

# IRE Transactions



## on ANTENNAS and PROPAGATION

Volume AP-6

JANUARY, 1958

Number 1

*Published Quarterly*

### TABLE OF CONTENTS

News and Views.....	1
---------------------	---

### CONTRIBUTIONS

An Analytical Study of Scattering by Thin Dielectric Rings.....	Lloyd L. Philipson	3
Theoretical Investigation of the Radiation Characteristics of a Quasi-Flush-Mounted Cardioid-Pattern Antenna.....	Howard E. Shanks	8
On the Propagation of Surface Waves Over an Infinite Grounded Ferrite Slab.....	Robert L. Pease	13
Polarization Fading Over an Oblique Incidence Path.....	D. A. Hedlund and L. C. Edwards	21
A Two-Dimensional Slotted Array.....	G. C. McCormick	26
Shunt and Notch-Fed HF Aircraft Antennas.....	Robert L. Tanner	35
On the Fresnel Approximation.....	R. B. Barrar and C. H. Wilcox	43
The Approximate Parameters of Slot Lines and Their Complement.....	G. H. Owyang and T. T. Wu	49
Propagation of Electromagnetic Pulses Around the Earth.....	B. R. Levy and J. B. Keller	56
Scattering of Electromagnetic Waves in Beyond-the-Horizon Radio Transmission.....	David I. Paul	61
Radio Echoes from Auroral Ionization Detected at Relatively Low Geomagnetic Latitudes.....	R. L. Leadabrand and A. M. Peterson	65
The Geometry of Auroral Communications.....	R. L. Leadabrand and I. Yabroff	80
A Statistical Model for Forward Scattering of Waves Off a Rough Surface.....	L. M. Spetner	88
A Method for Evaluating Antennas.....	Judd Blass	95
Wide-Angle Scanning with Microwave Double-Layer Pillboxes.....	Walter Rotman	96
Surface-Wave Beacon Antennas.....	Robert E. Plummer	105
Mechanical and Electrical Tolerances for Two-Dimensional Scanning Antenna Arrays.....	Robert S. Elliott	114
Fundamental Relations in the Design of a VLF Transmitting Antenna.....	Harold A. Wheeler	120
Fundamental Limitations of a Small VLF Antenna for Submarines.....	Harold A. Wheeler	123
The Prolate Spheroidal Antenna: Current and Impedance.....	C. P. Wells	125
An Application of Parageometrical Optics to the Design of a Microwave Mirror.....	L. Ronchi and G. Toraldo di Francia	129
End-Fire Echo Area of Long, Thin Bodies.....	Leon Peters, Jr.	133
Back-Scattering Cross Section of a Center-Loaded Cylindrical Antenna.....	Yueh-Ying Hu	140
Electromagnetic Diffraction by Dielectric Strips.....	David C. Stickler	148

### COMMUNICATION

A Line Source with Variable Polarization.....	J. N. Hines and J. Upson	152
Contributors.....		154

PUBLISHED BY THE  
Professional Group on Antennas and Propagation



### Administrative Committee

J. I. Bohnert, *Chairman*

R. L. Mattingly, *Vice-Chairman*

H. G. Booker

Arthur Dorne

J. W. Findlay

F. T. Haddock, Jr.

J. W. Herbstreit

D. D. King

R. K. Moore

W. H. Radford

J. B. Smyth

O. G. Villard, Jr.

### Ex Officio Members

P. S. Carter

D. C. Ports

A. H. Waynick

### Honorary Member

L. C. Van Atta

---

IRE TRANSACTIONS® PGAP IS A QUARTERLY PUBLICATION  
DEVOTED TO EXPERIMENTAL AND THEORETICAL PAPERS ON  
ANTENNAS AND WIRELESS PROPAGATION OF ELECTROMAGNETIC WAVES

---

**MANUSCRIPTS** should be submitted to John B. Smyth, Editor, Smyth Research Associates, 3930 4th Avenue, San Diego 3, Calif. Manuscripts should be original typewritten copy, double spaced, plus one carbon copy. References should appear as footnotes and include author's name, title, journal, volume, initial and final page numbers, and date. Each paper must have a summary of not more than 200 words. News items concerning PGAP members and group activities should be sent to the News Editor, Mr. Arthur Dorne, Dorne and Margolin, Inc., 30 Sylvester Street, Westbury, L.I., N.Y.

**ILLUSTRATIONS** should be submitted as follows: All line drawings (graphs, charts, block diagrams, cutaways, etc.) should be inked uniformly and ready for reproduction. If commercially printed grids are used in graph drawings, author should be sure printer's ink is of a color that will reproduce. All half-tone illustrations (photographs, wash, airbrush, or pencil renderings, etc.) should be clean and ready to reproduce. Photographs should be glossy prints. Call-outs or labels should be marked on a registered tissue overlay, not on the illustration itself. No illustration should be larger than 8 x 10 inches.

---

*Copies can be purchased from*  
**THE INSTITUTE OF RADIO ENGINEERS**  
**1 East 79 St., New York 21, N.Y.**

**PRICE PER COPY:** members of the Professional Group on Antennas and Propagation, \$3.85; members of the IRE, \$5.80; nonmembers, \$11.55.

**ANNUAL SUBSCRIPTION PRICE:** PGAP members, included in PGAP fee of \$4.00; IRE members, \$8.50; Colleges and public libraries, \$10.00; nonmembers, \$17.00.

IRE TRANSACTIONS ON ANTENNAS AND PROPAGATION  
Copyright © 1958, by The Institute of Radio Engineers, Inc.

Entered as second-class matter, at the post office at Menasha, Wisconsin, under the act of August 24, 1912. Acceptance for mailing at a special rate of postage is provided for in the act of February 28, 1925, embodied in Paragraph 4, Section 412, P. L. & R., authorized October 26, 1927.



# news and views

## ADMINISTRATIVE NEWS

Last year, when the IRE Executive Committee decided to permit advertising in the various TRANSACTIONS, it set the TRANSACTIONS rate at twice that of PROCEEDINGS. The reason for this was to ensure that advertisers did not transfer en masse from the PROCEEDINGS to the TRANSACTIONS. Of course, if this were to happen, the effect would be disruptive to the procedures and customs of the entire organization.

Recently, IRE decided to increase the rate for PROCEEDINGS advertising by 25 per cent (in two steps) while maintaining the two-to-one ratio of the TRANSACTIONS rate.

The PGAP Administrative Committee worked most diligently to persuade the IRE Executive Committee to waive the two-to-one requirement (at least temporarily) in order to permit the rate for TRANSACTIONS to stay unchanged. It was PGAP's feeling that an increase in the already high rates of TRANSACTIONS would make the sale of advertising so much more difficult that PGAP's future income was likely to be reduced drastically. They believed that the original purpose of protecting the PROCEEDINGS against losing its advertising would be as fully accomplished with a 1.8 rate as with the original 2.0-to-one rate.

PGAP's efforts were unsuccessful. The IRE Executive Committee denied the request at its meeting of December 11, 1957.

The following letter explains its position.

DR. J. I. BOHNERT  
Chairman, PGAP Administrative Committee

Your letter of December 5, 1957, with reference to TRANSACTIONS advertising rates, was thoroughly discussed by the IRE Executive Committee at the December meeting. This followed the discussion, at an earlier meeting, of the policy in general, and the PGAP situation in particular, so that you may be assured that all considerations have been taken into account by the Executive Committee. It was the final decision of the Executive Committee that the present policy on TRANSACTIONS advertising rates should not be changed.

The Executive Committee also reviewed the present financial situation of the PGAP, as well as a conservative projection for the next few years. The financial situation for 1958 is assured, and the data submitted indicated no need for reduction in pages published in 1959, but even suggested the possibility of switching funds to increase the number of pages.

I wish to emphasize the strong feeling of the Executive Committee, that no group should be forced by inadequate financing to forego the publication of important and valuable material. If such a situation should arise, we wish to be informed promptly, and shall give consideration to the merits of the case.

Very truly yours,  
JOHN T. HENDERSON,  
President

Quite obviously, the views expressed by Dr. Henderson are at variance with those of the PGAP Administrative Committee. Although PGAP's financial position has improved appreciably during the past six months, its Administrative Committee feels that complete recovery has not been accomplished. It feels that it will be only after a means has been found to increase its income.

## CHAPTER NEWS

### Albuquerque

On November 20 a joint meeting with the PGMTT was held at the University of New Mexico. B. J. Bittner of Gulton Industries spoke on "A Wide-Band Wide Scanning Angle, Microwave Antenna."

### Akron

The election of officers has been announced. They are G. H. Welch, *Chairman*; H. F. Mathis, *Vice-Chairman*, and J. R. Shoemaker, *Secretary*, all of whom may be addressed at the Goodyear Aircraft Corporation.

### Chicago

A meeting was held on December 13, at which Edward F. Harris, President of the Mark Products Company, talked on "Continuously-Loaded Helical Whip Antennas."



### Denver-Boulder

A technical meeting was held on December 11 in a lecture room at the Boulder Laboratories of the National Bureau of Standards. The subject discussed was "Sputnik—A Report on NBS Observations of Satellite Radio Signals."

Three speakers presented the several phases and aspects of the observations carried out by NBS on the radio emission by the two Russian satellites. J. W. Herbstreit described the principles of launching the satellite and measurement of phase of the received signal. R. S. Lawrence disclosed the results of measurements using an interferometer technique. R. M. Gallet related the results of frequency measurements and the determinations of the orbit using the Doppler frequency shift technique.

### Long Island

A move is afoot to organize a chapter with the intention of operating it jointly with the local PGMTT Chapter. To stimulate this activity, the PGMTT is devoting its April 8 and May 22 meetings to antennas. P. S. Carter will talk at the first meeting about his experiences as witness to and key participant in early antenna work on Long Island. Much of the important pioneering work in our field was conducted there.

### Los Angeles

The following were elected to serve for 1957-1958:

Robert J. Stegen, Canoga Corporation, *Chairman*; Thomas Kinaga, Hughes Aircraft Company, *Vice-Chairman*, and Dean B. Anderson, Autonetics Division of North American Aviation, *Secretary-Treasurer*.

The first meeting was September 12. Kenneth C. Kelly of Hughes spoke on "Recent Annular Slot Array Experiments," and Joseph A. Barkson, also of Hughes, presented a talk on "Coupling of Rectangular Waveguides."

Dr. John Smyth of Smyth Research Associates was the speaker on November 14. His topic was "Radio Wave Transmission by Way of the Troposphere."

### Washington, D. C.

A meeting was held on December 2. Roger W. Clapp spoke on "Scanning Array Antennas and Their Application to Radio Astronomy." Mr. Clapp is associated with the Hughes Aircraft Company, where he is now Associate Head of the Antenna Department. There were 125 in attendance and the meeting was co-sponsored by the

Washington Section of the IRE and the Washington Chapter of PGMTT.

The next meetings will be held in the PEPCO Auditorium. On January 27, J. H. Chisholm of the Lincoln Laboratory spoke on "Recent Research in Extended Range Ionospheric and Tropospheric Propagation." On February 3, Allen M. Peterson, Stanford Research Institute, discussed "Meteor Burst Communications." This was a Washington Section meeting, sponsored jointly by PGAP and PGCS.

### PERSONNEL NOTES

Dr. John I. Bohnert, PGAP Chairman, has been named Superintendent of the Electronics Division at the Naval Research Laboratory. He received the B.S. degree in mathematics from Carnegie Institute of Technology in 1932, and the M.A. and Ph.D. degrees in mathematics from the University of Pittsburgh in 1935 and 1940. From 1942 to 1945, he was a staff member of the Antenna Group at the M.I.T. Radiation Laboratory. He joined the Naval Research Laboratory in 1945. Dr. Bohnert is a senior member of the IRE and had an important part in organizing PGAP.

Norman Ritchey, formerly head of the Tube Application Engineering Section at Sylvania, Kew Gardens, N. Y., has joined Dorne and Margolin, Inc., Westbury, N. Y., as Senior Project Engineer; he will work on systems development.

### INDUSTRIAL NOTE

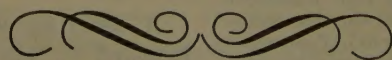
Gulton Industries has opened a new laboratory in Albuquerque, N. M., which boasts a four-ton rotator.

### URSI

On December 5, the unprecedented task of bringing into agreement the national primary standards of microwave power of two countries was carried out by Glenn F. Engen of the radio standards division of the National Bureau of Standards, and Dr. Denji Ishikawa, Japanese scientist. Dr. Ishikawa hand-carried Japan's standard for power measurements to the Boulder laboratories. The comparisons were made at 9375 megacycles and 10 milliwatts. As soon as possible, additional comparisons will be made at many other frequencies and power levels.

This meeting between the Japanese and U. S. scientists is a result of the efforts of the International Scientific Radio Union which held its 12th triannual assembly in Boulder during the summer of 1957.

*Note:* A detailed report of this Assembly is being published in the PROCEEDINGS.





# contributions

## An Analytical Study of Scattering by Thin Dielectric Rings\*

LLOYD L. PHILIPSON†

**Summary**—An analysis of the scattering effect of a thin dielectric ring on an electromagnetic field is developed under two assumptions: the incident field is the free space field of the source, and the scattered field tends asymptotically to zero as the radial thickness of the ring approaches zero. When an integral equation of Barrar and Dolph,<sup>1</sup> derived directly from Maxwell's equations, is employed, a formal expansion of the field in powers of the thickness is obtained, and then it is proved that the *linear approximation* obtained from it is indeed asymptotically equal to the total field. The sufficiency of this approximation is justified by experimental evidence. The far-zone pattern function of the ring is next obtained, and the resulting formulas are applied to the situation where the incident field is generated by a dipole antenna coaxial with the ring for which experimental comparisons are possible.

### I. INTRODUCTION

**A** THEORY for the scattering effect of a thin dielectric ring on an electromagnetic field is established under the following two assumptions: 1) the field incident on the ring is given by the free space field of the source, 2) the total field, incident plus scattered, tends asymptotically to the incident field as the radial thickness of the ring approaches zero.

Under assumption 1), Barrar and Dolph<sup>1</sup> have derived from Maxwell's equations a pair of integral equations giving the electric and magnetic vectors of the total field generated by a system of radiating sources

and a scattering obstacle embedded in an isotropic homogeneous nonconducting medium ("free space"). Their equation for the magnetic vector will be employed, but this vector will be related to the electric vector directly by Maxwell's equations in the discussion in Section II. The basic technique leading from the integral equation to a formal expansion for the vectors of the total field in powers of the radial thickness of the ring is essentially due to J. B. Keller.<sup>2</sup>

It is observed from actual measurements<sup>3</sup> that the scattered field is, at least in the far zone, very nearly a linear function of the volume of small diffracting obstacles introduced into a radiation field. For thin rings of constant inner radius and height, in particular, the degree of scattering appears to be nearly proportional to thickness. Thus, in Section III only the relatively simple terms through the first power of the thickness in the expansion obtained are considered in detail. Furthermore, it is shown by an elementary argument that, under assumption 2), this linear approximation is indeed valid asymptotically as the thickness of the ring tends to zero. The asymptotic relation is uniform for all points bounded away from the ring.

In Section IV, far-zone expressions for the components of the total field and power pattern function arising from the source-ring system are established using

\* Manuscript received by the PGAP, June 28, 1956; revised manuscript received February 24, 1957. Extracted from Res. Labs., Hughes Aircraft Co., Tech. Memo. No. 416; January, 1956.

† Litton Industries, Beverly Hills, Calif.

<sup>1</sup> R. B. Barrar and C. L. Dolph, "On a three-dimensional transmission problem of electromagnetic theory," *J. Rational Mechanics and Analysis*, vol. 3, pp. 725-743; November, 1954.

<sup>2</sup> J. B. Keller, "Reflection and Transmission of Electromagnetic Waves by Thin Curved Shells," N. Y. U. Washington Square College, Math. Res. Group, Rep. No. 172-5; February, 1948.

<sup>3</sup> V. Galindo and D. E. Adler, "Experimental Studies on Dependence of Boresight Error on Various Obstacle Parameters," Res. Labs., Hughes Aircraft Co., Tech. Memo. No. 431; January, 1956.



this linear evaluation. Finally, in Section V these expressions are applied to the special case, permitting an actual laboratory approximation, in which the source consists of a half-wave dipole coaxial with the ring.

## II. THE FORMAL EXPANSION

Let  $\mathbf{E}_i$ ,  $\mathbf{H}_i$  be the electric and magnetic vectors of a given (incident) field in free space. Suppose a thin cylindrical ring with constitutive parameters  $\epsilon, \mu, \sigma=0$  is placed in the field. As indicated in the figures, construct a cylindrical coordinate system  $(r, \theta, z)$  about the point 0, so that the ring is described by  $a \leq r \leq a+h$ ,  $0 \leq \theta \leq 2\pi$ ,  $-l \leq z \leq l$ .

Let  $S$  be the inner ring surface ( $r=a^+$ ,  $0 \leq \theta \leq 2\pi$ ,  $-l \leq z \leq l$ ), and  $V$  the ring volume (see Fig. 1). Define the coordinate  $\eta$  such that  $r=a+h\eta$ . Then the ring may be given by  $0 \leq \eta \leq 1$  and the above  $\theta, z$  ranges.

Let  $P=(r, \theta, z)$  denote an arbitrary field point,  $P_1=(r_1, \theta_1, z_1)=(a+h\eta, \theta_1, z_1)$ , an arbitrary point in  $V$ . Then, assuming that the interposition of the ring in the field does not affect the source distribution giving rise to it, as required by assumption 1) of the introduction, it can be shown [eq. (5.2) of Barrar and Dolph<sup>1</sup>] that at any point  $P$  inside or outside of  $V$  the resultant magnetic and electric vectors of the total field satisfy

$$\mathbf{H}(P) = \mathbf{H}_i(P) - \gamma \int_V \mathbf{F}(P, P_1) dV_1 \quad (1)$$

where

$$\gamma = \frac{k^2 - k_0^2}{4\pi i \omega \mu_0} \quad (2)$$

$$\mathbf{F}(P, P_1) = \nabla_1 \left( \frac{e^{ik_0 R}}{R} \right) \times \mathbf{E}(P_1) \quad (3)$$

with

$$\begin{aligned} k^2 &= \omega^2 \epsilon \mu_0 \\ k_0^2 &= \omega^2 \epsilon_0 \mu_0 \end{aligned} \quad (4)$$

and  $R=R(P, P_1)$  the distance between  $P$  and  $P_1$ :

$$R = \sqrt{r^2 + r_1^2 - 2rr_1 \cos(\theta - \theta_1) + (z - z_1)^2}. \quad (5)$$

In (1) it is assumed that  $\mu=\mu_0$  and that variation of the field vectors with time is given by the usual  $e^{-i\omega t}$  factor. The subscript 0 refers to the medium (free space) surrounding  $V$ . The subscript 1 refers to the point of integration  $P_1$ .

A further relation between  $\mathbf{E}$  and  $\mathbf{H}$  outside a neighborhood of the sources is Maxwell's equation,

$$\mathbf{E}(P) = \frac{i\omega\mu_0}{k^2} \nabla \times \mathbf{H}(P) \quad (6)$$

for  $P$  in  $V$ , and the same equation with  $k$  replaced by  $k_0$  for  $P$  outside  $V$ . For  $P$  on the interior of the boundary surface of  $V$ , (6) is interpreted as a limit over interior points of  $V$  and, for  $P$  on the exterior surface, as a limit over exterior points with  $k$  replaced by  $k_0$ .

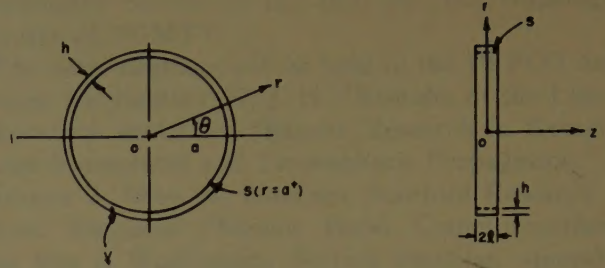


Fig. 1—Geometry for the thin cylindrical ring.

Formally, it can be written that

$$\begin{aligned} \mathbf{F}(P, P_1) &= \mathbf{F}(r, \theta, z; a + h\eta, \theta_1, z_1) \\ &= \sum_{m=0}^{\infty} \frac{(h\eta)^m}{m!} \left[ \frac{\partial^m}{\partial r_1^m} \mathbf{F} \right]_{r_1=a^+}. \end{aligned} \quad (7)$$

Furthermore, the element of ring volume can be expressed as

$$\begin{aligned} dV_1 &= r_1 dr_1 d\theta_1 dz_1 \\ &= (a + h\eta) h d\eta \frac{dS_1}{a} \end{aligned} \quad (8)$$

where  $dS_1$  is the element of area of the inner ring surface  $S(r=a^+)$ . Then (1) becomes, after substitution of (7) and (8) followed by an integration with respect to  $\eta$ ,

$$\begin{aligned} \mathbf{H}(P) &= \mathbf{H}_i(P) \\ &\quad - \frac{\gamma h}{a} \sum_{m=0}^{\infty} \left( \frac{a}{m+1} + \frac{h}{m+2} \right) \frac{h^m}{m!} \mathbf{G}_m(P) \end{aligned} \quad (9)$$

where

$$\mathbf{G}_m(P) = \int_S \left[ \frac{\partial^m \mathbf{F}}{\partial r_1^m} \right]_{r_1=a^+} dS_1. \quad (10)$$

In formally solving (9) by a power series in  $h$ , it can be written that

$$\mathbf{H}(P) = \mathbf{H}_i(P) + \sum_{n=1}^{\infty} h^n \mathbf{H}_n(P) \quad (11)$$

with  $\mathbf{H}_n$  to be determined. Note that the zero-order term is taken to be just the incident vector, following assumption 2) of the introduction. The analogous series for  $\mathbf{E}(P)$  is also assumed with the  $\mathbf{E}_n$  and  $\mathbf{H}_n$  related by Maxwell's (6). Upon substitution of (11) into (9) and equating like powers of  $h$ , the desired formula for  $\mathbf{H}_n$  is arrived at:

$$\begin{aligned} \mathbf{H}_{p+1}(P) &= \frac{\gamma}{a} \left\{ \sum_{m+n=p} \sum_{-p} \frac{a \mathbf{I}_{mn}(P)}{(m+1)!} + \sum_{m+n+1=p} \sum_{-p} \frac{\mathbf{I}_{mn}(P)}{(m+2)m!} \right\} \end{aligned} \quad (12)$$

where

$$\mathbf{I}_{mn}(P) = - \int_S \left[ \frac{\partial^m}{\partial r_1^m} \left( \nabla_1 \left( \frac{e^{ik_0 R}}{R} \right) \times \mathbf{E}_n(P_1) \right) \right] dS_1. \quad (13)$$

It is seen that (12) is an iteration formula; to calculate  $\mathbf{H}_n$ , the vectors  $\mathbf{H}_i, \mathbf{H}_1, \dots, \mathbf{H}_{n-1}$  are required.



Note in particular, however, that since  $I_{00}$  in (13) requires only  $E_i$  on  $S$ , the linear approximation for  $H$ ,

$$H(P) = H_i(P) + \gamma h I_{00}(P) \tag{14}$$

is simple to evaluate directly. Calculations of the higher order approximations are rather more complex and, with the exception of the second, probably impractical. For the second, an examination of (12) with  $p=1$  shows that  $E_i$  and its  $r$  derivative and  $E_1$  but not its derivative are required to be known on  $S$ , and these vectors are obtainable without undue effort from the initial data and the results of the first approximation.

The vector integration in (13) is conveniently carried out if the fixed cylindrical unit vectors  $r, \theta, z$  at the point of observation  $P$  are introduced. They are related to the unit vectors at the point of integration  $P_1$  by

$$\begin{aligned} r_1 &= -\sin(\theta - \theta_1)\theta + \cos(\theta - \theta_1)r \\ \theta_1 &= \cos(\theta - \theta_1)\theta + \sin(\theta - \theta_1)r \\ z_1 &= z. \end{aligned} \tag{15}$$

Now from the  $n$ th stage of the iteration  $E_n(P_1)$  has the form<sup>4</sup>

$$E_n(P_1) = e_{n1}(P_1)r_1 + e_{n2}(P_1)\theta_1 + e_{n3}(P_1)z_1. \tag{16}$$

Also

$$\nabla_1 \left( \frac{e^{ik_0 R}}{R} \right) = g_1 r_1 + g_2 \theta_1 + g_3 z_1 \tag{17}$$

where

$$\begin{aligned} g_1 &= (r_1 - r \cos(\theta - \theta_1))\rho(R) \\ g_2 &= -r \sin(\theta - \theta_1)\rho(R) \\ g_3 &= -(z - z_1)\rho(R) \end{aligned} \tag{18}$$

with

$$\rho(R) = \left( ik_0 - \frac{1}{R} \right) \frac{e^{ik_0 R}}{R^2}. \tag{19}$$

Thus, when (15) is introduced, and  $dS_1$  is replaced by  $ad\theta_1 dz_1$ , (13) can be written

$$I_{mn} = I_{mn}^{(r)}r + I_{mn}^{(\theta)}\theta + I_{mn}^{(z)}z \tag{20}$$

where

$$\begin{aligned} I_{mn}^{(r)} &= -a \int_0^{2\pi} \int_{-l}^l [C_{n1}^{(m)} \cos(\theta - \theta_1) \\ &\quad + C_{n2}^{(m)} \sin(\theta - \theta_1)] dz_1 d\theta_1 \\ I_{mn}^{(\theta)} &= -a \int_0^{2\pi} \int_{-l}^l [-C_{n1}^{(m)} \sin(\theta - \theta_1) \\ &\quad + C_{n2}^{(m)} \cos(\theta - \theta_1)] dz_1 d\theta_1 \\ I_{mn}^{(z)} &= -a \int_0^{2\pi} \int_{-l}^l C_{n3}^{(m)} dz_1 d\theta_1 \end{aligned} \tag{21}$$

in which

<sup>4</sup>  $r_1, \theta_1, z_1$  denote the unit cylindrical coordinate vectors at  $P_1$ .

$$\begin{aligned} C_{n1}^{(m)} &= \frac{\partial^m}{\partial r_1^m} (g_2 e_{n3} - g_3 e_{n2}) \Big|_{r_1=a+} \\ C_{n2}^{(m)} &= \frac{\partial^m}{\partial r_1^m} (g_3 e_{n1} - g_1 e_{n2}) \Big|_{r_1=a+} \\ C_{n3}^{(m)} &= \frac{\partial^m}{\partial r_1^m} (g_1 e_{n2} - g_2 e_{n1}) \Big|_{r_1=a+} \end{aligned} \tag{22}$$

These formulas permit the calculation of  $H_{n+1}$  and  $E_{n+1}$  in the  $(n+1)$ th stage of the iteration.

III. ESTABLISHMENT OF THE ASYMPTOTIC VALIDITY OF THE FIRST ORDER APPROXIMATION

As discussed in the introduction, from this point only the terms through the first order in (11) will be considered; that is, writing  $\psi = e^{ik_0 R}/R$

$$H(P) \doteq H_i(P) + hH_1(P) \tag{23}$$

with

$$H_1(P) = -\gamma \int_S [\nabla_1 \psi \times E_i(P_1)] dS_1. \tag{24}$$

When assumption 2) of the introduction is employed, it can be proved that (23), obtained formally, does indeed hold for sufficiently small  $h$ .

For brevity the explicit dependence of  $V$  on  $h$  in the following will be indicated by  $V_h$ .

Theorem: Define  $H_1(P)$  by (24). Assume that<sup>5</sup>

$$E(P) = E_i(P) + O(h) \tag{25}$$

is valid for  $h \rightarrow 0$ , uniformly for  $P$  in  $V_{h_0}$ , for some  $h_0 > 0$ .

Then if  $H$  is the solution of (1) related to  $E$  through Maxwell's equations,

$$H(P) = H_i(P) + hH_1(P) + O(h^2) \tag{26}$$

is valid for  $h \rightarrow 0$ , uniformly for  $P$  bounded away from  $S$ .

For the proof of the theorem, it should be noted that the restriction on  $P$  in (26) permits finding an  $h^* > 0$  such that for all  $h < h^*$ ,  $P$  is exterior to  $V_h$ .

The fundamental assumption (25) [2] in the introduction] appears to be difficult to justify rigorously in general, but it is known to be valid in certain situations at least. The scattered wave arising from a plane wave incident on an infinite plane dielectric slab, for instance, tends continuously to the incident wave as the thickness of the slab approaches zero.

The proof of the theorem is elementary. Eq. (26) evidently results by virtue of (1), if it is shown that

$$-\gamma \int_V F dV_1 - hH_1 = O(h^2)$$

or, employing (24) and (8), that

<sup>5</sup> Eq. (25) signifies that  $h^{-1} |E(P) - E_i(P)|$  is a bounded function of  $h$  and  $P$  for  $h < h_0$  and  $P$  in  $V_{h_0}$ .



$$-\gamma h \int_S \left\{ \int_0^1 \left( \frac{a + h\eta}{a} \right) F d\eta - [\nabla_1 \psi \times \mathbf{E}_i] \right\} dS_1 = 0(h^2).$$

Since with respect to  $h$   $S$  is a fixed domain of integration, this statement holds true if

$$\int_0^1 \left( \frac{a + h\eta}{a} \right) F d\eta - [\nabla_1 \psi \times \mathbf{E}_i(P_1)]_{r_1=a^+} = 0(h) \quad (27)$$

uniformly in  $\theta_1, z_1$  on  $S$  and in the coordinates of  $P$ .

Now the assumption (25) implies that for  $P_1$  in  $V_h$  with  $h < h_0$ ,

$$F(P, P_1) = \nabla_1(P, P_1) \times \mathbf{E}_i(P_1) + |\nabla_1 \psi(P, P_1)| 0(h). \quad (28)$$

Since  $\mathbf{E}_i(P_1)$  and  $\nabla_1 \psi(P, P_1)$  are continuous at all points in  $V_h$ , provided  $h < h^*$  (so that  $P$  is exterior to  $V_h$ ; see the remark following the statement of the theorem), it is certainly true that

$$\begin{aligned} \nabla_1 \psi(P, P_1) \times \mathbf{E}_i(P_1) \\ = [\nabla_1 \psi(P, P_1) \times \mathbf{E}_i(P_1)]_{r_1=a} + 0(|r_1 - a|) \end{aligned}$$

for  $|r_1 - a|$  sufficiently small. But  $|r_1 - a| = h|\eta|$ , so in fact for  $h < h^*$

$$\begin{aligned} \nabla_1 \psi(P, P_1) \times \mathbf{E}_i(P_1) \\ = [\nabla_1 \psi(P, P_1) \times \mathbf{E}_i(P_1)]_{r_1=a} + 0(h) \end{aligned} \quad (29)$$

uniformly in  $0 \leq \eta \leq 1, \theta_1, z_1$  on  $S$ , and in the  $P$  variables.

Substitution of (28) and (29) into the left side of (27) now shows that it is indeed of first order in  $h$ , and the theorem is proved.

#### IV. FAR-ZONE EVALUATIONS

General formulas can now be obtained for the linear approximation to the total magnetic vector and the power pattern in the far zone. For the calculation of the far-zone expressions it is convenient to express the field point  $P$  in spherical coordinates  $\sigma, \theta, \phi$  about the center of the ring which are related to the cylindrical coordinates so far employed by

$$r/\sigma = \sin \phi, \quad z/\sigma = \cos \phi, \quad \theta = \theta. \quad (30)$$

The far-zone formulas are then given by asymptotic evaluations for  $\sigma \rightarrow \infty$ .

For the distance  $R$ ,

$$R = \sigma - f + 0(\sigma^{-1}) \quad (31)$$

where

$$\begin{aligned} f &= f(r_1, \theta_1, z_1; \theta, \phi) \\ &= r_1 \sin \phi \cos(\theta - \theta_1) + z_1 \cos \phi. \end{aligned} \quad (32)$$

From (19) then

$$\rho(R) = \frac{ik_0 e^{ik_0(\sigma-f)}}{\sigma^2} + 0(\sigma^{-3}) \quad (33)$$

so the  $g_k$  in (18) and the  $C_{0k}$  in (22) can be evaluated. Writing

$$f_a = f(a, \theta_1, z_1; \theta, \phi) = a \sin \phi \cos(\theta - \theta_1) + z_1 \cos \phi \quad (34)$$

(21) then becomes

$$\begin{aligned} I_{00}^{(r)} &= \frac{ik_0 e^{ik_0 \sigma}}{\sigma} a \cos \phi \int_0^{2\pi} \int_{-l}^l [\sin(\theta - \theta_1) e_{01} \\ &\quad - \cos(\theta - \theta_1) e_{02}] e^{-ik_0 f_a} dz_1 d\theta_1 + 0(\sigma^{-2}) \end{aligned}$$

$$\begin{aligned} I_{00}^{(\theta)} &= \frac{ik_0 e^{ik_0 \sigma}}{\sigma} a \int_0^{2\pi} \int_{-l}^l [-\sin \phi e_{03} + \cos \phi \\ &\quad \cdot [\sin(\theta - \theta_1) e_{02} + \cos(\theta - \theta_1) e_{01}]] e^{-ik_0 f_a} dz_1 d\theta_1 \\ &\quad + 0(\sigma^{-2}) \end{aligned}$$

$$I_{00}^{(z)} = -\tan \phi I_{00}^{(r)} + 0(\sigma^{-2}). \quad (35)$$

Substitution into (26) of the evaluations (35), together with the far-zone expressions for the given components of the incident magnetic vector  $\mathbf{H}_i$ , results in the desired far-zone evaluation of the total magnetic vector  $\mathbf{H}$  to  $0(h^2)$ . It can be assumed, in making these substitutions, that  $\mathbf{H}_i$  can be written in the form

$$\mathbf{H}_i(P) = \frac{e^{ik_0 \sigma}}{\sigma} \mathbf{h}_i(P) \quad (36)$$

where  $|\mathbf{h}_i(P)|$  is bounded as  $\sigma \rightarrow \infty$ . Then  $\mathbf{H}$  appears also as a bounded function multiplied by  $e^{ik_0 \sigma}/\sigma$ .

It is to be noted from (35) that the far-zone relation  $H^{(\sigma)} = 0$  to  $0(\sigma^{-1})$ , required for any physical magnetic vector (see the discussion following), does indeed hold for  $\mathbf{H}_i$ , and hence for  $\mathbf{H}$  as given by (14).

In calculating the far-zone power pattern of  $\mathbf{H}$ , the magnitude for  $\sigma \rightarrow \infty$  of the time averaged Poynting's vector  $\mathbf{S}$  must be considered:

$$\mathbf{S} = \frac{1}{2} R \{ \mathbf{E} \times \mathbf{H}^* \}. \quad (37)$$

( $R$  indicates "real part of.") Now it can be shown<sup>6</sup> that the electric and magnetic vectors in free space always satisfy in the far zone<sup>7</sup>

$$\mathbf{E} = \sqrt{\frac{\mu_0}{\epsilon_0}} (\mathbf{H} \times \boldsymbol{\sigma}) + o(\sigma^{-1}). \quad (38)$$

Thus,

$$|\mathbf{S}| = \frac{1}{2} \sqrt{\frac{\mu_0}{\epsilon_0}} |\mathbf{H}|^2 + o(\sigma^{-2}) \quad (39)$$

or, in terms of cylindrical components,

$$\begin{aligned} |\mathbf{S}| &= \frac{1}{2} \sqrt{\frac{\mu_0}{\epsilon_0}} [ |H^{(r)}|^2 + |H^{(\theta)}|^2 + |H^{(z)}|^2 ] \\ &\quad + o(\sigma^{-2}). \end{aligned} \quad (40)$$

The far-zone power pattern function  $\mathcal{P}$  is defined as proportional to  $\lim_{\sigma \rightarrow \infty} \sigma^2 |\mathbf{S}|$ , so it can be written that

$$\begin{aligned} \mathcal{P} &= \lim_{\sigma \rightarrow \infty} K [ |\sigma e^{-ik_0 \sigma} H^{(r)}|^2 + |\sigma e^{-ik_0 \sigma} H^{(\theta)}|^2 \\ &\quad + |\sigma e^{-ik_0 \sigma} H^{(z)}|^2 ] + o(1) \end{aligned} \quad (41)$$

<sup>6</sup> S. Silver, "Microwave Antenna Theory and Design," M.I.T. Rad. Lab. Ser., No. 12, McGraw-Hill Book Co., Inc., New York, pp. 84-85, 1949.

<sup>7</sup> Eq. (38) signifies that  $\sigma^2 |\mathbf{E} - \sqrt{\mu_0/\epsilon_0} (\mathbf{H} \times \boldsymbol{\sigma})|$  tends to zero as  $\sigma \rightarrow \infty$ , uniformly in  $\theta$  and  $\phi$ .



or, from (26), (35), and (36),

$$\mathcal{P} = K[|p^{(r)}|^2 + |p^{(\theta)}|^2 + |p^{(z)}|^2] + o(1) \quad (42)$$

where  $K$  is a constant of proportionality of no interest, and to  $0(h^2)$ ,

$$\begin{aligned} p^{(r)} &= h_i^{(r)} + \gamma h i k_0 a \cos \phi \int_0^{2\pi} \int_{-l}^l [\sin(\theta - \theta_1) e_{01} \\ &\quad - \cos(\theta - \theta_1) e_{02}] e^{-ik_0 f a} dz_1 d\theta_1 \\ p^{(\theta)} &= h_i^{(\theta)} + \gamma h i k_0 a \int_0^{2\pi} \int_{-l}^l [-\sin \phi e_{03} + \cos \phi \\ &\quad \cdot [\sin(\theta - \theta_1) e_{02} + \cos(\theta - \theta_1) e_{01}]] e^{-ik_0 f a} dz_1 d\theta_1 \\ p^{(z)} &= -\tan \phi p^{(r)}. \end{aligned} \quad (43)$$

$h_i^{(r)}$  and  $h_i^{(\theta)}$  denote the  $r, \theta$  components of  $h_i$ .

After calculation of the terms in (42), it is found that

$$\mathcal{P} = [\mathcal{P}_i + h\mathcal{P}_p + 0(h^2)] + o(1) \quad (44)$$

where  $\mathcal{P}_i$  is the far-zone pattern function of the incident field alone and  $\mathcal{P}_p$  is the "first order perturbation" pattern function giving the effect on the pattern of the ring to  $0(h^2)$ . The component pattern functions in (44) explicitly are, recalling (2) and (4),

$$\begin{aligned} \mathcal{P}_i &= K\{[h_{iR}^{(r)}]^2 + [h_{iI}^{(r)}]^2 + [h_{iR}^{(\theta)}]^2 + [h_{iI}^{(\theta)}]^2 \\ &\quad + [h_{iR}^{(z)}]^2 + [h_{iI}^{(z)}]^2\} \end{aligned} \quad (45)$$

$$\begin{aligned} \mathcal{P}_p &= K \frac{\omega(\epsilon - \epsilon_0)}{2\pi} k_0 a \{ \cos \phi [h_{iR}^{(r)} J_R^{(r)} + h_{iI}^{(r)} J_I^{(r)}] \\ &\quad + [h_{iR}^{(\theta)} J_R^{(\theta)} + h_{iI}^{(\theta)} J_I^{(\theta)}] \\ &\quad + \sin \phi [h_{iR}^{(z)} J_R^{(z)} + h_{iI}^{(z)} J_I^{(z)}] \} \end{aligned} \quad (46)$$

where subscripts  $R$  and  $I$  denote real and imaginary parts, respectively, and

$$\begin{aligned} J_R^{(r)} + iJ_I^{(r)} &= \int_0^{2\pi} \int_{-l}^l [\sin(\theta - \theta_1) e_{01} \\ &\quad - \cos(\theta - \theta_1) e_{02}] e^{-ik_0 f a} dz_1 d\theta_1 \\ J_R^{(\theta)} + iJ_I^{(\theta)} &= \int_0^{2\pi} \int_{-l}^l [-\sin \phi e_{03} + \cos \phi \\ &\quad \cdot (\sin(\theta - \theta_1) e_{02} + \cos(\theta - \theta_1) e_{01})] e^{-ik_0 f a} dz_1 d\theta_1 \\ J_R^{(z)} + iJ_I^{(z)} &= -[J_R^{(r)} + iJ_I^{(r)}]. \end{aligned} \quad (47)$$

## V. SPECIAL CASE OF A COAXIAL DIPOLE SOURCE

The previous discussion can be applied to a special case which will permit an experimental verification. As illustrated in Fig. 2, a half-wave dipole antenna, coaxial with the ring, on which a sinusoidal current distribution with a single maximum at the center and vanishing at the ends exists, is considered. It is assumed that the wavelength on the wire is the same as in free space. Then

$$L = \frac{\pi}{2k_0}. \quad (48)$$

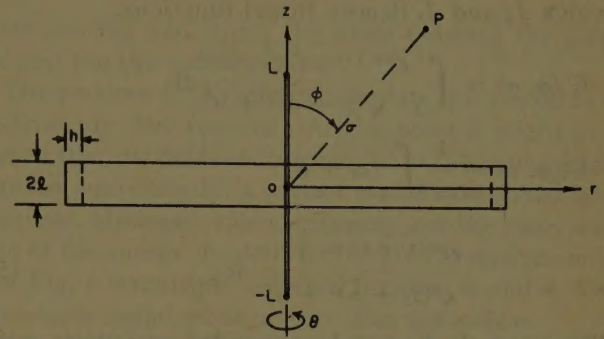


Fig. 2—Ring and coaxial half-wavelength dipole.

In Stratton,<sup>8</sup> it is shown that the nonzero cylindrical components of the free space field of the antenna are:

$$\begin{aligned} E_i^{(r)} &= -\frac{ik_0 I_0}{4\pi\epsilon_0\omega} \left\{ \left( \frac{z-L}{r} \right) \frac{e^{ik_0 r_2}}{r_2} + \left( \frac{z+L}{r} \right) \frac{e^{ik_0 r_1}}{r_1} \right\} \\ E_i^{(z)} &= \frac{ik_0 I_0}{4\pi\epsilon_0\omega} \left\{ \frac{e^{ik_0 r_2}}{r_2} + \frac{e^{ik_0 r_1}}{r_1} \right\} \\ H_i^{(\theta)} &= \frac{-iI_0}{4\pi r} \{ e^{ik_0 r_2} + e^{ik_0 r_1} \} \end{aligned} \quad (49)$$

where

$$\begin{aligned} r_1 &= \sqrt{r^2 + (z+L)^2} \\ r_2 &= \sqrt{r^2 + (z-L)^2} \end{aligned} \quad (50)$$

are the distances of the observation point from the ends of the wire at  $z = \mp L$ , respectively.

The evaluation of the  $\theta$  component of the incident magnetic vector in the far zone is immediately obtained from (49) and (50), using (30):

$$H_i^{(\theta)} = \frac{e^{ik_0 \sigma}}{\sigma} h_i^{(\theta)} \quad (51)$$

where

$$h_i^{(\theta)} = \frac{-iI_0}{2\pi} \frac{\cos(\pi/2 \cos \phi)}{\sin \phi} + 0(\sigma^{-1}). \quad (52)$$

By (45) then, the incident power pattern function is

$$\mathcal{P}_i = K \left( \frac{I_0}{2\pi} \right)^2 \frac{\cos^2(\pi/2 \cos \phi)}{\sin^2 \phi}. \quad (53)$$

For the calculation of the perturbation pattern  $\mathcal{P}_p$ , the  $J$  integrals in (47) must be evaluated. From (49) the functions  $e_{0k}$  are obtained [see (16)]. Upon their insertion into (47) and consideration of only  $\theta=0$ ,  $0 \leq \phi \leq \pi/2$  for the observation point as permitted by symmetry, it follows that

$$\begin{aligned} J^{(r)} &= J^{(z)} = 0 \\ J^{(\theta)} &= \frac{-ik_0 I_0}{2\epsilon_0\omega} \{ \sin \phi J_0(k_0 a \sin \phi) (K_1(\phi, L) + K_1(\phi, -L)) \\ &\quad - i \cos \phi J_1(k_0 a \sin \phi) (K_2(\phi, L) + K_2(\phi, -L)) \} \end{aligned} \quad (54)$$

<sup>8</sup> J. A. Stratton, "Electromagnetic Theory," McGraw-Hill Book Co., Inc., New York, pp. 454-457; 1941.



in which  $J_0$  and  $J_1$  denote Bessel functions,

$$K_1(\phi, \alpha) = \int_{-l}^l \frac{e^{ik_0(\sqrt{(z_1+\alpha)^2+a^2}-\cos\phi z_1)}}{\sqrt{(z_1+\alpha)^2+a^2}} dz_1$$

$$K_2(\phi, \alpha) = \frac{1}{a} \int_{-l}^l (z_1 + \alpha) \frac{e^{ik_0(\sqrt{(z_1+\alpha)^2+a^2}-\cos\phi z_1)}}{\sqrt{(z_1+\alpha)^2+a^2}} dz_1. \quad (55)$$

The integrals  $K_i$  can be expanded as infinite series involving Bessel functions or evaluated numerically without difficulty. Employing (46) then permits the calculation of the approximate power pattern (44). When this function is compared with the corresponding measured pattern of an actual half-wave antenna and ring system, an indication of the applicability of the general theory should result.

A number of such comparisons have been carried out. The accompanying graph (Fig. 3) shows in  $30^\circ \leq \phi \leq 90^\circ$  excellent agreement of the theoretical with the measured power pattern for the following set of parameter values:

$$\begin{aligned} \epsilon/\epsilon_0 &= 6.3 \\ a &= 2.32 \lambda \\ l &= 0.195 \lambda \\ h &= 0.043 \lambda. \end{aligned}$$

The agreement in this case was the best obtained and, considering that the measurements were made fairly hastily since qualitative verification only was sought, perhaps fortuitous. However, in all other cases investigated, qualitative agreement was good to excellent and quantitative agreement fair to good in the range  $30^\circ \leq \phi \leq 90^\circ$  and for  $h$  less than about  $.04\lambda$ . In the low-power range  $0 \leq \phi \leq 30^\circ$  the measurements were not accurate and agreement was in general only fair.

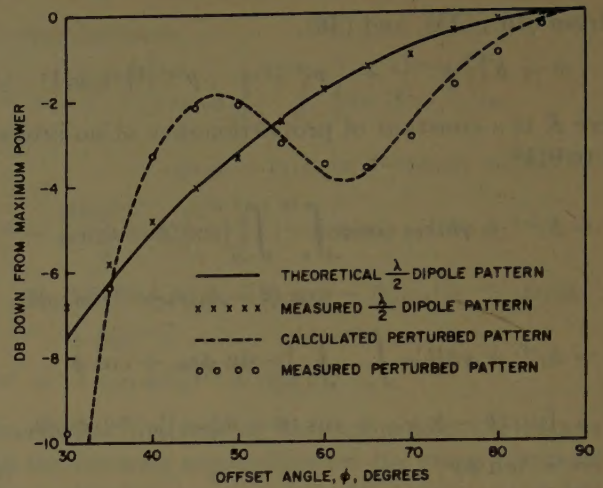


Fig. 3—Calculated and measured ring patterns with dipole source.

## VI. CONCLUSION

As with any asymptotic formulation, it must be understood that a given accuracy in the description of the physical situation considered in this paper will be assured only if the ring thickness  $h$  is taken sufficiently small, an unavoidably vague prescription. However, on the basis of comparisons with experiment, typified by the results of Fig. 3, the conclusion appears justified that the analysis presented is of merit in the description of the perturbative effect on an electromagnetic field by a dielectric ring whose thickness is of the order of a few hundredths of a wavelength.

## ACKNOWLEDGMENT

The author wishes to express his appreciation to his colleagues at Hughes Aircraft Company, D. E. Adler and G. Hanoaka, who carried out the measurements, and J. Pachares, who supervised the numerical calculations reported on in this paper.

# Theoretical Investigation of the Radiation Characteristics of a Quasi-Flush-Mounted Cardioid-Pattern Antenna\*

HOWARD E. SHANKS†

**Summary**—This paper determines the radiation characteristics of a semi-flush-mounted cardioid-pattern antenna on a theoretical basis. The antenna is similar to one described by Clapp in a report of

\* Manuscript received by the PGAP, June 29, 1956. Work was partially supported by USAF under Contract No. AF 19(604)-1317 with AF Cambridge Res. Center, Cambridge, Mass.

† Hughes Aircraft Company, Los Angeles, Calif.

the Electronic Research Laboratory of the University of California.

By judicious use of image theory in a radial transmission line formed by extending the antenna surfaces to infinity, the approximate fields of the principal polarization in the antenna are determined. If these fields are terminated in the aperture by a magnetic current sheet, the exterior radiation fields are obtained by integration over the aperture, according to the well-known equivalence theorem. Experimental patterns are given for comparison.



## INTRODUCTION

BECAUSE interest had developed (particularly from the U. S. Navy Bureau of Ships) in a quasi-flush-mounted communications antenna having a cardioid pattern in the azimuth plane, an analysis was made of a prototype of such an antenna based on an antenna developed in empirical fashion by F. D. Clapp of the University of California Electronic Research Laboratory, and for which radiation patterns and impedance characteristics are given in Clapp's report.<sup>1</sup>

It was felt that a theoretical analysis of a prototype antenna would be useful, not only as an analysis of this particular antenna, but also as an example of techniques which might prove valuable in similar applications. For instance, an explanation of the antenna's extreme sensitivity to a dielectric aperture cover (*i.e.*, radome) was particularly desired.

An illustration of the prototype cardioid-pattern antenna is given in Fig. 1, showing a low vertical silhouette enabling use where quasi-flush mounting is desirable.



Fig. 1—Prototype cardioid-pattern antenna.

## SUMMARY OF THEORETICAL PROCEDURE

Because of the unknown matching conditions across the antenna aperture (Fig. 1), an exact solution of the wave equation to fit all boundary conditions on the antenna plus the radiation condition at infinity is impractical. By the well-known equivalence principle, if the exact fields in the antenna could be determined, the exterior radiation pattern would be obtained by integration of this antenna field over any closed surface surrounding the source region. In this paper an approximation to the antenna field is achieved and the equivalence principle applied in the usual way.

If the top plate is extended to infinity in all directions, the fields between the parallel plates are readily found by the application of radial transmission line theory. In particular, if the back plate is also allowed to extend to infinity in the direction parallel to the ground plane, the primary feed may be imaged in this plate and the field to the right of the image plane becomes the superposition of two TEM radial modes diverging from different centers. However, this field is not due to the original radial line configuration, since it includes the contributions from the currents on the extended portions of the back plate. Nevertheless, it is assumed here that these contributions are negligible for small feed-to-back

plate spacing and, thus, the fields between the planes are just the two radial modes.

The portions of the infinite top plate extraneous to the antenna are then removed. At this point it might be assumed that the fields are unchanged in the antenna aperture, or equivalently, a perfect match postulated at the aperture. However, this is certainly not the case; a portion of the energy incident on the lateral sections *m* and *n* of Fig. 2 is multiply reflected between *m* and *n*. Thus, the simple radial mode picture does not suffice.

An analogy may be made between this problem and that of the cavity with finite impedance walls. The problem can be solved by assuming a perfect match and then making a first order correction for the reflection caused by the real part of the impedance mismatch between the aperture and external space. This is, in effect, a first order high frequency approximation to the correction factor but will be shown to have a substantial effect on the radiation pattern. In this manner, the sensitivity to a dielectric aperture cover, mentioned before, is adequately explained.

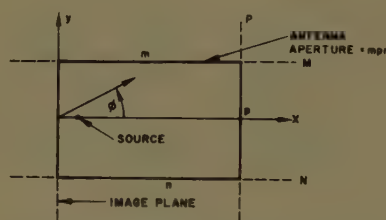


Fig. 2—Aperture of cardioid antenna.

If a magnetic current sheet terminates the antenna fields in the aperture, the radiation expressions are obtained by integration over the aperture. However, by analogy with radiation from horns or open-ended waveguide,<sup>2</sup> the aperture portions *m*, *n*, and *p* act as though they were in infinite vertical conducting planes *M*, *N*, and *P* and, thus, radiate only  $\pm 90^\circ$  to either side of their broadside directions. Due to symmetry of the antenna about the *x* axis, the pattern in the first quadrant ( $0 \leq \phi \leq 90^\circ$ ) is of interest and is the result of contributions from sections *m* and *p*.

The integrals over the aperture are the well-known integrated vector wave equations applied to an equivalent surface inclosing the source distribution; that is

$$\bar{E}_p = \frac{-j}{4\pi\omega\epsilon} \int_{\text{Aperture}} \{ -j\omega\epsilon \bar{J}_m \times \bar{\nabla} \} \frac{e^{-ikr}}{r} ds$$

and

$$\bar{H}_p = \frac{-j}{4\pi\omega\mu} \int_{\text{Aperture}} \{ (\bar{J}_m \cdot \bar{\nabla}) \bar{\nabla} + k^2 \bar{J}_m \} \frac{e^{-ikr}}{r} ds \quad (1)$$

where *r* is the distance between the variable source point

<sup>1</sup> F. D. Clapp, "Semi-Flush-Mounted Cardioid-Pattern Antenna for the 225-400 MC Band," Univ. of Cal., Div. of Elec. Eng., Berkeley, Calif., Rep. No. 109;

<sup>2</sup> S. Silver, "Microwave Antenna Theory and Design," M.I.T. Rad. Lab. Ser., McGraw-Hill Book Co., Inc., New York, N. Y., vol. 12, pp. 334-336; 1949.







These integrals are very difficult to solve in closed form; however, for specific values of the antenna parameters, they allow numerical solutions.

### Evaluation of the Factor ( $K$ )

The use of a correction factor ( $K$ ) to account for the internal reflections at the antenna aperture is qualitatively justified by the very presence of these reflections. Good quantitative evidence will subsequently be presented to show that values of ( $K$ ) can be found for which close agreement is obtained with experimental data. However, it is felt that an approximate analytic treatment is also in order.

It will be recalled that the integral expressions over the aperture take the following general form

$$E = Af(R) \int F(x, y, z) G(x, y, z; \theta, \phi) ds \quad (8)$$

where  $F(x, y, z)$  represents the source function over the aperture and  $G(x, y, z; \theta, \phi)$  represents a type of Green's function connecting the source point to the observation point. If  $F(x, y, z)$  is known accurately, the correct field will be obtained. As a first approximation to  $F$ , the radial mode analysis has been used; however, it was pointed out earlier that the internal reflections must be taken into account.<sup>2</sup> The latter may be formally achieved by the injection of a factor  $\tau(x, y, z)$  into the integrand of (8), giving

$$E = Af(R) \int \tau(x, y, z) F(x, y, z) G(x, y, z; \theta, \phi) ds \quad (9)$$

where  $\tau(x, y, z)$  is the dominant mode transmission coefficient associated with the reflections at various points in the aperture. If  $\tau$  is a slowly varying function over the aperture, it can be replaced by its mean value without incurring appreciable error. This condition is assumed in the following analysis.

Correction of the fields in the lateral sections of the aperture relative to the front section will be attempted as a means of establishing a theoretical value of  $K$ . Hence,  $\bar{\tau}$  becomes the average transmission coefficient of the internal waves incident at various points on the side portions of the aperture. We consider the waves impinging at points on the aperture to be cylindrical waves traveling in a radial transmission line incident on a transition to free space.

These concepts are illustrated pictorially in Fig. 4 showing the cylindrical wave impinging on the aperture at an angle of incidence ( $\beta$ ).

The wave impedance normal to the aperture is given by<sup>3</sup>

$$z_c = j\eta \frac{H_0^{(2)}(kr)}{H_1^{(2)}(kr)} \sec \beta. \quad (10)$$

However, the values of  $r$  encountered in this problem make  $z_c \approx \eta \sec \beta$ . Therefore, the reflection coefficient

$$\rho(x) = \frac{d - \sqrt{d^2 + x^2}}{d + \sqrt{d^2 + x^2}}. \quad (11)$$

The mean value of  $\rho$  over the lateral portion of the aperture is then

$$\bar{\rho} = \frac{1}{e} \int_0^e \frac{d - \sqrt{d^2 + x^2}}{d + \sqrt{d^2 + x^2}} dx \quad (12)$$

which represents, within the limit of our approximation, the proportion of the field incident on the lateral aperture which is reflected and assumed to be almost entirely reradiated by the front aperture. The proportion transmitted by each lateral aperture is then  $\bar{\tau} = 1 + \bar{\rho}$ . For the particular antenna under discussion, the ratio  $K$  of the lateral radiation to the front radiation becomes

$$K = \frac{1 + \bar{\rho}}{1 - 2\bar{\rho}} = 0.43.$$

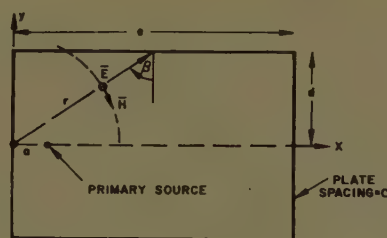


Fig. 4—Cylindrical wave incident on the aperture.

### EXPERIMENT

Frequencies of 750 and 900 mc were chosen as representative because these values bracket 800 mc, the frequency at which the omnidirectional character should become dominant. Thus, comparisons are made with the computed patterns for these values.

Using the symbolism of Fig. 3, the antenna parameters used were

$$\begin{aligned} a &= 0.9 \text{ inch} & e &= 12.7 \text{ inches} \\ d &= 3.9 \text{ inches} & c &= 2.6 \text{ inches.} \end{aligned}$$

Figs. 5 and 6 show experimental azimuth patterns compared with the theoretical patterns in which no correction has been made ( $K=1.0$ ). Figs. 7 and 8 indicate the marked improvement obtained by using values of  $K=0.20$  and  $K=0.33$ , respectively. The use of these correction factors results in agreement within  $\pm 1$  db over the major portion of the front  $180^\circ$  of the patterns. As expected, much closer agreement with the theoretical value of  $K=0.43$  is obtained at the higher of the two frequencies.

The poor agreement between theory and experiment for the rear  $180^\circ$  of the patterns is due to neglecting the flow of current on the top plate in the theory and the

<sup>3</sup> S. Ramo and J. R. Whinnery, "Fields and Waves in Modern Radio," John Wiley & Sons, Inc., New York, N. Y., p. 396; 1953.



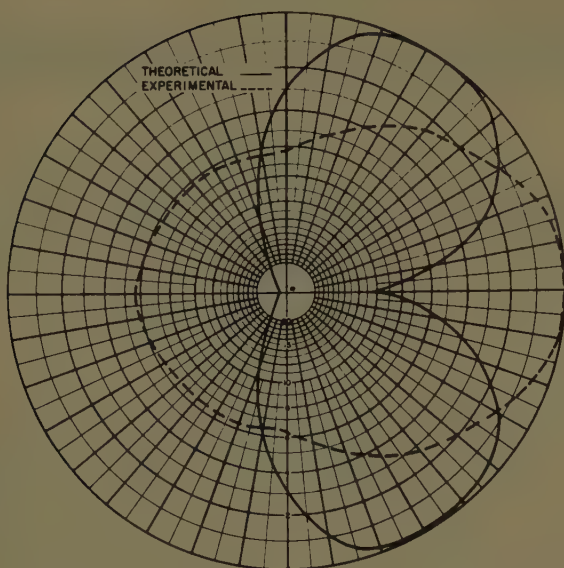


Fig. 5—Theoretical and experimental azimuth patterns:  
 $f=750$  mc and  $K=1.0$ .

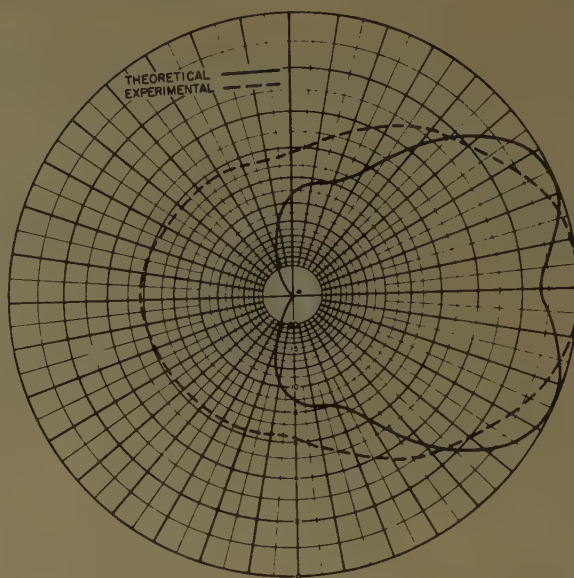


Fig. 7—Theoretical and experimental azimuth patterns:  
 $f=750$  mc and  $K=0.20$ .

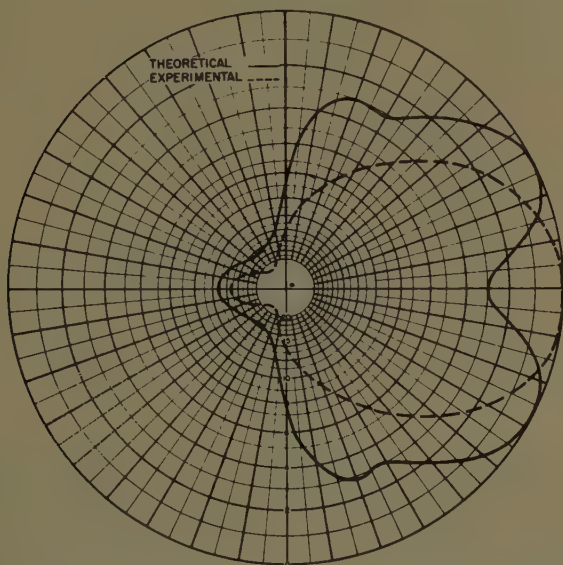


Fig. 6—Theoretical and experimental azimuth patterns:  
 $f=900$  mc and  $K=1.0$ .

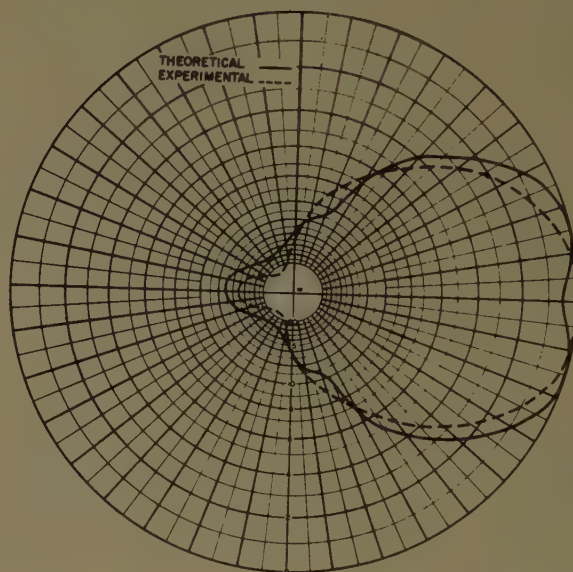


Fig. 8—Theoretical and experimental azimuth patterns:  
 $f=900$  mc and  $K=0.33$ .

presence of a finite ground plane in the experiment. Such a discrepancy is common in the solution of radiating horn problems.

#### CONCLUSION

The theoretical procedure established here has been reasonably successful in predicting the radiation patterns of the cardioid-type antenna with a minimum of mathematical difficulties. Antennas of similar type, having various shaped top plates, are amenable to this method of attack, however, with a probable increase in computational difficulties.

Analysis of the internal reflections indicates that antennas of wider angular coverage could be constructed by shaping the top plate so as to increase the average transmission coefficient of the aperture. Substantial pattern control can also be accomplished by judicious choice of radome dimensions.

#### ACKNOWLEDGMENT

The writer wishes to express his gratitude to Dr. R. W. Bickmore for his constant aid and encouragement during the preparation of this paper.





# On the Propagation of Surface Waves Over an Infinite Grounded Ferrite Slab\*

ROBERT L. PEASE†

**Summary**—A theoretical study is made of the propagation of surface waves along an infinite plane conductor coated with a layer of ferrite material subjected to a constant external magnetic field. For three directions of the external field, the electric and magnetic fields are computed for the separate media, and the relations between them arising from boundary conditions are expressed as transcendental equations. In the limiting case of small ferrite layer thickness (because of the loss problem of greatest physical interest), the fields and propagation constants may be expressed as simple closed forms.

## INTRODUCTION

CONSIDERABLE interest,<sup>1</sup> both theoretical and experimental, has been manifested recently in surface waves—electromagnetic waves guided along the surface of a conductor by virtue either of finite conductivity<sup>2</sup> or of the presence of a surface inhomogeneity such as a dielectric coating<sup>3,4</sup> or surface corrugations.<sup>5</sup> Such finite conductivity or surface inhomogeneity allows the satisfaction of Maxwell's equations by a wave propagating parallel with the surface but attenuated in a direction at right angles to it.

Another field, that of ferromagnetism, also has been the object of considerable recent investigation. It can be shown<sup>6</sup> that a ferromagnetic material subject to a large constant magnetic field exhibits a tensor permeability towards an additional small alternating field; if the constant magnetic field is along the  $x_k$  axis, the relation between magnetic induction and magnetic field strength may be represented as

$$\begin{pmatrix} B_i \\ B_j \\ B_k \end{pmatrix} = \begin{pmatrix} \mu & -j\kappa & 0 \\ j\kappa & \mu & 0 \\ 0 & 0 & \mu_0 \end{pmatrix} \begin{pmatrix} H_i \\ H_j \\ H_k \end{pmatrix} \quad (1)$$

( $i, j, k = \text{cycl. } 1, 2, 3$ )

\* Manuscript received by the PGAP, September 19, 1956; revised manuscript received April 15, 1957. This work was supported by the Air Force Cambridge Res. Ctr; the present paper is a condensation of Sci. Rep. No. 12 on Contract AF 19 (604)-1317, Hughes Aircraft Co., June 30, 1956.

† Lincoln Lab., Mass. Inst. Tech., Lexington, Mass. Formerly with Hughes Aircraft Co., Culver City, Calif.

<sup>1</sup> No attempt will be made here to reproduce the extensive bibliography which exists on surface waves. Most references to earlier work may be found in the literature.

<sup>2</sup> A. Sommerfeld, "Fortpflanzung elektrodynamischer wellen an einem zylindrischen leiter," *Ann. Phys. u. Chemie*, vol. 67, pp. 233-290; December, 1899 and later papers.

See also J. A. Stratton, "Electromagnetic Theory," McGraw-Hill Book Co., New York, N. Y.; pp. 527 ff.; 1941.

<sup>3</sup> G. Goubau, "Surface waves and their application to transmission lines," *J. Appl. Phys.*, vol. 21, pp. 1119-1128; November, 1950. Also see "Single-conductor surface-wave transmission lines," *Proc. IRE*, vol. 39, pp. 619-624; June, 1951.

<sup>4</sup> S. S. Attwood, "Surface-wave propagation over a coated plane conductor," *J. Appl. Phys.*, vol. 22, pp. 504-509; April, 1951.

<sup>5</sup> R. S. Elliott, "On the theory of corrugated plane surfaces," *IRE TRANS.*, vol. AP-2, pp. 71-81; April, 1954.

<sup>6</sup> D. Polder, "On the theory of ferromagnetic resonance," *Phil. Mag.*, vol. 40, pp. 99-115; 1949.

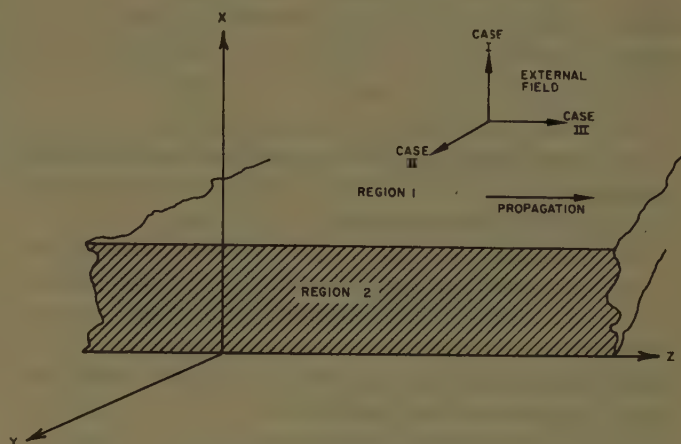


Fig. 1—Propagation media.

where  $\mu$  and  $\kappa$  are functions of the material and of the frequency of the alternating field. While this property is of great theoretical interest, it is not of practical significance for common ferromagnetic materials (such as iron) at microwave frequencies because the finite conductivity precludes penetration into the material. Recently, however, there has been developed a special class of ferromagnetic materials known as ferrites which possess very low conductivity over the microwave range<sup>7</sup> and to which (1) therefore, is applicable at such frequencies. Such a material, for example, if placed on the surface of a conductor, would allow control of surface-wave velocity by variation of an external magnetic field. The aim of the present paper is to investigate this phenomenon for a very simple configuration—an infinite conducting plane coated with a uniform ferrite<sup>8,9</sup> layer as shown in Fig. 1.

Let the infinite half space above the  $yz$  plane be divided into two regions:

Region 1,  $x > a$ , occupied by an homogeneous, isotropic, nonconducting, charge- and current-free substance with parameters  $\mu_1$ ,  $\epsilon_1$ , and

Region 2,  $0 < x < a$ , occupied by an homogeneous, nonconducting, charge- and current-free ferrite, subject to an external magnetic field and obeying constitutive relations (1), and let the  $yz$  plane be conducting perfectly ( $\sigma = \infty$ ). Then it is desirable to obtain solutions of Maxwell's equations

<sup>7</sup> See for instance, C. L. Hogan, "Ferromagnetic Faraday effect at microwave frequencies and its applications," *Rev. Mod. Phys.*, vol. 25, pp. 253-262; January, 1953.

<sup>8</sup> Attwood, *op. cit.* treats the TM case for a dielectric ( $\mu_2 = \mu_1$ ).  
<sup>9</sup> R. C. Hansen, "Single Slab Circular Polarization Surface Wave Structure," Sci. Rept. No. 9 on Contract AF 19 (604)-1317, Hughes Aircraft Co., Res. Lab., February, 1956, treats both TM and TE cases for a dielectric and presents design curves.



$$\text{curl } E = -\partial B/\partial t \quad (2a)$$

$$\text{curl } H = \partial D/\partial t \quad (2b)$$

$$\text{div } B = 0 \quad (2c)$$

$$\text{div } D = 0 \quad (2d)$$

$$B_x = \mu_0 H_x \quad (5a)$$

$$B_y = \mu_2 H_y - j\kappa H_z \quad (5b)$$

$$B_z = j\kappa H_y + \mu_2 H_z \quad (5c)$$

subject to the usual boundary conditions and to any further (consistent) conditions which it is desirable to impose in order to limit the class of solutions. There are four of these:

1) The waves shall be monochromatic, *i.e.*,  $u \sim \exp(j\omega t)$ , where  $\omega$  is real and positive and the scalar  $u$  represents any one of the 12 components of the four field vectors  $E, H, B, D$ .

2) The waves shall propagate undamped along the positive  $z$  direction, *i.e.*,  $u \sim \exp(-j\beta z)$ , where  $\beta$  is real and positive. (This solution ignores the loss in the material media in the direction of propagation.)

3) The waves shall preserve a constant amplitude in the  $y$  direction, *i.e.*,  $\partial u/\partial y = 0$ .

4) The amplitude of the waves shall be quadratically integrable on  $x$ , and there shall be no propagation in the  $x$  direction. (These conditions set the boundary condition at  $x = \infty$ .)

In Region 1, all six field components of  $E$  and  $H$  obey the wave equation

$$\partial^2 u^{(1)}/\partial x^2 + (\omega^2 \mu_1 \epsilon_1 - \beta^2) u^{(1)} = 0 \quad (3)$$

which in itself admits of sinusoidal or exponential solutions. From the surface-wave condition 4), however, only decreasing exponential solutions are allowed, or

$$u^{(1)} \sim \exp(-\alpha x), \quad \alpha \text{ real and positive,} \quad (4a)$$

$$\alpha^2 = \beta^2 - \omega^2 \mu_1 \epsilon_1. \quad (4b)$$

The resulting solutions in Region 1 may be divided into TM and TE waves, as there is no coupling between the two modes; in general this is not true for the fields in the ferrite. General solutions satisfying conditions 1) through 4) are given in Appendix I as (33). It is of interest to note that the TE solutions are the same as the TM solutions with  $E \rightarrow H$ ,  $H \rightarrow -E$ , and  $\mu_1 \rightleftharpoons \epsilon_1$ ; this equivalence does not hold in the ferrite because of asymmetry of boundary conditions.

The analysis of the fields in Region 2, and the matching with the Region 1 fields to obtain surface wave solutions will be carried out separately for the three external magnetic field directions shown in Fig. 1. Case I will be considered in some detail, due to ease of application of external magnetic field and ease of control of propagation constant; the treatments of the other two cases are quite analogous and will be considered more briefly.

#### PROPAGATION OVER FERRITE SLABS: CASE I

When the external magnetic field is in the  $x$  direction (perpendicular to the slab), the fields in Region 2 obey from (1) the constitutive relations:

Substitution of (5) together with the scalar constitutive relation  $D = \epsilon E$  into Maxwell's (2) leads to a set of equations for  $E$  and  $H$  in which the TE and TM modes are now coupled:

$$j\beta E_y^{(2)} = -j\omega\mu_0 H_x^{(2)} \quad (6a)$$

$$-j\beta E_x^{(2)} - \frac{\partial E_z^{(2)}}{\partial x} = -j\omega\mu_2 H_y^{(2)} - \omega\kappa H_z^{(2)} \quad (6b)$$

$$\frac{\partial E_y^{(2)}}{\partial x} = \omega\kappa H_y^{(2)} - j\omega\mu_2 H_z^{(2)} \quad (6c)$$

$$j\beta H_y^{(2)} = j\omega\epsilon_2 E_x^{(2)} \quad (6d)$$

$$-j\beta H_x^{(2)} - \frac{\partial H_z^{(2)}}{\partial x} = j\omega\epsilon_2 E_y^{(2)} \quad (6e)$$

$$\frac{\partial H_y}{\partial x} = j\omega\epsilon_2 E_z^{(2)} \quad (6f)$$

$$\mu_0 \frac{\partial H_x^{(2)}}{\partial x} + \kappa\beta H_y^{(2)} - j\beta\mu_2 H_z^{(2)} = 0 \quad (6g)$$

$$\frac{\partial E_z^{(2)}}{\partial x} - j\beta E_x^{(2)} = 0. \quad (6h)$$

Elimination of the magnetic or electric fields leads to the respective sets of coupled equations:

$$\begin{aligned} \frac{\partial^2 E_x^{(2)}}{\partial x^2} - \left[ \beta^2 - \omega^2 \mu_2 \epsilon_2 \left( 1 - \frac{\kappa^2}{\mu_2 \mu_2^2} \right) \right] E_x^{(2)} \\ + \frac{\beta\kappa}{\mu_2} \frac{\partial E_y^{(2)}}{\partial x} = 0 \end{aligned} \quad (7a)$$

$$\frac{\partial^2 E_y^{(2)}}{\partial x^2} - \left( \frac{\mu_2}{\mu_0} \beta^2 - \omega^2 \mu_2 \epsilon_2 \right) E_y^{(2)} - j\omega^2 \kappa \epsilon_2 E_x^{(2)} = 0 \quad (7b)$$

$$\begin{aligned} \frac{\partial^2 E_z^{(2)}}{\partial x^2} - (\beta^2 - \omega^2 \mu_2 \epsilon_2) E_z^{(2)} \\ - j \frac{\kappa}{\mu_0} (\beta^2 - \omega^2 \mu_0 \epsilon_2) E_y^{(2)} = 0 \end{aligned} \quad (7c)$$

$$\frac{\partial^2 H_x^{(2)}}{\partial x^2} - \left( \frac{\mu_2}{\mu_0} \beta^2 - \omega^2 \mu_2 \epsilon_2 \right) H_x^{(2)} + \frac{\beta\kappa}{\mu_0} \frac{\partial H_y^{(2)}}{\partial x} = 0 \quad (7d)$$

$$\frac{\partial^2 H_y^{(2)}}{\partial x^2} - (\beta^2 - \omega^2 \mu_2 \epsilon_2) H_y^{(2)} - j\omega^2 \kappa \epsilon_2 H_x^{(2)} = 0 \quad (7e)$$

$$\begin{aligned} \frac{\partial^2 H_z^{(2)}}{\partial x^2} - \left( \frac{\mu_2}{\mu_0} \beta^2 - \omega^2 \mu_2 \epsilon_2 \right) H_z^{(2)} \\ - \frac{j\kappa}{\mu_0} (\beta^2 - \omega^2 \mu_0 \epsilon_2) H_y^{(2)} = 0. \end{aligned} \quad (7f)$$



The task of the present section is to find solutions of (6) [and hence of (7)] which satisfy boundary conditions<sup>10</sup> at  $x=0$ , the surface of the conductor, and which join properly to the Region 1 solutions at  $x=a$ .

As a first step, the two simultaneous equations (7b) and (7c) may be reduced by the functional substitutions

$$E_y \sim \frac{\sin}{\cos} \gamma x, \quad E_z \sim \frac{\sin}{\cos} \gamma x$$

to the two simultaneous linear equations

$$\left( \gamma^2 + \frac{\mu_2}{\mu_0} \beta^2 - \omega^2 \mu_2 \epsilon_2 \right) E_y^{(2)} + j \omega^2 \kappa \epsilon_2 E_z^{(2)} = 0$$

$$\frac{j \kappa}{\mu_0} (\beta^2 - \omega^2 \mu_0 \epsilon_2) E_y^{(2)} + (\gamma^2 + \beta^2 - \omega^2 \mu_2 \epsilon_2) E_z^{(2)} = 0$$

for which a nonzero solution for the fields exists only if the determinant of the coefficients is zero; solution of the determinantal equation yields the two values for  $\gamma$  for a given  $\beta$ :

$$\begin{aligned} \gamma_{(\pm)}^2 = & -\frac{1}{2} \left[ \beta^2 \left( 1 + \frac{\mu_2}{\mu_0} \right) - 2 \omega^2 \mu_2 \epsilon_2 \right] \\ & \pm \frac{1}{2} \left[ \beta^4 \left( 1 - 2 \frac{\mu_2}{\mu_0} + \frac{\mu_2^2}{\mu_0^2} \right) \right. \\ & \left. - 4 \frac{\beta^2 \omega^2 \kappa^2 \epsilon_2}{\mu_0} + 4 \omega^4 \kappa^2 \epsilon_2^2 \right]^{1/2}. \quad (8) \end{aligned}$$

The same equation also results when the other pair of coupled equations, (7e) and (7f), is solved simultaneously. The most general Region 2 solutions satisfying Maxwell's (6) and the boundary conditions at  $x=0$  are given in Appendix I as (35); the definition

$$h_{(\pm)} \equiv \gamma_{(\pm)}^2 + \frac{\mu_2}{\mu_0} \beta^2 - \omega^2 \mu_2 \epsilon_2 \quad (9)$$

is adopted for convenience. In general, both the  $\gamma_{(+)}$  and the  $\gamma_{(-)}$  terms must be present to meet boundary conditions at  $x=a$ .

Matching Region 1 solutions (34) to Region 2 solutions (35) at  $x=a$  leads to four coefficient conditions:

$$\frac{j \omega \mu_1}{\alpha} B e^{-\alpha a} = C_{(+)} \sin \gamma_{(+)} a + C_{(-)} \sin \gamma_{(-)} a \quad (10a)$$

$$A e^{-\alpha a} = \frac{j}{\omega^2 \kappa \epsilon_2} (h_{(+)} C_{(+)} \sin \gamma_{(+)} a + h_{(-)} C_{(-)} \sin \gamma_{(-)} a) \quad (10b)$$

$$-\frac{j \omega \epsilon_1}{\alpha} A e^{-\alpha a}$$

$$= \frac{1}{\omega \kappa} \left( \frac{h_{(+)} C_{(+)}}{\gamma_{(+)}} \cos \gamma_{(+)} a + \frac{h_{(-)} C_{(-)}}{\gamma_{(-)}} \cos \gamma_{(-)} a \right) \quad (10c)$$

$$B e^{-\alpha a} = -\frac{j}{\omega \mu_0} (\beta^2 - \omega^2 \mu_0 \epsilon_2) \cdot \left( \frac{C_{(+)}}{\gamma_{(+)}} \cos \gamma_{(+)} a + \frac{C_{(-)}}{\gamma_{(-)}} \cos \gamma_{(-)} a \right). \quad (10d)$$

Then the Region 1 amplitudes  $A$  and  $B$  may be eliminated, and finally the ratio  $C_{(-)}/C_{(+)}$  eliminated to obtain the transcendental equation given in Appendix II as (38). From (38), (4b), (8), and (9), all propagation parameters may be obtained in principle, and amplitudes may be obtained by working backwards from the ratio  $C_{(-)}/C_{(+)}$ , but the actual solution of such a system of equations would be extremely difficult.

Fortunately, however, the case of greatest physical interest, that of thin films, is amenable under certain conditions to a much simpler solution. If the assumptions<sup>11</sup>  $\gamma_{(+)} a \ll 1$ ,  $\gamma_{(-)} a \ll 1$  are made, the sines in (38) are replaced by their arguments and the cosines by unity; between (38), (4b), (8), and (9) it is possible to obtain a quadratic equation for  $\alpha$  which may be solved by formula to yield

$$\alpha = \frac{-\frac{1}{a} \pm \left\{ \frac{1}{a^2} - 4 \omega^2 \mu_1 \epsilon_1 \left[ \left( \frac{\epsilon_1}{\epsilon_2} \right)^2 - \left( \frac{\mu_2}{\mu_1} \right)^2 \right] \right\}^{1/2}}{2 \left( \frac{\epsilon_1}{\epsilon_2} + \frac{\mu_2}{\mu_1} \right)} \quad (\gamma_a \ll 1). \quad (11)$$

Under the conditions

$$\frac{\epsilon_1}{\epsilon_2} + \frac{\mu_2}{\mu_1} > 0, \quad \left( \frac{\epsilon_1}{\epsilon_2} \right)^2 - \left( \frac{\mu_2}{\mu_1} \right)^2 < 0 \quad (12)$$

the denominator of (11) is positive and the magnitude of the radical is greater than  $(1/a)$ . The positive root may be chosen and the radical expanded binomially to give

$$\alpha \simeq \frac{\epsilon_1}{\epsilon_2} \omega^2 a (\mu_2 \epsilon_2 - \mu_1 \epsilon_1) \quad (\gamma_a \ll 1) \quad (13)$$

which turns out to be formally the same as in the dielectric case, as to this order it is independent of  $\kappa$ . From (4b) the propagation constant  $\beta$  may be expressed in terms of the Region 1 (free space) propagation constant  $k \equiv \omega \sqrt{\mu_1 \epsilon_1}$  as

$$\frac{\beta}{k} = \left[ 1 + \left( \frac{\epsilon_1}{\epsilon_2} \right)^2 \left( \frac{\mu_2 \epsilon_2 - \mu_1 \epsilon_1}{\mu_1 \epsilon_1} \right)^2 (ka)^2 \right]^{1/2} \quad (\gamma_a \ll 1). \quad (14)$$

<sup>10</sup> Tangential  $E$  ( $E_y$  and  $E_z$ ) and normal  $B$  ( $B_x$ ) zero. For Case I only, this second condition may be written  $H_x=0$ . (No conditions can be formulated for tangential  $H$  or normal  $D$  since the conductor supports surface current and charge.)

<sup>11</sup> The thin-slab approximation should be used with caution when the surface-wave phase velocity is more than a few percent below free-space velocity.



The surface waves propagate with a phase velocity  $v = \omega/\beta$ , which differs from the plane-wave velocity in Region 1 only to second order in  $a$ . It is convenient to define a parameter  $\epsilon_1^{12}$  through

$$\cos \eta \equiv \frac{\text{plane-wave velocity}}{\text{surface-wave velocity}} = \frac{k}{\beta};$$

then it follows that for thin slabs  $\eta$  is directly proportional to the slab thickness  $a$ :

$$\eta \simeq \frac{\epsilon_1}{\epsilon_2} \left( \frac{\mu_2 \epsilon_2 - \mu_1 \epsilon_1}{\mu_1 \epsilon_1} \right) (ka) \quad (\gamma a \ll 1) \quad [(12) \text{ holding}] \quad (15)$$

With the substitution

$$G' \equiv \sqrt{\frac{\mu_1}{\epsilon_1}} \frac{\gamma_{(+)} C_{(+)} + \gamma_{(-)} C_{(-)}}{\omega \kappa} \quad (16)$$

and considerable manipulation, the fields may be expressed to order  $a$  as shown in (41) of Appendix III. As would be expected from the dielectric case, the waves for thin slabs are primarily TM; a small TE component is necessary to satisfy the  $\text{div } \mathbf{B}$  (6<sup>-</sup>).

Ferrites possess positive dielectric constants, whence  $(\epsilon_1/\epsilon_2) > 0$ . Then it follows from (12) that the inequality

$$\frac{\mu_2}{\mu_1} > \frac{\epsilon_1}{\epsilon_2} > 0 \quad (17)$$

may be taken as the condition (in addition to  $\gamma a \ll 1$ ) that (12) holds. For conditions other than (12), no thin-slab approximation is possible.

#### PROPAGATION OVER FERRITE SLABS: CASE II

Let the steady magnetic field be along the  $y$  axis; then the fields in the ferrite will obey constitutive relations:

$$B_x = j\kappa H_z + \mu_2 H_x \quad (18a)$$

$$B_y = \mu_0 H_y \quad (18b)$$

$$B_z = \mu_2 H_z - j\kappa H_x \quad (18c)$$

The fields in Region 1 are given again by (34); the fields in Region 2 are now obtained by substituting (18) and  $D = \partial E$  into Maxwell's (2).

In Case II only, the constitutive relations do not introduce connections between the TM and TE fields; hence there are two separate sets of wave equations, and two uncoupled sets of Region 2 solutions shown as (36) of Appendix I. The propagation constants are related through

<sup>12</sup> Physically,  $\eta$  corresponds to the material limitation on the amount by which the radiation from a long slab without ground plane may be scanned. The beam-tilt angle (Elliott, *op. cit.*) for a radiating surface of length  $l \gg \lambda$  may be expressed as

$$\theta_T^2 \simeq \frac{2.33\lambda}{\pi l} - \eta^2 - \mu_{\text{max}}^2 - \eta^2;$$

the beam may be tilted from maximum to zero provided the constitutive parameters of the slab may be varied over a sufficiently large range.

$$\gamma_m^2 = \omega^2 \mu_0 \epsilon_2 - \beta^2 \quad (\text{TM}) \quad (19a)$$

$$\gamma_e^2 = \omega^2 \mu_2 \epsilon_2 \left[ 1 - \frac{\kappa^2}{\mu_2^2} \right] - \beta^2 \quad (\text{TE}) \quad (19b)$$

The TM solutions are the same as those for the isotropic case except that  $\mu_0$  is substituted for  $\mu_2$ ; the velocity of propagation is not controllable by an external magnetic field. Transcendental equations are given in Appendix II as (39).

In the thin-slab approximation, the various propagation constants for the TM mode have the same forms as in Case I except for the substitution of  $\mu_0$  for  $\mu_2$ , *i.e.*,

$$\alpha \simeq \frac{\epsilon_1}{\epsilon_2} \omega^2 a (\mu_0 \epsilon_2 - \mu_1 \epsilon_1) \quad (\gamma_m a \ll 1, \text{TM}) \quad (20)$$

$$\frac{\beta}{k} \simeq \left[ 1 + \left( \frac{\epsilon_1}{\epsilon_2} \right)^2 \left( \frac{\mu_0 \epsilon_2 - \mu_1 \epsilon_1}{\mu_1 \epsilon_1} \right)^2 (ka)^2 \right]^{1/2} \quad (\gamma_m a \ll 1, \text{TM}) \quad (21)$$

$$\eta \simeq \frac{\epsilon_1}{\epsilon_2} \left( \frac{\mu_0 \epsilon_2 - \mu_1 \epsilon_1}{\mu_1 \epsilon_1} \right) (ka) \quad (\gamma_m a \ll 1, \text{TM}), \quad (22)$$

while the fields assume the forms shown in Appendix III as (42), with the substitution

$$G'' \equiv -j \frac{\epsilon_2}{\epsilon_1} \sqrt{\frac{\mu_1 \epsilon_1}{\mu_0 \epsilon_2 - \mu_1 \epsilon_1}} C'' \quad (23)$$

For TE waves over thin slabs, transcendental equation (39b) may be rewritten with the help of (4b) and (19b) as

$$\frac{1}{a} = -\alpha \frac{\mu_2}{\mu_1} \left( 1 - \frac{\kappa^2}{\mu_2^2} \right) + \frac{\beta \kappa}{\mu_2} \quad (24)$$

Due to the presence of the off-diagonal  $\kappa$  term, it may be possible to satisfy (24) under certain conditions, but the results cannot in general be expressed in simple form.

#### PROPAGATION OVER FERRITE SLABS: CASE III

If the steady magnetic field is along the  $z$  axis (*i.e.*, along the direction of propagation), constitutive relations

$$B_x = \mu_2 H_x - j\kappa H_y \quad (25a)$$

$$B_y = j\kappa H_x + \mu_2 H_y \quad (25b)$$

$$B_z = \mu_0 H_z \quad (25c)$$

hold. As in Case I, there are connections between the TM and TE groups of fields; the substitutions

$$E_x \sim \frac{\sin}{\cos} \gamma x, \quad E_y \sim \frac{\sin}{\cos} \gamma x$$

lead to simultaneous algebraic equations for which a solution exists only if the determinant of the coefficients is zero. The resulting condition may be solved to yield two values for the  $x$ -wave number:



$$\begin{aligned}
\gamma_{(\pm)}^2 = & -\frac{1}{2} \left[ (\beta^2 - \omega^2 \mu_2 \epsilon_2) \left( 1 + \frac{\mu_0}{\mu_2} \right) + \frac{\omega^2 \kappa^2 \epsilon_2}{\mu_2} \right] \\
& \pm \frac{1}{2} \left[ (\beta^4 + \omega^4 \mu_2^2 \epsilon_2^2) \left( 1 - 2 \frac{\mu_0}{\mu_2} + \frac{\mu_0^2}{\mu_2^2} \right) \right. \\
& - 2\beta^2 \omega^2 \mu_2 \epsilon_2 \left( 1 - \frac{\mu_0}{\mu_2} + \frac{\mu_0^2}{\mu_2^2} \right) \\
& + \frac{2\beta^2 \omega^2 \kappa^2 \epsilon_2}{\mu_2} \left( 1 + \frac{\mu_0}{\mu_2} \right) \\
& \left. - 2\omega^4 \kappa^2 \epsilon_2^2 \left( 1 - \frac{\mu_0}{\mu_2} \right) + \frac{\omega^4 \kappa^4 \epsilon_2^2}{\mu_2^2} \right]^{1/2}. \quad (26a)
\end{aligned}$$

The Region 2 solutions satisfying Maxwell's equations and suitable boundary conditions are given in Appendix I as (37), with the definition

$$f_{(\pm)} \equiv \gamma_{(\pm)} \left[ \frac{\mu_0}{\mu_2} (\beta^2 - \omega^2 \mu_2 \epsilon_2) + \gamma_{(\pm)}^2 \right] \quad (26b)$$

adopted for convenience. Matching at  $x=a$  yields, as in Case I, four independent equations which, after elimination of amplitudes, yield in turn a transcendental equation (40) of Appendix II. Again it is possible, in principle, to find the propagation constants, but as in Case I such a set of equations would be extremely difficult to deal with in practice.

Fortunately, the thin slab case is again relatively simple. With the assumptions  $\gamma_{(+)}a \ll 1$ ,  $\gamma_{(-)}a \ll 1$ , it can be shown from (40), (4b), (25), and (26) that the attenuation constant

$$\alpha = \frac{-\frac{\mu_1}{\mu_0 a} \pm \left\{ \frac{\mu_1^2}{\mu_0^2 a^2} - 4 \left( 1 + \frac{\mu_1 \epsilon_1}{\mu_0 \epsilon_2} \right) \frac{\omega^2 \mu_1 \epsilon_1}{\mu_0 \epsilon_2} \left[ \mu_1 \epsilon_1 - \mu_2 \epsilon_2 \left( 1 - \frac{\kappa^2}{\mu_2^2} \right) \right] \right\}^{1/2}}{2 \left( 1 + \frac{\mu_1 \epsilon_1}{\mu_0 \epsilon_2} \right)} \quad (\gamma a \ll 1). \quad (27)$$

The denominator of (27) is always positive. Hence, in order that the attenuation constant be positive, it is necessary that the  $+$  sign be used in the numerator and that the magnitude of the square root be greater than  $(\mu_1/\mu_0 a)$ , i.e., that

$$\mu_2 \epsilon_2 \left( 1 - \frac{\kappa^2}{\mu_2^2} \right) - \mu_1 \epsilon_1 > 0. \quad (28)$$

Since the first term in the radical is very large, the radical may be expanded binomially to yield to order  $a$ ,

$$\alpha \simeq \frac{\epsilon_1}{\epsilon_2} \omega^2 a \left[ \mu_2 \epsilon_2 \left( 1 - \frac{\kappa^2}{\mu_2^2} \right) - \mu_1 \epsilon_1 \right] \quad (\gamma a \ll 1) \quad (29)$$

which differs from the attenuation constant (13) of Case I by the presence of the term in  $\kappa^2$ . Then the propagation constant to second order is

$$\frac{\beta}{k} \simeq \left[ 1 + \left( \frac{\epsilon_1}{\epsilon_2} \right)^2 \left[ \frac{\mu_2 \epsilon_2 \left( 1 - \frac{\kappa^2}{\mu_2^2} \right) - \mu_1 \epsilon_1}{\mu_1 \epsilon_1} \right]^2 \right]^{1/2} \quad (\gamma a \ll 1) \quad (30)$$

and the parameter

$$\eta \simeq \frac{\epsilon_1}{\epsilon_2} \left[ \frac{\mu_2 \epsilon_2 \left( 1 - \frac{\kappa^2}{\mu_2^2} \right) - \mu_1 \epsilon_1}{\mu_1 \epsilon_1} \right] (ka) \quad (\gamma a \ll 1). \quad (31)$$

Thin-slab solutions, in terms of the amplitude

$$G''' \equiv \frac{-j\mu_2}{\omega^2 \kappa \epsilon_1 \mu_0} [\gamma_{(+)}^2 - \gamma_{(-)}^2] D \quad (32)$$

are given in Appendix III as (43).

### CONCLUSION

Due to the complexity of the exact solutions to the problem of surface waves on ferrites and to the necessity for as low losses as practicable, it is expected that most design work will be based upon, or at least guided by, the results under the thin-slab approximation. These are summarized in Tables I and II (next page). Table I gives a brief description of allowed modes and lists the parameter  $\eta$  for each case; the attenuation and propagation constants may be computed from the tilt angle by the simple relations

$$\frac{\alpha}{k} = \eta \quad (33a)$$

$$\frac{\beta}{k} = 1 + \frac{\eta^2}{2}. \quad (33b)$$

Table II gives in more detail the relative magnitudes of field components for each case. For materials encountered in practice, the parameter restrictions (12) and (28) merely amount to the requirement that the parameter  $\eta$  be positive.

As would be expected, the TM mode is predominant for thin slabs. The TM mode of Case II is not of use for any applications involving changing  $\beta$ , however, as the result is independent of external field; further, since the TE solutions appear to exist under unusual conditions if at all, Case II might not have much application.

Finally, two limitations of the present analysis will be mentioned again: the thin-slab approximation is only accurate for quite small values of  $\eta$ , and the magnitude of the rf component of the magnetic field must be much smaller than the magnitude of the steady external component.



TABLE I  
RESULTS IN THIN-SLAB APPROXIMATION

Case	Direction of External Field	Allowed Modes	$\eta$
Isotropic	None	TM	$\frac{\epsilon_1}{\epsilon_2} \frac{\mu_2 \epsilon_2 - \mu_1 \epsilon_1}{\mu_1 \epsilon_1} (ka)$
I	$\perp$ Slab Plane ( $\perp$ Propagation)	TM+TE*	$\frac{\epsilon_1}{\epsilon_2} \frac{\mu_2 \epsilon_2 - \mu_1 \epsilon_1}{\mu_1 \epsilon_1} (ka)$
II	$\parallel$ Slab Plane $\perp$ Propagation	TM TE(?)	$\frac{\epsilon_1}{\epsilon_2} \frac{\mu_0 \epsilon_2 - \mu_1 \epsilon_1}{\mu_1 \epsilon_1} (ka)$ $N$
III	( $\parallel$ Slab Plane) $\parallel$ Propagation	TM+TE**	$\frac{\epsilon_1}{\epsilon_2} \frac{\mu_2 \epsilon_2 \left(1 - \frac{\kappa^2}{\mu_2^2}\right) - \mu_1 \epsilon_1}{\mu_1 \epsilon_1} (ka)$

\* Small.

\*\* Very small.

?—May be possible under certain conditions.

N—Not computed.

TABLE II  
RELATIVE FIELD COMPONENT AMPLITUDES IN  
THIN-SLAB APPROXIMATION

	Isotropic	Case I	Case II	Case III
TM $\begin{cases} E_x \\ E_z \\ H_y \end{cases}$	$\begin{matrix} L \\ S \\ L \end{matrix}$	$\begin{matrix} L \\ S \\ L \end{matrix}$	$\begin{matrix} L \\ S \\ L \end{matrix}$	$\begin{matrix} L \\ S \\ L \end{matrix}$
TE $\begin{cases} H_x \\ H_z \\ E_y \end{cases}$	$\begin{matrix} X \\ X \\ X \end{matrix}$	$\begin{matrix} S \\ V \\ S \end{matrix}$	$\begin{matrix} N \\ N \\ N \end{matrix}$	$\begin{matrix} V \\ V \\ V \end{matrix}$

L—large.

S—small [order  $(\gamma_a)$  less than large].

V—vanishingly small [order  $(\gamma_a)^2$  less than large].

X—prohibited by boundary conditions.

N—not computed—no simple results.

## APPENDIX I

### GENERAL SURFACE-WAVE SOLUTIONS

#### Region 1:

$$\left. \begin{aligned} E_x^{(1)} &= -\frac{j\beta}{\alpha} A e^{-\alpha x} \\ E_z^{(1)} &= A e^{-\alpha x} \\ H_y^{(1)} &= -\frac{j\omega\epsilon_1}{\alpha} A e^{-\alpha x} \end{aligned} \right\} \quad (\text{TM}) \quad (34)$$

$$\left. \begin{aligned} H_x^{(1)} &= -\frac{j\beta}{\alpha} B e^{-\alpha x} \\ H_z^{(1)} &= B e^{-\alpha x} \\ E_y^{(1)} &= \frac{j\omega\mu_1}{\alpha} B e^{-\alpha x} \end{aligned} \right\} \quad (\text{TE})$$

#### Region 2, Case I:

$$E_x^{(2)} = \frac{\beta}{\omega^2 \kappa \epsilon_2} \left( \frac{h_{(+)} C_{(+)}}{\gamma_{(+)}} \cos \gamma_{(+)} x + \frac{h_{(-)} C_{(-)}}{\gamma_{(-)}} \cos \gamma_{(-)} x \right)$$

$$E_y^{(2)} = C_{(+)} \sin \gamma_{(+)} x + C_{(-)} \sin \gamma_{(-)} x$$

$$E_z^{(2)} = \frac{j}{\omega^2 \kappa \epsilon_2} (h_{(+)} C_{(+)} \sin \gamma_{(+)} x + h_{(-)} C_{(-)} \sin \gamma_{(-)} x)$$

$$H_x^{(2)} = -\frac{\beta}{\omega \mu_0} (C_{(+)} \sin \gamma_{(+)} x + C_{(-)} \sin \gamma_{(-)} x)$$

$$H_y^{(2)} = \frac{1}{\omega \kappa} \left( \frac{h_{(+)} C_{(+)}}{\gamma_{(+)}} \cos \gamma_{(+)} x + \frac{h_{(-)} C_{(-)}}{\gamma_{(-)}} \cos \gamma_{(-)} x \right)$$

$$H_z^{(2)} = -\frac{j}{\omega \mu_0} (\beta^2 - \omega^2 \mu_0 \epsilon_2)$$

$$\cdot \left( \frac{C_{(+)}}{\gamma_{(+)}} \cos \gamma_{(+)} x + \frac{C_{(-)}}{\gamma_{(-)}} \cos \gamma_{(-)} x \right). \quad (35)$$

#### Region 2, Case II:

$$\left. \begin{aligned} E_x^{(2)} &= -\frac{j\beta}{\gamma_m} C'' \cos \gamma_m x \\ E_z^{(2)} &= C'' \sin \gamma_m x \\ H_y^{(2)} &= -\frac{j\omega\epsilon_2}{\gamma_m} C'' \cos \gamma_m x \end{aligned} \right\} \quad (\text{TM}).$$

$$\left. \begin{aligned} H_x^{(2)} &= \frac{j\beta}{\gamma_e} \frac{\mu_2^2}{\mu_2^2 - \kappa^2} D'' \sin \gamma_e x \\ &\quad - \frac{j\mu_2 \kappa}{\mu_2^2 - \kappa^2} D'' \cos \gamma_e x \\ H_z^{(2)} &= \frac{\mu_2^2}{\mu_2^2 - \kappa^2} D'' \cos \gamma_e x \\ &\quad - \frac{\beta}{\gamma_e} \frac{\mu_2 \kappa}{\mu_2^2 - \kappa^2} D'' \sin \gamma_e x \\ E_y &= -\frac{j\omega\mu_2}{\gamma_e} D'' \sin \gamma_e x \end{aligned} \right\} \quad (\text{TE}). \quad (36)$$



Region 2, Case III:

$$\begin{aligned}
 E_x^{(2)} &= \frac{-j\mu_2}{\omega^2\kappa\epsilon_2\mu_0} \left[ C \left( \frac{f_{(+)}}{\gamma_{(+)}} \sin \gamma_{(+)}x - \frac{f_{(-)}}{\gamma_{(-)}} \sin \gamma_{(-)}x \right) + D \left( \frac{f_{(+)}}{\gamma_{(+)}} \cos \gamma_{(+)}x - \frac{f_{(-)}}{\gamma_{(-)}} \cos \gamma_{(-)}x \right) \right] \\
 E_y^{(2)} &= C \left( \sin \gamma_{(+)}x - \frac{f_{(+)}}{f_{(-)}} \sin \gamma_{(-)}x \right) + D (\cos \gamma_{(+)}x - \cos \gamma_{(-)}x) \\
 E_z^{(2)} &= \frac{-\mu_2}{\omega^2\kappa\epsilon_2\mu_0\beta} [Cf_{(+)}(\cos \gamma_{(+)}x - \cos \gamma_{(-)}x) + D(-f_{(+)} \sin \gamma_{(+)}x + f_{(-)} \sin \gamma_{(-)}x)] \\
 H_x^{(2)} &= \frac{\beta}{\omega\mu_0} \left\{ C \left[ \left( \frac{f_{(+)}}{\beta^2\gamma_{(+)}} - \frac{\mu_0}{\mu_2} \right) \sin \gamma_{(+)}x + \left( \frac{-f_{(-)}}{\beta^2\gamma_{(-)}} + \frac{\mu_0}{\mu_2} \frac{f_{(+)}}{f_{(-)}} \right) \sin \gamma_{(-)}x \right] \right. \\
 &\quad \left. + D \left[ \left( \frac{f_{(+)}}{\beta^2\gamma_{(+)}} - \frac{\mu_0}{\mu_2} \right) \cos \gamma_{(+)}x + \left( \frac{-f_{(-)}}{\beta^2\gamma_{(-)}} + \frac{\mu_0}{\mu_2} \right) \cos \gamma_{(-)}x \right] \right\} \\
 H_y^{(2)} &= \frac{-j\mu_2}{\beta\omega\kappa\mu_0} \left[ C \left( \frac{f_{(+)}}{\gamma_{(+)}} \sin \gamma_{(+)}x - \frac{f_{(-)}}{\gamma_{(-)}} \sin \gamma_{(-)}x \right) + D \left( \frac{f_{(+)}}{\gamma_{(+)}} \cos \gamma_{(+)}x - \frac{f_{(-)}}{\gamma_{(-)}} \cos \gamma_{(-)}x \right) \right] \\
 H_z^{(2)} &= \frac{j}{\omega\mu_0} \left[ C \left( \gamma_{(+)} \cos \gamma_{(+)}x - \frac{f_{(+)}}{f_{(-)}} \gamma_{(-)} \cos \gamma_{(-)}x \right) + D (-\gamma_{(+)} \sin \gamma_{(+)}x + \gamma_{(-)} \sin \gamma_{(-)}x) \right]. \quad (37)
 \end{aligned}$$

## APPENDIX II

### TRANSCENDENTAL EQUATIONS

Case I:

$$\begin{aligned}
 &\left[ \frac{\mu_0\epsilon_1(h_{(+)} - h_{(-)})}{\mu_1\epsilon_2(\beta^2 - \omega^2\mu_0\epsilon_2)} \right] \sin \gamma_{(+)}a \sin \gamma_{(-)}a + \left[ \frac{h_{(+)} - h_{(-)}}{\gamma_{(+)}\gamma_{(-)}} \right] \cos \gamma_{(+)}a \cos \gamma_{(-)}a \\
 &\quad + \left[ \frac{-\epsilon_1 h_{(+)}}{\gamma_{(-)}\epsilon_2\alpha} + \frac{\mu_0\alpha h_{(-)}}{\gamma_{(-)}\mu_1(\beta^2 - \omega^2\mu_0\epsilon_2)} \right] \sin \gamma_{(+)}a \cos \gamma_{(-)}a \\
 &\quad + \left[ \frac{\epsilon_1 h_{(-)}}{\gamma_{(+)}\epsilon_2\alpha} - \frac{\mu_0\alpha h_{(+)}}{\gamma_{(+)}\mu_1(\beta^2 - \omega^2\mu_0\epsilon_2)} \right] \cos \gamma_{(+)}a \sin \gamma_{(-)}a = 0. \quad (38)
 \end{aligned}$$

Case II:

$$\gamma_m \tan \gamma_m a = \alpha \frac{\epsilon_2}{\epsilon_1} \quad (\text{TM}) \quad (39a)$$

$$\gamma_e \cot \gamma_e a = -\alpha \frac{\mu_2}{\mu_1} \left( 1 - \frac{\kappa^2}{\mu_2^2} \right) + \beta \frac{\kappa}{\mu_2} \quad (\text{TE}). \quad (39b)$$

Case III:

$$\begin{aligned}
 &\left[ \frac{\mu_1\epsilon_2}{\mu_0\epsilon_1} \left( \frac{\gamma_{(+)}}{\gamma_{(+)}} + \frac{\gamma_{(-)}}{\gamma_{(-)}} \right) - \left( \frac{f_{(+)}}{f_{(-)}} + \frac{f_{(-)}}{f_{(+)}} \right) \right] \sin \gamma_{(+)}a \sin \gamma_{(-)}a \\
 &\quad + \left[ -2 + \frac{\mu_1\epsilon_2}{\mu_0\epsilon_1} \left( \frac{f_{(+)}}{f_{(-)}} \frac{\gamma_{(-)}}{\gamma_{(+)}} + \frac{f_{(-)}}{f_{(+)}} \frac{\gamma_{(+)}}{\gamma_{(-)}} \right) \right] \cos \gamma_{(+)}a \cos \gamma_{(-)}a \\
 &\quad + \left[ \frac{\mu_1}{\alpha\mu_0} \gamma_{(+)} \left( 1 - \frac{f_{(+)}}{f_{(-)}} \frac{\gamma_{(-)}}{\gamma_{(+)}} \right) - \frac{\alpha\epsilon_2}{\epsilon_1} \frac{1}{\gamma_{(+)}} \left( 1 - \frac{f_{(-)}}{f_{(+)}} \frac{\gamma_{(+)}}{\gamma_{(-)}} \right) \right] \sin \gamma_{(+)}a \cos \gamma_{(-)}a \\
 &\quad + \left[ \frac{\mu_1}{\alpha\mu_0} \gamma_{(-)} \left( 1 - \frac{f_{(-)}}{f_{(+)}} \frac{\gamma_{(+)}}{\gamma_{(-)}} \right) - \frac{\alpha\epsilon_2}{\epsilon_1} \frac{1}{\gamma_{(-)}} \left( 1 - \frac{f_{(+)}}{f_{(-)}} \frac{\gamma_{(-)}}{\gamma_{(+)}} \right) \right] \cos \gamma_{(+)}a \sin \gamma_{(-)}a + 2 - 2 \frac{\mu_1\epsilon_2}{\mu_0\epsilon_1} = 0. \quad (40)
 \end{aligned}$$



### APPENDIX III

#### THIN-SLAB SOLUTIONS

Case I:

$$E_x^{(1)} = G' e^{-\alpha(x-a)}$$

$$E_y^{(1)} = \omega \kappa \sqrt{\frac{\epsilon_1}{\mu_1}} G' a e^{-\alpha(x-a)}$$

$$E_z^{(1)} = j\omega \sqrt{\frac{\epsilon_1}{\mu_1}}$$

$$\cdot \frac{(\mu_2 \epsilon_2 - \mu_1 \epsilon_1)}{\epsilon_2} G' a e^{-\alpha(x-a)}$$

$$H_x^{(1)} = -\frac{\omega \kappa \epsilon_1}{\mu_1} G' a e^{-\alpha(x-a)}$$

$$H_y^{(1)} = \sqrt{\frac{\epsilon_1}{\mu_1}} G' e^{-\alpha(x-a)}$$

$$H_z^{(1)} = 0$$

$$E_x^{(2)} = \frac{\epsilon_1}{\epsilon_2} G'$$

$$E_y^{(2)} = \omega \kappa \sqrt{\frac{\epsilon_1}{\mu_1}} G' x$$

$$E_z^{(2)} = j\omega \sqrt{\frac{\epsilon_1}{\mu_1}}$$

$$\cdot \left( \frac{\mu_2 \epsilon_2 - \mu_1 \epsilon_1}{\epsilon_2} \right) G' x$$

$$H_x^{(2)} = -\frac{\omega \kappa \epsilon_1}{\mu_0} G' x$$

$$H_y^{(2)} = \sqrt{\frac{\epsilon_1}{\mu_1}} G'$$

$$H_z^{(2)} = 0.$$

Case II:

$$E_x^{(1)} = G'' e^{-\alpha(x-a)}$$

$$E_y^{(1)} = j\omega \sqrt{\frac{\epsilon_1}{\mu_1}}$$

$$\cdot \frac{(\mu_0 \epsilon_2 - \mu_1 \epsilon_1)}{\epsilon_2} G'' a e^{-\alpha(x-a)}$$

$$H_y^{(1)} = \sqrt{\frac{\epsilon_1}{\mu_1}} G'' e^{-\alpha(x-a)}$$

$$E_x^{(2)} = \frac{\epsilon_1}{\epsilon_2} G''$$

$$E_z = j\omega \sqrt{\frac{\epsilon_1}{\mu_1}} \frac{(\mu_0 \epsilon_2 - \mu_1 \epsilon_1)}{\epsilon_2} G'' x$$

$$H_y = \sqrt{\frac{\epsilon_1}{\mu_1}} G''$$

( $\gamma_m a \ll 1$ , TM). (41)

Case III:

$$E_x^{(1)} = G''' e^{-\alpha(x-a)}$$

$$E_y^{(1)} = 0$$

$$E_z^{(1)} = j\omega \sqrt{\frac{\epsilon_1}{\mu_1}} \frac{\mu_2 \epsilon_2 \left( 1 - \frac{\kappa^2}{\mu_2^2} \right) - \mu_1 \epsilon_1}{\epsilon_2} G''' a e^{-\alpha(x-a)}$$

$$H_x^{(1)} = 0$$

$$H_y^{(1)} = \sqrt{\frac{\epsilon_1}{\mu_1}} G''' e^{-\alpha(x-a)}$$

$$H_z^{(1)} = 0$$

$$E_x^{(2)} = \frac{\epsilon_1}{\epsilon_2} G'''$$

$$E_y^{(2)} = 0$$

$$E_z^{(2)} = j\omega \sqrt{\frac{\epsilon_1}{\mu_1}} \frac{\mu_2 \epsilon_2 \left( 1 - \frac{\kappa^2}{\mu_2^2} \right) - \mu_1 \epsilon_1}{\epsilon_2} G''' x$$

$$H_x^{(2)} = \frac{j\kappa}{\mu_2} \sqrt{\frac{\epsilon_1}{\mu_1}} G'''$$

$$H_y^{(2)} = \sqrt{\frac{\epsilon_1}{\mu_1}} G'''$$

$$H_z^{(2)} = -\frac{\kappa \omega \epsilon_1}{\mu_2} G''' (a - x).$$

(43)

$$(\gamma a \ll 1)$$

$$\frac{\epsilon_1}{\epsilon_2} + \frac{\mu_2}{\mu_1} > 0 \quad (41)$$

$$\left( \frac{\epsilon_1}{\epsilon_2} \right)^2 - \left( \frac{\mu_2}{\mu_1} \right)^2 < 0.$$

#### ACKNOWLEDGMENT

This problem originated in a proposal made by Dr. R. C. Hansen. I am greatly indebted to Dr. Hansen and to Dr. R. W. Bickmore for valuable criticisms of the manuscript.



# Polarization Fading Over an Oblique Incidence Path\*

D. A. HEDLUND† AND L. C. EDWARDS†

**Summary**—This paper discusses the results of an investigation of polarization fading conducted over a one-hop F2 layer path from eastern Massachusetts approximately 1000 miles westward. Continuous recordings of pulse transmissions were made to study the instantaneous variations in amplitude of the vertically and horizontally polarized components of the received signal.

Results are presented which show a strong dependence between the amplitudes of the two components. Deep fades on one component were found to be accompanied by maxima of the other. A possible interpretation is presented which involves interference between the magneto-ionic components and leads to some interesting conclusions regarding their characteristics. Results are also included to illustrate the variations in these signal levels as the MUF is approached.

## INTRODUCTION

DURING 1954 and 1955 an investigation of polarization fading was carried out by Raytheon for the Air Force Cambridge Research Center. The purpose of the program was to evaluate, by measurement, the polarization characteristics of radio waves propagated over a one-hop F2 layer path. One specific point of interest was whether or not a particular polarization predominated over the chosen path.

It is well known that a linearly polarized wave transmitted by way of the ionosphere is split into several elliptically polarized components.<sup>1</sup> It was the intention of this program to measure the polarization of the predominant component.

In order to separate in time the various components, insofar as possible, and to provide synchronization, a pulse slave beacon system was chosen. Since the elliptically polarized signal can be completely specified by its component horizontal and vertical field intensities and the phase angle between them, equipment and antennas appropriate to the measurement of these parameters was used.

## CHOICE OF PARAMETERS

For convenience, an east-west path was picked. Raytheon maintains an ionosphere sounding station at South Dartmouth, Mass., and this served as the master station. Angles of arrival in the neighborhood of 15° would allow use of relatively simple antennas at normal heights above ground, and such angles would correspond to a path length of approximately 1500 km. The slave station was therefore located at Greenville College in Greenville, Ill., a distance of 1588 km. This path is approximately normal to the direction of the earth's

magnetic field. A frequency was desired so that one-hop F2 propagation was possible for most of the day. For the period of the investigation one of the available frequencies, 12.730 mc, satisfied this requirement.

## INSTRUMENTATION

At South Dartmouth a 20-kw (peak pulse power) transmitter fed a three-element horizontal Yagi antenna, interrogating a 1-kw pulse transponder beacon at Greenville. The beacon antenna, used both for reception and transmission, was a horizontal half-wave dipole. The pulse widths were 100  $\mu$ sec and the rate 20 pulses per second.

All measurements were made at South Dartmouth. A block diagram of the receiving and recording system is shown in Fig. 1. The receiving antenna system comprised crossed horizontal and vertical half-wave dipoles, a full wavelength above ground. This simple antenna array was chosen because known directivity patterns are necessary for determination of field strength. Fig. 2 is a picture of the actual antenna installation. The crossed dipoles were supported one wavelength above the ground between two poles 135 feet apart. This arrangement was decided upon when it was found that any supporting structures near the antenna had an effect on the impedance, and consequently on the calculated field intensities. The feedlines were brought back horizontally from the antennas a distance of about one wavelength to minimize possible effects on the directivity patterns and were carefully arranged to prevent intercoupling.

The patterns of the two elements of the antenna were first calculated, assuming suitable ground constants, and later were checked by actual measurement. To obtain this measure a small battery powered transmitter feeding either a horizontal loop or vertical whip antenna was carried aloft by a captive weather balloon. The calculated pattern of the horizontal element was verified quite closely and the agreement between calculation and measurement for the vertical element was within 10 per cent.

As seen in Fig. 1, the signals from the two elements of the polarimeter antenna were fed through a gated mixer to a single receiver channel whose bandwidth was 25 kc. The timing and mixing circuits were arranged to gate out alternate pulses from each antenna element and feed the resulting 10-cycle pulses from the horizontal and vertical elements alternately to the receiver. This method was chosen to avoid difficulties encountered early in the program in keeping separate receiver channels identical in both amplitude and phase.

The video output of the receiver was fed, through amplifiers, to an A-scope monitor and to one of the

\* Manuscript received by the PGAP, August 13, 1956; revised manuscript received, April 12, 1957.

† Raytheon Mfg. Co., Wayland, Mass.

<sup>1</sup> H. G. Booker, "Some general properties of the formulae of the magneto-ionic theory," *Proc. Roy. Soc. A*, vol. 147, pp. 352-382; November, 1934.



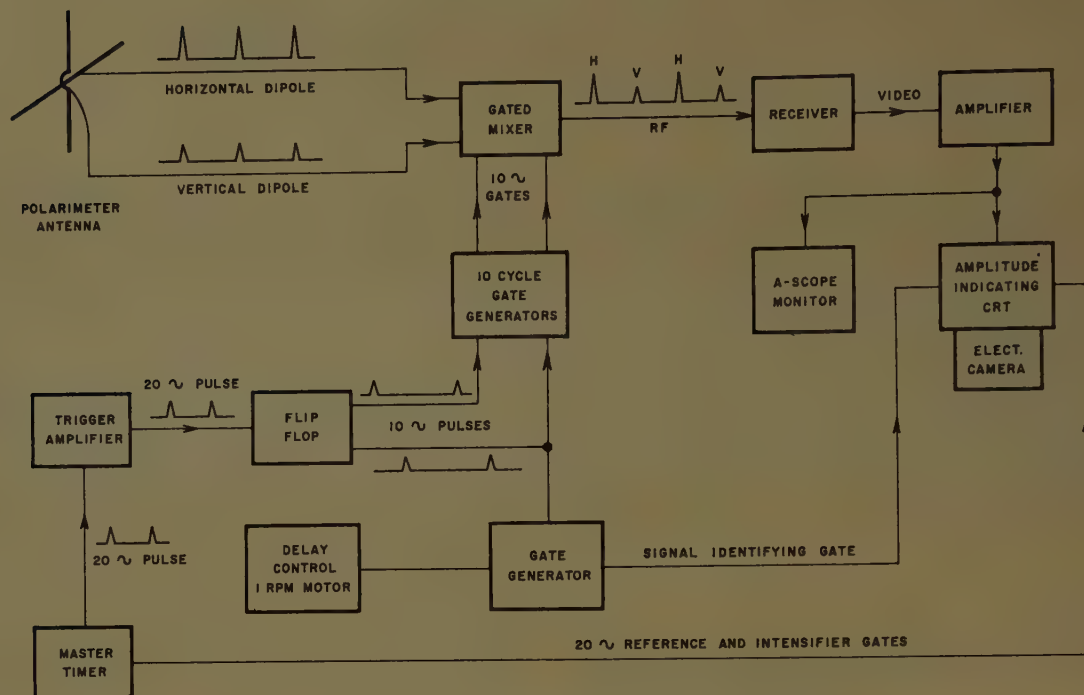


Fig. 1—Block diagram of polarization measurement system.

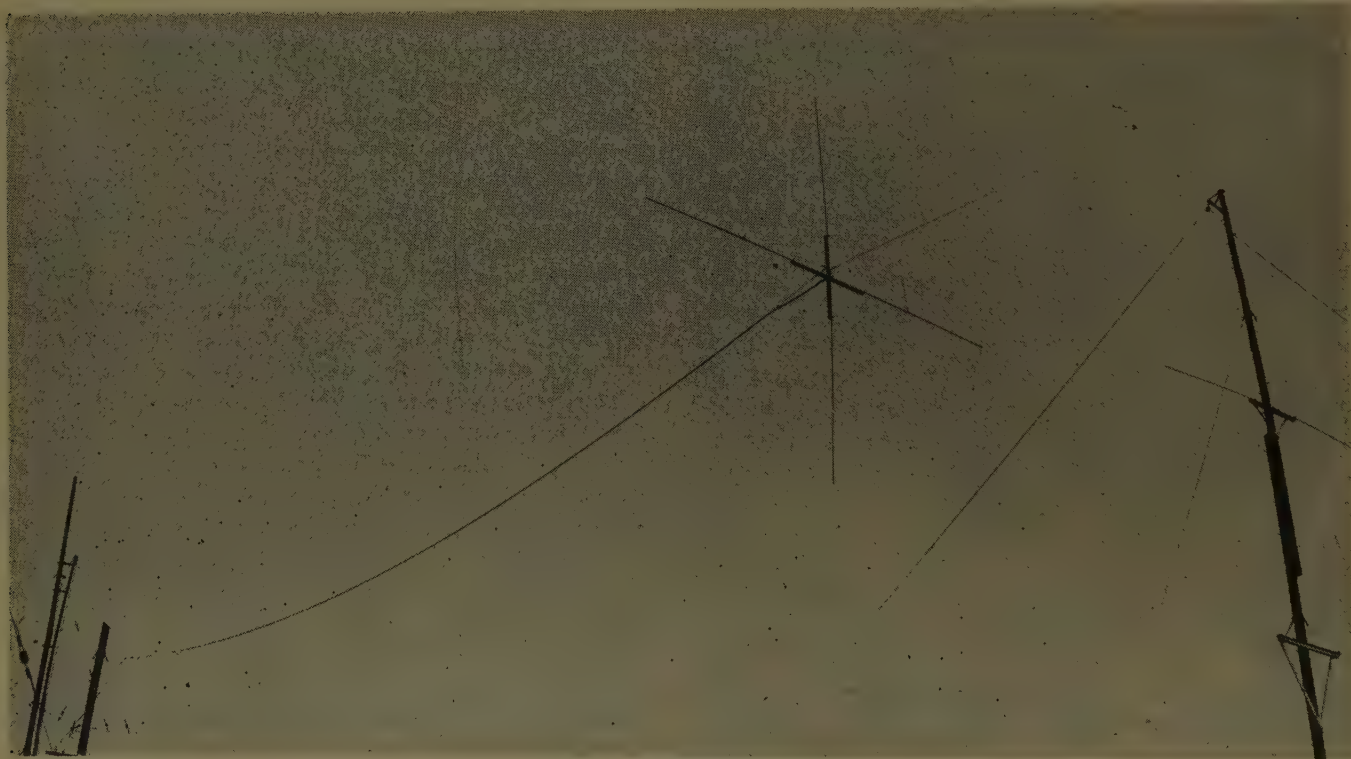


Fig. 2—Polarimeter antennas.

horizontal deflection plates of a crt. The deflection of the spot on the crt was proportional to the amplitude of the applied video signals. The tube was intensified for 10  $\mu$ sec near the center of the received pulse and, to provide a zero reference, for a short time when no signal was present. By continuously moving 35-mm film in front of the tube a record was obtained of the instantaneous variations in amplitude of both the horizon-

tally and vertically polarized components of the received signal. An identifying and timing pulse was applied at one-minute intervals to the signal from the vertical element to aid in data analysis.

Fig. 3 illustrates a sample of the data collected. The reference line is at the bottom and the two continuously varying lines represent the signals received on the horizontal and vertical elements of the polarimeter antenna.

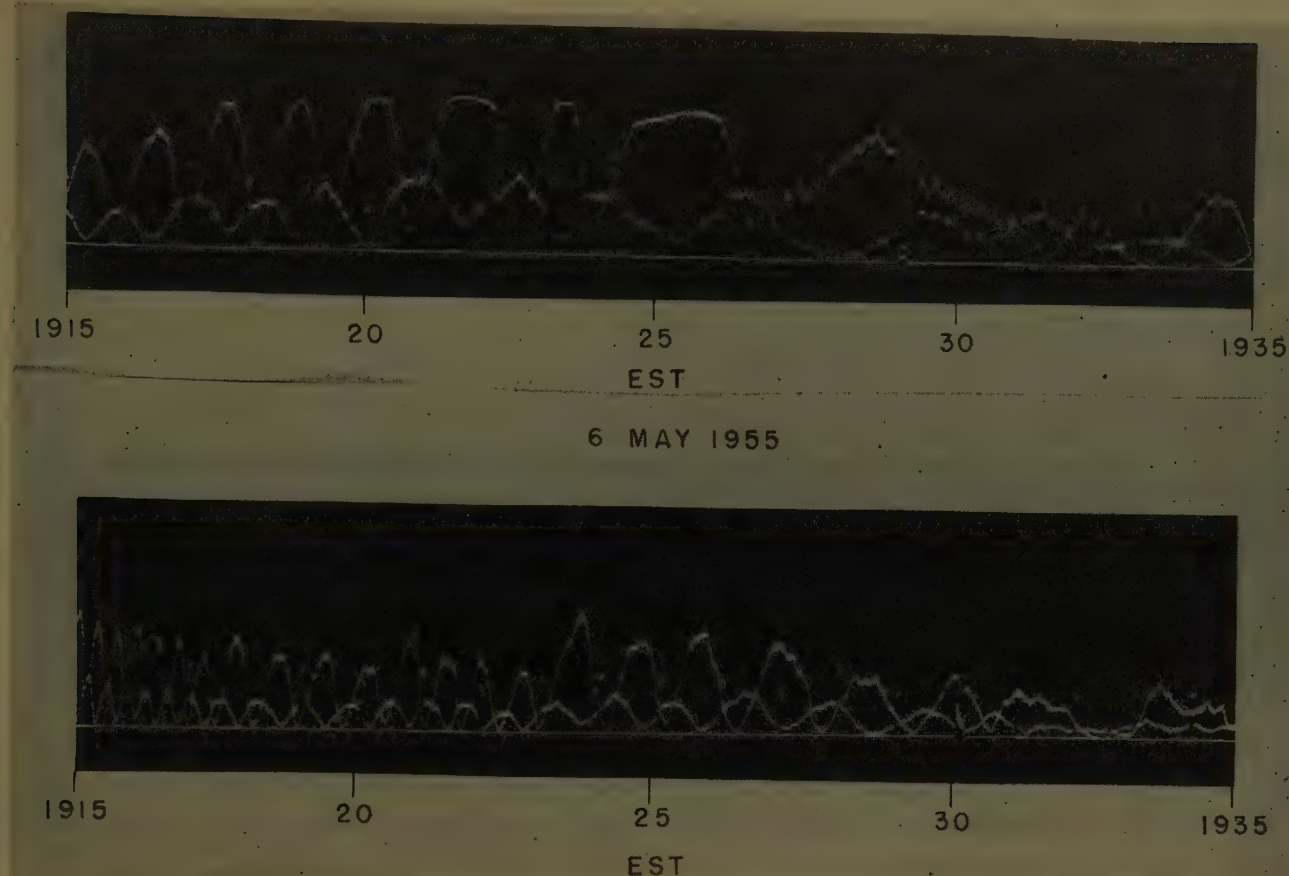


Fig. 3—Sample of typical recorded data. Note: Vertically polarized signal shown notched at one-minute intervals.

Note the notch which appears regularly in one of the lines identifying it as representing the output of the vertical element. It is evident from this record that variations are slow enough to be represented adequately by the 10-cycle sampling rate.

#### ANALYSIS OF DATA

Data were collected on the path during April and May, 1955. Of course, the path was open only in the daylight hours which limited the time of operation. Also, noise and interference, especially during the middle of the day when signal strength is lowest, made much of the data unusable. However, it is felt that sufficient quantities of good data were obtained to be representative of the path. The mode on which attention was focused was the one-hop F2 layer low angle ray. In general this mode could be easily identified at least when signals were strong enough for good recording. Of course when operating very near the MUF for the path, it was often impossible to resolve the low and high angle rays.

The actual strength of the incoming fields can be obtained from these records by application of suitable calibration constants and antenna directivity factors. The records were sampled at regular intervals and a statistical analysis showed that the average amplitudes of the horizontal and vertical components were essentially equal.

The instantaneous values, however, were found to be quite different. This is illustrated in Fig. 3 and particularly in Fig. 4 where the two components are seen to vary in almost exactly opposite fashion. The horizontal signal is seen to be maximum when the vertical is minimum and vice versa. Note also that the minima of both signals approach zero. This was found to be typical of a large percentage of all the data, and therefore, a special study was made to determine possible reasons for such behavior. The fading of the components suggests that the received signals are the result of two rays of different polarization and varying relative phases interfering at the antennas. The question then arises as to what characteristics of these two rays can be derived from the measurements performed.

Let us assume that there are two rays, each constant in amplitude and polarization. They can then be represented as shown below where the lower case letters indicate instantaneous values and the upper case letters amplitudes.

#### First Ray

$$e_x' = E_x' \cos \omega t$$

$$e_y' = E_y' \cos (\omega t + \phi').$$

#### Second Ray

$$e_x'' = E_x'' \cos (\omega t + \alpha)$$

$$e_y'' = E_y'' \cos (\omega t + \alpha + \phi''),$$



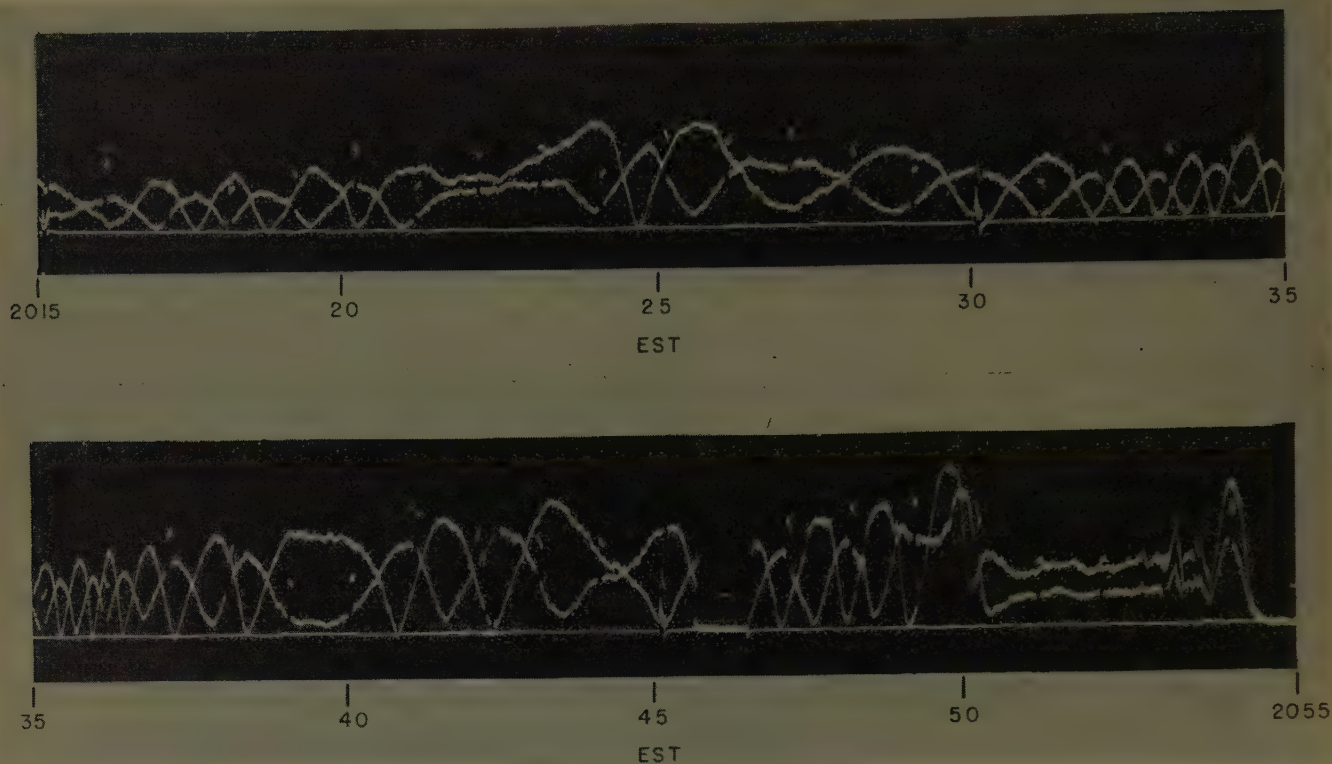


Fig. 4—Sample of data illustrating signal variations. Note: Vertically polarized signal shown notched at one-minute intervals.

The only variable other than time is the phase difference between the rays, namely  $\alpha$ . The polarization of each ray is determined by the relative amplitude of its horizontal and vertical components as well as the phase difference between them. Fading of the type shown earlier can then result from variations in  $\alpha$ .

The signal  $e_x$  received on the horizontal antenna will be the sum of the horizontal components of the individual rays.

#### Combined $x$ Component

$$e_x = e_x' + e_x'' = E_x \cos(\omega t + \psi_x)$$

$$E_x = \sqrt{E_x'^2 + E_x''^2 + 2E_x'E_x'' \cos \alpha};$$

similarly for the vertical component  $e_y$ .

#### Combined $y$ Component

$$e_y = e_y' + e_y'' = E_y \cos(\omega t + \psi_y)$$

$$E_y = \sqrt{E_y'^2 + E_y''^2 + 2E_y'E_y'' \cos(\phi'' - \phi' + \alpha)}.$$

It is seen now that the horizontal amplitude component  $E_x$  is a maximum when  $\alpha=0$  and a minimum when  $\alpha=180^\circ$ . The vertical amplitude component  $E_y$  is maximum when  $\phi'' - \phi' + \alpha = 0$  and a minimum when  $\phi'' - \phi' + \alpha = 180^\circ$ . Remembering that each component was a maximum while the other was a minimum, these expressions can be solved simultaneously, yielding the relationship that  $\phi'' - \phi' = 180^\circ$ . It is recalled that  $\phi''$  and  $\phi'$  are the phase differences between the vertical and horizontal components of the two rays.

Another interesting result regarding these rays can be derived from the data. Since the minima were very deep, often approximating zero, the similar components of the two rays must be nearly equal. In terms of these equations this means that  $E_x' \approx E_x''$  and  $E_y' \approx E_y''$ . Recalling that the average values of the resulting  $E_x$  and  $E_y$  are essentially the same and noting that  $E_x'$  and  $E_x''$  contribute equally to  $E_x$ , and  $E_y'$  and  $E_y''$  contribute equally to  $E_y$ , it is concluded that all four components are approximately the same. In other words,  $E_x' \approx E_x'' \approx E_y' \approx E_y''$ .

What does this mean regarding the polarization ellipses of the two rays? First, the major axes will be inclined at approximately  $45^\circ$  since the components are nearly equal. However, the two ellipses will be inclined on opposite sides of the vertical. This results from the fact that the phase angles  $\phi''$  and  $\phi'$  differ by  $180^\circ$ . This also results in ellipses which rotate in opposite directions. The exact shapes of the ellipses are not specified because the phase angles are unknown but possible polarizations of the rays are given in Fig. 5 for several values of  $\phi''$  and  $\phi'$ .

The polarizations that have been derived seem to agree quite well with descriptions of the ordinary and extraordinary rays resulting from the double refraction phenomena in the ionosphere. The magneto-ionic theory, at least in the case of no collision, predicts that the two ellipses will be  $90^\circ$  apart and will rotate in opposite senses.<sup>1</sup> Thus it seems reasonable to identify these rays as ordinary and extraordinary. The variations in  $\alpha$

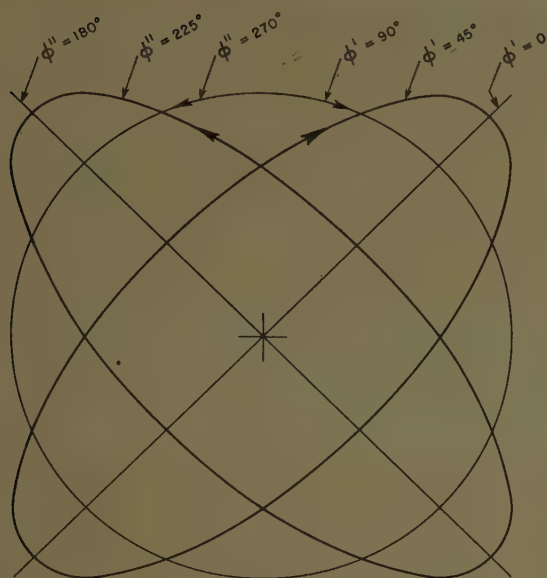


Fig. 5—Possible polarizations of received rays.

are undoubtedly caused by small changes in path length of one ray with respect to the other. It is interesting to compare these polarizations with those that might be expected from the magneto-ionic theory. If the limiting polarization,<sup>2,3</sup> that is, the polarization which the ray has when leaving the E layer, is assumed to be the same as that at the receiving site, the expected polarization can be computed.<sup>2</sup> In this case the direction of propagation of the downcoming ray makes an angle of  $105^\circ$  with the earth's magnetic field at the 100-km height. Neglecting the effects of collision, the polarization of the ordinary ray will be an ellipse whose major axis is tilted  $17^\circ$  out of the plane of incidence and whose ratio of major to minor axis is 1:23. The polarization of the extraordinary ray will be an ellipse of the same shape but with major axis tilted  $73^\circ$  on the other side of the plane of incidence.

These results of course differ from the ones obtained from the data which suggested axis tilts of  $45^\circ$  either side of the plane of incidence. However, these computed ellipses differ very little from circles for which the concept of axis tilt becomes meaningless. If these two

ellipses are assumed to be the ones interfering at the receiving antennas, the maximum signal occurring on the vertical element will be accompanied by one over 20 db less on the horizontal element and vice versa. Thus, in spite of the differences in computed and measured tilts, it seems reasonable to identify the received signals with the ordinary and extraordinary rays resulting from the double refraction effect of the ionosphere.

This identity is further substantiated by reference to Fig. 4 again. Note that the signal disappeared just before 2055 hours. At this time the skip distance moved across the beacon site. The fading is not present for the last five minutes. The skip is slightly longer for the ordinary ray than for the extraordinary ray. The ordinary ray evidently dropped out at 2050 hours. If so, only the extraordinary ray was present from 2050 to 2055. This perhaps accounts for the lack of fading during that period. A later attempt was made to observe these two rays independently when they would be separated by the greatest amount of time. This would occur when operating near the MUF. However, during the period of observation, conditions were never such that separate rays could be definitely identified. Nevertheless, it does seem likely that much of the fading occurring on linearly polarized antennas is of this type where minima of one polarization are accompanied by maxima of the other.

#### CONCLUSION

On the basis of these results it appears that polarization diversity should eliminate many of the deep fades present on linear antennas. This would certainly be the case when operating near enough to the MUF that one mode predominates and the ordinary and extraordinary rays are of comparable amplitude. However, even in those cases when several statistically independent modes are present, polarization diversity should be useful since there appears to be as much energy in the vertical signal as in the horizontal.

#### ACKNOWLEDGMENT

This work was done in connection with contracts sponsored by the Air Force Cambridge Research Center, Air Research and Development Command. Special thanks are due Dr. Phillip Newman of Air Force Cambridge Research Center and William A. Whitcraft, Jr. of Raytheon for their encouragement and assistance in making the material available for publication.

<sup>2</sup> H. Bremmer, "Terrestrial Radio Waves," Elsevier Press, Inc., New York, N. Y., pp. 321-322; 1949.

<sup>3</sup> S. K. Mitra, "The Upper Atmosphere," Asiatic Society, Calcutta, India, p. 207; 1952.





# A Two-Dimensional Slotted Array\*

G. C. McCORMICK†

**Summary**—A two-dimensional slotted array of which the radiating surface is one face of a parallel-plate region is discussed. This configuration differs from others previously reported in that a higher mode is utilized in the parallel-plate region. The array is equivalent thereby to a number of slotted waveguides parallel to each other. The stability of the desired mode requires that the array amplitude be uniform laterally; however, it may have an arbitrary taper longitudinally. The radiation field of the array is discussed with particular regard to the generation of second-order beams. The performance of several such arrays is described.

## INTRODUCTION

ONCE it was realized that a slot in a cavity or waveguide could be an efficient radiator, the further development into a linear array of slots followed rapidly.<sup>1,2</sup> A two-dimensional slotted array then could be obtained by placing slotted waveguides parallel to each other; and such a device, in fact, has been used in a practical antenna.<sup>2</sup> A basic difficulty in an array of this kind is the exterior coupling among the elements. The use of quarter-wave decoupling chokes has been considered.<sup>2</sup>

This paper treats a two-dimensional array of slots fed, not from parallel guides, but from a single waveguide of width sufficient to propagate a number of modes. The coupling problem can be dealt with, in certain special cases, by elementary image considerations. It will seem that higher mode operation unnecessarily complicates a problem, as yet unsolved, but certain practical considerations appear to justify the investigation of this case.

## THE PRINCIPLES OF OPERATION

Fig. 1 shows a broad waveguide excited in a higher mode, say  $TE_0$ . It will be observed that the fields in each of the four regions,  $AB$ ,  $BC$ ,  $CD$ , and  $DE$ , are the same as for a guide of one quarter the width operating in its lowest mode. The only physical difference is along the imaginary partitions  $BB'$ ,  $CC'$ ,  $DD'$ , where the currents are zero for the higher mode device. This may be of interest in exceptionally long arrays where ohmic losses are significant.<sup>3</sup>

Rows of slots are disposed along the lines of maximum field intensity as shown. Slots must be oppositely offset in adjacent rows on account of the phase reversal of the

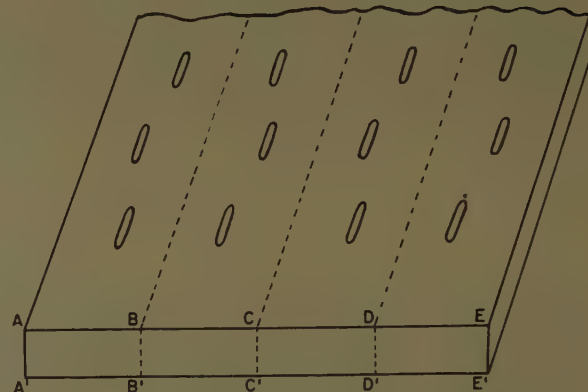


Fig. 1—Broad waveguide excited in a higher mode.

field. Slot admittances may be adjusted according to the well-developed practice for a single guide.<sup>2</sup> It now remains to consider the questions of mode stability and slot interaction.

It is supposed that initially only the desired mode is excited. A mixture of propagating modes is obviously undesirable. Their propagation constants are different and the slot spacing can be related to only one of them. Hence, if more than one mode were present the radiation from each would be directed toward different angles in space.

It is evident that in order to maintain only the desired mode along the course of the guide, energy must be abstracted equally in magnitude and phase from all parts of the regions  $AB$ ,  $BC$ , etc. In brief, the necessary and sufficient condition for the maintenance of the desired mode is that slot admittances be equalized laterally across the array. In this regard, the factor of primary importance which must be taken into consideration is that of slot interaction. Another matter of lesser concern is whether manufacturing tolerances are impractically restrictive.

The electric field in a slot is essentially perpendicular to the slot. As such it can be conceived of as originating from positive charges along one of its sides and equal negative charges along the other side. If offsets are equal and slot voltages equal laterally, it will be observed that the slot charges are symmetrically disposed, except for a sign reversal, about each of the nodal planes  $BB'$ ,  $CC'$ , etc. That is, each of these planes acts as a virtual image plane.<sup>4</sup> This arrangement is applicable

\* Original manuscript received by the PGAP, November 15, 1956; revised manuscript received, April 1, 1957.

† Radio and Electrical Eng. Div., Natl. Res. Council, Ottawa, Ont., Canada.

<sup>1</sup> A. L. Cullen and F. K. Goward, "The design of a waveguide-fed array of slots to give a specified radiation pattern," *J. IEE*, vol. 93, pp. 683-692; 1946.

<sup>2</sup> W. H. Watson, "Waveguide Transmission and Antenna Systems," Oxford University Press, New York, N.Y., p. 151; 1947.

<sup>3</sup> H. Gruenberg, "A waveguide array for solar noise studies," *IRE TRANS.*, vol. AP-3, pp. 147-152; October, 1954.

<sup>4</sup> Image plane considerations having some features in common with those presented here may be found, for example, in: H. A. Wheeler, "The radiation resistance of an antenna in an infinite array or waveguide," *Proc. IRE*, vol. 36, pp. 478-487; 1948, and G. Broussaud, "Étude de la diffraction des ondes électromagnétiques par un réseau de plaques percées de trous," *Ann. de Radioélectricité*, vol. 10, pp. 42-63; January, 1955.

both internally and externally. Therefore, for an infinitely long array, slot interaction is adequately accounted for by virtual conducting planes erected internally and externally along the lines  $BB'$ ,  $CC'$ , etc. Thus, the interior mode is effectively that which would be obtained with parallel guides, while each row of slots feeds into what is effectively a parallel-plate region having a width equal to the separation of the slot rows.

For the interior region, the sides  $AA'$ ,  $EE'$  are themselves the necessary image planes. In the exterior region, flanges must be erected as shown in the photographs, Figs. 2 and 3, to effect the lateral termination of the image plane system. Theoretically, for an ideally imaged system the flanges should be of infinite height. It is found in practice that the deterioration in the performance of the array may not be serious for flange heights as small as one-half wavelength.

The requirement so far imposed is that slot offsets and admittances be equal laterally. In the longitudinal direction they can be given any desired distribution; that is, the array amplitude will be uniform laterally, resulting in 22 per cent side lobes in  $E$  plane, but may have any desired taper in  $H$  plane. It should be noted, however, that the finite length of the flanges introduces errors in the admittances of slots near the two ends of the array. It is to be expected, therefore, that arrays requiring the critical adjustment of elements near the ends will be difficult to attain in practice. This consideration applies especially to the Dolph-Tchebycheff distribution and to a less extent to cosine squared distributions.

#### THE EXCITATION OF THE HIGHER MODE

The broad guide is easily excited in the higher mode by means of a slotted cross-guide feeding into one end. The cross-guide slots are cut in line; their offsets do not alternate across the center line as is the usual custom. The result is that adjacent regions in the broad guide are equally excited in opposite phase, which is the required condition of excitation. The slot admittance is the same as for a slot feeding into the end of the corresponding rectangular waveguide of width equal to the separation of the nodal planes.

Since the cross guide has low-power handling capacity, some other arrangement would have to be employed in devices using high power.

#### THE RADIATION FIELD OF A TWO-DIMENSIONAL ARRAY

The field due to electric and magnetic currents on a surface  $S$  is given by<sup>5</sup>

$$\begin{aligned} \vec{E}(X, Y, Z) \\ = 1/4\pi \int_S \left[ \frac{i}{\omega\epsilon} ((\vec{K} \cdot \nabla) \nabla + k^2 \vec{K}) \phi - \vec{K}^* \times \nabla \phi \right] da \quad (1) \end{aligned}$$

<sup>5</sup> J. A. Stratton, "Electromagnetic Theory," McGraw-Hill Book Co., Inc., New York, N.Y., p. 467; 1941.



Fig. 2—Two-dimensional array: displaced shunt slots.



Fig. 3—Two-dimensional array, feed withdrawn: inclined series slots.

where the electric and magnetic currents are,

$$\vec{K} = -\vec{n} \times \vec{H}$$

$$\vec{K}^* = \vec{n} \times \vec{E}$$

$\phi = \exp(ikr)/r$ , and  $\vec{n}$  points into the radiating surface.

When  $S$  is an infinite plane surface, it may be shown by Babinet's principle, or otherwise, that the electric and magnetic terms of (1) are equal and that

$$\vec{E}(X, Y, Z) = -1/2\pi \int_S (\vec{K}^* \times \nabla \phi) da. \quad (2)$$

A qualitative approach to the error in (2) for finite surfaces is possible from a comparison with (1), but a quantitative estimate is difficult. Eq. (2) has been used below for obtaining the distant field from the value of  $\vec{K}^*$  at the face of the flanges of a two-dimensional array, or from the value of  $\vec{K}^*$  at the face of the array itself when no flanges are present. Therefore, its accuracy may be expected to be about the same as when used for a horn of the same width. While some of the results below are extended to a linear slotted array, the error in (2) is much greater for this case.

The two-dimensional arrays under discussion will be like that shown in Fig. 4. It has two types of radiating elements, indicated by  $o$  and  $x$ , with equal spacings  $d$  and  $\sigma$  in the  $Y$  and  $X$  directions. First to be considered will be two basic arrays having distant fields  $f_{01}$  and  $f_{02}$  for the cases, respectively, of all elements identical in magnitude and phase and all elements identical in magnitude but with a phase reversal in going from one ele-



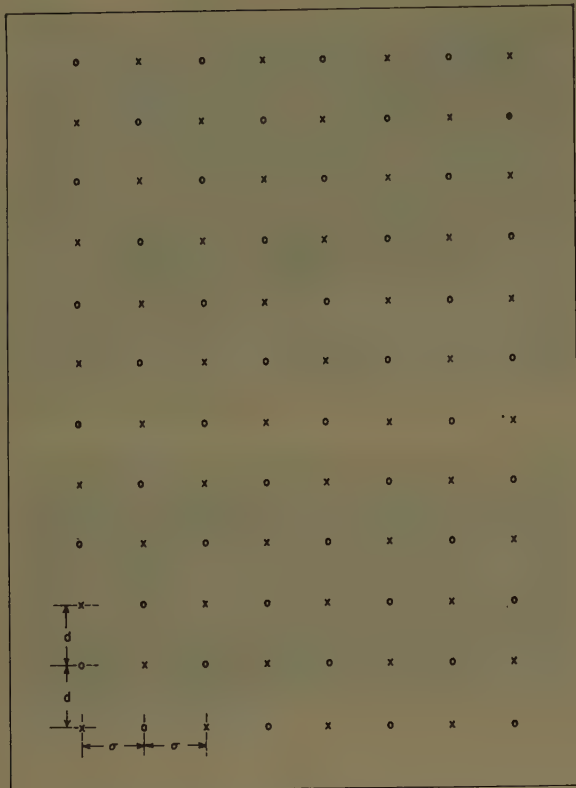


Fig. 4—A general two-dimensional array.

ment to an adjacent element. That is,  $\sigma = x$  in the first case, and  $\sigma = -x$  in the second.

$$f_{01} = \sum_i \exp \left[ -\frac{ik}{R} (x_i X + y_i Y) \right] \quad (3)$$

where  $(x_i, y_i)$  are co-ordinates of the  $i$ th radiator, and  $(X, Y, Z)$  are co-ordinates of the field point in a right-handed system with the origin at the lower left-hand element. The index  $i$  will be used to enumerate the two-dimensional set of radiating elements.

For the present, even numbers of radiators, respectively  $M$  and  $N$  in the  $X$  and  $Y$  directions, will be assumed. The summation in (3) gives<sup>6</sup>

$$f_{01} = \exp \left\{ -\frac{ik}{2R} [(N-1)dY + (M-1)\sigma X] \right\} \frac{\sin \left( \frac{kM\sigma X}{2R} \right) \sin \left( \frac{kNdY}{2R} \right)}{\sin \left( \frac{k\sigma X}{2R} \right) \sin \left( \frac{k d Y}{2R} \right)} \quad (4)$$

Similarly,

$$f_{02} = \sum_i (-1)^P \exp \left[ -\frac{ik}{R} (x_i X + y_i Y) \right] \quad (5)$$

where  $P$  is the number of intervals traversed from the origin to the radiator  $i$ . Completing the summation,

$$f_{02} = -\exp \left\{ -\frac{ik}{2R} [(M-1)\sigma X + (N-1)dY] \right\} \frac{\sin \left( \frac{kM\sigma X}{2R} \right) \sin \left( \frac{kNdY}{2R} \right)}{\cos \left( \frac{k\sigma X}{2R} \right) \cos \left( \frac{k d Y}{2R} \right)} \quad (6.1)$$

Alternatively,

$$f_{02} = \exp \left\{ -\frac{ik}{2R} [(M-1)\sigma X' + (N-1)dY'] \right\} \frac{\sin \left( \frac{kM\sigma X'}{2R} \right) \sin \left( \frac{kNdY'}{2R} \right)}{\sin \left( \frac{k\sigma X'}{2R} \right) \sin \left( \frac{k d Y'}{2R} \right)} \quad (6b)$$

where

$$X' = X \pm \frac{R\lambda}{2\sigma}, \quad Y' = Y \pm \frac{R\lambda}{2d}, \quad \lambda = \frac{2\pi}{k}$$

The dimensions of the array will be assumed such that  $\lambda/2 < d < \lambda$  and  $\lambda/2 < \sigma < \lambda$ .  $f_{01}$  is a two-dimensional grating pattern for  $MN$  radiators having a single first order.  $f_{02}$  has the same structure about the directions  $(X'/R, Y'/R)$  subject to  $(X'^2 + Y'^2)/R^2 \leq 1$ .

If the excitations of the individual elements are not all equal but are specified by the array factors,  $V_1(x, y)$  and  $V_2(x, y)$ , then the corresponding patterns will be

$$f_1 = \sum_i V_1(x_i, y_i) \exp \left[ -\frac{ik}{R} (x_i X + y_i Y) \right] \quad (7)$$

$$f_2 = \sum_i (-1)^P V_2(x_i, y_i) \exp \left[ -\frac{ik}{R} (x_i X + y_i Y) \right] \quad (8a)$$

$$= \sum_i \tilde{V}_2(x_i, y_i) \exp \left[ -\frac{ik}{R} (x_i X' + y_i Y') \right] \quad (8b)$$

It is clear from (8b) that if an aperture function  $V_2(x, y)$  has a distant field centered about  $(X_o, Y_o)$ , then  $f_2$  has maxima centered about,

$$\begin{aligned} X_o' &= X_o \pm (R\lambda)/(2\sigma) \\ Y_o' &= Y_o \pm (R\lambda)/(2d) \end{aligned} \quad (9)$$

The field of an actual slotted array will be expressed in terms of the vector potential,

$$\vec{F} = 1/4\pi \int (\vec{n} \times \vec{E}) \frac{\exp(i\vec{k} \cdot \vec{r})}{r} da$$

where

$$\vec{n} \times \vec{E} = \vec{e}(V_1/w) \cos \frac{\pi\eta}{l},$$

$\vec{e}$  is a unit vector along the length of the slot,  $V_1$  is the slot voltage,  $w$  the slot width,  $\eta$  the co-ordinate along the slot, and  $l$  the slot length.

<sup>6</sup> Ibid., p. 451.

The cases of inclined slots and longitudinal displaced slots will be treated separately. For displaced slots the vector  $\vec{e}$  is in the  $Y$  direction. The field in the plane of the array is a convolution of the slot field with the array excitation. Hence the vector potential in the distant field is given by,

$$F_y = F_{oo} \sum_i V_1(x_i, y_i) \cdot \exp \left\{ -\frac{ik}{R} [(x_i + (-1)^P \delta_i)X + y_i Y] \right\}$$

where  $\delta_i$  is the offset of the  $i$ th slot and  $F_{oo}$  is the vector potential in the distant field of a slot of unit voltage. Since  $k\delta_i$  is small, it follows that,

$$\begin{aligned} F_y &= F_{oo} \sum_i V_1(x_i, y_i) \exp \left[ -\frac{ik}{R} (x_i X + y_i Y) \right] \\ &\quad - \frac{ikXF_{oo}}{R} \sum_i (-1)^P V_1(x_i, y_i) \delta(x_i, y_i) \\ &\quad \cdot \exp \left[ -\frac{ik}{R} (x_i X + y_i Y) \right] \\ &= F_{1y} + F_{2y}, \end{aligned}$$

where  $F_{1y}$  and  $F_{2y}$  are fields of the types discussed above. In particular,

$$\begin{aligned} F_{1y} &= F_{oo} f_1 \\ F_{2y} &= -\frac{ikXF_{oo}}{R} f_2 \end{aligned} \quad (10)$$

where,  $V_2(x, y) = V_1(x, y)\delta(x, y)$ .

For inclined slots let the angle of inclination be  $(-1)^P \epsilon_i$ . If  $(R, \psi, \chi)$  are spherical co-ordinates about the  $Z$  axis, the field of a single slot equals  $F_{oo}(\psi, \chi - \chi_0) \vec{e}_1$  where  $\chi_0$ , the orientation of the slot in the aperture plane, equals  $(-1)^P \epsilon_i$ . Expanding in a Taylor's series and retaining only terms of first order in  $\epsilon_i$ ,

$$\begin{aligned} F_{oo}(\psi, \chi - \chi_0) &= F_{oo}(\psi, \chi) + \chi_0 \left( \frac{\partial F_{oo}}{\partial \chi} \right)_{\chi_0=0, R, \psi, \text{ constant}} \\ &= F_{oo}(\psi, \chi) - \chi_0 \left( \frac{\partial F_{oo}}{\partial \chi} \right)_{\chi_0=0, R, \psi, \text{ constant}} \\ F_{oo}(\psi, \chi) &= \frac{\exp(ikR)}{4\pi R} \int_{-1/2}^{1/2} \cos \frac{\pi\eta}{l} \frac{\exp(ikY\eta)}{R} d\eta \\ &= \frac{l}{2\pi^2} \frac{\exp(ikR)}{R} c(u) \end{aligned} \quad (11)$$

where

$$c(u) = \frac{\cos u}{1 - \left(\frac{2u}{\pi}\right)^2}, \quad u = \frac{\pi l}{\lambda} \cos \theta \quad \text{and} \quad (R, \theta, \phi)$$

is a spherical co-ordinate system about the  $Y$  axis. The co-ordinate systems are related as follows:

$$\begin{aligned} X &= R \sin \psi \sin \chi = R \sin \theta \sin \phi \\ Y &= R \sin \psi \cos \chi = R \cos \theta \\ Z &= R \cos \psi = R \sin \theta \cos \phi. \end{aligned} \quad (12)$$

Then

$$\begin{aligned} \left( \frac{\partial F_{oo}}{\partial \chi} \right)_{R, \psi} &= \left( \frac{\partial F_{oo}}{\partial (\cos \theta)} \right) \left( \frac{\partial (\cos \theta)}{\partial \chi} \right)_{R, \psi} \\ &= -\frac{l}{2} \frac{kX}{R} g(u) F_{oo} \end{aligned}$$

where

$$\begin{aligned} g(u) &= \frac{1}{c(u)} \frac{d}{du} (c(u)) \\ &= \frac{1}{(\pi/2) - u} - \frac{1}{(\pi/2) + u} - \tan u \end{aligned} \quad (13)$$

$$\begin{aligned} \therefore F_{oo}(\psi, \chi - (-1)^P \epsilon_i) \\ &= F_{oo} \left( 1 + (-1)^P \frac{\epsilon_i l}{2} \frac{kX}{R} g(u) \right) \end{aligned} \quad (14)$$

and,

$$\begin{aligned} F_{1y} &= F_{oo} f_1 \\ F_{2x} &= F_{oo} f_2 \\ F_{2y} &= \frac{l}{2} \frac{kX}{R} g(u) F_{oo} f_2 \end{aligned} \quad (15)$$

Eq. (2) may be rewritten,

$$\vec{E} = 2(\nabla \times \vec{F}) \quad (2b)$$

which in the distant field becomes,

$$\vec{E} = 2ik(\vec{R}_1 \times \vec{F}) \quad (16)$$

where  $\vec{R}_1$  is the unit radial vector.

The second-order beam  $\vec{T}$  will be defined as the ratio of the electric field of Type 2 to the maximum value of the electric field of Type 1. Using the approximation, (16),

$$\vec{T} = \frac{\vec{R}_1 \times \vec{F}_2}{(\vec{R}_1 \times \vec{F}_1)_{\max}} \quad (17)$$

$\vec{T}$  comprises in general, a direct polarized component  $\vec{\phi}_{1s}(\theta, \phi)$ , and a cross-polarized component  $\vec{\theta}_{1t}(\theta, \phi)$ .

The unit vector relationships between the relevant co-ordinate systems are given by,

$$\begin{aligned} \vec{j} &= \nabla Y = \vec{R}_1 \cos \theta - \vec{\theta}_1 \sin \theta \\ \vec{i} &= \nabla X = \vec{R}_1 \sin \theta \sin \phi + \vec{\theta}_1 \cos \theta \sin \phi + \vec{\phi}_1 \cos \theta. \end{aligned} \quad (18)$$

Then for longitudinal slots,



$$\begin{aligned} |\vec{R}_1 \times \vec{F}_1|_{\max} &= |\vec{R} \times j\vec{F}_{1y}|_{\max} = |\sin \theta F_{00} f_1|_{\max} \\ \vec{R}_1 \times \vec{F}_2 &= \vec{R}_1 \times j\vec{F}_{2y} = \vec{\phi}_1 (ik \sin^2 \theta \sin \phi F_{00} f_2). \end{aligned}$$

Therefore,

$$\begin{aligned} s(\theta, \phi) &= k \frac{\sin^2 \theta \sin \phi F_{00} f_2}{|F_{00} f_1 \sin \theta|_{\theta=\theta_0}} \\ l(\theta, \phi) &= 0, \end{aligned} \quad (19)$$

where  $\theta = \theta_0$  specifies the angle at which the main beam has its maximum value.

For inclined slots,

$$\begin{aligned} |\vec{R}_1 \times \vec{F}_1|_{\max} &= |\vec{R}_1 \times j\vec{F}_{1y}|_{\max} = (\sin \theta F_{00} f_1)_{\theta=\theta_0} \\ \vec{R}_1 \times \vec{F}_2 &= (\vec{R}_1 \times (i\vec{F}_{2x} + j\vec{F}_{2y})) \\ &= \vec{\phi}_1 F_{00} f_2 \sin \phi \left( \cos \theta - \frac{\pi l}{\lambda} g(u) \sin^2 \theta \right) \\ &\quad - \vec{\phi}_1 \cos \phi F_{00} f_2 \\ &\quad \sin \phi \left( \cos \theta - \frac{\pi l}{\lambda} g(u) \sin^2 \theta \right) F_{00} f_2 \\ \therefore s(\theta, \phi) &= \frac{\sin \phi \left( \cos \theta - \frac{\pi l}{\lambda} g(u) \sin^2 \theta \right) F_{00} f_2}{|F_{00} f_1 \sin \theta|_{\theta=\theta_0}} \\ l(\theta, \phi) &= - \frac{\cos \phi F_{00} f_2}{(F_{00} f_1 \sin \theta)_{\theta=\theta_0}}. \end{aligned} \quad (20)$$

However,

$$\frac{F_{00}}{(F_{00} f_1 \sin \theta)_{\theta=\theta_0}} \approx \frac{c(u)}{\sum V_i},$$

and if it is further assumed that  $l = \lambda/2$ , (19) and (20) reduce to the following:

$$\begin{aligned} s(\theta, \phi) &= \frac{2\pi}{\lambda} \frac{\sin \phi \cos u f_2}{\sum V_i} \\ l(\theta, \phi) &= 0 \end{aligned} \quad (21)$$

and

$$\begin{aligned} s(\theta, \phi) &= \frac{\sin \phi \left[ \frac{\pi}{2} \sin u - \frac{2}{\pi} u c(u) \right] f_2}{\sum V_i} \\ l(\theta, \phi) &= \frac{\cos \phi c(u) f_2}{\sum V_i} \end{aligned} \quad (22)$$

where

$$u = \frac{\pi}{2} \cos \theta, \quad c(u) = \frac{\cos \left( \frac{\pi}{2} \cos \theta \right)}{\sin^2 \theta}.$$

Eqs. (21) and (22) lend themselves both to a useful physical picture of the nature of second-order beams and to an easy numerical estimate of their position and magnitude. In these expressions there is the term  $f_2(\theta, \phi)$ . The field  $f_2$  is that of an array of elements of

alternated phase having an array function equal to that of the array multiplied by the excitation parameter. It therefore depends on the size of the array, the array function, and the excitation parameter. It can be visualized as a four-pronged pattern of lobe width basically determined by the size of the array, but widened due to: 1) the additional taper resulting from multiplication by the excitation parameter; and 2) the oblique angle which the beams make to the array normal. The oblique angle is especially significant with respect to variation in  $\phi$ ; for if the main beam radiates in the plane  $\phi = 0$ , the second-order beams will lie near  $\phi = 90^\circ$ .

If the array is fed by radiation traveling in the positive  $Y$  direction with propagation constant  $k_g = (2\pi)/\lambda_g$ ,

$$V_1 = |V_1| \exp \left[ i \left( k_g - \frac{\pi}{d} \right) y \right]$$

and where  $(\theta_0, \phi_0)$  specify the position of the main lobe of  $f_1$  and  $(\theta', \phi')$  the positions of the lobes of  $f_2$ , then it follows that

$$\cos \theta_0 = (\lambda/\lambda_g) - (\lambda/2d) \quad (23)$$

and from (9),

$$\cos \theta' = (\lambda/\lambda_g), \text{ or } (\lambda/\lambda_g) - (\lambda/d) \quad (24)$$

and

$$\sin \phi' = \pm \frac{\lambda/2\sigma}{\sin \theta'} \quad (25)$$

For the higher mode array previously discussed

$$\frac{\lambda}{\lambda_g} = \sqrt{1 - (\lambda^2/4\sigma^2)},$$

and of the values of  $\phi'$  which satisfy (25), the two in the forward direction ( $\theta < 90^\circ$ ) are given by

$$\phi' = \pm \frac{\pi}{2}.$$

The other two values are or are not possible, according to whether  $\cos \theta_0 \geq 0$ .

The principal maxima of  $f_2$  can be located now.  $\theta'$  is normally in the neighborhood of  $45^\circ$  and  $135^\circ$ . For the forward maxima ( $\theta' \approx 45^\circ$ ),  $\phi' = \pm 90^\circ$ ; that is, the maxima lie in the plane of the array for all slot spacings. The maxima to the rear for resonant spacing,  $1/(4\sigma^2) + 1/(4d^2) = 1/\lambda^2$ , are also given by  $\phi' = \pm 90^\circ$ . For  $1/(4d^2) + 1/(4\sigma^2) < 1/\lambda^2$ , there are two maxima to the rear at  $|\phi'| < 90^\circ$ . If  $1/(4\sigma^2) + 1/(4d^2) > 1/\lambda^2$ , there are no maxima to the rear, and the second-order power is radiated mainly into the forward lobes.

For a two-dimensional array using multiple guides, (23) to (25) must be used with the additional relation,

$$\frac{\lambda}{\lambda_g} = \sqrt{1 - \lambda^2/(4a^2)}$$

and the results obtained will be slightly different.

Since for practical arrays  $f_2$  has the maximum value  $\sum_i V_i \delta_i$  for longitudinal slots and  $\sum_i V_i \tan \epsilon_i$  for inclined slots, an estimate of the maximum value of the second-order beams may be obtained by substitution in (21) and (22). For the direct polarized beams, using a  $\theta = 45^\circ$ ,  $\phi = 90^\circ$ ,

$$s_{\max} \approx 2.8 \frac{\sum_i V_i \frac{\delta_i}{\lambda}}{\sum_i V_i} \quad (27)$$

for longitudinal slots, and

$$s_{\max} \approx 0.78 \frac{\sum_i V_i \tan \epsilon_i}{\sum_i V_i} \quad (28)$$

for inclined slots.

No similar formula can be given, in general, for  $t_{\max}$ . However, for a single row of slots, using  $\theta = 45^\circ$ ,  $\phi = 0^\circ$ ,

$$t_{\max} \approx 0.89 \frac{\sum_i V_i \tan \epsilon_i}{\sum_i V_i} \quad (29)$$

Eqs. (27) and (29) apply for slots in an infinite plane and are not directly applicable to an array of slots in a single waveguide. For the latter, (27) may be compared with the formula given by Gruenberg,<sup>7</sup>

$$s_{\max} = 1.5 \frac{\delta}{\lambda} \quad (30)$$

Substituting  $\theta = 90^\circ$ ,  $\phi = 45^\circ$ , a single row of slots in the  $x$  direction, corresponding to an array of edge-cut slots, gives

$$t_{\max} \approx 0.71 \frac{\sum_i V_i \tan \epsilon_i}{\sum_i V_i} \quad (31)$$

#### ARRAY IN A PARALLEL-PLATE REGION

The preceding discussion of the radiation field of an array has referred to a plane array without the flanges shown in Figs. 2 and 3. With the flanges the radiation field becomes a problem of an array radiating into a parallel-plate region of width  $M\sigma$ . The derivation of the complete fields within the region (neglecting those generated by currents on and outside the edges of the flanges) is a straightforward but lengthy procedure, and the results will be quoted without derivation. The exterior fields which result (neglecting edge currents) when flanges of height  $w$  are introduced on arrays of either longitudinal or inclined slots are obtained simply by making the following substitutions for the fields  $f_1$  and  $f_2$ ,

$$f_1 \rightarrow f_1 s \left( \frac{\pi \sigma}{\lambda} \sin \theta \sin \phi \right)$$

$$f_2 \rightarrow \frac{4}{\pi} f_2 c \left( \frac{\pi \sigma}{\lambda} \sin \theta \sin \phi \right) \exp [ik(\gamma - 1)w] \quad (32)$$

where

$$s(u) = (\sin u)/u, \quad c(u) = (\cos u)/1 - \left( \frac{2u}{\pi} \right)^2,$$

$$\gamma = \sqrt{\sin^2 \theta - (\lambda/2\sigma)^2}.$$

At the position of the second-order beams substitution of  $\theta = \theta'$  from (24) leads to

$$\gamma' = \sqrt{1 - (\lambda/\lambda_g)^2 - (\lambda/2\sigma)^2} \text{ or}$$

$$\sqrt{1 - (\lambda/\lambda_g - \lambda/d)^2 - (\lambda/2\sigma)^2} \quad (33)$$

Examination of (33) will determine whether, through a suitable choice of parameters, the second-order beams can be suppressed by rendering  $\mu'$  imaginary. It will be noted, incidentally, that (33) gives the attenuation constant of second-order beams for a linear array radiating into a parallel-plate region of width  $\sigma$ .

#### EXPERIMENTAL RESULTS

A broad waveguide, 3.6 inches  $\times$  0.4 inches, was made up to accommodate a two-dimensional array, 4 slots by 10 slots. Three interchangeable plates, two shunt-cut and one series-cut, were used with the assembly, various components of which are shown in the photographs, Figs. 2 and 3. The arrays are all resonant at the design frequency, 9270 mc. The feed is also a resonant section, four slots in length, with the slots radiating in antiphase.

The use of flanges 1.1 inches in height was regarded as standard procedure. Patterns were also taken with no flanges, and with flanges of height 0.5 inch.

Fig. 5 shows a typical curve of vswr vs frequency. No

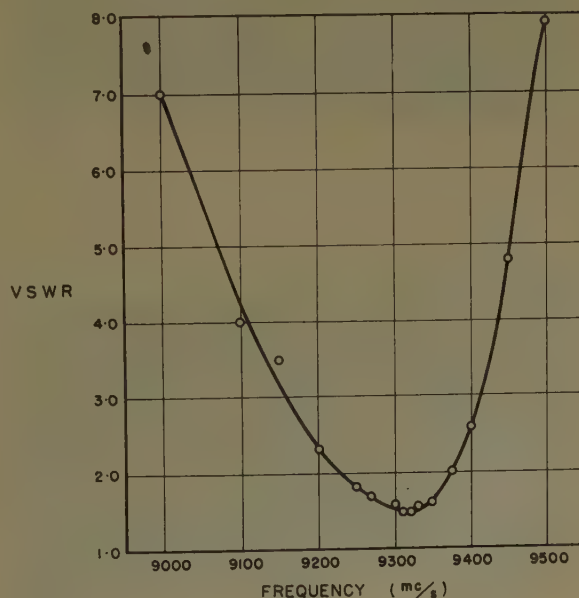


Fig. 5—VSWR vs frequency (Plate No. 3).

<sup>7</sup> H. Gruenberg, "Second-order beams of slotted waveguide arrays," *Can. J. Phys.*, vol. 31, pp. 55-69; January, 1953.



attempt was made in the design of the array to obtain an exact match. The positioning of the feed need not be very precise. Its displacement by  $\pm 0.025$  inch produces only a slight change in the array performance.

Plate No. 1, using displaced (shunt) slots, consisted of one slot with zero offset, followed by nine cut to a 7 per cent Dolph-Tchebycheff taper. The first slot was intended to explore the extent of extraneous modes; the radiation from it appeared to be very slight. Plate No. 2, using displaced slots, was cut to a cosine taper. Plate No. 3, using inclined (series) slots, was also cut to a cosine taper.

Patterns<sup>8</sup> for the three plates with and without flanges are shown in Figs. 6 to 12. The theoretical beamwidths at half-amplitude for the cosine patterns are  $13.2^\circ$  in the  $H$  plane and  $24.6^\circ$  in  $E$  plane. It will be noted that the measured beamwidths are about  $0.5^\circ$  less in each case. The side-lobe characteristics of the patterns in  $H$  plane differ appreciably from those based on the aperture design function. This is probably due to phase error since with inadequate information regarding resonant slot lengths, all slots were given the same

<sup>8</sup> One main division equals one-half inch on all original patterns.

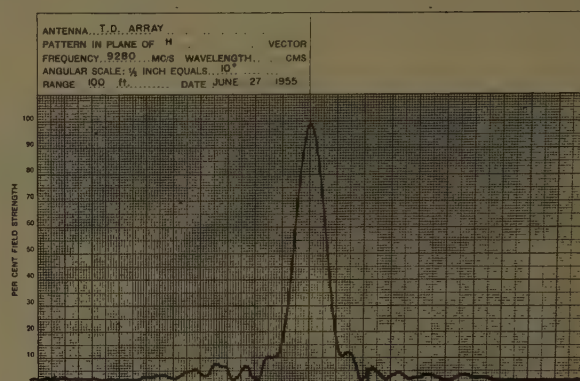
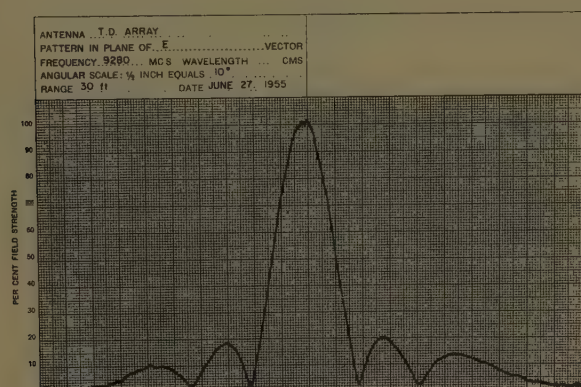


Fig. 6—Radiation patterns,<sup>8</sup>  $E$  and  $H$  planes (Plate No. 1) 1.1-inch flanges.

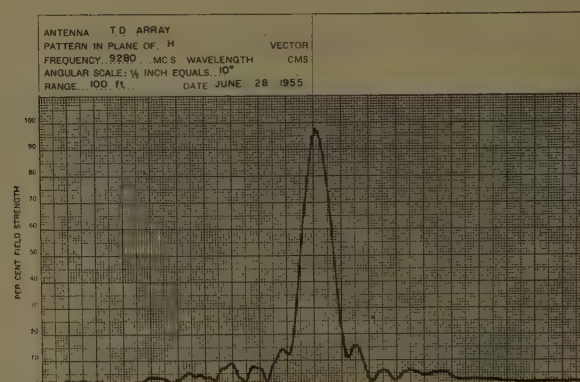
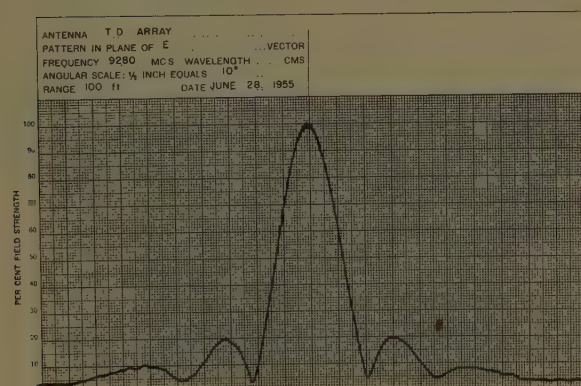


Fig. 7—Radiation patterns,  $E$  and  $H$  planes (Plate No. 1) 0.5-inch flanges.

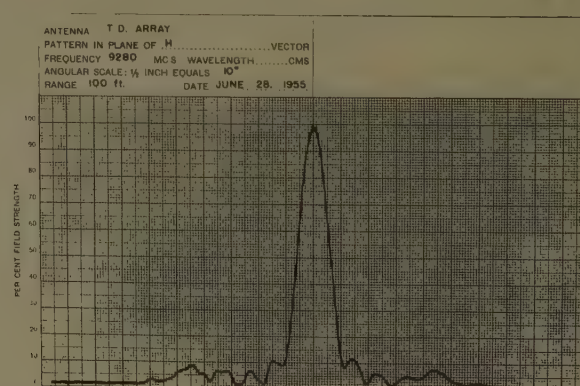
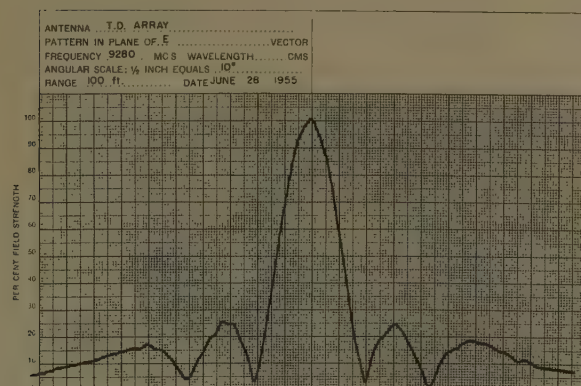
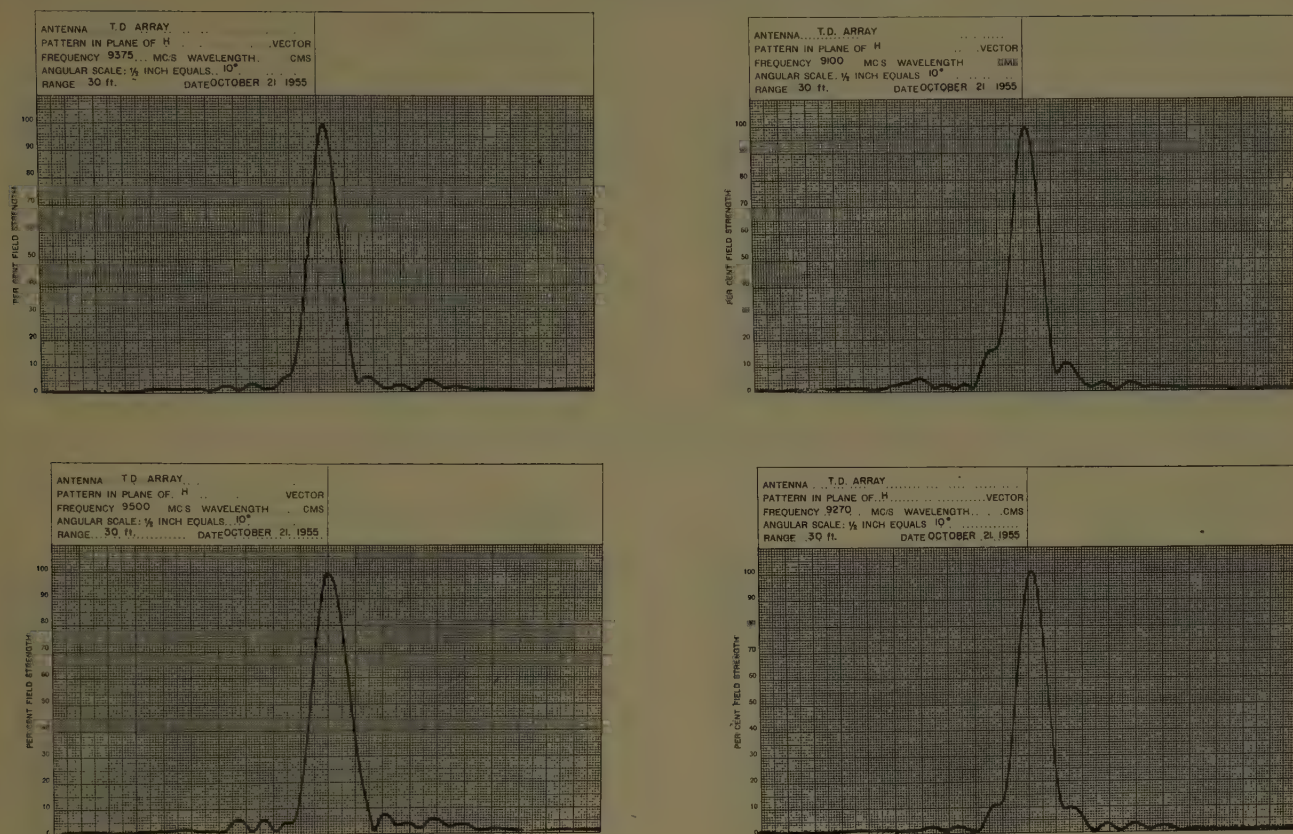
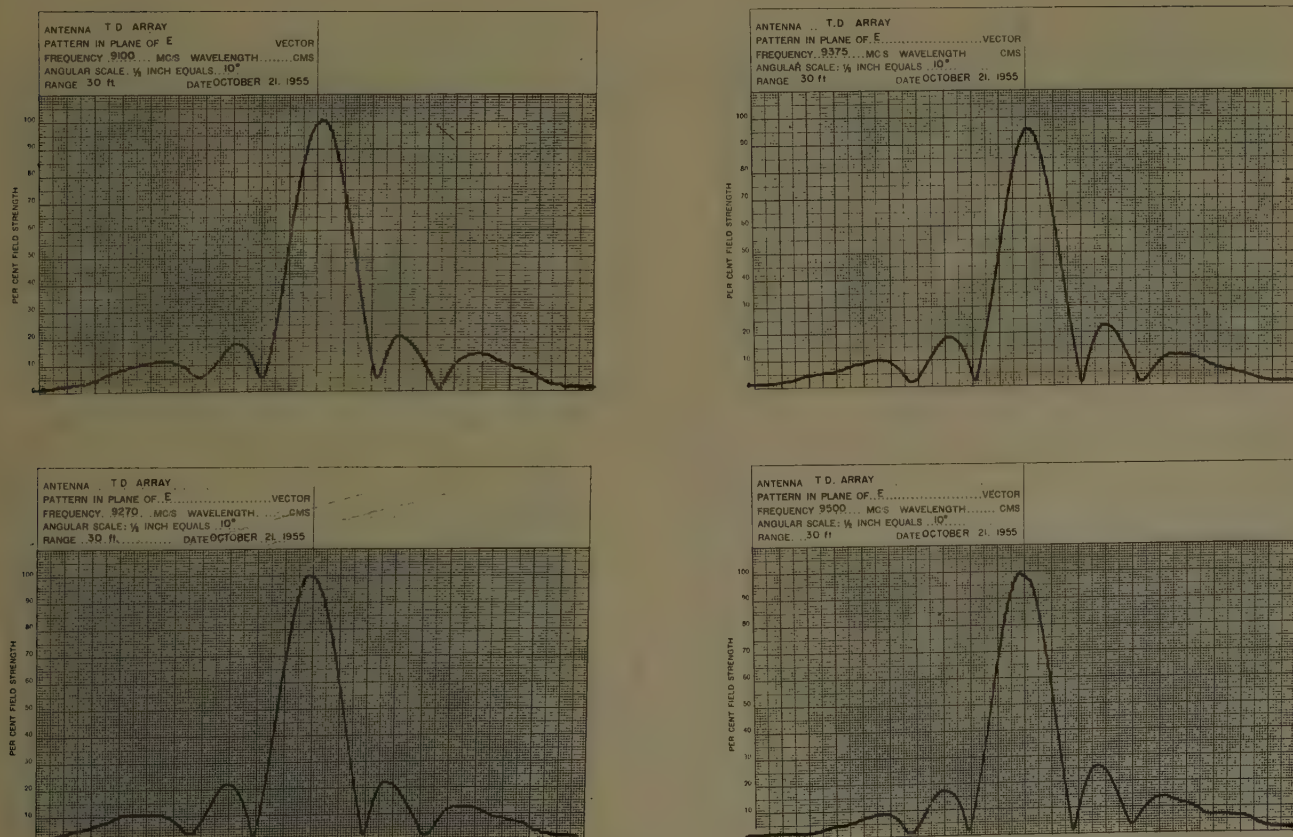
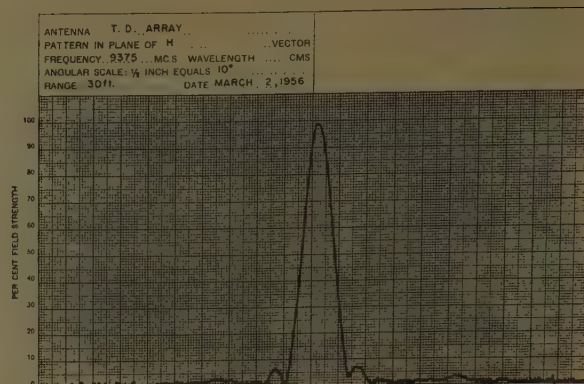
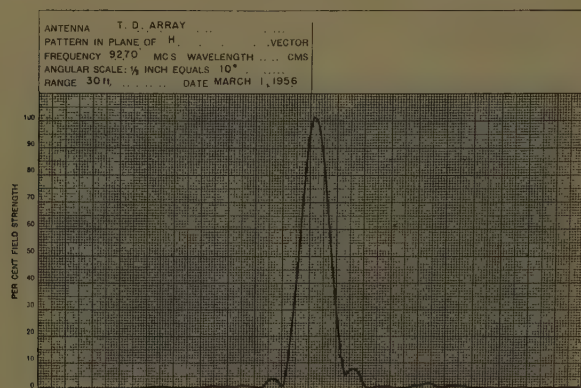
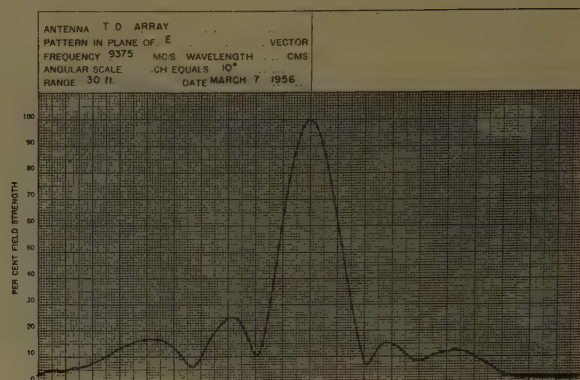
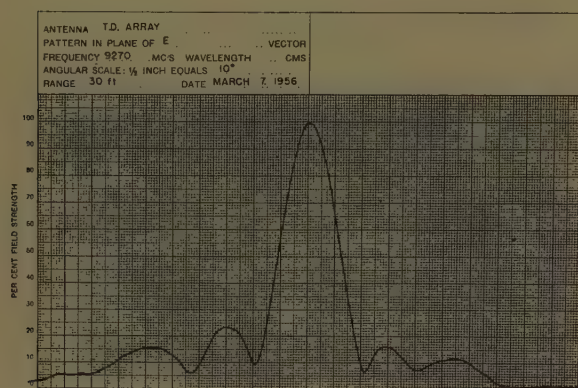
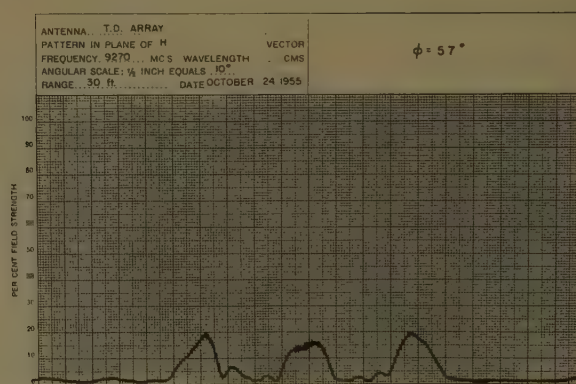
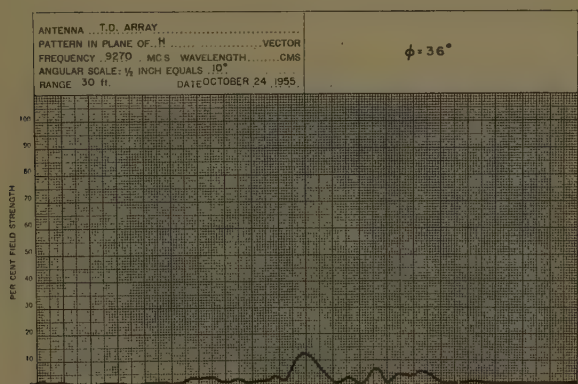


Fig. 8—Radiation patterns,  $E$  and  $H$  planes (Plate No. 1) no flanges.



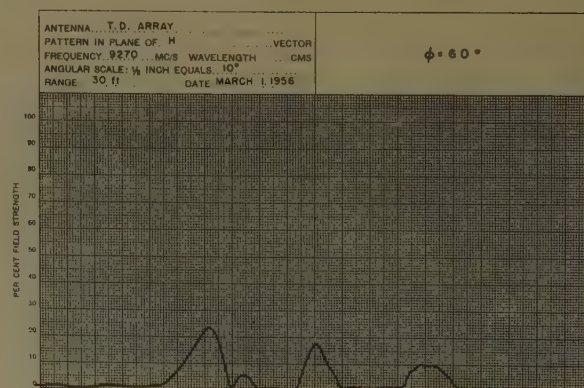
Fig. 9—Radiation patterns, *H* plane (Plate No. 2).Fig. 10—Radiation patterns, *E* plane (Plate No. 2).



Fig. 11—Radiation patterns,  $H$  plane (Plate No. 3).Fig. 12—Radiation patterns,  $E$  plane (Plate No. 3).Fig. 13—Second-order beams, direct-polarized (Plate No. 2) normalized to main lobe amplitude equals 100 per cent,  $\phi = 36^\circ$  and  $\phi = 57^\circ$ 

length. In  $E$  plane the pattern is very close to the ideal for a uniform array in the case of Plate No. 2, but differs appreciably for Plate No. 3. The asymmetry of the latter would suggest that mechanical imperfections were present.

Second-order beams, both direct-polarized and cross-polarized, were observed in substantial agreement with the preceding section. Typical patterns are shown in Figs. 13 to 15. Eq. (27) gives a value of  $s_{\max} = 14.7$  per cent. The observed value was 10 per cent for the array without flanges and 19 per cent with flanges. In the latter case, the parallel-plate region is resonant to the mode from which the second-order beams originate. Distortion of these beams can, therefore, be expected.

Fig. 14—Second-order beams, direct-polarized (Plate No. 3), normalized to main lobe amplitude equals 100 per cent,  $\phi = 60^\circ$ .



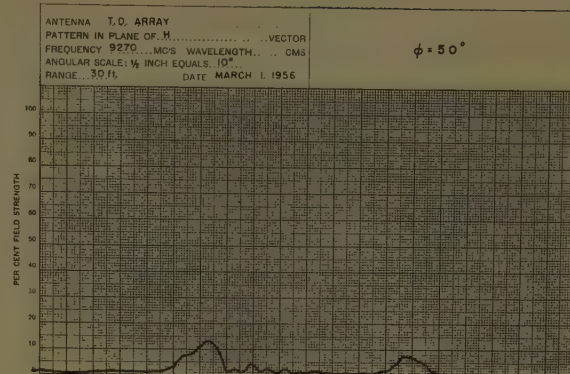
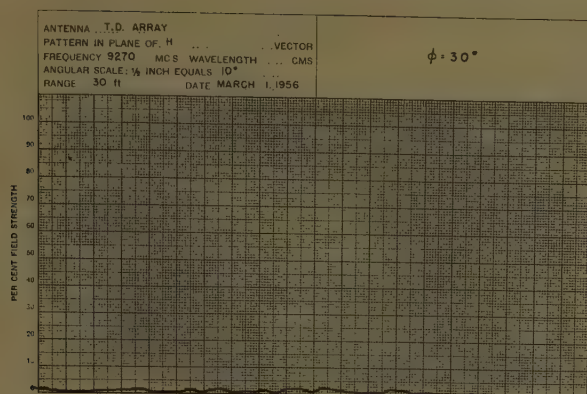


Fig. 15—Second-order beams cross polarized (Plate No. 3) normalized to main lobe amplitude equals 100 per cent,  $\phi = 30^\circ$  and  $\phi = 50^\circ$ .

### CONCLUSION

It is possible to construct a two-dimensional slotted array fed from a parallel-plate region, subject to the condition that the aperture function in one direction be uniform.

### ACKNOWLEDGMENT

The author expresses to Dr. G. A. Miller his appreciation for suggesting that the project be undertaken, and for his continued interest. Thanks are extended to Dr. H. Gruenberg for reading the original manuscript.

## Shunt and Notch-Fed HF Aircraft Antennas\*

ROBERT L. TANNER†

**Summary**—In the hf range radiation from aircraft must be accomplished by exciting radiating currents on the airframe itself. One method of exciting such currents is by shunts or notches which electrically penetrate the airframe.

The strength of coupling of such devices is analyzed and shown to be proportional to the square of the normal mode current which they interrupt.

A theory is developed and substantiated by experimental data, which enables the prediction of the impedance characteristics of such antennas. It is shown that these antennas are most effective when located in a region of high current concentration, and that the current concentration which occurs in the fillet area of swept-wing aircraft makes this area particularly favorable for their installation.

Shunt and notch antennas, when they can be used, have a number of structural advantages over cap-type antennas, and certain electrical advantages also. They require no special lightning protection and eliminate the need for special isolating devices. In general, they are capable of handling higher powers before encountering high-altitude voltage breakdown.

### INTRODUCTION

IN THE hf range the dimensions of most aircraft are comparable with a wavelength so that any type of antenna, including the fixed wire antennas which for many years were the standard hf aircraft antenna, tends to excite currents on the airframe itself. With the

advent of high speed aircraft, the possibilities for reducing drag which are afforded by an antenna which excites the airframe without resort to external structure have appealed strongly to aircraft designers. Basically, only two methods for accomplishing excitation are possible. These may be compared with the voltage probe and the current loop used to feed cavity resonators. The counterpart of the voltage probe is the cap-type antenna which has been used successfully on several aircraft of recent design. In the cap antenna excitation is accomplished by isolating one of the extremities of the aircraft and applying the driving voltage to the isolated portion. The principal characteristics of cap-type antennas are described by Granger.<sup>1</sup>

Aircraft antennas in which coupling is accomplished magnetically, corresponding to the loop coupling used in resonators, are the so called shunt- and notch-fed antennas.<sup>2-4</sup>

<sup>1</sup> J. V. N. Granger, "Wing-Cap and Tail-Cap Aircraft Antennas," Stanford Res. Inst. Tech. Rep. no. 6, Proj. 188, AF Contract No. AF 19(122)-78; March, 1950.

<sup>2</sup> J. V. N. Granger, "Shunt-excited flat-plate antennas with applications to aircraft structures," *Proc. IRE*, vol. 28, pp. 280-287; March, 1950.

<sup>3</sup> J. V. N. Granger and J. T. Bolljahn, "Aircraft antennas," *Proc. IRE*, vol. 43, pp. 533-550; May, 1955.

<sup>4</sup> W. L. Jones, "Notch Coupling to the Electromagnetic Resonances of a Delta Wing Aircraft," Stanford Res. Inst. Tech. Rep. no. 53, Contract AF 19(604)-266; December, 1955.

\* Original manuscript received by the PGAP, October 4, 1956; revised manuscript received, April 11, 1957. This work was supported by the U. S. Air Force under Contract No. AF 19(604)-1296.

† Stanford Research Institute, Menlo Park, Calif.



Although most flush mounted hf antennas which have so far been installed on operating aircraft have been tail caps, shunt and notch-fed installations have been proposed from time to time. Unfortunately, an inadequate understanding of the true nature of the mechanism by which the notch or shunt couples to the airframe currents has resulted in the proposal of feed configurations considerably less satisfactory than might otherwise have been achieved. Inadequate understanding has also been responsible for some inaccurate claims having been made for such methods of feed. It is hoped that the present paper will provide the information necessary to arrive at designs more nearly approaching the optimum and to appraise better the merits of shunt and notch-fed antennas relative to other types of antennas.

### CRITERIA FOR COMPARING HF ANTENNAS

To evaluate different antennas, we must have a set of criteria by which they can be compared. One important criterion is radiation pattern behavior. For hf antennas pattern behavior can be compared on the basis of radiation pattern efficiency as defined by Moore.<sup>5</sup> The pattern efficiency of an antenna is a measure of the proportion of total radiated power directed by the antenna into useful angular sectors.

Other quantities of importance in evaluating antennas are their efficiencies, the efficiencies of the circuits required to match them, and their relative susceptibilities to voltage breakdown. It can be shown that all of these characteristics are improved by increasing the ratio of antenna radiation resistance to antenna reactance. Since radiation is due to currents excited on the airframe, it is evident that the radiation resistance is increased by increasing the degree of coupling between the antenna feed and the airframe currents. The reactance component of the impedance, on the other hand, is associated to a very large extent with the local fields in the vicinity of the feed. It follows, therefore, that the performance of the antenna will be improved in all the respects mentioned if the strength of coupling is increased.

### ANALYSIS OF COUPLING MECHANISM

The mechanism of coupling in notch and shunt-fed antennas is most easily analyzed in terms of the two-terminal-pair equivalent network shown in Fig. 1. The admittance coefficients for the network,  $Y_{11}$ ,  $Y_{22}$ , and  $Y_{12}$ , are defined in the usual way:  $Y_{11}$  is the admittance at Terminals 1 with Terminals 2 shorted and similarly for  $Y_{22}$ , while  $-Y_{12}$  is the value of  $I_2$  with Terminals 2 shorted and unit voltage applied to Terminals 1 or vice versa. It will be observed that if Terminals 1 are shorted and a current  $I_2$  impressed at Terminals 2, that for the current directions and admittances as defined in Fig. 1,

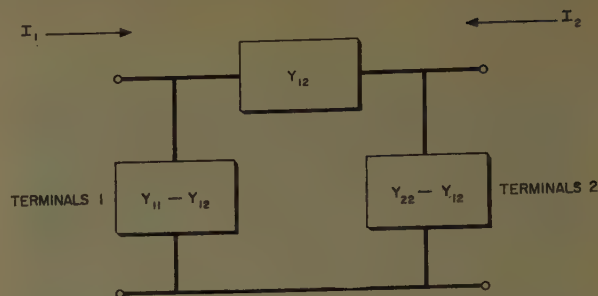


Fig. 1—Equivalent circuit for analysis of coupling mechanism.

we can write the relation

$$\frac{I_1}{I_2} = -\frac{Y_{12}}{Y_{22}} \quad (1)$$

To relate the equivalent circuit of Fig. 1 to the actual antenna feed, consider the notch-fed plate shown in Fig. 2. The plate may be considered as an idealization of a notch fed wing for which Terminals 1 are the notch feed terminals. Assume that a total linear current  $I_2$  is excited on the plate by some outside agency. If the width of the plate is small relative to a wavelength, the current will distribute itself across the plate in a manner dictated by TEM field considerations, with concentration at the edges as illustrated by the increased density of current lines. At the plane of the notch the current divides somewhat as shown, part flowing through Terminals 1 which are short-circuited, and the remainder flowing through the unsevered portion of the plate. Now consider the situation illustrated in Fig. 2(b). The plate has been severed at the plane of the notch to form a second pair of terminals, and a generator has been applied to these terminals. It is assumed that the generator is distributed so that it excites linear currents on the plate having the same transverse distribution as illustrated in Fig. 2(a). The linear currents shown in the diagrams of Fig. 2 represent the radiating currents excited on the plate; the situation of Fig. 2(b) represents the most efficient or tightest possible coupling to these currents—the entire plate is isolated and driven as an antenna. The problem of determining the coupling between the notch and the radiating currents, therefore, is in essence the problem of determining the coupling between the two sets of terminals shown in Fig. 2(b). To determine this coupling, we make use of the equivalent circuit shown in Fig. 1.

It is evident from the definition of the admittance coefficients given earlier that  $Y_{11}$ , which is the admittance looking into Terminals 1 with Terminals 2 shorted—thereby permitting linear antenna currents to flow on the plate—will be the total effective antenna input admittance, including radiation. On the other hand, if Terminals 2 are opened, blocking the radiating currents, the admittance seen looking into Terminals 1 will be the self-admittance of the notch. This admittance, which we will call  $Y_n$ , is essentially a pure sus-

<sup>5</sup> E. J. Moore, "Performance Specification and Evaluation of Liaison Antennas," Stanford Res. Inst. Final Rep, Proj. 606, Task III, AF Contract No. AF 33(616)-83; November, 1953.

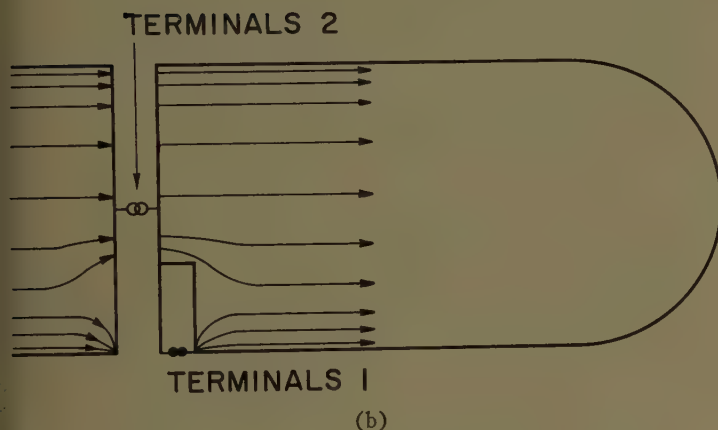
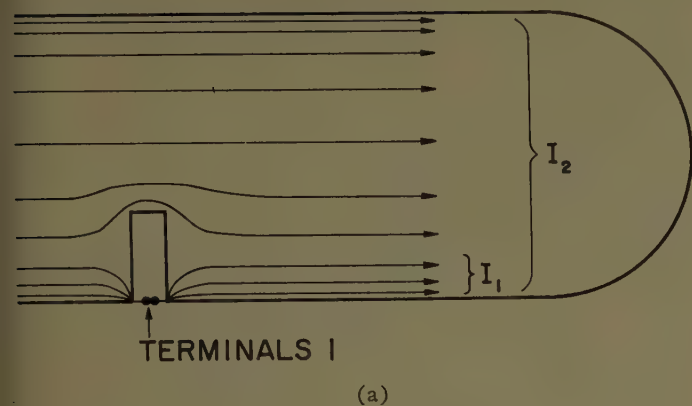


Fig. 2—(a) Notch-fed plate. (b) Definition of hypothetical coupled terminals for notch-fed plate.

ceptance and will not include any component due to radiation. From inspection of the equivalent circuit of Fig. 1, it is evident that  $Y_n$  is given by

$$Y_n = Y_{11} - Y_{12} + \frac{Y_{12}(Y_{22} - Y_{12})}{Y_{22}},$$

which reduces to

$$Y_n = Y_{11} - \frac{Y_{12}^2}{Y_{22}}. \quad (2)$$

Rearranging, we have

$$Y_{11} = Y_n + Y_{22} \left( \frac{Y_{12}}{Y_{22}} \right)^2. \quad (3)$$

Eq. (3) states that the antenna input admittance is made up of two components, the first of which,  $Y_n$ , is the admittance of the notch, while the second is  $Y_{22}$  multiplied by a dimensionless factor. This second component represents the coupling between the notch and the airframe currents. The strength of the coupling depends upon the magnitude of the factor multiplying  $Y_{22}$ . Stated as it is in (3), the expression is not especially illuminating. Referring to (1), however, we see that the factor  $Y_{12}/Y_{22}$ , which measures the strength of coupling, is equal to the current division ratio illustrated in Fig. 2(a). Eq. (3) can therefore be rewritten as

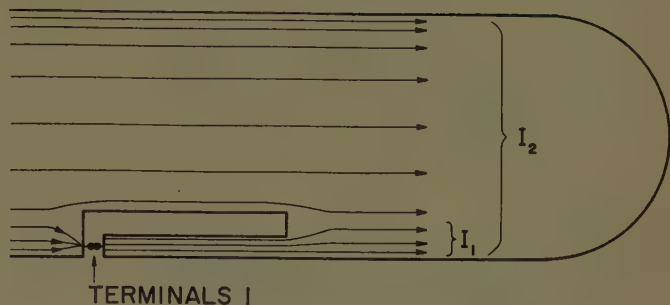


Fig. 3—Shunt-fed plate.

$$Y_{11} = Y_n + Y_{22} \left( \frac{I_1}{I_2} \right)^2. \quad (4)$$

It is obvious that the technique of analysis applied to the notch antenna can also be applied to the shunt-fed antenna illustrated in Fig. 3. In the case of the shunt antenna,  $Y_n$  represents, essentially, the susceptance of the section of the shorted transmission line formed by the shunt, while  $Y_{22}$  is, as before, the admittance seen if the entire section outboard of the feed terminals is isolated and driven as an antenna.

Eq. (4), which gives the input admittance of shunt and notch fed antennas, indicates several facts concerning the performance of such antennas and how the performance might be improved. In antennas of this type, the radiation conductance component of the input admittance comes almost entirely from the coupled admittance term, while the susceptance is largely due to  $Y_n$ . It follows from the previous discussion, therefore, that any measure which improves the ratio of these terms will improve the electrical performance of the antenna.

#### COUPLING IN TYPICAL AIRFRAMES

##### General

The coupling relationship just developed indicates several important facts concerning the use of notch and shunt feeds for aircraft antennas. The two of greatest importance are first, the dependence of the coupling upon the square of the current division ratio and, second, that the coupled admittance is closely proportional to the admittance obtained by severing the aircraft structure at the plane of the notch or shunt feed terminals. From the first of these it is evident that for greatest effectiveness, the feed must be located where current concentration is greatest. Fortunately, considerable concentration occurs at the edges of airfoil surfaces, which are reasonably accessible from the structural standpoint. The second consideration, that the coupled admittance is proportional to the admittance which would be obtained by severing the structure at the plane of the feed terminals, means that the feed should be placed as far away from the extremities of the aircraft as possible in order that  $Y_{22}$  be high. Both of these considerations indicate that from the efficiency and impedance standpoints



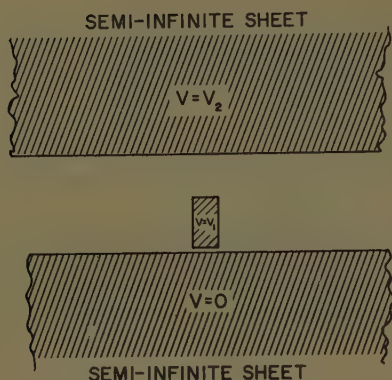


Fig. 4—Slot complement of notch-fed plate.

the wing-root area is perhaps the most favorable spot on the aircraft in which to install such an antenna.

#### Flat-Plate Idealization of Airfoil Surface

A feeling for the degree of coupling obtainable by notches or shunts in wings and other airfoil surfaces is gained by investigation of the current distributions on flat plates. In the wing section shown in Fig. 2(a), we desire to know the current division ratio  $I_1/I_2$ . This quantity can be calculated relatively easily if we assume that the actual wing can be approximated by a flat plate and that the width of the plate is small relative to a wavelength. If the latter assumption holds, we know that the current will take a distribution across the plate which is governed by the TEM wave conditions—the transverse distribution of currents and fields obeys the two-dimensional Laplace equation. This distribution is the same as the distribution of electric field between two semi-infinite plates as shown in Fig. 4. The configuration of Fig. 4 is essentially the slot complement of a notch-fed plate. The relation between the voltage,  $V_1$ , taken by the small isolated rectangular plate and the voltage,  $V_2$ , across the total gap is the same as the relation between the current flowing through the antenna terminals and the total current flowing on the plate. In other words,

$$\frac{I_1}{I_2} = \frac{V_1}{V_2}$$

This ratio can be calculated by means of the reciprocity theorem using the voltage distribution in the gap in the absence of the small plate. The latter is well known; it is obtained by a simple conformal transformation. Fig. 5 is a plot of the current division ratio, and the square of this ratio as calculated in the manner outlined, vs the fraction of total plate width occupied by the feed notch.

The fact that we can calculate the current division ratio enables us to check experimentally the coupling theory developed earlier. To do this, a flat plate was placed in a shielded cage as indicated schematically in Fig. 6. Terminals were provided as shown in Fig. 6 to simulate complete isolation of the plate [Fig. 6(a)] or

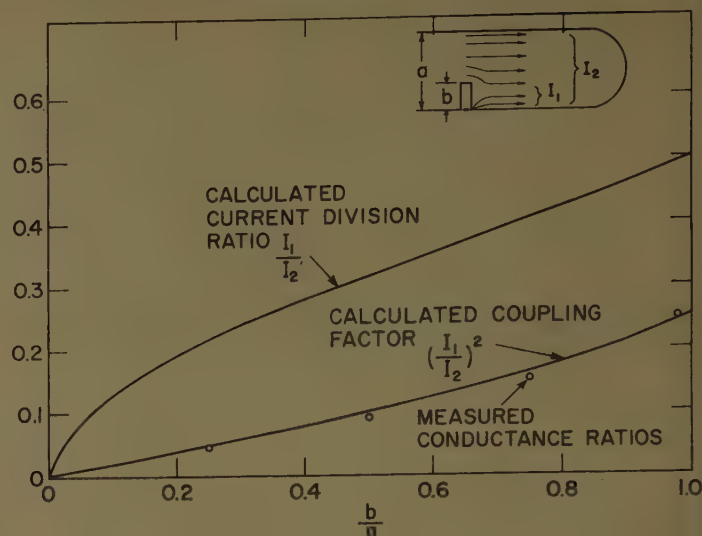


Fig. 5—Calculated coupling factor and comparison with measured values of coupled conductance.

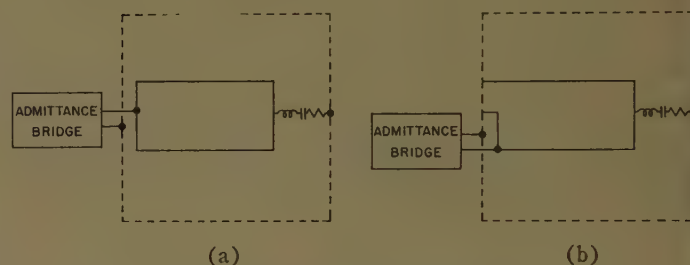


Fig. 6—Measurements on flat plate in shielded cage to verify notch coupling relations.

notch feed [Fig. 6(b)]. The plate was tuned at the far end for a series resonance of convenient peak conductance when measured with the setup of Fig. 6(a). With the tuning unaltered, the plate was then shorted at the driving end and the admittance measured over a range of frequencies in the vicinity of resonance for different lengths of feed notches as illustrated in Fig. 6(b).

In this latter condition, the measured conductance arises entirely from the coupling to the linear currents flowing on the plate. It therefore corresponds exactly to the radiation conductance of a notch-fed wing antenna, which is due to coupling to the linear radiating currents flowing on the wing. If the theory of coupling is correct, the relation between the conductance measured with different lengths of feeding notches and the conductance measured with the driven end of the plate isolated should be the same as the squares of the current division ratios for the same length notches. Points representing the measured conductance ratios are shown on the graph of Fig. 5 along with the curve representing the calculated values for  $(I_1/I_2)^2$ . It is seen that the agreement is essentially perfect, substantiating the analysis.

The flat plate model also permits easy investigation of the characteristics of shunt-fed antennas. For such antennas, where the length of the shunt is long compared to its transverse dimension, the current division ratio is governed by the two-dimensional Laplace equation and

can be investigated using electrolytic tank or resistance paper techniques.

In the consideration of shunt-fed antennas, an additional factor affecting the efficiency of the feed system must be taken into account. If we are given a certain space at the edge of a wing in which to install the antenna, we must decide what proportion of the space will be conductor and what proportion will be dielectric. If we make the conductor very broad and the gap narrow, the coupled conductance is a maximum, but the susceptance introduced by the shunting transmission line mode increases even more rapidly than does the conductance, so that the ratio of antenna susceptance to antenna conductance is higher than necessary. On the other hand, if the gap is wide and the conductor narrow, the shunt susceptance is minimum, but so also is the current division ratio. The optimum proportion exists somewhere between these extremes and can be determined. It depends somewhat upon what fraction of the total breadth of the wing is occupied by the shunt feed. A figure of 50 per cent; *i.e.*, conductor width and gap spacing equal, is very close to the optimum for shunt antennas of practical dimensions. Assuming equal space devoted to feed conductor and separating gap, we can then determine the current division ratio as a function of the fraction of wing breadth occupied by the shunt feed. The coupling factor, or square of the current division ratio, obtained using resistance paper (dry electrolytic tank) is shown in Fig. 7. The coupling data given in the figure as well as the validity of the coupling theory as applied to shunt fed plates were substantiated by experimental measurements made on a setup equivalent to that for notch antennas shown in Fig. 6.

#### Effect of Wing Sweep-Back on Coupling of Notches

The foregoing analysis of the flat plate model, in addition to substantiating the theory of coupling, provides a feeling for the degree of coupling which can be expected using notch and shunt feeds. The figures obtained apply quite accurately to shunt feeds or to notch feeds on straight wing aircraft over most of the hf frequency range. For swept-wing aircraft, and also to some extent for straight wing aircraft, the coupling at low frequencies of notch antennas at the wing roots is actually considerably stronger than indicated by Fig. 5.

The reason for the above is illustrated by Fig. 8. The diagram in this figure illustrates the main path of current flow at frequencies toward the low end of the hf range. The currents flow along the fuselage, divide at the wing junction, and flow out along the wing. At the trailing edge of the wing root the current flow lines tend to "cut the corner," resulting in increased current concentration in the fillet area. A greater degree of sweep back results in a sharper corner and a correspondingly greater concentration of current. With swept-back wings, some concentration occurs also for the mode of current flow illustrated in Fig. 8(b).

The current concentration which occurs in the fillet

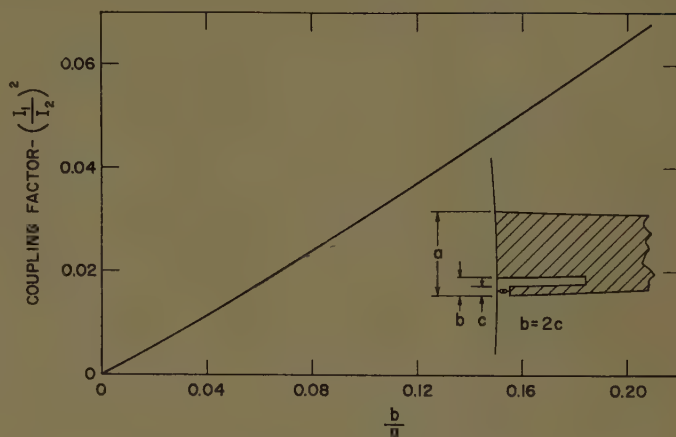


Fig. 7—Coupling factor for shunt-fed wings.

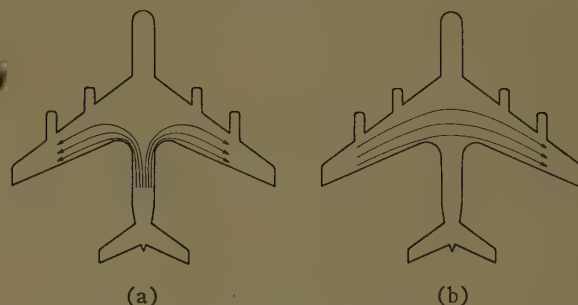


Fig. 8—Concentration of current in fillet region of swept-wing aircraft.

area for swept-wing aircraft enhances the coupling for notches in that area. Because of the complicated geometry, the coupling in such a situation cannot be calculated exactly. It can be measured experimentally, however, using a technique which will not be described here due to space limitations. The measured coupling factor  $(I_1/I_2)^2$ , for both of the current flow modes illustrated in Fig. 8 is given in the curves of Fig. 9. The coupling factor for a notch in a flat plate is replotted on the same chart for comparison. In the tests resulting in the curves of Fig. 9 the width of the wing dimension  $a$  is small relative to a wavelength, never exceeding  $\lambda/8$ .

#### ESTIMATED PERFORMANCE OF SHUNT AND NOTCH ANTENNAS

##### General

To estimate the performance of shunt and notch antennas, it is necessary to have, in addition to the coupling factors given in Fig. 7 and Fig. 9, the admittance with the wing isolated at the root. It is also necessary to know the shunt susceptance,  $Y_n$ , introduced by the shunt or notch. The measured admittance at the terminals of an isolated wing for a typical straight wing airframe having a 150-foot wing span is shown in Fig. 10, above.<sup>6</sup> While these data might be construed as applying

<sup>6</sup> These admittance data were obtained by actual measurement on a full scale mock-up of a light aircraft with a wing span of 36 feet. The measurements were made with the aircraft mounted on an insulating tower 40 feet high. An appropriate scaling factor is used.



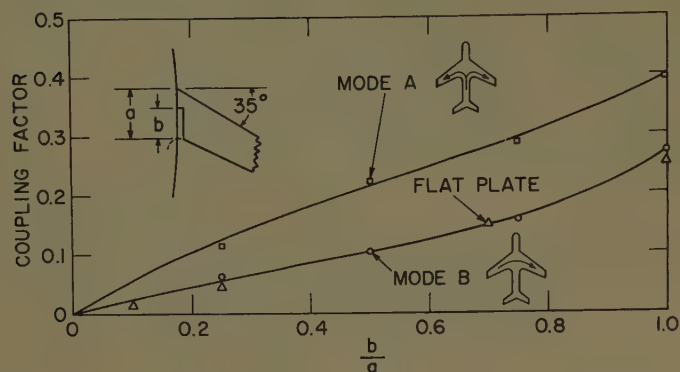


Fig. 9—Coupling factor for fillet notch in swept-wing aircraft.

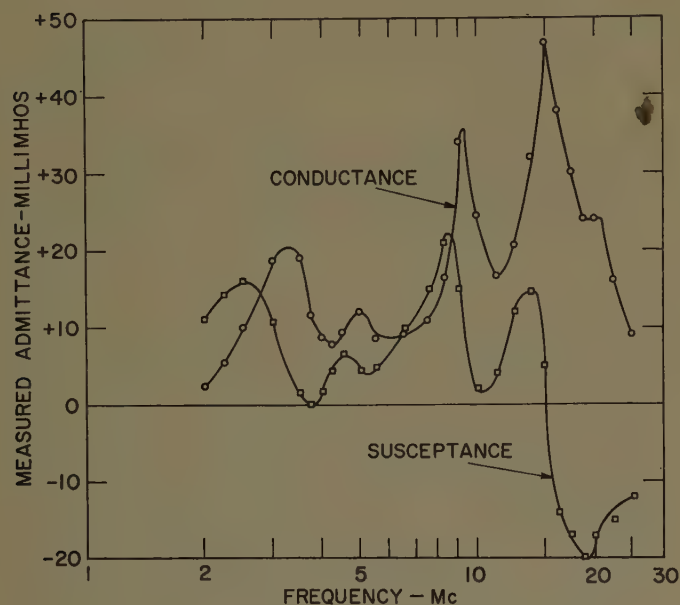


Fig. 10—Admittance of isolated wing on straight-wing airframe: 150-foot wing span.

only to a specific airframe, they are actually of considerably more general applicability. The isolated-wing admittance of any airframe, whether straight wing or swept wing, is of the general form shown in Fig. 10.

If scaling adjustments are made so that the lengths of the principal members correspond, good quantitative estimates of notch and shunt antenna admittance can be obtained. For example, the admittance of a notch antenna in the Douglas YC-132, a large, swept-wing, turboprop aircraft, was predicted using the data of Fig. 10 and the methods outlined in this paper. The predicted impedance characteristics were later compared with measurements on a 1/10-scale model of the aircraft. In the lower half of the hf range the predicted and measured curves coincided almost exactly. In the upper portion of the hf range the measured and predicted curves diverged but were similar in form.<sup>7</sup>

<sup>7</sup> This example is cited through the courtesy of the Douglas Aircraft Co., Tulsa Division. G. A. O'Reilly of Douglas supervised the model measurements.

For the shunt antenna the shunting susceptance,  $Y_n$ , is readily calculated or measured since it is the susceptance of the unbalanced transmission line forming the shunt. For the conductor configuration yielding optimum coupling efficiency; *i.e.*, equal conductor width and gap spacing, the characteristic admittance is approximately 0.005 mhos ( $Z_0 = 200$  ohms). The length of the shunt is determined by the space available, but should not be so long that it becomes equal to  $\lambda/2$  in the frequency range over which the antenna will be used, since at that frequency the susceptance of the line becomes very high, tending to short out the antenna.<sup>8</sup>

The susceptance of a notch cannot be calculated as simply as that of a shunt, especially since the notch may be of irregular shape. It can be determined with accuracy, however, by simple mock-up measurements. Sufficiently accurate measurements can be obtained by mocking up only the structure in the vicinity of the notch.

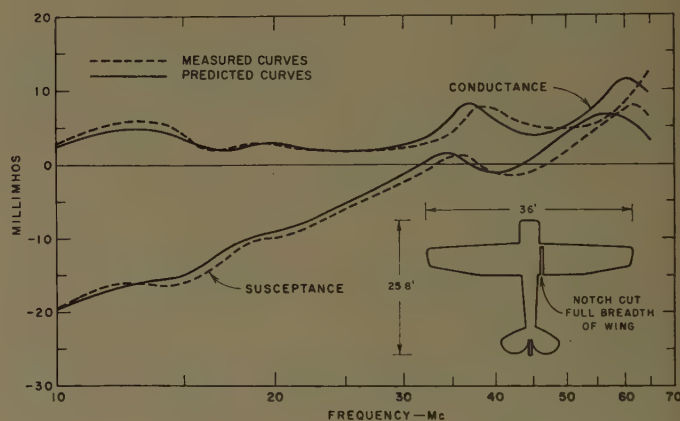


Fig. 11—Comparison of predicted and measured values of wing notch admittance.

### Experimental Verification

A further test of the accuracy with which the theory outlined is able to predict the impedance characteristics of notch antennas is provided by the data shown in Fig. 11. The two sets of curves shown in the figure are the admittance of a notch antenna predicted by the methods outlined in this paper and the admittance as actually measured. The data shown apply to a light aircraft having the dimensions indicated on the inset in the figure. The notch in this case extended the full breadth of the wing as shown. Equally good agreement was obtained with a notch cut half the breadth of the wing. No measurements were made for smaller notches because of the difficulty of obtaining accurate conductance measurements for the highly susceptible admittances which the smaller notches present.

<sup>8</sup> The simple theory as stated here neglects the radiation resistance due to the loop or transmission line mode. This component is the major contributor to the actual impedance at the frequency which makes the shunt  $\lambda/2$  in length.

It is evident from the agreement between the two sets of curves shown that the theory is surprisingly successful in predicting the actual behavior. In particular, it should be noted that the agreement between predicted and measured values extends to a frequency at which the breadth of the wing is nearly a half wavelength. The theory thus appears to apply with reasonable accuracy to a much higher frequency than might be inferred from the fact that the breadth of the wing was assumed small compared to a wavelength in estimating the transverse distribution of current on the wing. It would be expected that the theory would apply less accurately at high frequencies for swept-wing than for straight-wing aircraft. The example of the YC-132 cited earlier would appear to substantiate this expectation.

#### Performance of Shunt Antennas

From the data given and methods described, it is possible to calculate the impedance to be expected from a shunt antenna on a representative airframe. Such calculations have been made for a shunt antenna installed on an aircraft having a 150-foot wing span with the shunt feed section 18 feet long and occupying 10 per cent of the wing breadth. The feed terminals are at the root of the wing. The resulting impedance is shown in Fig. 12. From the calculated impedance, together with available data on the loss characteristics of typical dielectric materials likely to be used in fabricating the antenna, the antenna efficiency can be calculated and the matching efficiency estimated. The calculations indicate that the over-all power transfer efficiencies averaging 80 per cent can be obtained. For the example of Fig. 12 the efficiency at 2 mc is approximately 60 per cent. At higher frequencies the efficiency tends to drop due to increasing dielectric loss as the length of the shunt begins to approach a half wavelength.

Radiation patterns for a shunt antenna on a C-54 aircraft, representative of the straight-wing airframe, were taken, and the radiation pattern efficiency was evaluated according to the method given by Moore. The pattern efficiency obtained was comparable to that of a tail-cap antenna on the same aircraft, both having efficiencies near 50 per cent.

#### Performance of Notch Antennas

One would expect the performance of notch antennas to be considerably inferior to that of caps or of shunt-fed antennas. This is because the susceptance of the notch is high relative to the coupling which can be obtained with notches of sizes compatible with structural requirements. On large swept-wing aircraft similar to the Boeing 707 or the Douglas DC-8, however, the enhancement of coupling due to current concentration in the fillet area suggests that notch antennas installed in that area might be satisfactory. Approximate calculations indicate that this is true. As indicated previously, the admittance which would be measured with the wing severed at the root on such an aircraft is similar to that

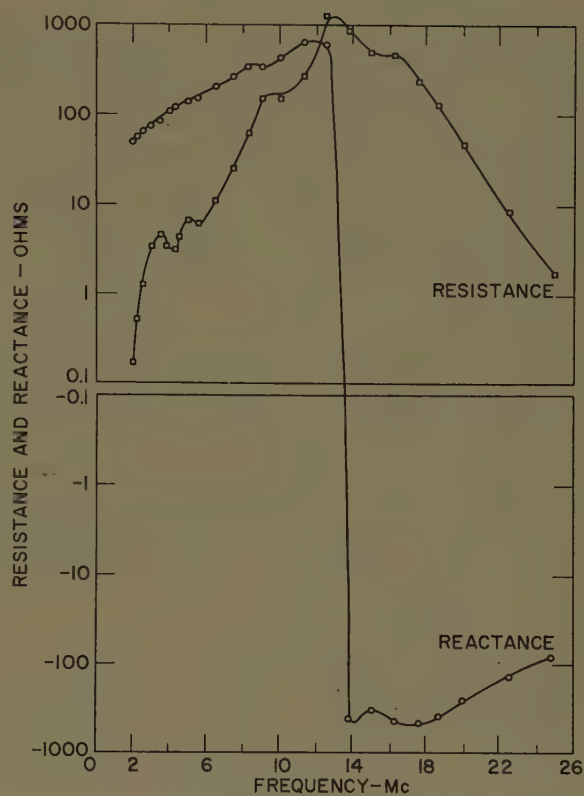


Fig. 12—Calculated impedance of shunt antenna on 150-foot span straight wing aircraft.

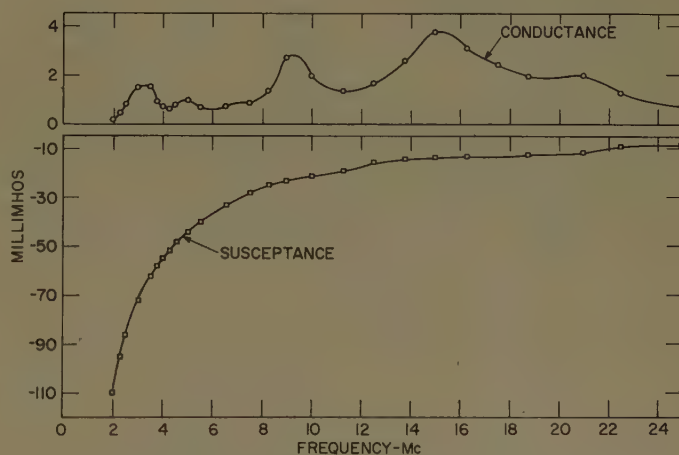


Fig. 13—Computed admittance of 1- by 4-foot notch on DC-8.

shown in Fig. 10. Using these data and a coupling factor obtained from Fig. 9 the impedance of a notch 4 feet deep and 1 foot wide was calculated. The slant breadth at the wing root was taken as 28 feet. The computed admittance curve for the notch antenna is given in Fig. 13. The computed admittance shown in the figure will quite accurately represent the true admittance at low frequencies. For the reasons mentioned earlier, however, the values at high frequencies, although representative of the true values, are not as good an approximation.

Computation of the over-all power transfer efficiency indicates that for the examples shown the notch antenna is somewhat superior to the shunt, averaging approxi-



mately 90 per cent. At 2 mc, however, the notch has an efficiency of only 45 per cent compared with 60 per cent for the shunt. The superiority of the notch at all but the extreme low frequency is, in this instance, principally due to the enhancement of coupling mentioned. The performance of a notch of this size on a straight-wing aircraft or one installed at a point other than the wing root area would almost certainly be inferior to the shunt antenna.

In discussing notches vs shunts, some comment is appropriate regarding their relative structural merits. It has been pointed out that the best place for installation from the standpoint of electrical efficiency is the trailing edge of the wing near the root. For notch antennas, in fact, this appears to be the only acceptable place. On modern aircraft, this area is occupied by flaps and it would seem improbable that compatible designs for shunt antennas, which require substantial distance along the trailing edge, could be worked out. It seems entirely possible, however, that a notch only 1 foot wide could be installed in the fillet area.

Radiation pattern data for a wing-root notch installed on a DC-8 aircraft indicate that the pattern efficiency of the notch is also comparable to that of a tail-cap antenna.

#### Multiple Turn Notches

Worthy of comment in connection with the discussion of notch antennas is a suggestion by Dr. A. Weissfloch of the Soci  t   Technique d'Application et de Recherche Electronique (STAREC) to use multiple turn loop coupling instead of a simple notch (see Fig. 14).

This case has been analyzed and it has been shown theoretically and substantiated by experiment that the admittance of a two-turn notch (one loop plus the notch itself) of the type illustrated is

$$Y_b = Y_a \frac{\cos \beta l + j \frac{Y_0}{Y_a} \sin \beta l}{2(1 + \cos \beta l) + j \frac{Y_a}{Y_0} \sin \beta l} \quad (5)$$

where

$Y_b$  = input admittance of two-turn notch

$Y_a$  = input admittance of simple notch

$Y_0$  = characteristic admittance of transmission line formed by feed loop and wall of notch

$\beta l$  = electrical length of transmission line formed by feed loop and wall of notch.

The transmission line for which the quantities  $Y_0$  and  $\beta$  in (5) apply may either be open as illustrated in Fig. 14, or coaxial.

Consideration of (5), above, makes it clear that use of multiple turns does not increase coupling. The principal

effect at low frequencies is merely an impedance transformation equivalent to that obtained by using a transformer having a 2:1 turns ratio at the input of a simple notch. At higher frequencies the effect, while much more complicated, is, in general, to degrade the impedance characteristic by increasing the ratio of reactance to resistance. Also, when the length of the peripheral transmission line becomes  $\lambda/2$  the antenna is effectively shorted out.

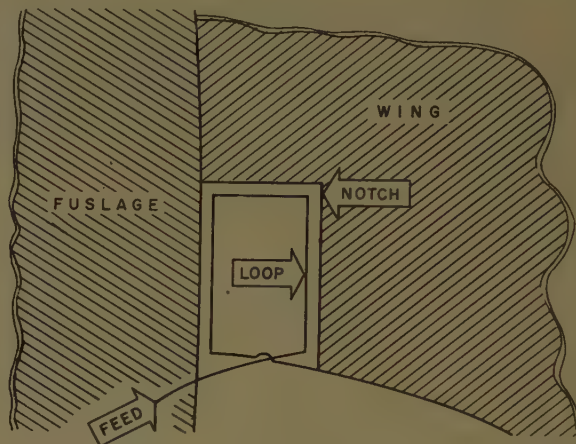


Fig. 14—Multiple-turn loop coupling in fillet area.

#### CONCLUSION

We have explored the nature of the coupling of notches and shunts to airframe radiating currents and have shown that if properly designed, antennas using these feed methods should be comparable in electrical performance to cap antennas. In particular, the investigation of the coupling in the wing root area indicates that in large swept-wing aircraft, current concentration at that point leads to enhanced coupling which makes feasible the use of relatively small notches. On small aircraft notches appear to be of dubious value.

Nothing authoritative can be asserted regarding the relative structural advantages of shunt fed and notch fed antennas. It would appear, however, that notches in particular, when they can be used, should have significant structural advantages over both shunts and caps. Both the notches and shunts have the advantage that they avoid the necessity of severing main spars as is required in cap antennas, although the interference with the landing flap installation which occurs with shunts may present even more serious structural difficulties. The leading edges of wings, while less satisfactory for the installation of shunt antennas than the trailing edges, nevertheless might be used for shunt antennas although achieving structural compatibility with the de-icing systems which occupy the wing-leading edges of almost all modern aircraft would undoubtedly present serious problems.

An undisputed advantage of shunt or notch antennas is that they avoid the necessity of using the special isolating devices required with cap antennas when the iso-

lated section contains other electrical devices such as navigation lights or higher frequency antennas. They also avoid the necessity for special lightning protection measures required with cap-type antennas. A characteristic of both shunt and notch antennas that may be a significant advantage, although it poses special problems in the design of antenna couplers to match them, is the fact that their impedance levels are relatively low. This means that voltage breakdown of the antennas is not a serious problem even with high radiated powers.

## On the Fresnel Approximation\*

R. B. BARRAR<sup>†</sup> AND C. H. WILCOX<sup>‡</sup>

**Summary**—The purpose of this paper is to show the power of the Sommerfeld expansion in computing Fresnel and near fields of antennas, a matter which has become of increasing importance in high resolution antennas. A connection is shown between the Fresnel and Fraunhofer approximations for radiation fields which is derived by using Sommerfeld's expansion of the field in inverse powers of radial distance. This expansion permits an estimate of the error incurred in using the Fresnel approximation. Higher-order corrections to the phase and amplitude portion of the Fresnel approximation are also exhibited. By way of illustrating the power of the Sommerfeld expansion of the fields in the Fresnel (intermediate) region of a radiation source, numerical calculations of amplitude, phase, and power patterns have been made for a finite line source of length  $D$  with an equiphase cosine-on-a-pedestal current distribution. It is found that the first five terms of the series are sufficient to obtain accurate results when  $r \geq D^2/2\lambda$ , as compared with the Fraunhofer approximation which is usually considered valid for  $r \geq 2D^2/\lambda$ . Non-Fraunhofer zone effects on the power pattern and phase front are discussed as a function of distance  $r$  and the type of current distribution.

### INTRODUCTION

INCREASED resolution requirements on microwave antennas have led to the use of long linear arrays at very short wavelengths. The possibility exists that such antennas will be tested and even used at closer range than their Fraunhofer regions. Thus, it has become increasingly important to be able to compute the Fresnel and near fields.

The computation of Fraunhofer fields can be done in many cases since the computation involves Fourier transforms for which many excellent tables exist. However, the computation of Fresnel and near fields can only be done in relatively few cases where the integrals

### ACKNOWLEDGMENT

The author acknowledges with gratitude his debt to Dr. J. V. N. Granger whose enduring interest in aircraft antenna systems has provided much of the motivation for the investigation reported here, and to Dr. J. T. Bolljahn for many helpful technical discussions. He is also indebted to A. V. McKenzie who carried out most of the numerous measurements and to Dr. Jack Cline for discussions regarding multiple turn coupling in notches.

can be reduced to tabulated Fresnel integrals. The purpose of this paper is to point out that the Sommerfeld expansion is a promising method of computing these near and Fresnel fields.

### THE SOMMERFELD EXPANSION

Although in spherical coordinates a solution of the scalar wave equation

$$\nabla^2 U + k^2 U = 0 \quad (1)$$

is usually given in terms of an infinite series involving products of spherical Bessel functions and tesseral harmonics,<sup>1</sup> Sommerfeld<sup>2</sup> has suggested that the expansion

$$U = r^{-1} \exp(-jkr) \sum_{n=1}^{\infty} a_n(\theta, \phi) / (-jkr)^{n-1} \quad (2)$$

be considered.

Concerning this expansion, Barrar and Kay<sup>3</sup> have derived the following theorem:<sup>4</sup>

Let  $U$

- 1) be a solution of (1) for real  $k$ ;
- 2) be twice continuously differentiable on, and exterior to, a sphere  $S$ , of radius  $r_0$ ; and,
- 3) satisfy the radiation condition  $r(\partial U / \partial r + jkU) \rightarrow 0$  uniformly with respect to  $\theta$  and  $\phi$  as  $r \rightarrow \infty$ .

Then, when  $r > r_0 + \epsilon$ , for arbitrary  $\epsilon$ , the expansion (2) converges uniformly and absolutely and may be differ-

<sup>1</sup> J. A. Stratton, "Electromagnetic Theory," McGraw-Hill Book Co., Inc., New York, N. Y., sec. 7.3, 7.4; 1941.

<sup>2</sup> A. Sommerfeld, "Partial Differential Equations in Physics," Academic Press, Inc., New York, N. Y., p. 191; 1949.

<sup>3</sup> R. B. Barrar and A. F. Kay, "A series development of a solution of the wave equation in powers of  $1/r$ ," Paper presented at the URSI meeting, Washington, D. C.; May, 1954.

<sup>4</sup> Similar results have been obtained by W. Magnus, "Über Eindeutigkeitsfragen bei einer Randwertaufgabe von  $\Delta u + k^2 u = 0$ ," *Jahresber. Deutschen Math. Vereinig.*, vol. 52, pp. 177-188, 1943, and F. V. Atkinson, "On Sommerfeld's radiation condition," *Phil. Mag.* vol. 40, pp. 645-651, 1949.

\* Manuscript received by the PGAP, October 10, 1956; revised manuscript received, May 10, 1957. Much of the work described in this paper has been reported more fully in Hughes Aircraft Co. Sci. Rep. No. 4 on AF Cambridge Res. Ctr. Contract AF 19(604)-1317, February 15, 1955, and was presented at the URSI-Michigan Symposium on Electromagnetic Wave Theory, June, 1955.

<sup>†</sup> Hoffman Labs., Inc., Los Angeles 7, Calif.

<sup>‡</sup> Microwave Lab., Hughes Aircraft Co., Culver City, Calif.



entiated any number of times with respect to  $r$ ,  $\theta$ , and  $\phi$ . Any series resulting from such differentiations will also converge uniformly and absolutely.

If the expansion (2) is substituted into the scalar wave equation (1), written in spherical coordinates, and like powers of  $1/r$  are equated to zero, one obtains the recursion relation

$$a_{n+1} = \frac{1}{2n} \left[ n(n-1)a_n + \frac{1}{\sin \theta} \frac{\partial}{\partial \theta} \left( \sin \theta \frac{\partial a_n}{\partial \theta} \right) + \frac{1}{\sin^2 \theta} \frac{\partial^2 a_n}{\partial \phi^2} \right]. \quad (3)$$

These formal manipulations are justified by the theorem of Barrar and Kay.

#### CONNECTION WITH THE FRAUNHOFER AND FRESNEL EXPANSIONS

In order to see the connection between the series (2) and the Fresnel and Fraunhofer approximations, let us compute the field of the finite line source shown in Fig. 1.

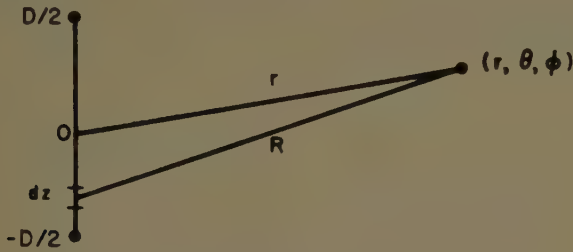


Fig. 1—Geometry for line-source calculation.

In terms of the Hertz potential  $\Pi_z$ , the formal solution to this problem is given by<sup>5</sup>

$$\Pi_z = (-j/4\pi\omega\epsilon) \int_{-D/2}^{D/2} I(z) R^{-1} \exp(-jkR) dz \quad (4)$$

$$\mathbf{H} = j\omega\epsilon \text{curl}(\Pi_z \mathbf{z}) \quad (5)$$

$$\mathbf{E} = (-j/\omega\epsilon) \text{curl} \mathbf{H} \quad (6)$$

where the factor  $e^{j\omega t}$  has been suppressed,  $I(z)$  is the current, and  $\mathbf{z}$  is the unit vector in the  $z$  direction. The Fraunhofer and Fresnel approximations to  $\Pi_z$  are, respectively,

$$\Pi_z = \Pi_z^{\text{Fraunhofer}} + O(1/r^2),^6 \text{ with}$$

$$\Pi_z^{\text{Fraunhofer}} = (-j/4\omega\epsilon r) \exp(-jkr) \int_{-D/2}^{D/2} I(z) \exp(jkzw) dz \quad (7)$$

$$\Pi_z^{\text{Fresnel}} = (-j/4\omega\epsilon r) \exp(-jkr) \int_{-D/2}^{D/2} I(z) [\exp(jkzw)] \cdot [\exp(-jkz^2(1-w^2)/2r)] dz, \quad (8)$$

with  $w = \cos \theta$  in both (7) and (8).

On the other hand,  $\Pi_z$  is a solution of (1); hence, the expansion (2) and (3) applies. Thus,

$$\Pi_z = r^{-1} \exp(-jkr) \sum_{n=1}^{\infty} b_n(\theta, \phi) / (-jkr)^{n-1} \quad (9)$$

and the  $b_n(\theta, \phi)$  satisfy the recursion relation (3).

By comparing (7) and (9), it can be seen that

$$b_1(\theta, \phi) = (-j/4\omega\epsilon) \int_{-D/2}^{D/2} I(z) \exp(jkzw) dz, \quad (10)$$

or that  $b_1(\theta, \phi)$  is just a constant multiplied by the Fraunhofer field.

The connection between the expansion (9) and the Fresnel approximation was first pointed out by Logan.<sup>7</sup> He observes that if one uses the series expansion for  $\exp[-jkz^2(1-w^2)/2r]$  and (10) for  $b_1(\theta, \phi)$ , one obtains for the Fresnel approximation (8):

$$\begin{aligned} \Pi_z^{\text{Fresnel}} &= (-j/4\omega\epsilon r) [\exp(-jkr)] \int_{-D/2}^{D/2} I(z) \exp(jkzw) \\ &\quad \cdot \exp[(ikz^2(1-w^2)/2(-jkr)] dz \\ &= (-j/4\omega\epsilon r) [\exp(-jkr)] \sum_{n=0}^{\infty} [(1-w^2)^n / 2^n (-jkr)^n n!] \\ &\quad \cdot \int_{-D/2}^{D/2} I(z) (jkz)^{2n} \exp(jkzw) dz \\ &= (-j/4\omega\epsilon r) [\exp(-jkr)] \sum_{n=0}^{\infty} [(1-w^2)^n / 2^n (-jkr)^n n!] \\ &\quad \cdot \frac{d^{2n}}{dw^{2n}} b_1(w). \end{aligned} \quad (11)$$

On the other hand, if one uses the exact formula (3) with  $w = \cos \theta$ , one obtains

$$\begin{aligned} b_{n+1}(w) &= (2^n n!)^{-1} \left[ (1-w^2)^n \frac{d^{2n}}{dw^{2n}} b_1(w) \right. \\ &\quad \left. - 2n^2 w (1-w^2)^{n-1} \frac{d^{2n-1}}{dw^{2n-1}} b_1(w) \right] \\ &\quad + T \left( \frac{d^{2n-2}}{dw^{2n-2}} b_1(w) \right), \end{aligned} \quad (12)$$

where

$$T \left( \frac{d^{2h-1}}{dw^{2h-1}} b_1(w) \right)$$

means other terms that involve, at most, the  $(2n-2)$  derivative with respect to  $w$ .

On comparing (11) and (12), one sees that the Fresnel approximation corresponds to the exact series (9), if the term  $b_{n+1}(w)$  is replaced by the leading term in its development (12), i.e.,

$$b_{n+1}(w) \sim \frac{1}{2^n n!} (1-w^2)^n \frac{d^{2n}}{dw^{2n}} b_1(w).$$

Perhaps a better way to see that the term

<sup>5</sup> Stratton, *op. cit.*, sec. 8.7.

<sup>6</sup>  $O(1/r^2)$  means all other terms vanish at least as fast as  $1/r^2$ .

<sup>7</sup> N. A. Logan, AF Cambridge Res. Ctr., private communication.

$$\frac{1}{2^n n!} (1 - w^2)^n \frac{d^{2n}}{dw^{2n}} b_1(w)$$

should be the leading term in  $b_{n+1}(w)$  is to note first that  $b_1(w)$  is actually a function of  $(kDw)$ , for example,  $c(kDw)$ , so that the  $n$ th derivative  $b_1^{(n)}(w) = (kD)^n c^{(n)}(kDw)$ . Hence,  $b_{n+1}(w)$  is a polynomial in  $(kD)$  of degree  $2n$ , and for large  $(kD)$ , the term in  $(kD)^{2n}$  is the most important one. This was found to be definitely so in the calculations described below.

#### AN IMPROVEMENT ON THE FRESNEL APPROXIMATION

It is always difficult to decide what is the range of validity of the Fresnel approximation and what is the next best approximation to that of Fresnel. The series (11) and (12) furnishes a partial answer to these questions. If the Fresnel approximation is

$$b_{n+1}^{\text{Fresnel}} = [(1 - w^2)^n / 2^n n!] \frac{d^{2n}}{dw^{2n}} b_1(w), \quad (13)$$

then the next approximation should be

$$b_{n+1}^{\text{Fresnel}+} = (2^n n!)^{-1} \left[ (1 - w^2)^n \frac{d^{2n}}{dw^{2n}} b_1(w) - 2n^2 w (1 - w^2)^{n-1} \frac{d^{2n-1}}{dw^{2n-1}} b_1(w) \right]. \quad (14)$$

If (14) is inserted into (9), the resulting series can be summed as follows:

$$\begin{aligned} \Pi_z^{\text{Fresnel}+} &= [r^{-1} \exp(-jkr)] \sum_{n=0}^{\infty} [2^n n! (-jkr)^n]^{-1} \left[ (1 - w^2)^n \frac{d^{2n}}{dw^{2n}} b_1(w) - 2n^2 w (1 - w^2)^{n-1} \frac{d^{2n-1}}{dw^{2n-1}} b_1(w) \right] \\ &= \Pi_z^{\text{Fresnel}} + [(j/4\omega\epsilon r) \exp(-jkr)] \sum_{n=1}^{\infty} [2nw(1 - w^2)^{n-1} / 2^n (-jkr)^n (n-1)!] \left[ \int_{-D/2}^{D/2} I(z) (jkz)^{2n-1} \exp(jkzw) dz \right]. \quad (15) \end{aligned}$$

Now, by letting  $m = n - 1$ , (15) becomes

$$\begin{aligned} \Pi_z^{\text{Fresnel}+} &= \Pi_z^{\text{Fresnel}} + [(j/4\omega\epsilon r) \exp(-jkr)] \int_{-D/2}^{D/2} [I(z) \exp(jkzw)] \sum_{m=0}^{\infty} [(m+1)w(1 - w^2)^m (jkz)^{2m+1} / 2^{m+1} (-jkr)^{m+1} m!] dz \\ &= (-j/4\omega\epsilon r) [\exp(-jkr)] \int_{-D/2}^{D/2} I(z) [1 + (wz/r) - jkwz^3(1 - w^2)/2r^2] \exp[jkzw - jkz^2(1 - w^2)/2r] dz. \quad (16) \end{aligned}$$

These correction terms which should be added to the Fresnel amplitude approximation are easy to interpret; the  $wz/r$  term comes from the next approximation to  $1/R$ , and the term  $jkwz^3(1 - w^2)/2r^2$  comes from the next approximation to  $\exp(-jkR)$ , as follows:

$$\begin{aligned} R^{-1} \exp(-jkR) &= (1/r) [1 + wz/r + 0(z^2)] [\exp(-jk)(r - zw + z^2(1 - w^2)/2r + w(1 - w^2)z^3/2r^2 + 0(z^4))] \\ &\cong (1/r) [1 + wz/r - jkw(1 - w^2)z^3/2r^2] [\exp(-jk)(r - zw + z^2(1 - w^2)/2r)]. \end{aligned}$$

Thus, according to the above theory:

1) The Fresnel approximation is good for

$$1 \gg \left| \frac{Dw}{2r} - \frac{jkwD^3(1 - w^2)}{16r^2} \right|, \text{ or, if } r = qD^2/\lambda,$$

$$1 \gg \frac{\lambda}{D} \left| \frac{w}{2q} - j \frac{\pi w(1 - w^2)}{8q^2} \right|.$$

2) The next best approximation to that of Fresnel is obtained by inserting the amplitude factor

$$[1 + zw/r - jkwz^3(1 - w^2)/2r^2]$$

in the Fresnel integral.

3) The next approximation to that of Fresnel must improve on both the amplitude and phase approximations.

#### THE FIELD OF A FINITE LINE SOURCE

The theory developed above resulted from an attempt to compute the field of a finite line source by means of the exact (9). For the calculations, the current distribution assumed was of the form

$$I(z) = I + A \cos(\pi z/D), \quad (17)$$

where  $A$  was chosen to give a 10-, 15-, or 20-db power taper. The power taper  $T$  is related to the coefficient  $A$  in (17) by

$$T = 10 \log_{10}(1 + A)^2. \quad (18)$$

The calculations were performed by using five terms in the series (9) to find  $\Pi_z$ , and then by applying (5) and (6) to find  $\mathbf{E}$  and  $\mathbf{H}$ . To apply these equations one must first express  $\mathbf{H}_\phi$  in cylindrical coordinates:

$$\begin{aligned} H_\phi &= -j\omega\epsilon \frac{\partial}{\partial \rho} (\Pi_z) \\ H_\rho &= 0 \quad H_z = 0 \end{aligned} \quad (19)$$

Now, changing to spherical coordinates, (19) becomes

$$\begin{aligned} H_\phi &= -j\omega\epsilon \left[ \sin \theta \frac{\partial \Pi_z}{\partial r} + \frac{\cos \theta}{r} \frac{\partial \Pi_z}{\partial \theta} \right] \\ H_r &= 0 \quad H_\theta = 0 \end{aligned} \quad (20)$$



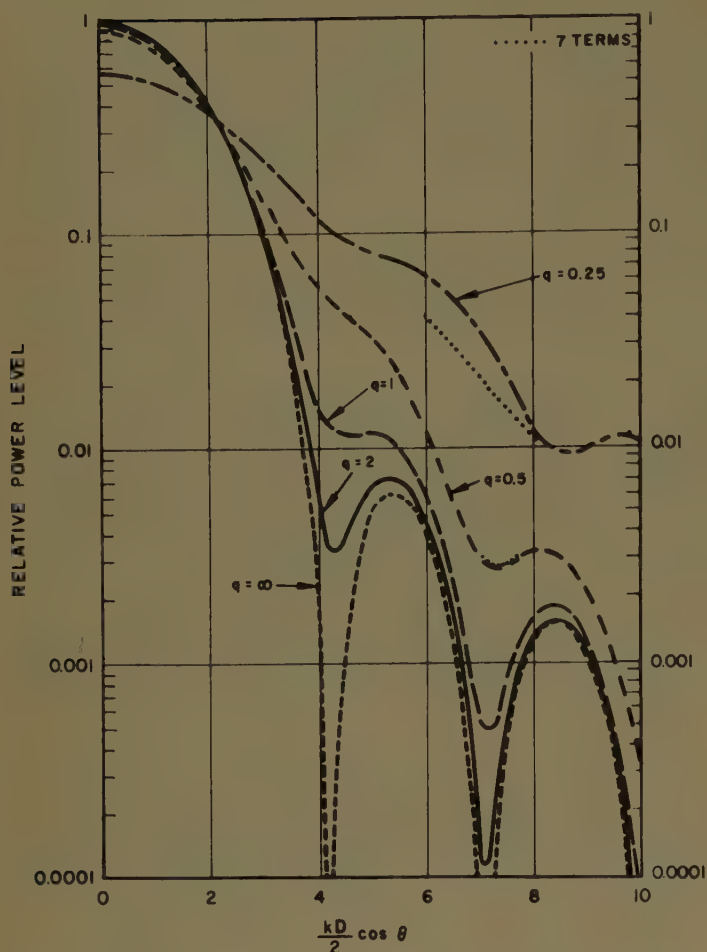


Fig. 2—Power patterns as a function of  $q$  for 15-db power taper.

Since  $\mathbf{H}$  is given by (20) in spherical coordinates, (6) can be applied in spherical coordinates to yield

$$\left. \begin{aligned} E_\theta &= -\frac{1}{r} \left[ \sin \theta \frac{\partial}{\partial r} \left( r \frac{\partial \Pi_z}{\partial r} \right) + \cos \theta \frac{\partial^2}{\partial r \partial \theta} \Pi_z \right] \\ E_r &= \frac{1}{r \sin \theta} \left[ \frac{\partial}{\partial \theta} \left( \sin^2 \theta \frac{\partial \Pi_z}{\partial r} \right) + \frac{\partial}{\partial \theta} \left( \frac{\sin^2 \theta}{2r} \frac{\partial \Pi_z}{\partial \theta} \right) \right] \\ E_\phi &= 0 \end{aligned} \right\} \quad (21)$$

By the theorem of Barrar and Kay,<sup>3</sup> it is permissible to perform all the differentiations indicated in (20) and (21) on the exact series for  $\Pi_z$ .

In the course of the numerical computations it was found that (13) was very good, which shows, at least in the present case, that the term in  $(kD)^{2n}$  is the dominant one in  $b_{n+1}(w)$ . Using (13) in the present calculation is equivalent to using the Fresnel approximation for the computation of  $\Pi_z$ , and then evaluating the Fresnel integral asymptotically. Actually, the present example is one for which the results of Lechtreck<sup>8</sup> may be used to compute  $\Pi_z^{\text{Fresnel}}$ . However, the method developed in this paper will apply to any problem for which one can compute the Fraunhofer field, and thus is applicable to

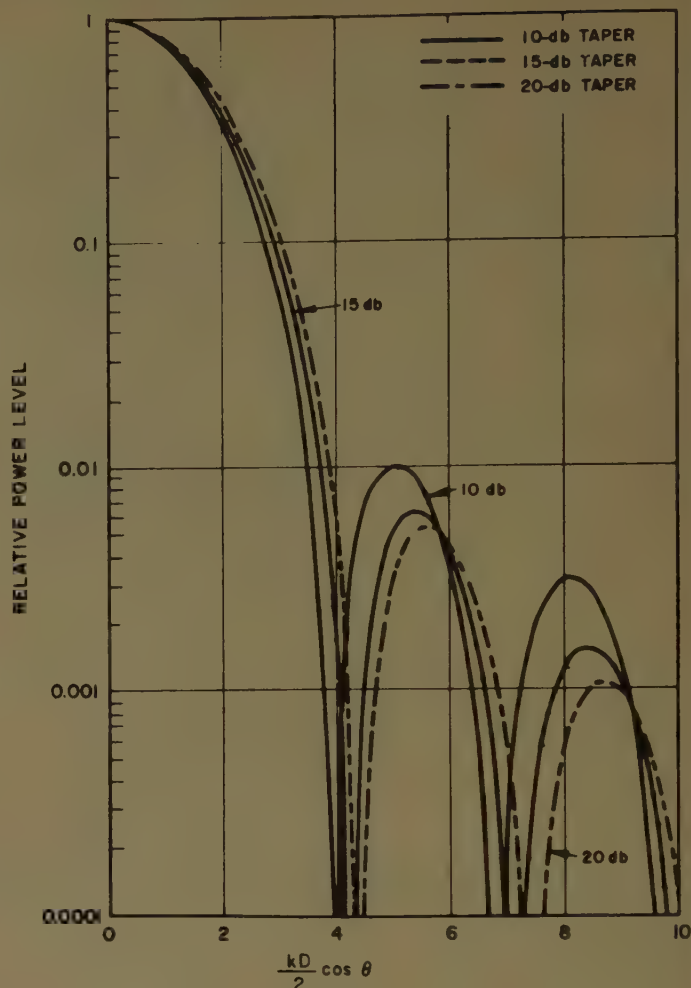


Fig. 3—Far-field patterns as a function of power taper.

problems which cannot be handled by Fresnel integrals.

By carrying out the steps, one can either first perform the differentiations (20) and (21) on the integral representation (4) for  $\Pi_z$ , and then make the Fresnel approximations in the integral representations for  $\mathbf{E}$  and  $\mathbf{H}$  to compute the series answers; or one can perform the indicated differentiations on  $\Pi_z^{\text{Fresnel}}$  to obtain  $\mathbf{E}$  and  $\mathbf{H}$  directly. The latter would have to be done to Lechtreck's results<sup>8</sup> to make them apply to the vector case.

In the illustrations,  $r$  is replaced by the dimensionless quantity  $q$  by means of

$$r = qD^2/\lambda.$$

Fig. 2 is a graph of the power pattern as a function of  $q$  (or distance). This calculation has been made for a 15-db power taper, and all curves in this and the succeeding figures have been normalized to the far-field coefficient  $|b_1(w)|^2$ . As the distance decreases from the far field ( $q = \infty$ ) to fractions of  $D^2/\lambda$ , the following effects are evident. First, as  $q$  decreases from  $\infty$  to 2, there is an appreciable change in the depth of the first minimum. Second, at a given  $q$ , the first sidelobe is more affected than the second. Third, the main beam maximum decreases as  $q$  decreases, though this effect is small

<sup>8</sup> L. W. Lechtreck, "Fresnel antenna patterns," IRE TRANS., vol. AP-3, pp. 138-140; July, 1955.

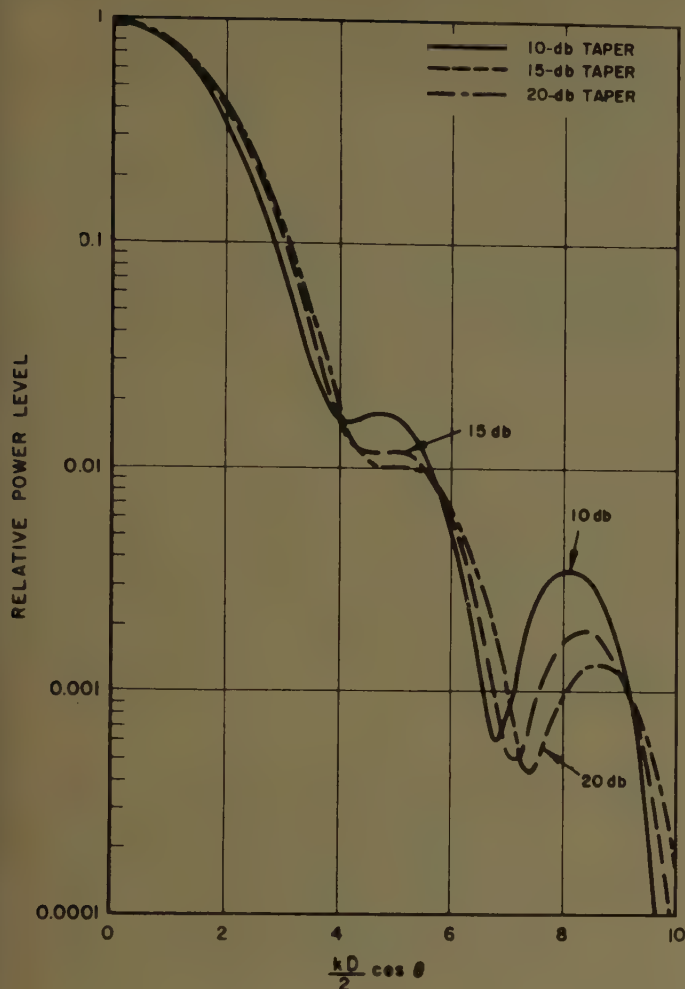


Fig. 4—Power patterns as a function of power taper for  $q=1$ .

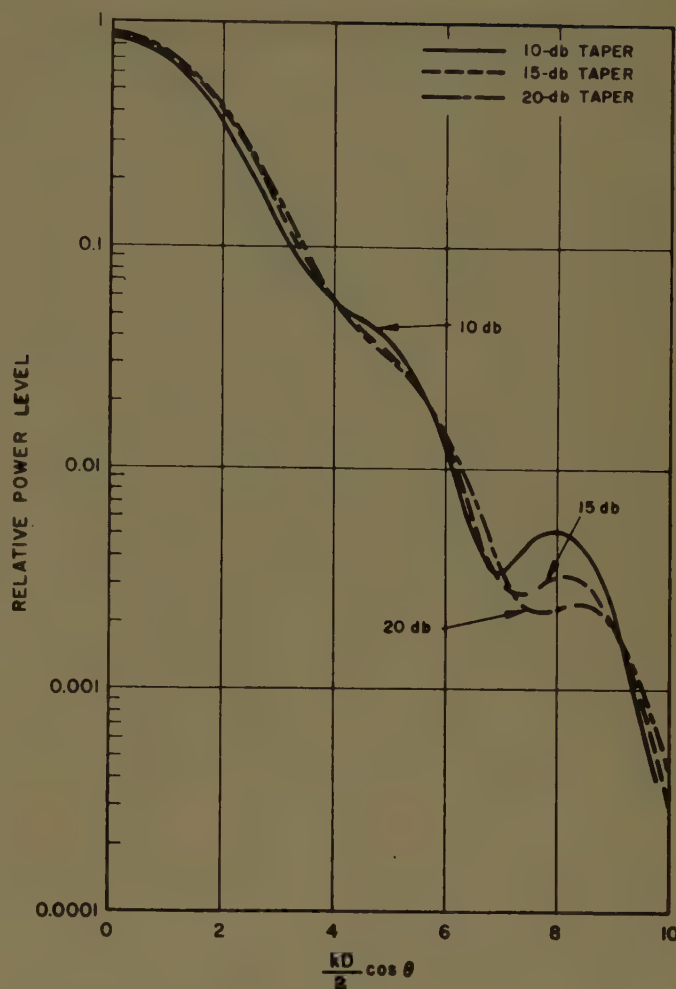


Fig. 5—Power patterns as a function of power taper for  $q=0.5$ .

until  $q < 0.5$ . Note that even at  $q = 0.25$  the first Fresnel minimum has not yet been reached. Fourth, the main beam is slightly broadened, and the loss of the first minimum effectively broadens the beam still further. This broadening is small, however, at the 3-db point. Fifth, the first sidelobe has disappeared at  $q = 1$ , and the second sidelobe at  $q < 0.5$ . Sixth, the main-beam-to-sidelobe ratio decreases as  $q$  decreases. This statement loses meaning, however, when the sidelobes disappear. The sidelobes also shift position slightly toward broadside.

It is evident that these results are least accurate for values of  $kD \cos \theta / 2$  near the far-field minima. To check the accuracy of the computation using five terms, additional power patterns were calculated in the neighborhood of the far-field minima using seven terms of the expansion. In Fig. 2, the dotted lines for the cases in which  $q = 0.5$  and  $0.25$  show the corrected patterns. It is seen that at  $q = 0.5$  the correction is negligible at the first minimum, and barely noticeable at the second minimum; hence, the first five terms are sufficient. At  $q = 0.25$ , however, even the first seven terms are not enough to give three-figure accuracy, as was evident from the relative magnitude of the seventh term. The curve shown for  $q = 0.25$  based on five terms is an indication only and is not quantitatively correct.

Fig. 3–Fig. 5 show the radiation patterns as a function of aperture-distribution power taper for three values of  $q$ . Fig. 3 shows the normalized far-field patterns for 10-, 15-, and 20-db tapers. Fig. 4 and Fig. 5 show the same patterns for  $q = 1.0$  and  $0.5$ , respectively. All curves are normalized to the far-field values.

Several conclusions can be drawn. First, Fresnel effects occur more markedly at a given  $q$  for the smaller power tapers. This phenomenon has been known for a long time in connection with phase-error effects in apertures.<sup>9</sup> It does not matter whether the phase difference at the field point is due to the geometry or to improper aperture illumination. The more peaked the aperture distribution, or the greater the illumination taper, the less the phase errors that are produced by off-center currents will be at a given field point. Second, the main-beam-to-side lobe ratio is a sensitive function of taper, especially as the taper approaches zero and the distribution becomes uniform. Third, although it is difficult to state that this conclusion is valid for arbitrary current distributions, in the present calculation the patterns for differing taper become more similar as  $q$  decreases. This

<sup>9</sup> S. Silver, "Microwave Antenna Theory and Design," McGraw-Hill Book Co., Inc., New York, N. Y., pp. 186–199; 1949.



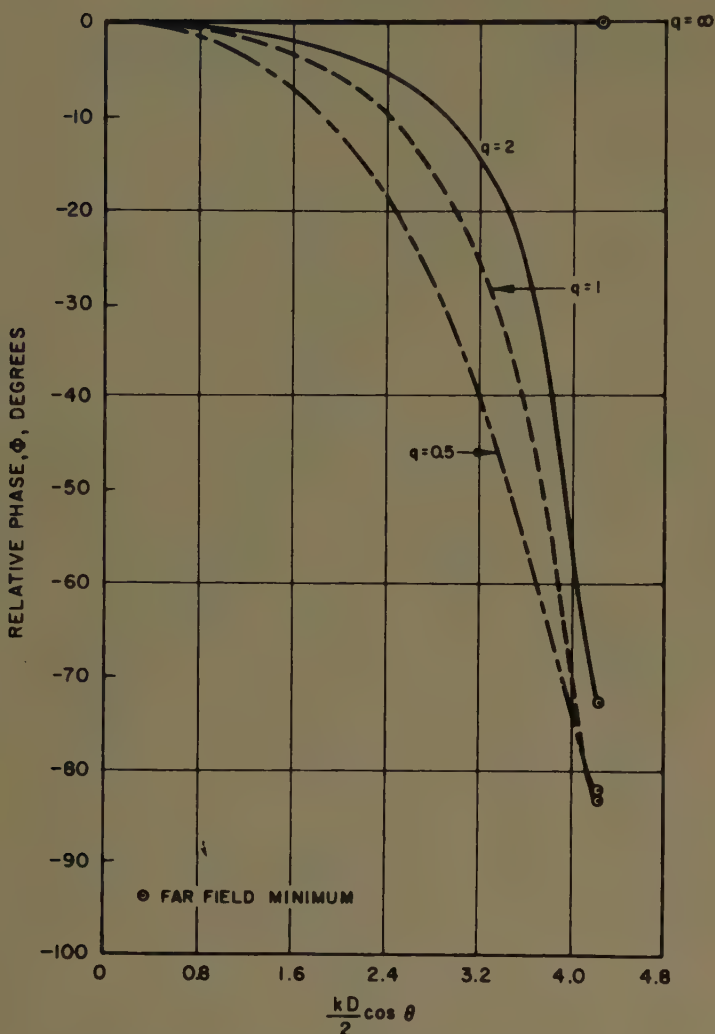


Fig. 6—Phase variation across the main beam as a function of  $q$  for 15-db power taper.

conclusion suggests that inferring far-field patterns from Fresnel field measurements would require very accurate knowledge of the Fresnel field and, hence, would be impractical.

For  $q = \infty$ , the phase variation would be zero across the main beam, and then alternate  $\pi$  radians in each successive sidelobe. As  $q$  decreases, it is natural to expect that the phase fronts would no longer be planes. The phase was calculated by noting that, although  $H_\phi$  is real in the far zone, for finite  $q$  it is complex, in general, and may be written

$$H_\phi = \alpha + j\beta, \quad (22)$$

where  $\alpha$ ,  $\beta$  are positive or negative real numbers. Then the phase angle is

$$\Phi = \tan^{-1} (\beta/\alpha). \quad (23)$$

The relative sign of  $\alpha$  and  $\beta$  determines the quadrant of  $\Phi$ . Fig. 6 presents the calculated relative phase variation across the main beam as a function of  $q$ . Notice that even at  $q = 2$  the phase variation has departed considerably from the uniform phase front characteristic of the true "far zone."

#### ACKNOWLEDGMENT

The authors acknowledge the assistance of several members of the Analysis Group, Systems Analysis Dept., Hughes Aircraft Company, particularly Dr. M. Steinberg for programming the calculation and checking some of the derivations, and Miss V. Stewart for performing the numerical computations. Benefit was derived from conversations with Dr. R. W. Bickmore and Dr. R. C. Hansen and from the encouragement and support of Dr. R. S. Elliott. Thanks also are due to N. A. Logan and the reviewers for their very helpful suggestions.



# The Approximate Parameters of Slot Lines and Their Complement\*

G. H. OWYANG† AND T. T. WU‡

**Summary**—An approximate attenuation coefficient due to ohmic loss is derived for both parallel slots and parallel strip lines. The capacitance per unit length, as well as the inductance per unit length of the lines are also obtained. The properties of a transmission line immersed in a lossless dielectric are thus completely determined. The attenuation coefficient due to lossy dielectric may be approximated by similar procedure.

## I. INTRODUCTION

**S**LOT ANTENNAS are usually fed by waveguides. A main disadvantage of this method of driving is the bulkiness of the waveguide. As an alternative, slot transmission lines as shown in Fig. 1 are being studied. The specific purpose of this report is to investigate properties of complementary wire and slot transmission lines.

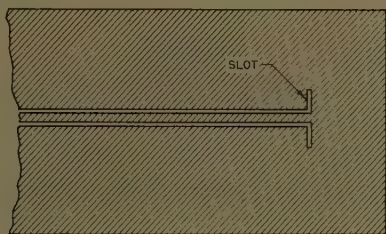


Fig. 1.

The rigorous solution of the transverse problem encountered with parallel transmission lines constructed of strips with finite thickness involves very complicated functions such as hyperelliptic integrals. However, for a thickness very small compared with the width and the separation, an approximate answer may be obtained by a first-order perturbation method.

The contour of the conducting strips is transformed by the Schwarz-Christoffel mapping into infinitely thin strips whose properties are already known. The actual distribution of current density is then calculated approximately from the known current density on the infinitely thin strips and the mapping factor. From the current density and the surface resistance of the material, the ohmic loss, and hence the attenuation, is obtained. The line constants are obtained as part of the analysis.

The problem of parallel slots is solved by a similar procedure in Section IV.

\* Original manuscript received by the PGAP, October 22, 1956; revised manuscript received, March 25, 1957. The work was supported in part by the Office of Naval Res. under Contract Nonr 1866(16), the U. S. Signal Corps, U. S. Army, and U. S. Air Force.

† Div. of Eng. Appl. Phys., Harvard University, Cambridge, Mass.

‡ Junior Fellow of the Society of Fellows, Harvard University, Cambridge, Mass.

## II. INFINITELY THIN STRIPS

It is well known that by means of the Schwarz-Christoffel transformation<sup>1</sup>

$$\frac{dz}{dw} = C_1 \prod_{(\alpha)} (w - w_{\alpha})^{-\gamma_{\alpha}} \quad (1)$$

the interior of the rectangle bounded by 1-2-3-4-1 in the  $z$  plane can be mapped onto the upper half  $w$  plane (Fig. 2). In the above equation,  $\gamma_{\alpha}\pi$  is defined as the change in direction of progression along the corresponding regions in the  $z$  plane. Since the strips are symmetrical with respect to the  $y$  axis in the  $z$  plane, by proper choice of the origin in the  $w$  plane, the planar parallel strips can be made symmetrical to the  $v$  axis. The transformation is found to be

$$\frac{dz}{dw} = C_1 [(w^2 - A^2)(w^2 - D^2)]^{-1/2}. \quad (2)$$

The constant  $C_1$  acts as scale and rotation factor.

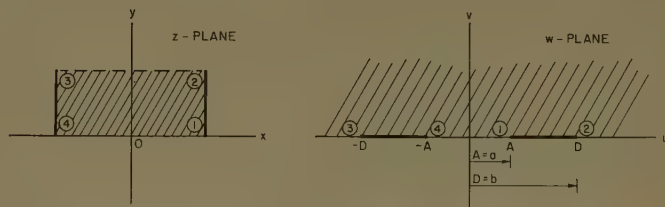


Fig. 2.

In Fig. 2, it is assumed that the vertical sides 1-2 and 3-4 are electric walls and the horizontal sides 1-4 and 2-3 are magnetic walls (in the  $z$  plane). Therefore, all  $E$ -field flux lines are straight and parallel to the  $x$  axis and all equipotential lines are parallel to the  $y$  axis. Consequently, in the  $w$  plane, the segments between 1-2 and 3-4 on the  $u$  axis are occupied by perfect electric conductors, and perfect magnetic conductors fill up the rest of the  $u$  axis. From (2) with the proper factor the  $E$ -field distribution exterior to the electric conductors and the current distributions in the electric conductors may be obtained. This is also true for the case of two planar strips placed in air, since in the  $w$  plane, the removal of the perfect magnetic conductor will not disturb the field.

The rms potential difference is obtained by integrating (2) in the space between the strips,

<sup>1</sup> E. Weber, "Electromagnetic Fields," John Wiley and Sons, Inc., New York, N. Y., vol. 1; 1950.



$$\begin{aligned}
 V &= 2 \int_{(0)}^{(1)} E_0 |dz| \\
 &= 2E_0 \int_0^A |dw[(w^2 - A^2)(w^2 - D^2)]^{-1/2}| \\
 &= \frac{2E_0}{D} K(k), \quad (3)
 \end{aligned}$$

where  $k \equiv A/D = a/b$ ,  $E_0$  is a scalar factor,  $K(k)$  is the complete elliptic integral of the first kind and  $k$  is the modulus.

The total charge per unit length is obtained by integrating the surface density of charge  $\eta$ ,<sup>2</sup>

$$\eta = -\epsilon_0 \hat{n} \cdot \vec{E},$$

over the surface of the strip,

$$\begin{aligned}
 q &= -2\epsilon_0 E_0 \int_{(1)}^{(2)} |dz| \\
 &= -2\epsilon_0 E_0 \int_A^D |dw[(w^2 - A^2)(w^2 - D^2)]^{-1/2}| \\
 &= -\frac{2\epsilon_0 E_0}{D} K(k_1), \quad (4)
 \end{aligned}$$

where

$$k_1 \equiv (1 - k^2)^{1/2}.$$

The factor 2 is due to the integration over both the top and bottom surfaces of the strip.

The total rms current may be obtained by integrating (2) over the surface of the strip.

$$i = \int_{(1)}^{(2)} i_0 |dz| = \frac{2i_0}{D} K(k_1), \quad (5)$$

where  $i_0$  is a scale factor.

The capacitance per unit length is

$$c = \frac{q}{V} = \epsilon_0 \frac{K(k_1)}{K(k)}, \quad (6)$$

and the inductance per unit length is

$$l = \frac{1}{v_0^2 c} = \mu_0 \frac{K(k)}{K(k_1)}, \quad (7)$$

where

$$v_0 = \frac{1}{\sqrt{\mu_0 \epsilon_0}}.$$

Maximum stored magnetic energy per unit length is

$$P_H = \frac{1}{2} l i_{\max}^2 = \frac{4i_0^2}{b^2} \mu_0 K(k) K(k_1). \quad (8)$$

The maximum stored electric energy per unit length is

$$P_E = \frac{1}{2} c V_{\max}^2 = \frac{4V_0^2}{b^2} \epsilon_0 K(k) K(k_1). \quad (9)$$

In order that the maximum stored electric energy equals the maximum stored magnetic energy, it is necessary that

$$\frac{V_0}{i_0} = \left( \frac{\mu_0}{\epsilon_0} \right)^{1/2} = \zeta_0,$$

which is true for TEM modes.

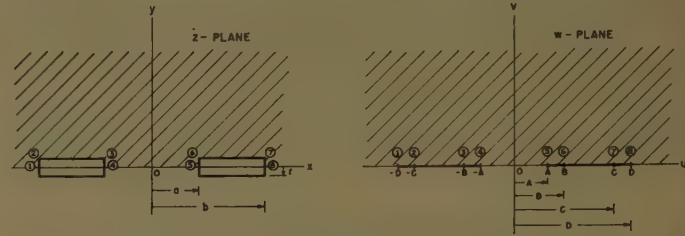


Fig. 3.

### III. STRIPS WITH FINITE THICKNESS

Let us consider two parallel strips of infinite length perpendicular to the paper, with a thickness  $2t$  and width  $(b-a)$ , and placed at a distance  $2a$  apart as shown in Fig. 3 in the  $z$  plane. By applying equation (1), the upper  $z$  plane exterior to the strips may be mapped into the upper half  $w$  plane. The transformation is

$$\frac{dz}{dw} = [(w^2 - B^2)(w^2 - C^2)]^{1/2} [(w^2 - A^2)(w^2 - D^2)]^{-1/2}. \quad (10)$$

Since the constant  $C_1$  in (1) is a magnitude factor and may be chosen to be independent of the thickness  $t$ , it is set equal to unity in the above expression.

In the following investigation, it is assumed that inequalities

$$t \ll a \quad \text{and} \quad t \ll (b-a) \quad (11)$$

are true.

Integration of equation (10) between points (5) and (6) in the  $z$  plane gives

$$\begin{aligned}
 i &= \int_{(5)}^{(6)} dz = \int_A^B [(w^2 - B^2)(w^2 - C^2)]^{1/2} [(w^2 - A^2)(w^2 - D^2)]^{-1/2} dw \\
 &= j \int_{A'}^{B'} \left[ \frac{B' - M}{M - A'} \right]^{1/2} \left\{ \frac{\left(1 + \frac{M + C'}{a + b}\right) \left(1 + \frac{C' - M}{b - a}\right) \left(1 + \frac{M + B'}{2a}\right)}{\left(1 + \frac{M + A'}{2a}\right) \left(1 + \frac{M + D'}{a + b}\right) \left(1 + \frac{D' - M}{b - a}\right)} \right\}^{1/2} dM. \quad (12)
 \end{aligned}$$

<sup>2</sup> R. W. P. King, "Electromagnetic Engineering," McGraw-Hill Book Co., Inc., New York, N. Y., 1945.

For a first-order theory, the higher-order terms in the brace are neglected so that

$$t \doteq \int_{A'}^{B'} \sqrt{\frac{B' - M}{M - A'}} dM \doteq \frac{\pi}{2} (B' - A'). \quad (13)$$

The above result is attained by making the following substitutions in (12):

$$\begin{aligned} A &= A' + a, \\ B &= B' + a, \\ C &= C' + b, \\ D &= D' + b, \end{aligned} \quad (14)$$

and then setting

$$M = w - a. \quad (15)$$

Note that  $A'$ ,  $B'$ ,  $C'$ , and  $D'$  are small quantities for small values of  $t$ , since as  $t$  approaches zero,  $A$  and  $B$

approach  $a$ , and  $C$  and  $D$  approach  $b$  (see Fig. 3). Integrating equation (10) from points (7) to (8) in the  $z$  plane gives

$$-jt = \int_{(7)}^{(8)} dz = \int_C^D dw [(w^2 - A^2)(w^2 - D^2)]^{-1/2} \cdot [(w^2 - B^2)(w^2 - C^2)]^{1/2}$$

or

$$t \doteq \int_{C'}^{D'} \left[ \frac{N - C'}{D' - N} \right]^{1/2} dN \doteq \frac{\pi}{2} (D' - C'). \quad (16)$$

A similar procedure is followed here except that the variable is replaced by

$$N = w - b. \quad (17)$$

The integration of equation (10) between the origin and point (5) gives

$$\begin{aligned} a &= \int_0^A dw [(w^2 - A^2)(w^2 - D^2)]^{-1/2} [(w^2 - B^2)(w^2 - C^2)]^{1/2} \\ &\doteq \int_{-a}^{A'} \left[ \frac{M - B'}{M - A'} \right]^{1/2} dM \left\{ 1 + \frac{1}{2} \left[ \frac{B' - A'}{M + 2a} + \frac{C' - D'}{M + b + a} + \frac{C' - D'}{b - a - M} \right] \right\} \\ &= [(A' + a)(B' + a)]^{1/2} + \frac{t}{\pi} \left\{ \left[ \frac{\frac{B'}{2a} + 1}{\frac{A'}{2a} + 1} \right]^{1/2} \ln \left| \frac{2 \left[ \left( \frac{A'}{2a} + 1 \right) \left( \frac{B'}{2a} + 1 \right) (a + A')(a + B') \right]^{1/2} + \left( \frac{B'}{2a} + 1 \right) (a + A') + \left( \frac{A'}{2a} + 1 \right) (B' + a)}{\frac{t}{\pi}} \right| \right. \\ &\quad - \left. \left[ \frac{\frac{B'}{\Delta} + 1}{\frac{A'}{\Delta} + 1} \right]^{1/2} \ln \left| \frac{2 \left[ \left( \frac{A'}{\Delta} + 1 \right) \left( \frac{B'}{\Delta} + 1 \right) (a + A')(a + B') \right]^{1/2} + \left( \frac{B'}{\Delta} + 1 \right) (a + A') + \left( \frac{A'}{\Delta} + 1 \right) (a + B')}{\frac{2t}{\pi} \left( 1 - \frac{a}{\Delta} \right)} \right| \right. \\ &\quad - \left. \left[ \frac{1 - \frac{B'}{\delta}}{1 - \frac{A'}{\delta}} \right]^{1/2} \ln \left| \frac{2 \left[ \left( 1 - \frac{A'}{\delta} \right) \left( 1 - \frac{B'}{\delta} \right) (a + B')(a + A') \right]^{1/2} + \left( 1 - \frac{B'}{\delta} \right) (A' + a) + \left( 1 - \frac{A'}{\delta} \right) (B' + a)}{\frac{2t}{\pi} \left( 1 + \frac{a}{\delta} \right)} \right| \right\}, \end{aligned} \quad (18)$$

where  $\Delta = b + a$ ,  $\delta = b - a$ , and equations (13) to (16) are used in obtaining the above equation.

Integration between points (6) and (7) in the  $z$  plane gives

$$\begin{aligned} b - a &= \int_B^C [(w^2 - B^2)(w^2 - C^2)]^{1/2} [(w^2 - A^2)(w^2 - D^2)]^{-1/2} dw \\ &\doteq \int_g^{C'} \left( \frac{C' - N}{D' - N} \right)^{1/2} dN \left\{ 1 + \frac{1}{2} \left[ \frac{B' - A'}{N + a + b} - \frac{B' - A'}{N + b - a} + \frac{C' - D'}{N + 2b} \right] \right\} \\ &= [(C' - g)(D' - g)]^{1/2} + \frac{t}{\pi} \left\{ 2 \ln \left| \frac{(D' - g)^{1/2} - (C' - g)^{1/2}}{(C' - g)^{1/2} + (D' - g)^{1/2}} \right| \right. \\ &\quad + \left[ \frac{\frac{C'}{\Delta} + 1}{\frac{D'}{\Delta} + 1} \right]^{1/2} \ln \left| \frac{2 \left[ \left( \frac{C'}{\Delta} + 1 \right) \left( \frac{D'}{\Delta} + 1 \right) (g - C')(g - D') \right]^{1/2} + \left( \frac{C'}{\Delta} + 1 \right) (D' - g) + \left( \frac{D'}{\Delta} + 1 \right) (C' - g)}{\frac{2t}{\pi} \left( 1 + \frac{g}{\Delta} \right)} \right| \\ &\quad - \left[ \frac{\frac{C'}{\delta} + 1}{\frac{D'}{\delta} + 1} \right]^{1/2} \ln \left| \frac{2 \left[ \left( \frac{C'}{\delta} + 1 \right) \left( \frac{D'}{\delta} + 1 \right) (g - C')(g - D') \right]^{1/2} + \left( \frac{C'}{\delta} + 1 \right) (D' - g) + \left( \frac{D'}{\delta} + 1 \right) (C' - g)}{\frac{2t}{\pi} \left( 1 + \frac{g}{\delta} \right)} \right| \\ &\quad - \left. \left[ \frac{\frac{C'}{2b} + 1}{\frac{D'}{2b} + 1} \right]^{1/2} \ln \left| \frac{2 \left[ \left( \frac{C'}{2b} + 1 \right) \left( \frac{D'}{2b} + 1 \right) (g - C')(g - D') \right]^{1/2} + \left( \frac{C'}{2b} + 1 \right) (D' - g) + \left( \frac{D'}{2b} + 1 \right) (C' - g)}{\frac{2t}{\pi} \left( 1 + \frac{g}{2b} \right)} \right| \right\}, \end{aligned} \quad (19)$$



where  $g = B' - \delta$ . Equations (13), (14), (16) and (17) are used in obtaining the above equation. With equations (13), (16), (18), and (19), it is possible to determine the four unknowns  $A'$ ,  $B'$ ,  $C'$ , and  $D'$ .

The ohmic loss per unit length is

$$P_L = \frac{1}{2} \int i_{\max}^2 R^s |dz|,$$

where  $i_{\max}$  is the peak current density, and  $R^s$  is the surface resistance<sup>3</sup> of the strip. The rms current density distribution on the strips in the  $w$  plane is given by equation (2); i.e.,

$$i = i_0 [(w^2 - A^2)(w^2 - D^2)]^{-1/2},$$

where  $i_0$  is a scale factor. This may be transformed into  $z$  plane by dividing it by the mapping factor as given by equation (10). Thus,

$$i = i_0 \left| \frac{dw}{dz} [(w^2 - A^2)(w^2 - D^2)]^{-1/2} \right|.$$

This is the distribution of current density for the right-hand strip in the  $z$  plane of Fig. 3.

The integral for  $P_L$  may be expressed as follows:

$$\begin{aligned} P_L &= 4R^s \int_I |dz| \left| i_0 \frac{dw}{dz} [(w^2 - A^2)(w^2 - D^2)]^{-1/2} \right|^2 \\ &= 4i_0^2 R^s \int_A^D P(w) dw, \end{aligned}$$

The leading term in the integrand of  $p_2$  when  $w$  is far away from both  $B$  and  $C$  is  $[(w^2 - A^2)(D^2 - w^2)]^{-1}$ . This suggests that  $p_2$  may be evaluated by adding two suitable correction terms to the integral

$$\int_B^C dw [(w^2 - A^2)(D^2 - w^2)]^{-1}$$

as follows:

$$\begin{aligned} p_2 &\equiv \int_B^C P(w) dw \doteq \int_B^C dw [(w^2 - A^2)(D^2 - w^2)]^{-1} \\ &\quad + \int_B^{B+\epsilon} dw \{ [(D^2 - w^2)^2 (w^2 - A^2)(w^2 - B^2)]^{-1/2} \\ &\quad - [(w^2 - A^2)(D^2 - w^2)]^{-1} \} \\ &\quad + \int_{C-\epsilon}^C dw \{ [(w^2 - A^2)^2 (C^2 - w^2)(D^2 - w^2)]^{-1/2} \\ &\quad - [(w^2 - A^2)(D^2 - w^2)]^{-1} \}. \end{aligned}$$

In this equation,  $\epsilon$  is a positive quantity which is small compared with the width of the slot and very large compared with  $t$ . Further evaluation yields the following to a first order:

$$\begin{aligned} p_2 &\doteq \frac{1}{D^2 - A^2} \int_B^C dw \left[ \frac{1}{w^2 - A^2} + \frac{1}{D^2 - w^2} \right] + \frac{1}{2a(b^2 - a^2)} \int_B^{B+\epsilon} dw \{ [(w - A)(w - B)]^{-1/2} - (w - A)^{-1} \} \\ &\quad + \frac{1}{2b(b^2 - a^2)} \int_{C-\epsilon}^C dw \{ [(C - w)(D - w)]^{-1/2} - (D - w)^{-1} \} \\ &\doteq \frac{1}{2(b^2 - a^2)} \left\{ \frac{1}{a} \ln \left( \frac{4a\pi}{t} \frac{b - a}{b + a} \right) + \frac{1}{b} \ln \left( \frac{4b\pi}{t} \frac{b - a}{b + a} \right) \right\}. \end{aligned}$$

where

$$P(w) = |[(w^2 - A^2)(w^2 - B^2)(w^2 - C^2)(w^2 - D^2)]^{-1/2}|,$$

and  $I$  is the contour (5)-(6)-(7)-(8) in the  $z$  plane of Fig. 3. Using the equations (14), (15), and (17), these integrals may be evaluated.

The first integral is

$$\begin{aligned} p_1 &= \int_A^B P(w) dw \\ &\doteq \frac{1}{2a(b^2 - a^2)} \int_{A'}^{B'} dM [(M - A')(B' - M)]^{-1/2} \\ &= \frac{\pi}{2a(b^2 - a^2)}. \end{aligned}$$

Lastly,

$$\begin{aligned} p_3 &\equiv \int_C^D P(w) dw \doteq \frac{1}{2b(b^2 - a^2)} \\ &\quad \cdot \int_{C'}^{D'} dN [(N - C')(D' - N)]^{-1/2} = \frac{\pi}{2b(b^2 - a^2)}. \end{aligned}$$

The ohmic loss per unit length is, therefore,

$$\begin{aligned} P_L &= 4i_0^2 R^s [p_1 + p_2 + p_3] \\ &= \frac{2i_0^2 R^s}{b^2 - a^2} \left\{ \frac{1}{a} \left[ \pi + \ln \left( \frac{4a\pi}{t} \frac{b - a}{b + a} \right) \right] \right. \\ &\quad \left. + \frac{1}{b} \left[ \pi + \ln \left( \frac{4b\pi}{t} \frac{b - a}{b + a} \right) \right] \right\}. \quad (20) \end{aligned}$$

<sup>3</sup> R. W. P. King: "Transmission-Line Theory," McGraw-Hill Book Co., Inc. New York, N. Y., 1955.

The attenuation constant per unit length due to ohmic loss is given by

$$\alpha_c = \frac{P_L}{2v_0 P_{H \max}}$$

$$= \frac{b^2 R^s}{8\zeta_0(b^2 - a^2)K(k)K(k_1)} \left\{ \frac{1}{a} \left[ \pi + \ln \left( \frac{4a\pi}{t} \frac{b-a}{b+a} \right) \right] + \frac{1}{b} \left[ \pi + \ln \left( \frac{4b\pi}{t} \frac{b-a}{b+a} \right) \right] \right\}, \quad (21)$$

where

$$\zeta_0 = \sqrt{\frac{\mu_0}{\epsilon_0}}$$

and  $p_H$  is obtained from equation (18). This is permissible because the total charge and the potential difference are the same before and after the mapping. To express the attenuation constant in terms of the separation and width of the strips,

$$\alpha_c = \frac{(\Delta + \delta)^2 R^s}{32\delta\Delta K(k)K(k_1)\zeta_0} \left\{ \frac{2}{\Delta - \delta} \left[ \pi + \ln \frac{2\delta\pi(\Delta - \delta)}{t\Delta} \right] + \frac{2}{\Delta + \delta} \left[ \pi + \ln \frac{2\delta\pi(\Delta + \delta)}{t\Delta} \right] \right\}, \quad (22)$$

where

$$k = \frac{a}{b}, \quad k_1 = [1 - k^2]^{1/2}$$

as before.

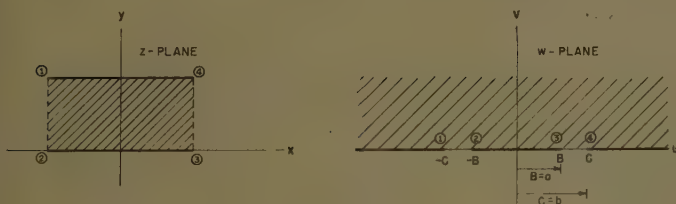


Fig. 4.

#### IV. PARALLEL SLOTS IN INFINITELY THIN SHEET

This is the complementary case of the infinitely thin strips and therefore the various quantities may be obtained by duality (Fig. 4). The transformation is

$$\frac{dz}{dw} = [(w^2 - B^2)(w^2 - C^2)]^{-1/2}. \quad (23)$$

The potential difference across the strips is

$$V = -\frac{E_0}{b} K(k_1),$$

where

$$k_1 = [1 - k^2]^{1/2}, \quad k = \frac{B}{C} = \frac{a}{b}. \quad (24)$$

The total charge per unit length is

$$q = -\frac{4\epsilon_0 E_0}{b} K(k). \quad (25)$$

The total current is

$$i = \frac{4i_0}{b} K(k). \quad (26)$$

The capacitance per unit length is

$$c = \frac{q}{V} = 4\epsilon_0 \frac{K(k)}{K(k_1)}, \quad (27)$$

and the inductance per unit length is

$$l = \frac{1}{v_0^2 c} = \frac{\mu_0}{4} \frac{K(k_1)}{K(k)}. \quad (28)$$

The total stored energy per unit length is

$$P_{\max} = \frac{1}{2} li_{\max}^2 = \frac{1}{2} cV_{\max}^2 = \frac{4i_0^2}{b^2} \mu_0 K(k)K(k_1). \quad (29)$$

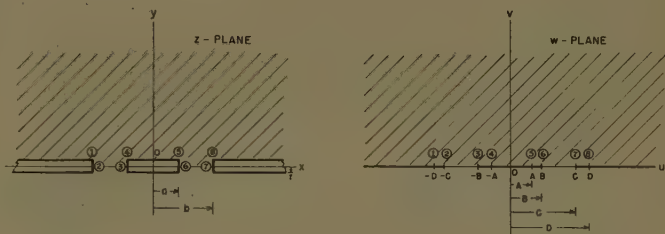


Fig. 5.

#### V. PARALLEL SLOTS ON METAL SHEET WITH FINITE THICKNESS

The parallel slots under consideration are on metal screen with a thickness  $2t$  as shown in the  $z$  plane (Fig. 5). In the solution of this problem almost exactly the same procedure is followed as in the case of parallel strips with finite thickness. It is assumed that the inequalities [equation (11)] are true.

The transformation of upper  $z$  plane exterior to the conductors into the upper half  $w$  plane is

$$\frac{dz}{dw} = [(w^2 - A^2)(w^2 - D^2)]^{1/2} [w^2 - B^2)(w^2 - C^2)]^{-1/2}. \quad (30)$$

This expression is normalized as before.

The unknowns  $A, B, \dots$  in the  $w$  plane may be determined by integrating equation (30) along specified paths in the  $z$  plane. In evaluating these integrals, the integrands are first written in factors of first degree, then equations (14) and (15) or (17) are substituted. The following integrals are sufficient for evaluating a first-order solution.

Integration of equation (30) from point (5) to point (6), in the  $z$  plane gives



$$-jt = \int_A^B \frac{1}{j} dw [(D^2 - w^2)(w^2 - A^2)]^{1/2} \\ \cdot [(C^2 - w^2)(B^2 - w^2)]^{-1/2},$$

$$\text{or } t \doteq \int_{A'}^{B'} \left[ \frac{M - A'}{B' - M} \right]^{1/2} dM = (B' - A') \frac{\pi}{2}. \quad (31)$$

And integration of equation (30) from point (7) to point (8) in the  $z$  plane gives

$$it = \int_C^D j dw [(D^2 - w^2)(w^2 - A^2)]^{1/2} \\ \cdot [w^2 - B^2)(w^2 - C^2)]^{1/2},$$

$$\text{or } t \doteq \int_{C'}^{D'} \left[ \frac{D' - M}{M - C'} \right]^{1/2} dM = (D' - C') \frac{\pi}{2}. \quad (32)$$

Integration of equation (30) between point (0) and point (5) in the  $z$  plane gives

$$a = \int_0^A dw [(A^2 - w^2)(D^2 - w^2)]^{1/2} [(B^2 - w^2)(C^2 - w^2)]^{-1/2} \\ = \int_{-a}^{A'} \left[ \frac{A' - M}{B' - M} \right]^{1/2} dM \left\{ 1 + \frac{1}{2} \left[ \frac{D' - C'}{b + a + M} + \frac{D' - C'}{b - a - M} + \frac{A' - B'}{2a + M} \right] \right\} \\ = [(A' + a)(B' + a)]^{1/2} + \frac{t}{\pi} \left\{ \left( \frac{A' + \Delta}{B' + \Delta} \right)^{1/2} \ln \left| \frac{2[(A' + a)(B' + a)(A' + \Delta)(B' + \Delta)]^{1/2} + (A' + \Delta)(B' + a) + (B' + \Delta)(A' + a)}{(\Delta - a)(B' - A')} \right| \right. \\ \left. - \left( \frac{A' + 2a}{B' + 2a} \right)^{1/2} \ln \left| \frac{2[(A' + a)(B' + a)(A' + 2a)(B' + 2a)]^{1/2} + (A' + 2a)(B' + a) + (B' + 2a)(A' + a)}{a(B' - A')} \right| \right. \\ \left. + \left( \frac{\delta - A'}{\delta - B'} \right)^{1/2} \ln \left| \frac{2[(A' + a)(B' + a)(\delta - A')(\delta - B')]^{1/2} + (\delta - A')(B' + a) + (\delta - B')(A' + a)}{(\delta + a)(B' - A')} \right| \right\}. \quad (33)$$

Integrating equation (30) from point (6) to point (7) in the  $z$  plane gives

$$b - a = \int_B^C dw [(D^2 - w^2)(w^2 - A^2)]^{1/2} [(C^2 - w^2)(w^2 - B^2)]^{-1/2} \\ \doteq \int_g^{C'} dN \left( \frac{D' - N}{C' - N} \right)^{1/2} \left\{ 1 + \frac{1}{2} \left[ \frac{A' - B'}{\Delta + N} - \frac{A' - B'}{\delta + N} + \frac{D' - C'}{2b + N} \right] \right\} \\ = [(D' - g)(C' - g)]^{1/2} + \frac{t}{\pi} \left\{ 2 \ln \left| \frac{(D' - g)^{1/2} + (C' - g)^{1/2}}{(C' - g)^{1/2} - (D' - g)^{1/2}} \right| \right. \\ \left. - \left( \frac{D' + \Delta}{C' + \Delta} \right)^{1/2} \ln \left| \frac{2[(D' - g)(C' - g)(D' + \Delta)(C' + \Delta)]^{1/2} + (D' + \Delta)(C' - g) + (C' + \Delta)(D' - g)}{(\Delta + g)(D' - C')} \right| \right. \\ \left. + \left( \frac{D' + \delta}{C' + \delta} \right)^{1/2} \ln \left| \frac{2[(D' - g)(C' - g)(D' + \delta)(C' + \delta)]^{1/2} + (D' + \delta)(C' - g) + (C' + \delta)(D' - g)}{(\delta + g)(D' - C')} \right| \right. \\ \left. + \left( \frac{D' + 2b}{C' + 2b} \right)^{1/2} \ln \left| \frac{2[(D' - g)(C' - g)(D' + 2b)(C' + 2b)]^{1/2} + (D' + 2b)(C' - g) + (C' + 2b)(D' - g)}{(g + 2b)(D' - C')} \right| \right\}. \quad (34)$$

The ohmic loss per unit length is

$$P_L = \frac{1}{2} \int_I R^s i_{m,x}^2 |dz| = 4i_0^2 R^s \int_0^\infty P(w) dw,$$

where

$$P(w) = |[(w^2 - A^2)(w^2 - B^2)(w^2 - C^2)(w^2 - D^2)]^{-1/2}|.$$

The rms current density is given by equation (23) with a scale factor  $i_0$ , and the mapping factor is from equation (30). Let

$$p_1 \equiv \int_0^A P(w) dw \doteq \frac{1}{2(b^2 - a^2)} \left\{ \frac{1}{a} \ln \frac{4a\pi}{t} - \frac{1}{b} \ln \frac{b + a}{b - a} \right\},$$

$$p_2 \equiv \int_A^B P(w) dw \doteq \frac{\pi}{2a(b^2 - a^2)},$$

$$p_3 \equiv \int_C^D P(w) dw \doteq \frac{\pi}{2b(b^2 - a^2)},$$

and

$$p_4 \equiv \int_D^\infty P(w) dw \doteq \frac{1}{2(b^2 - a^2)} \left\{ \frac{1}{b} \ln \frac{4b\pi}{t} + \frac{1}{a} \ln \frac{b - a}{b + a} \right\}.$$

Therefore, the ohmic loss per unit length is

$$P_L = 4i_0^2 R^s [p_1 + p_2 + p_3 + p_4]$$

$$\doteq \frac{2i_0^2 R^s}{(b^2 - a^2)} \left\{ \frac{1}{a} \left[ \pi + \ln \left( \frac{4a\pi}{t} \frac{b - a}{b + a} \right) \right] \right.$$

$$\left. + \frac{1}{b} \left[ \pi + \ln \left( \frac{4b\pi}{t} \frac{b - a}{b + a} \right) \right] \right\}. \quad (35)$$

The attenuation constant per unit length due to ohmic loss is, from equations (29) and (27),

$$\alpha_c = \frac{1}{2v_0} \frac{P_L}{P_{H \max}} \doteq \frac{b^2 R^s}{8(b^2 - a^2) \zeta_0 K(k) K(k_1)} \left\{ \frac{1}{a} \left[ \pi + \ln \left( \frac{4a\pi}{t} \frac{b-a}{b+a} \right) \right] + \frac{1}{b} \left[ \pi + \ln \left( \frac{4b\pi}{t} \frac{b-a}{b+a} \right) \right] \right\}. \quad (36)$$

The attenuation constant may be expressed in terms of the separation and the width of the slots.

$$\alpha_c = \frac{(\Delta + \delta)^2 R^s}{32\delta \Delta \zeta_0 K(k) K(k_1)} \left\{ \frac{2}{\Delta - \delta} \left[ \pi + \ln \frac{2\delta\pi(\Delta - \delta)}{t\Delta} \right] + \frac{2}{\Delta + \delta} \left[ \pi + \ln \frac{2\delta\pi(\Delta + \delta)}{t\Delta} \right] \right\}, \quad (37)$$

where

$k = a/b$ ,  $k_1 = [1 - k^2]^{1/2}$ ,  $\Delta = a + b$  is the center-to-center separation, and  $\delta = b - a$  is the width of a slot.

## VI. SUMMARY OF FORMULAS

The attenuation constant per unit length for the slot lines or their complement due to ohmic losses in the conductors is

$$\alpha_c = \frac{(\Delta + \delta) R^s}{32\delta \Delta \zeta_0 K(k) K(k_1)} \left\{ \frac{2}{\Delta - \delta} \left[ \pi + \ln \frac{2\delta\pi(\Delta - \delta)}{t\Delta} \right] + \frac{2}{\Delta + \delta} \left[ \pi + \ln \frac{2\delta\pi(\Delta + \delta)}{t\Delta} \right] \right\}$$

where  $\Delta$  is the center-to-center separation, and  $\delta$  is the width of the slots or the strips. This formula is a good approximation when the thickness  $2t$  is very small compared with the width and the separation of the strips (or slots), but large compared with the skin depth so that the surface resistance  $R^s$  is meaningful. The capacitance and inductance per unit length are:  
for parallel strips

$$c = \epsilon_0 \frac{K(k_1)}{K(k)}, \quad l = \mu_0 \frac{K(k)}{K(k_1)},$$

for parallel slots

$$c = 4\epsilon_0 \frac{K(k)}{K(k_1)}, \quad l = \frac{\mu_0}{4} \frac{K(k_1)}{K(k)}.$$

In the above formulas  $k = (\Delta - \delta)/(\Delta + \delta)$ . The conductance per unit length in either of the above cases is zero since the dielectric is air. For a slightly conducting dielectric with dielectric constant  $\epsilon$  and conductivity  $\sigma$ , the capacitance per unit length is as given above with  $\epsilon$  substituted for  $\epsilon_0$ ; the conductance  $g$  per unit length is given by the formulas for capacitance per unit length if  $\epsilon_0$  is replaced by  $\sigma$ . In this case  $\alpha = \alpha_c + \alpha_d$  where  $\alpha_d = gR_c/2$ . The resistance per unit length of transmission line can be calculated from

$$r = 2\alpha_c R_c,$$

where

$$R_c = \sqrt{\frac{l}{c}}.$$

## VII. CONCLUSION

It has just been found that the first-order solution of attenuation per unit length is the same in form for both strip lines and slot lines.

With the capacitance per unit length, inductance per unit length, and the attenuation per unit length, the resistance per unit length can be calculated from the relation  $\alpha_c = r/2R_c$  or  $r = 2\alpha_c R_c$ , where  $R_c = \sqrt{l/c}$  is the characteristic impedance of the transmission line. Since the lines are assumed to be in air, the conductance per unit length is zero in both cases. Thus the properties of the strip lines and slot lines are completely determined.

## VIII. ACKNOWLEDGMENT

The writers are indebted to Professor Ronold W. P. King for his guidance and encouragement in carrying out this theory and his correction of the manuscript.





# Propagation of Electromagnetic Pulses Around the Earth\*

B. R. LEVY† AND J. B. KELLER†

**Summary**—The propagation of electromagnetic pulses around the earth is investigated analytically. The pulses are assumed to be produced by a vertical electric or magnetic dipole. The earth is treated as a homogeneous sphere of either finite or infinite conductivity and the atmosphere is assumed to be homogeneous. It is found that very short pulses become longer the further they propagate, in addition to diminishing in amplitude. The duration of a pulse which is initially a delta-function increases as  $\theta^3$ , where  $\theta$  is the angle between source and receiver. The results are represented as products of several factors, which we call the amplitude factor, the pulse-shape factor, the time-dependent height-gain factors for the source and receiver, and the conductivity factor. Graphs of these factors and of the pulse shape for several cases are given.

## I. INTRODUCTION

SUPPOSE an electromagnetic pulse of given shape and amplitude is emitted by a source on or near the ground. We wish to find its shape, amplitude, and arrival time at any point beyond the horizon on or near the ground. In particular, we wish to determine the effects of the ground conductivity along the propagation path. We will assume that the source is a vertical dipole of either electric or magnetic type and that the earth is a homogeneous sphere. By a slight modification of our procedure, we could also treat the case in which the ground conductivity varies along the propagation path.

The method of solution consists of two steps. First, we must obtain the Hertz vector which represents the field due to a time harmonic or periodic source. Then, by Fourier superposition of these periodic fields, we can obtain the Hertz vector for a delta-function source. Other pulse-type sources can be treated by superposition of delta-function fields. Wait<sup>1</sup> also has analyzed the inversion of the resulting Fourier integrals by several methods for various types of time dependence of the source.

Since the field due to a periodic source has been determined by numerous authors, our first step is simple—we need merely copy the Hertz vector of this field. This is done in Section II, the books of Fock<sup>2</sup> and Bremmer<sup>3</sup> being used as sources. In Section III, we write the Fourier integral representing the Hertz vector of the field due to a delta-function source. Then we evaluate this integral by the saddle point method and obtain a

\* Manuscript received by the PGAP, March 29, 1957; revised manuscript received October 1, 1957. The research reported in this document has been sponsored by the AF Cambridge Res. Ctr., Air Res. and Dev. Comm., under Contract No. AF 19(604)1717.

† Inst. of Mathematical Sciences, Div. of Electromagnetic Res., New York University, New York 3, N. Y.

<sup>1</sup> J. R. Wait, "Transient fields of a vertical dipole over a homogeneous curved ground," *Can. J. Phys.*, vol. 34, pp. 27–35; January, 1956.

—, "A note on the propagation of the transient ground wave," *Proc. Symp. on Very Low Frequency Propagation*, Nat. Bur. Standards, Boulder, Colo.; 1957.

—, "The transient behavior of the electromagnetic ground wave on a spherical earth," *IRE TRANS.*, vol. AP-5, pp. 198–200; April, 1957.

<sup>2</sup> V. A. Fock, "Diffraction of radio waves around the earth's surface," *Acad. Sci. USSR, Moscow, Russia*; 1946.

<sup>3</sup> H. Bremmer, "Terrestrial Radio Waves," Elsevier Pub. Co., New York, N. Y.; 1949.

simple formula as the result for each type of dipole. In Section IV, some graphs based on these formulas and a discussion of the results are given.

## II. THE FIELD OF A PERIODIC SOURCE

Suppose a vertical electric dipole is located at the point  $r = \rho$ ,  $\theta = 0$  of a polar-coordinate system with the origin at the center of the earth. Then its field can be expressed in terms of a Hertz vector having only a radial component  $rU_e(r, \theta, t)$ , by:

$$\begin{aligned} E &= \nabla \times \nabla \times (\bar{r}U_e) \\ H &= \left( \epsilon \frac{\partial}{\partial t} + \sigma \right) \nabla \times (\bar{r}U_e). \end{aligned} \quad (1)$$

Similarly, the field of a vertical magnetic dipole at  $r = \rho$ ,  $\theta = 0$  can be expressed in terms of a radial Hertz vector  $rU_m(r, \theta, t)$  by:

$$\begin{aligned} E &= -\mu \frac{\partial}{\partial t} \nabla \times (\bar{r}U_m) \\ H &= \nabla \times \nabla \times (\bar{r}U_m). \end{aligned} \quad (2)$$

In these equations  $\epsilon$ ,  $\mu$ , and  $\sigma$  are the dielectric constant, permeability, and conductivity, respectively. These quantities are assumed to have the constant values  $\epsilon_1$ ,  $\mu_1$ ,  $\sigma_1$  inside the earth ( $r < a$ ) and the constant values  $\epsilon$ ,  $\mu$ ,  $\sigma = 0$  outside it.

If the field is time harmonic with angular frequency  $\omega$ , then

$$U_e = u_e(r, \theta)e^{-i\omega t}, \quad U_m = u_m(r, \theta)e^{-i\omega t}. \quad (3)$$

We now define the propagation constants  $k$  and  $k_1$  by

$$k = \omega\sqrt{\epsilon\mu}, \quad k_1^2 = \omega^2\epsilon_1\mu_1 + i\mu_1\sigma_1\omega. \quad (4)$$

It is convenient also, to define  $\delta_e$  and  $\delta_m$  by

$$\delta_e = \frac{ik_1^2/k^2}{(ka)^{1/3}\sqrt{(k_1^2/k^2) - 1}} \quad (5)$$

$$\delta_m = \frac{i}{(ka)^{1/3}\sqrt{(k_1^2/k^2) - 1}}. \quad (6)$$

For large  $ka$  both the electric and magnetic Hertz potentials  $u_e(r, \theta)$  and  $u_m(r, \theta)$  can be expressed in terms of a single function  $f(r, \theta, \delta)$

$$u_e(r, \theta) = f(r, \theta, \delta_e), \quad u_m(r, \theta) = f(r, \theta, \delta_m). \quad (7)$$

The function  $f(r, \theta, \delta)$  is defined by

$$\begin{aligned} f &= \frac{[2\pi i \sin \theta]^{1/2}}{2\pi a \sin \theta} (ka)^{1/6} \sum_{s=0}^{\infty} \frac{\exp [i\{ka\theta + \tau_s(ka)^{1/3}\theta\}]}{2\tau_s - \delta^{-2}} \\ &\quad \cdot \left[ \frac{w(2^{1/3}\tau_s - y_1)}{w(2^{1/3}\tau_s)} \frac{w(2^{1/3}\tau_s - y_2)}{w(2^{1/3}\tau_s)} \right]. \end{aligned} \quad (8)$$

This function also can be written in the form

$$f = \frac{[2\pi i \sin \theta]^{1/2}}{2\pi a \sin \theta} \frac{(ka)^{1/6}}{2^{2/3}} \sum_{s=0}^{\infty} \frac{\exp[i\{ka\theta + \tau_s(ka)^{1/3}\theta\}]}{2\tau_s \delta^2 - 1} \cdot \left[ \frac{w(2^{1/3}\tau_s - y_1)}{w'(2^{1/3}\tau_s)} \cdot \frac{w(2^{1/3}\tau_s - y_2)}{w'(2^{1/3}\tau_s)} \right]. \quad (9)$$

The quantities  $y_1$  and  $y_2$  in (8) and (9) are defined by

$$y_1 = \frac{2^{1/3}}{a} (ka)^{2/3} (r - a) \quad (10)$$

$$y_2 = \frac{2^{1/3}}{a} (ka)^{2/3} (\rho - a). \quad (11)$$

The function  $w(x)$  is the Airy function

$$w(x) = \frac{1}{\sqrt{\pi}} \int_{\Gamma} e^{(x-z^3/3)} dz. \quad (12)$$

Here  $\Gamma$  is a contour going from infinity to zero along the ray  $\arg z = -2\pi/3$  and from zero to infinity along the positive real axis. The numbers  $\tau_s$ , which depend upon  $\delta$ , are the roots of

$$\frac{w'(2^{1/3}\tau_s)}{w(2^{1/3}\tau_s)} = -\frac{1}{2^{1/3}\delta}. \quad (13)$$

It is easily seen, by use of (13), that (9) follows from (8).

For a perfectly conducting earth,  $\sigma_1 = \infty$ , it follows from (4), (5), and (6) that  $\delta_e = \infty$  and  $\delta_m = 0$ . The roots  $\tau_s$  are denoted by  $\tau_s^\infty$  when  $\delta = \infty$  and by  $\tau_s^0$  when  $\delta = 0$ . Upon expanding  $\tau_s$  in powers of  $\delta^{-1}$  for  $\delta$  large, and in powers of  $\delta$  for  $\delta$  small, one obtains

$$\tau_s = \tau_s^\infty - \frac{1}{2\tau_s^\infty \delta} - \frac{1}{8\tau_s^\infty \delta^2} + \dots \quad (14)$$

$$\tau_s = \tau_s^0 - \delta - \frac{2}{3} \tau_s^0 \delta^2 + \dots \quad (15)$$

The numbers  $\tau_s^\infty$  and  $\tau_s^0$  are complex, lying on the ray  $\arg \tau = \pi/3$ . The  $\tau$ 's of smallest absolute value are

$$\tau_0^\infty = 0.808 e^{i\pi/3} \quad (16)$$

$$\tau_0^0 = 1.856 e^{i\pi/3}. \quad (17)$$

For a highly conducting earth  $\sigma_1$  is large so  $\delta_e$  is large and  $\delta_m$  is small. Therefore, the series (14) is useful for computing  $\tau_s$  in the electric case and (15) is useful in the magnetic case. For the same reason, (8) is more convenient for computing  $f$  in the electric case, and (9) is in the magnetic case.

### III. THE FIELD OF A DELTA-FUNCTION SOURCE

The Hertz potential  $U(r, \theta, t)$  of the field due to a vertical electric or magnetic dipole having any time dependence can be obtained by Fourier superposition of the periodic potentials  $u(r, \theta)e^{-i\omega t}$  described above. Since  $k = \omega/c$ , where  $1/c = \sqrt{\epsilon\mu}$ , we can integrate with respect to  $k$  instead of  $\omega$  and obtain

$$U(r, \theta, t) = \frac{c}{2\pi} \int_{-\infty}^{\infty} A(k) u(r, \theta) e^{-ikct} dk. \quad (18)$$

In (18) the Fourier amplitude  $A(k)$  is determined by the time dependence and amplitude of the source. With the function  $u(r, \theta)$  defined as in the preceding section, a delta-function source has the amplitude  $A(k) \equiv 1$ . In the absence of the earth, the Hertz potential of the field due to such a dipole would be

$$U_0 = \frac{\delta\left(t - \frac{R}{c}\right)}{4\pi R}. \quad (19)$$

Here  $R = (r^2 + \rho^2 - 2\rho r \cos \theta)^{1/2}$  is the distance from the source to the receiver. Thus with  $A(k) \equiv 1$ , (18) will yield the diffracted pulse due to the incident pulse (19).

To evaluate (18) we introduce the time  $T$  defined by

$$T = t - \frac{a\theta}{c} + \frac{a}{c} \cos^{-1}\left(\frac{a}{\rho}\right) + \frac{a}{c} \cos^{-1}\left(\frac{a}{r}\right). \quad (20)$$

This time  $T$  is just the time measured from the arrival of the diffracted wave front at the point  $(r, \theta)$ , assuming that the source starts at  $t=0$ . We now insert (8) or (9) into (18) and set  $A(k) = 1$ . Let us consider first, the case of a perfectly conducting earth. In this case,  $\tau$  is independent of  $k$  and  $\delta$  is either infinity or zero. Then for  $T > 0$  the contour in (18) can be closed in the upper half-plane to yield the value zero for  $U$ . Of course, this is to be expected from the definition of  $T$ . For  $T > 0$  we evaluate (18), by the saddle point method. This yields the first term in the asymptotic expansion of the diffracted field as  $T$  tends to zero. In the electric case we use (8) in (18), set  $\delta_e = \infty$  and obtain

$$U_e(r, \theta, t) = \sum_s \frac{c\theta}{2^{5/2} 3^{1/2} \pi a^{1/2} (\sin \theta)^{1/2}} \cdot \frac{1}{(cT)^{3/2}} \exp\left[-\frac{2}{3^{3/2}} \frac{|\tau_s^\infty|^{3/2} \theta^{3/2} a^{1/2}}{(cT)^{1/2}}\right] \cdot \frac{v\left\{|\tau_s^\infty|^{2/3} \left(\frac{\theta(r-a)}{3cT} - 1\right)\right\}}{v(-|\tau_s^\infty|^{2/3})} \cdot \frac{v\left\{|\tau_s^\infty|^{2/3} \left(\frac{\theta(\rho-a)}{3cT} - 1\right)\right\}}{v(-|\tau_s^\infty|^{2/3})}. \quad (21)$$

In the magnetic case we use (9) in (18), set  $\delta_m = 0$  and obtain

$$U_m(r, \theta, t) = \sum_s \frac{c\theta |\tau_s^0|}{2^{5/2} 2^{1/3} 3^{1/2} \pi a^{1/2} (\sin \theta)^{1/2}} \cdot \frac{1}{(cT)^{3/2}} \exp\left[-\frac{2}{3^{3/2}} \frac{|\tau_s^0|^{3/2} \theta^{3/2} a^{1/2}}{(cT)^{1/2}}\right] \cdot \frac{v\left\{|\tau_s^0|^{2/3} \left(\frac{\theta(r-a)}{3cT} - 1\right)\right\}}{v'(-2^{1/3} |\tau_s^0|)} \cdot \frac{v\left\{|\tau_s^0|^{2/3} \left(\frac{\theta(\rho-a)}{3cT} - 1\right)\right\}}{v'(-2^{1/3} |\tau_s^0|)}. \quad (22)$$



The function  $v$  in (21) and (22) is the imaginary part of the Airy function,  $v = \text{Im}w$ . For large positive  $z$ ,  $v(z)$  is asymptotic to  $\frac{1}{2}z^{-1/4} \exp[-\frac{2}{3}z^{3/2}]$  while for large negative  $z$ ,  $v(z)$  is asymptotic to

$$(-z)^{-1/4} \sin \left[ \frac{2}{3} (-z)^{3/2} + \frac{\pi}{4} \right].$$

In the intermediate region the values of  $v(z)$  have been tabulated by Fock.<sup>2</sup>

Now let us consider the case of a finitely conducting earth. In the electric case we will use for  $\tau_s$  the first two terms of (14) with  $\delta = \delta_e$ . Upon inserting (8) into (18), with this value of  $\tau_s$ , and putting  $A(k) = 1$ , we obtain an expression for  $U_e(r, \theta, t)$ . For  $T < 0$  this expression is zero, as before. For  $T > 0$  we again use the saddle point method. Since  $\delta_e$  is a function of  $k$ , determination of the saddle point is more complicated than in previous cases. Thus, we neglect the term  $-1/(2\tau_s^\infty \delta_e)$  compared with  $\tau_s^\infty$  in determining the saddle point. Then we obtain

$$U_e(r, \theta, t) = \sum_s \frac{c\theta |\tau_s^\infty|^{1/2}}{2^{3/2} 3^{1/2} \pi a^{1/2} (\sin \theta)^{1/2}} \cdot \frac{1}{2 |\tau_s^\infty| + \frac{1}{|\tau_s^\infty| |\delta_e^*|}} \cdot \frac{1}{(cT)^{3/2}} \exp \left[ -\frac{2}{3^{3/2}} \frac{\left[ |\tau_s^\infty| + \frac{1}{2 |\tau_s^\infty|} \cdot \frac{1}{|\delta_e^*|} \right]^{3/2} \theta^{3/2} a^{1/2}}{(cT)^{1/2}} \right] \cdot \frac{v \left\{ |\tau_s^\infty| 2^{1/3} \left( \frac{\theta(r-a)}{3cT} - 1 \right) \right\}}{v(-|\tau_s^\infty| 2^{1/3})} \cdot \frac{v \left\{ |\tau_s^\infty| 2^{1/3} \left( \frac{\theta(\rho-a)}{3cT} - 1 \right) \right\}}{v(-|\tau_s^\infty| 2^{1/3})}. \quad (23)$$

In (23),  $\delta_e^*$  is the value of  $\delta_e$  at the stationary point. Its absolute value is given by

$$|\delta_e^*| = \left( \frac{3T}{|\tau_s^\infty| T_2} \right)^{1/2} \cdot \frac{\frac{\epsilon_1}{\epsilon} + \frac{3^{3/2} \sigma_1 \mu c a}{|\tau_s^\infty|^{3/2}} \left( \frac{T}{T_2} \right)^{3/2}}{\sqrt{\frac{\epsilon_1}{\epsilon} - 1 + \frac{3^{3/2} \sigma_1 \mu c a}{|\tau_s^\infty|^{3/2}} \left( \frac{T}{T_2} \right)^{3/2}}}. \quad (24)$$

Here  $T_2 = \theta a/c$  is the travel time for the pulse to reach the point  $\theta$  from the source at  $\theta = 0$ .

In the magnetic case we use the first two terms in (15) for  $\tau_s$  with  $\delta = \delta_m$ . Then using (9) in (18) with  $A(k) = 1$  we obtain an expression for  $U_m(r, \theta, t)$ . As before, this expression is zero for  $T < 0$ , while for  $T > 0$  we obtain

$$U_m(r, \theta, t) = \sum_s \frac{c\theta |\tau_s^0|^{1/2}}{2^{5/2} 2^{1/3} 3^{1/2} \pi a^{1/2} (\sin \theta)^{1/2}} \cdot \frac{1}{2 |\delta_m|^2 (|\tau_s^0| - |\delta_m^*|) + 1} \cdot \frac{1}{(cT)^{3/2}} \exp \left[ -\frac{2}{3^{3/2}} \frac{[|\tau_s^0| - |\delta_m^*|]^{3/2} \theta^{3/2} a^{1/2}}{(cT)^{3/2}} \right] \cdot \frac{v \left\{ |\tau_s^0| 2^{1/3} \left( \frac{\theta(\rho-a)}{3cT} - 1 \right) \right\}}{v'(-2^{1/3} |\tau_s^0|)} \cdot \frac{v \left\{ |\tau_s^0| 2^{1/3} \left( \frac{\theta(r-a)}{3cT} - 1 \right) \right\}}{v'(-2^{1/3} |\tau_s^0|)}. \quad (25)$$

Here  $\delta_m^*$  is the value of  $\delta_m$  at the stationary point and  $|\delta_m^*|$  is given by

$$|\delta_m^*| = \left( \frac{3cT}{|\tau_s^0| \theta a} \right)^{1/2} \cdot \frac{1}{\sqrt{\frac{\epsilon_1}{\epsilon} - 1 + \frac{\sigma \mu c 3^{3/2} (cT)^{3/2}}{|\tau_s^0|^{3/2} a^{1/2} \theta^{3/2}}}}. \quad (26)$$

#### IV. DISCUSSION OF RESULTS

We have calculated the Hertz vector of the field due to a vertical electric or magnetic dipole with a delta-function time dependence. For a perfectly conducting earth we obtain (21) and (22), while for finite conductivity we obtain (23) and (25). Of course (23) reduces to (21) and (25) to (22) as  $\sigma_1 \rightarrow \infty$ . These results are useful at points beyond the horizon and, therefore, only the first term ( $s=0$ ) in each result need be retained. This is so because the other terms have relatively rapidly decaying exponential factors. Consequently, our results are rather simple formulas.

Let us examine  $U_e(r, \theta, t)$  for the perfectly conducting case when both the source and observation point are on the ground ( $\rho = a$  and  $r = a$ ). Then (21) becomes

$$U_e(a, \theta, t) = A_e(\theta) S(T/T_{e0}). \quad (27)$$

Here the amplitude  $A_e(\theta)$  is the maximum value of  $U_e$ , the build-up time  $T_{e0}(\theta)$  is the time at which the maximum occurs and  $S(T/T_{e0})$  is the pulse-shape factor.  $A_e$ ,  $T_{e0}$ , and  $S$  are given by

$$A_e = \frac{3^7 c}{|\tau_0^\infty|^{5/2} 2^{11/2} \pi e^3 a^2} \cdot \frac{1}{\sqrt{\theta^7 \sin \theta}} = (1.64 \times 10^{-5}) \frac{1}{\sqrt{\theta^7 \sin \theta}} \sim (1.64 \times 10^{-5}) \frac{1}{\theta^4}, \quad (28)$$

$$T_{e0} = \frac{4 |\tau_0^\infty|^{3/2} a}{3^5 c} \theta^3 = (1.85 \times 10^{-4}) \theta^3, \quad (29)$$

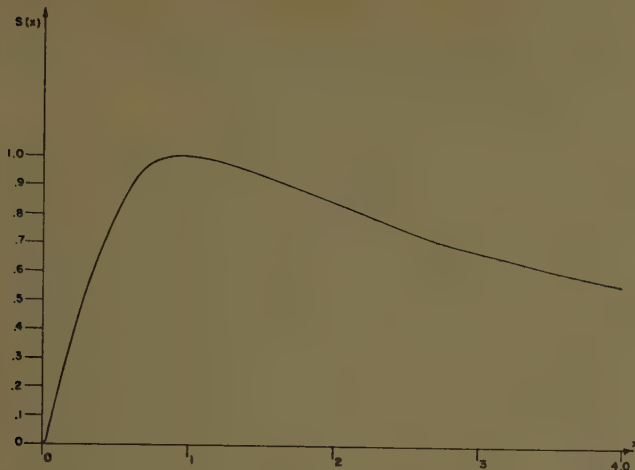


Fig. 1—The pulse shape factor  $S(x) = x^{-3/2} \exp [3(1 - x^{-1/2})]$ .

$$S(T/T_{e0}) = (T_{e0}/T)^{3/2} \exp 3[1 - (T_{e0}/T)^{1/2}]. \quad (30)$$

A graph of the pulse shape factor  $S$  is given in Fig. 1.  $U_e$  is obtained from this graph by multiplying the vertical scale by  $A_e(\theta)$ , which is given by (28).

If the observation point is above the ground ( $r > a$ ),  $U_e$  is obtained by multiplying (27) by the time dependent height-gain factor  $H_e(T/T_{e1}(r))$  defined by

$$H_e\left(\frac{T}{T_{e1}(r)}\right) = \frac{v[T_{e1}(r)/T - 2^{1/3}|\tau_0^\infty|]}{v[-2^{1/3}|\tau_0^\infty|]}. \quad (31)$$

In (31) the time  $T_{e1}(r)$  is defined by

$$T_{e1}(r) = 2^{1/3}|\tau_0^\infty|\theta(r - a)/3c. \quad (32)$$

A graph of  $H_e(T/T_{e1}(r))$  is shown in Fig. 2. If the source is above the ground ( $\rho > a$ ) a similar height-gain factor must be introduced. Thus in general we have for the perfectly conducting case

$$U_e(r, \theta, t) = A_e(\theta)S(T/T_{e0})H_e(T/T_{e1}(r))H_e(T/T_{e1}(\rho)). \quad (33)$$

A graph of  $U_e$  is shown in Fig. 3.

If the times  $T_{e1}(r)$  and  $T_{e1}(\rho)$  are both small compared to the build-up time  $T_{e0}$ , both height-gain factors are effectively equal to unity. Then  $U_e$  is essentially the same as it is for both source and receiver on the ground. On the other hand, if  $T_{e1}(r)$  and  $T_{e1}(\rho)$  are large compared to  $T_{e0}$ , the maximum of  $U_e$  is less than its value for  $r = a, \rho = a$  by the factor  $H_e(T_0/T_{e1}(r))H_e(T_0/T_{e1}(\rho))$ . In this case the shape of the pulse is also slightly altered.

In case of finite conductivity, (23) shows that  $U_e$  is obtained by multiplying (33) by the conductivity factor  $C_e(T/T_{e0}, T/T_2)$ . This factor is given by

$$C_e = \exp \left[ 3(T_0/T)^{1/2} \left( 1 - \left[ 1 + \frac{1}{2|\tau_0^\infty|^2|\delta_e^*|} \right]^{3/2} \right) \right] \cdot \frac{1}{1 + \frac{1}{2|\tau_0^\infty|^2|\delta_e^*|} + \frac{1}{2|\tau_0^\infty|^2|\delta_e^*|^2}}. \quad (34)$$

The quantity  $|\delta_e^*|$ , which depends upon  $T/T_2$  and upon  $\sigma_1$ , is given by (24) with  $s = 0$ . Thus we have, denoting by  $U_e^\infty$  the result (33) for perfect conductivity,

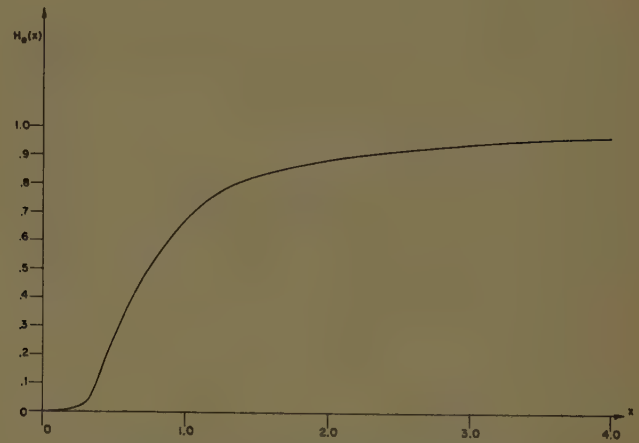


Fig. 2—The time dependent height-gain factor  $H_e(x)$  for the electric dipole case, from (31).

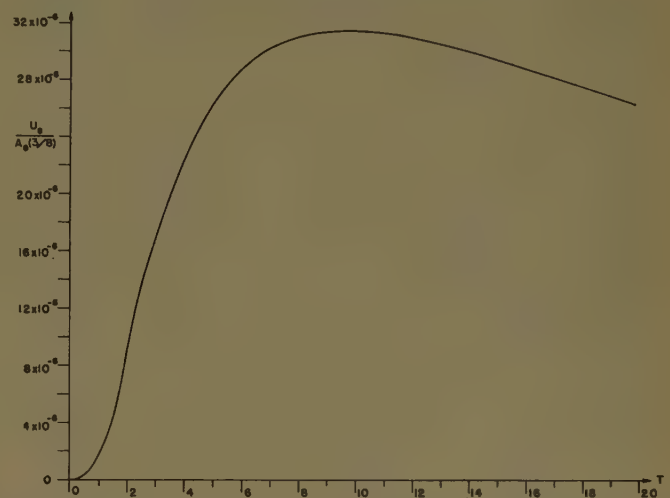


Fig. 3—The Hertz potential  $U_e(T)$  for the electric dipole case, based on (33). The source and receiver are both 25 meters above the ground, which is assumed to be perfectly conducting, and the angle  $\theta = 3/8$ . The vertical scale is the value of  $U_e(T)/A_e(3/8)$ , where  $A_e$  is given by (28).

$$U_e(r, \theta, t) = U_e^\infty(r, \theta, t)C_e(T/T_{e0}, T/T_2). \quad (35)$$

If we insert (33) for  $U_e^\infty$  this becomes

$$U_e(r, \theta, t) = A_e(\theta)S(T/T_{e0})H_e(T/T_{e1}(r)) \cdot H_e(T/T_{e1}(\rho))C_e(T/T_{e0}, T/T_2). \quad (36)$$

A graph of  $C_e$  is shown in Fig. 4 and one of  $U_e$  in Fig. 5.

A quite similar analysis is also possible in the magnetic case. From (22) we find that the analog of (33) for  $U_m$  in the case of perfect conductivity is

$$U_m(r, \theta, t) = A_m(\theta)S(T/T_{m0})H_m(T/T_{m1}(r))H_m(T/T_{m1}(\rho)). \quad (37)$$

The shape factor  $S$  is the same as in the electric case but the amplitude  $A_m(\theta)$ , the build-up time  $T_{m0}$ , the times  $T_{m1}(r)$  and  $T_{m1}(\rho)$  and the height-gain factors  $H_m$  are slightly different. These quantities are given by

$$A_m(\theta) = \frac{37c}{2^{11/2}2^{1/3}\pi e^3|\tau_0^0|^4 a^2} \cdot \frac{1}{\sqrt{\theta^7 \sin^2 \theta}}$$



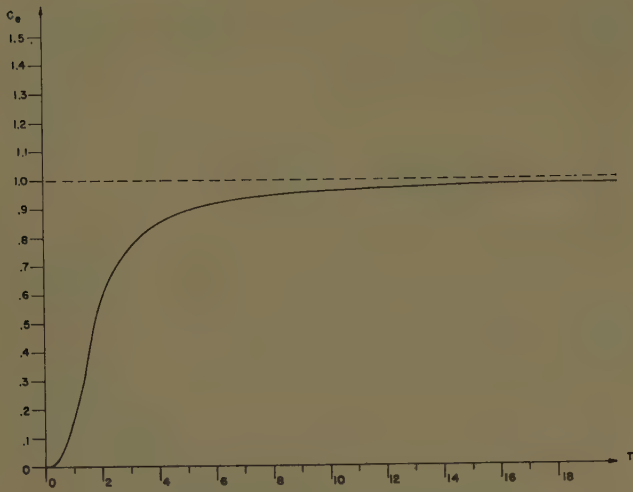


Fig. 4—The conductivity correction factor  $C_e(T)$  for the electric dipole case, based on (34). The conductivity  $\sigma_1 = 4$  mho/meter, appropriate to sea water, while  $\theta = 3/8$ ,  $\epsilon_1/\epsilon = 81$  and  $\mu = 4\pi \cdot 10^{-7}$  henry/meter.

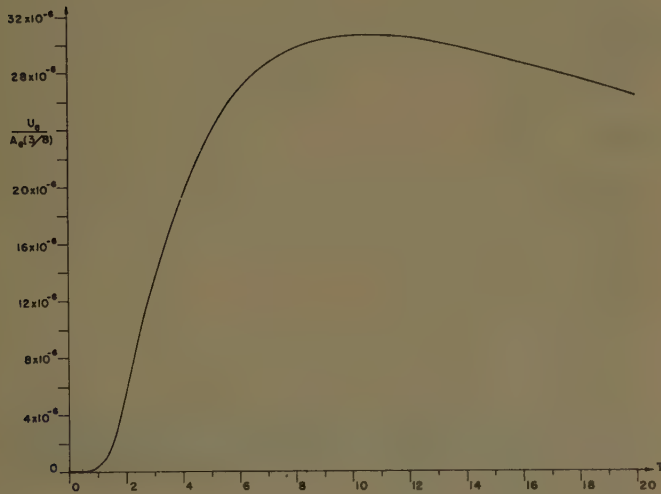


Fig. 5—The Hertz potential  $U_e(T)$  for the electric dipole case and a finitely conducting earth. The source and receiver are both 25 meters above the ground, the conductivity  $\sigma_1 = 4$  mho/meter,  $\theta = 3/8$ ,  $\epsilon_1/\epsilon = 81$  and  $\mu = 4\pi \cdot 10^{-7}$  henry/meter. The vertical scale is the value of  $U_e(T)/A_e(3/8)$  with  $U_e$  given by (36) and  $A_e$  by (28).

$$= (3.78 \times 10^{-3}) \frac{1}{\sqrt{\theta^7 \sin \theta}} \sim (3.78 \times 10^{-3}) \frac{1}{\theta^4}, \quad (38)$$

$$T_{m0} = \frac{4 |\tau_0^0|^3 a}{3^5 c} \theta^3 = (2.24 \times 10^{-9}) \theta^3, \quad (39)$$

$$T_{m1}(r) = 2^{1/3} |\tau_0^0| \theta (r - a) / 3c, \quad (40)$$

$$H_m(T/T_{m1}(r)) = \frac{v [T_{m1}(r)/T - 2^{1/3} |\tau_0^0|]}{v' [-2^{1/3} |\tau_0^0|]}. \quad (41)$$

A graph of the height-gain factor  $H_m$  is given in Fig. 6. This height-gain factor is zero at the ground. Therefore, graphs of  $U_m$  are given for  $r > a$  and  $\rho > a$  in Fig. 7.

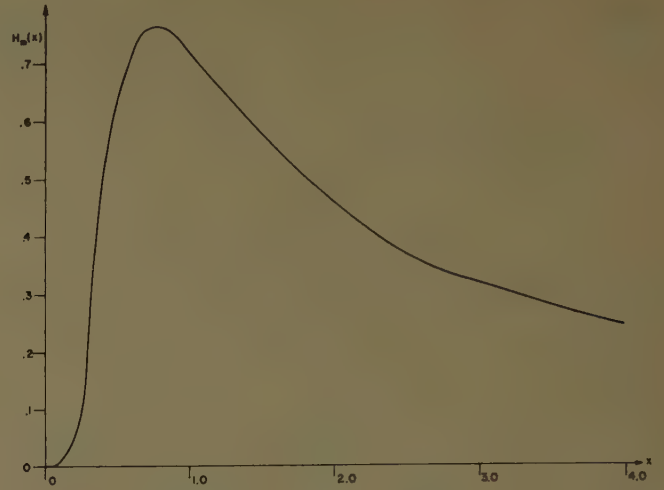


Fig. 6—The time dependent height-gain factor  $H_m(x)$  for the magnetic dipole case. The graph, based on (41), is for a height of 25 meters.

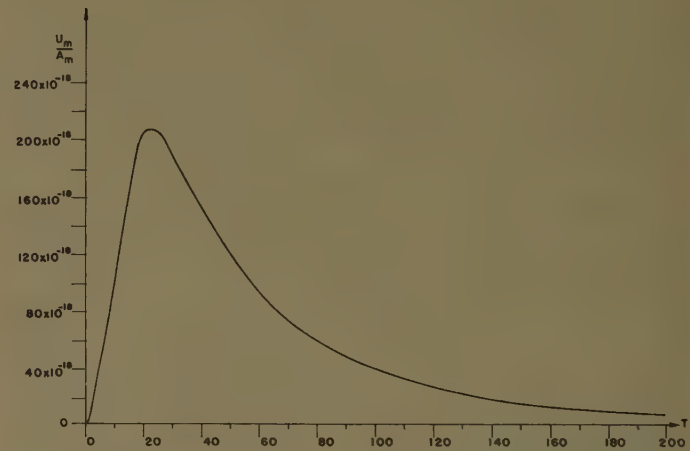


Fig. 7—The Hertz potential  $U_m(T)$  for the magnetic dipole case. The source and receiver are both 25 meters above the ground. The graph is based upon (37) for a perfectly conducting earth and upon (44) for a finitely conducting earth with  $\sigma_1 = 4$  mho/meter. The two results are indistinguishable. The vertical scale shows the value of  $U_m(T)/A_m$ , for  $\theta = 3/8$  with  $A_m$  given by (38). For any other value of  $\theta$ , say  $\theta = 3/8\alpha$ , the vertical scale must be multiplied by  $\alpha^{-17/2}$  and the horizontal scale by  $\alpha^{-3}$ .

In the case of finite conductivity, we find from (25) that  $U_m$  can be obtained by multiplying the result (37) by the conductivity factor  $C_m(T/T_{m0}, T/T_2)$ . This factor is

$$C_m(T/T_{m0}, T/T_2) = \frac{\exp \left[ 3 \left( \frac{T_0}{T} \right)^{1/2} \left( 1 - \left[ 1 - \frac{|\delta_m^*|}{|\tau_0^0|} \right]^{3/2} \right) \right]}{2 |\delta_m^*|^2 (|\tau_0^0| - |\delta_m^*|) + 1}. \quad (42)$$

The quantity  $|\delta_m^*|$  depends upon  $T/T_2$  and upon  $\sigma_1$ . It is given by (26) with  $s = 0$ . If we denote the result (37) for perfect conductivity by  $U_m^\infty$  we now have

$$U_m(r, \theta, t) = U_m^\infty(r, \theta, t) C_m(T/T_{m0}, T/T_2). \quad (43)$$

If we replace  $U_m^\infty$  by means of (37) this becomes

$$U_m(r, \theta, t) = A_m(\theta) S(T/T_{m0}) H_m(T/T_{m1}(r)) \cdot H_m(T/T_{m1}(\rho)) C_m(T/T_{m0}, T/T_2). \quad (44)$$

If  $\sigma_1 = 4$  mhos/meter, which is the conductivity of sea water,  $C_m$  differs from unity by less than one per cent for all values of  $\theta$ . Therefore in this case  $U_m$  is essentially the same as  $U_m^\infty$ , which is shown in Fig. 7.

The field components can be found from the Hertz vector by (1) in the electric case and by (21) in the magnetic case. In the electric case  $E_\phi = 0$ , and  $E_\theta = 0$  at  $r = a$  in the perfectly conducting case. The main non-zero component of  $E$  is  $E_r$ . By using (1) and (18) we find, for finite or infinite conductivity, that

$$E_r = -\frac{1}{a} \left[ \frac{|\tau_0^\infty| T_2}{3T} \right]^3 U_e. \quad (45)$$

In the magnetic case  $E_r = E_\theta = 0$ . From (2) and (18) we find for the only nonzero component of  $E$ ,

$$E_\phi = \frac{\mu c}{a} \left[ \frac{|\tau_0^0| T_2}{3T} \right]^3 U_m. \quad (46)$$

When the source has a time dependence  $f(t)$  instead of  $\delta(t)$ , the result for the Hertz vector or the field components can be obtained from those for the delta-function source. If  $U'$  denotes the Hertz vector (electric or magnetic) due to the source  $f$ , and  $U^\delta$  the corresponding Hertz vector due to the delta-function source, then by superposition

$$U'(r, \theta, t) = \int_{-\infty}^{\infty} f(\tau) U^\delta(r, \theta, t - \tau) d\tau. \quad (47)$$

From this equation we see that the minimum resolution time in  $U'$  is the appropriate build-up time  $T_{e0}$  or  $T_{m0}$ . Thus frequencies higher than  $1/T_{e0}$  or  $1/T_{m0}$  are essentially lost from the pulse. We may describe this by saying

that diffraction has the effect of a low-pass filter. This is understandable since high-frequency fields do not so readily diffract around the earth.

An alternative to (47), which may be easier to compute from, is

$$U'(r, \theta, t) = \bar{f}(ck^*) U^\delta(r, \theta, t). \quad (48)$$

Here  $\bar{f}$  is the Fourier transform of  $f(t)$  and  $k^*$  is the value of  $k$  at the saddle point. It is given by

$$ck^* = \frac{ic}{a} \left[ \frac{|\tau_0| T_2}{3T} \right]^{3/2}. \quad (49)$$

Here  $\tau_0$  is  $\tau_0^\infty$  in the electric case and  $\tau_0^0$  in the magnetic case. Although (47) is valid for arbitrary  $f(t)$ , (48) applies only when  $f(t)$  represents a pulse. This limitation results because the phase of  $\bar{f}$  was ignored in determining the saddle point.

Finally we must point out a limitation on our result (33) in the electric dipole case for a finitely conducting earth. This limitation pertains to small values of  $T$ . For such values of  $T$  the stationary value of  $k$  or  $\omega$  is large in the integral (18) for  $U_e$ . But our approximate calculation of  $\tau_s$ , which occurs in that integral, is based on an expansion for large  $\sigma$  and it is not valid when  $\omega$  is also large. Therefore, the result (23) is not accurate for small  $T$ . However this range of  $T$  is confined to a small interval which terminates long before the maximum occurs, in the case we have considered. No such limitation occurs in the magnetic dipole case, however, since then the expansion for large  $\sigma$  becomes more accurate when  $\omega$  is large.

#### ACKNOWLEDGMENT

We wish to acknowledge our indebtedness to Prof. Bernard Friedman who previously analyzed the field due to a pulsed line source near a perfectly conducting cylinder.

## Scattering of Electromagnetic Waves in Beyond-the-Horizon Radio Transmission\*

DAVID I. PAUL†

**Summary**—A formula is developed for the cross section in electromagnetic wave propagation beyond the horizon. The theory assumes that the propagation is the result of scattering by ellipsoidal shaped inhomogeneities in the atmosphere causing variations in the dielectric constant. The method of derivation is straightforward and gives a clear physical picture of the nature of the process. Simplifications concerning the geometric shape, size, and distribution of these

inhomogeneities yield 1) the semi-empirical formula of Norton and 2) the formula derived by Gordon for large sized inhomogeneities. Thus, the physical implications contained in these formulas are clearly demonstrated.

IN recent years, the phenomenon of electromagnetic wave propagation beyond the horizon in the uhf range of the frequency band has assumed increasing importance. It is agreed generally that this propagation is the result of a single (nonmultiple) scattering of the

\* Manuscript received by the PGAP, January 29, 1957; revised manuscript received, May 22, 1957. This work was initiated at Bell Telephone Laboratories.

† University of California, Los Angeles, Calif.



incident electromagnetic wave by inhomogeneities in the region of the atmosphere defined by the intersection of the transmitting and receiving beams. These inhomogeneities manifest themselves by variations in the dielectric constant of the atmosphere.

It is the purpose of this paper to develop a formula for the scattering cross section in beyond-the-horizon radio transmission. It is felt that the method presented is straightforward and gives a clear physical picture of the nature of the process. A general formula for the cross section is obtained. Then, by making various simplifications concerning the geometric shape, size, and distribution of the inhomogeneities in the atmosphere, we obtain 1) the semi-empirical formula given by Norton [1] which has had some success in predicting median values of signal intensity, and 2) the formula derived by Gordon [2]. Thus, the physical implications contained in these formulas are clearly demonstrated.

First we consider the effect of an electromagnetic wave incident on a single blob of atmosphere, distinct from its surroundings by virtue of its dielectric properties. The blob is chosen as ellipsoidal in shape with arbitrary semi-axes ( $l_1, l_2, l_3$ ). Using the methods of quantum mechanics we obtain a first Born approximation for the electric vector and compute the intensity. Then we assume a random distribution of such blobs ( $l_1, l_2, l_3$ ) in an arbitrary region of the atmosphere and obtain the total scattered intensity and thus the cross section for scattering from blobs of this size. Finally, we recognize that there is a distribution of blob sizes centered about some mean size. Assuming a Gaussian distribution of blob sizes centered about ( $l_1, l_2, l_3$ ), we add up the contribution from each blob size and obtain the formula for the scattering cross section in beyond-the-horizon radio transmission.

Applying Maxwell's equations where the dielectric constant,  $\epsilon$ , is a function of position and assuming time harmonic dependence, we obtain as the differential equation satisfied by the electric vector

$$(\nabla^2 + k^2)\vec{E} = -k^2\beta(r)\vec{E} + \nabla(\nabla \cdot \vec{E}), \quad (1)$$

where

$$\beta(r) = \frac{\epsilon}{\epsilon_0} - 1. \quad (2)$$

Wheelon [3] has shown that if the change of the dielectric constant,  $\beta(r)$ , is less than its rms value in one wave length, the term  $\nabla(\nabla \cdot \vec{E})$  is small. Thus, this term may be neglected in the first Born approximation which we now write as

$$\psi_s = k^2 \int G(r|r_0)\beta(r)\psi_i(r)d\vec{r}, \quad (3)$$

where  $\vec{E} = \psi_s \vec{e}$ ,  $G(r|r_0)$  is the Green's function for the Helmholtz equation, and  $\psi_i(r)$  is our first trial function. The quantity  $\beta(r)$  is used to define our ellipsoidal blob.

The evaluation of the integral in (3) is performed in the Appendix. We obtain the result

$$\psi_s = \frac{(\Delta\epsilon)E_0 \sin \chi e^{ikr_0} l_1 l_2 l_3 \eta^3 \pi^{3/2} k^2}{4\pi r_0} \exp -\frac{1}{2}\eta^2 k^2 B^2, \quad (4)$$

where

$$B^2 = l_1^2(\sin \alpha - \cos \theta_0)^2 + l_2^2(\cos \alpha \cos \phi_i - \sin \theta_0 \cos \phi_0)^2 + l_3^2(\cos \alpha \sin \phi_i - \sin \theta_0 \sin \phi_0)^2.$$

The angles ( $\theta_0, \phi_0$ ) define the direction of the scattered wave  $\vec{r}_0$ , while

$$\left(\frac{\pi}{2} - \alpha, \phi_i\right)$$

define the direction of the incident wave  $\vec{k}_i$  with respect to the coordinate system of Fig. 1 [see (26)]. The quantities  $l_1, l_2$ , and  $l_3$  are the semi-axes of the ellipsoid along the  $z, x$ , and  $y$  directions, respectively, while  $\eta$  is an additional parameter which varies the over-all size of the blob [see (23) and Fig. 1]. The quantity  $E_0 \sin \chi$  is the absolute value of the incident wave where  $\sin \chi$  compensates for deviations from  $\frac{1}{2}\pi$  in the angle between  $\vec{E}_i$  in the blob, and in the direction from the blob to the receiver.

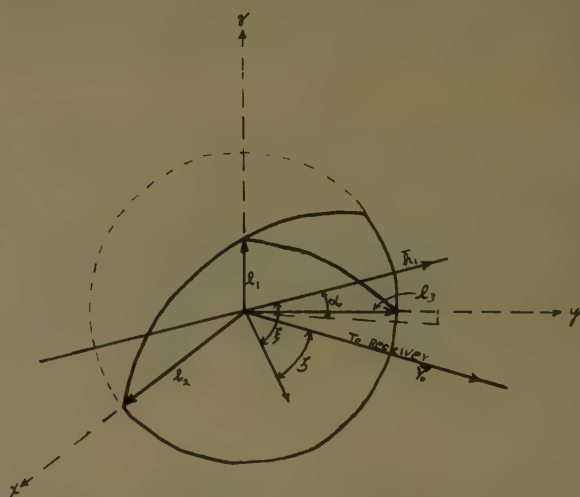


Fig. 1—Ellipsoidal shaped blob.

The intensity from a single blob with respect to free space intensity is given by  $I_b = |\psi_s|^2/E_0^2$ . Thus,

$$I_b = \frac{(\Delta\epsilon)^2 \eta^6 (l_1 l_2 l_3)^2 \pi^2 k^4 \sin^2 \chi}{16r_0^2} \exp -\frac{1}{2}\eta^2 k^2 B^2. \quad (5)$$

To find the total intensity,  $I_t$ , for a random distribution of such blobs, we merely sum the intensities of the individual blobs,  $I_b$ , in the scattering volume  $V_i$ ; i.e., if  $N$  is the number of blobs in  $V_i$ ,  $I_t = NI_b$ . If  $\nu$  is a factor  $< 1$  indicative of the closeness of the blobs to each other and  $V_b$  is the volume of an individual blob, i.e.,  $V_b = (4/3)\pi \eta^3 l_1 l_2 l_3$ , then  $N = \nu V_i / V_b$ .

The cross section for a random distribution of blobs of size  $(l_1, l_2, l_3)$  in the region  $V_i$  may be approximated as

$$\sigma_i \sim I r_0^2 / V_i$$

$$= \frac{3}{64} (\Delta\epsilon)^2 \eta^3 l_1 l_2 l_3 \nu k^4 \sin^2 \chi \exp - \frac{1}{2} \eta^2 k^2 B^2, \quad (6)$$

where the assumption is made that the angles do not vary considerably in the scattering region  $V_i$  (see Fig. 2). Thus,  $\alpha$ ,  $\theta_0$ ,  $\phi_0$ , and  $\phi_i$  are now average or mean values in the scattering region. Eq. (6) is equivalent to (17) and (21) of Booker [4] for an anisotropic medium, and to (23) of Wheelon [3] for an isotropic medium where Gaussian autocorrelation functions were assumed.

In accordance with our general plan outlined above, we now assume a Gaussian distribution of blob sizes centered about a predominant size  $(l_1, l_2, l_3)$  and sum the contributions from each different size. Thus, using the density function

$$\rho(\eta) = \exp - (1 - \eta)^2 / \delta^2 \quad (7)$$

where  $\delta$  is a measure of the width of the size distribution (see Fig. 3), we write as our formula for the scattering cross section in beyond-the-horizon radio transmission

$$\sigma = \frac{\int \rho(\eta) \sigma_i d\eta}{\int \rho(\eta) d\eta} \quad (8)$$

Substituting (6) and (7) into (8), we get

$$\sigma = \frac{3}{64} \frac{(\Delta\epsilon)^2 \nu k^4 l_1 l_2 l_3 \sin^2 \chi}{\int_{-\infty}^{\infty} \exp - (1 - \eta)^2 / \delta^2 d\eta} \int_{-\infty}^{\infty} \eta^3 \exp - (1 - \eta)^2 / \delta^2 d\eta$$

$$\cdot \exp - \frac{1}{2} \eta^2 k^2 B^2 d\eta, \quad (9)$$

where due to the nature of the density function (see Fig. 3) it is permissible to extend the integration to include the entire real  $\eta$  axis. The integration may be performed exactly, and we obtain the expression

$$= \frac{9}{128} \frac{(\Delta\epsilon)^2 \nu k^4 l_1 l_2 l_3 \delta^2 \sin^2 \chi}{[1 + \frac{1}{2} k^2 \delta^2 B^2]^{5/2}} \exp - \frac{1}{2} k^2 B^2 / (1 + \frac{1}{2} k^2 \delta^2 B^2)$$

$$\cdot \{1 + \frac{2}{3} \delta^{-2} (1 + \frac{1}{2} k^2 \delta^2 B^2)^{-1}\}. \quad (10)$$

#### SPHERICAL BLOBS

We now consider, as a special case, spherical blobs ( $l_1 = l_2 = l_3 = l$ ) and obtain a formula for the cross section which is identical to that obtained by Norton [1] except for a constant factor. Thus, recognizing that for spherical blobs  $B^2 = 4l^2 \sin^2 \frac{1}{2} \gamma$ , where  $\gamma$  is the angle between the incident beam and the receiving beam (*i.e.*, the scattering angle, see Fig. 2), we obtain

$$\sigma_{sp} = \frac{9}{128} \frac{(\Delta\epsilon)^2 \nu k^4 l^3 \delta^2 \sin^2 \chi}{[1 + 2k^2 l^2 \delta^2 \sin^2 \frac{1}{2} \gamma]^{5/2}} \exp - \frac{2k^2 l^2 \sin^2 \frac{1}{2} \gamma}{1 + 2k^2 l^2 \delta^2 \sin^2 \frac{1}{2} \gamma}$$

$$\cdot \{1 + \frac{2}{3} \delta^{-2} (1 + 2k^2 l^2 \delta^2 \sin^2 \frac{1}{2} \gamma)^{-1}\}. \quad (11)$$

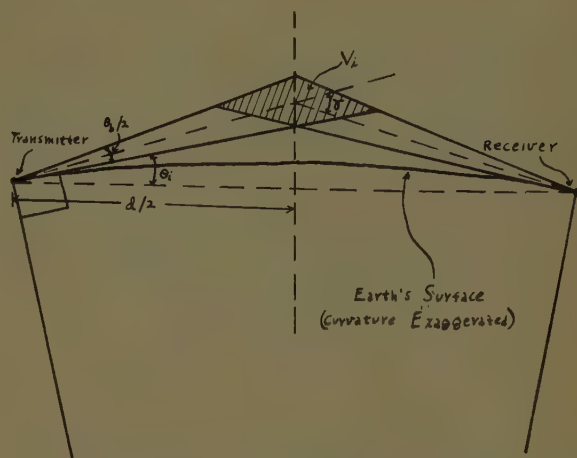


Fig. 2—Geometry of beyond-the-horizon scatter transmission.

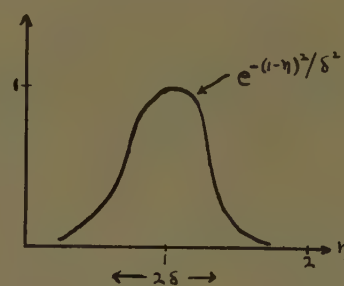


Fig. 3—Distribution of blob sizes.

Applying the condition

$$2\delta^2 l^2 k^2 \sin^2 \frac{1}{2} \gamma \gg 1 \quad (12)$$

analogous to that used by Gordon and letting  $\sin \frac{1}{2} \gamma = \frac{1}{2} \gamma$ , (11) may be written as

$$\sigma_{sp} \sim \frac{\nu (\Delta\epsilon)^2 \lambda \sin^2 \chi e^{-1/\delta^2}}{16 l^2 \delta^3 \gamma^5} \left\{ 1 + \frac{\lambda^2}{12 \pi^2 \delta^4 l^2 \sin^2 \frac{1}{2} \gamma} \right\}, \quad (13)$$

where  $\lambda$  is the wavelength. Again applying (12), we get

$$\sigma_{sp} \sim \frac{\nu (\Delta\epsilon)^2 \lambda \sin^2 \chi}{16 l^2 \delta^3 \gamma^5} e^{-1/\delta^2}. \quad (14)$$

Except for two extra parameters  $\nu$  and  $\delta$  contained in our formula, which emphasize the density and size distribution of the blobs, (14) is the same as the formula given by Norton [1] which has had some success in predicting median values. If we choose  $\nu = \delta = 0.6$  and an average radius  $l = 20$  meters, (14) and Norton's formula are identical. We note the sensitivity of  $\sigma_{sp}$  to the two parameters  $\nu$  and  $\delta$ , and suggest that variations in these parameters might account for the slow fading (as distinguished from the Rayleigh fast fading) observed in scatter propagation.

#### ELLIPSOIDAL BLOBS

Experimental evidence indicates that the inhomogeneities in the atmosphere are not spherical. On the contrary, measurements by Wong, Herbstreit, and



Norton indicate that the blobs are more ellipsoidal in shape with the semimajor axis parallel to the earth's surface and the semiminor axis in the vertical direction. Thus, we return to (10) giving the scattering cross section for ellipsoidal-type blobs which we now approximate as<sup>1</sup>

$$\sigma \sim \frac{9}{128} \frac{(\Delta\epsilon)^2 \nu k^4 l_1 l_2 l_3 \delta^2 \sin^2 \chi}{\left\{1 + \frac{1}{2} k^2 \delta^2 [l_1^2 \gamma^2 + \frac{1}{8} l_2^2 \theta_b^2]\right\}^{5/2}} \cdot \exp - \frac{\frac{1}{2} k^2 [l_1^2 \gamma^2 + \frac{1}{8} l_2^2 \theta_b^2]}{1 + \frac{1}{2} k^2 \delta^2 [l_1^2 \gamma^2 + \frac{1}{8} l_2^2 \theta_b^2]} \cdot \left\{1 + \frac{2}{3} \delta^{-2} [1 + \frac{1}{2} k^2 \delta^2 (l_1^2 \gamma^2 + \frac{1}{8} l_2^2 \theta_b^2)]^{-1}\right\} \quad (15)$$

where  $\theta_b$  is the beamwidth.

Imposing the condition analogous to (12)

$$\frac{1}{2} k^2 \delta^2 (l_1^2 \gamma^2 + \frac{1}{8} l_2^2 \theta_b^2) \gg 1 \quad (16)$$

and assuming  $l_2 = l_3$ , *i.e.*, assuming neither direction is preferred in space, we obtain

$$\sigma \sim \frac{\nu (\Delta\epsilon)^2 \lambda l_1 l_2^2 \sin^2 \chi}{16 \delta^3 [l_1^2 \gamma^2 + \frac{1}{8} l_2^2 \theta_b^2]^{5/2}} e^{-1/\delta^2} \quad (17)$$

A functional dependence on the beamwidth for anisotropic media was noted in (27) of Norton [1].

Using the relations

$$\gamma = 2\theta_i + \frac{1}{2} \theta_b = \frac{d}{a} + \frac{1}{2} \theta_b, \quad \theta_b^0 \sim 69\lambda/D,$$

where  $D$  is the diameter of the antenna dish,  $a$  is the radius of the earth, and  $d$  is the distance between the transmitter and the receiver, we see that for  $f=300$  mc,  $d=600$  miles,  $D=60$  feet, the factor  $\gamma^2$  is approximately 340 times  $\theta_b^2/8$ , while at  $d=200$  miles,  $\gamma^2$  is approximately 52 times  $\theta_b^2/8$ . Thus, we note that if  $l_2$  is of the same size as  $l_1$ , then  $l_2^2 \theta_b^2/8 \ll l_1^2 \gamma^2$ , and (17) reduces to (14) for a spherical blob. However, if  $l_2$  is large compared to  $l_1$ ; *i.e.*,  $l_2 \sim 10l_1$ , these terms will be approximately the same order of magnitude and an additional factor of 10 may appear in the denominator or numerator of the right-hand side of (17) (depending on the size of  $\theta_b$  compared to  $\gamma$  and  $l_2$  compared to  $l_1$ ). The parameters  $\nu$ ,  $\delta$ ,  $l_1$ , and  $l_2$ , of course, are functions of the atmospheric conditions prevalent during the time of propagation. Scattering amplitude predictions (except for average values based on experimental observation) await the determination of precise relationships between the atmospheric environment and these parameters, and the ability to determine or predict such environment at the altitude where scattering occurs.

<sup>1</sup> Referring to Fig. 2, we note that the angle of the incident wave  $\alpha$  is small and thus  $\cos \alpha \sim 1$ . Further, the angles  $\theta_0$ ,  $\phi_0$ , and  $\phi_i$  are close to  $\frac{1}{2}\pi$ ; (*i.e.*,  $\theta_0 \sim \alpha + \frac{1}{2}\pi$ ,  $\phi_0 = \frac{1}{2}\pi \pm \phi_0'$ ,  $\phi_i = \frac{1}{2}\pi + \phi_i'$ ). From Figs. 1 and 2, we see that the average values of  $\phi_0'$  and  $\phi_i'$  are functions of the half-beamwidth  $\frac{1}{2}\theta_b$ ; *i.e.*,  $\phi_0' = \phi_i' = \theta_b/4\sqrt{2}$ , while  $\alpha = \frac{1}{2}\gamma$ . Thus, the term  $(\sin \alpha - \cos \theta_0)^2 \sim \gamma^2$ , the term  $(\sin \theta_0 \cos \phi_0 - \cos \alpha \cos \phi_i)^2 \sim \theta_b^2/8$ , and the term  $(\cos \alpha \sin \phi_i - \sin \theta_0 \sin \phi_0)^2$  is of order  $\theta_b^4$  and may be neglected.

## DERIVATION OF GORDON'S FORMULA

It is of interest to note that by assuming a constant density function (*i.e.*, assuming that all size blobs are present in equal amounts in space) we can derive Gordon's formula [2] for large  $l$ . Thus, we write in place of (7)

$$\rho(\eta) = 1, \quad 0 < \eta \leq L, \quad (18)$$

where  $L$  is determined by the maximum range of blob sizes. Then

$$\sigma_G = \frac{1}{L} \int_h^L \sigma_i d\eta, \quad (19)$$

where  $h$  is a very small number close to zero. Since we merely desire to obtain Gordon's formula we can simplify the writing by immediately assuming spherical blobs ( $l_1 = l_2 = l_3 = l$ ) in (6) and substitute the resultant value in the above expression, obtaining

$$\sigma_G = \frac{3}{64} (\Delta\epsilon)^2 l^3 \nu k^4 \sin^2 \chi \cdot \frac{1}{L} \int_h^L \eta^3 \exp - 2\eta^2 k^2 l^2 \sin^2 \frac{1}{2}\gamma d\eta. \quad (20)$$

The integration may be performed exactly yielding

$$\sigma_G = \frac{3}{64} (\Delta\epsilon)^2 l^3 \nu k^4 \sin^2 \chi \left\{ \frac{1 - \exp - 4l^2 k^2 L^2 \sin^2 \frac{1}{2}\gamma}{8l^4 k^4 L \sin^4 \frac{1}{2}\gamma} - \frac{L \exp - 4l^2 k^2 L^2 \sin^2 \frac{1}{2}\gamma}{4l^2 k^2 \sin^2 \frac{1}{2}\gamma} \right\}. \quad (21)$$

Since obviously the size of the blobs are limited, we may put  $L$  equal to unity; *i.e.*,  $0 < \eta \leq 1$ .  $l$  must then be associated with a large size blob. Applying Gordon's condition  $2k^2 l^2 \sin^2 \frac{1}{2}\gamma \gg 1$ , the exponential terms can be neglected, and we obtain

$$\sigma_G = \frac{3}{32} \frac{(\Delta\epsilon)^2 \nu \sin^2 \chi}{l \gamma^4}. \quad (22)$$

If we choose  $\nu = \frac{1}{2}$ , (22) is equivalent to Gordon's formula [2].

## APPENDIX

In this Appendix we evaluate the expression

$$\psi_s = k^2 \int G(r| r_0) \beta(r) \psi_i(r) dr$$

given in (3). If we examine Fig. 2 showing the geometry of beyond-the-horizon scatter transmission, we note that a plane wave constitutes a satisfactory approximation for  $\psi_i(r)$ . The quantity  $\beta(r)$  given by (2) is now used to define our ellipsoidal shaped blob. Let us take the origin of our coordinate system as coincident with the center of the blob. The  $yz$  plane will be parallel to the plane defined by the line joining the transmitter and the receiver, and the center of the earth, while the  $z$  axis is perpendicular to this line and passes through the center

of the earth (see Fig. 1). Then, our blob is defined by the equation

$$\beta(r) = (\Delta\epsilon) \exp - \frac{1}{\eta^2} \left( \frac{z^2}{l_1^2} + \frac{x^2}{l_2^2} + \frac{y^2}{l_3^2} \right), \quad (23)$$

where  $l_1$ ,  $l_2$ , and  $l_3$  are the semi-axes of the ellipsoid along the  $z$ ,  $x$ , and  $y$  directions respectively, and  $\eta$  is an additional parameter for the over-all size of the blob which will prove useful.

Utilizing the coordinate system of Fig. 1, we may expand the Green's function,  $G(r|r_0)$ , where the distance from the blob to the observer is considered large with respect to the size of the blob. Thus, we obtain

$$G(r|r_0) = \frac{e^{ikR}}{4\pi R} = \frac{e^{ikr_0 - ikr \cos \zeta}}{4\pi r_0}, \quad (24)$$

where  $\vec{r}$  is the vector from the origin to the variable point of integration in the blob,  $\vec{r}_0$  is the vector from the origin to the receiver,  $\zeta$  is the angle between  $\vec{r}$  and  $\vec{r}_0$ , and  $R = |\vec{r} - \vec{r}_0|$ . The plane wave  $\psi_i$  may be written as

$$\psi_i = E_0 \sin \chi e^{i\vec{k}_i \cdot \vec{r}} = E_0 \sin \chi e^{ikr \cos \xi}, \quad (25)$$

where  $\sin \chi$  compensates for deviations from  $\frac{1}{2}\pi$  in the angle between  $\vec{E}$  in the blob and the direction from the blob to the receiver, and  $\xi$  is the angle between the incident beam and the vector  $\vec{r}$  (see Fig. 1). Noting that

$$\begin{aligned} \cos \zeta &= \cos \theta \cos \theta_0 + \sin \theta \sin \theta_0 \cos (\phi - \phi_0) \\ \cos \xi &= \cos \theta \sin \alpha + \sin \theta \cos \alpha \cos (\phi - \phi_i) \end{aligned} \quad (26)$$

and recognizing that  $r \sin \theta \cos \phi = x$ ,  $r \sin \theta \sin \phi = y$ , and  $r \cos \theta = z$ , we can substitute (23), (24), and (25) into (3) and obtain

$$\begin{aligned} \psi_s &= \frac{(\Delta\epsilon) E_0 k^2 \sin \chi e^{ikr_0}}{4\pi r_0} \iiint \exp - \frac{1}{\eta^2} \left( \frac{z^2}{l_1^2} + \frac{x^2}{l_2^2} + \frac{y^2}{l_3^2} \right) \\ &\quad \cdot \exp ikz(\sin \alpha - \cos \theta_0) + ikx(\cos \alpha \cos \phi_i - \sin \theta_0 \cos \phi_0) \\ &\quad + iky(\cos \alpha \sin \phi_i - \sin \theta_0 \sin \phi_0) dx dy dz. \end{aligned} \quad (27)$$

Although the integral in (26) is to be taken over the volume of the blob, the limits of integration may be extended to cover all space because of the strong zero behavior of  $\beta(r)$  outside of the blob. Thus, recognizing that

$$\int_{-\infty}^{\infty} \exp - (u^2 \eta^2 l^2) + i a u du = n l \pi^{1/2} \exp - \frac{1}{4} (a l \eta)^2,$$

we may integrate directly and obtain (4) given in the text of this paper.

#### ACKNOWLEDGEMENT

The author wishes to express his thanks for the interest and encouragement of K. Bullington, A. L. Durkee, and Dr. S. O. Rice of the Bell Telephone Research Laboratories.

#### BIBLIOGRAPHY

- [1] Norton, K. A., "Point to Point Radio Relaying via the Scatter Mode of Tropospheric Propagation," IRE TRANSACTIONS, Vol. CS-4, (March, 1956), pp. 39-49.
- [2] Gordon, W. E., "Radio Scattering in the Troposphere," PROCEEDINGS OF THE IRE, Vol. 43 (January, 1955), pp. 23-28.
- [3] Wheelon, A. D., "Near-Field Corrections to Line-of-Sight Propagation," PROCEEDINGS OF THE IRE, Vol. 43 (October, 1955), pp. 1459-1466.
- [4] Booker, H. G., "A Theory of Scattering by Non-Isotropic Irregularities with Application to Radar Reflections from the Aurora," *Journal of Atmospheric and Terrestrial Physics*, Vol. 8 (1956), pp. 204-221.
- [5] Staras, H., "Antenna-to-Medium Coupling Loss," IRE TRANSACTIONS, Vol. AP-5 (April, 1957), pp. 228-231.

## Radio Echoes from Auroral Ionization Detected at Relatively Low Geomagnetic Latitudes\*

R. L. LEADABRAND† AND A. M. PETERSON†

**Summary**—High-frequency radio echoes from ionization associated with the Aurora Borealis have been identified at Stanford University (geomagnetic latitude 43.75°). The echoes occur at ranges between 1400 km and 4700 km corresponding to reflection from ionization in the zone of maximum auroral occurrence located far to the north of Stanford. The formation of the ionization is attributed to the bombardment of the upper atmosphere by high-speed charged particles emitted from the sun. The echoes have great amplitudes with duration times between one second and one hour. Their appearance and disappearance is quite similar to the behavior of visual auroras; the occurrence of the echoes has been found to be related

to geomagnetic disturbances. The heights of reflection appear to be between 100 km and 1200 km above the surface of the earth. The paths which the auroral signals travel over the relatively enormous distance from Stanford to the auroral zone (and back) are greatly influenced by the presence of the normal ionospheric layers. The echoes have been observed at ranges and bearings which indicate reflection from ionization at points along the auroral zone all the way from eastern Canada to Alaska.

#### INTRODUCTION

DURING studies of the ionosphere by means of the long-distance back-scatter technique [1], a new type of echo has been observed at Stanford University [2]. It is believed that these echoes are

\* Manuscript received by the PGAP, June 9, 1956; revised manuscript received August 5, 1957.

† Stanford University, Stanford, Calif.



the result of reflections from ionization associated with the Aurora Borealis. The echoes are detected at ranges of 1400 km to 4700 km in the direction of geomagnetic latitude of Stanford ( $43.75^\circ$ ) and place the reflection centers well within and to the north of the zone of maximum auroral occurrence.

These reflections were first noticed at Stanford at a frequency of 6.425 mc. Subsequent examinations of continuous scatter-sounding records, made at frequencies of 17.31 mc and 30.66 mc, have resulted in numerous instances in which these echoes have been found to occur under suitable conditions at 17 mc. Until recently, the fall of 1955, none have been identified on the 30-mc records. Additional investigations using a frequency of 12.8625 mc also have resulted in echoes of this type.

The majority of previous radio investigations [3-20] of auroral ionization have been carried out at geomagnetic latitudes ( $53-67^\circ$ ), which place the observers within or very close to the auroral zone. This is in contrast to the Stanford investigations, which are made at a location several thousand kilometers south of the auroral zone at the relatively low geomagnetic latitude of  $43.75^\circ$ . Also, previous investigations of the auroras by radio techniques generally have been made at frequencies above 30 mc, while at Stanford frequencies of 6 mc to 30 mc have been used successfully for these purposes.

## EXPERIMENTAL RESULTS

### Equipment

The equipment used to detect the auroral echoes at Stanford was developed primarily for the study of the ionosphere by the long-distance back-scatter technique [21].

### Echo Characteristics

The echoes observed at Stanford have a number of unique characteristics which distinguish them from the usual ground-scatter echoes.

**Depth of Range and Echo Shape:** One of the most striking characteristics of these reflections is the shape of the echo when observed on an *A* scope. It is about 1 pulse-width (1.5 millisecond) in range with a rapid rise and decay as illustrated by Fig. 1. Thus, it is easily distinguishable from the slow decay with range exhibited by the usual scatter echo. On occasion, closely spaced groups of echoes are observed, each 1 pulse-width and separated by less than the width of the transmitted pulse. Examples of such groups of auroral echoes are shown in Fig. 2 for 6 mc.

At times, a more diffuse form of echo is observed. It is spread in range by as much as 2 to 3 pulse widths and is characteristically lower in amplitude. This echo usually is observed shortly before and shortly after the occurrence of the discrete type of echo. An example of a diffuse echo is shown in Fig. 3.

**Range and Variations in Range with Time:** The echoes are observed at ranges between 1400 km and 4700 km.

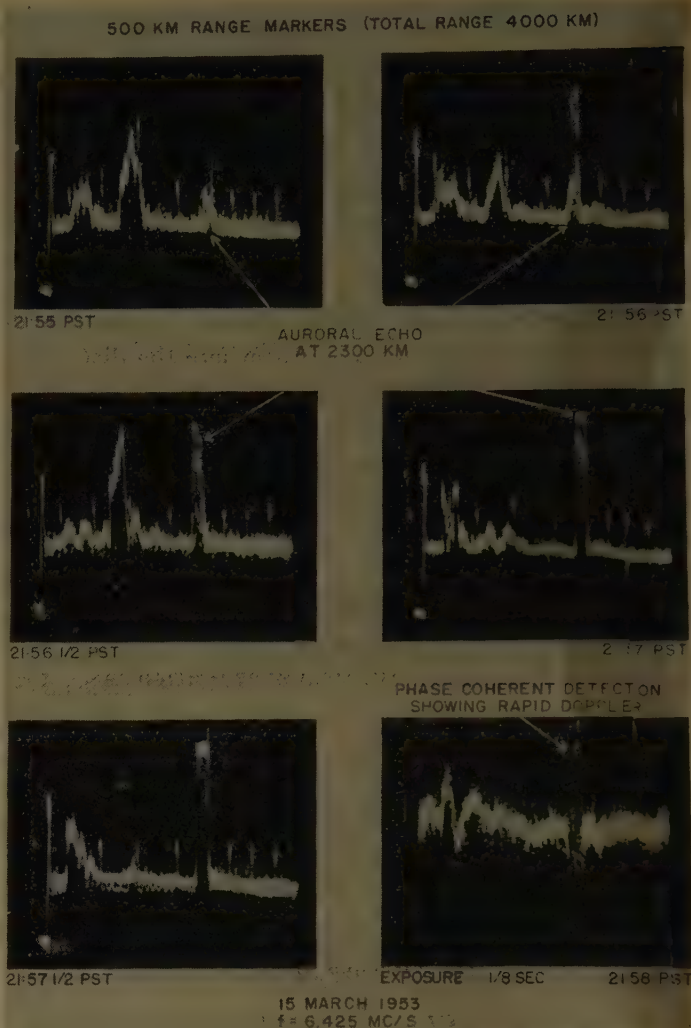


Fig. 1—A-scope displays of auroral-zone echo with phase detector to illustrate rapid Doppler frequency at 6.425 mc.

Examples of echoes at 17 mc are shown in Figs. 4 and 5, p. 68. In Fig. 4, the echoes are shown on a ppi display and are at a range of 1600 km; in Fig. 5, they are at a range of 3800 km and 4300 km. At 17 mc, sufficient data are available to illustrate the distribution of relative occurrence with range; this is shown in the form of a histogram in Fig. 6. The maximum number of echoes occurs at ranges between 3500 km and 4000 km. The range of maximum echo occurrence, as shown in Fig. 6, coincides with the range from Stanford to the zone of visual auroral occurrences.

During active periods, a change in echo range with time has been observed. A frequent form of this change in range consists of a series of echoes occurring first at relatively long range and then at successively shorter ranges in discontinuous steps. During one such example, the echo first appeared at a range of 2800 km and then moved in a step-like manner to 2300 km in a period of 15 minutes. Less frequently, an echo is observed to move continuously to a shorter range through approximately 200 km. The apparent velocities represented by the changes in range are frequently as high as 1500 km per hour.

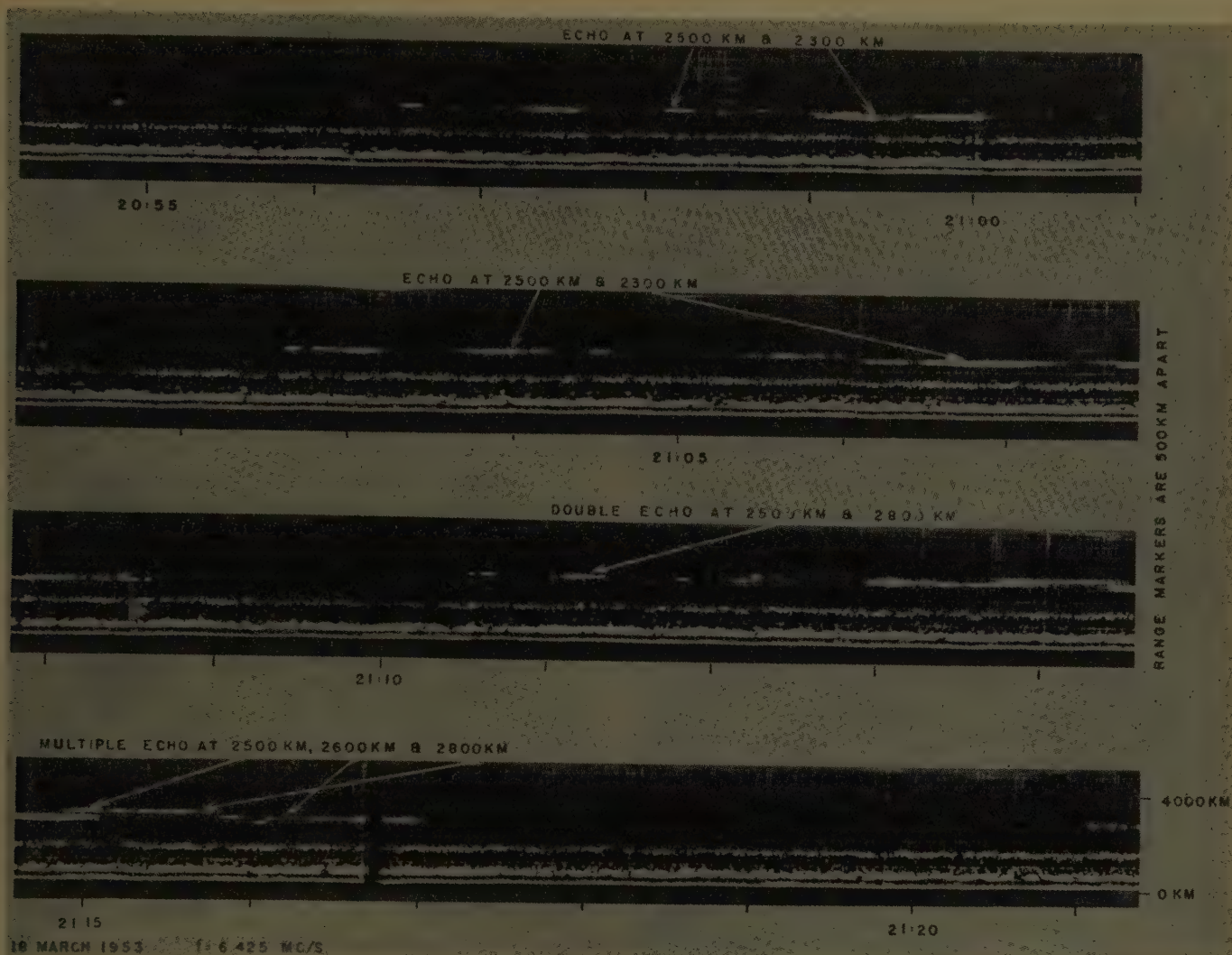


Fig. 2—Range-time display of auroral-zone echoes at 6.425 mc.

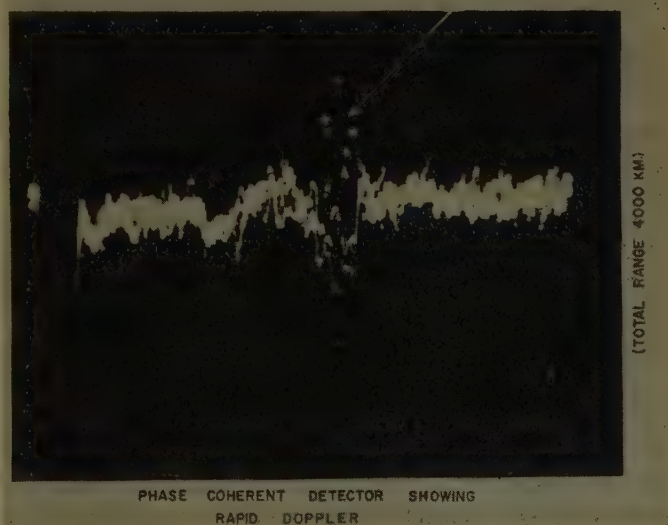
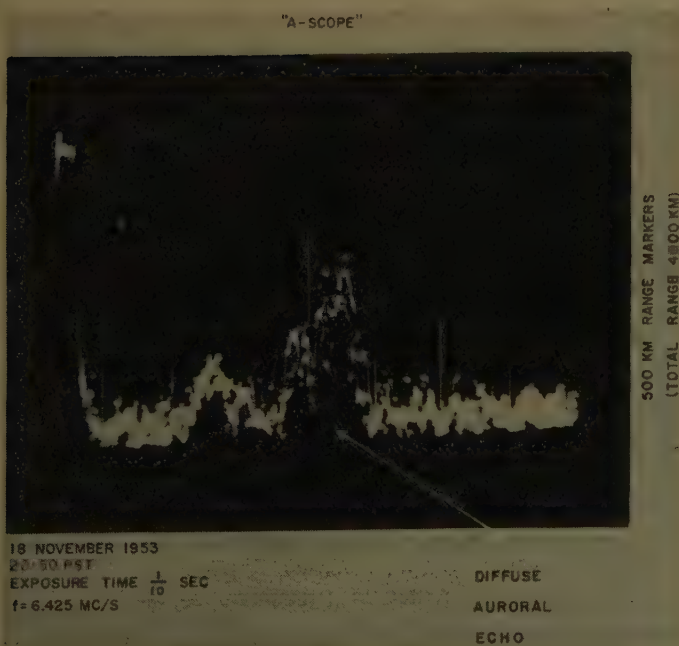


Fig. 3—A scope and Doppler display of a diffuse-type auroral-zone echo at 6.425 mc.



3 APRIL 1953  
19:31-19:40 PST

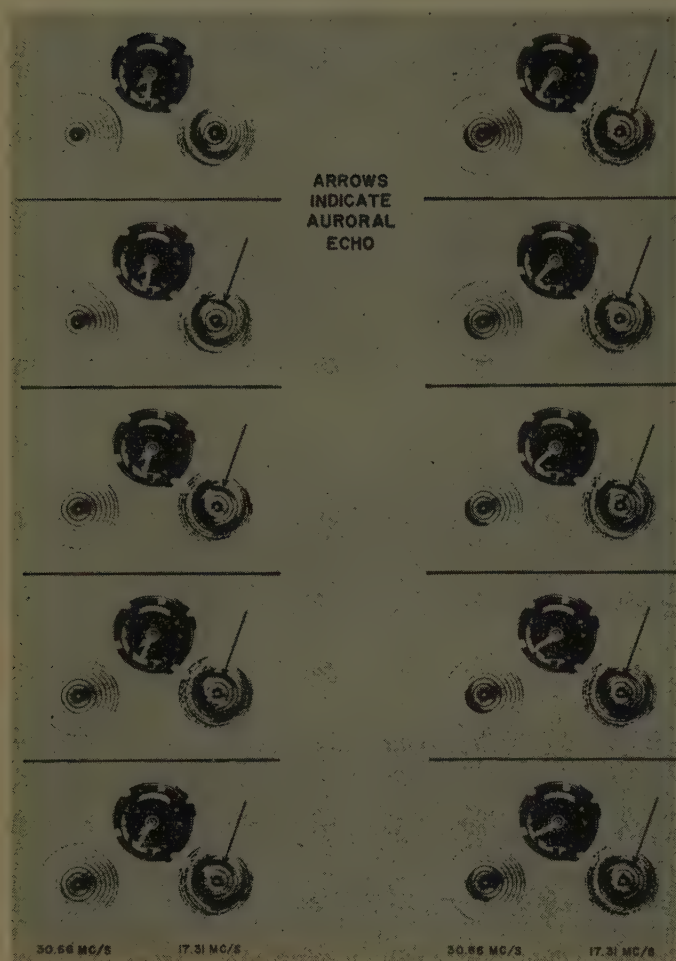


Fig. 4—PPI scatter-soundings showing auroral-zone echo at 1600-km range at 17.31 mc.

20 NOVEMBER 1952  
07:39-07:48 PST

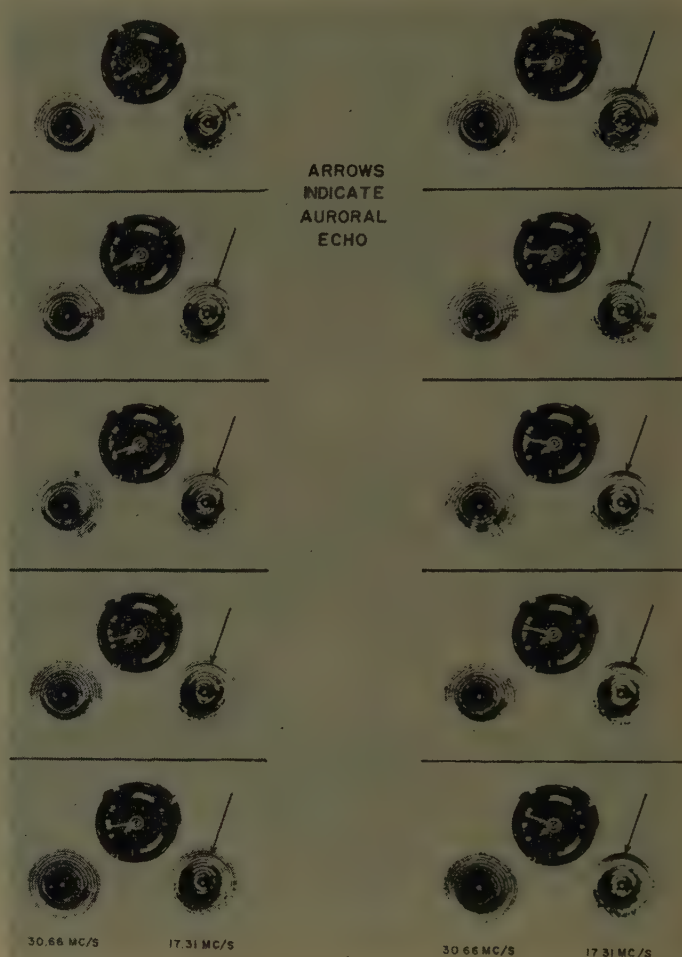


Fig. 5—PPI scatter-soundings showing auroral-zone echoes at 3800 km and 4300-km range at 17.31 mc.

*Direction of Occurrence:* The bearings of the echoes are, in most cases, somewhat east of north, which corresponds roughly to geomagnetic north at Stanford. Occasionally, echoes are seen in directions other than geomagnetic north; they appear at azimuths as much as  $45^\circ$  east and west of geomagnetic north, corresponding to reflection over northeastern Canada to Alaska.

On infrequent occasions a discontinuous change in range with azimuthal direction is found to occur. A jump of 200 km or more in range has been observed with a  $30^\circ$  change in azimuth on 6.4 mc.

*Amplitude Fluctuations and Doppler Shifts:* The discrete echoes appear suddenly and rise in a fraction of a second to full amplitude, remain for a length of time, varying from a few seconds to many minutes, then disappear. Fig. 2 is a good example of this behavior. The echo usually is found to vary rapidly and discontinuously in amplitude and Doppler shift of the returned energy. The availability of Doppler detection (phase-path) equipment greatly facilitates the separation of this echo from ground-scatter echoes which may be pres-

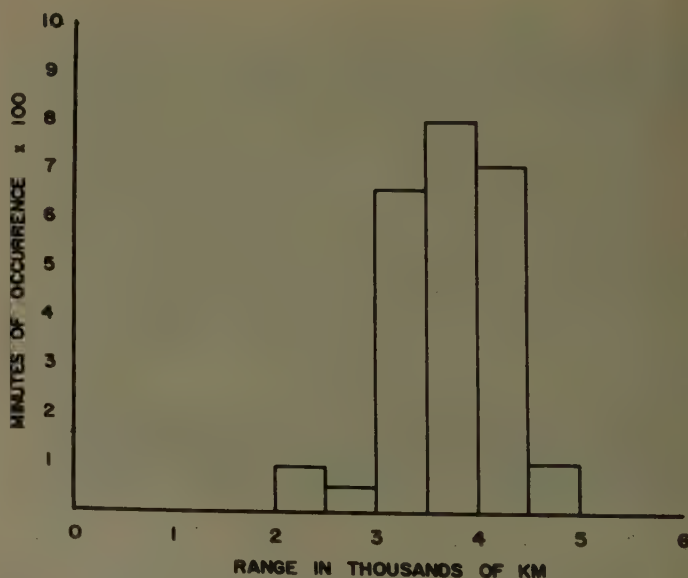


Fig. 6—Minutes of occurrence of auroral-zone echoes at 17.31 mc plotted vs range for the period between October, 1952 and March, 1953.

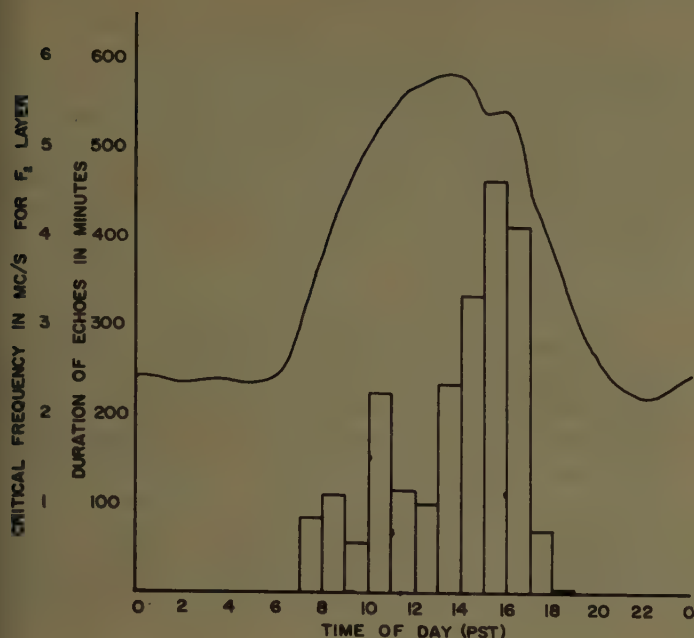


Fig. 7—Auroral-zone echo occurrence at 17.31 mc compared with  $F$ -layer criticals at Winnipeg, Man., Can., for the period between October, 1952 and March, 1953.

ent at the same time. The Doppler shift of the auroral echo is much more rapidly varying and erratic than that of the usual ground-scatter echo. Ground-scatter echoes seldom are observed with Doppler shifts exceeding 5 cps, while the auroral echoes have Doppler shifts as great as 100 cps. These differences are illustrated by the phase-coherent detector output shown in Fig. 1. An auroral echo, superimposed on a ground-scatter echo, is easily identified when using phase-path recording.

The amplitude variations and Doppler shifts of the diffuse echoes are quite similar to those of the discrete echo. The diffuse echo generally is of smaller amplitude than the discrete echo.

The amplitude fluctuations and Doppler shifts are so rapid that they appear on the customary  $A$  scope displays as discontinuous jumps at the prf used. In order to resolve the fading frequency of the echoes, a high prf would be required. This is not practical because of the long range at which these echoes appear, and the simultaneous presence of ground-scatter echoes. However, an effect similar to a high prf may be obtained by transmitting, at the customary prf, groups of two pulses which are separated by a small time delay. By varying the spacing between these two pulses, it is possible to determine the separation at which successive echoes begin to differ appreciably in amplitude. Results from this double-pulsing technique have indicated that the amplitude fluctuations occur at rates as high as 100 to 200 cps.

**Time of Occurrence:** At 17 mc, the echoes are found to occur mostly during daytime hours. The relationship between the rate of occurrence at 17 mc and time of day is shown in Fig. 7. The average value of  $F$ -layer-critical frequencies for Winnipeg, Can., during the same period also is shown in Fig. 7. Comparison of the two curves

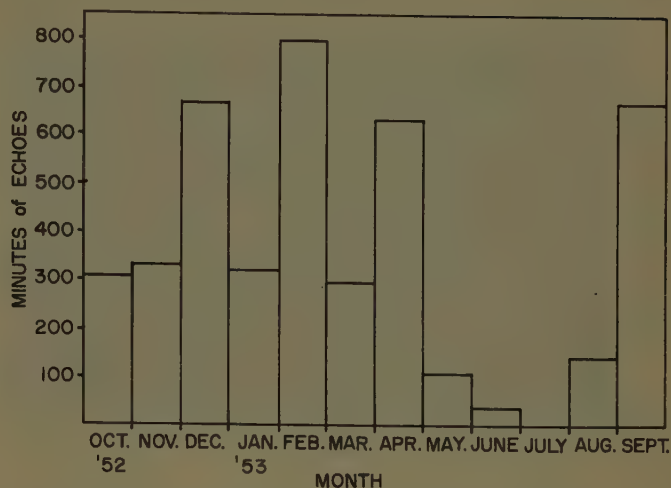


Fig. 8—Histogram showing minutes of auroral-zone echoes as a function of the month of the year, for the period between October, 1952 and October, 1953.

suggests a possible relationship between  $F$ -layer ionization and the occurrence of echoes at 17 mc. At 6 mc the echoes occur at nearly all times of day. The hours of maximum frequency of occurrence are between 1700 and 2300 PST.

The seasonal variation of these echoes has been obtained from the continuous 17-mc scatter-soundings and is shown in Fig. 8. The echoes appear to be observed most frequently during the equinoctial and winter solstice periods. Very few auroral echoes are detected during the summer months. In Fig. 9, the number of minutes of auroral echoes seen at 17 mc are shown for each day for a period of one year between October, 1952 and October, 1953.

Occasionally, echoes have been found to occur simultaneously on 17 mc and 6 mc. More frequently, simultaneous occurrence is detected at 6 mc and 12 mc. In several instances, it has been found that rapid increases in amplitude of the echoes (bursts) occur at identical times on both frequencies, suggesting that both the 6-mc and 12-mc echoes are the result of reflection from the same auroral form.

#### Observations at Other Locations

Observations of these auroral-zone echoes have been made at locations other than Stanford. During the period between March 19 and March 30, 1954, a field station was operated at a location near Tacoma, Wash. Also a portable scatter-sounder was operated at Spokane, Wash. from February 20 to April 20, 1955. Numerous auroral-zone echoes were recorded simultaneously at Spokane and Stanford during this period. These simultaneous occurrences were useful in the determination of propagation paths.

The characteristics of the auroral echoes observed at these more northern locations were similar to those seen at Stanford. More recently, such echoes have been observed as far south as Sacramento Peak, N. M. (geomagnetic latitude  $40^\circ$ ).



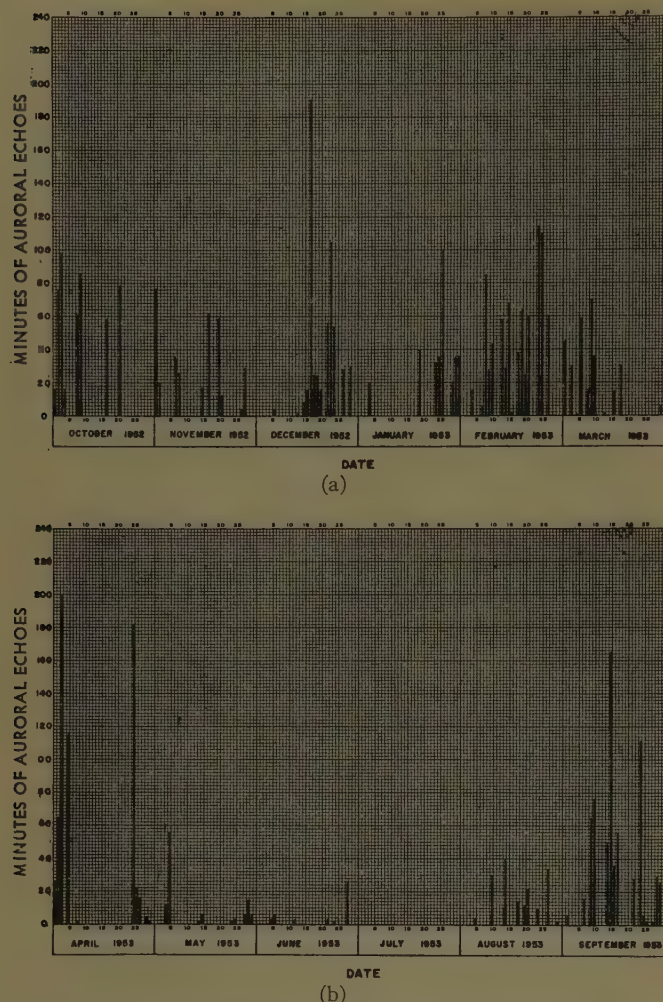


Fig. 9—(a) Histogram showing minutes of occurrence of auroral-zone echoes for each day of the one year period between October, 1952 and October, 1953. (b) Histogram showing minutes of occurrence of auroral-zone echoes for each day of the one year period between October, 1952 and October, 1953.

#### Correlation with Auroral Activity

The seasonal variations in the echo occurrence rate as observed at 6 mc and 17 mc are consistent with the seasonal variations of visual auroral activity. The time of occurrence at 6 mc appears to be in excellent accord with visual auroral activity. Differences in occurrence times at 6 mc and 17 mc appear inconsistent, but this may be justified by the mode of propagation.

A correlation of magnetic activity ( $k$  figures) with frequency of echo occurrence has been investigated. The coefficient of correlation has been found to be 0.85. The result of the correlation indicates a close relationship between the auroral echoes and magnetic activity.

The sudden appearance and disappearance of these echoes, as illustrated in Fig. 2, is typical of visual auroral behavior. The multiple echoes occasionally observed can be explained by the presence of several auroral forms at different magnetic latitudes. Visual auroras are known to show apparent motion, thus giving a possible explanation for the echoes which exhibit changes in range.

It also should be pointed out that the rapid-amplitude fluctuations, high-Doppler shifts, and direction of occurrence of these echoes gave the first clues to their origin. In these respects, the echoes detected at Stanford are similar to auroral echoes observed at more northern latitudes. Workers using vhf radio waves have shown the relation between vhf radio echoes and visual auroras [7].

#### EXPLANATIONS OF THE OBSERVATIONS

It has been possible for workers using frequencies in the vhf range at locations close to the auroral zone to determine propagation paths and to offer explanations of the reflection mechanisms [14], [16], and [19]. Since the auroral-zone echoes at Stanford are observed on frequencies in the hf range, the normal ionospheric layers and sporadic- $E$  ionization have great influence on the propagation paths of the auroral signals. Possible reflection mechanisms and propagation paths are discussed in this section.

#### Reflection Mechanism

The great amplitude of the auroral echoes and the retention of the transmitted pulse shape by the reflected signals (as illustrated by Fig. 1) suggest specular reflection from a relatively large ionized surface. Such ionized surfaces might be related to auroral arcs which are known to lie along the earth's magnetic field lines. Auroral arcs are, perhaps, a kilometer thick and extend many hundreds of kilometers along the auroral zone.

In order to determine the electron density of the auroral form necessary for reflection, some reflection mechanism must be visualized which produces echoes with the rapid amplitude fluctuations and Doppler shifts observed experimentally. The actual reflection mechanism for auroral echoes is not definitely known, although several mechanisms have appeared in the literature [14], [16], and [19]. The mechanism which best explains the rapid Doppler shifts is the one described by Moore [24], who proposes that the ionization consists of many small ionized trails formed by bundles of incoming auroral protons.

For the auroral echoes observed at Stanford, the reflecting surface is visualized as an ionized surface made up of many of these small ionized trails. Thus, the Doppler frequencies and amplitude fluctuations of the echoes may be explained by the rate of formation of ionization in the reflecting surface.

There have been many cases of auroral echoes which occur at 6 mc and 17 mc simultaneously, but more have been seen on a frequency of 30 mc at this same time; this allows an upper limit to be placed on the density of auroral ionization assuming a critical reflection mechanism. For the 17-mc frequency, an ionization density of  $3.72 \times 10^6$  electrons per cc is obtained, and for 30 mc, a density of  $1.1 \times 10^7$  electrons per cc. Thus, the ionization density of the auroral forms must lie between these two values:



$$1.11 > 10^7 > N > 3.72 \times 10^6.$$

Since the occurrence rate of auroral echoes is greater on the lower frequencies, many of the auroral forms must have ionization densities which are smaller than  $3.72 \times 10^6$  electrons per cc. Only  $5 \times 10^6$  electrons per cc are required for critical reflection at 6.4 mc.

If it is assumed that the auroral reflector is a plane-ionized surface having unity coefficient, then the reflector, of one Fresnel zone diameter, would give the maximum obtainable amplitude of reflected signal.

Calculation of the Fresnel-zone diameter for frequencies of 6 mc, 12 mc, and 17 mc give values between 7 km and 22 km for the frequencies and ranges involved at Stanford.

The amount of power available at the receiver antenna terminals after reflection, from a reflector with unity reflection coefficient, may be calculated using the familiar radar equation

$$P_R = \frac{\lambda^2 P_T G^2 S}{(4\pi)^3 R^4} \quad (1)$$

The symbols have the following meanings:

$P_R$  = received power in watts,

$P_T$  = transmitted power in watts,

$G$  = antenna gain,

$S$  = radar cross section in meters<sup>2</sup> ( $R^2$  for a Fresnel-zone reflector),

$R$  = range in meters,

$\lambda$  = wavelengths in meters.

The auroral-zone echoes quite frequently are observed to be as great as ten times the noise level of the receiving system when observed on  $A$  scope. The sensitivity of the 17-mc equipment is limited by the atmospheric noise level. The average noise level was found to be approximately  $6 \times 10^{-14}$  watts. The calculated values for received power are considerably above the noise level for all ranges. Assuming a Fresnel-zone reflector, the reflection coefficient is smaller than unity. Also, the ionization densities would be less than the values necessary for critical reflection. An alternative interpretation would be that the reflector is a perfect reflector much smaller in size. However, the relatively enormous size of auroral forms would tend to favor the partial reflection interpretation.

The sensitivity of the radar is such that a Fresnel-zone size sheet of auroral ionization with a very small reflection coefficient may be detected. The reflection coefficient  $\rho_K$ , is defined as the ratio of actual received power ( $P_A$ ) to the calculated received power for a perfect Fresnel reflector.

$$\rho_K = \frac{P_A}{P_R}$$

The value of this reflection coefficient has been calculated for observed values of received signal ( $P_A$ ) equal to 10 times and 100 times the noise level of  $6 \times 10^{-14}$

watts. For 17 mc, it was found that  $\rho_K$ , the reflection coefficient, may vary between  $3 \times 10^{-8}$  and  $1.5 \times 10^{-8}$  for the ranges and signal strengths involved.

Assuming partial reflection, it is possible to calculate the ionization densities implied by the above reflection coefficient. For 17 mc, the ionization densities implied by reflection coefficients of  $10^{-4}$  and  $10^{-8}$  are  $1.5 \times 10^4$  and  $1.4 \times 10^2$  electrons per cc, respectively.

Also it is conceivable that increased signal strengths may be obtained at times on account of the geometrical configurations of the aurora. Such increases could aid the detecting of very weak auroras. It is well known that visual auroras tend to lie along lines which are coincident with geomagnetic latitude lines. Although these forms appear convex in the horizontal direction, some focusing may be possible because of folds appearing in the surfaces. Such folds are commonly observed by visual means [22].

### Propagation Paths<sup>1</sup>

The paths that the transmitted signals travel from Stanford to the auroral reflector and back are very difficult to determine precisely because of the great distance from Stanford to the auroral zone. Workers located at more northern latitudes, using vhf radars, can easily determine propagation paths by the consideration of antenna patterns and angles of arrival. At these more northern locations, the propagation paths generally are straight lines from the transmitter to the auroral ionization. At Stanford, the auroral investigations are made on frequencies (6 mc to 30 mc) that are affected appreciably by the normal ionospheric layers. It is found that the existence of the normal ionospheric layers plays an essential part in the observation of the longer range auroral echoes. No single model will explain adequately the transmission paths of all the long-range auroral-zone echoes seen at Stanford. It appears that several models are necessary, depending upon the range of the echoes and the ionization density existing in the normal and sporadic ionospheric layers.

For the majority of the echoes detected at ranges of 1400 km–1800 km, a simple straight-line propagation path is believed to exist. Reflection occurs at the point where a ray from Stanford is incident on the earth's magnetic field lines at right angles (see Fig. 10).

At times there is sufficient  $F$ -layer ionization in the direction of geomagnetic north to return the transmitted signal to the earth. Auroral echoes observed during these times appear to involve an  $F$ -layer reflection followed by an earth reflection in propagating the signal from Stanford to the auroral ionization. Such a propagation path is illustrated in Fig. 11.

Quite frequently, at 17.31 mc, there is not sufficient

<sup>1</sup> Additional transmission modes of importance in the production of Long Distance Auroral Echoes have been reported. See S. Stein, Stanford University, Stanford, Calif., Radio Propagation Lab., Tech. Rep. No. 21, August 20, 1957 and O. Stark, Geophysical Inst., Final Rep., Task B, Contract DA 36-039-SC-71137, October, 1957.



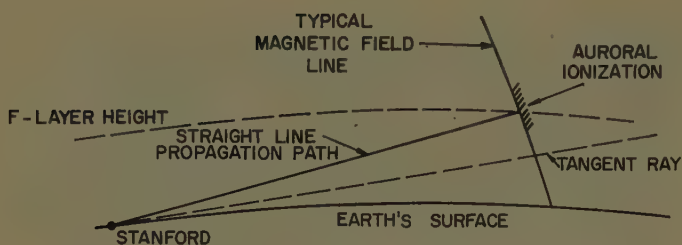


Fig. 10—Sketch showing typical straight line propagation path for auroral-zone echoes.

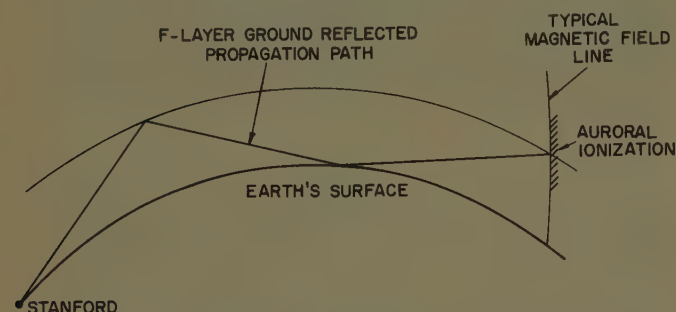


Fig. 11—Sketch showing *F*-layer-ground reflected propagation path for auroral-zone echoes.

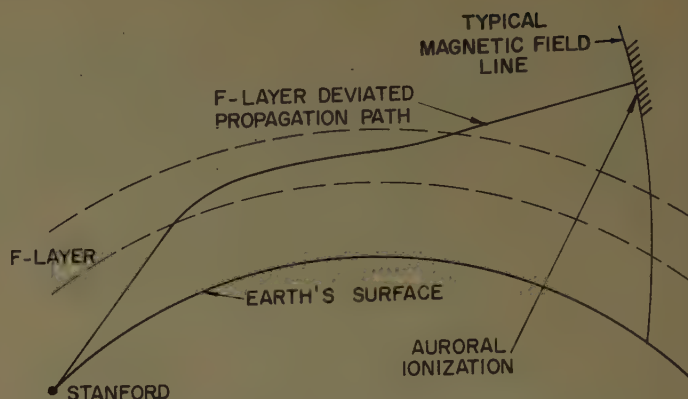


Fig. 12—Sketch showing *F*-layer deviated propagation path for auroral-zone echoes.

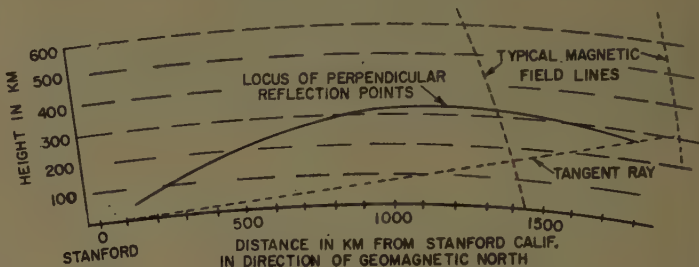


Fig. 13—Locus of those points at which a line of sight from Stanford intersects the earth's magnetic field lines at perpendicular incidence for the magnetic north direction from Stanford.

*F*-layer ionization present in the direction of geomagnetic north to return the transmitted signal to the earth. However, auroral echoes are seen frequently during these times at ranges as great as 4700 km. On first inspection, a straight-line path for such echoes does not appear realistic, as the point of reflection for zero take-off angle would be located 1800 km above the earth's surface. Also, intersection of such a long-range straight-line path with the earth's magnetic field lines does not satisfy the perpendicularity requirement. The scatter-sounding records for the times when auroral echoes occur under these conditions indicate that sufficient *F*-layer ionization is present to bend the ray path and thus lower the height of reflection. A propagation path involving ionospheric bending is depicted in Fig. 12.

**Straight-Line Path:** Auroral echoes occasionally have been observed at Stanford at ranges as short as 1400 km. For echoes observed at these ranges, a simple straight-line propagation path has been found to exist.

If it is assumed that reflection occurs at perpendicular incidence with the earth's magnetic field lines, then it is possible to determine the height of reflection. In Fig. 13, the locus of all points of perpendicular intersection of a ray from Stanford and the earth's magnetic field is shown. For echoes appearing at ranges less than 1850 km, the perpendicularity requirement may be satisfied.

As seen from this geometry, the height of reflection is near 300 km for ranges between 1400 km and 1800 km. Angle-of-arrival measurements using variable-height antennas have shown that reflection is actually taking place at *F*-region heights.

These reflection heights are considerably above the reflection heights (*E* region) reported by workers at more northern locations using radio waves in the vhf range [7], [8], and [19]. However, the ionization densi-

ties required (in the *F* region) for the reflection of the Stanford signals are several orders of magnitude less than those required at very high frequencies for *E*-region reflection [13]. It is known [22] that ionization formed by positive particle bombardment is directly proportional to the luminosity produced. Luminosity as a function of height has been determined by Vegard and Krogness [25] for various auroral forms, showing that the luminosity of the *E*-region aurora is several orders of magnitude greater than luminosity of the aurora at higher *F*-region heights. Thus, the ionization density required for reflection at *F*-layer heights appears to be consistent with the density required for vhf reflection at *E*-layer heights.

**Ground Reflected Path:** The auroral echoes detected at Stanford at frequencies of 6 mc and 12 mc are observed nearly always at times when *F*-layer ground-scatter echoes are seen in the direction of geomagnetic north. This condition is occasionally satisfied on 17 mc but very rarely satisfied on 30 mc. The auroral echoes seen during these ionospheric conditions are visualized as having propagation paths which consist of an *F*-layer or sporadic *E*-layer reflection with a subsequent ground reflection. A sketch showing an *F*-layer ground reflected path is shown in Fig. 11.

In this section, the propagation paths of auroral echoes consisting of reflection from the *E* and *F* layers with subsequent ground reflections are discussed. It is evident that many different combinations of such reflections are possible depending upon the normal and sporadic ionospheric conditions existing at the times of auroral occurrence. During certain of these conditions,

the end points of these paths and hence, auroral reflection, appears to lie within the *E* layer. During other conditions, the end points appear to lie within the *F* layer. As direct auroral reflections from the *E* layer of the ionosphere are fairly well known the particular example chosen for discussion in this section appears to have a reflection height coinciding with the upper *F* layer. However, the discussion, except for the height of reflection, will apply equally as well to those echoes having *E*-layer reflection heights.

In order to test for the existence of this type of propagation path, an additional experiment was performed. The experiment consisted of locating a monitor receiver at Tacoma, Wash., approximately 1150 km to the north of Stanford. This distance corresponds roughly to the distance from Stanford to the ground-reflection point for *F*-layer ground-scatter echoes seen at 6 mc during the hours of maximum auroral occurrences (2000 to 2300 PST). Thus it was possible to monitor the pulse transmission from Stanford in order to detect any auroral echoes at Tacoma which are propagated over the proposed *F*-layer ground-reflected path shown in Fig. 11.

The monitor receiver was operated during the period between March 19 and March 30, 1954, a period of high-auroral activity. During that period, many echoes were observed at Stanford and Tacoma simultaneously. The simultaneous occurrences had time delays which indicated reflections from a common auroral reflector. The auroral echoes seen at Stanford, and not at Tacoma, do not necessarily disprove the *F*-layer ground-reflected path. These auroral echoes may have had propagation paths in which the ground-reflection point does not coincide with Tacoma location.

Additional experimental evidence for the existence of the *F*-layer ground-reflected path has been obtained more recently. A 17.31-mc scatter-sounder (the frequency of the Stanford equipment) was located at Spokane, Wash. Spokane is 1200 km from Stanford in the direction of geomagnetic north. The equipment was operated continuously between February and May, 1955.

During the period of this test, numerous auroral echoes were observed at Spokane and Stanford. There were simultaneous occurrences which have aided appreciably in verifying the *F*-layer ground-reflected propagation path.

The majority of the simultaneous occurrences were observed when *F*-layer ground-scatter echoes seen at Stanford indicated that the Stanford signals were being returned to the earth in the geomagnetic north direction. At this same time there were no *F*-layer ground-scatter echoes seen in the geomagnetic north direction on the Spokane records.

From a typical simultaneous occurrence it is possible to reconstruct the probable propagation paths of the auroral echoes. The paths are shown in Fig. 14 for both Stanford and Spokane echoes. The Spokane propagation path must be a straight-line path if it is assumed that

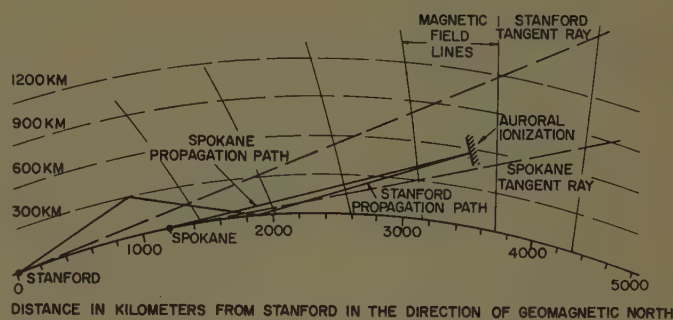


Fig. 14—Cross section of earth's surface and magnetic field lines showing probable propagation path of a typical simultaneous occurrence of auroral-zone echoes seen at Stanford and Spokane at 17.31 mc.

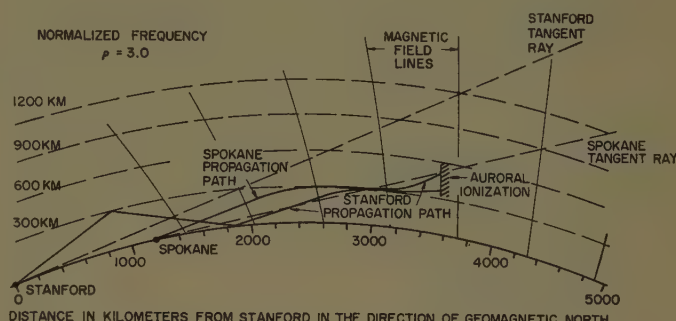


Fig. 15—Cross section of earth's surface and magnetic field lines showing probable propagation path, including *F*-layer deviation, for a typical simultaneous occurrence of auroral-zone echoes seen at Stanford and Spokane at 17.31 mc.

there is no *F*-layer or sporadic-*E* ionization in the direction of geomagnetic north from Spokane. A ray path, tangent to the earth's surface at Spokane, is seen to be at a height of 450 km for a range of 2400 km. Thus, the reflection center must have been above a height of 450 km.

The Stanford propagation path in this case is believed to consist of reflection from the *F* layer and then the ground (near the edge of the skip zone) as shown in Fig. 14. The range of the Stanford echo (3400 km) allows the reflection center for the Stanford echo and the Spokane echo to coincide at a height greater than 450 km. Such great heights do not appear unreasonable, because visual auroras are known to occur at heights up to 1200 km [22].

The absence of *F*-layer ground-scatter is evidence that insufficient *F*-layer ionization is present in the geomagnetic north direction to reflect the Spokane signal to the earth. Also, it does not appear likely that the Stanford signal is returned to the earth a second time. However, it is possible that enough *F*-layer ionization is present to the north of Spokane to cause these signals to deviate appreciably. The deviation (based on calculations in a later section) is illustrated by the ray paths shown in Fig. 15. It is seen that there is sufficient deviation to allow the ray path to be incident upon the magnetic field lines at more nearly perpendicular incidence. For the particular example shown in Fig. 15, the ray path intersects the magnetic field lines at an angle of  $10^\circ$  from the perpendicular. Also, as a result of devia-



tion, the height of reflection has been lowered to that determined by the tangent ray at Spokane.

The nature of the auroral ionization would indicate that an appreciable amount of energy is scattered at angles near perpendicular incidence. Dyce [11] has shown that off-perpendicular angles as great as  $6^\circ$  to  $8^\circ$  will allow an auroral echo to be detected with vhf radars.

**F-Layer Influenced Paths:** Many auroral echoes have been observed at Stanford at 17 mc during periods when the  $F$  layer was not of sufficient density (in the geomagnetic north direction) to return the radar signals to the earth (see, for example, Fig. 5). It does not appear realistic to assume that straight-line propagation paths exist for these echoes since the great ranges (up to 4700 km) place the reflecting centers up to 1800 km above the earth's surface. Thus, propagation paths are sought which have reflection centers not higher than the height of the  $F$ -layer maximum since the Stanford short-range auroral echoes are known to occur at these heights. Such paths would then undergo bending in the  $F$  regions; suitable bending could possibly lower the height of reflection.

The scatter-sounding records showing the auroral echoes also give an index of the  $F$ -layer ionization present in the direction of geomagnetic north. It is seen from Fig 5 that no  $F$ -layer ground-sound echoes are present in the geomagnetic north direction; they do appear, however, in directions slightly away from geomagnetic north. Thus it is not unreasonable to assume that there may be sufficient density to cause bending of the ray path in the geomagnetic north direction.

**F-Layer Deviated Paths:** The  $F$ -layer deviated path is depicted by the geometry in Fig. 12. This path is one in which the  $F$ -layer ionization density is too low to reflect the ray back to the earth's surface. In such a case the path is only deviated by the  $F$  layer. The effect of deviation, as far as geometrical relationships are concerned, is the same as that of being able to radiate at a vertical angle less than the zero take-off angle. This would place the ray path at an angle much more favorable for its intersection of a magnetic field line at perpendicular incidence and would allow a lower height of reflection.

In order to evaluate the effect of deviation, two limiting cases of  $F$ -layer ionization distributions have been considered. The actual  $F$ -layer ionization distribution lies between these two limiting cases. In one case, the  $F$ -layer deviation is a minimum, and in the other the deviation is a maximum. The actual deviation is between these two limits.

The first ionization distribution considered (parabolic  $F$  layer) is one in which the deviation is less than the actual case. The deviated path is described in terms of the geometry of a curved earth and ionosphere (Fig. 16). The derivation of the equations describing ionospheric deviation is given in Appendix I.

The results of the calculation of ionospheric deviation described in Appendix I are presented in Fig. 17 for the

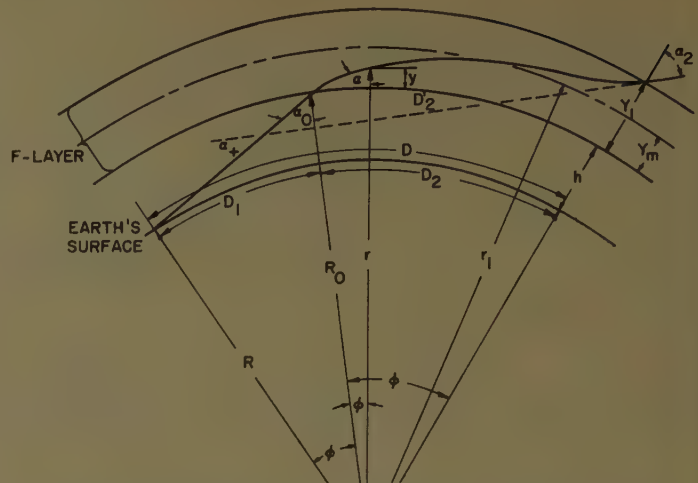


Fig. 16—Geometry of curved-earth curved-ionosphere  $F$ -layer deviated propagation path.

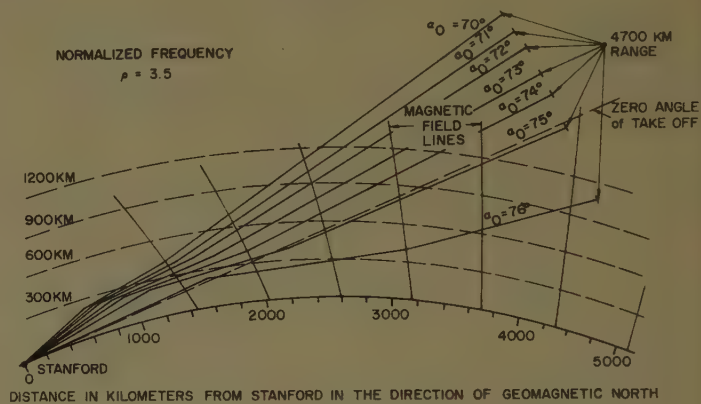
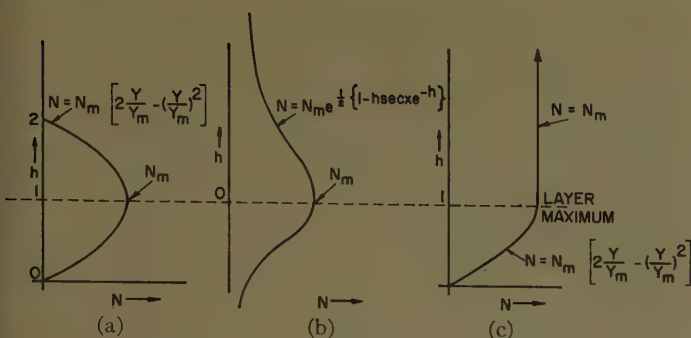
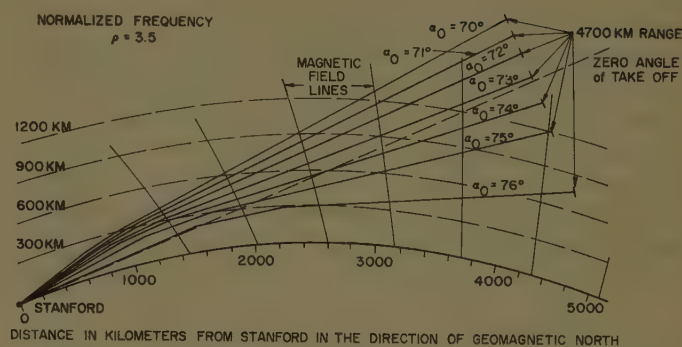
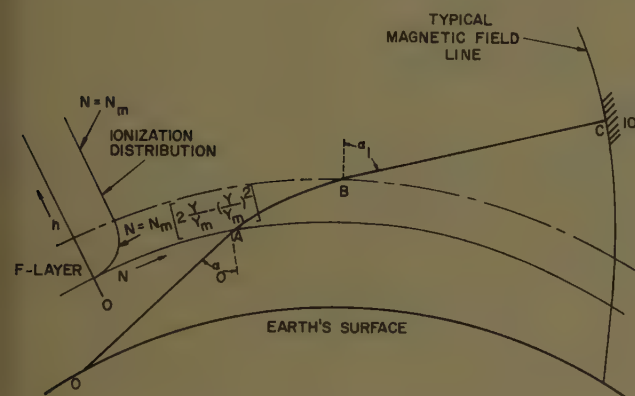
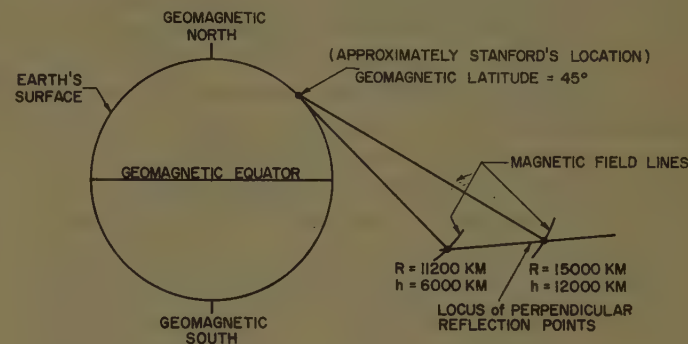


Fig. 17—Sketches of  $F$ -layer deviated ray paths for normalized frequency of  $\rho = 3.5$ .

ionization density profile in Fig. 18(a) and in Fig. 20 for the profile shown in Fig. 18(c) and Fig. 19. The two figures represent the maximum amount of deviation ( $g = 3.5$ ) for the two electron density profiles shown in Fig. 18(a) and Fig. 18(c). The ionospheric portions of these paths are shown in the drawings as straight lines for the sake of convenience.

Thus, even with bending (parabolic case) we are left with ray paths of which the lowest or most horizontal corresponds nearly to the tangent ray. Paths for the echoes at ranges of 4700 km have their end points at heights greater than 1500 km above the surface of the earth. Also, these paths do not intersect the earth's magnetic field lines at right angles, but at an angle of  $20^\circ$  off perpendicular incidence. For the ionization density profile in Fig. 19, there is considerably more bending than for the simple parabolic layer. Such bending places the height of reflection as low as 800 km above the earth's surface.

The actual deviation due to an ionization profile as shown in Fig. 18(b) (Chapman layer) lies between these two examples calculated (Fig. 17 and Fig. 20). This places the lowest possible height of reflection between 800 km and 1200 km. The angle at which the ray path

Fig. 18—Sketches of *F*-layer ionization density distributions.Fig. 20—Sketches of *F*-layer deviated ray paths for normalized frequency of  $\rho = 3.5$ , assuming a limiting ionization distribution.Fig. 19—Sketch of *F*-layer deviated ray path for the limiting ionization distribution shown.Fig. 21—Geometry of transequatorial auroral echoes for a location at  $45^\circ$  geomagnetic latitude (approximately Stanford University).

intersects the earth's magnetic field lines is between  $10^\circ$  and  $20^\circ$  away from perpendicular incidence.

The fact that reflection does not occur at right angles to the earth's magnetic field lines for these very long-range auroral zone echoes is not difficult to justify. There are several possible interpretations.

One interpretation is that given by Chapman [26]. He has stated that there is apparently no reason to believe that the auroral particles are precisely constrained by the earth's magnetic field at all heights above the surface of the earth. For the great heights of reflection found at Stanford, the auroral ionization may not be in alignment with the magnetic field lines.

Another interpretation considers the possibility of a distorted magnetic field. As pointed out by Harang [22], there is evidence that the earth's magnetic field is distorted during an auroral display. The distortion consists of depression of the earth's field towards the south. Such distortion would allow a signal from Stanford to be incident upon the auroral forms at more nearly perpendicular incidence.

It has been shown by Chapman [26] that auroral echoes would not be expected at geomagnetic latitudes above  $64^\circ$  because the perpendicular reflection points lie below a height of 80 km, which is the lowest known height of the aurora. However, auroral echoes are seen consistently at such locations as College [7], Tromsø [14], and Point Barrow [11], which are at geomagnetic latitudes of  $64^\circ$ ,  $67^\circ$ , and  $68^\circ$ , respectively. All these lo-

cations lie in the *forbidden* region. However, due to the high sensitivity of the radar equipments and the nature of auroral ionization it appears that echoes may be detected at reasonable off-perpendicular angles. It has been shown by Dyce [11] that near-perpendicular incidence is obtained for the auroral echoes seen at College and Point Barrow. Auroral echoes are seen quite regularly at both locations, and are most frequently found when the angle of incidence on the auroral ionization is most nearly perpendicular. Echoes are seen at these locations with angles of  $6^\circ$  to  $8^\circ$  from the perpendicular.

The long-range auroral echoes seen at Stanford are believed to be due to near-perpendicular reflections from ionization aligned with the magnetic field lines.

The extreme heights of reflection associated with the auroral zone echoes (1200 km) suggests that reflections may take place from streams of primary auroral particles. In a discussion of the detection of such streams, Chapman [26] also has discussed the possibility of detecting transequatorial echoes. Such echoes, as observed in the northern hemisphere, would be reflections from the primary auroral particles causing the Aurora Australis. The geometry of the echoing streams is shown in Fig. 21 for a location of  $45^\circ$  geomagnetic latitude (approximately the same location as Stanford). The detection of echoes corresponding to transequatorial reflection would be positive evidence that the Stanford echoes, occurring at great heights, are due to reflection from primary auroral particles.

The 17-mc and 30-mc radars, with three-element yagi



antennas, 1 and 1.7 wavelengths above ground, respectively, have been in continuous operation for a period of three years (October, 1952 to September, 1955). No echoes of this type have been observed even during magnetically disturbed periods. It does not seem likely that such echoes can be seen from Stanford with such low-power radars. The optimum parameters for a radar which could be used to search for such streams are given in the next section.

#### RECOMMENDATIONS FOR FURTHER STUDY

There are several aspects of the long-range auroral-zone echoes which need further investigation. The most important of these appears to be the determination of the exact origin of the echoes occurring at great heights (apparently as great as 1200 km above the earth's surface). The detection of transequatorial echoes [26], would be evidence that these echoes are due to reflection from the primary auroral streams producing the Aurora Borealis. Although no transequatorial echoes have been detected at Stanford during the three years of continuous investigations, their detection may be possible with a suitably designed radar. The range at which transequatorial echoes would occur, for a geomagnetic latitude such as that of Stanford, would be approximately 15,000 km [2]. The height of reflection would be above 6000 km. Based on the detection of 4700-km echoes at Stanford, using a radar operating with 2-kw peak power, a radar which could be used to detect 15,000 km echoes should have at least 20-kw peak power. The pulse length, prf, and receiver bandwidth may be adjusted to optimum values for the detection of echoes at these ranges. The frequency which should be used for the search of transequatorial echoes must be above the muf for  $F$ -layer propagation. A frequency in the range between 15 mc and 30 mc would appear to be above the  $F$ -layer muf for the majority of the time. The radar antenna should have a low radiation angle, the lower the better.

Another aspect of the long-range aurora-zone echoes which needs further investigation is related to their fading rates and Doppler shifts. Measurements made by Bowles [7] show that echoes from the rayed structures of the aurora, which are the highest of any of the auroral forms, have negative Doppler frequencies. The negative Doppler frequencies have been interpreted to indicate upward discharges. Also, the measurements of the  $H_a$  spectral line in the aurora by Meinel [27] have suggested that the rayed structures of the aurora are not due to proton bombardment inasmuch as  $H_a$  spectral lines are not found in aurora with rayed structure.

In the case of the auroral-zone echoes at Stanford, the small off-perpendicular angle of intersection with a magnetic field line indicates that a Doppler shift should be observed. The detection of positive Doppler shifts associated with the Stanford echoes would be evidence that reflection is from the primary auroral streams rather than from auroras with rayed structures.

The long-range auroral-zone echoes also will come under study during the International Geophysical Year [28]. It is not possible to predict the results of such studies at this time, except that many statistics concerning their behavior should be obtained. The increased number of observations during IGY should make it possible to correlate the echoes more closely with the occurrence of visual auroras. Also, it is not possible to determine, at this time, the geomagnetic latitudes for the stations which may detect these echoes. It is known that they are detectable from Spokane with much the same characteristics as at Stanford. The fact that Spokane is 1200 km to the north of Stanford gives an indication of the wide latitude spread of locations that are useful for these studies.

#### CONCLUSION

The characteristics of the auroral-zone echoes, occurring at great ranges from Stanford, have been described. These echoes are similar in many respects to auroral echoes seen at locations with geomagnetic latitudes closer to the auroral zone. The occurrence of the auroral-zone echoes, seen at Stanford, have been found to be correlated with magnetic disturbances. The Stanford echoes have been observed at locations along the west coast of the United States which are separated by 1200 km (Spokane, geomagnetic latitude  $44^\circ$ ).

The reflection mechanism of the auroral-zone echoes has been discussed on the basis of a partially reflecting, semi-infinite, ionized sheet. The ionization densities required for reflection are consistent with previous radio measurements and also with the values obtained from absolute auroral brightness measurements.

No single propagation path model will fit all the experimental data. Instead, it is necessary to consider several such models, depending upon the conditions of the normal ionospheric layers at the times when the auroral echoes are found to occur.

For the shorter range echoes (1400 to 1800 km), the propagation path is a straight line from Stanford to the auroral form. Reflection occurs at right angles to the earth's magnetic field lines, and the reflection centers are located at heights of approximately 300 km.

When there is sufficient  $F$ -layer ionization in the direction of geomagnetic north to return the transmitted signal to the earth, the auroral echoes are propagated over paths involving an  $F$ -layer reflection, followed by an earth reflection. The majority of the auroral echoes seen at 6 mc and 12 mc and some of the 17-mc echoes appear to have such propagation paths. When this propagation mode is involved, reflections are believed to sometimes take place in the  $E$  and sometimes in the upper  $F$  layer.

The intersection of the ray path and the earth's magnetic field lines does not always form a  $90^\circ$  angle. Instead, auroral echoes apparently may still be observed with off-perpendicular angles as great as  $10^\circ$ .

At 17 mc, there quite frequently are times when there

is not sufficient  $F$ -layer ionization present in the direction of geomagnetic north to return a transmitted signal to the earth. Auroral-zone echoes seen during these times apparently have paths which are nearly straight lines from the transmitter to the auroral ionization, with deviation occurring when the signal passes through the  $F$  layer. Such paths appear to be the only ones possible for the ionospheric conditions involved. Under these conditions the heights of reflection seem to be in excess of 1000 km for the 4700-km echoes. Such great heights of reflection have never before been obtained, although it is well known that sunlit auroras are seen at heights of 1200 km [25].

It is considered possible that reflection at great heights takes place from streams of primary auroral particles. However, during the three years of continuous observations, made at 30 mc and 17 mc, no echoes of this type have been seen in the direction of geomagnetic south. Such echoes would correspond to reflection from the primary auroral particles producing the Aurora Australis; the height of reflection, assuming perpendicular incidence on magnetic field lines, would be in excess of 6000 km. The detection of these echoes would tend to confirm the hypothesis that the Stanford echoes, occurring at great heights in the magnetic north direction, are due to reflection from the primary auroral particles.

#### APPENDIX I

##### CURVED-EARTH CURVED-IONOSPHERE RAY PATH DERIVATIONS

These ray path derivations are made for the purpose of evaluating the amount of deviation that a signal undergoes in passing obliquely through the  $F$  layer. Deviation is important in the investigation of the propagation paths for the auroral zone echoes detected at Stanford. In particular, it is important for those echoes occurring when there is not sufficient  $F$  layer present in the direction of geomagnetic north to return the Stanford signal to the earth.

The desired ray paths are described in terms of the ground distances  $D_1$  and  $D_2$  (see Fig. 16) for the non-ionospheric and ionospheric portions of the path, respectively.

The nonionospheric portion,  $D_1$ , is obtained from

$$D_2 = \rho R R_0 Y_m \sin \alpha_0 \int_0^{y_1} \frac{dy}{(R_0 + Y_m y)^2 \left\{ \rho^2 - 2y + y^2 - \frac{R_0^2 \rho^2 \sin^2 \alpha_0}{(R_0 + Y_m y)^2} \right\}^{1/2}} \quad (10)$$

simple geometrical relations and is

$$D_1 = R \left[ \alpha_0 - \frac{\pi}{2} + \cos^{-1} \left( \frac{R_0}{R} \sin \alpha_0 \right) \right] \quad (2)$$

The ground distance for the ionospheric part of the path is

$$D_2 = \int_0^\phi R d\phi \quad (3)$$

The incremental angle  $d\phi$  may be expressed in terms of  $\alpha$ ,  $r$ , and  $Y_m$  by consideration of the incremental triangle in Fig. 16. Thus,

$$D_2 = R Y_m \int_0^{y_1} \frac{\sin \alpha}{r \sqrt{1 - \sin^2 \alpha}} dy, \quad (4)$$

where  $y_1$  is the normalized height corresponding to integrating over an angle  $\phi_1$ . Applying Bouguer's rule (Snell's law for spherical geometry)

$$\mu r \sin \alpha = \mu_0 R_0 \sin \alpha_0,$$

where  $\mu$  is the index of refraction in the layer and  $\mu_0$  the free-space value ( $\mu_0 = 1$ ), we obtain

$$D_2 = R R_0 Y_m \int_0^{y_1} \frac{\sin \alpha_0}{\sqrt{\mu^2 r^4 - r^2 R_0^2 \sin^2 \alpha_0}} dy. \quad (5)$$

A parabolic distribution of ionization density with height is assumed and is given as

$$N = N_m \left[ 2 \frac{Y}{Y_m} - \left( \frac{Y}{Y_m} \right)^2 \right], \quad (6)$$

where  $N_m$  is the maximum ionization density of the layer. The index of refraction of an ionized region may be expressed in terms of the ionization density as follows:

$$\mu = 1 - \frac{N e^2}{m \pi f^2}, \quad (7)$$

where  $e$  is the electron charge,  $m$  the mass of the electron, and  $f$  the wave frequency. Defining the critical, or penetration, frequency of the layer as

$$f_c^2 = \frac{N_m e^2}{m \pi} \quad (8)$$

we may describe the index of refraction in normalized form as

$$\mu = 1 - \frac{1}{\rho^2} (2y - y^2), \quad (9)$$

where  $\rho = f/f_c$  is the normalized frequency variable and  $y = Y/Y_m$  is the normalized height variable. Noting that  $r = (R_0 + Y_m y)$ , we may express  $D_2$  as

Writing  $(R_0 + Y_m y) = R_0(1 - \xi y)$ , where  $\xi = Y_m/R_0$ , and obtaining the binomial expansion of  $[R_0(1 - \xi y)]^{-2}$  we have

$$[R_0(1 - \xi y)]^{-2} = \frac{1}{R_0^2} (1 - 2\xi + 3\xi^2 y^2 \dots).$$

Neglecting third and higher-order curvature terms, because they are of order less than  $10^{-6}$ ,  $D_2$  is then given



by

$$D_2 = M \int_0^{y_1} \frac{1 - 2\xi y + 3\xi^2 y^2}{[y^2 - 2by + c]^{1/2}} dy \quad (11)$$

where

$$b = 1 - \xi \rho^2 \sin^2 \alpha_0$$

$$c = \frac{\rho^2 \cos^2 \alpha_0}{1 - 3\rho^2 \xi^2 \sin^2 \alpha_0}$$

$$M = \rho \frac{R}{R_0} Y_m \sin \alpha_0 (1 - 3\rho^2 \xi^2 \sin^2 \alpha_0)^{-1/2}.$$

Eq. (11) may now be integrated readily as the sum of three standard integrals. Performing this integration and neglecting second-order curvature terms, because their contribution is of order  $10^{-2}$ , we obtain

$$D_2 = \frac{R}{R_0} \rho Y_m \sin \alpha_0 \left\{ (1 - 2\xi) \log \frac{y_1 - b + \sqrt{y_1^2 - 2by_1 + c}}{\sqrt{c} - b} + 2\xi [\sqrt{c} - (y_1^2 - 2by_1 + c)^{1/2}] \right\}. \quad (12)$$

The constants  $m$ ,  $b$ , and  $c$  have also been reduced by neglecting second-order curvature terms and they are

$$b = 1 - \xi \rho^2 \sin^2 \alpha_0$$

$$c = \rho^2 \cos^2 \alpha_0$$

$$m = \frac{R}{R_0} \rho Y_m \sin \alpha_0.$$

In the case where the ray is not returned to the earth by the ionized layer, the end point of the path describing the ground distance  $D_2$  is at the top of the layer, or at  $y_1 = 2$ . This gives an expression for  $D_2$ , the ground distance, such that

$$D_2 = \frac{R}{R_0} \rho Y_m \sin \alpha_0 \left[ (1 - 2\xi) \log \frac{1 + \xi \rho^2 \sin^2 \alpha_0 + \sqrt{4\xi \rho^2 \sin^2 \alpha_0 + \rho^2 \cos^2 \alpha_0}}{\rho \cos \alpha_0 + \xi \rho^2 \sin^2 \alpha_0 - 1} + 2\xi (\rho \cos \alpha_0 - \sqrt{4\xi \rho^2 \sin^2 \alpha_0 + \rho^2 \cos^2 \alpha_0}) \right]. \quad (13)$$

Evaluating the constants,  $D_2$  reduces to

$$D_2 = 94\rho \sin \alpha_0 \log \left( \frac{1 + 0.01523 \sin^2 \alpha_0 + \sqrt{0.06092 \rho^2 \sin^2 \alpha_0 + \rho^2 \cos^2 \alpha_0}}{\rho \cos \alpha_0 + 0.01523 \rho^2 \sin^2 \alpha_0 - 1} + 2.953 \rho \sin \alpha_0 (\rho \cos \alpha_0 - \sqrt{0.0692 \rho^2 \sin^2 \alpha_0 + \rho^2 \cos^2 \alpha_0}) \right). \quad (14)$$

The values which  $\alpha_0$  may take are limited by that  $\alpha_0$  which corresponds to the ray being reflected from the layer. The value of  $\alpha_0$  corresponding to reflection is  $\alpha_{0c}$  and is determined by that value which makes  $D_2$  be-

come infinite; i.e., when the denominator in the logarithmic term goes to zero, or

$$\rho \cos \alpha_{0c} + 0.1523 \rho^2 \sin^2 \alpha_{0c} - 1 = 0. \quad (15)$$

Thus, the value  $\alpha_0$  in (14) must have the following limits:

$$0 < \alpha_0 < \alpha_{0c},$$

where  $\alpha_{0c}$  is determined from (15).

In order to determine the amount of deviation, (2) and (14) were evaluated by means of the IBM card programmed calculator of the Stanford Computation Center for various values of the frequency variable  $\rho$  and for all applicable  $\alpha_0$ .

The arguments presented have been based upon ray-path derivations in which it has been assumed that the  $F$ -layer ionization density varies parabolically with height as given in (6). This parabolic ionization distribution, shown in Fig. 18(a), is a convenient first approximation to the actual ionization distribution in the layer. Although the actual distribution of the  $F$  layer is not completely known, the most probable ionization distribution of the  $F$  layer is that given by Chapman [see Fig. 18(b)], and is known as a Chapman layer [23]. The lower half of the Chapman layer has been shown to be a good approximation to the actual distribution by experimental measurements. However, for the Chapman layer, the ionization distribution lying above the layer maximum is obtained from calculations based on the theory of production of the  $F$  layer. No experimental evidence is available to substantiate this ionization distribution.

Ray path results based upon parabolic-layer assumptions, in which only reflection is considered, have been shown to be in good agreement with experimental results. The use of the Chapman distribution in such calculations has been limited by the mathematical difficulty involved in the ray path analysis. For ray paths which penetrate the maximum of the  $F$  layer, it is

necessary to carefully evaluate the limitations involved in using the parabolic-layer assumptions.

This may be accomplished by considering the ionization distribution shown in Fig. 18(c). This distribution

makes use of the parabolic assumption for the part of the layer below the maximum. For the portion of the layer above the parabolic maximum, a constant distribution of ionization density with height is assumed to be a limiting case. The true distribution, no doubt, is not constant but resembles the Chapman distribution, Fig. 18(b), more or less closely. However, inasmuch as the actual distribution is not definitely known, it is believed that this limiting case is useful in showing the maximum amount of *F*-layer deviation that may be obtained. Re-evaluation of the ray path tracings shown in Fig. 17 are made, using this limiting case distribution shown in Fig. 18(c).

For the distribution shown in Fig. 18(c), the deviated ray path will resemble that shown in Fig. 19. The non-ionospheric portion of the path is given by the length *OA*. The ray will be made to deviate, as in previously calculated examples, by the lower half of the layer, and is shown as path *AB*. In reaching the maximum of the layer, the ray will no longer be deviate, but will continue in a straight line until it strikes the hypothetical auroral reflector *C*. The angle  $\alpha_1$  between the ray and the radius vector at the layer maximum may be computed by using the relations developed in Appendix I. That is, the angle  $\alpha_1$  may be expressed in terms of  $\alpha_0$  by means of Bouguer's rule (Snell's law for curved geometry) as

$$\sin \alpha_1 = \frac{\mu_0 R_0 \sin \alpha_0}{\mu_1 r_1} \quad (16)$$

where

$\mu_0$  = index of refraction of free space ( $=1$ ),

$\mu_1$  = index of refraction at the maximum of the layer,

$R_0$  = radius of the earth plus the height of the bottom of the layer,

$r_1$  =  $R_0$  plus  $Y_m$ , the half-thickness of the layer.

The index of refraction at the maximum of the layer is given in normalized form by

$$\mu_1 = \sqrt{1 - 1/\rho^2} \quad (17)$$

where

$\mu_1$  = index of refraction at the maximum of the layer,

$\rho$  = normalized frequency variable ( $f/f_c$ ).

Thus, the  $\alpha_1$  is given by

$$\alpha_1 = \sin^{-1} \left[ \frac{R_0 \sin \alpha_0}{r_1 \left(1 - \frac{1}{\rho^2}\right)^{1/2}} \right] \quad (18)$$

where

$R_0 = 6367 + 200$  km,

$r_1 = 6367 + 300$  km.

The angle  $\alpha_1$  is calculated for the applicable values of  $\alpha_0$  and  $\rho$ .

## BIBLIOGRAPHY

- [1] Peterson, A. M. "The Mechanism of *F*-layer Propagated Back-Scatter Echoes," *Journal of Geophysical Research*, Vol. 56 (June, 1951), pp. 221-237.
- [2] Peterson, A. M. and Leadabrand, R. L. "Long Range Radio Echoes from Auroral Ionization," *Journal of Geophysical Research*, Vol. 59 (June, 1954), pp. 306-309.
- [3] Aspinall, A. and Hawkings, G. S. "Radio Echo Reflections from the Aurora Borealis," *Journal of the British Astronomical Association*, Vol. 60 (April, 1950), pp. 130-135.
- [4] Booker, H. G., Gartlein, C. W., and Nichols, B. "An Interpretation of Radio Reflections from the Aurora," *Journal of Geophysical Research*, Vol. 60 (March, 1955), pp. 1-22.
- [5] Bowles, K. "The Fading Rate of Ionospheric Reflections from the Aurora Borealis at 50 Mc/s," *Journal of Geophysical Research*, Vol. 57 (June, 1952), pp. 191-196.
- [6] Bowles, K. "Doppler Shifted Radio Echoes from the Aurora," *Journal of Geophysical Research*, Vol. 59 (December, 1954), pp. 553-555.
- [7] Bowles, K. "Some Recent Experiments with VHF Radio Echoes from Aurora and Their Possible Significance in the Theory of Magnetic Storms and Auroras," Ph.D. dissertation, School of Electrical Engineering, Cornell University, Ithaca, N. Y., June 1, 1955.
- [8] Bullough, K. and Kaiser, T. R. "Radio Reflections from Aurorae," *Journal of Atmospheric and Terrestrial Physics*, Vol. 5 (September, 1954), pp. 189-200.
- [9] Currie, B. W., Forsyth, P. A., and Vawter, F. E. "Radio Reflections from the Aurora," *Journal of Geophysical Research*, Vol. 58 (June, 1953), pp. 179-200.
- [10] Davidson, D. "Reflexion of High Frequencies During Auroral Activity," *Nature (London)*, Vol. 167 (September, 1951), pp. 277-278.
- [11] Dyce, R. "Communication Aspects of VHF Auroral Reflections," Ph.D. dissertation, School of Electrical Engineering, Cornell University, Ithaca, N. Y., June 1, 1955.
- [12] Flood, W. A. "Ionospheric Fading-Measurements," Master's thesis, School of Electrical Engineering, Cornell University, Ithaca, N. Y., June, 1952.
- [13] Forsyth, P. A. "Radio Measurements and Auroral Electron Densities," *Journal of Geophysical Research*, Vol. 58 (March, 1953), pp. 53-66.
- [14] Harang, L. and Landmark, B. "Radio Echoes Observed During Aurorae and Geomagnetic Storms Using 35 and 74 Mc/s Waves Simultaneously," *Journal of Atmospheric and Terrestrial Physics*, Vol. 4, (January, 1954), pp. 332-338.
- [15] Harang, L. and Stoffregen, W. "Echoversuche auf Ultra Kurzwellen," *Hochfrequenztech. und Elektroakust.*, Vol. 55 (1940).
- [16] Hellgren, G. and Meos, J. "Localization of Aurorae with 10-mm High-Power Radar Technique Using a Rotating Antenna," *Tellus*, Vol. 3 (March, 1952), pp. 249-261.
- [17] Lovell, A. C. B., Clegg, J. A., and Ellyett, C. D. "Radio Echoes from the Aurora Borealis," *Nature (London)*, Vol. 160 (September 13, 1947), p. 273.
- [18] McKinley, D. W. R. and Millman, P. M. "Long-Duration Echoes from Aurora, Meteors, and Ionospheric Back-Scatter," *Canadian Journal of Physics*, Vol. 31 (February, 1953), pp. 171-181.
- [19] McNamara, A. G. and Currie, B. W. "Radio Echoes During Auroras," *Journal of Geophysical Research*, Vol. 59 (June, 1954), pp. 279-285.
- [20] Thayer, R. E. "Radar Echoes from the Aurora Borealis," Master's thesis, School of Electrical Engineering, Cornell University, Ithaca, N. Y., June, 1952.
- [21] Peterson, A. M. *A Scatter-Sounder for the Study of Sporadic Ionization in the Upper Atmosphere*, Stanford: Stanford University, Radio Propagation Laboratory, Technical Report 1, Contract DA-04-200-ORD-181, September, 1953.
- [22] Harang, L. *The Aurorae*. New York: John Wiley & Sons, Inc., 1951.
- [23] Mitra, S. K. "The Upper Atmosphere," *The Asiatic Society of Calcutta*, (June, 1952), pp. 419-420.
- [24] Moore, R. K. "Theory of Radio Scattering from the Aurora," *IRE TRANSACTIONS*, Vol. PGAP-3 (August, 1952), pp. 217-229.
- [25] Vegard, L. and Krogness, O. "The Position in Space of the Aurora Polaris," *Geophysical Publication (Oslo)*, Vol. 1 (1920).
- [26] Chapman, S. "The Geometry of Radio Reflections from Aurorae," *Journal of Atmospheric and Terrestrial Physics*, Vol. 3 (January, 1952), pp. 1-29.
- [27] Meinel, A. B. "Doppler-Shifted Auroral Hydrogen Emission," *Astrophysical Journal*, Vol. 113 (January, 1951), p. 50.
- [28] Peterson, A. M. and Villard, O. G., Jr. *A Preliminary Proposal for Fixed-Frequency Back-Scatter Sounding During IGY*, Stanford: Stanford University, Radio Propagation Laboratory, Memorandum, February 18, 1955.



# The Geometry of Auroral Communications\*

R. L. LEADABRAND† AND I. YABROFF†

**Summary**—As early as 1939, radio amateurs found auroral ionization useful for communication purposes. Such ionization makes hf and vhf propagation possible over paths as great as several hundred kilometers when other more normal ionospheric propagation modes do not exist. The geometry of reflection is investigated for a variety of transmitter locations based upon the assumption of specular reflection from columnar ionization aligned with the earth's magnetic field lines. The results of the investigations outline the region of useful auroral ionization and the regions on the earth within which the auroral propagation is possible. The probability has been determined of obtaining propagation from a particular transmitter location to any receiver location within the region of propagation. These geometrical studies allow the communicator to predict the most useful transmitter and receiver locations in utilizing auroral ionization for communication purposes. The studies also may suggest methods of minimizing the effects of auroral propagation when it is considered a detrimental propagating mode, for example, when it results in undesirable multipath effects.

## I. INTRODUCTION

THIS REPORT deals with the geometrical aspects of radio communication by means of reflections from auroral ionization. Based upon the results of these geometrical calculations, interpretations are given of the possible modes of propagation for previously reported auroral communications.

Many investigators<sup>1-10</sup> of the ionosphere have established that radio propagation by means of reflection from auroral ionization is possible. This phenomenon, first observed by radio amateurs in 1939,<sup>11</sup> has been investigated more recently at several locations by Dyce<sup>1-3</sup> and was reported by Bailey, *et al.*<sup>4</sup> The geometry of radio reflections from the aurora was discussed by Chapman<sup>12</sup> for the case in which the transmitter and receiver are at the same location (radar case). Chapman's analysis

was based upon the interpretation that echoes should be received when a ray from the transmitter intersects the earth's magnetic field lines at perpendicular incidence.

The normal incidence restriction is not asserted. Instead, the reflections are considered to be specular (or nearly specular) from small auroral columns of ionization that are aligned with the earth's magnetic field lines. This interpretation is consistent with the present knowledge of auroral reflections.<sup>13,14</sup> The dipole approximation to the earth's magnetic field is assumed.

## II. GEOMETRICAL DERIVATIONS

The relations developed in this section were obtained for later evaluation by means of a Model 650 IBM calculator at the Stanford Computation Center. Hence, the order of derivation follows the scheme most easily programmed for computer solution.

The location of the auroral column with respect to the transmitter is described in terms of  $\xi$ ,  $\tau_1 r$ ,  $D$ , and  $G$  (see Fig. 1) where

$\xi$  = azimuthal bearing to the column (measured from magnetic north),

$G$  = distance represented by the difference in geomagnetic latitude of the column and the transmitter,

$D$  = distance represented by the difference in geomagnetic longitude of the column and the transmitter, and

$\tau_1 r$  = great-circle distance from the transmitter to the column.

Thus, applying spherical trigonometry,

$$\cot \xi = \frac{\sin \frac{G}{r}}{\tan \frac{D}{r}} \quad (1)$$

$$\gamma_1 r = r \sin^{-1} \left[ \frac{\sin \frac{G}{r}}{\cos \frac{D}{r}} \right] \quad (2)$$

$$\gamma_1 = \sin^{-1} \left[ \frac{\sin \frac{G}{r}}{\cos \frac{D}{r}} \right] \quad (3)$$

\* Manuscript received by the PGAP, November 1, 1956.

† Stanford Research Institute, Menlo Park, Calif.

<sup>1</sup> R. Dyce, "Communication Aspects of V.H.F. Auroral Reflections," Cornell Univ. School of Elec. Eng., Ithaca, N. Y., Ph.D. dissertation (Tech. Rep. 23); June 1, 1955.

<sup>2</sup> —, "VHF auroral and sporadic-E propagation from Cedar Rapids, Iowa, to Ithaca, New York," IRE TRANS., vol. AP-3, pp. 76-80; April, 1955.

<sup>3</sup> —, "More about vhf auroral propagation," QST, vol. 39, pp. 11-15; January, 1955.

<sup>4</sup> D. K. Bailey, R. Bateman, and R. C. Kirby, "Radio transmission at vhf by scattering and other processes in the lower ionosphere," Proc. IRE, vol. 43, pp. 1181-1231; October, 1955.

<sup>5</sup> R. K. Moore, "A vhf propagation phenomena associated with aurora," J. Geophys. Res., vol. 56, March, 1951.

<sup>6</sup> N. C. Gerson, "A note on auroral interaction," J. Atmos. Terr. Phys., vol. 4, pp. 81-82; 1954.

<sup>7</sup> —, "Radio observations of the aurora on Nov. 19, 1949," Nature, vol. 167, pp. 804-807; 1951.

<sup>8</sup> K. Bowles, "The fading rate of ionospheric reflections from the aurora at 50 mc/s," J. Geophys. Res., vol. 57, pp. 191-196; June, 1952.

<sup>9</sup> —, "Doppler-shifted radio echoes from the aurora," J. Geophys. Res., vol. 59, pp. 553-555; December, 1954.

<sup>10</sup> R. E. Thayer, "Auroral effects of television," Proc. IRE, vol. 41, p. 160; January, 1953.

<sup>11</sup> Anonymous, QST, vol. 23, p. 78; 1939.

<sup>12</sup> S. Chapman, "The geometry of radio echoes from aurorae," J. Atmos. Terr. Phys., vol. 3, pp. 1-29; 1952.

<sup>13</sup> R. K. Moore, "Theory of radio scattering from the aurora," IRE TRANS., vol. AP-3, pp. 217-230; August, 1952.

<sup>14</sup> H. G. Booker, "A Theory of Scattering by Non-Isotropic Irregularities With Application to Radar Reflections from the Aurora," Cornell Univ., School of Elec. Eng., Ithaca, N. Y., Tech. Rep. 28; October 30, 1955.





where

$$R_2^2 = y_R^2 + x_R^2 + h^2 \quad (12)$$

and

$$R^2 = \frac{x_t^2 + y_t^2 + h^2}{(x_t \sin \theta - h \cos \theta)^2} \quad (13)$$

Thus

$$y_R^2 + (1 - R^2 \sin^2 \theta) x_R^2 + 2x_R R^2 h \cos \theta \sin \theta + h^2(1 - R^2 \cos^2 \theta) = 0. \quad (14)$$

In order to find where the curve formed by the intersection of the cone and the plane crosses the meridian line of the auroral column,  $y_R$  is set equal to zero. The value of  $x_R$  is then

$$x_R = \frac{-b \pm \sqrt{b^2 - 4ac}}{2a} \quad (15)$$

where

$$a = (1 - R^2 \sin^2 \theta)$$

$$b = 2R^2 h \cos \theta \sin \theta$$

$$c = (1 - R^2 \cos^2 \theta) h^2.$$

If the angle between the ray and the auroral column ( $\sigma_1$ ) is less than  $90^\circ$ , then the positive root in (15) must be chosen. If the angle between the ray and the auroral column is greater than  $90^\circ$ , the negative root in (15) must be chosen. Choosing the improper root would not give the receiver locus, but would give the transmitter locus for constant  $\sigma_1$ .

$$\cos \gamma_2 = \frac{-\frac{R_2}{R_1} \left\{ \sin \tau_1 \cos \gamma_1 \sin \theta - \left(1 + \frac{h}{r} - \cos \tau_1\right) \cos \theta \right\} + \left(1 + \frac{h}{r} - \cos \tau_2\right) \cos \theta}{\sin \tau_2 \sin \theta} \quad (23)$$

The great-circle distance  $\tau_2 r$  corresponding to  $x_R$  may now be obtained by plane-earth to curved-earth transformation as

$$\tau_2 r = r \left\{ \sin^{-1} \left( \frac{r+h}{r} \right) \sqrt{\frac{x_R^2}{x_R^2 + h^2}} - \tan^{-1} \frac{x_R}{h} \right\}. \quad (16)$$

In order to determine the remaining (nonmeridian) points of the locus, it is most convenient to revert to the geometry of a spherical earth with the center of the earth taken as the origin of the coordinate system. The equation of the transmitted ray in this coordinate system is

$$\frac{x}{r \sin \tau_1 \cos \gamma_1} = \frac{y}{r \sin \tau_1 \sin \gamma_1} = \frac{Z - (r+h)}{r \cos \tau_1 - (r+h)} \quad (17)$$

and has direction cosines

$$\cos \alpha = \frac{r}{R_1} \sin \tau_1 \cos \gamma_1$$

$$\cos \beta = \frac{r}{R_1} \sin \tau_1 \sin \gamma_1$$

$$\cos \gamma = \frac{r}{R_1} \left( \cos \tau_1 - 1 - \frac{h}{r} \right). \quad (18)$$

The direction cosines of the auroral column are

$$\cos \alpha = \sin \theta$$

$$\cos \beta = 0$$

$$\cos \gamma = \cos \theta. \quad (19)$$

Thus, the angle between the ray and the auroral column is  $\sigma_1$  where

$$\cos \sigma_1 = \frac{r}{R_1} \sin \tau_1 \cos \gamma_1 \sin \theta - \frac{r}{R_1} \left( 1 - \cos \tau_1 + \frac{h}{r} \right) \cos \theta. \quad (20)$$

The condition for reflection is

$$\cos \sigma_1 = -\cos \sigma_2 \quad (21)$$

or

$$\sin \tau_1 \cos \gamma_1 \sin \theta - \left( 1 + \frac{h}{r} - \cos \tau_1 \right) \cos \theta = -\frac{R_1}{R_2} \sin \tau_2 \cos \gamma_2 \sin \theta - \left( 1 + \frac{h}{r} - \cos \tau_2 \right) \cos \theta. \quad (22)$$

Solving for  $\cos \gamma_2$  where  $\gamma_2$  is the bearing from the auroral column to the receiver,

where

$$\frac{R_2}{r} = \sqrt{\sin^2 \tau_2 + \left( 1 + \frac{h}{r} - \cos \tau_2 \right)^2} \quad (24)$$

and

$$\frac{R_1}{r} = \sqrt{\sin^2 \tau_1 + \left( 1 + \frac{h}{r} - \cos \tau_1 \right)^2}. \quad (25)$$

The order of computation using these equations follows.

- 1) Specify  $G$ ,  $D$ ,  $\alpha_0$ , and  $h$ .
- 2) Compute  $\tau_1 r$  using (2).
- 3) Compute  $G/r$ .
- 4) Compute  $\gamma_1$  using (3).
- 5) Compute  $\theta$  using (4).
- 6) Compute  $x_t$  and  $y_t$  using (5) and (6).
- 7) Compute  $x_R$  using (15).
- 8) Compute  $\tau_2 r$  using (16).

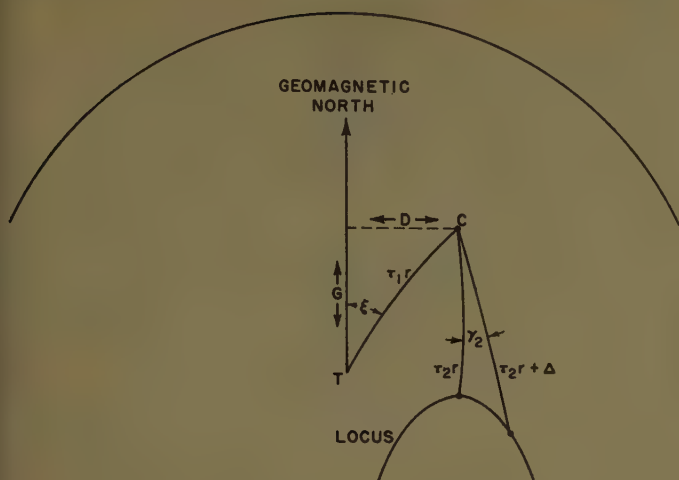


Fig. 4—Sketch describing the calculation of auroral communication locus.

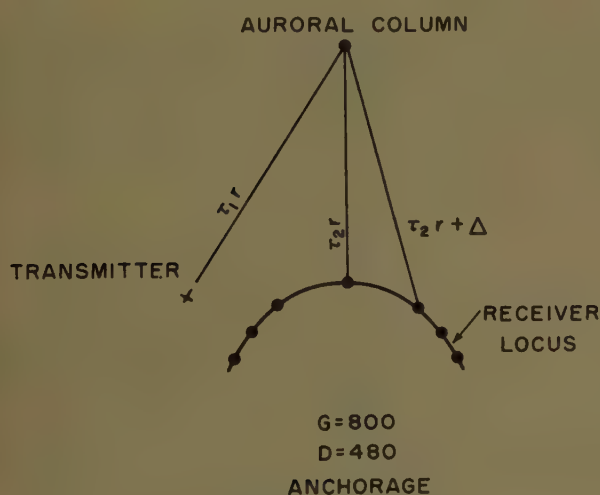


Fig. 5—Typical receiver locus.

- 9) Add 100 km to  $\tau_2 r$  and compute  $\gamma_2$  using (23) to (25).
- 10) Repeat step 9) until  $\tau_2 r$  exceeds great-circle distance, corresponding to a ray tangent to the earth's surface and intersecting the column at a height  $h$ .

The geometry of these calculations is shown in Fig. 4. The actual calculation results in a typical receiver locus as in Fig. 5. The effect of changing the height of reflection is shown in Fig. 6.

Calculations using the preceding relations have been made for the following transmitter locations, assuming a height of reflection of 100 km.

- 1) Anchorage, Alaska (geomagnetic colatitude =  $29^\circ$ );
- 2) Fargo, N. D. (geomagnetic colatitude =  $33.5^\circ$ ),
- 3) Cedar Rapids, Iowa (geomagnetic colatitude =  $37^\circ$ ),
- 4) College, Alaska (geomagnetic colatitude =  $26^\circ$ ), and
- 5) Goose Bay, Labrador (geomagnetic colatitude =  $26^\circ$ ).

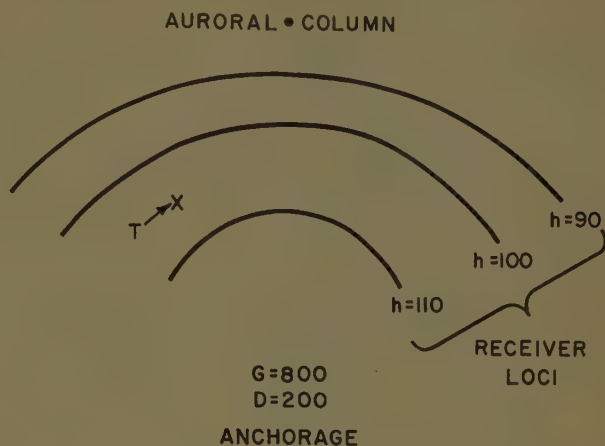


Fig. 6—Effect of changing height of reflection on typical receiver locus.

The region of useful ionization and the region of propagation are shown for each location in Fig. 7 through Fig. 9. (Calculations show that specular reflection from auroral columns at a height of 100 km will not return the signal to the earth for transmitters located at College and Goose Bay.) These regions were outlined by computing the receiver loci for auroral columns at many different locations. Auroral columns lying outside the useful region either do not reflect the transmitted signal back to the earth, or are not visible from the transmitter due to earth curvature.

### III. OFF-SPECULAR REFLECTION

Forsyth,<sup>15</sup> Dyce,<sup>16</sup> and Bowles<sup>17</sup> have shown that off-specular reflection from auroral ionization is obtained frequently. In fact, no radar echoes from auroral ionization could be obtained at such locations as College and Point Barrow if specular reflection were required.<sup>12</sup> For auroral radar echoes seen at Point Barrow, off-specular reflection by angles as great as  $7^\circ$  has been observed by Dyce.

If the configuration of the auroral ionization makes off-specular reflection possible in the radar case, then it should also be possible to have off-specular reflection when the transmitter and receiver are separated. Off-specular scattering would increase appreciably the area to which it would be possible to communicate via auroral reflections.

It is possible to evaluate to what extent the area of propagation may be increased due to off-specular reflection by using the same relationships that were developed in Section II. Physically, off-specular reflection by a constant angle corresponds to changing, by a con-

<sup>15</sup> P. A. Forsyth, "Radio Wave Reflections from Aurorae," *Geophys. Res. Dir., AFCRC, ARDC, Paper No. 30*; July, 1954.

<sup>16</sup> R. Dyce, "Auroral echoes observed north of the auroral zone," *J. Geophys. Res.*, vol. 60, September, 1955.

<sup>17</sup> K. Bowles, "Some Recent Experiments with VHF Radio Echoes from Aurora and Their Possible Significance in the Theory of Magnetic Storms and Auroras," *Cornell Univ. School of Elec. Eng., Ithaca, N. Y., Ph.D. dissertation*; June 1, 1955.



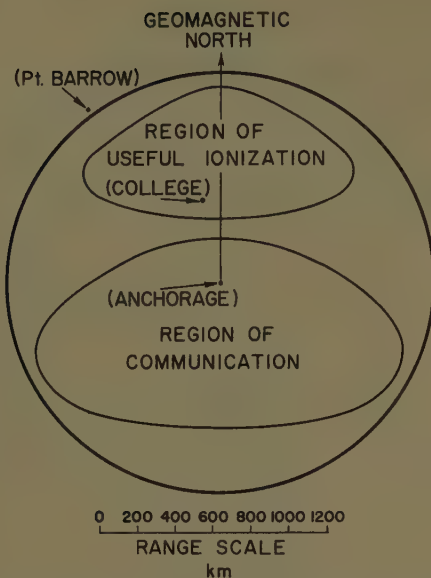


Fig. 7—Region of useful ionization and region of propagation for Anchorage, Alaska.

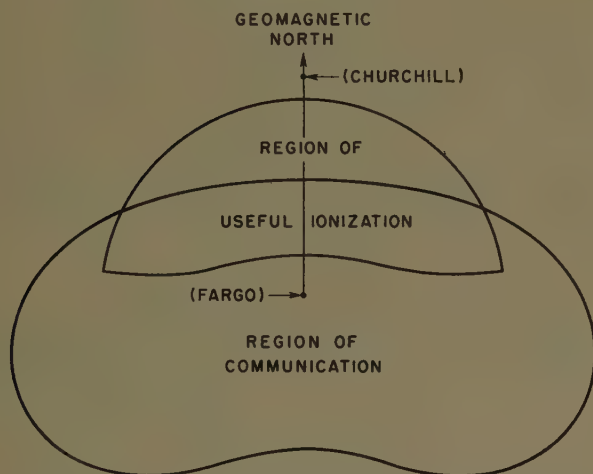


Fig. 8—Region of useful ionization and region of propagation for Fargo, N. D.

stant angle, the size of the conical surface describing the reflected signal. Thus, the reflected signal is considered to have a lobe structure, rather than being a ray as it was considered previously.

In computing the receiver locus for a constant off-specular scattering angle, the relationships used in Section II are used again. The computation scheme used in Section II is followed through step 6). In step 7) the opposite root from that chosen in Section II is taken for computing  $x_R$ . This value of  $x_R$  locates the transmitter on the meridian line of the auroral column at a point which keeps the angle between the transmitted ray and the column constant. That is, it finds the point where the transmitter locus crosses the meridian of the column (Fig. 10). Both the ray from  $T$  to the column and the ray from  $T'$  to the column intersect the axis of the auroral column at an angle,  $\sigma_1$ . Thus, either location of the transmitter  $T$  or  $T'$  gives the same receiver locus. At this point in the computations the angle between the

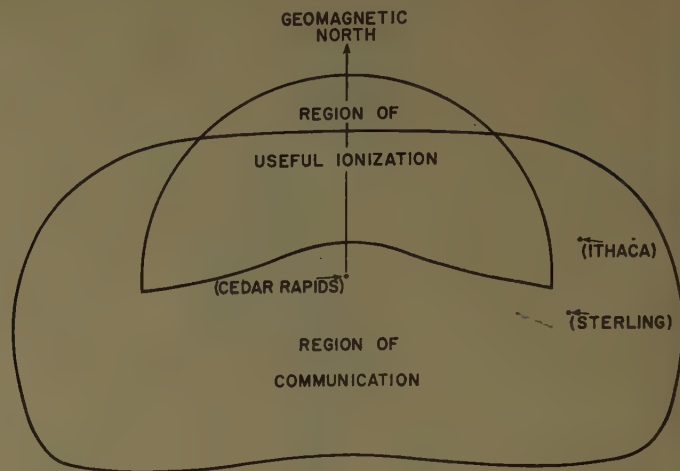


Fig. 9—Region of useful ionization and region of propagation for Cedar Rapids, Iowa.

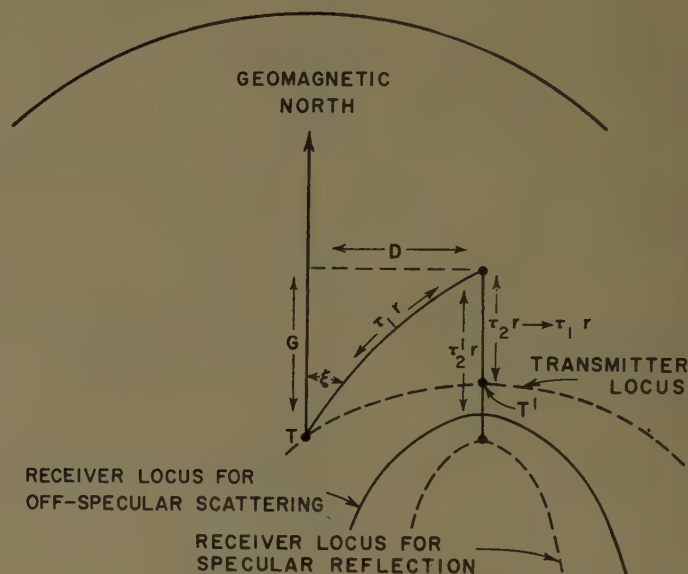


Fig. 10—Geometry of off-specular reflection.

ray from  $T'$  and the axis of the column is changed by a constant amount  $\epsilon$  (adding  $\epsilon$  to  $\theta$ ). The effect is to shift the receiver locus by an amount which is equivalent to off-specular reflection of  $2\epsilon$ .

The order of computation for the constant-angle off-specular reflection follows.

- 1) Follow steps 1) through 6) in Section II.
- 7) Compute  $x_R$  (choosing proper root) using (14).
- 8) Compute  $\tau_2 r$  using (15).
- 9) Call  $\tau_2 r \rightarrow \tau_1 r$ .
- 10) Set  $\gamma_1 = 0$ .
- 11) Add  $\epsilon$  to  $\theta$  and call  $\epsilon + \theta = \theta'$ .
- 12) Compute  $x_t$  using (5).
- 13) Compute  $x_R$  using (14) and  $\theta'$ .
- 14) Compute  $\tau_2' r$  using (15).
- 15) Add 100 to  $\tau_2' r$  and compute  $\tau_2' r$  using (25) to (27).
- 16) Repeat step 15) until  $\tau_2' r$  exceeds the great-circle distance corresponding to a ray tangent to the earth's surface and intersecting the column at a height  $h$ .

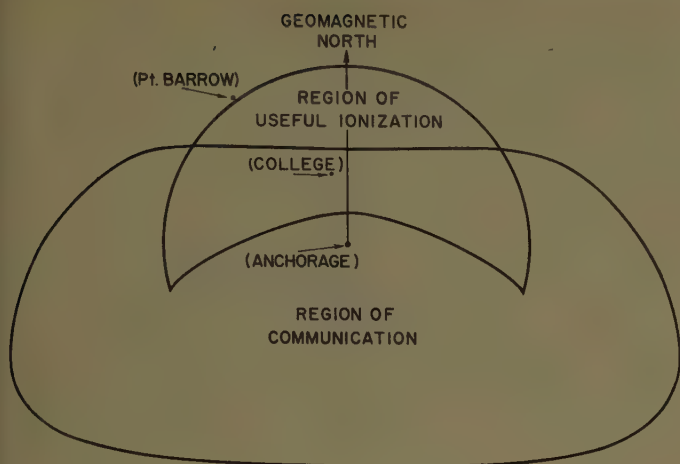


Fig. 11—Region of useful ionization and region of propagation for off-specular scattering at Anchorage, Alaska.

The effect of off-specular reflection has been evaluated for Anchorage, Alaska, using  $\epsilon = 3.5^\circ$  (corresponding to off-specular reflection of  $2\epsilon = 7^\circ$ ). The results are shown in Fig. 11. It is seen that the area of useful ionization and the area of propagation have been increased greatly.

#### IV. THE PROBABILITY OF AURAL COMMUNICATION

For the communicator it is important that knowledge of the probability of aural communication be available. The probability of aural communication is discussed here with the goal of being able to predict the frequency of aural communication for any particular transmitter and receiver location.

If it is assumed that the aurora is made up of a homogeneous distribution of small ionized columns all aligned with the earth's magnetic field lines, then certain regions on the earth's surface will be illuminated by more or fewer of these columns. Thus, the region of propagation for any particular transmitter location contains some receiver locations which are more likely to receive aural signals than are other receiver locations. The region of propagation for ionization lying along a latitude line is determined for small equal increments of latitude (see Fig. 12 for one such region) contained in the region of ionization. These small "regions of propagation" are then superimposed, forming the total "region of propagation." There are many of the small regions which overlap each other. By counting the number of overlapping regions and joining the regions having the same number of overlaps, it is possible to obtain a contour plot. Such a contour plot has been made for Anchorage, Alaska ( $h = 100$  km), and is shown in Fig. 13. The numbers assigned to each contour line have been normalized to the maximum to indicate the relative number of paths possible for each location. The physical interpretation of such a plot can be made as follows.

The receiver is placed at some point within the total region of propagation. The probability contour that

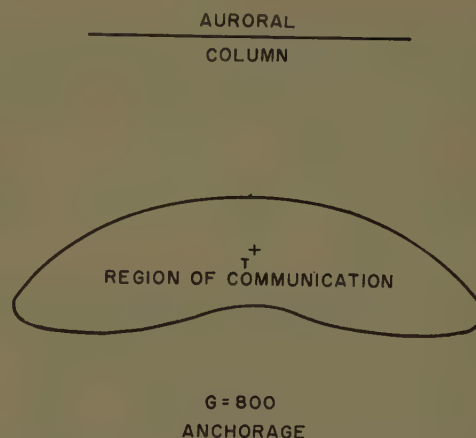


Fig. 12—Formation of region of propagation for auroral columns located along a constant latitude line.

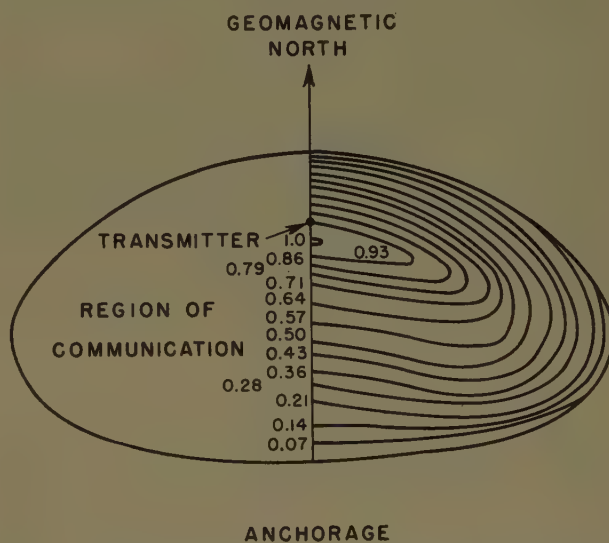


Fig. 13—Contour plot showing relative number of paths possible in the region of propagation for Anchorage, Alaska.

passes through the receiver location gives an indication of the probability of receiving a signal at the receiver. The contours also apply to an interchange of receiver and transmitter. That is, the receiver is placed at Anchorage (Fig. 13) and the transmitter at some other point within the region of propagation. The contour passing through the transmitter location gives an indication of the probability of receiving a signal at the receiver.

It is possible to take into account the distribution of the aurora across the auroral zone. Based upon a plot by Vestine, the number of auroral days vs latitude is charted in Fig. 14 for the region to the north of Anchorage. If it is assumed that the number of auroral days is a measure of the probability of auroral occurrence, then it is possible to consider the effect of this probability distribution in the contour plot of Fig. 13.

The contours in Fig. 14 are modified by calculating the joint probability associated with the overlapping of



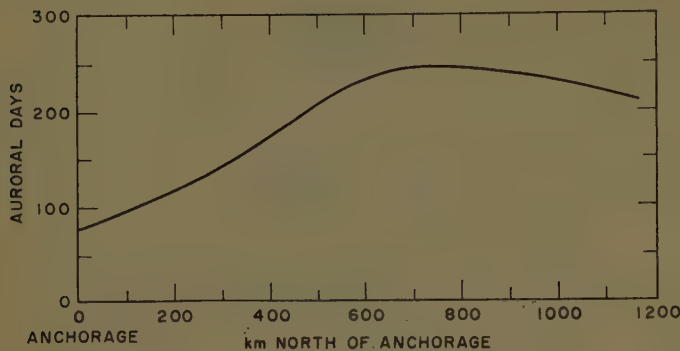


Fig. 14—Plot showing number of auroral days vs latitude (from Vestine).

the "regions of propagation" calculated for constant latitude auroral columns. This has been done, and the contour plot of Fig. 15 was obtained. Thus, a receiver at a particular location would be expected to receive a signal sometime during the night with the probability assigned to the contour at that location.

Examination of the contour plots of Fig. 13 and Fig. 15 illustrates several important facts in auroral communication. First, the most probable location for the detection of auroral propagated signals is in the region near the transmitter. Second, propagation over east-west paths is more probable than over north-south paths. For the communicator wishing to either maximize or minimize the presence of auroral propagation, these charts should prove useful.

#### V. INTERPRETATIONS

Reports of auroral communications have been made by many radio amateurs in the northeastern section of the United States.<sup>1,5,18,19</sup> The analysis of these reports by Dyce<sup>1</sup> has shown that east-west auroral propagation up to 800 miles is possible and north-south auroral propagation up to 400 miles is possible. Dyce<sup>2</sup> studied auroral propagation between Cedar Rapids, Iowa, and Ithaca, N. Y., for more than two years. Since considerable experimental data are available for these paths, the locus of auroral communication was computed for a transmitter located at Cedar Rapids, Iowa. The region of useful ionization, assuming that the auroral ionization occurs at a height of 100 km, covers the majority of the visible region. Ithaca lies well within the zone of communication.

Thus, the geometrical model developed here can explain the reported communications. Auroral communication between the two locations is possible for auroral ionization occurring within a large portion of the useful region.

For transmitter locations such as Anchorage and Fargo, it is seen that the locus of propagation does not satisfy the observed propagation. For example, consider the auroral propagation reported by Bailey, *et al.*, be-

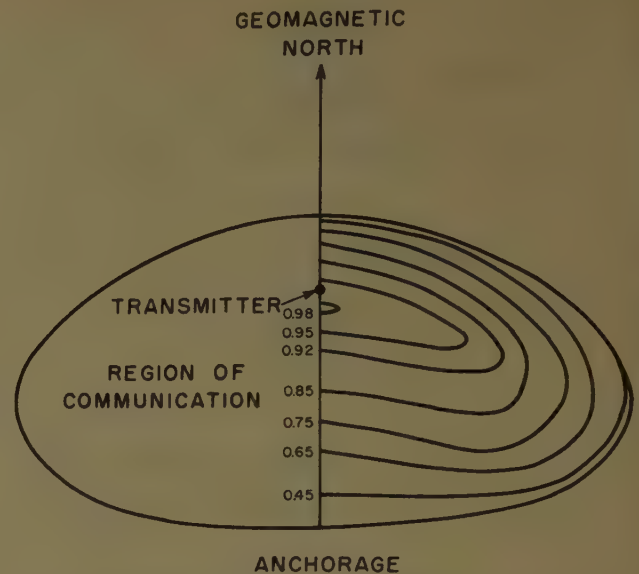


Fig. 15—Contour plot showing probability of auroral propagation for Anchorage, Alaska.

tween Anchorage and Point Barrow. As seen by Fig. 7, Point Barrow is outside the region of propagation assuming specular reflection at 100-km height. Thus the observed propagation may be due to some other mechanism than the 100-km height, specular reflection mechanism postulated here. However, relatively few cases of propagation between Anchorage and Point Barrow were found.

To investigate effects of off-specular reflection, the computations described in Section III were made. The amount of off-specular reflection was assumed to be equal to that observed by auroral radars, *i.e.*, 7°. The results of the off-specular calculations illustrated in Fig. 12 are seen to allow the use of a much greater area of auroral ionization and to increase sizeably the area of communication. However, for off-specular scattering of 7° and 100-km height of reflection the region of propagation does not include Point Barrow.

There remains two explanations of such observed communication. First, the height of reflection may be greater than 100 km. Second, the observed propagation may be due to reflection from a sporadic *E* layer formed by the aurora and located at the midpoint of the path.

It is not unreasonable to assume that reflections from the aurora can occur at heights in excess of 100 km. It has been shown at Stanford<sup>20</sup> that reflection from auroral ionization at heights in excess of 300 km can be obtained. Auroras lying at greater heights would appear useful since perpendicular or nearly perpendicular reflection is not necessary for auroral communication as it is for the detection of radar echoes. However, increasing the height of reflection does not increase the region of propagation. Instead, the region is decreased greatly because the transmitted ray meets the earth's magnetic

<sup>18</sup> F. P. Tilton, "On the very highs," *QST*, vol. 28, pp. 42-43; 1944.

<sup>19</sup> "The world above 50 mc," *QST*, vol. 38, pp. 61-62; June, 1954.

<sup>20</sup> R. L. Leadabrand, "Radio Echoes from Auroral Ionization Detected at Relatively Low Geomagnetic Latitudes," Stanford Univ. Radio Propagation Lab., Stanford, Calif., Tech. Rep. 98; December, 1955.

field lines at more oblique angles. Thus, reasonable off-specular reflection at 300-km heights cannot explain the relatively infrequent auroral propagation between Anchorage and Point Barrow observed by Bailey, *et al.*, or the one case of propagation between College and Point Barrow observed by Dyce.

For transmitters at such locations as College and Goose Bay, specular reflection from auroral columns aligned with the earth's field lines at a height of 100 km does not even return a signal to the earth's surface. Thus, specular reflection at a lower height can explain this case, as can off-specular reflection at 100-km height.

It is well known that the appearance of sporadic *E* is associated with auroras.<sup>21-25</sup> In fact, Harang<sup>21</sup> has dem-

onstrated that sporadic-*E* ionization increases in intensity when auroras are present. Sporadic *E*, formed by auroras at the midpoint of the communication path, could explain the observed propagation. Although a search for such propagation between College and Point Barrow was unsuccessful,<sup>1</sup> the geometry described here is evidence against other modes of auroral propagation.

## VI. CONCLUSION

Auroral propagation at medium magnetic latitudes may be explained by specular reflection from small auroral columns aligned with the earth's magnetic field with reflection occurring at a height of 100 km. However, the long north-south paths in the vicinity of the auroral zone cannot be explained by this model. Instead, off-specular reflection much greater than  $7^\circ$  or heights of reflection in excess of 100 km are necessary to explain the experimental observations. For propagation between Goose Bay, Labrador, and Sondre Stromfjord, Greenland, and other auroral paths, an alternate explanation is possible. The observed propagation may be due to reflection from sporadic-*E* ionization formed at the midpoint of the path by auroras.

The probability of auroral communications has been investigated for one transmitter location (Anchorage)

<sup>21</sup> L. Harang and B. Landmark, "Radio echoes observed during auroral and geomagnetic storms using 35 and 74 mc/s waves simultaneously," *J. Atmos. Terr. Phys.*, vol. 4, pp. 332-338; January, 1954.

<sup>22</sup> J. P. Heppner, E. C. Byrne, and A. E. Belon, "The association of absorption and E ionization with aurora at high latitudes," *J. Geophys. Res.*, vol. 57, pp. 121-134; March, 1952.

<sup>23</sup> R. W. Knecht, "Relationship between aurora and sporadic-E echoes" (abstract), *IRE TRANS.*, vol. AP-3, p. 213; August, 1952.

<sup>24</sup> J. H. Meek, "Correlations of magnetic auroral and ionospheric variations at Saskatoon, parts I and II," *J. Geophys. Res.*, vol. 58, pp. 445-456; December, 1953, and vol. 59, pp. 89-92; March, 1954.

<sup>25</sup> J. H. Meek and A. G. McNamara, "Magnetic disturbances, sporadic-E and radio echoes associated with the aurora," *Can. J. Phys.*, vol. 32, pp. 326-329; 1954.





# A Statistical Model for Forward Scattering of Waves Off a Rough Surface\*

L. M. SPETNER†

**Summary**—Using methods of physical optics, a statistical description of the scattering of waves off a rough surface is obtained. The rough surface is assumed to consist of a large number of independent point scatterers which fluctuate randomly in vertical position and also disappear and appear at random. The surface is divided into cells so that no more than one scatterer can occupy a cell, and the events in any two different cells are independent of each other. The average scattered signal, the mean square fluctuation, and the time covariance of the fluctuating portion of the signal are computed in terms of the mean-square scatterer height, the grazing angle, the radiation wavelength, the decay time for disappearance of scatterers, the time autocorrelation of a scatterer height, and the *a priori* probability of finding a given cell occupied by a scatterer.

## INTRODUCTION

THE PROBLEM of the scattering of waves from a statistically rough surface has been attacked theoretically by many investigators.<sup>1-8</sup> The approach of the present paper is to assume a surface which consists of a large number of independent scatterers. This model was first proposed in connection with the forward-scattering of microwaves off the ocean surface by Goldstein and Goldmuntz.<sup>3</sup> Here we extend their model in that we assume a random disappearance and appearance of scatterers. We also take into account the possibility of an effective exclusion area around each scatterer by dividing the surface into cells, and then postulating that no more than one scatterer can exist in any one cell. On the basis of these and other assumptions as to the nature of the scatterers, we compute the time covariance of the fluctuating signal components, as well as the average scattered signal. It should be pointed out that while one would not necessarily expect every rough surface to behave as a collection of independent scatterers all the time, it is felt that the model used here may

be descriptive of the actual situation in many important cases, such as microwave scattering off a rough ocean surface. In this case the wave crests act like independent scatterers.

Methods of physical optics are used throughout; consequently, there is no possibility of obtaining any information as to the polarization of the wave in the case of electromagnetic propagation. We shall treat the problem of a point source transmitting to a point receiver in the vicinity of a rough surface.

## DESCRIPTION OF THE MODEL

We shall assume that the rough surface consists of independent point scatterers. The surface is divided into cells whose size is determined by the consideration that no more than one scatterer can occupy any one cell at any time.<sup>9</sup> This condition helps to take into account cases such as scattering off the ocean surface, where wave crests play the role of scatterers. In this case, the wave itself occupies a small area and it is not possible to have another independent wave closer than some exclusion radius which will be a function of the sea state. It is important to point out that the cell size is not arbitrary, but is provided with both an upper and a lower bound, by the sea-state conditions. Its upper bound is determined by the condition that no more than one scatterer can occupy the cell, while its lower bound is set by the condition that events in different cells must be statistically independent. It is expected that the size of the cells will be fixed by the sea state.

Scatterers are distributed among the cells in a statistical manner, and they may disappear and new ones may appear at random. Any single scatterer exhibits a random vertical motion, and we shall further assume that if a scatterer disappears and if later another one appears in the cell, the two will be uncorrelated.

The vertical motion of the scatterers corresponds, in the case of the ocean surface to the vertical wave motion, while the disappearance and appearance of scatterers correspond to the phenomenon of shadowing and to the abrupt and apparently erratic changes in shape of the ocean surface.

## THE FORWARD-SCATTERED SIGNAL

We shall attempt to describe statistically the signal received at a point from a point source of waves in the neighborhood of a rough surface of the type described by our model.

\* Manuscript received by the PGAP, April 6, 1957; revised manuscript received, August 21, 1957.

† Applied Physics Lab., The Johns Hopkins Univ., Silver Spring, Md.

<sup>1</sup> S. O. Rice, "Reflection of electromagnetic waves from slightly rough surfaces," *Commun. Pure and Appl. Math.*, vol. 4, pp. 351-378; August, 1951.

<sup>2</sup> M. A. Isakovich, "Scattering of waves from a statistically rough surface," *J. Exp. and Theor. Physics (USSR)*, vol. 23, pp. 305-314; September, 1952. (Translated from the Russian by R. N. Goss, U. S. Naval Electronics Lab., San Diego, Calif.)

<sup>3</sup> H. Goldstein and L. A. Goldmuntz, "Mean Square Signal Computation," Nuclear Dev. Corp. of Amer., NDA-18-2, August 18, 1952.

<sup>4</sup> W. S. Ament, "Toward a theory of reflection by a rough surface," *Proc. IRE*, vol. 41, pp. 142-146; January, 1953.

<sup>5</sup> J. Feinstein, "Some stochastic problems in wave propagation. Part I," *IRE TRANS.*, vol. AP-2, pp. 23-30; January, 1954.

<sup>6</sup> J. W. Miles, "On nonspecular reflection at a rough surface," *J. Acous. Soc. Amer.*, vol. 26, pp. 191-199; March, 1954.

<sup>7</sup> H. Davies, "The reflection of electromagnetic waves from a rough surface," *Proc. IEE (London)*, pt. IV, vol. 101, pp. 209-214; August, 1954.

<sup>8</sup> W. C. Hoffman, "Scattering of electromagnetic waves from a random surface," *Quart. Appl. Math.*, vol. 13, pp. 291-304; October, 1955.

<sup>9</sup> C. Klahr and H. Goldstein, "Statistics of One-Way Microwave Transmission Over a Rough Sea," Nuclear Dev. Corp. of Amer., NDA-52-2, November 23, 1955.

The geometry is shown in Fig. 1.  $P_n$  represents the scatterer in the  $n$ th cell (if a scatterer exists there). We shall assume that the average vertical positions of all scatterers lie in a plane and we shall choose this plane as the zero reference for our measurement of the vertical, or  $z$ , coordinate of each scatterer. Let  $v_n$  represent the component of the received signal that is scattered from  $P_n$ . Then if we neglect multiple scattering we may write

$$v_n = \frac{K\epsilon_n s_n F_0(\theta_{0n}, \psi_{0n}) F_1(\theta_{1n}, \psi_{1n})}{R_{0n} R_{1n}} \exp[ik(R_{0n} + R_{1n})] \quad (1)$$

where

- $K$  = a constant independent of  $n$ ,
- $\epsilon_n$  = a random variable which takes the value 1 when there is a scatterer in the  $n$ th cell and 0 when there is no scatterer in the  $n$ th cell,
- $s_n$  = the scattering length of  $P_n$ ,
- $F_0$  = the antenna pattern of the transmitter,
- $F_1$  = the antenna pattern of the receiver,
- $R_{0n}$  = the distance from the transmitter to  $P_n$ ,
- $R_{1n}$  = the distance from  $P_n$  to the receiver,
- $k = 2\pi$  divided by the wavelength of the radiation,
- $\theta_{0n}, \psi_{0n}, \theta_{1n}, \psi_{1n}$  = the angles shown in Fig. 1.

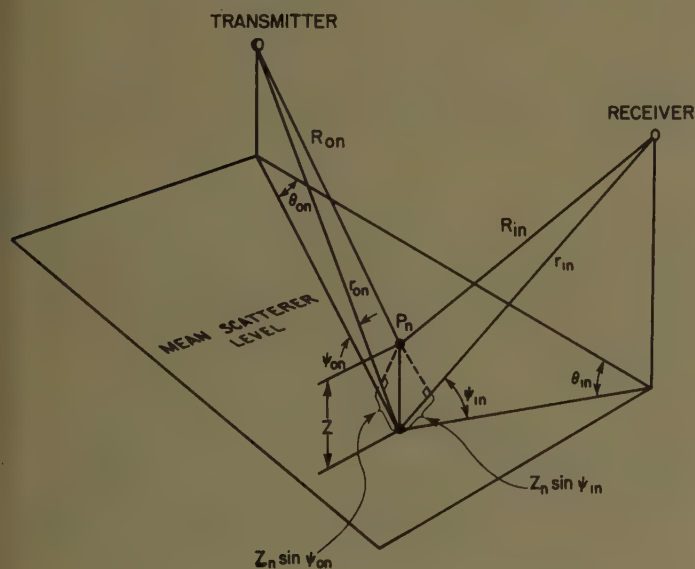


Fig. 1—The geometry of forward scattering.

From Fig. 1 we see that if we assume  $z_n \ll r_{0n} \sin \psi_{0n}$  and  $z_n \ll r_{1n} \sin \psi_{1n}$ , that

$$R_{0n} = r_{0n} - z_n \sin \psi_{0n}$$

$$R_{1n} = r_{1n} - z_n \sin \psi_{1n}$$

where  $r_{0n}$  and  $r_{1n}$  are, respectively, the distances from the transmitter and receiver to the projection of  $P_n$  on the mean scatterer plane. Then (1) can be written as

$$v_n = \frac{K\epsilon_n s_n F_0 F_1}{r_{0n} r_{1n}} \exp[ik(r_{0n} + r_{1n})] \cdot \exp[-ikz_n(\sin \psi_{0n} + \sin \psi_{1n})]. \quad (2)$$

If we let

$$a_n = (r_{0n} r_{1n})^{-1} K F_0(\theta_{0n}, \psi_{0n}) F_1(\theta_{1n}, \psi_{1n}) \quad (3)$$

and

$$\phi_n = kz_n(\sin \psi_{0n} + \sin \psi_{1n}), \quad (4)$$

then (2) may be rewritten as

$$v_n = \epsilon_n s_n a_n \exp[ik(r_{0n} + r_{1n})] \exp(-i\phi_n). \quad (5)$$

This expression for  $v_n$  shows that it is random since  $\epsilon_n$ ,  $s_n$ , and  $\phi_n$  are random. The statistics of  $v_n$  will depend, in general, upon the statistics of these quantities.

We may now sum over all cells and obtain the scattered signal as seen at the receiver

$$V = \sum_{n=1}^N v_n = \sum_{n=1}^N \epsilon_n s_n a_n \exp[ik(r_{0n} + r_{1n})] \exp(-i\phi_n) \quad (6)$$

where  $N$  = the total number of cells. If we assume that  $N$  is sufficiently large, if all  $v_n$ 's are identically distributed, and if the variances of the  $v_n$ 's are finite, then we may invoke the Central Limit Theorem to tell us that the real and imaginary parts of  $V$  are jointly Gaussian.<sup>10</sup> From (6) we obtain

$$V = V_x + iV_y = \sum_{n=1}^N \epsilon_n a_n s_n [\cos \phi_n \cos k(r_{0n} + r_{1n}) + \sin \phi_n \sin k(r_{0n} + r_{1n})] + i \sum_{n=1}^N \epsilon_n a_n s_n [\cos \phi_n \sin k(r_{0n} + r_{1n}) - \sin \phi_n \cos k(r_{0n} + r_{1n})]. \quad (7)$$

Eq. (7) then gives the real and imaginary parts of the signal scattered to the point receiver by the rough surface. (This excludes any signal which travels directly from the transmitter to the receiver.) It consists of a sum of the contributions from the scatterers located in the  $N$  cells into which the surface is divided.

#### THE AVERAGE FORWARD-SCATTERED SIGNAL

The first statistical parameter of  $V$  which we shall compute will be its average. We shall assume that for each cell  $n$ , the random quantities  $\epsilon_n$ ,  $s_n$ , and  $\phi_n$  (which depends upon  $z_n$ ) are statistically independent. Then from (6) we have

$$\langle V \rangle = \sum_{n=1}^N \langle \epsilon_n \rangle \langle s_n \rangle a_n \exp[ik(r_{0n} + r_{1n})] \langle \exp(-i\phi_n) \rangle. \quad (8)$$

Using (4) we see that  $\langle \exp(-i\phi_n) \rangle$  is just the characteristic function of the probability density of  $z_n$ . If we let the probability that  $\epsilon_n = 1$  be  $p_n$ ; i.e.,

$$P\{\epsilon_n = 1\} = p_n \quad (9a)$$

$$P\{\epsilon_n = 0\} = 1 - p_n \quad (9b)$$

<sup>10</sup> S. O. Rice, "Mathematical analysis of random noise," *Bell Sys. Tech. J.*, vol. 23, pp. 282-332; July, 1944. In particular see sec. 2.10, pp. 331-332.



then we find that

$$\langle \epsilon_n \rangle = p_n. \quad (10)$$

Let us further assume that  $z_n$  is identically distributed for all  $n$ .

We shall convert the summation of (8) to an integration. Let  $\Delta$  represent the area of a cell, then (8) becomes

$$\langle V \rangle = \iint p \Delta^{-1} \langle s \rangle a \exp [ik(r_0 + r_1)] \langle e^{-i\phi} \rangle dx dy.$$

If we replace the product  $p \Delta^{-1}$  with the symbol  $q(x, y)$ , then we may write

$$\langle V \rangle = \iint \langle s \rangle q(x, y) a(x, y) \exp [ik(r_0 + r_1)] \langle e^{-i\phi} \rangle dx dy. \quad (11)$$

The quantity  $q(x, y)$  will depend upon cell size, and it is expected that it will have a finite limit as  $\Delta \rightarrow 0$ , in that it represents the probability per unit area that a scatterer exists. It will be pointed out later that under these conditions, in the limit as  $\Delta \rightarrow 0$ , we arrive at a Poisson distribution for the total number of scatterers.

At this point, for the sake of definiteness we shall assume that the scatterer height  $z$  is Gaussian distributed. Then using (4), we have

$$\langle e^{-i\phi} \rangle = \exp \left[ -\frac{1}{2} h^2 k^2 (\sin \psi_0 + \sin \psi_1)^2 \right], \quad (12)$$

where  $h$  is the rms scatterer height. Then (11) becomes

$$\langle V \rangle = \iint \langle s \rangle q a \exp [ik(r_0 + r_1)] \cdot \exp \left[ -\frac{1}{2} h^2 k^2 (\sin \psi_0 + \sin \psi_1)^2 \right] dx dy. \quad (13)$$

It will be instructive to let  $h \rightarrow 0$  in (13) and examine the case of the smooth surface. Since in general one might expect  $\langle s \rangle$  and  $q(x, y)$  to depend upon  $h$ , let us explicitly write their smooth-surface values as

$$\lim_{h \rightarrow 0} \langle s \rangle q(x, y) = \langle s \rangle_0 q_0(x, y).^{11}$$

Then

$$\langle V \rangle_{\text{smooth}} = \iint \langle s \rangle_0 q_0(x, y) a(x, y) \cdot \exp [ik(r_0 + r_1)] dx dy. \quad (14)$$

For smooth surfaces it is customary to describe the reflected signal by the product of a reflection coefficient and the incident field. If we let the incident field be denoted by  $E_0$ , the complex reflection coefficient by  $r$ , and the path length from transmitter to receiver, via the point of specular reflection, by  $R_s$ , then one may write

$$\langle V \rangle_{\text{smooth}} = r E_0 \exp (ik R_s). \quad (15)$$

It can be demonstrated easily that this form for  $\langle V \rangle_{\text{smooth}}$  is correct since the integral of (14) upon being evaluated by the method of stationary phase will result in a contribution only from the neighborhood of the

stationary phase point; *i.e.*, the point of specular reflection.

Now the expression for  $\langle V \rangle$  in (13) can be related to the smooth-surface expression of (15) in the following way. Both the integral of (13) and that of (14) may be evaluated by the method of stationary phase, and both have the same stationary phase point. The only difference between the two integrals lies in the slowly varying parts of their integrands. Hence we may write

$$\langle V \rangle = r E_0 \exp (ik R_s) \frac{\langle s \rangle q}{\langle s \rangle_0 q_0} \exp [-2h^2 k^2 \sin^2 \psi] \quad (16)$$

where the  $q$ 's and  $\langle s \rangle$ 's are understood to be evaluated at the specular point, and  $\psi$  is the grazing angle at the specular point. Note that the last factor of (16) is the same as Ament's reflection coefficient for a rough surface<sup>4</sup> which he gives in his (19). The difference between his reflection coefficient and ours is that we have an additional factor of  $r \langle s \rangle q / \langle s \rangle_0 q_0$ . Without a knowledge of the dependence of this factor upon sea state and geometry it is difficult to choose between the two expressions for the case of the ocean. It may well be, however, that it is just this factor which is responsible for the points of Fig. 2 of Beard, Katz, and Spetner<sup>12</sup> falling above the curve.

#### SIGNAL FLUCTUATION

The fluctuating portions of the real and imaginary parts of the scattered signal  $V$  are given respectively by

$$X = V_x - \langle V_x \rangle \quad (17a)$$

$$Y = V_y - \langle V_y \rangle. \quad (17b)$$

Since  $X$  and  $Y$  are jointly Gaussian, their joint probability distribution is completely determined if one knows the quadratic averages  $\langle X^2 \rangle$ ,  $\langle Y^2 \rangle$ , and  $\langle XY \rangle$ . Furthermore, the time fluctuations of the signal are determined by the covariances

$$\langle X(t)X(t+\tau) \rangle, \langle Y(t)Y(t+\tau) \rangle, \text{ and } \langle X(t)Y(t+\tau) \rangle.$$

Since  $\langle X^2 \rangle$  is just  $\langle X(t)X(t+\tau) \rangle$  for  $\tau=0$ , and similarly for the others, we shall compute expressions for the above three covariances as functions of  $\tau$ .

If we let

$$G(\tau) = \langle V(t)V^*(t+\tau) \rangle - |\langle V \rangle|^2 \quad (18)$$

and

$$H(\tau) = \langle V(t)V(t+\tau) \rangle - \langle V \rangle^2, \quad (19)$$

then we have

$$\langle X(t)X(t+\tau) \rangle = \frac{1}{2} \text{Re} [G(\tau) + H(\tau)] \quad (20a)$$

$$\langle Y(t)Y(t+\tau) \rangle = \frac{1}{2} \text{Re} [G(\tau) - H(\tau)] \quad (20b)$$

$$\langle X(t)Y(t+\tau) \rangle = \frac{1}{2} \text{Im} [-G(\tau) + H(\tau)] \quad (20c)$$

$$\langle Y(t)X(t+\tau) \rangle = \frac{1}{2} \text{Im} [G(\tau) + H(\tau)]. \quad (20d)$$

<sup>11</sup> Goldstein and Goldmuntz, *op. cit.* This limiting value was discussed for the case of the ocean surface.

<sup>12</sup> C. I. Beard, I. Katz, and L. M. Spetner, "Phenomenological vector model of microwave reflection from the ocean." IRE TRANS., vol. AP-4, pp. 162-167; April, 1956.

Using (6) we can compute  $G(\tau)$  and  $H(\tau)$ . Thus

$$G(\tau) = \sum_{n=1}^N \sum_{m=1}^N a_n a_m \langle \epsilon_n(t) \epsilon_m(t+\tau) \rangle \langle s_n(t) s_m^*(t+\tau) \rangle \\ \cdot \exp [ik(r_{0n} + r_{1n} - r_{0m} - r_{1m})] \\ \cdot \langle \exp i[-\phi_n(t) + \phi_m(t+\tau)] \rangle - |\langle V \rangle|^2.$$

Now according to our model, distinct scatterers are statistically independent. Hence

$$G(\tau) = \sum_{n \pm m} a_n a_m \langle \epsilon_n \rangle \langle \epsilon_m \rangle \langle s_n \rangle \langle s_m^* \rangle \\ \cdot \exp [ik(r_{0n} + r_{1n} - r_{0m} - r_{1m})] \\ \cdot \langle \exp (-i\phi_n) \rangle \langle \exp (i\phi_m) \rangle \\ + \sum_{n=1}^N a_n^2 \langle \epsilon_n(t) \epsilon_n(t+\tau) \rangle \langle s_n(t) s_n^*(t+\tau) \rangle \\ \cdot \langle \exp i[-\phi_n(t) + \phi_n(t+\tau)] \rangle - |\langle V \rangle|^2 \\ = |\langle V \rangle|^2 - \sum_{n=1}^N a_n^2 \langle \epsilon_n \rangle^2 |\langle s_n \rangle|^2 |\langle \exp (-i\phi_n) \rangle|^2 \\ + \sum_{n=1}^N a_n^2 \langle \epsilon_n(t) \epsilon_n(t+\tau) \rangle \langle s_n(t) s_n^*(t+\tau) \rangle \\ \cdot \langle \exp i[-\phi_n(t) + \phi_n(t+\tau)] \rangle - |\langle V \rangle|^2 \\ = \sum_{n=1}^N a_n^2 \{ \langle \epsilon_n(t) \epsilon_n(t+\tau) \rangle \langle s_n(t) s_n^*(t+\tau) \rangle \\ \cdot \langle \exp i[-\phi_n(t) + \phi_n(t+\tau)] \rangle \\ - \langle \epsilon_n \rangle^2 |\langle s_n \rangle|^2 |\langle \exp (-i\phi_n) \rangle|^2 \}. \quad (21a)$$

Similarly we find

$$H(\tau) = \sum_{n=1}^N a_n^2 \exp [i2k(r_{0n} + r_{1n})] \{ \langle \epsilon_n(t) \epsilon_n(t+\tau) \rangle \\ \cdot \langle s_n(t) s_n(t+\tau) \rangle \langle \exp i[-\phi_n(t) - \phi_n(t+\tau)] \rangle \\ - \langle \epsilon_n \rangle^2 \langle s_n \rangle^2 \langle \exp (-i\phi_n) \rangle^2 \}. \quad (21b)$$

From the definition of  $\epsilon_n$  we see that  $\langle \epsilon_n(t) \epsilon_n(t+\tau) \rangle$  is just equal to the joint probability that a scatterer exists in the  $n$ th cell both at time  $t$  and at time  $t+\tau$ . This can be expressed as the sum of the probabilities of the following two mutually exclusive cases:

- 1) The scatterer which existed at  $t$  did not disappear and continued to exist at  $t+\tau$ .
- 2) The scatterer which existed at  $t$  disappeared before  $t+\tau$  and a different scatterer exists at  $t+\tau$ .

We shall define the following conditional probabilities.

Let  $A_n(t)$  be the probability that a scatterer exists in the  $n$ th cell at time  $t$  assuming it existed at  $t=0$  and did not disappear in the meantime.

Let  $B_n(t)$  be the probability that a scatterer exists in the  $n$ th cell at time  $t$  assuming one existed at  $t=0$ , but disappeared in the meantime.

Then using the assumption that a scatterer in the  $n$ th cell at  $t$  is statistically independent of a scatterer in the same cell at  $t+\tau$  if there has been at least one disap-

pearance in the interval between  $t$  and  $t+\tau$ , and using (10) we obtain

$$G(\tau) = \sum_{n=1}^N a_n^2 \{ p_n A_n(\tau) \langle s_n(t) s_n^*(t+\tau) \rangle \\ \cdot \langle \exp i[-\phi_n(t) + \phi_n(t+\tau)] \rangle \\ + [p_n B_n(\tau) - p_n^2] |\langle s_n \rangle|^2 |\langle \exp (-i\phi_n) \rangle|^2 \} \quad (22a)$$

and

$$H(\tau) = \sum_{n=1}^N a_n^2 \exp [i2k(r_{0n} + r_{1n})] \{ p_n A_n(\tau) \langle s_n(t) s_n(t+\tau) \rangle \\ \cdot \langle \exp i[-\phi_n(t) - \phi_n(t+\tau)] \rangle \\ + [p_n B_n(\tau) - p_n^2] \langle s_n \rangle^2 \langle \exp (-i\phi_n) \rangle^2 \}. \quad (22b)$$

If we specify the statistics of the appearance and disappearance of scatterers in a single cell, we shall be able to compute  $A_n(t)$  and  $B_n(t)$ . For convenience let us drop the subscript  $n$ . We define the parameters  $\beta$  and  $\gamma$  as follows:

$\beta dt$  is the probability that a scatterer appears in the cell during the interval between  $t$  and  $t+dt$ , on the condition that there was no scatterer in the cell at time  $t$ .

$\gamma dt$  is the probability that a scatterer disappears from the cell during the interval between  $t$  and  $t+dt$ , on the condition that a scatterer existed in the cell at time  $t$ .

In taking  $\beta$  and  $\gamma$  to be constants we are assuming that the probabilities per unit time of the appearance and disappearance of scatterers are uniform. It seems reasonable that  $\beta$  should be a monotonic function of the cell size and in the limit of vanishingly small cell size  $\beta$  should be proportional to the cell area. It is felt that  $\gamma$ , however, should be independent of the cell size.

We can now find  $A(t)$  by noting that for small  $dt$ ,  $A(t)$  satisfies the following:

$$A(t+dt) = A(t)(1 - \gamma dt).$$

Hence we have the differential equation,

$$\frac{dA}{dt} = -\gamma A.$$

Using the condition that  $A(0)=1$ , we have

$$A(t) = e^{-\gamma t}. \quad (23)$$

In order to find  $B(t)$  we first define  $C(t)$  as the probability that a scatterer exists in the cell at  $t$ , assuming that there was none at time 0. Then, clearly

$$B(t) = \int_0^t \gamma A(\tau) C(t-\tau) d\tau, \quad (24)$$

where  $A(\tau)\gamma d\tau$  represents the probability that the scatterer which existed at time 0, disappears in the interval between  $\tau$  and  $\tau+d\tau$ . In order to evaluate the integral of (24) we must first find  $C(t)$ . To do this we note that for sufficiently small  $dt$ ,

$$C(t+dt) = C(t)(1 - \gamma dt) + [1 - C(t)]\beta dt.$$



This leads to the differential equation,

$$\frac{dC}{dt} + (\beta + \gamma)C - \beta = 0.$$

Using the condition that  $C(0) = 0$ , we find that

$$C(t) = \frac{\beta}{\beta + \gamma} [1 - e^{-(\beta + \gamma)t}].$$

Inserting this and the expression for  $A(t)$  in (23) into the integral of (24) we obtain

$$B(t) = \int_0^t \gamma e^{-\gamma\tau} \frac{\beta}{\beta + \gamma} [1 - e^{-(\beta + \gamma)(t - \tau)}] d\tau.$$

Hence, we find that

$$B(t) = \frac{1}{\beta + \gamma} [\beta - (\beta + \gamma)e^{-\gamma t} + \gamma e^{-(\beta + \gamma)t}]. \quad (25)$$

We can also express  $p_n$ , the *a priori* probability of finding a scatterer in the  $n$ th cell, in terms of  $\gamma_n$  and  $\beta_n$  by noting that it should equal the steady-state value of  $B_n(t)$  or  $C_n(t)$ , that is (again dropping the subscript  $n$ ),

$$p = \lim_{t \rightarrow \infty} B(t) = \lim_{t \rightarrow \infty} C(t).$$

Hence

$$p = \frac{\beta}{\beta + \gamma}, \quad (26)$$

or

$$\beta = \gamma \frac{p}{1 - p}. \quad (27)$$

Then (22) becomes

$$\begin{aligned} G(\tau) &= \sum_{n=1}^N a_n^2 p_n \exp(-\gamma_n \tau) \\ &\cdot \left\{ \langle s_n(t) s_n^*(t + \tau) \rangle \langle \exp i[-\phi_n(t) + \phi_n(t + \tau)] \rangle \right. \\ &+ \left[ (1 - p_n) \exp\left(\frac{-p_n \gamma_n \tau}{1 - p_n}\right) - 1 \right] |\langle s_n \rangle|^2 \\ &\cdot |\langle \exp(-i\phi_n) \rangle|^2 \Big\} \end{aligned}$$

and

$$\begin{aligned} H(\tau) &= \sum_{n=1}^N a_n^2 \exp[i2k(r_{0n} + r_{1n})] p_n \exp(-\gamma_n \tau) \\ &\cdot \left\{ \langle s_n(t) s_n(t + \tau) \rangle \langle \exp i[-\phi_n(t) - \phi_n(t + \tau)] \rangle \right. \\ &+ \left[ (1 - p_n) \exp\left(\frac{-p_n \gamma_n \tau}{1 - p_n}\right) - 1 \right] \langle s_n \rangle^2 \\ &\cdot \langle \exp(-i\phi_n) \rangle^2 \Big\}. \end{aligned}$$

We shall now convert the above summations over

cells to integrations over the surface area. We shall drop the subscripts and replace the  $n$  dependence with a dependence on  $(x, y)$ , the position coordinates on the surface. If we let  $\Delta$  represent the area of a cell, then for small enough cell size we may write

$$\begin{aligned} G(\tau) &= \iint a^2 p \Delta^{-1} e^{-\gamma\tau} \\ &\cdot \left\{ \langle s(t) s^*(t + \tau) \rangle \langle \exp i[-\phi(t) + \phi(t + \tau)] \rangle \right. \\ &+ \left[ (1 - p) \exp\left(\frac{-p\gamma\tau}{1 - p}\right) - 1 \right] |\langle s \rangle|^2 \\ &\cdot |\langle e^{-i\phi} \rangle|^2 \Big\} dxdy \quad (28) \end{aligned}$$

and

$$\begin{aligned} H(\tau) &= \iint a^2 p \Delta^{-1} e^{-\gamma\tau} \exp[i2k(r_0 + r_1)] \\ &\cdot \left\{ \langle s(t) s(t + \tau) \rangle \langle \exp i[-\phi(t) - \phi(t + \tau)] \rangle \right. \\ &+ \left[ (1 - p) \exp\left(\frac{-p\gamma\tau}{1 - p}\right) - 1 \right] \langle s \rangle^2 \\ &\cdot \langle e^{-i\phi} \rangle^2 \Big\} dxdy. \quad (29) \end{aligned}$$

The average values  $\langle e^{-i\phi} \rangle$  and

$$\langle \exp i[-\phi(t) \pm \phi(t + \tau)] \rangle$$

can be computed on the assumption that  $z(t)$  and  $z(t + \tau)$  are jointly Gaussian with correlation coefficient  $\rho(\tau)$ . We first note that

$$\begin{aligned} \langle \exp i[-\phi(t) \pm \phi(t + \tau)] \rangle &= \langle \cos[-\phi(t) \pm \phi(t + \tau)] \rangle + i \langle \sin[-\phi(t) \pm \phi(t + \tau)] \rangle \\ &= \langle \cos \phi(t) \cos \phi(t + \tau) \rangle \pm \langle \sin \phi(t) \sin \phi(t + \tau) \rangle \\ &\quad - i \langle \sin \phi(t) \cos \phi(t + \tau) \rangle \pm i \langle \cos \phi(t) \sin \phi(t + \tau) \rangle. \end{aligned}$$

Using (4) and assuming the joint probability of  $z(t)$  and  $z(t + \tau)$  is given by

$$\begin{aligned} p[z(t), z(t + \tau)] &= \frac{1}{2\pi h^2 \sqrt{1 - \rho^2(\tau)}} \\ &\cdot \exp \left\{ \frac{z^2(t) + z^2(t + \tau) - 2\rho(\tau)z(t)z(t + \tau)}{-2h^2[1 - \rho^2(\tau)]} \right\} \end{aligned}$$

we find that

$$\begin{aligned} \langle \cos \phi(t) \cos \phi(t + \tau) \rangle &= \exp[-k^2 h^2 (\sin \psi_0 + \sin \psi_1)^2] \\ &\quad \cdot \cosh[\rho k^2 h^2 (\sin \psi_0 + \sin \psi_1)^2] \\ \langle \sin \phi(t) \sin \phi(t + \tau) \rangle &= \exp[-k^2 h^2 (\sin \psi_0 + \sin \psi_1)^2] \\ &\quad \cdot \sinh[\rho k^2 h^2 (\sin \psi_0 + \sin \psi_1)^2] \\ \langle \sin \phi(t) \cos \phi(t + \tau) \rangle &= 0 \\ \langle \cos \phi(t) \sin \phi(t + \tau) \rangle &= 0. \end{aligned}$$

Hence

$$\langle \exp i[-\phi(t) \pm \phi(t + \tau)] \rangle = \exp [-k^2 h^2 (1 \mp \rho) (\sin \psi_0 + \sin \psi_1)^2]. \quad (30)$$

Again using the assumption that  $z$  is Gaussian distributed we have

$$\langle e^{-i\phi} \rangle = \exp [-\frac{1}{2} k^2 h^2 (\sin \psi_0 + \sin \psi_1)^2]. \quad (31)$$

Then using (30) and (31), (28) and (29) become

$$\begin{aligned} G(\tau) = & \iint a^2 p \Delta^{-1} e^{-\gamma \tau} \left\{ \langle s(t) s^*(t + \tau) \rangle \right. \\ & \cdot \exp [-k^2 h^2 (1 - \rho) (\sin \psi_0 + \sin \psi_1)^2] \\ & + \left[ (1 - p) \exp \left( \frac{-p \gamma \tau}{1 - p} \right) - 1 \right] \langle s \rangle^2 \\ & \cdot \exp [-k^2 h^2 (\sin \psi_0 + \sin \psi_1)^2] \Big\} dx dy \end{aligned} \quad (32)$$

and

$$\begin{aligned} H(\tau) = & \iint a^2 p \Delta^{-1} e^{-\gamma \tau} \exp [i 2 k (r_0 + r_1)] \\ & \cdot \left\{ \langle s(t) s(t + \tau) \rangle \exp [-k^2 h^2 (1 + \rho) (\sin \psi_0 + \sin \psi_1)^2] \right. \\ & + \left[ (1 - p) \exp \left( \frac{-p \gamma \tau}{1 - p} \right) - 1 \right] \langle s \rangle^2 \\ & \cdot \exp [-k^2 h^2 (\sin \psi_0 + \sin \psi_1)^2] \Big\} dx dy. \end{aligned} \quad (33)$$

We note that the absolute value of the integrand of  $H(\tau)$  is always smaller than that of  $G(\tau)$ . Furthermore the integrand of  $H(\tau)$  contains the sinusoidally varying term  $\exp [i 2 k (r_0 + r_1)]$ . If we assume a geometry such that the integrand of  $G(\tau)$  is slowly varying over many Fresnel zones, which are defined by the  $\exp [i 2 k (r_0 + r_1)]$  term, then it is easily seen that  $|H(\tau)| \ll |G(\tau)|$ . In fact the upper limit of  $|H(\tau)| / |G(\tau)|$  is smaller than  $1/n$  where  $n$  is the number of Fresnel zones over which there is a significant contribution to the integral  $G(\tau)$ . For reasonable geometries, in the case of microwave scattering off the ocean surface,  $n$  can be of the order of 10 or 100. In what follows we shall make the approximation that  $H(\tau)$  is negligible. Hence using (20) we write

$$\langle X(t) X(t + \tau) \rangle \approx \langle Y(t) Y(t + \tau) \rangle \approx \frac{1}{2} \text{Re } G(\tau) \quad (34a)$$

$$\langle Y(t) X(t + \tau) \rangle \approx -\langle X(t) Y(t + \tau) \rangle \approx \frac{1}{2} \text{Im } G(\tau). \quad (34b)$$

If the scattering length  $s$  is real, then  $\text{Im } G(\tau) = 0$ .

The average power of the fluctuation is the sum of the variances of  $X$  and  $Y$ , or just  $G(0)$ .

$$\begin{aligned} G(0) = & \iint a^2 p \Delta^{-1} \{ \langle |s|^2 \rangle - p \langle s \rangle^2 \} \\ & \cdot \exp [-k^2 h^2 (\sin \psi_0 + \sin \psi_1)^2] dx dy. \end{aligned} \quad (35)$$

Eqs. (32) and (35) indicate that the variances and covariances of the fluctuating portion of the signal depend upon the value of  $p$ . It is instructive to examine  $G(0)$  and  $G(\tau)$  for the two limiting cases of  $p=0$ , and  $p=1$ .

#### Case I: Zero Cell Size

For vanishingly small cell size, *i.e.*, in the limit as  $\Delta \rightarrow 0$ , the *a priori* probability,  $p$ , that a scatterer exists in a given cell vanishes. If, in the limit of small  $\Delta$ ,  $\beta$  is proportional to  $\Delta$ , then (26) shows that  $p$  is also. Then the product  $p \Delta^{-1}$  will approach a finite limit which we shall call  $q$ .

The total number of cells  $N$  will approach infinity, while the product  $(Np)$ , which represents the average number of scatterers on the surface, approaches a finite limit. It is easy to show that the probability that  $\alpha$  scatterers exist at any time is Poisson distributed. Clearly the number of scatterers that exist is given by

$$\sum_{n=1}^N \epsilon_n.$$

The probability that this is equal to  $\alpha$  is just the probability that exactly  $\alpha$  of the  $\epsilon_n$ 's are equal to one, and the rest zero. If we further assume that  $p_n$ , the probability that  $\epsilon_n$  is unity, is independent of  $n$ , *i.e.*,  $p_n = p$  for all  $n$ , then we have

$$P(\alpha) = \binom{N}{\alpha} p^\alpha,$$

or in the limit as  $N \rightarrow \infty$ ,

$$P(\alpha) = \frac{(Np)^\alpha}{\alpha!}. \quad (36)$$

Hence, a vanishingly small cell size requires, under our assumptions, that the distribution of the number of scatterers on the surface be Poisson.

Let us now write the variance and time covariance of the signal components. These are determined by  $G(0)$  and  $G(\tau)$ , respectively. Letting  $p \rightarrow 0$  and  $p \Delta^{-1} \rightarrow q$  in (32) and (35), we obtain

$$\begin{aligned} G(\tau) = & \iint a^2 q e^{-\gamma \tau} \exp [-k^2 h^2 (1 - \rho) (\sin \psi_0 + \sin \psi_1)^2] \\ & \cdot \langle s(t) s^*(t + \tau) \rangle dx dy \end{aligned} \quad (37)$$

and

$$G(0) = \iint a^2 q \langle |s|^2 \rangle dx dy. \quad (38)$$

Note that the average power of the fluctuation, which is given by  $G(0)$  has no explicit dependence on the surface roughness, except insofar as  $\langle |s|^2 \rangle$  and  $q$  may themselves depend upon such roughness. The  $\tau$  dependence of  $G(\tau)$ , which is just the Fourier transform of the power frequency spectrum, can be expressed more simply than (37) if we assume that the contribution to the scattered



energy comes mainly from the region of the surface near the specular point. Then if we let  $\psi$  be the grazing angle at the specular point,

$$G(\tau) = C e^{-\gamma\tau} e^{-4k^2 h^2 \sin^2 \psi [1-\rho(\tau)]} \langle s(t) s^*(t+\tau) \rangle \quad (39)$$

where  $C$  is a constant of proportionality that does not depend on  $\tau$ .

### Case II: Nonvanishing Scatterers

The other extreme is that where  $p=1$ . From (26) we see that if  $p=1$ , then perforce  $\gamma=0$ . This situation refers to a surface which consists of fixed scatterers, one in each cell. These scatterers may fluctuate in height but they do not disappear and new ones do not appear.

Setting  $p=1$  and  $\gamma=0$  in (32) and (35) we obtain

$$G(\tau) = \int \int a^2 \Delta^{-1} \exp [-k^2 h^2 (1-\rho)(\sin \psi_0 + \sin \psi_1)^2] \cdot \langle s(t) s^*(t+\tau) \rangle - \exp [-k^2 h^2 \rho (\sin \psi_0 + \sin \psi_1)^2] | \langle s \rangle |^2 dx dy \quad (40)$$

and

$$G(0) = \int \int a^2 \Delta^{-1} \{ | \langle s \rangle |^2 - | \langle s \rangle |^2 \} \exp [-k^2 h^2 (\sin \psi_0 + \sin \psi_1)^2] dx dy. \quad (41)$$

We notice that in this case the average power of the fluctuation,  $G(0)$ , depends explicitly on the mean square scatterer height,  $h^2$ . If we assume a nonfluctuating scattering length and again assume that the major contribution to the scattered energy comes from the neighborhood of the specular point, then we may write approximately

$$G(0) \approx C [1 - e^{-4k^2 h^2 \sin^2 \psi}]. \quad (42)$$

Similarly, the  $\tau$  dependence of  $G(\tau)$  can be written as

$$G(\tau) = C' [e^{4k^2 h^2 \rho(\tau) \sin^2 \psi} - 1] \quad (43)$$

where  $C'$  is independent of  $\tau$ .

The above two cases represent the two limiting values of  $p$ , namely 0 and 1. The actual value of  $p$  will likely depend upon the size of the cell: the larger the cell, the larger  $p$ . We must remember that the size of the cell is not the result of an arbitrary construction but is determined by the nature of the surface. The cells must be small enough so that no more than one scatterer can occupy each, and they must be large enough so that events in separate cells are independent.

### CONCLUSION

The signal received at a point from a source which transmits waves in the vicinity of a fluctuating rough surface can be divided into the directly transmitted signal and a scattered one. The random surface will impart some of its randomness to the scattered signal which will add vectorially to the direct ray. Fig. 2 shows the various components of the received signal.  $D$  represents the

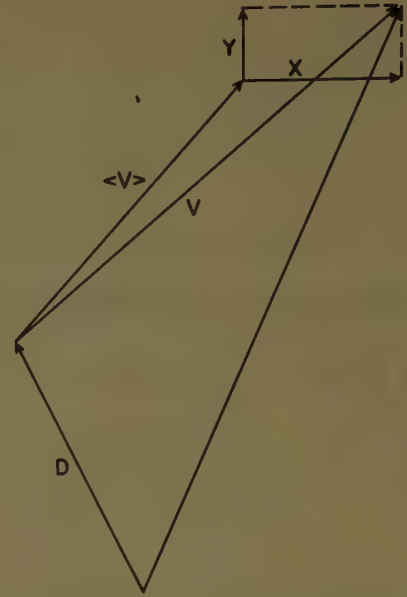


Fig. 2—Vector diagram of forward-scattered signal.

direct ray while  $V$  represents the scattered component. We see that  $V$  is the vector sum

$$V = \langle V \rangle + X + Y.$$

The average value  $\langle V \rangle$  is given by (16).  $X$  and  $Y$  are Gaussian. Their time covariances are given by

$$\langle X(t) X(t+\tau) \rangle = \langle Y(t) Y(t+\tau) \rangle = \frac{1}{2} \text{Re } G(\tau)$$

and

$$\langle Y(t) X(t+\tau) \rangle = - \langle X(t) Y(t+\tau) \rangle = \frac{1}{2} \text{Im } G(\tau).$$

For  $\tau=0$ , these take the forms

$$\langle X^2 \rangle = \langle Y^2 \rangle = \frac{1}{2} \text{Re } G(0).$$

$$\langle XY \rangle = 0.$$

$G(\tau)$  is given by (32). The above information provides a complete statistical description of these random quantities.

This description of the received signal closely parallels the description used by Beard, Katz, and Spetner<sup>12</sup> and encouragingly enough some of their experimental results on the measurement of the "coherent term" and "incoherent term" correspond to the predictions of our model for  $\langle V \rangle$  and  $\langle X^2 \rangle + \langle Y^2 \rangle$ , respectively. Also the work of Beard and Katz<sup>13</sup> shows a favorable comparison between our expressions for the time covariance and the measurements of signal spectra.

### ACKNOWLEDGMENT

More than a mere acknowledgment is due to Dr. Herbert Goldstein who not only suggested some of the approaches in this paper but also spent a considerable amount of his time reading the manuscript and offering constructive comments.

<sup>13</sup> C. I. Beard and I. Katz, "The dependence of microwave radio signal spectra on ocean roughness and wave spectra," IRE TRANS., vol. AP-5, pp. 183-191; April, 1957.

# A Method for Evaluating Antennas\*

JUDD BLASS†

**Summary**—An ideal figure of merit for a communications antenna is derived. This figure of merit is a measure of the time required to transmit a given message to an isotropic receiving antenna from a transmitter which uses the antenna under evaluation.

## I. INTRODUCTION

THE evaluation of a communications antenna should be based on the function of the antenna in the communication system. Since all communication systems have the common function of transmitting information from one point to another, the antennas, which are the connecting information chain, must quantitatively effect this transmission of information.

Fig. 1 illustrates the two basic elements of a communication system. The information introduced into the system at the transmitter is  $N_{in}$ ; and the information at the output of the transcriber is  $N_{out}$ . One practical measure of the communication system performance is the ratio of the output information to the input information in a given time. If this ratio ( $N_{out}/N_{in}$ ) is equal to unity, the system is perfect. If, however,  $N_{out}/N_{in} = 0$ , the system is obviously useless.

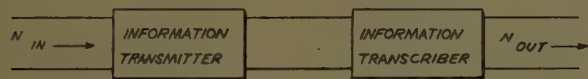


Fig. 1—Communication chain.

This ratio may also be derived from the rate at which the information is processed so that with a perfect transmitter, if  $C_T$  is the rate at which the information is introduced, and  $C_t$  is the rate at which it is transcribed, then  $N_{out}/N_{in} = C_t/C_T$ . Related to this figure of merit is the average time it takes to transmit a given amount of information through a given transcriber within a given limit of error.

The type of systems, in which most commercial antennas are linked, are those which utilize a single transmitter which transmits equally well to many transcribers. The two considerations of the previous paragraph, *i.e.*, information rate or information time, can be applied to this type of system as well. In the first case, the average ratio of output information to input information would be the figure of merit of the system,<sup>1</sup> *i.e.*,

$$\eta = \left( \frac{N_{out}}{N_{in}} \right) = \frac{1}{M} \sum_{i=1}^M \frac{C_{ti}}{C_T} = \frac{\bar{C}_t}{C_T} \quad (1)$$

where  $\bar{C}_t$  is the average transcription rate.

\* Manuscript received by the PGAP, November 10, 1956; revised manuscript received, June 21, 1957.

† The W. L. Maxson Corp., New York, N. Y.

<sup>1</sup> W. S. Lucke, "An Antenna Evaluation," Stanford Res. Inst., Menlo Park, Calif., Tech. Rep. No. 17 for Air Force Contract No. AF 19(122)78; April, 1951.

On the other hand, the average time of transmission,  $\bar{T}$  is

$$\bar{T} = \bar{T} \frac{1}{M} \sum_{i=1}^M \frac{C_T}{C_{ti}} = TC_T \left( \frac{1}{\bar{C}_t} \right) \quad (2)$$

where  $TC_T = N_{in}$ .

Note that for this method if one transcriber is inoperative, *i.e.*,  $C_{ti} = 0$  then  $\bar{T} = \infty$  and the communication system considered as a whole is useless. This is not an unusually stringent condition for system of transcribers if no single transcriber can be considered expendable.

For example, let us examine the case of the communication link between two ships that are transmitting their bearing to each other in order to avoid a collision. One ship has a transmitter which is sending information out in all directions, and the other ship, unknowingly, can receive the transmission only if it is coming from a given  $180^\circ$  sector. If all possible relative bearings are equally probable the system is obviously useless.<sup>2</sup> If the figure of merit was measured by averaging  $C_t$  over the angular region, a nonzero number would result for  $N_{out}/N_{in}$ . This would imply that the longer the transmission took place the greater the probability of getting the message through would be. That is, of course, not so in this example, if the ships are approaching each other and the  $180^\circ$  sector is forward. The average time, however, is infinite and the antenna, on the basis of this figure of merit, would be considered useless.

It certainly seems that the above mentioned methods for evaluating a communication system are basic and that any methods are really one form or the other of these two. In the specific case illustrated it appears that the time average method should apply to the evaluation of the antenna. Such an evaluation would consider an antenna useless which had a finite sector over which the signal was zero, *if the system was stationary*. If the transcriber is in motion, however, there is zero probability that it would remain in a given sector for an infinite length of time. Thus, to completely evaluate  $\bar{T}$  the relative velocity of the transcriber to transmitter would have to be taken into account.

In the next section, a mathematical account of how the average time method applies to a system using an antenna in the chain is discussed.

## II. APPLICATION OF AVERAGE TIME CONCEPT TO ANTENNA SYSTEMS

In order to find the most probable time of transcription without error, it is necessary to define the ap-

<sup>2</sup> It is, of course, better than one that could receive in only a  $90^\circ$  sector.



propriate transcription rate. This has been done<sup>3</sup> and is

$$C_t = W \log_2 \left( 1 + \frac{S}{N} \right) \quad (3)$$

where  $W$  is the bandwidth of the transcriber and  $S/N$  is the signal-to-noise ratio. In the case of an antenna system  $S/N$  is a function of the range and bearing between transmitter and receiver. The time to transcribe an amount of information without error to any point is simply

$$t = \frac{TC_T}{C_t(R, \theta, \phi)}$$

The average time of errorless transmission to any point on a sphere of given radius is then

$$\bar{T} = T_0 \int \frac{P(\theta, \phi) d\Omega}{\log_2 \left( 1 + \frac{S}{N} \right)} \quad (4)$$

where  $P(\theta, \phi)$  is the probability that transmission will be required at the bearing  $(\theta, \phi)$  at the given range.

$\bar{T}_0$  is the time to transcribe the information if the system to noise ratio were unity. If free space propagation applies

$$\frac{S}{N} = \left( \frac{R_0}{R} \right)^2 G(\theta, \phi) \quad (5)$$

where  $G(\theta, \phi)$  is the antenna gain and  $R_0$  is the range of

<sup>3</sup> C. E. Shannon, "Communication in the presence of noise," *Proc. IRE*, vol. 37, pp. 10-21; January, 1949.

the system at which  $\bar{T} = T_0$  when  $G(\theta, \phi) = 1$ . If the normalized function

$$\tau = \frac{\bar{T}}{T_0}$$

is substituted in (4) then the figure of merit of the system as a function of range is

$$\tau = \int \frac{P(\theta, \phi) d\Omega}{\log_2 \left[ 1 + \left( \frac{R_0}{R} \right)^2 G(\theta, \phi) \right]}$$

A particular system may require a given  $\tau$  for proper operation. Since  $R_0$  is a simple function of the system parameters, one can find the maximum possible range for a specific antenna by simply specifying the required  $\tau$ . The same antenna, with a different system (*i.e.*, utilizing a different  $\tau$ ) will result in a different range. For the special case where  $G(\theta, \phi)$  vanishes in such a way as to make the integral infinite.

$\tau =$  Minimum of

$$\left\{ \int_{\Sigma'} \frac{P(\theta, \phi) d\Omega}{\log_2 \left[ 1 + \left( \frac{R_0}{R} \right)^2 G(\theta, \phi) \right]} + \frac{T_c}{T_0} \right\} \quad (6)$$

where  $\Sigma'$  is taken over the surface not including the region where  $G(\theta, \phi)$  vanishes and  $T_c$  is the average time to traverse the excluded region. Eq. (6) is the general representation for the figure of merit of an antenna assuming free space propagation.

## Wide-Angle Scanning with Microwave Double-Layer Pillboxes\*

WALTER ROTMAN†

**Summary**—The double-layer pillbox is a microwave parallel-plate system in which the image space and the object space relative to a two-dimensional internal reflector are electrically separated by a metal septum. The double-layer prevents the shadowing effects and impedance mismatch that result in a single-layer pillbox when energy from the reflector reenters the primary feed. It also allows correction of the optical aberrations of the system in the image space, the object space, or both.

The pillbox with semicircular reflector has wide-angle scanning properties. Its inherent spherical aberration can be reduced by such elements as dielectric lenses, geodesic contours, quasi point-source feeds, and auxiliary reflectors. These techniques have been applied to the construction of pillboxes whose wide-angle scanning properties and improved radiation characteristics substantiate the theory.

\* Manuscript received by the PGAP, July 13, 1957; revised manuscript received, October 30, 1957.

† AF Cambridge Res. Center, Air. Res. and Dev. Command, Bedford, Mass.

### I. INTRODUCTION

PARALLEL-plate systems for microwave antennas, in which the radiation is essentially confined to two dimensions between conducting sheets, have found widespread use in radar and communication applications. When combined with curved conducting back walls (one-dimensional mirrors), which reflect and collimate the microwave energy, these systems are known as pillboxes or "cheese" antennas,<sup>1</sup> the chief distinction between them being that the pillbox supports only a single mode of propagation (usually either the TEM or the TE<sub>01</sub> mode) between the conducting sheets

<sup>1</sup> S. Silver, "Microwave Antenna Theory and Design," M.I.T. Rad. Lab. Ser., McGraw-Hill Book Co., Inc., New York, N. Y., vol. 12, pp. 459-464; 1949.

whereas the cheese antenna is capable of supporting several modes simultaneously.

The most common type of pillbox antenna is that used to collimate the energy from a point source, placed at the focal point of a parabolic reflecting surface and confined between conducting plates, into a plane wavefront. The radiation of this collimated energy from a linear aperture creates a line source which can serve either as the primary feed for an auxiliary reflector or as a direct source for a fanned radiation pattern.

The pillboxes used during World War II were mostly of the single-layer type—that is, the point source, the reflecting back wall, and the linear radiating aperture all lay in the same plane between the conducting sheets. The chief disadvantage of the single-layer antenna is that reflections from the rear wall into the primary feed are very large—much greater than those from full paraboloids.<sup>2</sup> Because of the “long-line” effect between feed and reflector, the phase of these reflected waves varies rapidly with frequency, making it difficult to broadband the pillboxes by using fixed tuning devices. This impedance fluctuation can be minimized by placing a metallic plate at the vertex of the parabolic reflecting surface, but only at the expense of a decrease in antenna gain and an increase in the side lobes of the radiation pattern. A better solution is to use a “folded” or “multiple-layer” structure in which a curved toroidal or 180° parallel-plate bend is substituted as the reflector; the linear radiating aperture and point source or waveguide feed are thus at different levels and the amount of reflection back into the feed system is consequently reduced. Early systems using this folded type of construction include the Robinson and the Schwarzschild Scanning Feeds,<sup>3</sup> both of which are electro-mechanical scanning devices; that is, the peak of the radiation pattern is moved through an angle in space by rotating the waveguide input instead of the entire mechanical structure. This technique permits much higher scanning rates because of the reduction in mechanical inertia, but the two systems mentioned are limited in scan angle by virtue of their geometry.

More recent antenna designs have attempted to produce wide-angle electrical scanning by means of circular symmetry in the antenna. Iams<sup>4</sup> of RCA has built a circular reflector with correction element, which is capable of scanning over  $\pm 30^\circ$ . Construction is of the double-layer circularly symmetric type, with a toroidal bend substituting as the reflector. A noncircular lens, which corrects for residual spherical aberrations of the system, is attached and moves with the waveguide in-

put. The double-layer construction, which eliminates reflections back to the waveguide, permits the use of multiple feeds without shadowing effects. These feeds are switched sequentially so that a rotary motion of the feed system produces a sawtooth motion of the radar beam. The chief disadvantages of this antenna are mechanical troubles in rotating the large mass of the lens elements, as well as limitations on lens size. Since only about half of the physical aperture of the antenna is effective in collimating the radiation, the beamwidth is greater than that for a parabolic reflector of the same size.

Since reflections back to the source are negligibly small, a major advantage of folded pillboxes is that microwave optical systems impossible to construct in single-layer form may easily be achieved. (This is why the double-layer pillbox was used with the Schwarzschild antenna.) For instance, correcting lenses to eliminate optical aberrations may be placed in front of, at, or even behind the reflecting “mirror.” Fairly complex quasi point-source feed systems can be constructed without fear of shadows or impedance mismatch. An example is the Microwave Schmidt System of Chait,<sup>5</sup> a double-layer circular pillbox with a nonconcentric dielectric lens of the Schmidt type placed in front of the mirror reflector. Other systems, using concentric correcting lenses, have also been built.

Another technique for producing wide-angle scanners distorts the flat conducting sheets of the parallel-plate system into special geometric shapes. Although one is accustomed to thinking of refraction or reflection in microwave optical systems as the chief parameter in determining the paths of the rays, the important factor is actually given by Fermat's principle which states that the optical path lengths in a system must have stationary values. If the conducting plates are distorted from their normally plane surface, the microwave energy will be constrained to follow “geodesic” (minimum optical distance) paths between the plates; differences in optical path lengths, which may be used for focusing effects, are thus obtained. An example of geodesic construction is given by the microwave Rinehart analog of the Luneberg lens. A folded version of this system, with the advantage of a smaller feed circle, has also been proposed by Rinehart.<sup>6</sup> One important feature of the Luneberg system is the complete circular symmetry and the corresponding ability to scan throughout the plane of the antenna. Extensive experimental and theoretic work on this subject has been reported from AFCRC and other laboratories.<sup>7</sup>

<sup>2</sup> W. Sichak and E. M. Purcell, “K-Band CSC<sup>2</sup> Antennas With a Line Source and Shaped Cylindrical Reflector,” M.I.T., Cambridge, Mass., Rad. Lab. Rep. No. 624; 1944.

<sup>3</sup> W. M. Cady, M. B. Karelitz, and L. A. Turner, “Radar Scanners and Radomes,” M.I.T. Rad. Lab. Series, McGraw-Hill Book Co., Inc., New York, N. Y., vol. 26, pp. 45-61; 1948.

<sup>4</sup> H. B. Devore and H. Iams, “Microwave optics between parallel conducting sheets,” *RCA Rev.*, vol. 9, pp. 730-732; December, 1948.

<sup>5</sup> H. N. Chait, “A Microwave Schmidt System,” Naval Res. Lab., Washington, D. C., NRL No. 3889; May, 1952. Also see “Wide-angle scan radar antennas,” *Electronics*, vol. 26, pp. 128-132; January, 1953.

<sup>6</sup> R. J. Rinehart, “A family of designs for rapid scanning radar antennas,” *Proc. IRE*, vol. 40, pp. 686-688; June, 1952.

<sup>7</sup> H. Jasik, “The Electromagnetic Theory of the Luneberg Lens,” Contractor's paper to Antenna Lab., AF Cambridge Res. Center, Cambridge, Mass.; May, 1953.



## II. PROPERTIES OF SEMICIRCULAR PILLBOXES

For wide-angle scanning, the semicircular pillbox with linear aperture (Fig. 1) has many applications as a line source. The pillbox is divided into two layers, the entrance layer containing the waveguide input and the exit layer containing the linear aperture. In transmission, microwave energy from the open end of the waveguide propagates within the entrance layer, passes to the exit layer through the parallel-plate bend where it is approximately collimated into a plane wavefront, and then radiates into space from the linear aperture.

From the symmetry of the model it can be seen that the radar beam may be scanned by moving the waveguide in a circle whose center coincides with the center of curvature of the model. A one-to-one relationship is obtained between the angular position of the feed and that of the beam if the velocity of propagation of the waves in the parallel plates is the same as that in free space. This condition is satisfied by the TEM waves in which the electric vector is normal to the conducting parallel plate. With the  $TE_{01}$  mode, in which the electric vector is parallel to the plates, the velocity between the plates is greater than free-space velocity in accordance with the relation

$$v_p = \frac{c}{\sqrt{1 - \left(\frac{\lambda}{2ma}\right)^2}}, \quad (1)$$

where

- $v_p$  = phase velocity in metal plate media,
- $c$  = free-space velocity of light,
- $m$  = mode number = 1, 2, 3, 4, etc. ( $m=1$  for fundamental mode),
- $a$  = separation of parallel plates,
- $\lambda$  = free-space wavelength;

and the rays are refracted at the linear aperture according to Snell's law

$$\frac{\sin \theta}{\sin \phi} = \sqrt{1 - \left(\frac{\lambda}{2ma}\right)^2}, \quad (2)$$

where  $\theta$  = angle with respect to normal of ray in free space,  $\phi$  = angle with respect to normal of ray in parallel-plate media. The position of the feed circle is the same for TEM and  $TE_{01}$  operation.

The only aberrations in a circularly symmetric system are of the on-axis types, such as spherical aberrations, and also shadowing effects. Off-axis aberrations, such as coma and astigmatism, are completely absent. If the system can be corrected for on-axis aberrations, it is completely corrected for all angles of scan except for effects caused by shadowing. Actually, the aberrations need not be completely eliminated but only reduced to the point where the deviation from linearity of the emerging wavefront is less than the  $\lambda/8$  limit set by

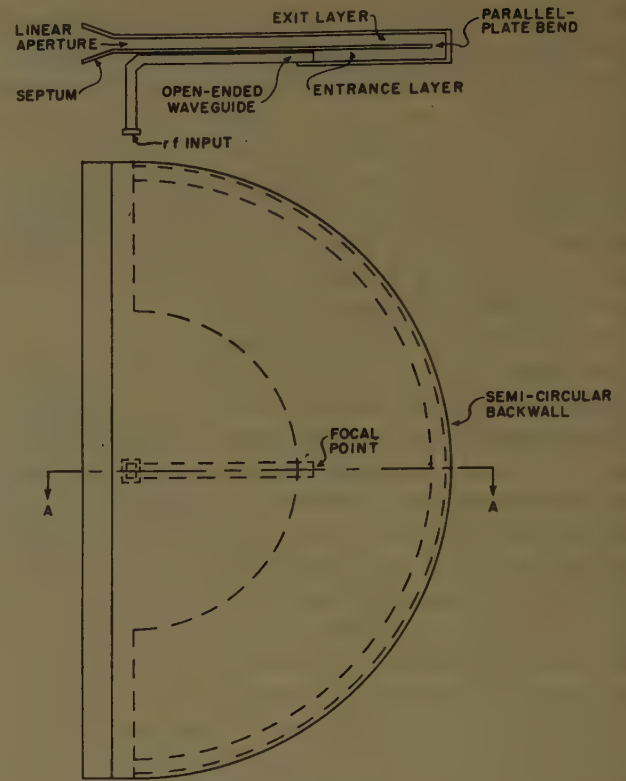


Fig. 1—Semicircular double-layer pillbox with linear aperture.

Rayleigh's<sup>8</sup> criterion or by the limit set by an analogous criterion determined by permissible deterioration of beamwidth and side-lobe level of the radiation pattern.

The effect of shadowing and spillover may be qualitatively determined by considering a circular reflector (Fig. 2) fed in the TEM mode by a directive horn so that only a small width  $w$  of the reflector is uniformly illuminated. For on-axis feeding [Fig. 2(a)], the same length  $l$  of the linear aperture is illuminated ( $l=w$ ), while off-axis  $l=w/\cos \theta$ . However,  $w$  and the gain of the antenna remain constant until the aperture is totally illuminated at an angle  $\theta_0$  [Fig. 2(b)] given by

$$\cos \theta_0 = w/A, \quad (3)$$

where  $A$  is the maximum aperture width. Beyond this critical angle, the gain decreases because of two factors. First, a loss of radiated energy by aperture shadowing (vignetting) causes a  $\cos \theta$  variation in gain; and second, the reduction in effective aperture due to the decrease in cross section of the wavefront broadens the main beam and thus decreases the gain further [Fig. 2(c)].

The side-lobe level of the far-field pattern also increases in intensity since the energy that does not reach the aperture is scattered. Note that the electrical center of radiation and the physical center of the aperture always coincide.

The radiation pattern of the primary feed must be carefully controlled in order to get the desired amplitude

<sup>8</sup> A. S. Dunbar, "Applications of the Rayleigh criterion," Symposium on Microwave Optics, McGill University, Montreal, Can.; June, 1953.

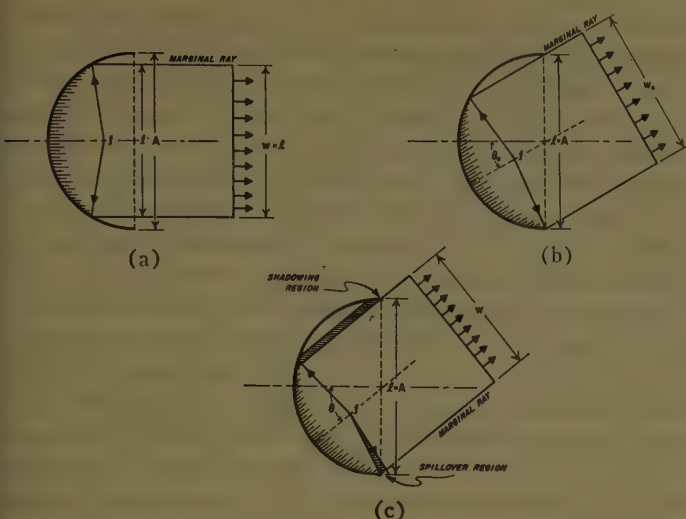


Fig. 2—Effective aperture of a circular reflection. (a) On-axis illumination. (b) Limits of aperture. (c) Spillover and shadowing effects.

distribution along the aperture. To ensure reasonably low side lobes, the intensity at the edges of the usable portion of the aperture should be about ten decibels below that at the center. Special primary waveguide feeds, incorporating metallic and dielectric protrusions or obstacles in the waveguide opening<sup>2,9-11</sup> may be required to obtain this wide-angle illumination.

### III. CONTROL OF ON-AXIS ABERRATIONS

Since spherical aberration causes deterioration of the radiation patterns of circular pillboxes, methods of controlling this aberration are of prime importance. For a plane wave incident upon the concave side of a spherical reflector, rays close to the axis are focused at the paraxial focus which is exactly half-way between the center of curvature and the vertex. Other rays cross the axis at points closer to the vertex. The distance from the paraxial focus to the intersection of a general ray and the axis may be expressed as

$$LA' = ay^2 + by^4 + cy^6 + \dots,$$

where  $y$  is the height of the incident ray,  $LA'$  is the longitudinal spherical aberration, and the various terms of the series in  $y^2$ ,  $y^4$ ,  $y^6$ , etc., respectively represent the primary, secondary, tertiary, etc., spherical aberrations. Thus, limitation of the illuminated portion of the aperture reduces the aberrations, at the least, as the square of the aperture dimensions. For a given reflector, if the effective aperture is made small enough in terms of wavelength, the aberrations may be reduced below the point where they are troublesome. The optical analog

is the use of field stops and diaphragms to obtain systems of large  $f$  numbers (ratio of focal length to effective diameter).

Uncorrected spherical reflectors have been used for radar applications by restricting the aperture and selecting sufficiently large radii of curvature for the reflector. Ashmead<sup>12</sup> describes a scanning antenna that has a horizontal beamwidth of less than  $1^\circ$  and scans through an angle of  $6^\circ$  by motion of the primary feed alone. His theoretical analysis indicates that the best focal point for an uncorrected spherical system is not at the paraxial focus  $r/2$  but is at one-half of the radius minus one-quarter of the depth of the reflector. For this position of focus, the maximum aperture  $A$  for which deviation from a plane wavefront is less than  $\lambda/8$  may be computed from  $A^4 = 250\lambda f^2$  where  $f$  = the focal length,  $A$  = maximum usable aperture,  $\lambda$  = wavelength. These results were obtained by comparison of the sphere with the optically perfect paraboloid.

Similar conclusions have been reached by the author through a slightly different technique. The spherical reflector is considered as a transmitter with a point source placed on axis; the optical path lengths from the source to a line normal to the axis are computed for the geometric rays. The differences in path lengths for the various rays are a measure of the phase deviation from linearity; the shape of the wavefront may be investigated as a function of position of feed. For the feed at the paraxial focus, the wavefront has the shape shown in Fig. 3(a). If the feed is moved closer to the reflector,

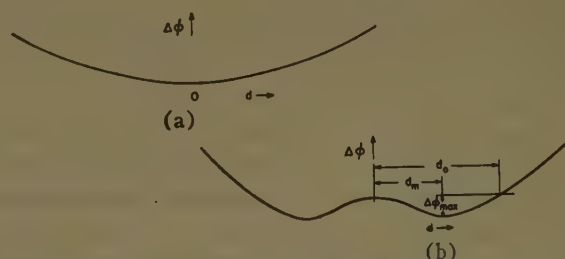


Fig. 3—Wavefront phase errors in axially symmetric systems. (a) Spherical mirror: primary source at paraxial focus. (b) Spherical mirror: primary source at "best" focus.

the wavefront is converted to the type shown in Fig. 3(b) in which the optical path length at some zone  $d_0$  is equal to the length of the paraxial ray. The position of focus for any value of  $d_0$  may be determined theoretically. If the maximum deviation,  $\Delta\phi_{\max}$ , for  $d_0 > d > 0$  is less than the Rayleigh criterion of  $\lambda/8$ , the aperture is usable over an area somewhat greater than these limits. This type of analysis has advantages over the Ashmead method in the study of a concentric, dielectric lens in a spherical mirror. By either method, however, the position of the feed for the best focus in an uncorrected mirror is almost identical.

<sup>9</sup> C. S. Pao, "Shaping the Primary Pattern of a Horn Feed," M.I.T., Cambridge, Mass., Rad. Lab. Rep. No. 655; January, 1945.

<sup>10</sup> L. J. Eyges, "Lens Feed for K-Band Pillboxes," M.I.T., Cambridge, Mass., Rad. Lab. Rep. No. 869; January, 1946.

<sup>11</sup> T. J. Keary, "AN/APS-32 and AN/APS-34 Airborne Navigational Radar Antennas at K-Band," M.I.T., Cambridge, Mass., Rad. Lab. Rep. No. 808; March, 1946.

<sup>12</sup> J. Ashmead and A. B. Pippard, "The use of spherical reflectors as microwave scanners," *J IEE (London)*, vol. 93, pt. IIIA, pp. 627-632; 1946.



If the phase errors are excessive, auxiliary techniques can be used to reduce the aberrations. These methods include:

- 1) Dielectric lens—concentric, Schmidt type, or auxiliary lens moving with feed,
- 2) Geodesic shapes,
- 3) Quasi point-source feeds—multiple point sources, extended line sources, or auxiliary reflectors,
- 4) Combinations of the three preceding methods.

Characteristics of these techniques will be discussed in detail in the following sections.

### *Dielectric Lenses*

Lenses of natural or synthetic materials may be placed in suitable locations between the parallel conducting sheets of pillboxes to minimize the spherical aberrations of the system. They may be concentric or nonconcentric. The nonconcentric types include the Schmidt systems and the movable lenses.<sup>4,5</sup>

The concentric dielectric lens has the advantage that it does not disturb the circular symmetry of the system; however, spherical aberration can never be entirely eliminated by this lens—it can only be reduced to an acceptable value. With no correction the rays in a spherical reflector are poorly focused. If a concentric dielectric shell is placed in front of the mirror, the focusing is improved regardless of the exact position or thickness of the shell. There are, of course, certain optimum dimensions of the lens that give minimum spherical aberration. Concentric lens-mirror combinations of this type have been used in optics for the construction of microscope, telescope, and photographic objectives, and have received extensive theoretical treatment by Bowers.<sup>13</sup>

In the double-layer pillbox application, the two-dimensional concentric lens may be located in either the entrance or the exit layers (containing the waveguide or the linear aperture, respectively) or both. The lens always acts as an optical element of weak power but with spherical aberration of opposite sign to that of the concave mirror. If the lens is placed in the exit layer, only that portion of the linear aperture that corresponds to the smaller inside diameter of the lens may be used for radiation. For this reason the lens is usually located in the entrance layer. Increasing the dielectric constant of the lens reduces the aberrations of the system and moves the focal point closer to the center of curvature. The latter effect results in a smaller feed circle, which is an advantage in rapid scanning.

### *Geodesic Shapes*

We have mentioned that the conducting surfaces of the pillbox may be distorted into special geometric shapes to obtain better focusing. The theory of such "geodesic" systems for electromechanical scanning pur-

poses has been analyzed by Myers<sup>14</sup> who discusses several interesting solutions. He shows the design of a parallel-plate system in which the feed moves in a circle, the aperture is a straight line, and the energy leaves the aperture as a directed beam that tilts as the source moves. His solution to the wide-angle scanning problem is a "surface of revolution scanner" in which the linear aperture lies along a diameter. This design satisfies all conditions except the aberration problem. It has been shown<sup>15</sup> that no geodesic surface can completely eliminate the spherical aberration. However, by proper selection of contour, the optical errors may be minimized and conceivably reduced below the point where they are troublesome. Of the several possible solutions, the one which appears most practical is the right circular cylinder similar to that shown in Fig. 9. Its aberrations are only about one-third that of the uncorrected flat pillbox and even less than that for a system with a polystyrene dielectric correcting lens. A combination of appropriate dielectric lenses and geodesic contours can reduce the aberrations to a still smaller value.

A pillbox incorporating these principles was constructed and will be described later. If the mean surface were exactly a right circular cylinder, abrupt 90° bends which might reflect energy would be required. A modified mean surface (Fig. 9) was therefore selected so that gradual toroidal bends<sup>16</sup> could be substituted.

### *Quasi Point-Source Feeds*

The methods for correction of spherical aberration described so far attempt to collimate the energy from a point source into a perfect plane wave at the aperture. The alternate approach is to consider a plane wave incident upon the antenna from external sources and to attempt the interception of the imperfectly focused rays by placing several waveguide receiving elements near the focal regions where the energy is concentrated. Examples include the multipoint source feed which minimizes lateral spherical aberration, and the corrected line source feed which operates upon the longitudinal spherical aberration.

Still another approach is to collimate the energy to a perfect focus by means of a small auxiliary nonconcentric reflector placed near the paraxial focus of the pillbox. This auxiliary reflector is considered part of the primary feed and can be moved with the waveguide for scanning purposes.

<sup>14</sup> S. B. Myers, "Parallel Plate Optics for Electrical Scanning," M.I.T., Cambridge, Mass., Rad. Lab. Rep. No. 646; December, 1944; also see "Parallel plate optics for rapid scanning," *J. Appl. Phys.*, vol. 18, pp. 221–229; February, 1947.

<sup>15</sup> The proof that no geodesic surface can completely eliminate the spherical aberration was first derived by Dr. R. C. Spencer at M.I.T. Rad. Lab. in 1943. A similar conclusion was later obtained by Dr. S. B. Myers through an alternate formulation of the problem. The improved characteristics of an appropriate combination of geodesic surfaces and dielectric lenses were first demonstrated by Dr. C. Robinson at M.I.T. Rad. Lab.

<sup>16</sup> E. M. T. Jones and R. C. Honey, "Millimeter Wavelength Antenna Studies," Stanford Res. Inst., Stanford, Calif., Seventh Quarterly Progress Report, Project No. 430 (Contract No. DA-36-039-SC-5503), pp. 23–31; January, 1953.

<sup>13</sup> A. Bowers, "Achievements in Optics," Elsevier Publishing Co., New York, N. Y., pp. 25–330; 1946.

Sletten<sup>17</sup> has attempted to correct the spherical aberrations in a three-dimensional, spherical reflector by placing several point source feeds transverse to the reflector axis in the concentrated field distribution (known as the Airy disk) near the paraxial focal region. This technique has met with considerable success, but performance suffers from the shadowing effects of the moderately large feed system.

The design of the multiple point-source feed is simplified when applied to the two-dimensional case of the double-layer pillbox;<sup>18</sup> furthermore, shadowing effects are eliminated.

For this application, a typical multiple-source feed consists of three open-ended waveguides spaced about one wavelength apart, with the center one near the paraxial focus and the other two on either side (Fig. 6). Power is fed into the center guide and distributed at a lower intensity to the auxiliary guides by means of multihole directional couplers.

In contrast to this multiple-source feed, which is transverse to the reflector axis and therefore modifies the fields in the lateral plane, correction of aberrations may also be achieved by operation upon the longitudinal fields. In the latter case, receiving elements are distributed along the axis of the system and phased to intercept the rays at the point where they cross the axis. These elements form a phased line source<sup>19</sup> which can consist of a traveling-wave array located between the parallel plates and made of waveguide with radiating slots or dipoles in the side walls. Scanning is achieved by rotating the array about the center of curvature of the reflector.

Phased line sources have been constructed and tested for spherical reflectors but not for parallel plate systems. The chief difficulty is the limited knowledge of the design principles for linear arrays between parallel plates.

Since most of the energy, even in an optical system with large spherical aberrations, is concentrated fairly close to the focus, a small auxiliary reflector can intercept and focus the rays from an incoming wave [Fig. 4(a)]. This auxiliary reflector can be moved with the waveguide feed for scanning purposes. Since the shape of the reflector is determined from geometric optics, it should be several wavelengths in aperture to avoid the diffraction effects encountered with small openings. Proper illumination of the auxiliary reflector without shadowing necessitates its construction in double-layer form [Fig. 4(b)], making the pillbox a triple-layer structure.

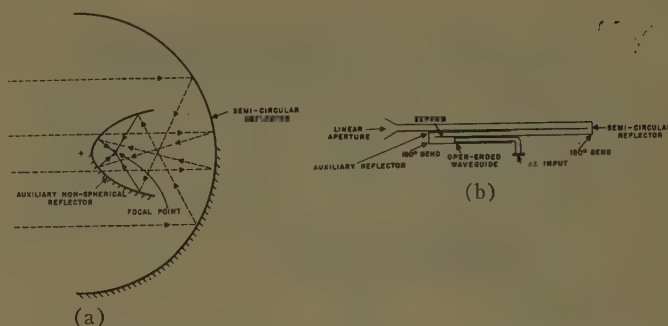


Fig. 4—Semicircular double-layer pillbox with auxiliary reflector. (a) Basic configuration. (b) Double-layer pillbox form.

### Combinations

Among the methods discussed for correction of spherical aberration, the Schmidt system, the phased line source, and the auxiliary reflector are the only ones capable of perfect focusing. The concentric dielectric lens, geodesic shapes, and multiple-point source feeds minimize the aberrations but do not eliminate them entirely. For small apertures (in terms of wavelength), the residual aberration may be acceptable; but for the larger apertures required for high-resolution radar systems, the deviation from linearity of the wavefronts may exceed the permissible amount.

Several of these methods can be combined to reduce the aberrations to acceptable limits. One example, previously mentioned, is the use of concentric dielectric lenses in geodesic structures. Other combinations include geodesic shapes with either corrected line sources, multiple-point sources, auxiliary reflectors, or Schmidt lenses. The following combinations for correcting circular pillbox reflectors have been found practical:

- 1) Small apertures ( $5-10\lambda$ )—no correction needed beyond tapered illumination.
- 2) Medium apertures ( $10-20\lambda$ )—tapered illumination plus geodesic shapes.
- 3) Large apertures ( $20-40\lambda$ )—tapered illumination plus geodesic shapes plus multiple-point source feeds.
- 4) Very large apertures ( $40\lambda$  and above)—tapered illumination plus geodesic shapes plus auxiliary reflectors.

### IV. EXPERIMENTAL RESULTS

Several double-layer pillboxes were constructed to evaluate the techniques. Three of these models—a semi-circular pillbox with triple-horn feed and two geodesic pillboxes with a triple-horn feed and with an auxiliary reflector respectively—are described here. These types were selected as optimum with respect to angle of scan and aperture efficiency. Other models whose characteristics are discussed in the author's reports<sup>20</sup> include a

<sup>17</sup> C. J. Sletten and W. G. Mavroides, "A Method of Side-lobe Reduction," Naval Res. Lab., Washington, D. C., NRL No. 4043, pp. 1-12; April, 1952.

<sup>18</sup> B. Berkowitz and J. D'Agostino, "A Geodesic Antenna for Flush Mounted Applications," (Classified Paper), Georgia Inst. of Tech., Atlanta, Ga., Symposium Record of Georgia Tech.-SCEL Meeting on Scanning Antennas, pp. 283-293; December, 1956.

<sup>19</sup> R. C. Spencer, C. J. Sletten, and J. E. Walsh, "Correction of Spherical Aberration by a Phased Line Source," AF Cambridge Res. Labs., Cambridge, Mass., AFCRL Rep. No. E 5069; May, 1951.

<sup>20</sup> W. Rotman, "A Study of Microwave Double-Layer Pillboxes; Part I, Line Source Radiators," AF Cambridge Res. Center, Cambridge, Mass., Tech. Rep. AFCRC-TR-102; July, 1954; Part II, "Multiple Reflector Systems," Tech. Rep. AFCRC-TR-101; January, 1956.





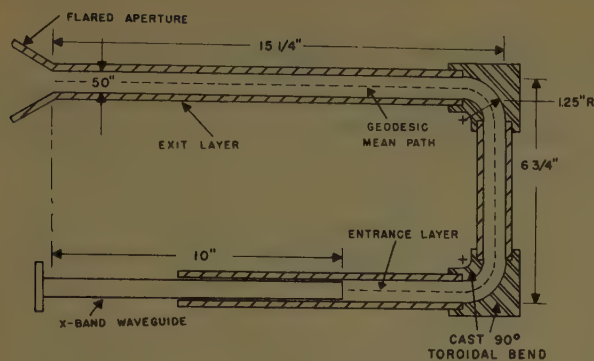


Fig. 9—Semicircular geodesic pillbox.

tween a vswr of 2.2 and 1.1 in the X-band range of frequencies. This bad mismatch is not due to any inherent property of the pillbox, but was traced to internal reflections from the coupling holes within the three-element primary feed. A simple redesign of these holes (Fig. 6) in accordance with good directional coupler practice should correct this trouble.

The semicircular flat pillbox with triple-horn feed is acceptable for moderate aperture efficiencies and sidelobe levels. The geodesic pillbox, which has inherently smaller spherical aberrations and better aperture efficiencies, will now be discussed.

#### Semicircular Geodesic<sup>24</sup> Pillbox With Triple-Horn Feed

This pillbox is a wide-angle scanning antenna operating at X band in the TEM mode. The special contour is dictated by geodesic principles applied to limit the spherical aberration to a smaller residual value than that achieved in the flat, uncorrected, semicircular pillbox. The triple-horn feed is used to reduce the sidelobes caused by the residual aberrations to acceptable values. Construction is similar to the flat semicircular pillbox, with the exception of the "surface of revolution" shape which is a right circular cylinder.

The optimum geodesic contour suggested by Myers<sup>14</sup> is a right circular cylinder (Fig. 9). For this 30-inch diameter model the wavefront has a maximum phase error of less than  $\lambda/8$  at K band and  $\lambda/16$  at X band.

Since right-angle bends reflect a considerable portion of the incident energy, circularly curved bends are used. This change modifies the optimum geodesic contours and increases the spherical aberrations by a small, second-order amount. An attempt to compensate for the effects of the bends was made by adjusting the geodesic height. The equations<sup>16</sup> can be used to calculate this adjustment exactly.

The triple horn feed (Fig. 6) was used as the primary source for the geodesic pillbox (Fig. 9). The relative power fed to the horns was controlled by variable at-

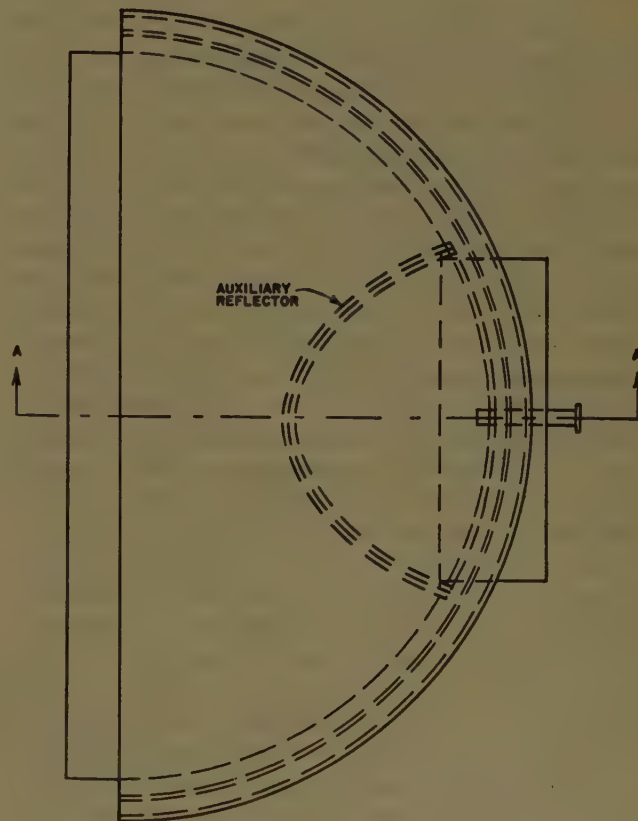
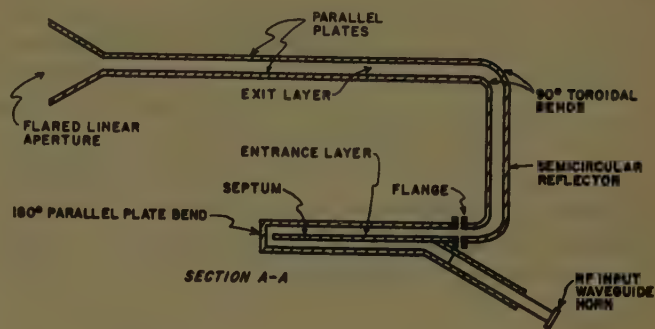


Fig. 10—Semicircular pillbox with auxiliary reflector.

tenuators which were used to adjust the radiation pattern to a sidelobe level of 20 db and a half-power beamwidth of  $3.6^\circ$ . Scanning patterns taken with this feed show that the radiation pattern has not appreciably deteriorated even at scan angles up to  $50^\circ$ .

The aperture efficiency of the experimental geodesic pillbox is better, by a factor of about 30 per cent, than that of the flat pillbox of equivalent aperture size. In terms of volume efficiency, however, the flat pillbox is vastly superior to the geodesic, and in some applications its smaller volume may make it more desirable than the geodesic type. In this case, a larger aperture would be required for equivalent beamwidths.

#### Semicircular Geodesic Pillbox With Auxiliary Reflector

The pillbox with auxiliary reflector (Fig. 10) has three main parts: 1) the stationary semicircular reflector, whose mean surface is that of a right circular cylinder,

<sup>24</sup> The term "geodesic" is used here as a descriptive title for an antenna system, rather than as an implication that geodesic principles do not apply to most other antenna types. An alternate designation "semicircular separated layer pillbox," based upon the geometric configuration, has also been employed in several communications.



TABLE I  
SUMMARY CHART, CHARACTERISTICS OF DOUBLE-LAYER SEMICIRCULAR PILLBOXES

Type	Wavelength (cm)	Aperture (inches)	Half-Power Beamwidth	Side-Lobe Level (On-Axis) (db)	Useful Angle of Scan (1-db loss)	Aperture Efficiency (per cent)
Dielectric lens	3.3	40	3.8°	22.5	±55°	55
Flat shape with triple-horn feed	3.3	40	3.4°	19.5	±55°	60
Geodesic shape with triple-horn feed	3.3	30	3.6°	20.0	±55°	80
Geodesic shape with triple-horn feed	1.25	30	1.6°	16.0	±50°	67
Geodesic shape with auxiliary reflector	3.2	30	3.3°	15.0	±50°	78

2) the auxiliary reflector and, 3) the primary waveguide feed. In scanning, the latter two move as one unit.

When the system operates as a receiving antenna, a plane wave that impinges on the linear aperture of the semicircular reflector is imperfectly focused in the entrance layer. The auxiliary noncircular reflector serves to focus this energy perfectly at the location of the primary feed. Both the auxiliary and the semicircular reflectors are built in double-layer form to minimize reflections and improve optical properties. The radar beam can be scanned by moving the auxiliary reflector and primary feed together about the axis of revolution of the semicircular reflector. For a pillbox operating in the TEM mode the beams move through the same angle as the feed. Geodesic principles specify that the entrance and exit layers of the semicircular reflector must be separated to bring the rays in the entrance layer to a better focus and to keep the size of the auxiliary reflector small. This separation also increases the effective linear aperture and improves collimation of the beam.

If the layers of a semicircular pillbox are not separated, a ray that enters the system further from the center than  $\sqrt{2}/2$  of the radius of the semicircular reflector crosses the axis in the entrance layer at an angle greater than 90°. It cannot be focused by any auxiliary reflector that is concavely symmetric about that axis because it strikes the convex side of the reflector first. An interspace between layers, limited to about one-sixth the diameter of the pillbox to prevent intersection between the auxiliary and semicircular reflectors, decreases the angle at which the ray strikes the axis and provides an effective aperture of between 85 and 90 per cent of the physical aperture. The auxiliary reflector is subject to the following requirements:

- 1) It must be contained within the physical bounds of the semicircular reflector.
- 2) It must be so positioned that two separate rays cannot strike it at the same point. Otherwise, perfect focusing will be impossible.
- 3) It must intercept all the radiation from the effective linear aperture and focus it on the primary feed. Since the beamwidth of the radiation pattern produced by a waveguide horn, the usual feed, is less than 140°, the angle of rays incident upon the feed is preferably less than 70° from the paraxial ray.

- 4) It must be as small as possible for mechanical reasons. The details for computing the shape of the auxiliary reflector and the primary box horn feed from ray-tracing may be found in the author's AFCRC reports.<sup>20</sup>

The pillbox antenna selected as an example is designed for a wavelength of 3.2 cm. Its linear aperture of 30 inches produces a beamwidth of about 3°. The 90° bends in the semicircular reflector are toroidal. This complicates geometric ray-tracing but prevents the reflections that would occur if the bends were at sharp right angles. Fortunately, ray-tracing formulas<sup>26</sup> take the toroids into account. The sharp 180° bend in the auxiliary reflector has moderately small reflections at the design frequency. Near-field measurements correlate the far-field measurements with the properties of the pillbox. Although the measured and the computed near-field amplitude patterns along the linear aperture agree with each other substantially, both differ from the theoretical optimum in not having a smooth taper. The expected effect of this variation is evidenced by higher side-lobes and a wider main beam in the far-field pattern. This could be remedied by modifying the waveguide feed.

Scanning patterns, taken by moving the auxiliary reflector and the box horn feed about the center of curvature of the pillbox, show that the radiation pattern does not appreciably deteriorate even for scan angles greater than ±30°. The measured beamwidth corresponds to an aperture efficiency of about 78 per cent (relative to uniform illumination).

#### Summary Chart

A summary chart of the principal properties of the various pillboxes is given in Table I. Of all these models the semicircular geodesic pillbox has the best aperture efficiency in the X-band region.

The choice of pillbox for a given application depends upon volume, weight, and size requirements, in addition to the desired angle of scan and electrical characteristics. The data given in the table are not optimum but rather are results achieved within a restricted time schedule.

<sup>26</sup> E. M. T. Jones, R. C. Honey, and R. A. Folsom, "Millimeter Wavelength Antenna Studies," Stanford Res. Inst., Stanford, Calif., Final Rep., Project 430, Contract DA-36-039-SC-5503, pp. 26-31; July, 1953.

## V. CONCLUSION

Some of the characteristics of double-layer pillboxes have been applied to the design of wide-angle scanning antenna systems of semicircular construction. Methods of eliminating or reducing the spherical aberration have been tested and their limitations indicated.

The triple-horn feed, for example, reduces the intensity of the first sidelobe. The other sidelobes can be reduced by additional horns, but this would add to the complexity of the system.

Geodesic contours minimize spherical aberrations and, therefore, increase the aperture efficiency. They can be used to improve performance in conjunction with other techniques.

The auxiliary reflector can focus perfectly all rays which enter its aperture. One of its advantages, which is not possessed by any pillbox of semicircular type other than the Schmidt and the Iams correcting lenses, is that its techniques can be applied to pillboxes of arbitrarily large dimensions. With proper design it produces a narrower beam for a given physical aperture than either of the other two types. Its scan angle, unlike that of the Schmidt system, is independent of beamwidth.

The chief disadvantage of this pillbox is the fairly large mass of the auxiliary reflector. This may prove a slight hindrance in high-speed scanning although the

circular focal path allows the auxiliary reflector to be mounted in a disk and rotated at constant angular velocity. Several scans per revolution of the disk could be obtained by combining a number of reflectors.

Another application for wide-angle double-layer pillboxes is in multiple beam generation or reception. Since no aperture blocking is caused by the feeds, a number of inputs may be located around the focal arc and used either simultaneously or sequentially to generate many independent beams.

## ACKNOWLEDGMENT

The author gratefully acknowledges the contributions of several individuals who assisted in compiling the material included in this article. The concepts of the multi-point source feed, the line source feed, the auxiliary reflector, and much of the information on tuned posts were all provided by C. J. Sletten. L. Parad and H. Foster derived formulas used for ray tracing. J. Christian made many of the computations.

The author is also grateful to W. J. Kearns who performed the measurements. Numerous technical discussions with Dr. R. C. Spencer served to stimulate interest in this subject with which he has been actively concerned for many years.

# Surface-Wave Beacon Antennas\*

ROBERT E. PLUMMER†

**Summary**—Experimental results with center-fed corrugated and dielectric-clad spherical-cap antennas are presented and compared with the theory. The spherical surface waves supported by these structures give rise to radiation field patterns which are omnidirectional in the azimuth plane and which can be shaped in the elevation plane over a considerable range. The corrugated sphere provides vertical polarization while the dielectric sphere can support either polarization. The spherical caps are shown to have a natural application as low-drag beacon antennas when the surface geometries and sphere radii are appropriately adjusted.

## I. INTRODUCTION

THE RESULTS of an experimental investigation of surface waves on spheres are described in this report. The performance of center-fed corrugated and dielectric-clad spherical-cap antennas is compared

with the theory<sup>1</sup> and with the performance of their flat-disk counterparts. It is demonstrated that when the sphere radii and the surface geometries are appropriately adjusted, the spherical caps exhibit radiation patterns which closely approximate ideal beacon antenna performance.

The existence of guided modes of wave propagation over corrugated and dielectric-clad conducting surfaces has been known for many years. Until recently, investigators have been concerned primarily with the guiding properties rather than the radiation characteristics of these surfaces. The consideration of surface waves for application to antenna problems was motivated, to a large extent, by the need for antenna configurations which are compatible with the severe requirements of present-day and future airframes, and also by the desirability of low-silhouette antenna structures for many ground and shipboard installations.

\* Manuscript received by the PGAP, February 20, 1957; revised manuscript received, June 26, 1957. The work described in this paper was supported in part by the AF Cambridge Res. Ctr., Air Res. and Dev. Comm., Contract No. AF 19(604)-1317. The paper was presented at the NEC, Chicago, Ill., October, 1955, and was issued as Hughes Aircraft Co., Res. Labs., Tech. Memo No. 422, April, 1956.

† Hughes Aircraft Co., Culver City, Calif.

<sup>1</sup> R. S. Elliott, "Surface waves on spheres with an application to beacon antennas," *IRE TRANS.*, vol. AP-4, pp. 422-428; July, 1956.



Because of their low-gain, endfire-type radiation characteristics and their poor adaptability to scanning, surface-wave antennas have somewhat limited application. The elevation pattern of a flat, linear trapping surface is characterized by deep nulls, and when the surface is operated with a fore-shortened ground plane, diffraction at the end causes the main beam to tilt up from the plane of the surface.

## II. DISK ANTENNAS

As a first step in the experimental work, corrugated and dielectric-clad disk antennas were constructed and tested. It was felt that the performance of these structures (which are limiting examples of the spherical structures described in Section III) would provide a suitable gauge for measuring the improvements in performance anticipated with the spherical caps. The spherical coordinate system diagrammed in Fig. 1 will be convenient in describing the radiation characteristics of the experimental antennas.

Earlier work by Elliott<sup>2,3</sup> demonstrated that the nulls in the elevation pattern of a flat, linear surface-wave antenna could be filled in and the main beam tilted down for good horizon coverage by curving the trapping surface into a cylindrical shape and tapering the depth of the trapping medium.

Beginning in 1951, the antenna group at Stanford Research Institute reported a series of experiments with annular-ring antennas.<sup>4,5</sup> By corrugating a flat disk and feeding it at the center, they were able to obtain an endfire-type omnidirectional radiation pattern. The elevation pattern of the disk exhibited the characteristic deep nulls, the main beam was tilted up considerably from the plane of the disk, and the corrugations limited the application to perpendicular polarization. In view of the pattern shaping and beam placement achieved by curving flat, linear antennas, it was felt that the pattern of the disk antenna could be similarly improved if the disk were replaced by a spherical cap. Furthermore, if the corrugations were replaced by a dielectric film,<sup>6</sup> the limitation to perpendicular polarization would be removed.

A theoretical analysis of surface waves on spheres was made by Elliott<sup>1</sup> in order that a starting point for the design of spherical-cap antennas would be available. This analysis revealed two basic facts. 1) Essentially unimodal propagation of surface waves on spheres is possible if the curvature is not excessive. 2) The single

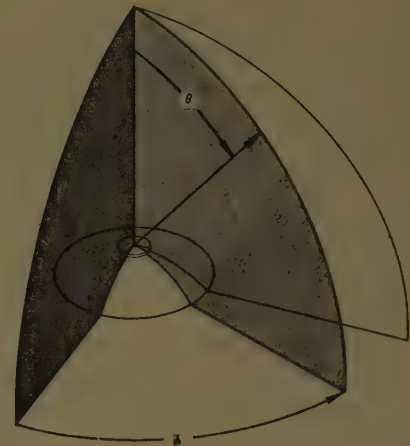


Fig. 1—Coordinate system used in pattern measurements.

mode leaks, and the leakage depends on curvature and depth of the trapping medium.

### Corrugated Disk

The experimental corrugated disk is shown in Fig. 2. The disk was fed at the center with a coaxial waveguide supporting propagation of the TEM mode. The center conductor of the coaxial guide extended slightly above the corrugations where it flared into a flat metal disk. The corrugations under this top plate were tapered from zero depth at the point of entry of the guide to the 1/16-inch depth at the "splash plate" extremity.

This taper was introduced to provide a gentle transition from the TEM radial-waveguide mode under the splash plate to the circularly symmetric TM surface-wave mode.

The theoretical elevation pattern of a corrugated disk which has the given parameters and is embedded in an infinite ground plane exhibits a beamwidth of  $17^\circ$ , a sidelobe level of  $-12$  db, and a gain of  $8.5$  db.<sup>1</sup>

Experimental radiation patterns were obtained for the corrugated disk at X-band frequencies ranging from 8200 mc to 10,000 mc. The elevation and azimuth plane patterns at 9600 mc, shown in Fig. 3 and Fig. 4, are typical of those observed over the entire frequency band. The only notable changes in pattern shape over the band were the anticipated lowering and narrowing of the main beam with increasing frequency. The finite extent of the disk causes diffraction which accounts for the main beam tilt of  $14^\circ$  and the broadening of the beamwidth to  $20^\circ$  noticeable in Fig. 3. The sidelobe level is only  $-2.5$  db and the gain figure obtained by pattern integration was  $6.5$  db relative to an isotropic radiator. The azimuth pattern displays the high degree of omnidirectionality of the antenna. Except for the sidelobe level, the departure of the experimental antenna performance from the theory is reasonable and can be explained in terms of the finite ground plane. By probing the field over the corrugated disk via the radial slot evident in Fig. 2, the cause for the poor sidelobe figure was traced to inefficient mode conversion at the

<sup>2</sup> R. S. Elliot, "Azimuthal surface waves on circular cylinders," *J. Appl. Phys.*, vol. 26, pp. 368-376; April, 1955.

<sup>3</sup> —, "Pattern Shaping with Surface Wave Antennas," Hughes Aircraft Co., Res. Labs., Tech. Memo. No. 360; March, 1955.

<sup>4</sup> A. S. Dunbar, et al., "Ridge and Corrugated Antenna Studies," Stanford Res. Inst., Menlo Park, Calif., Final Rep.; January, 1951.

<sup>5</sup> E. M. T. Jones, "An annular corrugated-surface antenna," *Proc. IRE*, vol. 40, pp. 721-725; June, 1952.

<sup>6</sup> A dielectric-clad disk antenna was also described by the Stanford group, but their interest seemed to be confined to perpendicular polarization.



Fig. 2—Corrugated disk antenna.

feed, indicating that the direct feed radiation was not adequately suppressed.<sup>7</sup> The fine lobe structure in the broadside (on-axis) region is due to diffraction of energy around the feed splash plate; methods for reducing the level of this radiation have been developed.

#### Dielectric Disk

The corrugated surface antenna of the preceding section can support only TM modes, and, consequently, polarization is perpendicular to the surface. A dielectric-clad surface, on the other hand, can support either TM or TE modes, thereby making a study of both polarizations possible. The structure of the TM mode essentially is the same whether propagating over a corrugated or a dielectric-guiding surface, so that the performance of a corrugated surface antenna is assumed to imply the performance of a dielectric-surface antenna of similar

<sup>7</sup> M. J. Ehrlich and L. Newkirk, "Corrugated-Surface Antennas," Hughes Aircraft Co., Res. Labs., Tech. Memo No. 297; February, 1953.

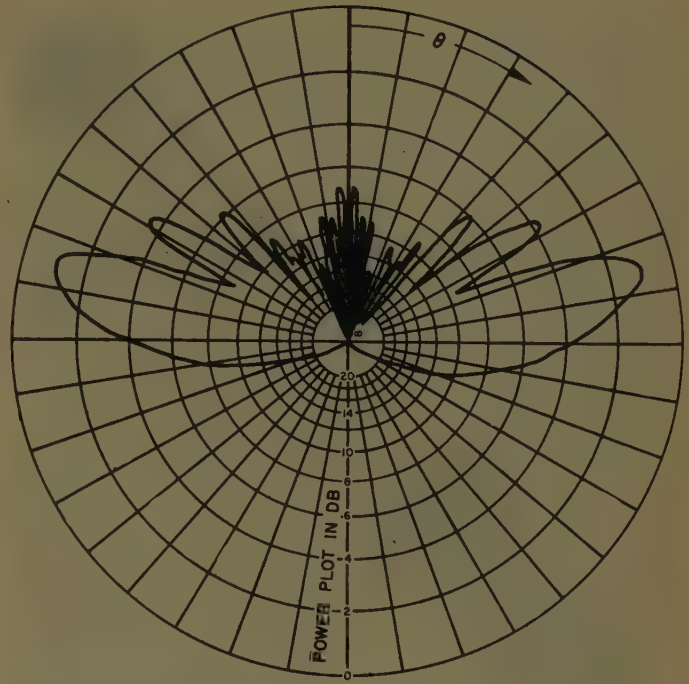


Fig. 3—Elevation pattern for corrugated disk at 9600 mc.

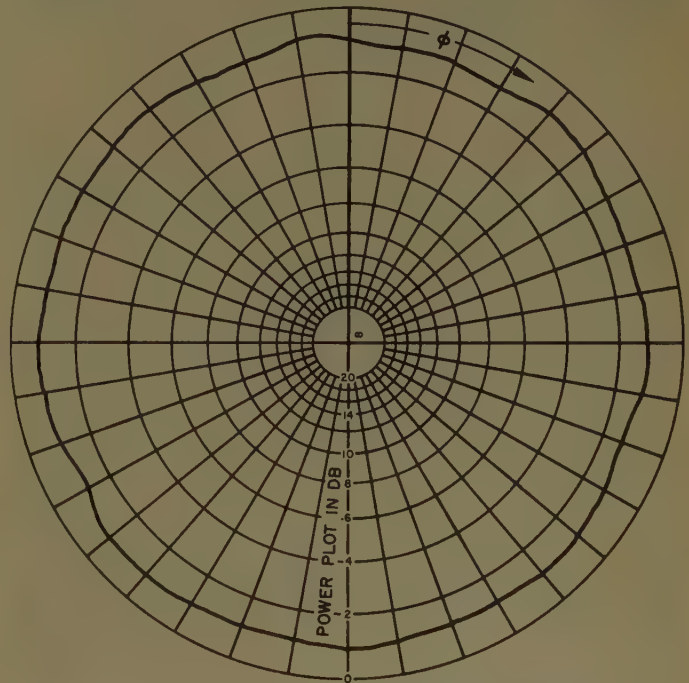
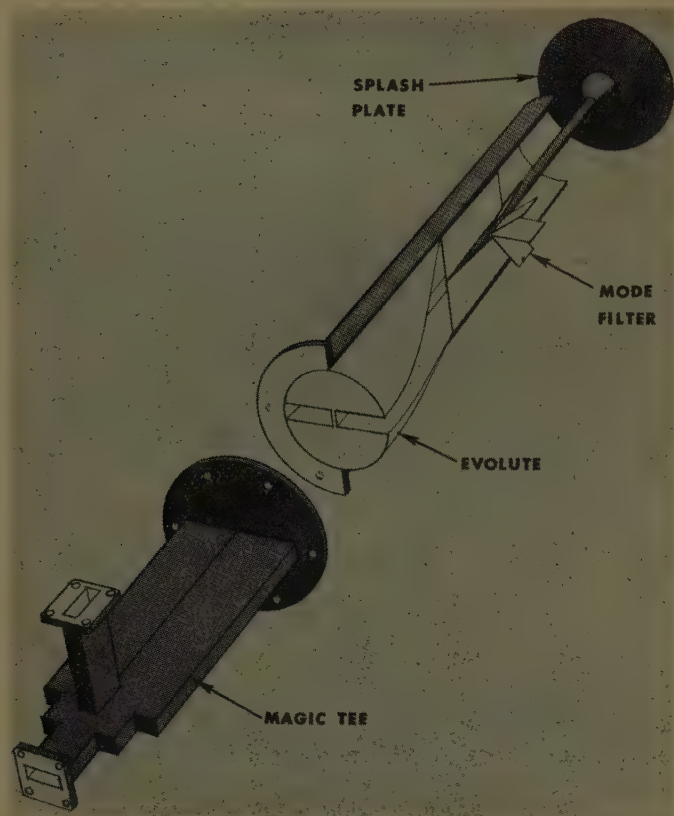


Fig. 4—Azimuth pattern for corrugated disk at 9600 mc.

geometry which is operating with the dominant TM mode. Thus, in the experimental study of spherical surface waves on dielectric surfaces, the emphasis was placed on the TE surface-wave mode for which the electric field is parallel to the surface.

The experimental dielectric disk antenna consisted of a lucite slab bounded on one side by a ground plane. The lucite slab and its ground plane had a diameter of 24 inches, and the thickness of the dielectric layer was



Fig. 5—Cutaway sketch of coaxial  $TE_{01}$  mode feed.

cut to 0.260 inch to appropriately trap the  $TE$  mode. The feed at the center of the disk consisted of a coaxial waveguide which was large enough to support the  $TE_{01}$  mode. The cutaway sketch of this feed shown in Fig. 5 indicates the means of launching and isolating the coaxial  $TE_{01}$  mode. The coaxial guide is fed in tandem by a magic tee whose side arms are folded in the  $H$  plane so that they lie side by side. A signal coupled into the difference arm of the tee divides in the side arms so that the electric fields in the arms are of equal amplitude but of opposite phase in a given transverse plane. When each of the broad walls of the side arms is bent slowly through  $90^\circ$  via the evolute section shown, the fields in the two arms finally join and a resultant field with circular shape emerges which forms the  $TE_{01}$  mode. The radial fins form a mode filter which destroys all the modes lower than the  $TE_{01}$  mode. The center conductor of the system is included primarily to provide support for the splash plate which is located slightly above the dielectric surface.

Radiation pattern measurements with the dielectric disk are typified by those shown in Fig. 6 and Fig. 7, which were recorded at a frequency of 9000 mc. The measurements covered a band from 8600 to 9600 mc over which the pattern shape is well represented by that of Fig. 6. Again, the finite disk size explains the beam tilt of  $11^\circ$  and the  $20^\circ$  beamwidth (Fig. 6), while the high sidelobe level of  $-2$  db is once more probably due

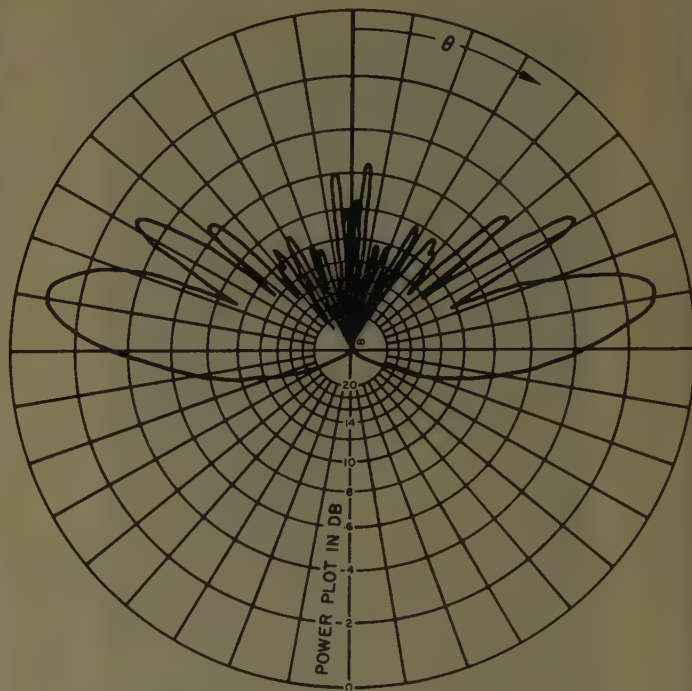


Fig. 6—Elevation pattern for dielectric disk at 9000 mc.

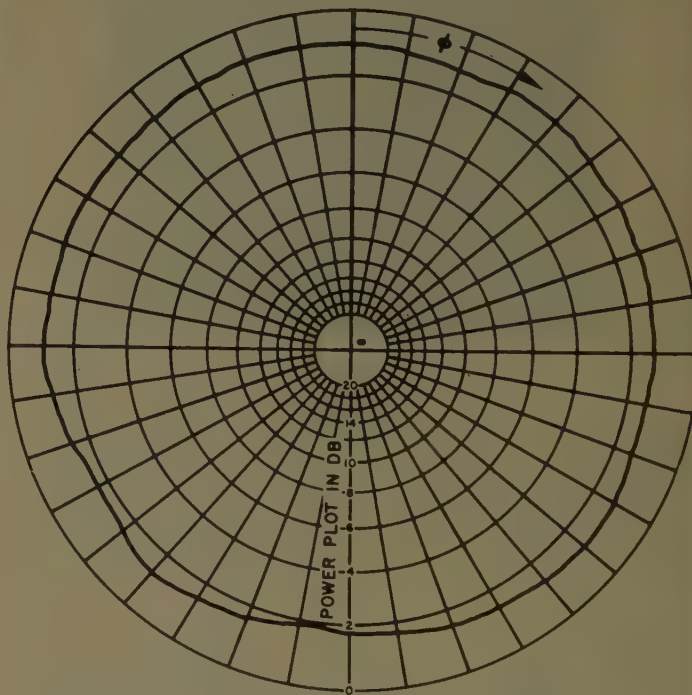


Fig. 7—Azimuth pattern for dielectric disk at 9000 mc.

to inefficient mode conversion at the feed. Additional evidence of the poor mode conversion is seen in the shallow nulls. The gain of the dielectric disk as determined by pattern integration is 6.0 db relative to an isotropic radiator. The azimuth pattern of Fig. 7 displays the good circularity obtained with the coaxial  $TE_{01}$  mode.

### Discussion

The elevation plane patterns of both the corrugated disk and the dielectric-clad disk exhibit nulls which are too deep for applications requiring solid high-angle coverage, while the upward tilt of the main beams prevents good horizon coverage for a horizontal installation of an antenna of this type. Both of these deficiencies can be overcome by the introduction of a curvature of the trapping surface, supplemented with tapering of the surface depth. It has been demonstrated<sup>3</sup> that these modifications give rise to a complex propagation coefficient for the surface wave which implies that the wave is no longer completely trapped but "leaks" as it traverses the modified surface.

This leakage radiation tends to fill in the nulls of the elevation pattern while affecting the pattern maxima very little; pattern shaping can be accomplished if the amount of this leakage radiation can be controlled over a sufficient range. Furthermore, if the radius of curvature is properly chosen, the main beam of the pattern can be tilted downward for good horizon coverage, since the "unleaked" part of the wave is launched at an angle below the horizon which is determined by the surface curvature.

### III. EXPERIMENTAL SPHERICAL-CAP ANTENNAS

The theoretical analysis of surface waves on spheres by Elliott<sup>1</sup> shows that, for both corrugated and dielectric-clad surfaces, the approximate propagation coefficient is a complex number  $\gamma = \beta + i\alpha$ , where  $\beta$  is the phase coefficient and  $\alpha$  is the attenuation coefficient which essentially measures the "leakage" of the quasi-trapped wave. For spheres of large radius, it is shown that  $\beta \gg \alpha$  and, consequently, a first approximation to the propagation equation assumes  $\gamma \cong \beta$ . This approximation improves as the sphere radius increases. A plot of  $\beta$  as a function of sphere radius  $a$  shows that  $\beta$  is a slowly varying function of  $a$  and smoothly approaches the value for a flat disk as  $a$  is increased. The first approximation  $\beta$  is then employed by Elliott<sup>1</sup> to calculate  $\alpha$  and a new value of  $\beta$ . Results of this type of calculation are included here in Table I for ease of reference. It is seen from Table I that  $\alpha$  has a considerable range as a function of the sphere radius and the corrugation geometry. The results of this theoretical analysis indicate that an essential tool is available for improving the patterns of the disk antennas. By shaping the trapping surface in the form of a spherical cap, the leaked portion of the spherical surface wave gives rise to a pattern similar to that of the flat disk, except that the energy is launched at an angle below the horizon determined by the radius of the sphere. The leaked part of the wave contributes energy which tends to fill in the nulls of the pattern of the leaked part. By choosing the sphere radius and surface parameters appropriately, the resultant pattern can be made to exhibit essentially solid

TABLE I

FIRST AND SECOND APPROXIMATIONS TO PROPAGATION CONSTANTS FOR LATITUDINAL SURFACE WAVES OVER CORRUGATED SPHERES

$ka$	$C^*$	First Approximation ( $\beta a$ )	Second Approximation ( $\gamma a$ )
60	0.267	62.5	63 + 0.9 <i>i</i>
	0.419	65.5	65.5 + 0.2 <i>i</i>
	0.751	74.5	74.5 + 2 × 10 <sup>-6</sup> <i>i</i>
	1.128	89.5	89.5 + 3 × 10 <sup>-16</sup> <i>i</i>
120	0.274	125.5	125.5 + 0.5 <i>i</i>
	0.443	131.5	131.5 + 0.01 <i>i</i>
	0.751	149.5	149.5 + 7 × 10 <sup>-12</sup> <i>i</i>
	1.123	179.5	179.5 + 7 × 10 <sup>-23</sup> <i>i</i>
480	0.311	503.5	503.5 + 0.002 <i>i</i>
	0.455	527.5	527.5 + 3 × 10 <sup>-11</sup> <i>i</i>
	0.750	599.5	599.5 + 4 × 10 <sup>-47</sup> <i>i</i>
	1.119	719.5	719.5 + 4 × 10 <sup>-184</sup> <i>i</i>
960	0.316	1007.5	1007.5 + 10 <sup>-7</sup> <i>i</i>
	0.457	1055.5	1055.5 + 3 × 10 <sup>-26</sup> <i>i</i>
	0.750	1199.5	1199.5 + 2 × 10 <sup>-95</sup> <i>i</i>
	1.119	1439.5	1439.5 + 10 <sup>-208</sup> <i>i</i>

\*  $C$ , which is a function of the corrugation geometry defining the role of the corrugation parameters in the determination of the propagation coefficients, is given by:

$$C = \sqrt{\frac{\epsilon_0}{\epsilon}} \frac{\theta_g}{\theta_g + \theta_t} \tan k(a - b)$$

where

$(a - b)$  = corrugation gap depth,

$\theta_g$  = central angle subtended by a gap,

$\theta_t$  = central angle subtended by a tooth,

$k = 2\pi/\lambda$  = wave number for dielectric material in the gaps,

$\epsilon_0$  = permittivity of free space,

$\epsilon$  = permittivity of material in the gaps.

coverage in the elevation plane with the main beam on the horizon.

It is apparent from Table I that it is possible to achieve a desired  $\alpha$  with any one of a number of combinations of sphere radius and corrugation geometry. The design problem is simplified by restricting attention to spheres of large radius. Even with this restriction, there is not a straight forward procedure for optimum design of a spherical-cap antenna. (An optimum design is considered to be one which provides the desired solid coverage in the elevation plane with minimum surface curvature.)

The experimental spherical caps were designed by arbitrarily choosing a sphere radius and then adjusting the surface parameters to yield a desired phase coefficient. For maximum gain of an endfire antenna, the phase coefficient must satisfy

$$(\beta - k_0)l = \pi \quad (1)$$

where

$\beta$  = surface-wave phase coefficient,

$k_0 = 2\pi/\lambda_0$  = free-space wave number,

$l$  = length of antenna or surface.

(This expression is the well-known Hansen-Woodyard condition for maximum gain of endfire systems.) The experiments showed that, in order to make the sphere



radius large enough to satisfy a low-silhouette requirement and still achieve an adequate leakage (sufficiently large  $\alpha$ ), the phase coefficient had to be less than that specified by (1). Hence, (1) was used only as a guide in the spherical cap designs. After a value for  $\beta$  is chosen, the trapping surface can be designed by use of the appropriate propagation equation for a flat surface. The equations for flat surfaces are justified in this connection, since for large radii  $\beta$  is essentially independent of the sphere radius.

#### Corrugated Spherical-Cap Antenna

A photograph of the experimental corrugated spherical cap is shown in Fig. 8. The sphere radius was chosen as 25.5 inches (this radius was dictated by the fact that the maximum thickness of available aluminum plate was 3 inches). Except for the radius, the cap dimensions corresponded to those of the corrugated disk. The corrugated sphere was again driven with the coaxial TEM mode feed.

The normalized length of the trapping surface was chosen as 10 free-space wavelengths, so that (1) specifies  $\beta/k_0 = 1.05$ . This value is too large for the reasons discussed following (1). The ratio  $\beta/k_0$  is related to the corrugation parameters of a flat corrugated surface by<sup>8</sup>

$$\beta/k_0 = \sqrt{1 + \left(\frac{G}{G+T}\right)^2 \tan^2(k_0 h)} \quad (2)$$

where

- $\beta$  = surface wave phase coefficient,
- $k_0 = 2\pi/\lambda_0$  = free space wave number,
- $G$  = corrugation gap width,
- $T$  = corrugation tooth width,
- $h$  = corrugation tooth height.

For the experimental spherical cap,  $G = T = h = 1/16$  inch, so that  $\beta/k_0 \cong 1.015$  from (2) for the frequency 9600 mc.

The approximate theoretical complex propagation coefficient for this surface configuration in terms of the sphere radius was found to be  $\gamma a = \beta a + i\alpha a = 124 + i1.4$ , indicating a total leakage from the spherical surface wave of approximately 60 per cent of its original power content, since the power decays as  $\exp[-2\alpha a\theta]$ . If it is assumed that the trapped portion of the spherical surface wave radiates a pattern similar to that of Fig. 3, and that, to a crude approximation, the pattern of the leaked part is hemispherically isotropic, it could be expected that the first null of the elevation pattern would be filled in to a level of  $-3$  db, and succeeding nulls filled in correspondingly. Furthermore, the untrapped part of the wave is launched at an angle  $28^\circ$  below the horizon, so that the beam tilt could be expected to be less than



Fig. 8—Corrugated spherical-cap antenna.

the  $+14^\circ$  of Fig. 3, but no less than  $-14^\circ$ .

The experimental results obtained using the corrugated spherical cap generally substantiated these predictions. Fig. 9 displays the radiation pattern measured at 9600 mc. Generally, the shape of the patterns measured over a frequency band extending from 8200 to 10,000 mc was the same as that shown in Fig. 9, with the nulls filling in even more than as shown and the beam rising up toward the horizon level at the lower frequencies. Considerable null-filling was achieved providing solid coverage for about  $45^\circ$  of elevation. The beam is seen to be depressed about  $4^\circ$  below the horizon in Fig. 9 or a total of  $18^\circ$  depression relative to the pattern of Fig. 3. The calculated pattern gain at 9600 mc was 5.1 db (contrasted with 6.5 db for the corrugated disk), indicating the cost of null-filling and beam placement.

Additional improvement of the elevation patterns was obtained by tapering the corrugations of the spherical-cap antenna, thereby introducing additional leakage radiation. Fig. 10 shows the elevation pattern observed at 9600 mc after the corrugation gap depth was smoothly tapered latitudinally from  $1/16$  inch at the feed aperture to zero depth at the cap edge. The result shown is indicative of the pattern shaping that can be achieved with proper control of the surface geometry and the sphere radius. The beam is seen to remain somewhat below the horizon, but the improvement in null-filling is considerable. An improved design would require slightly less curvature of the trapping surface, a shallower initial corrugation depth, or a combination of both

<sup>8</sup> R. S. Elliott, "On the theory of corrugated plane surfaces," IRE TRANS., vol. AP-2, pp. 71-81; April, 1954.

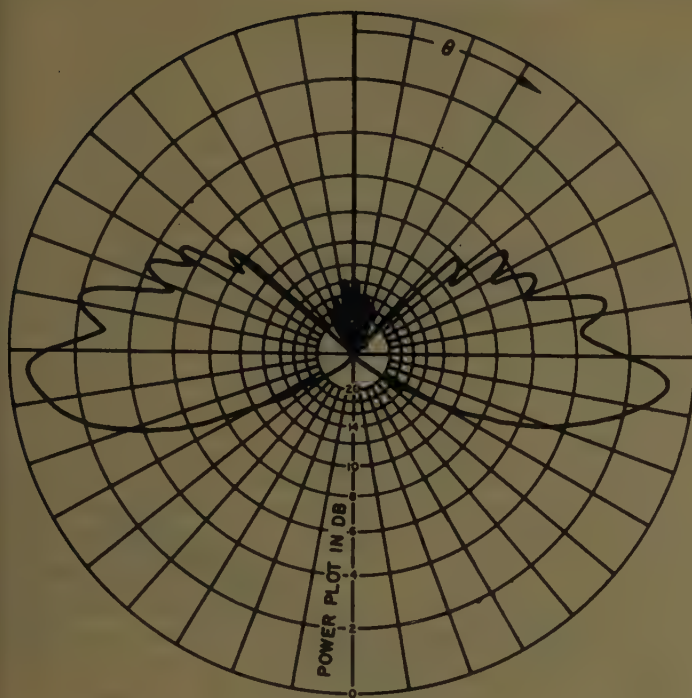


Fig. 9—Elevation pattern for corrugated sphere at 9600 mc.

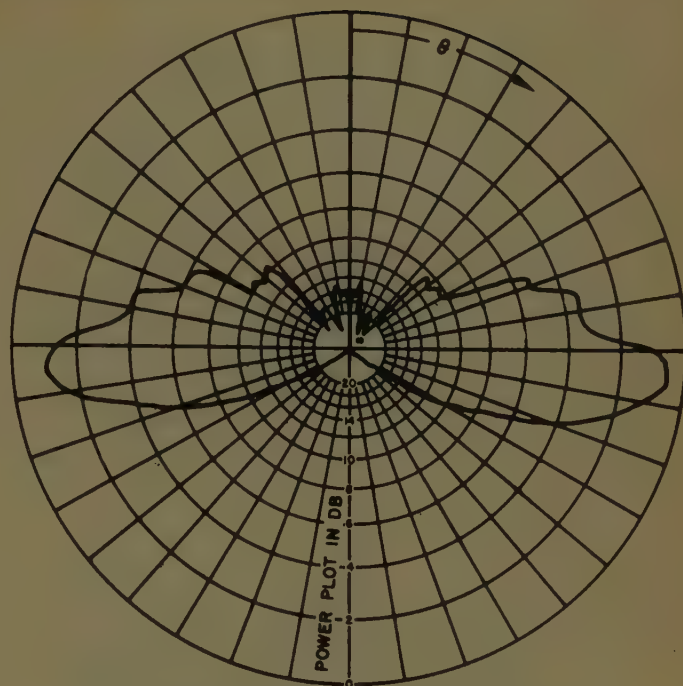


Fig. 10—Elevation pattern for tapered-tooth corrugated sphere at 9600 mc.

to direct the beam better and still provide the desired null-filling. Improved feed mode conversion efficiency should result in a better sidelobe level, permitting the attainment of a pattern shape approaching  $\csc^2\theta$  in elevation.

The input vswr of the corrugated spherical-cap was measured by inserting a probe through an axial slot in the outer conductor of the TEM coaxial mode feed. A plot of input vswr vs frequency is shown in Fig. 11.

#### Dielectric Spherical-Cap Antenna

The experimental dielectric spherical cap was constructed to provide the 25.5-inch sphere radius which was employed with the corrugated sphere and to maintain the surface parameters of the dielectric disk. The dielectric sphere was driven with the coaxial  $TE_{01}$  mode feed.

The surface parameters for both the disk and spherical cap were obtained from the transcendental relation

$$\cot [k_0 t \sqrt{\epsilon_r - (\beta/k_0)^2}] = (-) \sqrt{\frac{(\beta/k_0)^2 - 1}{\epsilon_r - (\beta/k_0)^2}} \quad (3)$$

where

- $\beta$  = surface wave phase coefficient,
- $k_0 = 2\pi/\lambda_0$  = free-space wave number,
- $t$  = thickness of dielectric layer,
- $\epsilon_r$  = relative permittivity of the dielectric material.

Eq. (3) relates the phase coefficient to the thickness of the uniform dielectric layer and to the dielectric constant for TE-type surface-wave modes over a flat dielectric surface. To obtain  $\beta/k_0 \cong 1.015$  as for the corrugated

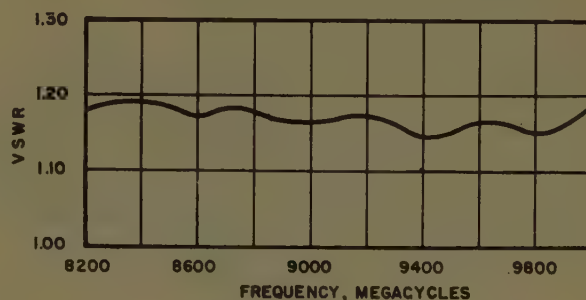


Fig. 11—Input vswr vs frequency for corrugated spherical-cap antenna.

surfaces, it was found that a lucite thickness of approximately 0.260 inch satisfied (3) for the 9000-mc design frequency.

Computation of the theoretical complex propagation coefficients for dielectric spheres is exceedingly difficult and has not been carried out; however, the results of computations for the propagation coefficients associated with azimuthal surface waves on circular cylinders suggested that, if two cylinders of the same radius had the same phase coefficient  $\beta$ , then they would have the same attenuation coefficient  $\alpha$  regardless of the method used to trap the waves or the polarization. If this "property" could be inferred to apply to the spherical geometry, then the results obtained for the corrugated sphere could be applied to the dielectric spheres. With this assumption and in view of the identical phase coefficients for the corrugated and dielectric spheres and their geometric similarity, the predictions of corrugated



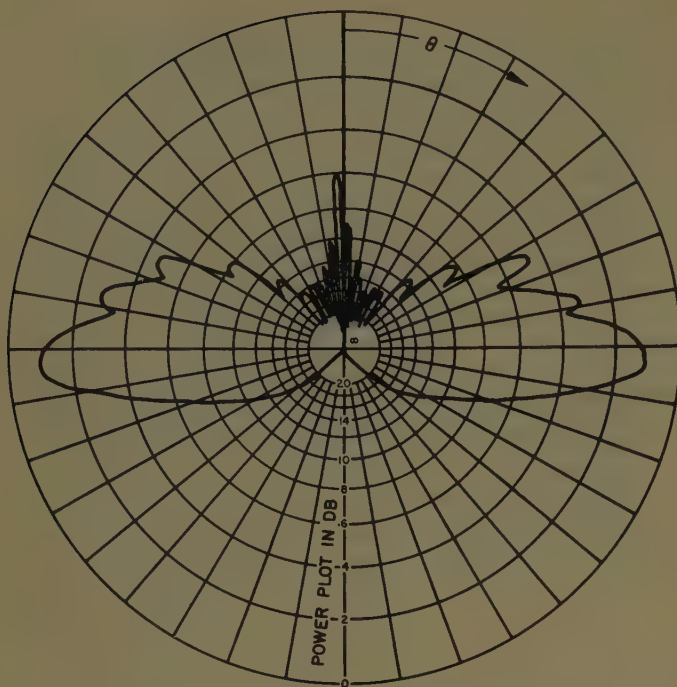


Fig. 12—Elevation pattern for dielectric sphere at 9000 mc.

sphere performance would also apply to the dielectric sphere.

Once more the broad predictions were borne out by experiment. The elevation pattern shown in Fig. 12 for the dielectric sphere at 9000 mc should be compared with the pattern of the dielectric disk (Fig. 6). The pattern shape for the sphere held up over a 8600 to 9600-mc frequency band. The null-filling achieved with the dielectric sphere was comparable to that characteristic of the corrugated sphere. Again, the main beam is depressed below the horizon about  $4^\circ$ , indicating that slightly less curvature, or reduced dielectric thickness, or both would be necessary in an improved design. The calculated pattern gain at 9000 mc was 5.5 db indicating a cost of only 0.5 db for the improvements, relative to the disk pattern.

No attempt was made to improve further the elevation pattern of the dielectric spherical-cap, but earlier experiments with a tapered dielectric disk indicated that additional null-filling could be achieved by introducing a smooth latitudinal taper of the dielectric thickness.

The input vswr of the dielectric spherical cap was measured by attaching an X-band slotted line to the difference arm of the magic-tee feed. The results of the measurement are shown in Fig. 13. These values could be improved by careful attention to the feed mechanism.

Experimental results for a dielectric sphere supporting the TM surface-wave mode are not presented here. It is felt that the performance of the corrugated sphere represents the case for perpendicular polarization and that inclusion of material for the TM mode over a dielectric surface would be redundant.

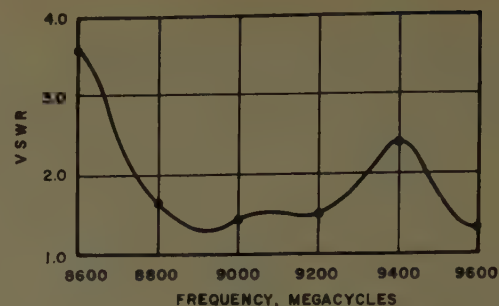


Fig. 13—Input vswr vs frequency for dielectric spherical-cap antenna.

### Discussion

The radiation patterns which have been presented for the corrugated and dielectric spherical-cap antennas do not necessarily represent the optimum in performance for such structures. A summary of the measured characteristics of these antennas is presented in Table II, with similar characteristics of the disk antennas. Some remarks have already been made with respect to design modifications which should yield improved pattern shapes. Sufficient data have been presented to show the capability of a spherical-cap antenna and to show the method of tailoring a spherical cap to a specific application.

The low-silhouette feature of surface-wave antennas was compromised only slightly with the spherical caps to achieve the improvements in performance relative to the flat disks; both the corrugated and the dielectric spherical caps had on-axis depths which did not exceed  $3\lambda_0$ .

### IV. DUAL-MODE STUDIES

The corrugated and dielectric-clad spherical-cap configurations which have been described offer a choice of either vertically or horizontally polarized beacon antennas. In the forms shown, neither of the antennas is capable of simultaneously supporting propagation of waves containing both polarization components in a desirable manner. A more versatile antenna is envisioned in which polarization could be switched from vertical to horizontal or to any arbitrary polarization without appreciably altering the pattern shape and position. The inability of the corrugated surface to support a TE trapped-wave mode would preclude its use in a "dual-polarization" arrangement. On the other hand, a dielectric-clad surface can be made to support either TE or TM modes.

A difficulty arises in attempting to combine both the TE and TM modes over a dielectric surface since, for a given dielectric constant and dielectric thickness, the two modes propagate with different velocities, and thus have radiation patterns which are different both in shape and position. At least two surface modifications are possible which *will* enable both modes to propagate with identical velocities and, hence, to exhibit essentially identical radiation patterns. One possibility would

TABLE II  
SUMMARY OF MEASURED CHARACTERISTICS OF EXPERIMENT ANTENNAS

Type of Antenna	Frequency Band (Megacycles)	Characteristics at Corresponding Optimum Frequency			
		Main Beam Tilt (degrees)	Beamwidth (degrees)	Sidelobe Level (db)	Gain (db)
Corrugated Disk	8200-10,000	+14	22	-2.5	6.5
Dielectric Disk	8600-9600	+11	21	-2.0	6.0
Corrugated Spherical Cap	8200-10,000	-4	*	-2.0	5.1
Tapered-Tooth					
Corrugated Spherical Cap	8200-10,000	-4	*	-3.0	5.6
Dielectric Spherical Cap	8600-9600	-4	*	-2.3	5.5

\* Measurement of beamwidth is meaningless at 3-db level.

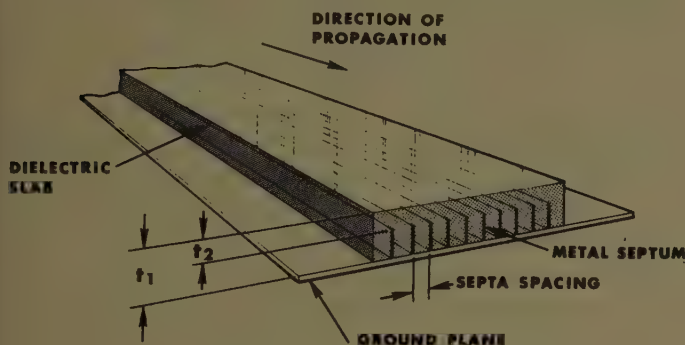


Fig. 14—Sketch of modified-dielectric surface for dual-mode propagation.

be to employ a double-layer or multiple-layer dielectric surface,<sup>9,10</sup> the thickness and dielectric constant of the material in each layer being determined so as to trap both modes to the same degree. An alternative method involves the use of a "mode filter" consisting of septa embedded within the single dielectric slab whose initial thickness and dielectric constant are adjusted for a given "trapping" of the TE mode. The diagram in Fig. 14 shows the cross section of a dielectric surface containing septa arranged in the manner described. The septa are spaced considerably less than  $\lambda/2$  in the dielectric medium so that electric field polarized parallel to them is reflected while polarization perpendicular to the septa does not see them if they are very thin. The thickness  $t_1$  shown in Fig. 14 would be initially chosen to trap the TE mode to the desired degree, while the height ( $t_1 - t_2$ ) of the septa would be adjusted so that the TM mode was trapped to that same degree or to any arbitrary degree desired.

An experimental study is presently in progress to evaluate methods for obtaining dual-mode surface-wave propagation and to determine design data for dual-polarization surface-wave antennas. Results thus far are very encouraging. Theoretical data on single-slab and double-slab arbitrary polarization surface-wave struc-

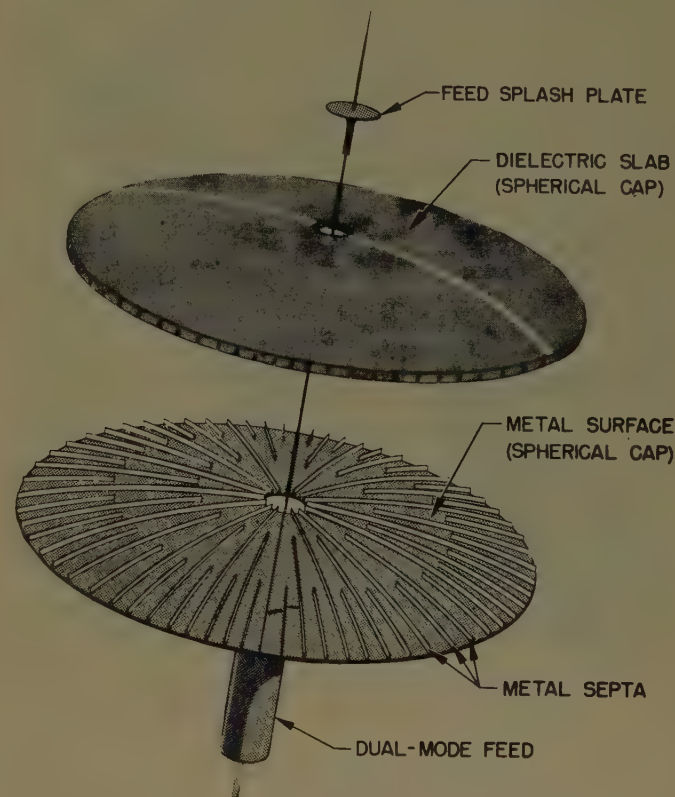


Fig. 15—Sketch of proposed dual-polarization beacon antenna.

tures also have been obtained.<sup>11</sup> It is believed that extension of methods outlined above to cylindrical and spherical geometries may be possible with at least one result being the realization of a beacon antenna allowing arbitrary polarization selection.

Fig. 15 shows a sketch of a proposed spherical cap configuration for dual polarization which utilizes a variation of the "mode filter" arrangement. Here, the septa are no longer parallel, so that additional, shorter lengths of septa are inserted as the spacing diverges beyond that necessary to ensure cutoff of the parallel polarized mode between the septa. Such an arrangement is conceptually plausible, but the difficulties of construction seem formidable.

Whatever the method used to provide for dual polar-

<sup>9</sup> H. Ehrenspeck, W. Gerbes, and F. J. Zucker, "Trapped wave antennas," 1954 IRE CONVENTION RECORD, pt. 1, pp. 25-30.

<sup>10</sup> R. E. Plummer and R. C. Hansen, "Double-Slab Arbitrary Polarization Surface-Wave Structure," IEE Monograph No. 238R; May, 1957. To be reprinted in pt. C, *Proc. IEE*.

<sup>11</sup> R. C. Hansen, "Single-slab arbitrary-polarization surface-wave structure," IRE TRANS., vol. MTT-5, pp. 115-120; April, 1957.





Fig. 16—Sketch of proposed dual-mode feed for beacon antenna.

ization of the spherical surface-wave fields, a dual-mode feed suitable for beacon antenna excitation would be necessary. Fig. 16 shows a sketch of a proposed feed which has the essential features required for this task. The proposed feed utilizes the  $TE_{01}$  coaxial mode feed used to drive the dielectric-clad surfaces with a modification consisting of an independent TEM coaxial line residing within the center conductor of the  $TE_{01}$  guide. The  $TE_{01}$  mode filter forms a transition section for the TEM line through gradual enlargement of the outer conductor until it coincides with the outer conductor of the  $TE_{01}$  guide. The center conductor of the inner system extends outward to support a splash plate which would be located above the trapping surface.

#### V. CONCLUSION

Experimental evidence has been given of the performance of corrugated and dielectric-clad spherical-cap antennas (see Table II). It has been demonstrated that, with appropriate control of surface geometries and sphere radii, the spherical caps exhibit radiation characteristics which make them suitable for beacon antenna applications, the corrugated sphere providing vertically polarized radiation, and the dielectric sphere providing either polarization. Both the corrugated and dielectric spherical-cap configurations have very low silhouettes, thus allowing their application to antenna problems where the vertical aspect must be minimized. Development of techniques for obtaining dual-polarization surface-wave propagation will materially extend the usefulness of these antennas.

#### ACKNOWLEDGMENT

The author is indebted to Dr. R. S. Elliott for his guidance of this study and to P. B. Pressman who assisted with the experiments.

## Mechanical and Electrical Tolerances for Two-Dimensional Scanning Antenna Arrays\*

ROBERT S. ELLIOTT†

**Summary**—An analysis is presented of the effect on radiation pattern of random errors in the construction of a two-dimensional scanning array.

\* Manuscript received by the PGAP, March 22, 1957; revised manuscript received, June 19, 1957. The research reported in this article was sponsored by the Rome Air Dev. Cr. and was performed under a consulting arrangement between the author and Hughes Aircraft Co.

† Rantec Corp., Calabasas, Calif.

Translational and rotational errors in the positions of all elements are assumed together with errors in the electrical excitations themselves. Translational errors are found to cause the dominant effect. A formula connecting side lobe level and errors is derived and representative curves are shown. For a given tolerance, pattern deterioration is found to decrease as the array is enlarged. For the same tolerance, pattern deterioration is less for a planar array of size  $L^2$  than it is for a linear array of length  $L$ . Side lobe increase due to random errors does not depend on scan angle.

## INTRODUCTION

THE subject of random errors in broadside antenna arrays has been treated previously by several authors. Ruze<sup>1</sup> considered the effect on the radiation pattern of random errors in the exciting currents. He used the restrictions that the magnitudes of all error currents be the same and that all phases of an error current be equally probable. The analysis essentially followed the method of Lord Rayleigh.<sup>2</sup> Ashmead<sup>3</sup> extended Ruze's work by assuming that each error current was the same fraction of the corresponding unperturbed current, all phases still being equally probable. For both cases, the probability distribution of the error radiation pattern is circular. Bailin and Ehrlich<sup>4</sup> took the problem one step further by considering the physical errors which cause the random errors in the exciting currents. They studied a symmetrical standing-wave-fed linear slot array and determined the effect on the radiation pattern of normally distributed errors in slot lengths and positions. As the authors point out, the analysis is equally applicable to a symmetrical broadside array of dipoles. Their work was furthered by O'Neill and Bailin<sup>5</sup> in a paper which provides results of many calculations based on the theory. Gilbert and Morgan<sup>6</sup> treated the effect on gain of random geometric errors in the general two-dimensional aperture.

The present analysis is intended to unify and extend these previous treatments. Of considerable current interest is the effect of random errors on the side lobe level of two-dimensional scanning arrays. Although this problem has not been studied previously, its solution can draw significantly from the prior theories. As a problem, it has the added advantage of generality and the problems treated in the earlier theories logically become special cases. Several interesting and significant conclusions can be stated for this general problem which were not evident in the special cases.

A two-dimensional array of dipoles is assumed, with three-dimensional translational errors of position permitted for each dipole, together with two-dimensional angular errors of orientation of individual dipoles. Random errors in the exciting current of each dipole are also included and the net effect on side lobe level is deduced. The theory considers only first-order errors but could be extended to grosser tolerances. The results can

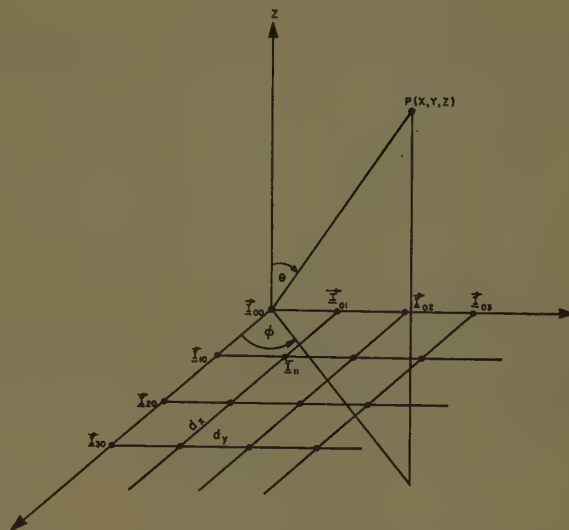


Fig. 1—Dipole arrangement and coordinate system.

also be applied to a two-dimensional dipole array backed by a ground plane and (with some care) to a two-dimensional slot array.

## THE RADIATION FIELD

Consider a two-dimensional array of dipoles arranged as shown in Fig. 1. The dipoles are meant to lie in the  $x-y$  plane with uniform separations  $d_x$  in the  $x$  direction and  $d_y$  in the  $y$  direction. The coordinates of the center of the  $m$ nth dipole are meant to be  $(md_x, nd_y, 0)$  but through constructional errors are actually  $(md_x + \xi_{mn}, nd_y + \eta_{mn}, \zeta_{mn})$  in which  $\xi_{mn}, \eta_{mn}, \zeta_{mn}$  are random errors. Similarly, the orientation of each dipole is meant to be parallel to the  $x$  axis, but through errors it is not. This is accounted for by writing the input current of the  $m$ nth dipole as<sup>7</sup>

$$\vec{I}_{mn} = \vec{u}_x I_{mn}^x + \vec{u}_y I_{mn}^y + \vec{u}_z I_{mn}^z \quad (1)$$

in which  $\vec{u}_x$  is a unit vector in the  $x$  direction, etc.

Define the angle that the projection of  $\vec{I}_{mn}$  on the  $x-y$  plane makes with the  $x$  axis as  $\alpha_{mn}$  and the angle that the projection of  $\vec{I}_{mn}$  on the  $x-z$  plane makes with the  $x$  axis as  $\beta_{mn}$ . Then, since  $I_{mn}^x, I_{mn}^y$ , and  $I_{mn}^z$  obviously have the same phase,

$$\begin{aligned} \sin \alpha_{mn} &= \frac{I_{mn}^y}{\sqrt{(I_{mn}^x)^2 + (I_{mn}^y)^2}} \cong \frac{I_{mn}^y}{I_{mn}}, \\ \cos \alpha_{mn} &\cong 1, \\ \sin \beta_{mn} &= \frac{I_{mn}^z}{\sqrt{(I_{mn}^x)^2 + (I_{mn}^z)^2}} \cong \frac{I_{mn}^z}{I_{mn}}, \end{aligned} \quad (2)$$

and

$$\cos \beta_{mn} \cong 1,$$

<sup>7</sup> An arrow over a quantity designates vector and a bar under it designates phasor.

<sup>1</sup> J. Ruze, "The effect of aperture errors on the antenna radiation pattern," *Suppl. Nuovo Cimento*, vol. 9, pp. 364-380; 1952.

<sup>2</sup> Lord Rayleigh, "Theory of Sound," Dover Publications, New York, N. Y., pp. 35-42; 1954.

<sup>3</sup> D. Ashmead, "Optimum design of linear arrays in the presence of random errors," *IRE TRANS.*, vol. AP-4, pp. 81-92; December, 1952.

<sup>4</sup> L. L. Bailin, and M. J. Ehrlich, "Factors affecting the performance of linear arrays," *PROC. IRE*, vol. 41, pp. 235-241; February, 1953.

<sup>5</sup> H. F. O'Neill, and L. L. Bailin, "Further effects of manufacturing tolerances on the performance of linear shunt slot arrays," *IRE TRANS.*, vol. AP-4, pp. 93-102; December, 1952.

<sup>6</sup> E. N. Gilbert and S. P. Morgan, "Optimum design of directive antenna arrays subject to random variations," *Bell Sys. Tech. J.*, vol. 34, pp. 637-663; May, 1955.



since  $I_{mn}^y$  and  $I_{mn}^z$  are small perturbations due to misalignment.  $\alpha_{mn}$  and  $\beta_{mn}$  will be chosen as the random errors which gauge the effect of this misalignment.

Now assume

$$\vec{I}_{mn} = \left( \vec{u}_x \frac{\overset{\circ}{I}_{mn}^x}{\overset{\circ}{I}_{mn}} + \vec{u}_y \frac{\overset{\circ}{I}_{mn}^y}{\overset{\circ}{I}_{mn}} + \vec{u}_z \frac{\overset{\circ}{I}_{mn}^z}{\overset{\circ}{I}_{mn}} \right) \cdot (\overset{\circ}{I}_{mn} e^{jm\Psi_x} e^{jn\Psi_y} + \overset{\circ}{i}_{mn}) \quad (3)$$

in which the superscript  $\circ$  indicates correct values<sup>8</sup> and  $\overset{\circ}{i}_{mn}$  is the complex random error current.  $\Psi_x$  and  $\Psi_y$  are the uniform progressive phase parameters which represent scanning.

Letting

$$\Omega_x = kd_x \sin \theta \cos \phi + \Psi_x, \quad (4)$$

$$\Omega_y = kd_y \sin \theta \sin \phi + \Psi_y \quad (5)$$

and approximating  $\sin \alpha_{mn}$ ,  $\sin \beta_{mn}$  by  $\alpha_{mn}$ ,  $\beta_{mn}$  respectively, one can deduce<sup>9</sup> that the far field is given by

$$\vec{H}(\theta, \phi) = f(\theta, \phi, l) \{ \vec{H}(\theta, \phi) + \delta \vec{H}(\theta, \phi) \} \quad (6)$$

in which  $f(\theta, \phi, l)$  is the ratio of the element pattern of the dipole of length  $l$  to the element pattern of an infinitesimal dipole, and

$$\begin{aligned} \vec{H} &= \vec{u}_\theta(h_1 + jg_1) + \vec{u}_\phi(h_2 + jg_2) \\ &= \vec{u}_\theta \sum_{m=0}^M \sum_{n=0}^N \sin \phi \overset{\circ}{I}_{mn} e^{jm\Omega_x} e^{jn\Omega_y} \\ &\quad + \vec{u}_\phi \sum_{m=0}^M \sum_{n=0}^N \cos \theta \cos \phi \overset{\circ}{I}_{mn} e^{jm\Omega_x} e^{jn\Omega_y} \end{aligned} \quad (7)$$

is the desired array pattern.

$$\begin{aligned} \delta \vec{H} &= \vec{u}_\theta(U_5 + jV_5) + \vec{u}_\phi(U_6 + jV_6) \\ &= \vec{u}_\theta(U_1 + jV_1 + U_2 + jV_2) \\ &\quad + \vec{u}_\phi(U_3 + jV_3 + U_4 + jV_4) \end{aligned} \quad (8)$$

is the error in the array pattern with

$$\begin{aligned} U_1 &= - \sum_{m=0}^M \sum_{n=0}^N \{ \sin \phi \sin(m\Omega_x + n\Omega_y) \cdot [k\xi_{mn} \sin \theta \cos \phi \\ &\quad + k\eta_{mn} \sin \theta \sin \phi + k\xi_{mn} \cos \theta] \\ &\quad + \cos \phi \cos(m\Omega_x + n\Omega_y) \cdot \alpha_{mn} \} \overset{\circ}{I}_{mn}, \end{aligned} \quad (9)$$

$$\begin{aligned} V_1 &= \sum_{m=0}^M \sum_{n=0}^N \{ \sin \phi \cos(m\Omega_x + n\Omega_y) \cdot [k\xi_{mn} \sin \theta \cos \phi \\ &\quad + k\eta_{mn} \sin \theta \sin \phi + k\xi_{mn} \cos \theta] \\ &\quad - \cos \phi \sin(m\Omega_x + n\Omega_y) \cdot \alpha_{mn} \} \overset{\circ}{I}_{mn}, \end{aligned} \quad (10)$$

<sup>8</sup> Here,  $\overset{\circ}{I}_{mn}^y$  and  $\overset{\circ}{I}_{mn}^z$  are considered "correct" in the sense that  $\overset{\circ}{I}_{mn}$  is correct and

$$\overset{\circ}{I}_{mn} = \sqrt{(\overset{\circ}{I}_{mn}^x)^2 + (\overset{\circ}{I}_{mn}^y)^2 + (\overset{\circ}{I}_{mn}^z)^2}.$$

<sup>9</sup> For the details of this analysis, the reader is referred to R. S. Elliott, "Mechanical and Electrical Tolerances for Two-Dimensional Scanning Antenna Arrays," Hughes Aircraft Co., Culver City, Calif., Tech. Memo. no. 354; July, 1956.

$$U_2 + jV_2 = \sum_{m=0}^M \sum_{n=0}^N \sin \phi \overset{\circ}{I}_{mn} e^{jm(\Omega_x - \Psi_x)} e^{jn(\Omega_y - \Psi_y)}, \quad (11)$$

$$\begin{aligned} U_3 &= - \sum_{m=0}^M \sum_{n=0}^N \{ \cos \theta \cos \phi \sin(m\Omega_x + n\Omega_y) \\ &\quad \cdot [k\xi_{mn} \sin \theta \cos \phi + k\eta_{mn} \sin \theta \sin \phi + k\xi_{mn} \cos \theta] \\ &\quad - \cos \theta \sin \phi \cos(m\Omega_x + n\Omega_y) \cdot \alpha_{mn} \\ &\quad + \sin \theta \cos(m\Omega_x + n\Omega_y) \cdot \beta_{mn} \} \overset{\circ}{I}_{mn}, \end{aligned} \quad (12)$$

$$\begin{aligned} V_3 &= \sum_{m=0}^M \sum_{n=0}^N \{ \cos \theta \cos \phi \cos(m\Omega_x + n\Omega_y) \\ &\quad \cdot [k\xi_{mn} \sin \theta \cos \phi + k\eta_{mn} \sin \theta \sin \phi + k\xi_{mn} \cos \theta] \\ &\quad + \cos \theta \sin \phi \sin(m\Omega_x + n\Omega_y) \cdot \alpha_{mn} \\ &\quad - \sin \theta \sin(m\Omega_x + n\Omega_y) \cdot \beta_{mn} \} \overset{\circ}{I}_{mn}, \end{aligned} \quad (13)$$

$$U_4 + jV_4 = \sum_{m=0}^M \sum_{n=0}^N \cos \theta \cos \phi \overset{\circ}{I}_{mn} e^{jm(\Omega_x - \Psi_x)} e^{jn(\Omega_y - \Psi_y)}. \quad (14)$$

#### PROBABILITY DISTRIBUTION OF THE RADIATION FIELD

If it is assumed that  $\xi_{mn}$ ,  $\eta_{mn}$ ,  $\zeta_{mn}$ ,  $\alpha_{mn}$ , and  $\beta_{mn}$  are all independent and normally distributed, with means zero, and variances  $\sigma_\xi^2$ ,  $\sigma_\eta^2$ ,  $\sigma_\zeta^2$ ,  $\sigma_\alpha^2$ , and  $\sigma_\beta^2$ , respectively, then, except in the region of the main beam,  $(U_1, V_1)$  and  $(U_3, V_3)$  have approximately symmetric bivariate normal distributions. If it is assumed that  $\overset{\circ}{i}_{mn}$  has a normally distributed amplitude, with variance  $\sigma_{mn}^2$ , and a uniformly distributed phase,<sup>10</sup> the distributions of  $(U_2, V_2)$  and  $(U_4, V_4)$  are also symmetric, bivariate normal. If it is assumed that  $U_1 + jV_1$  and  $U_2 + jV_2$  are independent, and that  $U_3 + jV_3$  and  $U_4 + jV_4$  are also independent,<sup>10</sup> the distributions of  $(U_5, V_5)$  and  $(U_6, V_6)$  can be derived. These distributions are also found to be symmetric bivariate normal.

Under all these foregoing assumptions, it is possible to find the random distribution of the entire array pattern. Let

$$U_7 + jV_7 = h_1 + jg_1 + U_5 + jV_5, \quad (15)$$

$$U_8 + jV_8 = h_2 + jg_2 + U_6 + jV_6. \quad (16)$$

Then  $U_7 + jV_7$  is the  $\theta$  component of the entire array pattern, including errors, and, likewise,  $U_8 + jV_8$  is the  $\phi$  component of the entire array pattern including errors.

The probability distributions of  $U_7^2 + V_7^2$  and  $U_8^2 + V_8^2$  follow readily. The means of these distributions are given by

$$\mathfrak{M}(U_7^2 + V_7^2) = h_1^2 + g_1^2 + 2\sigma_\theta^2, \quad (17)$$

$$\mathfrak{M}(U_8^2 + V_8^2) = h_2^2 + g_2^2 + 2\sigma_\phi^2, \quad (18)$$

in which

<sup>10</sup> These assumptions will be reconsidered later.

$$\begin{aligned} \sigma_\theta^2 = & \frac{1}{2} \{ k^2 \sigma_\xi^2 \sin^2 \theta \sin^2 \phi \cos^2 \phi + k^2 \sigma_\eta^2 \sin^2 \theta \sin^4 \phi \\ & + k^2 \sigma_\zeta^2 \cos^2 \theta \sin^2 \phi + \sigma_\alpha^2 \cos^2 \phi \} \sum_{m=0}^M \sum_{n=0}^N \dot{I}_{mn}^2 \\ & + \sin^2 \phi \sum_{m=0}^M \sum_{n=0}^N \sigma_{mn}^2, \end{aligned} \quad (19)$$

$$\begin{aligned} \sigma_\phi^2 = & \frac{1}{2} \{ k^2 \sigma_\xi^2 \sin^2 \theta \cos^2 \theta \cos^4 \phi \\ & + k^2 \sigma_\eta^2 \sin^2 \theta \cos^2 \theta \sin^2 \phi \cos^2 \phi \\ & + k^2 \sigma_\zeta^2 \cos^4 \theta \cos^2 \phi + \sigma_\alpha^2 \cos^2 \theta \sin^2 \phi \\ & + \sigma_\beta^2 \sin^2 \theta \} \sum_{m=0}^M \sum_{n=0}^N \dot{I}_{mn}^2 \\ & + \cos^2 \theta \cos^2 \phi \sum_{m=0}^M \sum_{n=0}^N \sigma_{mn}^2. \end{aligned} \quad (20)$$

### THE MEAN SIDE LOBE LEVEL

Let the main beam be pointed in the direction  $(\theta_T, \phi_T)$ . From (4) and (5), these angles are defined by

$$0 = kd_x \sin \theta_T \cos \phi_T + \Psi_x, \text{ and} \quad (21)$$

$$0 = kd_y \sin \theta_T \sin \phi_T + \Psi_y. \quad (22)$$

From (7)

$$\begin{aligned} |\vec{H}(\theta_T, \phi_T)|^2 = & \{ \sin^2 \phi_T + \cos^2 \theta_T \cos^2 \phi_T \} \\ & \cdot \left\{ \sum_{m=0}^M \sum_{n=0}^N \dot{I}_{mn}^2 \right\}^2. \end{aligned} \quad (23)$$

For a side lobe pointing in the direction  $(\theta, \phi)$ , the mean side lobe level is therefore

$$\mathfrak{M} = 10 \log_{10} \frac{(\sin^2 \phi_T + \cos^2 \theta_T \cos^2 \phi_T) \left( \sum_{m=0}^M \sum_{n=0}^N \dot{I}_{mn}^2 \right)^2 f^2(\theta_T, \phi_T, l)}{\{h_1^2 + g_1^2 + h_2^2 + g_2^2 + 2(\sigma_\theta^2 + \sigma_\phi^2)\} f^2(\theta, \phi, l)}. \quad (24)$$

The *design* side lobe level is customarily chosen with the main beam at broadside and the dipoles are customarily oriented so that  $f(\theta, \phi, l)$  has its maximum value at broadside. Under these assumptions, and with  $f(\theta, \phi, l)$  normalized,

$$D = 10 \log_{10} \frac{\left( \sum_{m=0}^M \sum_{n=0}^N \dot{I}_{mn}^2 \right)^2}{\{h_1^2 + g_1^2 + h_2^2 + g_2^2\} f^2(\theta, \phi, l)} \quad (25)$$

is the design side lobe level, in which  $D$  is given in db. Combining (24) and (25) one obtains

$$\begin{aligned} \mathfrak{M} = & D + 10 \log_{10} (\sin^2 \phi_T + \cos^2 \theta_T \cos^2 \phi_T) f^2(\theta_T, \phi_T, l) \\ & - 10 \log_{10} \left\{ 1 + \frac{2(\sigma_\theta^2 + \sigma_\phi^2) 10^{D/10} f^2(\theta, \phi, l)}{\left( \sum_{m=0}^M \sum_{n=0}^N \dot{I}_{mn}^2 \right)^2} \right\}. \end{aligned} \quad (26)$$

Eq. (26) is the principal result of the analysis and relates the rise in side lobe level to scanning and to

random errors. The second term raises the side lobe level and is due to scanning. It is present whether there are random errors or not. The third term

$$\mathfrak{L} = 10 \log_{10} \left\{ 1 + \frac{2(\sigma_\theta^2 + \sigma_\phi^2) 10^{D/10} f^2(\theta, \phi, l)}{\left( \sum_{m=0}^M \sum_{n=0}^N \dot{I}_{mn}^2 \right)^2} \right\} \quad (27)$$

also causes a rise in the side lobe level and is due to random errors. By making proper estimates of the mechanical and electrical tolerances and evaluating  $\sigma_\theta^2$  and  $\sigma_\phi^2$  from (19) and (20), one can then determine  $\mathfrak{L}$  from (27) and thus relate side lobe deterioration to tolerances.

### SIMPLIFICATIONS

Suppose one assumes an array of dipoles for which

$$\sigma_\xi^2 = \sigma_\eta^2 = \sigma_\zeta^2 = \sigma_1^2, \quad (28)$$

$$\sigma_\alpha^2 = \sigma_\beta^2 = \sigma_2^2, \quad (29)$$

$$\sigma_{mn}^2 = F^2 \dot{I}_{mn}^2, \quad (30)$$

with

$$0 \leq F \leq 1. \quad (31)$$

These are reasonable assumptions and serve to simplify (19) and (20) so that

$$\begin{aligned} \sigma_\theta^2 = & \frac{1}{2} \{ k^2 \sigma_1^2 \sin^2 \phi + \sigma_2^2 \cos^2 \phi + 2F^2 \sin^2 \phi \} \\ & \cdot \sum_{m=0}^M \sum_{n=0}^N \dot{I}_{mn}^2. \end{aligned} \quad (32)$$

$$\begin{aligned} \sigma_\phi^2 = & \frac{1}{2} \{ k^2 \sigma_1^2 \cos^2 \theta \cos^2 \phi + \sigma_2^2 (\cos^2 \theta \sin^2 \phi + \sin^2 \theta) \\ & + 2F^2 \cos^2 \theta \cos^2 \phi \} \sum_{m=0}^M \sum_{n=0}^N \dot{I}_{mn}^2. \end{aligned} \quad (33)$$

Recalling that  $f^2(\theta, \phi, l)$  is normalized, it follows from (32) and (33) that

$$\begin{aligned} \mathfrak{L}_{\max} < & 10 \log_{10} \left\{ 1 + 10^{D/10} [k^2 \sigma_1^2 + 2\sigma_2^2 + 2F^2] \right. \\ & \cdot \frac{\sum_{m=0}^M \sum_{n=0}^N \dot{I}_{mn}^2}{\left( \sum_{m=0}^M \sum_{n=0}^N \dot{I}_{mn}^2 \right)^2} \left. \right\}. \end{aligned} \quad (34)$$

An additional simplification arises when the array is square with the same symmetric aperture distribution in both the  $x$  and  $y$  directions. For then  $M=N$  and

$$\dot{I}_{mn} = \dot{I}_{0,n} \frac{\dot{I}_{mn}}{\dot{I}_{0,n}} = \dot{I}_{0,n} \frac{\dot{I}_{0,m}}{\dot{I}_{0,0}} = \dot{I}_m \dot{I}_n \quad (35)$$

in which  $\dot{I}_m$  is the design current of a linear distribution.



Thus

$$\sum_{m=0}^M \sum_{n=0}^N \dot{I}_{mn}^2 = \sum_{m=0}^M \dot{I}_m^2 \sum_{n=0}^M \dot{I}_n^2 = \left( \sum_{m=0}^M \dot{I}_m^2 \right)^2 \quad (36)$$

$$\begin{aligned} \left( \sum_{m=0}^M \sum_{n=0}^N \dot{I}_{mn} \right)^2 &= \left( \sum_{m=0}^M \dot{I}_m \sum_{n=0}^M \dot{I}_n \right)^2 \\ &= \left( \sum_{m=0}^M \dot{I}_m \right)^4 \end{aligned} \quad (37)$$

and (34) becomes

$$\mathcal{L}_{\max} < 10 \log_{10} \left\{ 1 + 10^{D/10} [k^2 \sigma_1^2 + 2\sigma_2^2 + 2F^2] \frac{\left( \sum_{m=0}^M \dot{I}_m^2 \right)^2}{\left( \sum_{m=0}^M \dot{I}_m \right)^4} \right\} \quad (38)$$

#### ILLUSTRATIVE EXAMPLE

Eq. (38) will be used to demonstrate the effects which random tolerances have on side lobe level. Consider a square array of dipoles for which the design currents have been chosen to yield the same Dolph-Tchebyscheff pattern in both principal planes. Using known data for the current distributions,<sup>11</sup> Table I has been constructed and relates the ratio

$$\frac{\left( \sum_{m=0}^M \dot{I}_m^2 \right)^2}{\left( \sum_{m=0}^M \dot{I}_m \right)^4}$$

to the number of elements and the desired side lobe level.

A study of Table I and (38) points up several important general features. First, for a given number of elements, the ratio

$$\frac{\left( \sum_{m=0}^M \dot{I}_m^2 \right)^2}{\left( \sum_{m=0}^M \dot{I}_m \right)^4}$$

increases as the side lobe level is further suppressed. Second, for a given side lobe level, the ratio decreases as the number of elements is increased. These statements are generally true, and not just true for the cases cited in Table I. Thus, the rise in side lobe level, due to random errors, for a given set of tolerances:

- 1) for a given design side lobe level, decreases as the number of elements increases.
- 2) for a given number of elements, increases as the side lobe level is further suppressed.

<sup>11</sup> L. L. Bailin, R. S. Wehner, and I. P. Kaminow, "Empirical Approximations to the Current Values for Large Dolph-Tschebyscheff Arrays," Hughes Aircraft Co., Culver City, Calif., Tech. Mem. No. 328; October, 1953.

TABLE I

$\frac{\left( \sum_{m=0}^M \dot{I}_m^2 \right)^2}{\left( \sum_{m=0}^M \dot{I}_m \right)^4}$ for a Dolph-Tchebyscheff distribution vs number of elements and side lobe level			
No. of elements	$\frac{\left( \sum_{m=0}^M \dot{I}_m^2 \right)^2}{\left( \sum_{m=0}^M \dot{I}_m \right)^4}$		
	20 db	30 db	40 db
24	$19.7 \times 10^{-4}$	$22.8 \times 10^{-4}$	$28.8 \times 10^{-4}$
48		$5.67 \times 10^{-4}$	$7.07 \times 10^{-4}$
144			$0.770 \times 10^{-4}$

The second of these two conclusions is not surprising, but the first appears contrary to intuition. It means that if a given tolerance of construction can be maintained, the bigger one makes an antenna the less damaging will be the effect of random errors on the pattern. The explanation for this seeming paradox is that the gain is increasing more rapidly than the contribution of random errors to the side lobe level.

Even more significant is the fact that if the tolerance is assumed to increase linearly with the size of the antenna (a most pessimistic assumption) the effect of random errors still decreases as the size of the antenna increases. This can be understood by appreciating that for a given side lobe level,

$$\frac{\left( \sum_{m=0}^M \dot{I}_m^2 \right)^2}{\left( \sum_{m=0}^M \dot{I}_m \right)^4}$$

behaves as  $M^{-2}$  if  $M$  is large. Thus, the achievable mechanical tolerance would have to increase at least as the square of the antenna size before one could state that the effect of random errors is more serious in large arrays. At most frequencies, this is decidedly not the case.

To gain a feeling for the magnitude of this random effect, let us assume that the arrays listed in Table I are operating in the vhf-uhf range of frequencies. Then it is reasonable to expect that  $\sigma_1$  will not exceed  $0.1\lambda$ ,<sup>12</sup> that  $\sigma_2$  will not exceed 0.1 radians, and that  $F$  will not exceed 0.25. The factor

$$k^2 \sigma_1^2 + 2\sigma_2^2 + 2F^2 \quad (39)$$

of (38) thus would have a maximum value

$$(0.395) + (0.02) + (0.125) = 0.540. \quad (40)$$

<sup>12</sup> This is to say that two-thirds of the dipoles will have their centers within  $0.1\lambda$  of the true position.

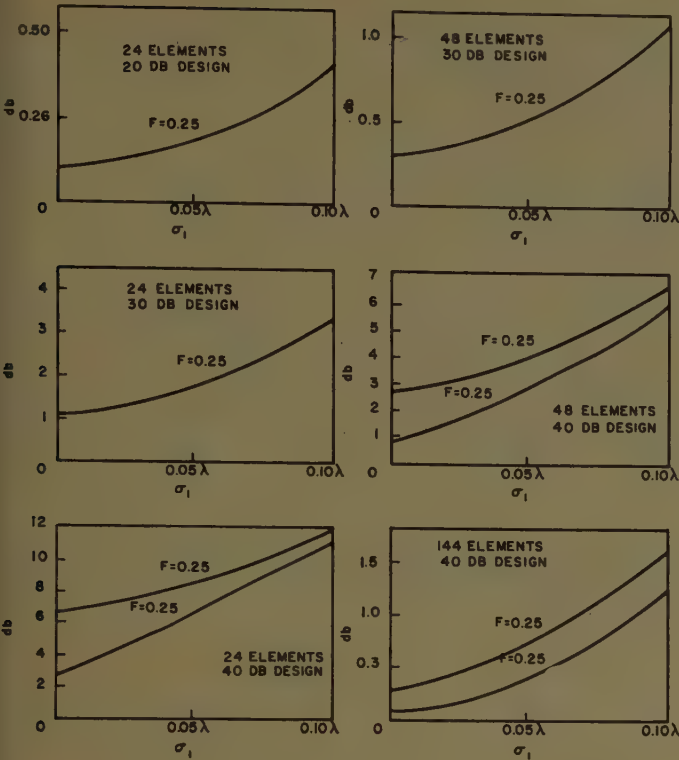


Fig. 2—Upper bound on rise in side lobe level due to random errors for various Dolph-Tchebycheff arrays as a function of the tolerances.

The calculation in (40) reveals that the dominant effect is translational errors in the dipole positions and that errors in their orientations are relatively unimportant, insofar as effect on side lobe level is concerned.

For the six cases of Table I, a plot of the upper bound of (38) is given in Fig. 2 as a function of  $\sigma_1$  for several values of  $F$ , assuming that  $\sigma_2=0$ . The curves clearly show the two points previously enumerated, namely, that the rise decreases with the number of elements for a given side lobe level design, and increases with the side lobe level design as the number of elements remains constant.

It should be emphasized that these calculations give the maximum *mean* rise in side lobe level due to random errors. The *actual* rise in a particular side lobe can be more or less than this and the probability can be determined from the distributions of  $U_1^2 + V_1^2$  and  $U_8^2 + V_8^2$ . The simplest case to consider is the pattern in either principal plane. For example, if the beam is scanned in the  $x$ - $z$  plane ( $\phi=0$ ), one finds from (6) that the significant field, including random errors terms, has only a  $\phi$  component in the  $x$ - $z$  plane. Thus, for any side lobe in this pattern, the random level has the distribution of  $U_8^2 + V_8^2$ . For the side lobe most seriously affected, the probability that the actual side lobe rise is less than the maximum mean side lobe rise is therefore

$$P = \int_0^{h_2^{10} \frac{2}{20}} \left\{ \frac{\rho I_0 \left( \frac{h_2 \rho}{\sigma_\phi^2} \right)}{\sigma_\phi^2} e^{-(\rho^2 + h_2^2 / 2\sigma_\phi^2)} \right\} d\rho \quad (41)$$

in which

$$\frac{2\sigma_\phi^2}{h_2^2} = 10^{2/10} - 1. \quad (42)$$

By making the substitutions

$$v = \frac{\rho}{\sigma_\phi}, \quad a = \frac{h_2}{\sigma_\phi} \quad (43)$$

this can be simplified to

$$P = 1 - \int_{a10^{2/20}}^{\infty} \{ v I_0(av) e^{-(v^2 + a^2/2)} \} dv. \quad (44)$$

The integral in (44) can be recognized as the  $Q$  function, for which tables are available. Returning to our example of 144 elements, designed for 40-db side lobes, if  $F=0.25$ ,  $\sigma_1=0.10$  and  $\sigma_2=0$ , then  $\mathcal{L}=1.6$  db. The probability that a side lobe in the  $x$ - $z$  plane does not suffer a rise greater than 1.6 db is therefore (from 44),

$$P = 1 - \int_{2.55}^{\infty} v I_0(2.12v) e^{-(v^2 + 4.5/2)} dv = 0.586. \quad (45)$$

Similar calculations can be made for the other cases.

To find the probability that *all* side lobes stay below a certain level, one would have to revert to the more precise expression (26) and account for the angular dependence of  $\sigma_\theta^2$  and  $\sigma_\phi^2$ . This probability would be approximately the product of the individual probabilities.

### DISCUSSION

The preceding section has shown how random errors in the construction of a two-dimensional dipole array can affect side lobe level. Several of the assumptions in the analysis deserve review. The somewhat unreal assumption was made that all error currents were randomly distributed in phase. A more drastic assumption would be that they are all distributed in such phase as to cause the most damaging effect on side lobe level. Under this assumption, the variance is only doubled and surprisingly little change is made in the calculation of mean side lobe rise. Thus, it can be concluded that the current assumptions are not giving overly optimistic results.

It was also assumed that the error currents were independent of the mechanical tolerances on dipole position and orientation. To the extent that changes in mutual coupling between dipoles cause error currents, this is not a valid assumption. However, this is a minor effect and the major sources of current errors will be improper lengths of transmission lines, improper lengths of dipoles, and improper coupling coefficients. The slight correlation should not affect the analysis to any significant degree.

The analysis can be extended to a dipole array backed by a ground plane in the following manner: the errors in shape and position of the ground plane are assumed to be gradual so that the image principle can be evoked. The image of a certain dipole is thus dis-



placed from its true position due to the positional errors of the dipole and due to the local error in the ground plane. The analysis then proceeds as before.

The analysis can be extended to a slot array in a ground plane by using the image principle and replacing the slots by magnetic dipoles. The analysis is similar to the one presented here, with  $\vec{E}$  and  $\vec{H}$  interchanged. If the slots are fed by waveguides, then some components of the positional errors in the slots are rigidly connected to the errors in transmission line lengths, and thus to the error currents. However, milling techniques usually make these particular tolerances so small that their effects can be ignored.

#### CONCLUSION

An analysis is presented of the effect of random constructional errors on the pattern of a two-dimensional dipole antenna array. The most serious tolerance ap-

pears to lie in the translational positions of the dipoles. Their angular positions are relatively unimportant. Of secondary importance are the errors in the radiating currents. An expression was derived which relates side lobe level to these errors, and representative calculations are displayed in the figures. Several noteworthy results were obtained from the analysis: 1) the rise in side lobe level due to random errors is independent of scan angle, 2) the rise is less the larger the antenna, for a given tolerance and a given design side lobe level, and 3) the rise is more the lower the side lobe level, for a given antenna size and a given tolerance.

The analysis can be extended to reflector-backed dipole arrays and to slot arrays.

#### ACKNOWLEDGMENT

The author wishes to thank Dr. James Pacharis for his helpful suggestions and Owen Tyson for his friendly encouragement.

## Fundamental Relations in the Design of a VLF Transmitting Antenna\*

HAROLD A. WHEELER†

**Summary**—For a VLF flat-top antenna much smaller than the radian sphere (a sphere whose radius is one radianlength), the effective height, effective area, and effective volume are defined. The required power factor of radiation proportionately determines the effective volume. For a specified power to be radiated, the effective height inversely determines the current and the effective area inversely determines the voltage. For a limited electric gradient on the overhead wires, the current requires a proportionate area of conductor surface. A corresponding total length of wire in the flat top is adequate if disposed for uniform distribution of charge and if spread out to realize the required effective area. These objectives are obtained more readily by some configurations, such as long parallel wires or concentric circles of wire. This study has been made for the U. S. Navy's high-power transmitter to be located in Maine, the first to radiate 1 megawatt continuously at 15 kc.

THE antenna for a high-power VLF transmitter is a large structure. It is important to know just what size is needed to meet any particular requirements. Therefore, concepts and formulas will be given for the fundamental relations that govern the design of such an antenna.

The principal objective is to radiate a specified amount of power over a sufficient bandwidth of fre-

quency. Efficient radiation requires that the bandwidth be provided largely by the radiation power factor, to which is added the power factor of all losses in the antenna circuit. For example, an efficiency of 0.50 requires that one half the bandwidth be provided by the radiation power factor.

The performance capabilities of the antenna are limited by its size and such other factors as the current for corona on the wires and the voltage of insulation. These will be formulated.

Fig. 1 outlines the type of antenna, having a flat-top web of wires suspended at a height above the ground. The antenna is assumed to be much smaller than the radian hemisphere (a hemisphere whose radius is one radianlength), behaving as a pure capacitance with negligible inductance. The relations are valid for single or multiple tuning; in the latter case, all the tuning circuits are regarded as connected in parallel to form a single circuit.

Some detrimental factors are included implicitly, such as the reduction of the effective height by the proximity of grounded supporting towers. Ground losses and other losses are omitted because they are outside the fundamental relations.

Since one of the principal limitations is imposed by corona on the wires, this topic is presented first as back-

\* Manuscript received by the PGAP, April 6, 1957; revised manuscript received, September 21, 1957. Presented at VLF Symposium, Boulder, Colo., January 23-25, 1957.

† Wheeler Laboratories, Great Neck, N. Y. Consultant to Developmental Engineering Corp., Leesburg, Va., and Continental Electronics Manufacturing Co., Dallas, Tex.

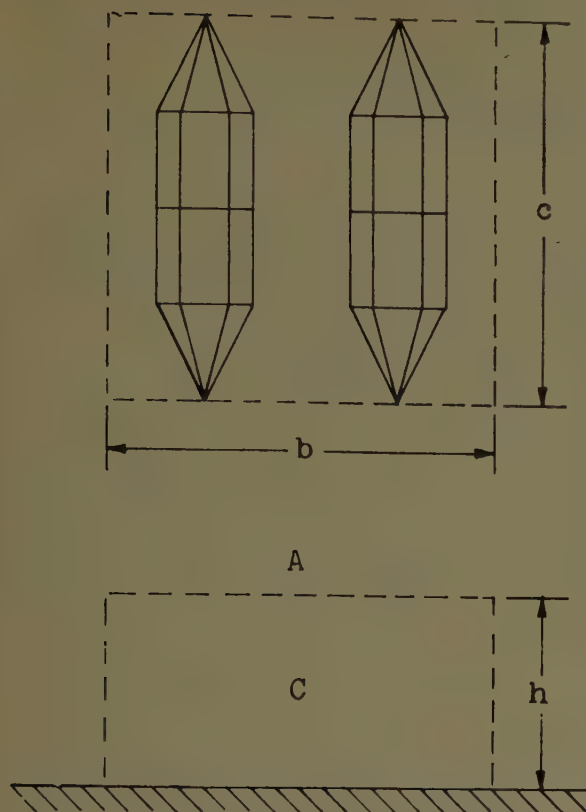


Fig. 1—Essential dimensions of flat-top antenna.

$C$  = capacitance.

$h$  = effective height.

$A = bc$  = effective area.

$A_a$  = conductor area (of surface of wires).

ground. In air as a dielectric or insulator, there is a fairly definite value of alternating-voltage gradient which is just sufficient to cause breakdown and sparking in a uniform electric field. In the vicinity of round wires far from other objects, a somewhat greater gradient is permissible on the conductor surface, because the gradient decreases with increasing distance from the surface. When the permissible gradient is exceeded on the surface, the wire is surrounded by a corona discharge rather than sparking.

An empirical formula has been published for evaluating the corona gradient on a round wire:<sup>1</sup>

$$E_c = E_b(1 + \sqrt{a_1/a}) \quad (1)$$

in which

$E_c$  = voltage gradient for corona on round wire (rms kv/mm),

$E_b = 2.05$  kv/mm = voltage gradient for breakdown in uniform field (rms),

$a_1 = 0.90$  mm = wire radius (mm) on which  $E_c = 2E_b$ ,  
 $a$  = wire radius (mm).

The most favorable condition is a uniform distribution of charge, and hence a uniform gradient, all over the conductor surface of the wires. To obtain a reasonable value of gradient for such a design,  $E_b$  is multiplied by several factors as follows:

1.27 for wires of diameter 1 inch, by (1) above.

1/2 for water drops in wet weather (approximate, based on some experience).

1/2 for doubtful factors, including departure from constant gradient.

The resulting value of gradient is

$$E_a = 0.65 \text{ kv/mm (rms).}$$

An example will be carried along with the formulas, based on these specifications:

$f = 15$  kc = frequency,

$\lambda = 20$  km = wavelength,

$p = 0.002$  = radiation power factor,

$P = 1$  megw = radiated power,

$V = 200$  kv = antenna voltage (rms),

$E_a = 0.65$  kv/mm = gradient on wires (rms), and

$R_e = 377$  ohms = wave resistance in air.

For radiation efficiency of 0.50, the total power factor would be 0.004; this fraction of the frequency gives a bandwidth of 60 cycles between the points of half-power response.

Several dimensions of the antenna are defined on an idealized basis with reference to Fig. 1.

The *effective height* ( $h$ ) is the average height of the charge on the antenna and downleads, relative to the average height of the opposite charge on the ground and supporting towers.<sup>2</sup> This is a statement of the accepted meaning. It is shown as the actual height in Fig. 1, but in practice the effective height is somewhat less. It determines the radiation resistance.

The *effective area* ( $A$ ) is the area of an idealized parallel-plate condenser, with plates separated by the effective height, which would have the same capacitance as the antenna.<sup>2,3</sup>

The *capacitance* ( $C$ ) establishes the relation between the preceding pair of dimensions, by the basic formula,

$$C = \epsilon_0 A/h \quad \text{farads (2)}$$

in which

$C$  = capacitance (farads),

$\epsilon_0$  = electrivity (electric permittivity) of air (farads/meter)

$A$  = effective area (meter<sup>2</sup>),

$h$  = effective height (meters).

This is the capacitance in a uniform field bounded by the rectangular prism shown in dotted lines in Fig. 1.

The *conductor area* ( $A_a$ ) is the area of the surface of all conductors forming the antenna and downleads. It is much smaller than the effective area. The conductor area, if uniformly charged, is capable of holding an amount of charge that is limited by corona. This charge

<sup>2</sup> This parallel usage of "effective height" and "effective area," as defined here, should not be confused with other usages of these same terms.

<sup>3</sup> J. T. Bolljahn and R. F. Reese, "Electrically small antennas and the aircraft antenna problem," IRE TRANS., vol. AP-1, pp. 46-54; October, 1953. (Equivalent area defined, same as effective area in present paper; no reference to voltage limitation for radiation power.)

<sup>1</sup> S. S. Attwood, "Electric and Magnetic Fields," John Wiley & Sons, Inc., New York, N. Y., 3rd ed.; 1949. (See p. 91, Peek's formula for extra gradient on round wire for sparkover.)



is proportional to the antenna current, regardless of the antenna voltage.

The first relation to be expressed is one which influences the frequency bandwidth and the radiation efficiency, but is independent of the amount of power.

The *effective volume* ( $Ah$ ) is proportional to the required value of the *radiation power factor* ( $p$ ).<sup>4</sup>

$$Ah = \frac{3p\lambda^3}{8\pi^2} \quad \text{meter}^3 \quad (3)$$

$$= 0.608 \text{ km}^3$$

in which

$Ah$  = effective volume (meter<sup>3</sup>),

$p$  = radiation power factor = ratio of radiation resistance/reactance, and

$\lambda$  = wavelength (meters).

The radiation power factor contributes to the total power factor which proportionately determines the frequency bandwidth. The radiation efficiency is the ratio of radiation power factor over total power factor.

The next pair of relations are determined by the amount of power to be radiated.

$$hI = \frac{\lambda}{2\pi} \sqrt{\frac{3\pi P}{R_o}} = \frac{\lambda}{4\pi} \sqrt{\frac{P}{10}} \quad \text{meter-amperes} \quad (4)$$

$$= 0.503 \text{ km-ka.}$$

$$AV = \left(\frac{\lambda}{2\pi}\right)^2 \sqrt{3\pi PR_o} = \frac{3\lambda^2}{2\pi} \sqrt{10P} \quad \text{meters}^2 \text{ volts} \quad (5)$$

$$= 604 \text{ km}^2 \text{kv}$$

in which

$I$  = antenna current (rms amperes),

$V$  = antenna voltage (rms volts),

$P$  = radiated power (watts), and

$R_o = 377 \text{ ohms}$  = wave resistance in air (ohms).

The former of these relations (meter-amperes) has been used as a rating of the radiated power. The latter (meter<sup>2</sup> volts) seems to be a new concept; it expresses an inverse proportionality between effective area and voltage.

The remaining relation involves the power and the average electric gradient on the conductor surface.

$$A_a h = \frac{\lambda^2}{4\pi^2 E_a} \sqrt{3\pi PR_o} = \frac{3\lambda^2}{2\pi E_a} \sqrt{10P} \quad \text{meters}^3 \quad (6)$$

$$= 930,000 \text{ m}^3$$

<sup>4</sup> H. A. Wheeler, "Fundamental limitations of small antennas," *Proc. IRE*, vol. 35, pp. 1479-1484; December, 1947. (Antenna smaller than the radian sphere.)

—, "VLF Antenna Notebook," Repts. 301 and 303 to Developmental Eng. Corp., Leesburg, Va.; 1956.

in which

$A_a$  = conductor area (meters<sup>2</sup>)

$E_a$  = average electric gradient on conductor surface (rms volts/meter).

This expresses an inverse relationship between the conductor area and the effective height.

These four relations will be applied here to determine the dimensions for the stated example.

$$(5) \quad A = (Ah)/h = 3.02 \text{ km}^2,$$

$$(3) \quad h = (Ah)/A = 0.200 \text{ km} = 200 \text{ m},$$

$$(6) \quad A_a = (A_a h)/h = 4650 \text{ m}^2.$$

For wire of 1-inch diameter, the required length of wire is 58 km. The wire must be distributed to give the required effective area, which is usually comparable with the actual area occupied by the flat-top pattern of wires. One of the most critical problems is the pattern of distribution of the wire to assure nearly constant gradient on nearly all of the conductor surface. Economy of conductor area is dictated by its proportionality to the wind loading or the ice-melting power, and approximately to the ice loading. For a certain area, the former is nearly independent of wire size and length, while the latter is substantially greater for smaller wires. The effective area is more dependent on the number of wires, so it is greater for a greater length of smaller wire; this rule is applicable where icing is not encountered.

Some other properties of this example are the following:

$R = 0.160 \text{ ohm}$  = radiation resistance,

$X = R/p = 80 \text{ ohms}$  = reactance,

$C = 0.133 \text{ } \mu\text{f}$  = capacitance,

$I = V/X = 2.5 \text{ ka}$  = antenna current.

The pattern of wires forming the flat top and down-leads presents an opportunity for much ingenuity in design and approximate computation. Fig. 1 shows an array of parallel wires, termed the "triatric" after the nautical term for the supporting catenaries across the array. This form offers an inherent tendency for uniform charge distribution, and also the simplest formulas for approximate computation. The two separate structures are intended to be connected together for normal operation, or either half operated independently at reduced power while the other half is out of service.

The relations given here are most useful for estimating the size of antenna needed for realizing a specified performance. They are also useful for evaluating the capabilities of an existing antenna. The emphasis has been placed on the simplest concepts relating the antenna structure with its operating requirements.

This study has been made in connection with the design of the U. S. Navy's high-power transmitter to be located in Maine. The computed example gives some idea of the size of antenna required to radiate 1 megawatt at 15 kc.

# Fundamental Limitations of a Small VLF Antenna for Submarines\*

HAROLD A. WHEELER†

**Summary**—A submarine requires a small VLF antenna for reception while submerged. Since the propagation in sea water is nearly vertical (downward from the surface), the only operative types are horizontal dipoles, electric and magnetic. The electric dipole is coupled by conduction and the magnetic dipole by induction in a loop. The former has no resonance and nearly unlimited bandwidth, but fails when not submerged. The latter, by resonance, is able to present much greater interception area and available power. The magnetic interception area is determined by the size of the radome and by the radianlength or skin depth in sea water (2 meters at 15 kc). The radiation power factor, which is essential to bandwidth and efficiency, is influenced also by the size of the inductor and by the magnetic permeability of an iron core. Simple formulas illustrate these relations for the idealized spherical shape of radome, coil and core. Omnidirectivity in azimuth requires crossed coils in a two-phase circuit.

THE fundamental limitations of a small antenna have been fairly well stated for a location above ground, but seem to have been neglected for a location under the surface of sea water. The latter is the problem of the small antenna mounted on a submarine for reception of VLF signals while submerged.

The propagation of a radio wave over a water surface is well understood. For present purposes, it will be summarized with reference to Fig. 1. Just above the

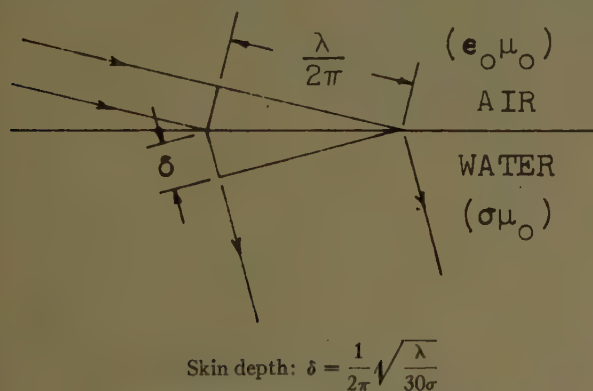


Fig. 1—Wave refraction at water surface.

surface, the direction of propagation is tilted downward and a fraction of the power is directed into the water. The index of refraction, as determined by the conductivity of the water, is very great, so the direction of propagation in the water is nearly vertical.

The propagation in the water is greatly attenuated by the skin effect which prevails in conductors. The *skin depth* or *napier depth* is defined as the depth at which the fields are attenuated one napier (8.7 db) below their value at the surface.

$$\delta = \sqrt{\frac{2}{\omega\mu_0\sigma}} = \sqrt{\frac{\lambda}{\pi R_c\sigma}} = \frac{1}{2\pi} \sqrt{\frac{\lambda}{30\sigma}} \quad (1)$$

$\delta$  = skin depth, napier depth, or radianlength in water (meters).

$\omega = 2\pi f$  = radian frequency (radians/second).

$\mu_0 = 0.4\pi \cdot 10^{-6}$  = magnetivity (permeability) in air or water (henries/meter).

$\sigma$  = conductivity in water (mhos/meter).

$\lambda$  = wavelength in air (meters).

$\lambda/2\pi$  = radianlength in air (meters).

$R_c = 120\pi$  = wave resistance in air (ohms).

The same distance ( $\delta$ ) is also the *radianlength* in the water, so the index of refraction is  $\lambda/2\pi\delta$  as diagrammed in Fig. 1.

The conductivity of sea water is about 4 mhos/meter. The lowest frequency in VLF service is about 15 kc, at which the skin depth is 2.0 meters. The index of refraction is 1600, so the direction of propagation in the water is practically vertical. The attenuation with depth is one napier per 2.0 meters, or 4.3 db/meter.

Vertical propagation downward in the water is accomplished by horizontal crossed electric and magnetic fields. The orientation of these fields in azimuth is determined by the direction of the wave over the surface. There is practically no pickup by a submerged vertical dipole of either kind, so there is no simple antenna for omnidirectional reception corresponding to the vertical electric dipole above the surface. Omnidirectional reception under the water is obtainable by a pair of crossed horizontal dipoles coupled to the receiver in phase quadrature. The further discussion is directed to a single horizontal dipole, submerged to a depth greater than the skin depth in the water.

The horizontal magnetic dipole is realized by a coil or loop whose axis is horizontal. Fig. 2 shows a spherical coil of radius  $a$  in the center of a spherical radome of larger radius  $a'$ . The coil is filled with a core of magnetic ratio  $k$ . The radome is the boundary of insulating material between the water outside and air inside. It is assumed much smaller than the radian sphere of radius  $\delta$  in the water. Following the principles that are recognized for small antennas in free space, we shall formulate the principal properties of the submerged coil antenna.

The *radiation power factor* of the coil determines its capabilities as an efficient radiator over a frequency bandwidth. It is a measure of the power coupled to the surrounding water, as compared with the reactive power in the inductance.

\* Manuscript received by the PGAP, April 6, 1957; revised manuscript received, September 21, 1957. Presented at VLF Symposium, Boulder, Colo., January 23–25, 1957.

† Wheeler Laboratories, Great Neck, N. Y.



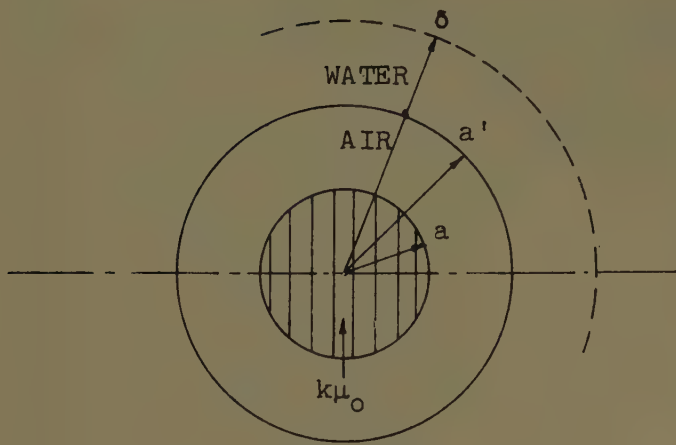


Fig. 2—Coil in submerged radome.

$$p = \frac{a^3}{a'\delta^2} \frac{1}{1/k + 1/2} \ll 1 \quad (2)$$

in which

- $p$  = radiation power factor,
- $a$  = radius of spherical coil,
- $a'$  = radius of spherical radome,
- $k$  = magnetic ratio of core in coil.

As in the case of a coil in free space, this power factor is proportional to the volume of the coil and is less for greater radianlength. In this case it also is less for greater size of radome. A greater magnetic ratio causes lesser magnetic energy in the coil and thereby increases the power factor.

The *interception area* of the coil is the usual concept for formulating its ability to take some power from the wave and make it available to a load. This area is here defined with reference to the power density in the air wave over the surface, so it can be compared with the same rating for a coil in the air.

$$A_m = \frac{3\pi^2 a' \delta^2}{2\lambda} \exp - \frac{2d}{\delta} \quad (3)$$

in which

- $A_m$  = interception area of submerged magnetic dipole,
- $d$  = depth of dipole from surface.

The first factor is the area before the attenuation by depth, and the second factor is that attenuation.

The available power, as a basis for defining the interception area, is the power that the antenna could deliver to an ideal matched load, by tuning out the coil reactance and matching the radiation resistance. As in the case of a coil above the surface, the interception area is determined by the environment of the coil and is independent of the properties of the coil itself. This area increases with the size of the radome. The first factor is independent of the wavelength, since this dimension appears in both numerator (implicitly in  $\delta^2$ ) and denominator.

A spherical coil as large as the radome, with a perfect magnetic core, is the ideal for fully utilizing the volume of the enclosed air space to obtain the greatest power factor of radiation. This would place a lower limit on the size of radome required to realize a certain power factor of radiation. If the radome is larger, the coil may be smaller, may be of different shape, and may dispense with the iron core. For a submarine, it is more important to reduce the size of the radome than to economize in the weight of the coil and core.

The alternative kind of antenna is the horizontal electric dipole, coupled with the water by conduction. It is essentially a pair of electrodes having their outer surfaces in contact with the water (directly or through thin dielectric walls of a radome). For comparison in the same spherical radome, the electric dipole is adapted to a spherical space; its electrodes are spherical caps of such size as to give nearly uniform field inside the sphere.

Unlike the coil, the electric dipole has the negligible reactance of short connecting wires. Its radiation resistance is that of the water outside the radome, which is of the order of 1 ohm. Therefore, the radiation power factor is practically unity and there is no difficulty coupling to a resonant circuit of any usual bandwidth.

The matched load for a spherical radome is a resistance whose value is one half as great as that of the same sphere filled with the same water. This is because the external resistance of a sphere is one half as great as its internal resistance if the mediums are the same. Such a matched load is assumed for evaluating the available power.

The interception area of the electric dipole is evaluated on the same basis.

$$A_e = \frac{3\pi^2 a'^3}{2\lambda} \exp - \frac{2d}{\delta} \quad (4)$$

in which

$A_e$  = interception area of submerged electric dipole.

The first factor is dependent on the size of radome and the wavelength but not on the conductivity of the water (involved in the skin depth).

On the present assumption of a radome much smaller than the radian sphere, the magnetic dipole or coil is much superior in its interception area.

$$A_m/A_e = (\delta/a')^2 \gg 1 \quad (5)$$

This ratio of superiority is directly proportional to the wavelength. As an example, take a radome of radius  $a' = 0.30$  meter or 1 foot; in sea water at 15 kc, this ratio of area or intercepted power is  $(2.0/0.30)^2 = 44$  (or 16.5 db).

In practice, the horizontal dipole may be rotated for maximum pickup and for direction finding. Here the coil has the advantage of convenience in rotation,

since the coil does not have to be very close to the wall of the radome.

Since the magnetic properties of air and water are similar, and the magnetic field is horizontal in both, the coil will operate nearly the same when above or below the surface. On the other hand, the conduction properties are opposite, and the electric fields are respectively vertical and horizontal, so the same electric dipole cannot operate in both mediums.

It is concluded that the magnetic dipole or coil antenna is the preferred kind for use on a submarine, and has a great advantage if limited to the interior of a small radome. Its radiation power factor and interception area are defined and formulated as representing its most significant ratings of performance.

## BIBLIOGRAPHY

- [1] Wheeler, H. A. "Formulas for the Skin Effect," PROCEEDINGS OF THE IRE, Vol. 30 (September, 1942), pp. 412-424.
- [2] ——. "Fundamental Limitations of Small Antennas," PROCEEDINGS OF THE IRE, Vol. 35 (December, 1947), pp. 1479-1484. (Antennas smaller than the radian sphere.)
- [3] ——. "Universal Skin-Effect Chart for Conducting Materials," *Electronics*, Vol. 25 (November, 1952), pp. 152-154. (Including sea water.)
- [4] ——. *The Radiansphere Around a Small Antenna*. Wheeler Laboratories Report 670, March 8, 1955. (Radiation power factor of spherical coil.)
- [5] ——. *The Spherical Coil as an Inductor, Shield, or Antenna*. Wheeler Laboratories Report 734, November, 1957. (Radiation power factor.)
- [6] Wait, J. R. "The Magnetic Dipole Antenna Immersed in a Conducting Medium," PROCEEDINGS OF THE IRE, Vol. 40 (October, 1952), pp. 1951-1952. (In a spherical cavity.)
- [7] ——. *The Insulated Loop Antenna Immersed in a Conducting Medium*. Washington, D. C.: National Bureau of Standards Report 5042, January, 1952. (Wire circle in sphere cavity.)

# The Prolate Spheroidal Antenna: Current and Impedance\*

C. P. WELLS†

**Summary**—This paper studies the near field of the prolate spheroidal antenna. By expanding the components of the electromagnetic field in terms of the spheroidal functions, we determine the current distribution over the antenna and the impedance at the gap. We consider both center and off-center gaps for  $kL=1, 1.49, 2, 3, 4$ , where  $k=2\pi/\lambda$ ,  $L$  is the semifocal length of the spheroid, and  $\lambda$  is the wavelength. The radiation resistance is calculated from the far field and found to be in excellent agreement with the resistance at the gap calculated from the near field.

## INTRODUCTION

THIS PAPER continues the recent work of Myers<sup>1</sup> on the prolate spheroidal antenna and extends it to include the near field. It also extends the earlier work of Chu and Stratton<sup>2</sup> which was restricted to center-fed antennas with infinitesimal gap. By using the spheroidal functions, we determine here the current distribution on the antenna and the impedance at the gap for finite gap widths and various gap locations. We also cover the range  $kL=1$  to  $kL=4$ , where  $k=2\pi/\lambda$ ,  $\lambda$  = the wavelength, and  $L$  = the semifocal length of the spheroid. Finally, we calculate the radiation resistance from the far field and compare with the resistance at the gap as measured by the real part of the impedance.

\* Manuscript received by the PGAP, March 16, 1957; revised manuscript received August 20, 1957. This work was done under contract with the Office of Ordnance Research.

† Dept. of Math., Michigan State University, East Lansing, Mich.

<sup>1</sup> H. A. Myers, "Radiation patterns of unsymmetrically fed prolate spheroidal antennas," IRE TRANS., vol. AP-4, pp. 58-64; January, 1956.

<sup>2</sup> L. J. Chu and J. A. Stratton, "Forced oscillations of a prolate spheroid," *J. Appl. Phys.*, vol. 12, pp. 241-248; March, 1941.

For the most part we follow the notation of Myers<sup>1</sup> and let  $u$  be the radial variable and  $v$  and  $\phi$  angular variables of the prolate spheroidal system. The radial functions are represented by  $U_n(u)$  and the angular functions by  $V_n(v)$ . The  $U_n(u)$  are functions of the third kind in that they behave like  $\exp(-icu)$  as  $u \rightarrow \infty$ , where  $c=kL$ . Further details concerning the functions  $U_n$  and  $V_n$  can be found in the paper by Myers and in the references cited there.

## THE FIELD COMPONENTS

As is well known, when rotational symmetry is assumed only three components  $E_u$ ,  $E_v$ , and  $H_\phi$  are needed to describe the electromagnetic field. These are given by<sup>3</sup>

$$E_u = -(\imath\beta/kL^2)[(u^2 - v^2)(1 - v^2)]^{-1/2} \frac{\partial A}{\partial v} \quad (1a)$$

$$E_v = (\imath\beta/kL^2)[(u^2 - v^2)(1 - v^2)]^{-1/2} \frac{\partial A}{\partial u} \quad (1b)$$

$$H_\phi = (1/L)[(u^2 - 1)(1 - v^2)]^{-1/2} A \quad (1c)$$

where  $\beta = (\mu/\epsilon)^{1/2}$  and  $A$  is given by

$$A = \sum_{n=0}^{\infty} a_n U_n(u) V_n(v). \quad (2)$$

<sup>3</sup> For example, see S. A. Schelkunoff, "Advanced Antenna Theory," John Wiley & Sons, Inc., New York, N. Y., pp. 111-125; 1952.



The coefficients  $a_n$  are determined from the orthogonality of the  $V_u$ , together with the boundary condition that the total tangential component of the electric field vanishes on the antenna. Thus, if  $E_v^a$  is the applied field, then we must have  $E_v + E_v^a = 0$  for  $u = u_0$ , and

$$a_n = \frac{kL^2}{i\beta N_n U_n'(u_0)} \int_{-1}^1 E_v^a(u_0, v) \cdot [(u_0^2 - v^2)/(1 - v^2)]^{1/2} V_n(v) dv. \quad (3)$$

Here  $u_0$  represents the particular spheroidal antenna and  $N_n$  is the norm of the  $V_n$ .

The current on the antenna is given by

$$I = L \int_0^{2\pi} H_\phi [(u^2 - 1)(1 - v^2)]^{1/2} d\phi = 2\pi A(u_0, v) \quad (4)$$

for any antenna  $u = u_0$ .

Some difficulties now present themselves when one attempts to use (4) to determine  $I$  numerically at various points  $v$  on a given spheroid  $u_0$ . First the nature of the applied field  $E^a$  must be known. One might assume that the antenna is fed by a two wire transmission line, but the field around the transmission line itself has never been exactly determined, much less the field of the line in the neighborhood of an antenna. Furthermore, any external feeding will, in general, destroy the rotational symmetry assumed by (1). Hence, one must make an arbitrary choice for the applied field and hope to check results against experiment.

The second difficulty lies in the slow convergence of the expansion (2) for the near field of the antenna. For  $1 \leq c < 2$ , at least 6 terms of the expansion are necessary for 3 significant figure accuracy. The computation of the radial functions for many  $c$  values becomes a formidable task even when the eigenvalues are known.<sup>4</sup> However, it is possible to cut down on this job somewhat by making use of asymptotic values with  $n$  of  $U_n(u)$  and  $U_n'(u)$ . More precisely, it can be shown that at least in the range of  $c$  considered here, the functions  $U_n(u)$  and  $U_n'(u)$  can be approximated by their asymptotic values in  $n$ ; i.e., as  $n \rightarrow \infty$ , for  $n > 4$ , in such a manner that the desired accuracy can be obtained. An outline of this can be found elsewhere.<sup>5</sup>

#### THE APPLIED FIELD ON THE ANTENNA

It is customary to assume that  $E^a$  is everywhere zero on the antenna except at the gap and there is equal to a constant voltage divided by the length of arc across the gap. For spheroids  $u_0 \approx 1$ , as we assume here, the variation of  $[(u_0^2 - v^2)/(1 - v^2)]^{1/2}$  is negligible over the gap and  $E^a$  is given by

$$E^a = \frac{-V^a}{L(v_1 - v_2)}, \quad v_1 < v < v_2, \\ = 0, \text{ elsewhere.}$$

In this case the coefficients  $a_n$  in (2) reduce to

$$a_n = \frac{-cV^a}{i\beta N_n U_n'(u_0)} B_n \quad (5)$$

where

$$B_n(v_1 - v_2) = \int_{v_1}^{v_2} V_n(v) dv.$$

At this point Chu and Stratton<sup>2</sup> assume an infinitesimal gap for which  $B_n = 1$  and which, as Infeld<sup>6</sup> has pointed out, leads to divergent series for current or admittance. All the following calculations are based on series whose coefficients are given by (5).

#### CURRENT AND IMPEDANCE

As noted earlier, the current on any spheroid  $u_0$  is given by  $I = 2\pi A(u_0, v)$ , where  $A$  is given by (2). Using unit voltage the current and the corresponding impedance have been computed for two spheroids  $u_0 = 1.001$  and  $u_0 = 1.00001$ . In general, the convergence of the series for  $A$  is faster for the smaller spheroid but even then six terms are needed to give 3-place accuracy. The convergence is also faster for smaller  $c$ ; i.e., for  $c \approx 1$ , and becomes slower as  $c$  increases. For this reason, we have limited our computations to  $c = 1, 1.49, 2, 3, 4$  for each of the two spheroids mentioned above. In order to show the effects of off-center feeding, we have included the following gaps:  $v_1 = 0.1$  to  $v_2 = 0.2$ ,  $v_1 = 0.3$  to  $v_2 = 0.4$ ,  $v_1 = 0.5$  to  $v_2 = 0.6$ . For comparison we have also included a center gap. It seems impractical to extend the computations until such time as: 1) more information is available concerning the applied field, and 2) the spheroidal functions have been computed over a wider range, a project which seems to be feasible only with electronic equipment.

The impedance at the gap is calculated from  $Z = V^a/I_0$ , where  $I_0$ , for off-center gaps, has been arbitrarily chosen to be the arithmetic average of the current at the ends of the gap. For center gaps  $I_0$  is to be  $I$  for  $v = 0$ .<sup>7</sup> Table I through Table IV give this impedance in ohms with unit voltage.

Since the only resistance is radiation resistance, we can check this part of the impedance using the far field. To do this we must integrate the normal component of  $S = \frac{1}{2} \text{Re}(E \times \tilde{H})$  over the far field. Here  $\tilde{H}$  means the complex conjugate of  $H$ . For the far field as  $u \rightarrow \infty$ ,

<sup>4</sup> All eigen values used here were furnished by the Computation Laboratory of the Bureau of Standards.

<sup>5</sup> C. P. Wells, "Mathematical Theory of Antenna Radiation," OOR Contract DA-20-018-ORD-13354, Final Rep.; July, 1957.

<sup>6</sup> L. Infeld, "The influence of the width of the gap upon the theory of antennas," *Quart. Appl. Math.*, vol. 5, pp. 113-132; July, 1947.

<sup>7</sup> This lack of uniqueness in defining impedance or admittance has been discussed by Infeld, *ibid.*

TABLE I

$v_1 = -0.05, v_2 = 0.05$		
	$u = 1.001$	$u = 1.00001$
$c$	$Z$	$Z$
1	24.3-215 <i>i</i>	24.1-395 <i>i</i>
1.49	64.2-28.7 <i>i</i>	63.8-48.8 <i>i</i>
2	153+99.6 <i>i</i>	152+236 <i>i</i>
3	444+97.2 <i>i</i>	133+666 <i>i</i>
4	97.2-156 <i>i</i>	188-441 <i>i</i>

TABLE II

$v_1 = +0.1, v_2 = +0.2$		
	$u = 1.001$	$u = 1.00001$
$c$	$Z$	$Z$
1	28.3-237 <i>i</i>	26.4-423 <i>i</i>
1.49	66.7-31.5 <i>i</i>	67.3-51.9 <i>i</i>
2	169+103 <i>i</i>	171+256 <i>i</i>
3	270-87.6 <i>i</i>	570-259 <i>i</i>
4	217-165 <i>i</i>	954-587 <i>i</i>

TABLE III

$v_1 = 0.3, v_2 = 0.4$		
	$u = 1.001$	$u = 1.00001$
$c$	$Z$	$Z$
1	48.6-350 <i>i</i>	28.7-494 <i>i</i>
1.49	82.4-43.7 <i>i</i>	83.2-68.2 <i>i</i>
2	292+61.8 <i>i</i>	323+363 <i>i</i>
3	103-51.7 <i>i</i>	123-123 <i>i</i>
4	223+135 <i>i</i>	308+580 <i>i</i>

TABLE IV

$v_1 = 0.5, v_2 = 0.6$		
	$u = 1.001$	$u = 1.00001$
$c$	$Z$	$Z$
1	121-701 <i>i</i>	31.6-669 <i>i</i>
1.49	120-85.1 <i>i</i>	129-120 <i>i</i>
2	380-241 <i>i</i>	1290-61.2 <i>i</i>
3	26.2-51.6 <i>i</i>	82.2-99.6 <i>i</i>
4	274-47.6 <i>i</i>	1270-306 <i>i</i>

$E_u \rightarrow 1/u^2$  and can be neglected while  $E_v \rightarrow \beta H_\phi$ . Hence the normal component of  $S$  becomes simply  $\beta H_\phi \tilde{H}_\phi / 2$ . If we now integrate over a sphere of radius  $r$  and let  $r \rightarrow \infty$ , we get the power radiated, which in terms of the spheroidal functions is

$$W = (2\pi c^2 / \beta) \sum_{n=0}^{\infty} B_n^2 / (N_n U_n' \tilde{U}_n'). \quad (6)$$

The radiation resistance is  $R = 2W / |I_0|^2$ . The series in (6) converges rapidly and usually only one or two terms are necessary to give sufficient accuracy. We evaluated  $R$  corresponding to each value of the impedance given in the tables and found excellent agreement.

For wider gaps this comparison is not quite as good but the difference is still scarcely significant. For example, for  $c=2$  and  $u_0=1.00001$ , we find the following:

$$v_1 = -0.1, v_2 = +0.1 \quad v_1 = -0.2, v_2 = +0.2$$

$$Z = 148 + 237i \quad Z = 146 + 298i$$

$$\text{Far field } R = 146 \quad \text{Far field } R = 142.$$

This agreement between the calculations of the resistance based on the near field with those based on the far field serves as an excellent check on our computations. No such check is available for the reactance. For this reason the real values in the tables are more reliable than the imaginary parts.

A comparison of our values of  $Z$  for the center-fed case with the graphs of resistance and reactance given in Chu and Stratton<sup>2</sup> shows at least qualitative agreement. The spheroid  $u_0=1.001$  corresponds to a length-thickness ratio of about 44, while the spheroid  $u_0=1.00001$  has a corresponding ratio of about 630. The resistance is approximately the same for both spheroids for  $c < 2$  and reaches a maximum for both near  $c=3$  or approximately a full wave antenna. Also, in both cases the reactance is zero near  $c=1.5$  or a half-wave antenna and again for  $c$  between 3 and 4. Similar statements apply to near center gaps as can be seen from the case  $v_1=0.1, v_2=0.2$ . For the other gaps more information would be necessary to locate zeros or maxima with any accuracy.

Fig. 1 through Fig. 7 show current distribution over the antenna. Actually we have plotted  $60|I|$  in amps on the vertical scale. For center-fed or near center-fed antennas the resonance-like behavior of the half-wave antenna shows up.<sup>8</sup> For the antenna nearest a full wave,  $c=3$ , the graph shows up as roughly sinusoidal. Locating the gap off center at  $v=0.3$  to  $0.4$  or  $0.5$  to  $0.6$ , brings the  $c=3$  graph to near resonance. Finally, it appears that the resonance or near resonance peaks for any  $c$  occur approximately at the same value of  $c$  regardless of gap location and differ only in magnitude for different gap locations.

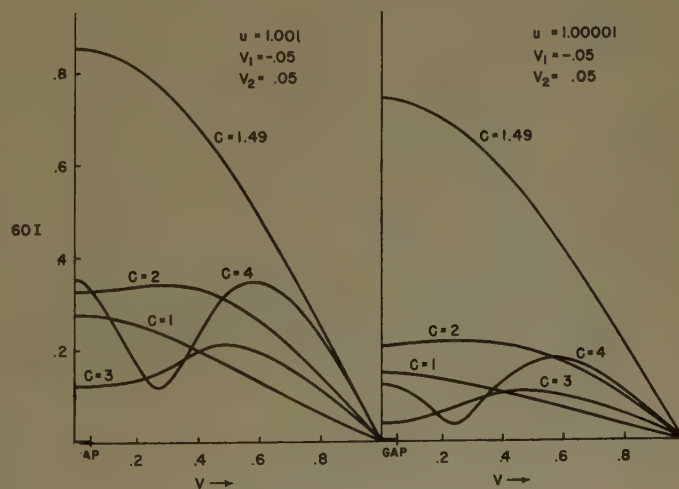


Fig. 1.

<sup>8</sup> Compare with R. King and C. W. Harrison, "The distribution of current along a symmetrical center-driven antenna," Proc. IRE, vol. 31, pp. 548-567; October, 1943.



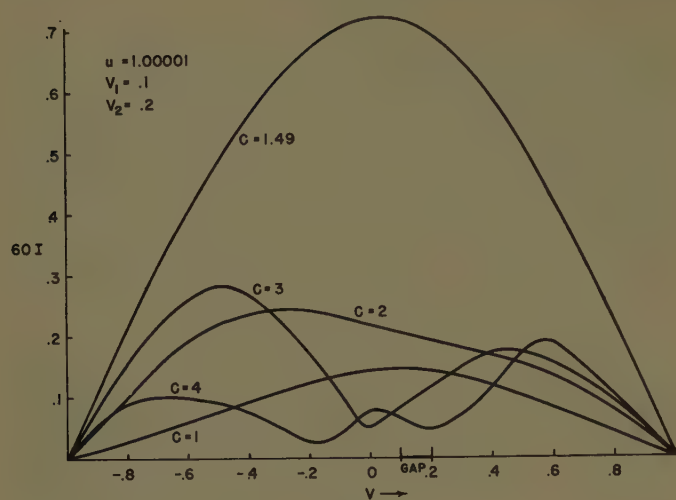


Fig. 2.

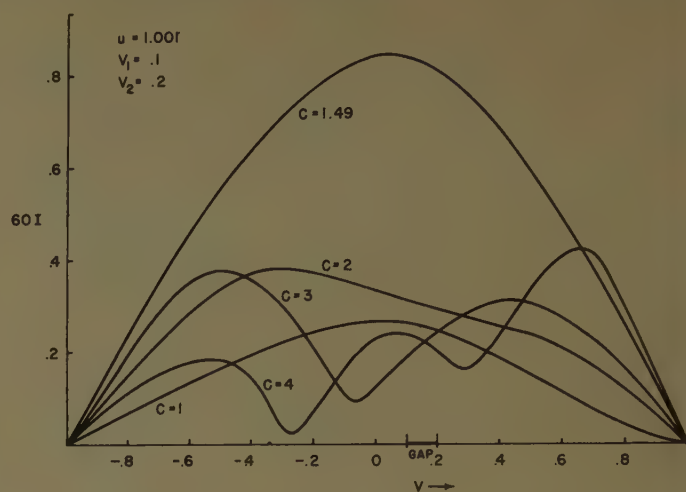


Fig. 5.

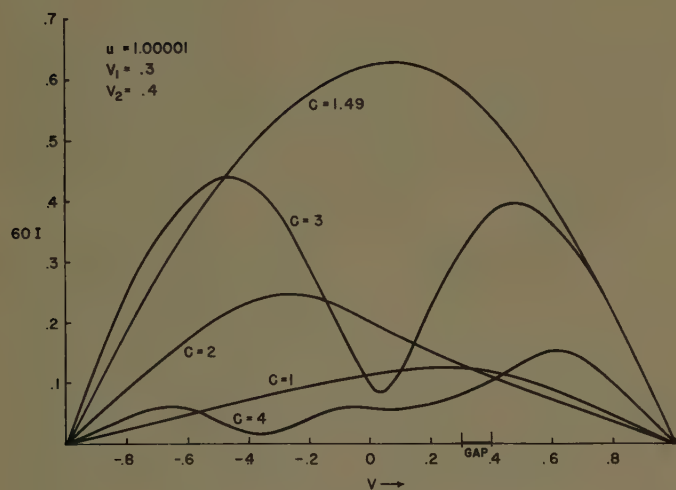


Fig. 3.

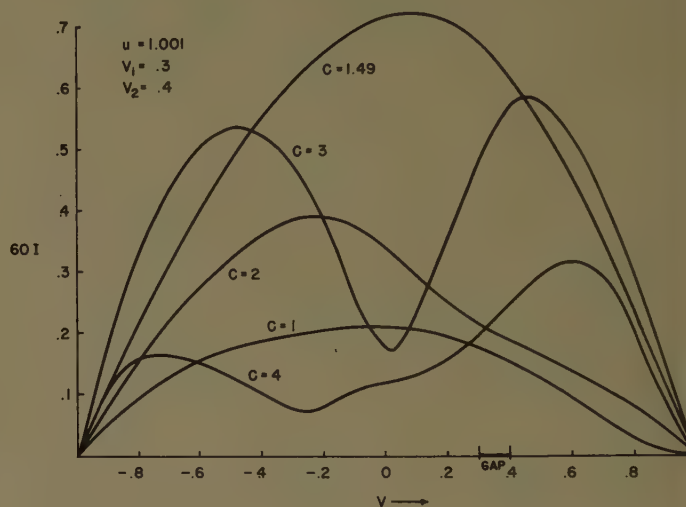


Fig. 6.

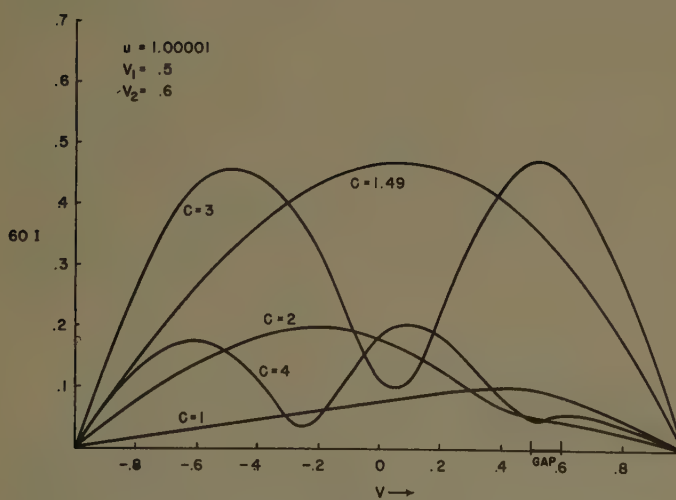


Fig. 4.

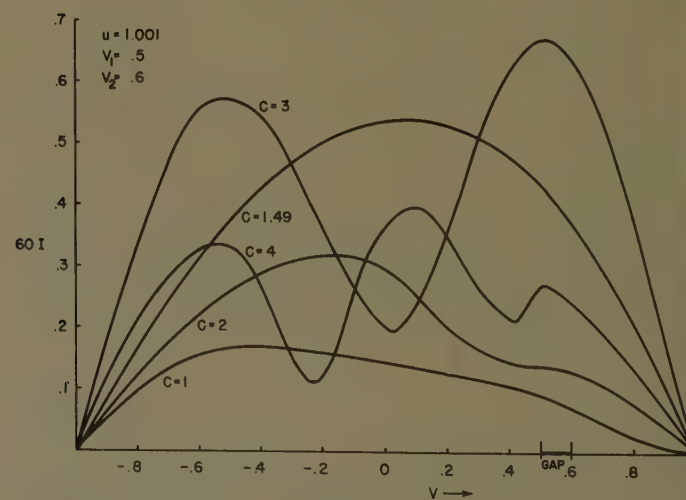


Fig. 7.



# An Application of Parageometrical Optics to the Design of a Microwave Mirror\*

L. RONCHI† AND G. TORALDO DI FRANCIA‡

**Summary**—A microwave device is described which collimates the radiation from a point feed into a parallel beam. The instrument operates by both reflection and diffraction. The offense against the sine condition is corrected perfectly, so that no monochromatic aberration is present for a moderate field even at very high apertures. The expressions of the aberrations are worked out and a graph is given where one can read the maximum values of the aperture and field for a given tolerance. It seems that the device described may be useful for radio astronomy and for rapid scanning.

## INTRODUCTION

IN some previous papers, one of the authors introduced *parageometrical optics*.<sup>1</sup> This is a kind of ray optics, intermediate between geometrical and wave optics, which holds when the wavelength is small, but not necessarily zero.

Consider a general surface  $\Sigma$  and an arbitrary set of curvilinear coordinates  $u, v$  on it. The surface  $\Sigma$  will be termed a *generalized grating* if its transmission or reflection coefficient is a periodic function of one coordinate, say  $u$ . If a general wave is incident on  $\Sigma$ , its diffraction can be treated ray by ray.<sup>2</sup> If  $s^i$  denotes a unit vector in the direction of the incident ray at a point  $P$  of  $\Sigma$ , and  $a$  the periodicity with respect to  $u$ , the diffracted ray of  $m$ th order can be specified by a unit vector  $s_m$ , according to the law<sup>3</sup>

$$s_m = s^i - m \frac{\lambda}{a} \text{grad}_\Sigma u + gN \quad (1)$$

where  $\lambda$  represents the wavelength,  $N$  the unit normal to  $\Sigma$  at  $P$ , and  $g$  a scalar quantity. By  $\text{grad}_\Sigma$  we understand the gradient in the two-dimensional domain  $\Sigma$ . This ray-by-ray technique is justified by a theorem,

\* Manuscript received by the PGAP, May 6, 1957; revised manuscript received, August 1, 1957. This research has been sponsored in part by the Air Res. and Dev. Comm., USAF, under Contract AF 61(514)-903, through the European Office, ARDC. Only the main results of the research are presented here. The detailed derivations may be found in Tech. Note n. 6 of the Contract.

† Centro Microonde, Florence, Italy.

‡ Istituto Nazionale di Ottica, Florence, Italy.

<sup>1</sup> G. Toraldo di Francia, "Parageometrical optics," *J. Opt. Soc. Amer.*, vol. 40, pp. 600-602; September, 1950, and "A fundamental theorem of parageometrical optics," *J. Opt. Soc. Amer.*, vol. 43, pp. 368-370; May, 1953.

<sup>2</sup> In spite of some analogies, this ray treatment of diffraction should not be confused with that introduced by Rubinowicz and recently developed and extended with success by Keller, where use is made of the rays diffracted by an edge. See also the panel discussion on this point in IRE TRANS., vol. AP-4, p. 544; July, 1956.

A. Rubinowicz, "Die Beugungswelle in der Kirchhoffschen Theorie der Beugungserscheinungen," *Ann. Phys.*, vol. 53, pp. 257-278; July, 1917.

J. B. Keller, "Diffraction by an Aperture," New York Univ. Inst. of Math. Sci., Div. of Electromagnetic Res., Res. Reps. EM-92 and EM-96; 1956.

<sup>3</sup> G. Toraldo di Francia, "Electromagnetic Waves," Interscience Publishers, New York, N. Y., p. 233; 1956.

analogous to that of Malus-Dupin, which states that if  $s^i$  represents a normal set of rays,  $s_m$  turns out to be a normal set of rays, too. In other words, whatever the shape of the incident wave, the set of diffracted rays  $s_m$  admit a set of normal surfaces, which represent the diffracted wave of the  $m$ th order. Several properties of conventional ray optics can be extended to parageometrical optics, in particular, Abbe's sine condition for an aplanatic image. This will be put in use in the present paper.

Our purpose will be to design a mirror which can collimate a microwave beam with substantial values of the aperture and field angle. The two most conventional types of mirrors each present an aberration which cannot be eliminated. The spherical mirror is affected by spherical aberration, and the parabolic mirror by coma.

An ideal mirror would be a spherical mirror capable of reflecting any ray parallel to the axis towards the center  $C$  of the mirror. In this way, spherical aberration obviously would be absent, and the sine condition would be fulfilled, since the sine of the aperture angle  $\theta$  is proportional to the height of incidence  $h$ . Of course, this behavior of the rays is absurd, if the rules of ordinary reflection are to be respected.

However, the situation is no longer absurd if diffraction is used in place of reflection. If the surface  $\Sigma$  of the mirror is an appropriate reflecting grating, the ray considered can be the diffracted ray of order  $m$ . In this way, the mirror will become a zoned mirror.

As is well known, besides the wave centered at  $C$ , other (approximately spherical) waves will arise by diffraction. One can get rid of these waves by a technique which is well known in grating manufacture. The rulings of a reflecting grating often are given a saw-tooth profile in order to enhance the brightness of one spectrum at the expense of the others. In particular, it can be proved that if the direction of ordinary reflection on the saw teeth coincides with the direction of a given spectrum, light is practically all concentrated in that spectrum. The same technique will be followed in the design of our mirror.

## THE ZONED SPHERICAL GRATING

In order to reduce chromatic aberration, we shall make use of the first-order diffracted wave.

Consider two incident rays  $AP$  and  $A'P'$  (Fig. 1) in a meridional plane;  $P$  and  $P'$  are the points of intersection of  $\Sigma$  with any two consecutive zones. The zones must be oriented so as to reflect both rays towards  $C$ . As the distances  $PC, P'C$  are evidently equal, the dif-



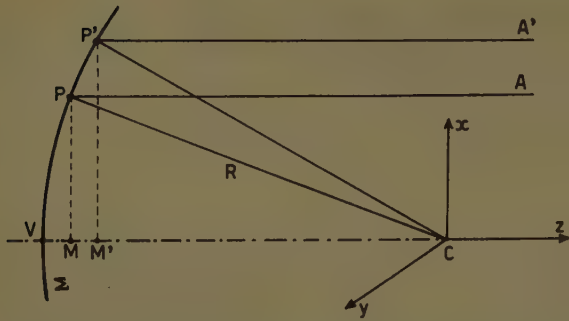


Fig. 1—Optical path difference  $MM'$  between two rays of the meridional plane which are incident at corresponding points of two consecutive zones.

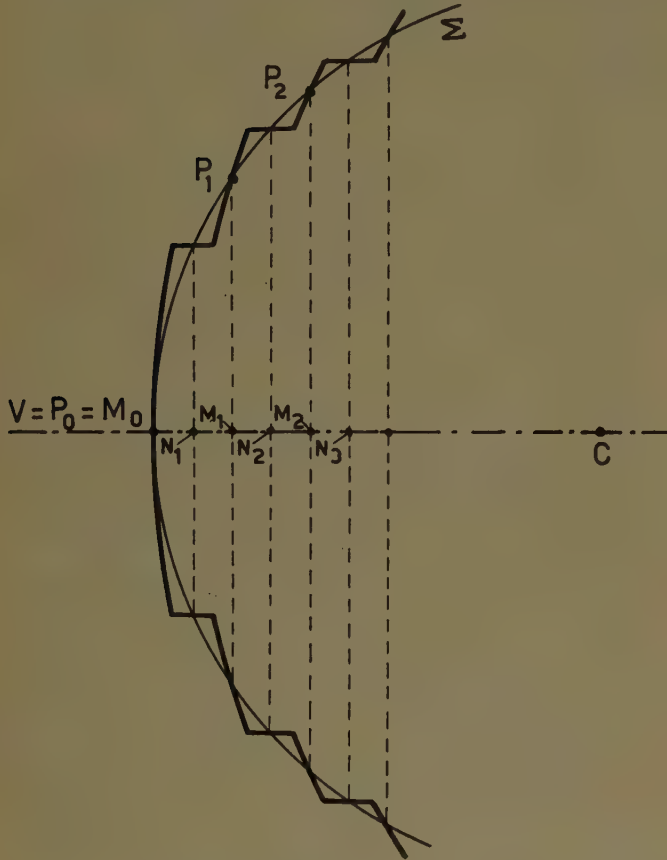


Fig. 2—Determination of the zones.

ference of optical path between the two rays is simply represented by  $MM'$ . As a consequence, we shall put  $MM' = \lambda$ .

Accordingly, the set of points  $P_0, P_1, P_2, \dots$ , of intersection of the zones with the spherical surface  $\Sigma$  will be determined by means of their projections on the axis  $M_0, M_1, M_2, \dots$ , as follows. We put  $P_0 \equiv M_0 \equiv V$  (Fig. 2), then  $VM_1 = \lambda$ ,  $M_1M_2 = \lambda$ , and so on.

The surface of the zoned mirror will be completed by sections of coaxial cylinders (Fig. 2), each representing the connection between two neighboring zones. The cylinders will intersect the spherical surface  $\Sigma$  along a set of circles, centered at  $N_1, N_2, N_3, \dots$ , respectively. Each point  $N$  will be assumed to be located midway between two consecutive points  $M$ . It will be noted that

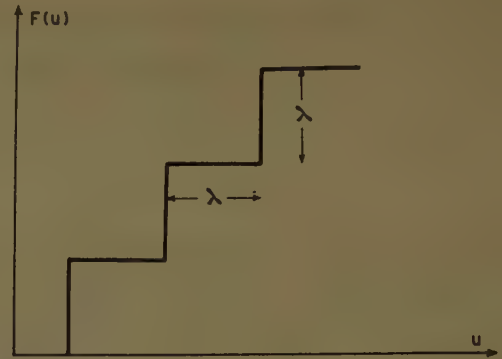


Fig. 3—Behavior of the phase of the first-order diffracted wave as a function of  $u$ .

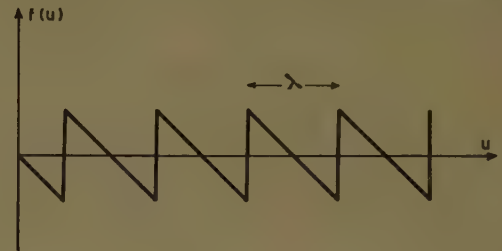


Fig. 4—Behavior of the argument of the complex reflection coefficient of  $\Sigma$  as a function of  $u$ .

the construction described is in many respects analogous to the classical construction of the Fresnel zones.

We shall refer to a rectangular system of coordinates  $x, y, z$  (unit vectors  $i, j, k$ ) with the origin at  $C$  and the  $z$ -axis coincident with the axis of the mirror and directed away from the mirror. Alternatively, we shall use the spherical coordinates  $r, \theta, \phi$  (unit vectors  $i_r, i_\theta, i_\phi$ ) with  $x = r \sin \theta \cos \phi$ ,  $y = -r \sin \theta \sin \phi$ ,  $z = -r \cos \theta$ .

The surface  $\Sigma$  will be referred to a system of curvilinear coordinates  $u, v$ , specified by  $u = R \cos \theta$ ,  $v = \phi$ , where  $R$  represents the radius of the sphere  $\Sigma$ . In terms of these coordinates and apart from an additive constant in the phase, the complex amplitude of the incident wave over  $\Sigma$  will have the form  $A^i \exp(iku)$ ,  $A^i$  being a real constant. The complex amplitude of the first-order diffracted wave, when referred to  $\Sigma$ , will have the form  $A^r \exp[ikF(u)]$ , where  $A^r$  is a real constant, and  $F(u)$  is the function represented (apart from a constant) in Fig. 3, consisting of a series of identical steps with both width and height equal to  $\lambda$ .

We will consider the diffracted wave as obtained by reflection of the incident wave by  $\Sigma$ ; to this end, we shall attribute to  $\Sigma$  an appropriate reflection coefficient  $\rho(u) = \rho_0(u) \exp[ikf(u)]$ ,  $\rho_0(u)$  being real. Accordingly, we shall write

$$A^r \exp[ikF(u)] = \rho_0(u) \exp[ikf(u)] A^i \exp(iku). \quad (2)$$

Hence, we have  $\rho_0 = A^r/A^i$  and

$$f(u) = F(u) - u. \quad (3)$$

The behavior of  $f(u)$  is represented in Fig. 4, which clearly shows that the reflection coefficient of the zoned

mirror corresponds (in curvilinear coordinates) to that of a conventional saw-tooth grating. The periodicity, with respect to  $u$ , is  $\lambda$ . Accordingly, in (1), we shall put  $a = \lambda$ . On the other hand, we have  $\text{grad}_z u = -i_\theta \sin \theta$ , and  $N = -i_r$ . As a result, (1) may be rewritten, for  $m = 1$

$$s_1 = s^i + i_\theta \sin \theta - i_r g. \quad (4)$$

The scalar quantity  $g$  should be determined by requiring that  $s_1^2 = 1$ . Two values will be found, one corresponding to  $s_1 \cdot i_r > 0$ , and the other to  $s_1 \cdot i_r < 0$ . Obviously we must choose the second one.

#### ABERRATIONS OF THE MIRROR

Let us consider a plane wave, whose direction of propagation  $s^i$  is parallel to the  $xz$  plane. This plane will be called the *meridional plane*. The field angle  $\Omega$ , or the angle made by  $s^i$  with the axis, will be assumed to be positive when the radiation comes from below the axis.

In order to visualize the aberrations of the diffracted wave, we make use of Herzberger's *diapoints*.<sup>4</sup> The diapoint of a given ray is defined as the point where the ray intersects the meridional plane.

The equation of the diffracted ray can be worked out by utilizing (4). In this way, the coordinates  $x, z$  of the diapoint are found to be

$$\frac{x}{R} = -\frac{\sin \Omega}{w} \quad (5)$$

$$\frac{z}{R} = -\frac{1 - \cos \Omega}{w} \quad (6)$$

where the quantity  $w$  is the negative root of the equation

$$w^2 + 2w[\sin \Omega \sin \theta \cos \phi - (1 - \cos \Omega) \cos \theta] - (2 \cos \Omega - 1) = 0 \quad (7)$$

and is related to  $g$  by  $w = \cos \theta - g$ .

Eqs. (5) and (6) show that the ratio  $z/x = \tan(\Omega/2)$  is independent of  $\theta$  and  $\phi$ . As a consequence, we have found that, once the value of  $\Omega$  is given, all the diapoints lie on a straight line  $CS$  (Fig. 5). The section of this line occupied by the diapoints will be termed the *sagittal focal line*. It is clear that  $S$  is the *sagittal focus* on the principal ray. The locus of the sagittal foci on the principal rays can be found from the geometry of Fig. 5 and turns out to be an hyperbola, represented by

$$\left[z + \frac{R}{3}\right]^2 - \frac{x^2}{3} = \left[\frac{R}{3}\right]^2. \quad (8)$$

The center of the hyperbola is located on the axis at  $z = -R/3$  and the asymptotes make angles of  $\pm 60^\circ$  with the axis (Fig. 6). Obviously, point  $C$  belongs to the hyperbola. The radius of curvature of the hyperbola at  $C$  turns out to be equal to  $R$ .

<sup>4</sup> M. Herzberger, "A new theory of optical image formation," *J. Opt. Soc. Amer.*, vol. 26, pp. 197-204; May, 1936.

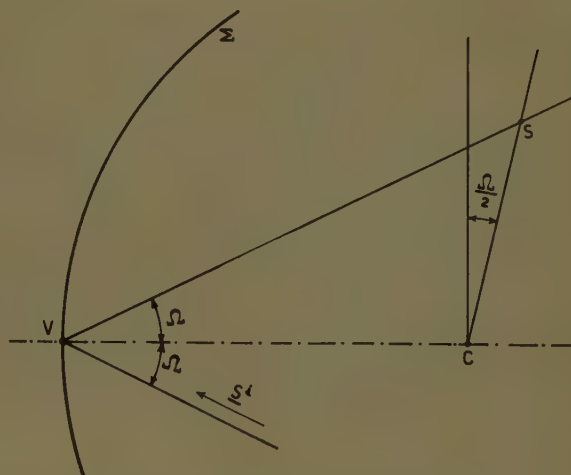


Fig. 5—Locus of the diapoints for a given field angle.

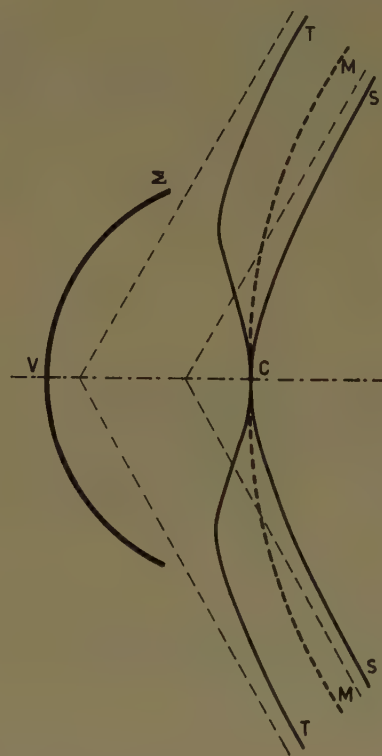


Fig. 6—Loci of the sagittal focus  $S$ , of the tangential focus  $T$ , and of the best focus  $M$ .

The sagittal coma  $C_s$  of a given zone  $\theta$  will be defined as the distance of the common diapoint of the rays  $\phi = \pi/2$ ,  $\phi = 3\pi/2$  from the principal ray, and will be taken positive or negative according to whether the diapoint is on the opposite or on the same side as the axis. By introducing these values of  $\phi$  into (7) and solving for  $w$ , and by making use of (5) and (6), it is an easy matter to find

$$C_s = -R \sin \Omega [1 - (1 - \cos \Omega) \cos \theta - \sqrt{\cos^2 \Omega - (1 - \cos \Omega)^2 \sin^2 \theta}]. \quad (9)$$

This expression is an odd function of  $\Omega$  and the first



term of its series expansion in powers of  $\sin \Omega$  turns out to be

$$C_s = -\frac{1}{2}R \sin^3 \Omega (1 - \cos \theta). \quad (10)$$

The absence of a term with the first power of  $\sin \Omega$  is a consequence of the sine condition being fulfilled. In particular, the third-order coma vanishes.

An analogous result can be obtained for the tangential coma  $C_t$ , which is defined as the distance of the intersection of the two rays  $\phi=0$ ,  $\phi=\pi$ , from the principal ray. The exact expression of  $C_t$  turns out to be rather complicated. For the sake of simplicity, we will limit ourselves to giving the first term of the series expansion of  $C_t$  in powers of  $\sin \Omega$ . It is found

$$C_t = -\frac{1}{2}R \sin^3 \Omega (1 - \cos \theta) (3 + \cos \theta). \quad (11)$$

As was to be expected,  $C_t$  also does not depend on the first power of  $\sin \Omega$ .

Next, we will find the position of the *tangential focus*  $T$  on the principal ray. This point may be defined as the limit of the intersection of the two meridional rays  $\phi=0$ ,  $\phi=\pi$ , for  $\theta=0$ . Starting from the equation of the diffracted ray, one can find

$$x_T = R \frac{\sin \Omega \cos^2 \Omega}{2 \cos \Omega - 1} \quad (12)$$

$$z_T = -R \left[ 1 - \frac{\cos^3 \Omega}{2 \cos \Omega - 1} \right] \quad (13)$$

where  $x_T$ ,  $z_T$  represent the coordinates of  $T$  in the meridional plane. The locus of  $T$  is the line shown in Fig. 6. In the neighborhood of  $C$ , the line is concave towards the mirror and its radius of curvature is exactly  $R$ , then the line turns away from the mirror and for  $|\Omega|=60^\circ$  goes to infinity. The corresponding asymptotes intersect the axis at  $z = -(5/6)R$ .

If the distance of the sagittal and tangential foci from the vertex  $V$  of the mirror are designated by  $\rho_s$  and  $\rho_T$  respectively, the astigmatism as usually defined in optics easily is found to be

$$A = \frac{1}{\rho_T} - \frac{1}{\rho_s} = \frac{1}{R} (2 \cos \Omega - 1) \tan^2 \Omega. \quad (14)$$

This expression vanishes for  $\Omega=0^\circ$  and  $|\Omega|=60^\circ$ .

An extremely surprising result which may be proved by means of the formulas of the preceding sections is that the diffracted wave for  $|\Omega|=60^\circ$  is exactly a plane wave up to  $\theta=30^\circ$ .

Finally, a few words will be said about chromatic aberration. Unfortunately, this aberration cannot be corrected with the present system and it will be useful to know its value. It is an easy matter to find

$$df = R \frac{d\lambda}{\lambda} \quad (15)$$

where  $df$  denotes the increment of the focal length due to an increment  $d\lambda$  of the wavelength.

## WAVE ABERRATION AND TOLERANCE

As is well known, the *wave aberration* is defined as the distance from a given reference sphere to the wave under consideration, in the direction of propagation. A particularly interesting case is obtained when both the reference sphere and the wave are at infinity.<sup>5</sup> The wave aberration at infinity  $W$  is a function of the ray (or direction) considered. If a ray is specified by its direction cosines  $\alpha$ ,  $\beta$ ,  $\gamma$ , one can put  $W=W(\alpha, \beta)$ . The fundamental property of the wave aberration at infinity is represented by

$$x = \frac{\partial W}{\partial \alpha}, \quad y = \frac{\partial W}{\partial \beta} \quad (16)$$

where  $x$  and  $y$  represent the coordinates of the intersection of the ray with the  $xy$  plane, the origin coinciding with the center of the reference sphere.

Starting from (16) and carrying out some calculations, one can prove that in our case the wave aberration at infinity, with respect to a reference sphere centered at the sagittal focus  $S$ , has the expression

$$W_s = R \left[ w - \alpha \frac{\sin \Omega}{2 \cos \Omega - 1} + (1 - \gamma) \frac{1 - \cos \Omega}{2 \cos \Omega - 1} + \text{constant} \right]. \quad (17)$$

The maximum excursion  $\Delta W_s$  of  $W_s$  over the whole mirror turns out to be

$$\frac{1}{R} \Delta W_s = \cos \Omega + w_1 \left[ 1 + \frac{(1 - \cos \Omega) \cos \theta - \sin \Omega \sin \theta}{2 \cos \Omega - 1} \right] \quad (18)$$

where  $\theta$  represents the semiaperture of the mirror, and  $w_1$  is the value of  $w$  for  $\phi=0$ .

Numerical computations have been carried out on the basis of (18) and the results are shown in Fig. 7, where  $\Delta W_s/R$  is plotted against  $\theta$  for different values of  $\Omega$ .

The graphs of Fig. 7 are useful in practice for introducing tolerances. For instance, once the radius  $R$  and aperture  $\theta$  of the mirror are fixed, one can read off from the graph the value of  $\Omega$  for which  $\Delta W_s = \lambda/16$  or  $\lambda/8$  or whatever tolerance one may choose as suitable.

Thus, the maximum field angle is determined which can be reached with that mirror. Of course, to make the best use of the tolerance, the image should be placed at the "best focus" for any field angle. In the case of pure astigmatism, the best focus should be located at  $M$ , midway between the sagittal and the tangential foci. The locus of  $M$  is shown in Fig. 6. Its curvature at point  $C$  vanishes, so the *mean field curvature is zero*.

<sup>5</sup> G. Toraldo di Francia, "Introduzione alla Teoria Geometrica e Interferenziale delle Onde Aberranti," Publ. Ist. Naz. di Ottica, Florence, Italy, No. 413, p. 6; 1947.

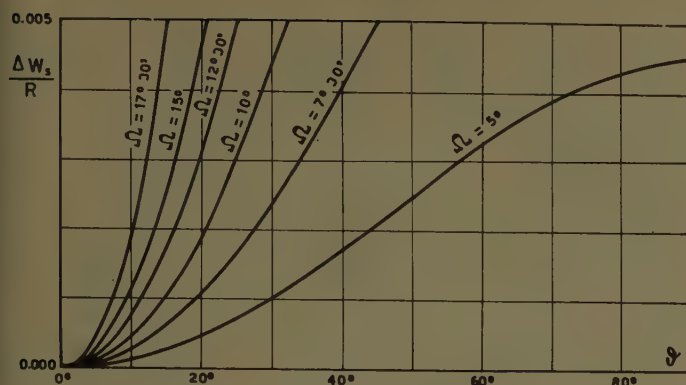


Fig. 7—Total excursion of the wave aberration plotted against  $\theta$  for different values of  $\Omega$ .

### CONCLUSION

We have described a microwave device, having the general shape of a spherical mirror with zonal steps. This mirror operates by both reflection and diffraction. Its main feature is a perfect correction for spherical aberration and for the offense against the sine condition, when the object (or the image) is at infinity. In agreement with optical theory, there is no coma of the first order with respect to the field.

Precise computations show that even higher-order coma is extremely small. The patterns obtained in the neighborhood of the focal plane are nearly those of pure astigmatism.

The only serious aberrations of the mirror are chromatic aberration and astigmatism. The former requires that the mirror be used with practically monochromatic radiation. As to the latter, its influence is negligible for small fields and, anyway, the tolerance can be read off from the graph of Fig. 7. It is probable that in radio astronomy the mirror may be used with a very large aperture and a moderate field. For scanning applications the point feed should travel along the mean image surface  $M$  (Fig. 6), which in the case of pure astigmatism represents the locus of the best focus. Alternatively, one may be interested in making the rays parallel only to the meridional plane or to a plane perpendicular to it. In this case the feed should simply travel along the line  $S$  or  $T$  respectively. Very large scanning angle could be reached by making a linear feed to match the sagittal or tangential Sturm lines, respectively.

A system of the type described in this paper is under construction at the Centro Microonde and experimental results regarding its performance will be published in due course.

## End-Fire Echo Area of Long, Thin Bodies\*

LEON PETERS, JR.†

**Summary**—The echo area resulting from traveling waves excited on the surface of long, thin bodies is considered. A means of predicting this echo area on the basis of antenna theory is derived. Computed and measured values are compared for a long wire, an ogive, and a shorted polyrod.

### INTRODUCTION

THE echo area of a long, thin body in the region of longitudinal incidence is derived by making use of the existing concepts of antenna theory. The body is considered as a traveling-wave antenna.

In general, the echo area due to an antenna mode may be computed from the proper application of the concept of scattered power of a receiving antenna. King<sup>1</sup> has made use of this in computing the echo area of a dipole at normal incidence. Here the concept is to be used to compute the echo area due to antenna modes set up on

certain bodies. For the bodies under consideration and the choice of antenna terminals that is made, only the component of scattered power that is reflected from the antenna terminals is needed to compute the echo area. Other modes do not contribute appreciably to scattering in the direction of interest. This component of the scattered power has been used previously by Sinclair, Jordan, and Vaughan<sup>2</sup> in an antenna pattern measurement scheme. An unmodulated source was used to illuminate an antenna whose pattern was to be measured. The power reflected from the antenna terminals was modulated by varying the load impedance periodically. A receiving system located at the same position of the source detected the modulated component of scattered power.

Of the scatterers to be treated here, the maximum echo area of the polyrod antenna has been derived by

\* Manuscript received by the PGAP, March 16, 1957; revised manuscript received, September 16, 1957.

† Antenna Lab., The Ohio State University, Columbus, Ohio.

<sup>1</sup> D. D. King, "The measurement and interpretation of antenna scattering," *PROC. IRE*, vol. 37, pp. 770-777; July, 1949.

<sup>2</sup> G. Sinclair, E. C. Jordan, and E. W. Vaughan, "The measurement of aircraft antenna patterns using models," *PROC. IRE*, vol. 35, pp. 1451-1467; December, 1947.



Horton and Watson<sup>3</sup> and also by Hame and Kennaugh.<sup>4</sup> Traveling waves have been considered by Sloan<sup>5</sup> and Tai<sup>6</sup> to obtain the echo of short wires.

Hansen and Schiff<sup>7</sup> conclude that for "any pointed object of revolution that has a smooth surface at the geometrical shadow with all appendages well within the shadow, the dominant back scattering comes from the point." Consequently the point has been treated as the dominant scatterer when computing the radar properties of the ogive.<sup>8</sup> This approximation has been shown to be valid only when the contribution due to the traveling-wave mode is negligible.<sup>9</sup> The research described in this paper is a direct result of the nonconformity of measurements and computations based on the above approximations. Deviations of as much as 40 db were noted.

### THEORY

The absorbed power  $P_a$  and the scattered power  $P_s$  of a receiving antenna are given in terms of the power intensity  $S_i$  of a plane wave incident on the antenna, the absorption cross section  $A_r$ , and the scattering cross section  $A_s$ , as<sup>10</sup>

$$\begin{aligned} P_a &= A_r S_i \\ P_s &= A_s S_i. \end{aligned} \quad (1)$$

Let us consider an antenna with a matched load. Then these two components of power can be defined as follows:

$P_{am}$  is the power flowing into the antenna terminals when the antenna is terminated in a matched load, and

$P_{sm}$  is the power scattered by a receiving antenna when it is terminated in a matched load.

<sup>3</sup> C. W. Horton and R. B. Watson, "On the back scattering of radar waves from the trailing edge of an aircraft wing," *Texas J. Science*, vol. 6, pp. 392-398; December, 1954.

<sup>4</sup> T. G. Hame and E. M. Kennaugh, "Interim Engineering Report on the Polarization Dependence of Radar Echoes," Antenna Lab., The Ohio State Univ. Res. Foundation, Rep. 612-3; July 1, 1955. Prepared under Contract AF 30(635)-2811, Rome Air Dev. Center, Griffiss Air Force Base, N. Y.

<sup>5</sup> R. Sloan, "Echo Area of Wires and Hollow Cylinders," Antenna Lab., The Ohio State Univ. Res. Foundation, Rep. 444-2; September 1, 1951. Prepared under Contract DA 36-039sc5506, Evans Signal Laboratory, Belmar, N. J.

<sup>6</sup> C. T. Tai, "Radar Response from Thin Wires," Stanford Research Institute, Menlo Park, Calif., Rep. SRI-18; March, 1951.

<sup>7</sup> W. W. Hansen and L. I. Schiff, "Theoretical Study of Electromagnetic Waves Scattered from Shaped Metal Surfaces," Microwave Lab., Dept. of Physics, Stanford Univ., Stanford, Calif., Quarterly Rep. No. 3; May, 1948.

<sup>8</sup> K. M. Siegel, H. A. Alperin, R. R. Bonkowski, J. W. Crispin, A. L. Maffet, C. E. Schensted, and I. V. Schensted, "Bistatic cross section of surfaces of revolution," *J. Appl. Phys.*, vol. 26, pp. 297-305; March, 1955.

<sup>9</sup> L. Peters, Jr., "Memorandum on the Echo Area of Ogives," Antenna Lab., The Ohio State Univ. Res. Foundation Rep. 601-7, January 30, 1956. Prepared under Contract AF 33(616)-3546, Air Res. and Dev. Command, Wright Air Dev. Center, Wright-Patterson Air Force Base, Ohio.

<sup>10</sup> S. Silver, "Microwave Antenna Theory and Design," McGraw-Hill Book Co., Inc., New York, N. Y., p. 42; 1949.

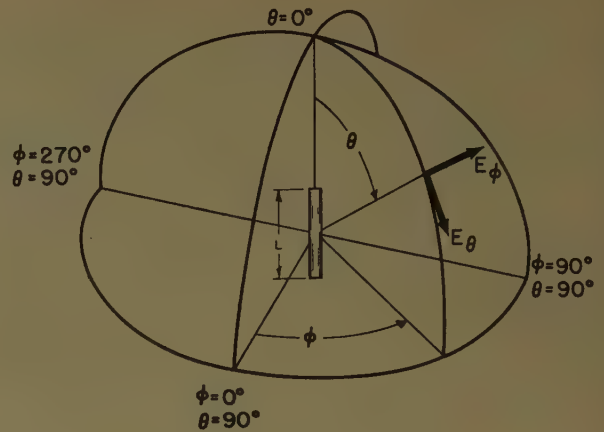


Fig. 1—Coordinate systems.

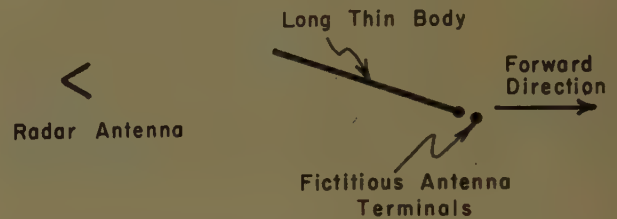


Fig. 2—Position of antenna terminals on long, thin body.

If the antenna is not terminated in a matched load, a portion of the power  $P_{am}$  is reradiated. This power to be designated as  $P_r$  is the component used to compute the echo area of the bodies of interest here.

The absorption cross section is<sup>11</sup>

$$A_r(\theta, \phi) = G(\theta, \phi) \frac{\lambda^2}{4\pi} \quad (2)$$

where  $G(\theta, \phi)$  is the gain function of the antenna and  $\lambda$  is the wavelength. When  $P_r = 0$ , substitution of (2) into (1) gives

$$P_{am} = G(\theta, \phi) \frac{\lambda^2}{4\pi} S_i \quad (3)$$

where  $\theta, \phi$  are angles shown in the coordinate system of Fig. 1.

To demonstrate that the power  $P_{sm}$  may be eliminated from the computations, the induced currents on the surface of the long, thin body may be broken into components as follows:

- the current reflected from the end of the body nearest the transmitter (see Fig. 2),
- the current reflected from the end most distant from the transmitter, and
- induced current produced by the incident field.

If one considers these currents from the viewpoint of traveling-wave antennas, it is apparent that the first and third of the above currents will set up radiation chiefly in the forward direction (see Fig. 2). They may

<sup>11</sup> *Ibid.*, p. 51.

therefore be neglected when computing echo area. For the above choice of terminals the induced current is the only current whose radiation contributes to the power  $P_{em}$ , and this power may therefore be eliminated from the computation.

Consequently the terminals of the antenna (representing the long, thin body) are chosen at the position shown in Fig. 2. Since this antenna is not terminated in a matched load, the power absorbed is less than that for a matched load.<sup>12</sup> The magnitude of the power reflected from the terminals is proportional to the square of the current reflection coefficient  $\gamma$ . This reflected power is

$$P_r = \gamma^2 \frac{G(\theta, \phi) \lambda^2}{4\pi} S_i.$$

The power intensity ( $S_r$ ) of the wave radiated in the direction of the transmitter is given by<sup>13</sup>

$$S_r = \frac{P_r G(\theta, \phi)}{4\pi R^2} = \left( \frac{\gamma G(\theta, \phi) \lambda}{4\pi R} \right)^2 S_i. \quad (4)$$

Applying the definition of echo area

$$\sigma = \lim_{R \rightarrow \infty} 4\pi R^2 \frac{S_r}{S_i} \quad (5)$$

gives the final result

$$\sigma = \gamma^2 \frac{G^2(\theta, \phi)}{4\pi} \lambda^2. \quad (6)$$

Note that this equation does not apply to the case of the dipole because the component of power  $P_{em}$  has been neglected.

The above result may be easily extended to obtain the equation for the bistatic echo area. If the angles  $\theta_R$  and  $\phi_R$  denote the position of the radar receiver (see coordinate system of Fig. 1) and  $\theta_T$  and  $\phi_T$  denote the position of radar transmitter, (3) becomes

$$S_r = \frac{P_r G(\theta_R, \phi_R)}{4\pi R^2} = \frac{\gamma^2 G(\theta_T, \phi_T) G(\theta_R, \phi_R)}{(4\pi R)^2} S_i.$$

Then (6) becomes

$$\sigma(\theta_T, \phi_T; \theta_R, \phi_R) = \frac{\gamma^2 G(\theta_T, \phi_T) G(\theta_R, \phi_R)}{4\pi} \lambda^2$$

which is the equation of the bistatic echo area of the target in the regions of interest in this report.

The choice of the position of the antenna terminals at one end of the body may not appear to be physically realizable but consider the traveling-wave antenna shown in Fig. 3. If the antenna terminals are shorted by means of a plate that fills the circular aperture of the coaxial cable, the coaxial cable may be removed as shown in Fig. 3(b). In this case the reflection coefficient is unity. The size of ground plane is then reduced. In the

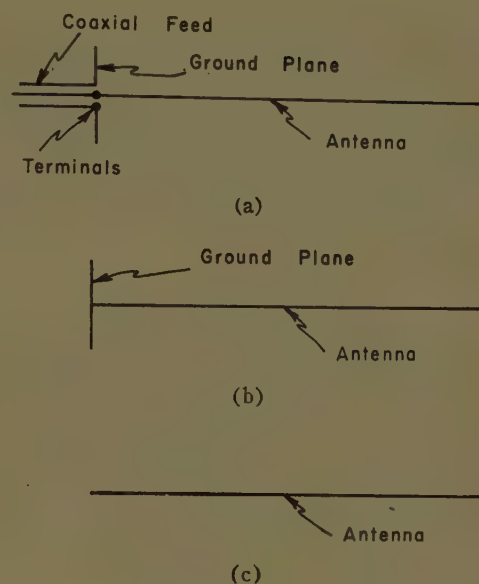


Fig. 3—Long, thin rod as a degenerate form of an antenna. (a) Traveling-wave antenna. (b) Same antenna with terminals shorted. (c) Same antenna as area of ground plane approaches zero.

limit the ground plane disappears and the configuration becomes that of the long, thin wire shown in Fig. 3(c). As the size of ground plane is reduced, the major change in electrical properties is that the reflection coefficient changes. This is indeed the manner in which the reflection coefficient is to be determined experimentally. The echo area patterns of the configurations of both Fig. 3(b) and 3(c) are measured for regions of longitudinal incidence of interest. The ratio of the two patterns is determined by the square of the ratio of reflection coefficients, as may be seen in (6). It is necessary to exclude the echo area of the flat plate in such considerations. However, for the size of plate (about  $1\lambda$  in diameter) considered, such effects are negligible, especially since the echo area maximum of the plate and the target usually do not occur for the same orientation.

#### EXPERIMENTAL TECHNIQUE

The equipment used to make the required echo area measurements is described in several technical reports.<sup>14-16</sup> Briefly it consists of a pulsed radar set with an attenuator placed in the waveguide to the receiver. This attenuator is servo driven to maintain the input signal to the receiver at a constant level. The attenuator

<sup>14</sup> D. R. Rhodes, "An Investigation of Pulsed Radar Systems for Model Measurements," Antenna Lab., The Ohio State Univ. Res. Foundation Rep. 475-6; December 1, 1953. Prepared under Contract AF 18(600)-19, Air Res. and Dev. Command, Wright Air Dev. Center, Wright-Patterson Air Force Base, Ohio.

<sup>15</sup> J. Bacon, "K-Band Radar Modifications," Antenna Lab., The Ohio State Univ. Res. Foundation, Rep. 475-12; June 30, 1954. Prepared under Contract AF 18(600)-19, Air Res. and Dev. Command, Wright Air Dev. Center, Wright-Patterson Air Force Base, Ohio.

<sup>16</sup> Modification of a Radar System for Automatic Recording of Back Scattering Radiation Patterns," Antenna Lab., The Ohio State Univ. Res. Foundation, Final Rep. 406-1, vol. 1; July 2, 1951. Prepared under Contract AF 33(038)-10101, Air Res. and Dev. Command, Wright Air Dev. Center, Wright-Patterson Air Force Base, Ohio.

<sup>12</sup> *Ibid.*, p. 53.

<sup>13</sup> J. D. Kraus, "Antennas," McGraw-Hill Book Co., Inc., New York, N. Y., p. 15; 1950.



is mechanically linked to a recorder. A standard target, in this case a 6-inch sphere, is used to calibrate the equipment. The target is string supported in such a manner that it can be continuously rotated. The echo area patterns are measured in the  $\phi = 0^\circ$  plane using  $E_\theta$  polarization as shown in the coordinate system of Fig. 1. Measurements were made at a frequency of 23,850 mc and a range of 275 feet.

### POLYROD ANTENNA

The first example to be considered is the polyrod antenna. The antenna configuration used is shown in Fig. 4. The antenna and its measured field pattern were provided by Professor George Mueller of the Electrical Engineering Department, The Ohio State University. A small conducting disk replaces the feed terminals, as is shown in Fig. 4, thus giving nearly complete reflection ( $\gamma = 1$ ). The measured echo area pattern of this antenna is shown in Fig. 5.

The directivity of the antenna is computed from the approximate equation<sup>17</sup>

$$D = \frac{41,253}{\phi_0 \theta_0}$$

where  $\phi_0$  and  $\theta_0$  are the half-power beamwidths obtained from the measured antenna pattern. It has been previously noted that polyrod antennas are not lossless devices, and that for the cases reported, the gain is approximately one db less than the directivity.<sup>18</sup> Therefore the gain ( $G$ ) is taken as one db less than the directivity computed by (9) for this example. The gain function of this antenna is

$$G(\theta) = G[f(\theta)]^2$$

where  $f(\theta)$  is the measured electric field pattern of the antenna.

Substituting into (6) gives

$$\sigma = \frac{G^2[f(\theta)]^4}{4\pi}$$

The measured and computed echo area patterns are compared in Fig. 5. Good agreement is obtained in the region when the echo area is due to traveling waves set up on the antenna (approximately  $0^\circ$  to  $30^\circ$ ).

### THE LONG, THIN ROD

A steel rod that is  $39\lambda$  long and  $\lambda/4$  in diameter is the second example to be considered. The magnitude of the first maximum of the echo area pattern of the steel rod is 9 square wavelengths. This magnitude is increased to 28.2 square wavelengths by using a silver rod. The measured echo area pattern of the silver rod is shown in

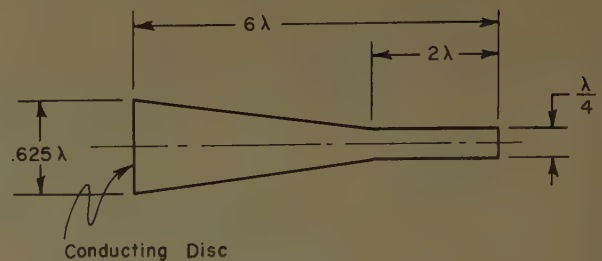


Fig. 4—Polyrod antenna.

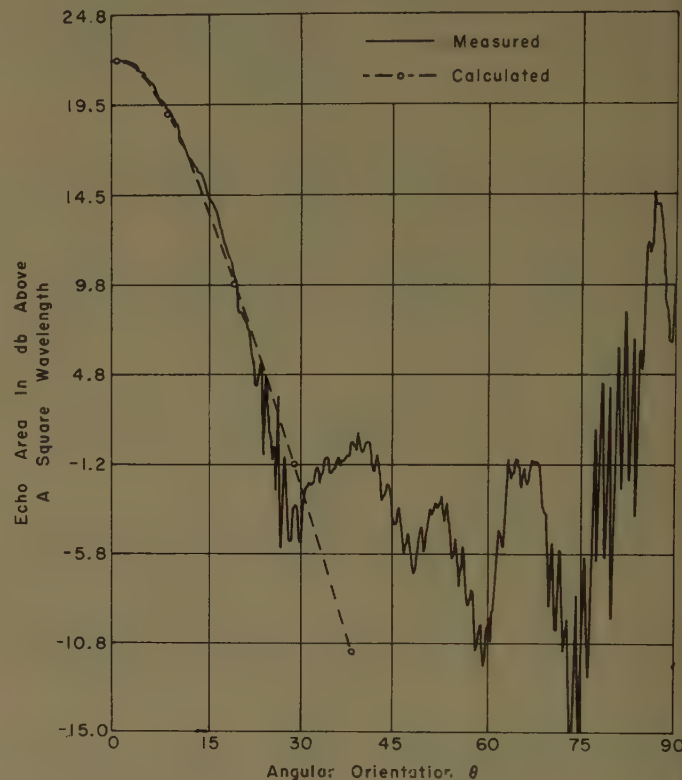


Fig. 5—Echo area of the polyrod antenna.

Fig. 6. The current reflection coefficient  $\gamma$  was found to be equal to 0.32 by the method described earlier.

The gain function of a thin, linear traveling-wave antenna with a relative phase velocity of one is derived in the Appendix (15). Substituting these values in (6) gives

$$\sigma = 0.000850 \left\{ \frac{\sin \theta}{1 - \cos \theta} \sin [124.5(1 - \cos \theta)] \right\}^4 \quad \text{square wavelengths} \quad (7)$$

Theoretical values obtained using this equation are also shown in Fig. 6. The first four lobes are plotted in detail. Excellent agreement is obtained.

It is to be noted that the theory predicts that the echo area due to the traveling-wave mode is sensitive to polarization. The incident wave must be polarized in the plane defined by the axis and the direction of wave propagation; *i.e.*, the polarization required is designated as  $E_\theta$  in Fig. 1. This is because of the polarization properties of a thin linear traveling-wave antenna.

<sup>17</sup> J. D. Kraus, *op. cit.*, p. 25.

<sup>18</sup> J. J. Panakal and G. E. Mueller, "An Investigation of Polystyrene Rod Antennas," Antenna Lab., The Ohio State Univ. Res. Foundation, Rep. 510-11; June 15, 1954. Prepared under Contract DA36-039sc15554, U. S. Army, Evans Signal Laboratory, Belmar, N. J.

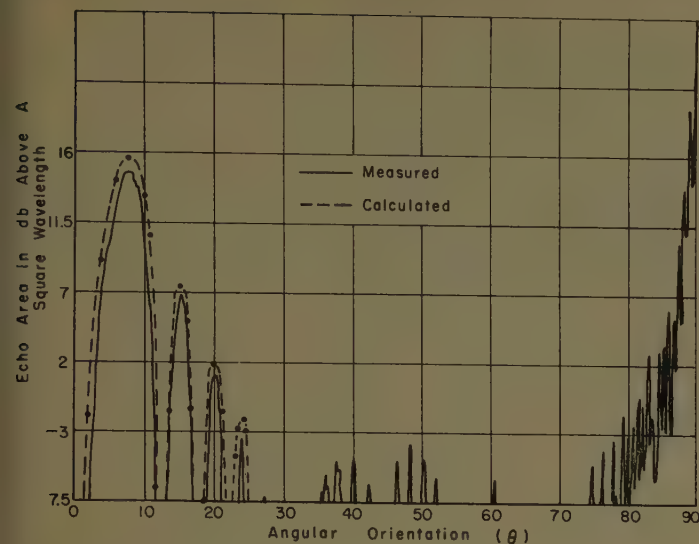


Fig. 6—Echo area of a long, thin rod.

### THE OGIVE

The theory is next applied to obtain the echo area of the ogive (an arc of a circle rotated about its chord) shown in Fig. 7. The measured echo area pattern of the ogive of Fig. 7 is shown in Fig. 8. The current reflection coefficient was found to be 0.7 by the method described earlier.

The ogive is considered as a traveling-wave antenna whose relative phase velocity equals the average relative phase velocity in the direction of the axis of symmetry when the current is traveling along the surface of the ogive at a relative phase velocity of one. This is expressed mathematically as follows:

$$(v_z)_{av} = \frac{1}{L} \int_0^L v_z dl$$

where  $L$  is the length of ogive,  $v_z$  is the component of relative phase velocity in the direction of the axis of symmetry, and  $(v_z)_{av}$  is the desired average relative phase velocity.

In this case  $(v_z)_{av} = 0.99$ . The ogive is then treated as a thin linear traveling-wave antenna in order to obtain its field pattern.

The gain function of a thin, linear traveling-wave antenna with a relative phase velocity of 0.99 is found in the Appendix (14). Substituting the appropriate values into (6) gives

$$\sigma = 0.0131 \left\{ \frac{\sin \theta}{1 - 0.99 \cos \theta} \sin [125.5(1 - 0.99 \cos \theta)] \right\}^4 \quad (8)$$

The calculated echo area pattern is plotted in detail for the first three lobes in Fig. 8. The agreement is good considering the approximations that are made. Also

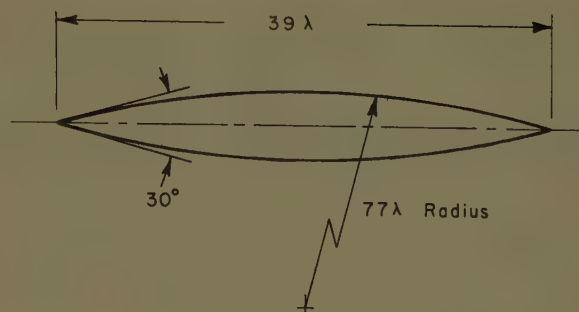


Fig. 7—Dimensional drawing of the ogive.

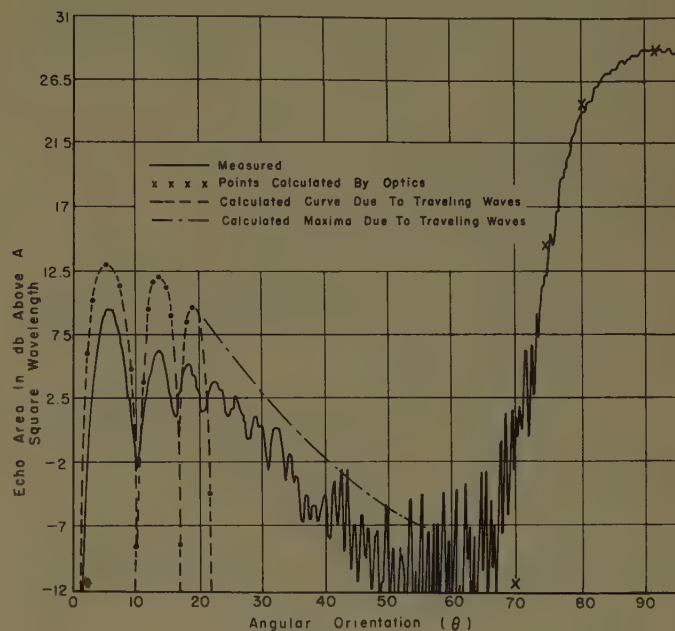


Fig. 8—Echo area of ogive.

shown in Fig. 8 is the envelope of the echo area pattern maxima, and points calculated from physical optics for aspects near broadside.

It is interesting to note that when a hollow  $0.9\lambda$  cylinder is placed over the far point of the ogive the maximum echo area falls to about one square wavelength. This clearly demonstrates that the point located in shadow region is of major significance in determining the echo area.

The echo area of the ogive is sensitive to polarization in the same manner as the long, thin wire, because of the polarization properties of a long, thin traveling-wave antenna.

### CONCLUSION

The agreement of the calculated and experimental values of echo area show that the traveling-wave mode must be considered in treating the echo area of these and similar bodies in near end-fire region. Since the maximum gain of a thin traveling-wave antenna increases with frequency it may further be concluded that this mode becomes even more significant as the frequency is increased.



## APPENDIX

## GAIN OF A THIN, LOSSLESS TRAVELING-WAVE ANTENNA

For a lossless antenna, the gain  $G$  equals the directivity  $D$  which is defined as<sup>19</sup>

$$D = \frac{4\pi U_m}{P} = \frac{4\pi(\text{maximum radiation intensity})}{\text{total power radiated}} \quad (9)$$

The magnitude of the magnetic field intensity  $H_\phi$  of a thin traveling-wave antenna is given by<sup>20</sup>

$$H_\phi = \frac{I_0 P}{2\pi R} \frac{\sin \theta}{1 - p \cos \theta} \left\{ \sin \frac{\beta L}{2} (1 - p \cos \theta) \right\}$$

where

$I_0$  = the current magnitude

$R$  = the range

$\theta$  = defined by the coordinate system of Fig. 1

$p = v/c$  = relative phase velocity

$v$  = the velocity of the wave

$c$  = the velocity of a wave in free space

$\beta = 2\pi/\lambda$  = the propagation factor along the surface of the antenna

$\lambda$  = the wavelength and

$L$  = the length of the antenna.

The radiation intensity  $U$  of such an antenna is<sup>21</sup>

$$U = R^2 S$$

$$= K^2 \left\{ \frac{\sin \theta}{1 - p \cos \theta} \left[ \sin \frac{\beta L}{2} (1 - p \cos \theta) \right] \right\}^2 \quad (10)$$

where  $S$  is the power intensity and  $K$  is a constant. The total power radiated is

$$P = \int \int U \sin \theta d\theta d\phi$$

$$= \int_0^{2\pi} \int_0^\pi K^2 \frac{\sin^3 \theta}{(1 - p \cos \theta)^2} \left[ \sin \frac{\beta L}{2} (1 - p \cos \theta) \right]^2 d\theta d\phi.$$

The directivity is

$$D = \frac{4\pi K^2 A^2}{K^2 \int_0^{2\pi} \int_0^\pi \frac{\sin^3 \theta}{(1 - p \cos \theta)^2} \left[ \sin \frac{\beta L}{2} (1 - p \cos \theta) \right]^2 d\theta d\phi} \quad (11)$$

where  $A$  is the maximum value of the pattern factor

$$\left\{ \frac{\sin \theta}{(1 - p \cos \theta)} \sin \frac{\beta L}{2} (1 - p \cos \theta) \right\}.$$

Integrating the denominator of (11) with respect to  $\phi$  gives

$$D = \frac{2A^2}{\int_0^\pi \frac{\sin^3 \theta}{(1 - p \cos \theta)^2} \left[ \sin \frac{\beta L}{2} (1 - p \cos \theta) \right]^2 d\theta} \quad (12)$$

The integral in the denominator can be evaluated by means of several changes of variables.

The first change of variables is  $x = 1 - p \cos \theta$ ; applying this to the integral in the denominator of (12),

$$\begin{aligned} & \int_0^\pi \frac{\sin^3 \theta}{(1 - p \cos \theta)^2} \left\{ \sin \left[ \frac{\beta L}{2} (1 - p \cos \theta) \right] \right\}^2 d\theta \\ &= \int_{1-p}^{1+p} \frac{p^2 - 1 + 2x - x^2}{p^3 x^2} \sin^2 \left( \frac{\beta L}{2} x \right) dx \\ &= \frac{1}{p^3} \int_{1-p}^{1+p} \left( -1 + \frac{2}{x} + \frac{p^2 - 1}{x^2} \right) \sin^2 \frac{\beta L}{2} x dx \\ &= \frac{1}{p^3} \left\{ \int_{1-p}^{1+p} \left( -\sin^2 \frac{\beta L}{2} x \right) dx + \int_{1-p}^{1+p} \frac{1 - \cos \beta L x}{x} dx \right. \\ & \quad \left. + \frac{1}{2} \int_{1-p}^{1+p} \frac{p^2 - 1}{x^2} dx - \frac{p^2 - 1}{2} \int_{1-p}^{1+p} \frac{\cos \beta L x}{x^2} dx \right\} \quad (13) \end{aligned}$$

The first integral on the right-hand side of (13) is approximately evaluated as follows:

$$\begin{aligned} -\frac{1}{p^3} \int_{1-p}^{1+p} \sin^2 \frac{\beta L}{2} x dx &= -\frac{1}{p^3} \left\{ \frac{x}{2} + \frac{\sin \beta L x}{2\beta L} \right\}_{1-p}^{1+p} \\ &\doteq -\frac{1}{p^2} \quad \text{for } \beta L \gg 1. \end{aligned}$$

The second integral on the right-hand side of (13) is evaluated by means of the change of variable  $y = \beta L x$ . Then

$$\begin{aligned} \frac{1}{p^3} \int_{1-p}^{1+p} \frac{1 - \cos \beta L x}{x} dx &= \frac{1}{p^3} \int_{\beta L(1-p)}^{\beta L(1+p)} \frac{1 - \cos y}{y} dy \\ &= \frac{1}{p^3} \{ \text{Cin } \beta L(1+p) - \text{Cin } \beta L(1-p) \} \end{aligned}$$

where  $\text{Cin } x$  is a tabulated modified cosine integral function.<sup>22</sup>

The third integral of (13) is simply

$$\frac{1}{2p^3} \int_{1-p}^{1+p} \frac{p^2 - 1}{x^2} dx = -\frac{1}{p^2}.$$

The last integral of (13) is evaluated by means of integral tables<sup>23</sup> giving

<sup>19</sup> J. D. Kraus, *op. cit.*, p. 23.

<sup>20</sup> *Ibid.*, p. 151.

<sup>21</sup> *Ibid.*, p. 15.

<sup>22</sup> *Ibid.*, p. 539.

<sup>23</sup> R. S. Burington, "Handbook of Mathematical Tables and Formulas," Handbook Publishers, Inc., Sandusky, Ohio, p. 81; 1947.

$$-\frac{p^2-1}{2p^3} \int_{1-p}^{1+p} \frac{\cos \beta L x}{x^2} dx = \frac{p^2-1}{2p^3} \left[ \frac{\cos \beta L(1+p)}{1+p} - \frac{\cos \beta L(1-p)}{1-p} + \beta L \int_{1-p}^{1+p} \frac{\sin \beta L x}{x} dx \right].$$

The final integral to be evaluated is the one remaining in the last expression above. It is evaluated by means of the change of variable  $y = \beta L x$ . Then

$$\begin{aligned} \beta L \frac{p^2-1}{2p^3} \int_{1-p}^{1+p} \frac{\sin \beta L x}{x} dx \\ = \frac{p^2-1}{2p^3} \beta L \int_{\beta L(1-p)}^{\beta L(1+p)} \frac{\sin y}{y} dy \\ = \frac{p^2-1}{2p^3} \beta L \{ \text{Si} [\beta L(1+p)] - \text{Si} [\beta L(1-p)] \} \end{aligned}$$

where  $\text{Si}(x)$  is a tabulated function<sup>24</sup> known as the sine integral.

Combining the solutions of these integrals gives

$$\begin{aligned} \int_0^\pi \frac{\sin^3 \theta}{(1-p \cos \theta)^2} \left\{ \sin \left[ \frac{\beta L}{2} (1-p \cos \theta) \right] \right\}^2 d\theta \\ = -\frac{2}{p^2} + \frac{\text{Cin} \beta L(1+p) - \text{Cin} \beta L(1-p)}{p^3} \\ + \frac{1}{2p^3} \{ (p-1) \cos \beta L(1+p) + (p+1) \cos \beta L(1-p) \\ + (p^2-1) \beta L [\text{Si} (\beta L\{1+p\}) - \text{Si} (\beta L\{1-p\})] \}. \end{aligned}$$

It is now only necessary to obtain a value for  $A$ , the pattern factor maximum, to completely evaluate (12). This may be done by either setting the derivative of the pattern factor equal to zero, which leaves a complicated

transcendental equation to be solved, or by plotting the pattern factor. The second method is used since the results are also useful in plotting the desired echo area.

The length and relative phase velocity of the two antennas which are of interest, and the values obtained by the methods described are tabulated below.

$\beta L$	$p$	$A$	$D=G$
251	0.99	6.37	23.5
249	1.00	13.2	60

Since the gain function  $G(\theta)$  of an antenna varies as the square of the field pattern, the gain functions of these two antennas are

$$G(\theta) = 0.580 \left\{ \frac{\sin \theta}{1 - 0.99 \cos \theta} \cdot \sin [125.5(1 - 0.99 \cos \theta)] \right\}^2 \quad (14)$$

for  $p=0.99$  and

$$G(\theta) = 0.345 \left\{ \frac{\sin \theta}{1 - \cos \theta} \sin [124.5(1 - \cos \theta)] \right\}^2 \quad (15)$$

for  $p=1$ .

#### ACKNOWLEDGMENT

It is a particular pleasure to acknowledge the encouragement and stimulating discussion provided by E. M. Kennaugh, C. T. Tai, and T. E. Tice. The assistance of O. Click and S. A. Redick in making measurements and calculations is also acknowledged. The research described in this paper was carried out under Contract AF 33(616)-2546, Air Research and Development Command, Wright Air Development Center, Wright-Patterson Air Force Base, Ohio.

<sup>24</sup> J. D. Kraus, *op. cit.*, p. 537.





# Back-Scattering Cross Section of a Center-Loaded Cylindrical Antenna\*

YUEH-YING HU†

**Summary**—A solution of the broadside back-scattering cross section,  $\sigma$ , of a center-loaded cylindrical antenna with any load impedance,  $Z_L$ , is obtained by a variational method through a four-terminal network approach. A simple formula for  $\sigma$ , in terms of  $Z_L$  and the parameters  $Z_{11}$ ,  $Z_{12}$ , and  $Z_{22}$  associated with the antenna has been derived. The impedances  $Z_{11}$ ,  $Z_{12}$ , and  $Z_{22}$  are independent of the load and they are determined by using the variational principle. Numerical results of the first order approximation are presented, and they are in good agreement with some measured results available in the literature.

## INTRODUCTION

THE back-scattering cross section,  $\sigma$ , of a cylindrical antenna with either no load (shorted) or matched load was studied both theoretically and experimentally by Dike and King.<sup>1</sup> The first order approximation of their theoretical result deviates from the measured result considerably in some cases. Moreover, higher order approximations are rather difficult to obtain by the integral equation method used, because the iteration process involves repeated integrals. Other approximations of  $\sigma$  are also obtained by Van Vleck, *et al.*,<sup>2</sup> using the emf method and by Tai,<sup>3</sup> using the variational method. Measured results are also reported by Sevick<sup>4</sup> in absolute values rather than the relative values presented by Dike and King. However, both the theoretical and experimental results by Van Vleck, Tai, and Sevick are limited to shorted cylindrical antennas—cylindrical wires. This paper presents a variational method to determine the back-scattering cross section of a center-loaded cylindrical antenna with any load impedance,  $Z_L$ , by using a four-terminal network approach. There are two advantages of the method used in this study. First, as a consequence of the four-terminal network approach, a simple logical formulation of  $\sigma$  in terms of  $Z_L$  and the antenna impedance parameters  $Z_{11}$ ,  $Z_{12}$ , and  $Z_{22}$  is obtained. Since the parameters  $Z_{11}$ ,  $Z_{12}$ , and  $Z_{22}$  are independent of the load and depend only on the geometrical configurations of the cylindrical antenna,

one needs only to determine these parameters for an antenna once in order to determine the back-scattering cross section of this antenna loaded with any impedance. Second, because of the stationary property of the variational expressions used for determining  $Z_{11}$ ,  $Z_{12}$ , and  $Z_{22}$ , rather accurate results are obtained. Furthermore, one can obtain more accurate results by using higher order approximations. There appears to be no analytical difficulty in finding higher order approximations by the present method.

## BACK-SCATTERING CROSS SECTION

The back-scattering cross section,  $\sigma$ , of an object is defined<sup>5</sup> as the equivalent area intercepting that amount of power from an incident electromagnetic plane wave which, when scattered isotropically, produces a back-scattered field equal to that observed from the object. Mathematically,  $\sigma$  of an object can be expressed in terms of the field quantities as

$$\sigma = 4\pi r_0^2 \frac{|E_r^s|^2}{|E_0^i|^2} \quad (1)$$

where  $E_0^i$  is the incident electric field intensity at the object, and  $E_r^s$  is the back-scattered field intensity at a distance  $r_0$  far away from the object. In this research, interest is limited to back-scattering cross sections of center-loaded cylindrical antennas with respect to a broadside incident plane wave, although the method can be applied to oblique incidence and to other types of antennas. A fictitious short dipole at a distance  $r_0$  far away from the cylindrical antenna, as shown by Fig. 1, is imagined both to serve as the source of a broadside incident field and to detect the back-scattered field at the same time. It is known that the incident field intensity in the direction of the antenna ( $z$  direction) produced by a short dipole of length  $\Delta l$  with dipole moment  $I_1(0)\Delta l$ , is

$$E_0^i = \frac{j\eta\beta}{4\pi} I_1(0)\Delta l \frac{e^{-i\beta r_0}}{r_0} \quad (2)$$

where

$$\eta = \sqrt{\mu/\epsilon} = 120\pi \text{ ohm}$$

$$\beta = \omega\sqrt{\mu\epsilon} = 2\pi/\lambda \text{ radians/meter.}$$

In order to determine  $\sigma$  by (1), one needs to determine the back-scattered field  $E_r^s$  at the short dipole from the

\* Manuscript received by the PGAP, March 8, 1957; revised manuscript received, June 17, 1957. The research reported in this paper was supported by Rome Air Dev. Center, Rome, N. Y., under Contract No. AF 30(635)-2808 between the Air Force and Syracuse University, from October, 1954 to September, 1956. This research was the early first part work of three parts under that contract.

† Dept. of Elec. Eng., Syracuse University, Syracuse, N. Y.  
<sup>1</sup> S. H. Dike and D. D. King, "The absorption gain and back-scattering cross section of the cylindrical antenna," *Proc. IRE*, vol. 40, pp. 853-860; July, 1952.

<sup>2</sup> J. H. Van Vleck, F. Block, and M. Hammermesh, "Theory of radar reflection from wires or thin metallic strips," *J. Appl. Phys.*, vol. 18, pp. 274-294; March, 1947.

<sup>3</sup> C. T. Tai, "Electromagnetic back-scattering from cylindrical wires," *J. Appl. Phys.*, vol. 23, pp. 909-916; August, 1952.

<sup>4</sup> J. Sevick, "Experimental and Theoretical Results on the Back-Scattering Cross Section of Coupled Antennas," *Cruft Laboratory, Harvard University, Cambridge, Mass., Tech. Rep. No. 150*; May, 1952.

<sup>5</sup> D. E. Kerr, "Propagation of Short Radio Waves," *M.I.T. Rad. Lab. Series*, McGraw-Hill Book Co., Inc., New York, N. Y., vol. 13, p. 33; 1951.

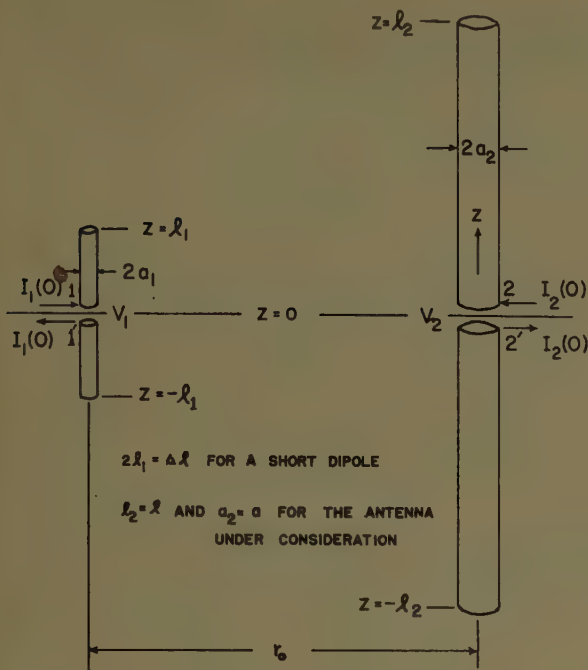


Fig. 1—A cylindrical antenna with its fictitious short dipole.

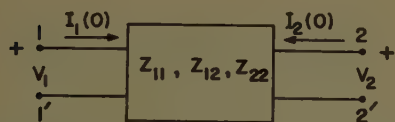


Fig. 2—The four-terminal network representation of an antenna.

cylindrical antenna. Notice that for the same cylindrical antenna,  $E_r^s$  varies with the load impedance connected across its feeding terminals. To determine  $E_r^s$  for any load impedance  $Z_L$ , a four-terminal network approach is used. Referring to Fig. 1, the feeding terminal pairs of both the short dipole and the cylindrical antenna constitute the terminal pairs 1-1' and 2-2', respectively, of a four-terminal network as shown in Fig. 2. Therefore the feeding terminal voltages and currents of the short dipole and the antenna become the terminal quantities of the four-terminal network. The terminal voltages and currents are related in terms of the four-terminal network impedance parameters  $Z_{11}$ ,  $Z_{12}=Z_{21}$ ,  $Z_{22}$  as follows

$$V_1 = Z_{11}I_1(0) + Z_{12}I_2(0) \quad (3)$$

$$V_2 = Z_{21}I_1(0) + Z_{22}I_2(0) \quad (4)$$

where  $V_1$ ,  $V_2$  = voltages across the feeding terminals of the short dipole and the antenna, respectively, and  $I_1(0)$ ,  $I_2(0)$  = currents flowing into the feeding terminals of the short dipole and the antenna, respectively. If a load impedance  $Z_L$  is connected to the terminal pair 2-2', then

$$V_2 = -Z_L I_2(0). \quad (5)$$

Substituting (5) into (4), solving for  $I_2(0)$  and then substituting  $I_2(0)$  into (3), one obtains

$$V_1 = \left[ Z_{11} - \frac{Z_{12}^2}{Z_{22} + Z_L} \right] I_1(0). \quad (6)$$

Recall that  $V_1$  is the voltage required to send a feeding current  $I_1(0)$  into the short dipole. This  $V_1$  consists of two parts. One is the voltage required to send  $I_1(0)$  into the short dipole with the cylindrical antenna removed. This part corresponds to the voltage drop  $Z_1 I_1(0)$ , where  $Z_1$  is the input impedance of the short dipole in free space alone. The other part, denoted by  $V_r^s$ , is due to the back-scattered field  $E_r^s$  because of the presence of the cylindrical antenna. Since  $E_r^s$  is in the same direction as the short dipole for broadside incidence, therefore

$$V_r^s = E_r^s \Delta l$$

and

$$V_1 = V_r^s + Z_1 I_1(0) = E_r^s \Delta l + Z_1 I_1(0). \quad (7)$$

Substituting (7) into (6), one has

$$E_r^s = \frac{I_1(0)}{\Delta l} \left[ (Z_{11} - Z_1) - \frac{Z_{12}^2}{Z_{22} + Z_1} \right]. \quad (8)$$

If the impedance  $Z_1$  of the short dipole and the self and mutual impedance  $Z_{11}$ ,  $Z_{12}$ , and  $Z_{22}$  of the coupled short dipole and the cylindrical antenna are determined, one is ready to compute  $\sigma$  for any  $Z_L$  from (1) by substituting in  $E_0^i$  from (2) and  $E_r^s$  from (8).

#### VARIATIONAL FORMULATIONS

The physical set-up of Fig. 1 may be considered as a special case of two coupled cylindrical antennas. In this case, the cylindrical antenna number 1 is a short dipole and the current distribution over it is assumed to be constant and equal to the feeding current. The method used in this research for determining the impedances of coupled antennas was found, after the numerical results were obtained, to have some similarities to the work of Levis and Tai.<sup>6</sup> However, the particular treatment here enables us to single out the variational expressions for  $Z_{11}$ ,  $Z_{12}$ , and  $Z_{22}$  one at a time by proper choice of feeding currents. As a consequence, the variational formulas for the impedances which will be derived in this section are simpler than their determinantal solutions of simultaneous equations.

Let the current distributions over the coupled cylindrical antennas number 1 and number 2 be  $I_1(z)$  and  $I_2(z)$ , respectively. Assume the feeding gaps are very small. Then  $I_1(z)$  and  $I_2(z)$  satisfy the following simultaneous integral equations.

$$\begin{aligned} & \delta(z) [Z_{11}I_1(0) + Z_{12}I_2(0)] \\ &= \int_{-l_1}^{l_1} \Gamma_{11}(z - z') I_1(z') dz' + \int_{-l_2}^{l_2} \Gamma_{12}(z - z') I_2(z') dz' \quad (9) \end{aligned}$$

<sup>6</sup> C. A. Levis and C. T. Tai, "A method of analyzing coupled antennas of unequal sizes," IRE TRANS., vol. AP-4, pp. 128-132; April, 1956.



$$\delta(z)[Z_{21}I_1(0) + Z_{22}I_2(0)] \\ = \int_{-l_1}^{l_1} \Gamma_{21}(z-z')I_1(z')dz' + \int_{-l_2}^{l_2} \Gamma_{22}(z-z')I_2(z')dz' \quad (10)$$

where

$$\Gamma_{11}(z-z') = \frac{j\eta\beta}{4\pi} \left(1 + \frac{1}{\beta^2} \frac{\partial^2}{\partial z^2}\right) \frac{1}{2\pi} \int_0^{2\pi} \frac{e^{-j\beta r}}{r} d\phi$$

$$r = [(z-z')^2 + 4a_1^2 \sin^2(\phi/2)]^{1/2}.$$

$\delta(z)$  = Dirac delta function.

In the above equations,  $a_1$  is the radius of antenna number 1,  $l_1$  and  $l_2$  are the half-lengths of antennas number 1 and number 2, respectively,  $\phi$  is the axial angle subtended by  $z$  and  $z'$ , where  $z$  is the field point and  $z'$  is the source point on the surface of the cylindrical antenna. The functions  $\Gamma_{22}(z-z')$  and  $\Gamma_{12}(z-z')$  are obtained by replacing  $2a_1 \sin(\phi/2)$  in  $r$  with  $2a_2 \sin(\phi/2)$  and  $r_0$ , respectively, where  $a_2$  is the radius of the antenna number 2 and  $r_0$  is the distance between the axes of the two cylindrical antennas.

Let  $I_1'(z)$  and  $I_2'(z)$  be another pair of current distributions corresponding to the feeding currents  $I_1'(0)$  and  $I_2'(0)$ . Then  $I_1'(z)$  and  $I_2'(z)$  also satisfy (9) and (10) with  $I_1(0)$  and  $I_2(0)$  replaced by  $I_1'(0)$  and  $I_2'(0)$ . If one multiplies (9) by  $I_1'(z)$  and integrates from  $-l_1$  to  $l_1$ , and multiplies (10) by  $I_2'(z)$  and integrates from  $-l_2$  to  $l_2$  by adding the results, then one obtains

$$I_1'(0)Z_{11}I_1(0) + I_1'(0)Z_{12}I_2(0) + I_2'(0)Z_{21}I_1(0) \\ + I_2'(0)Z_{22}I_2(0) \\ = \iint I_1'\Gamma_{11}I_1 + \iint I_1'\Gamma_{12}I_2 + \iint I_2'\Gamma_{21}I_1 \\ + \iint I_2'\Gamma_{22}I_2 \quad (11)$$

where

$$\iint I_i\Gamma_{ij}I_j = \int_{-l_i}^{l_i} \int_{-l_j}^{l_j} I_i(z)\Gamma_{ij}(z-z')I_j(z')dz'dz$$

with

$$i = 1, 2, \quad j = 1, 2.$$

Separate expressions for the impedances  $Z_{11}$ ,  $Z_{22}$ , and  $Z_{12}$  can be obtained from (11) by proper choice of feeding currents as follows:

1) For  $Z_{11}$ , choose  $I_2'(0) = 0$ ,  $I_2(0) = 0$  and  $I_1'(0)/I_1(0) = K_1$  (a constant). As a result of  $I_2'(0) = I_2(0) = 0$ , (11) reduces to an expression for  $Z_{11}$  alone,

$$I_1'(0)Z_{11}I_1(0) = \iint I_1'\Gamma_{11}I_1 + \iint I_1'\Gamma_{12}I_2 \\ + \iint I_2'\Gamma_{21}I_1 + \iint I_2'\Gamma_{22}I_2.$$

Since both sets of currents, with and without prime, satisfy the same set of simultaneous equations, (9) and

(10), one has  $I_1'(z) = K_1 I_1(z)$  and  $I_2'(z) = K_1 I_2(z)$  due to  $I_1'(0) = K_1 I_1(0)$ . The above equation then becomes

$$Z_{11}I_1^2(0) = \iint I_1\Gamma_{11}I_1 + 2 \iint I_1\Gamma_{12}I_2 \\ + \iint I_2\Gamma_{22}I_2. \quad (12)$$

2) For  $Z_{22}$ , choose  $I_1'(0) = 0$ ,  $I_1(0) = 0$  and  $I_2'(0)/I_2(0) = K_2$  (a constant). Similarly, (11) reduces to

$$Z_{22}I_2^2(0) = \iint I_1\Gamma_{11}I_1 + 2 \iint I_1\Gamma_{12}I_2 \\ + \iint I_2\Gamma_{22}I_2. \quad (13)$$

3) For  $Z_{12}$ , choose  $I_1(0) = 0$  and  $I_2'(0) = 0$ . Eq. (11) then reduces to

$$I_1'(0)Z_{12}I_2(0) = \iint I_1'\Gamma_{11}I_1 + \iint I_1'\Gamma_{12}I_2 \\ + \iint I_2'\Gamma_{21}I_1 + \iint I_2'\Gamma_{22}I_2. \quad (14)$$

The separate expressions for  $Z_{11}$ ,  $Z_{22}$ , and  $Z_{12}$  can be proved to be stationary with respect to the true current distributions corresponding to the particular choice of feeding currents for each case. This can be proved by subtracting from the first variation of (11) both: 1) the results of multiplying (9) by  $\delta I_1'(z)$  and integrating from  $-l_1$  to  $l_1$  and of multiplying (10) by  $\delta I_2'(z)$  and integrating from  $-l_2$  to  $l_2$ ; 2) the results with the currents with and without prime interchanged in the results of part 1). Hence

$$I_1'(0)\delta Z_{11}I_1(0) + I_1'(0)\delta Z_{12}I_2(0) + I_2'(0)\delta Z_{21}I_1(0) \\ + I_2'(0)\delta Z_{22}I_2(0) = 0. \quad (15)$$

Eq. (15) is true for any choice of  $I_1(0)$ ,  $I_2(0)$ ,  $I_1'(0)$ , and  $I_2'(0)$ . By choosing the feeding currents in different ways, as in obtaining the expressions for  $Z_{11}$ ,  $Z_{12}$ , and  $Z_{22}$ , one proves, from (15),  $\delta Z_{11} = 0$ ,  $\delta Z_{22} = 0$ , and  $\delta Z_{12} = 0$ , respectively. If antenna number 2 is removed, then  $Z_{11}$  reduces to the impedance of antenna number 1 in free space alone. This impedance is denoted by  $Z_1$  as used for the short dipole case. It is clear that a variational expression for  $Z_1$  can be obtained from (12) by putting  $I_2(z) = 0$  as follows:

$$Z_1 I_1^2(0) = \iint I_1\Gamma_{11}I_1. \quad (16)$$

If antenna number 1 is a short dipole at a distance  $r_0$  far away from antenna number 2, ( $r_0 \gg l_2$ ). The following reasonable approximations can be used

$$I_1(z) \simeq I_1(0)$$

$$\Gamma_{12}(z-z') \simeq \Gamma_{12}(0-z')$$

$$\Gamma_{21}(z-z') \simeq \Gamma_{21}(z-0).$$

In such a case, the variational expressions for the impedances  $Z_{11}-Z_1$ ,  $Z_{22}$ , and  $Z_{12}$  can be obtained from (12)–(14) and (16) as follows:

$$(Z_{11} - Z_1)I_1^2(0) = 2I_1(0)\Delta l \int \Gamma_{12}I_2 + \iint I_2\Gamma_{22}I_2 \quad (17)$$

$$Z_{22}I_2^2(0) = \iint I_2\Gamma_{22}I_2 \quad (18)$$

$$I_1(0)Z_{12}I_2(0) = I_1'(0)\Delta l \int \Gamma_{12}I_2 + \iint I_2'\Gamma_{22}I_2. \quad (19)$$

The impedance expressions by (17)–(19) are stationary with respect to the true current distribution  $I_2(z)$  corresponding to the respective feeding conditions. Since  $I_2(z)$  is not known, appropriate functions have to be chosen to represent  $I_2(z)$ .

Since antenna number 1 is a short dipole and antenna number 2 is the antenna under consideration, the subscript 2 is dropped hereafter from  $I_2$  and  $a_2$  for convenience.

#### FIRST ORDER APPROXIMATION

From general knowledge about the current distributions over linear antennas, it is reasonable to assume that  $I_2(z)$  is a linear combination of a constant term, a sine term and a cosine term as follows:

$$I_2(z) = a + b \cos \beta z + c \sin \beta z. \quad (20)$$

The current distribution is assumed to satisfy the following conditions:

- 1) symmetrical about  $z=0$ , i.e.,  $I_2(-z) = I_2(z)$ ,
- 2)  $I_2(0)$  = the feeding current of the cylindrical antenna,
- 3)  $I_2(z) = 0$  at  $z = \pm l$ .

According to condition 1),  $\sin \beta |z|$  is used in (20) instead of  $\sin \beta z$ . By applying conditions 2) and 3) in (20), constants  $a$  and  $b$  can be eliminated, and (20) then becomes

$$\begin{aligned} I_2(z) &= I_2(0) \frac{\cos \beta z - \cos \beta l}{1 - \cos \beta l} \\ &\quad + k[\sin \beta(l - |z|) + \sin \beta |z| - \sin \beta l] \\ &= I_{20}(z) + kI_{21}(z) \end{aligned} \quad (21)$$

where

$$k = \frac{c}{1 - \cos \beta l}$$

$$I_{20}(z) = I_2(0) \frac{\cos \beta z - \cos \beta l}{1 - \cos \beta l}$$

$$I_{21}(z) = \sin \beta(l - |z|) + \sin \beta |z| - \sin \beta l.$$

Notice that  $I_{20}(z)$  and  $I_{21}(z)$  have the following properties:

$$\begin{aligned} I_{20}(0) &= I_2(0), & I_{20}(\pm l) &= 0, \\ I_{21}(0) &= 0, & I_{21}(\pm l) &= 0. \end{aligned}$$

Since the trial function for  $I_2(z)$  in (21) contains one adjustable constant  $k$ , quantities related to it are called the first order approximations.

Using (21) as trial function for  $I_2(z)$  in the expressions for  $Z_{11}-Z_1$ ,  $Z_{22}$ , and  $Z_{12}$ , given by (17), (18), and (19), respectively, and at the same time applying the corresponding feeding conditions, one obtains

$$\begin{aligned} (Z_{11} - Z_1)I_1^2(0) &= 2I_1(0)\Delta l \int \Gamma_{12}(k_{11}I_{21}) + \iint (k_{11}I_{21})\Gamma_{22}(k_{11}I_{21}) \quad (22) \end{aligned}$$

$$Z_{22}I_2^2(0) = \iint (I_{20} + k_{22}I_{21})\Gamma_{22}(I_{20} + k_{22}I_{21}) \quad (23)$$

$$\begin{aligned} I_1'(0)Z_{12}I_2(0) &= I_1'(0)\Delta l \int \Gamma_{12}(I_{20} + k_{12}I_{21}) \\ &\quad + \iint (k_{12}'I_{21})\Gamma_{22}(I_{20} + k_{12}I_{21}) \quad (24) \end{aligned}$$

where  $k_{11}$ ,  $k_{22}$ ,  $k_{12}$ , and  $k_{12}'$  are adjustable constants in the trial functions for the corresponding impedances and all the integrations are from  $-l$  to  $l$ . Since the impedance expressions are stationary, all the  $k$ 's can be determined by setting  $\partial Z/\partial k = 0$  in the corresponding expressions. Substituting the solutions for the  $k$ 's back into (22)–(24), one obtains the expressions for the impedances in terms of the trial functions and the geometry of the system as:

$$(Z_{11} - Z_1)I_1^2(0) = - \frac{\left[ I_1(0)\Delta l \int \Gamma_{12}I_{21} \right]^2}{\iint I_{21}\Gamma_{22}I_{21}} \quad (25)$$

$$Z_{22}I_2^2(0) = \iint I_{20}\Gamma_{22}I_{20} - \frac{\left[ \iint I_{20}\Gamma_{22}I_{21} \right]^2}{\iint I_{21}\Gamma_{22}I_{21}} \quad (26)$$

$$\begin{aligned} I_1'(0)Z_{12}I_2(0) &= I_1'(0)\Delta l \int \Gamma_{12}I_{20} \\ &\quad - \frac{\left[ I_1'(0)\Delta l \int \Gamma_{12}I_{21} \right] \left[ \iint I_{20}\Gamma_{22}I_{21} \right]}{\iint I_{21}\Gamma_{22}I_{21}}. \quad (27) \end{aligned}$$

The different integrals involved in (25)–(27) can be evaluated approximately. If  $l \gg a$  and  $r_0 \gg l$ , the approximated results of the integrals are listed in the Appendix in terms of quantities  $A$ ,  $B$ ,  $C$ ,  $D$ ,  $E$ ,  $F$ ,  $G$ , and  $H$ . These quantities are complicated expressions dependent only on  $\beta l$  and  $\Omega = 2 \ln 2l/a$  and independent of  $\Delta l$ ,  $r_0$ , and the feeding currents. By using the approximate results of the integrals, (25)–(27) become



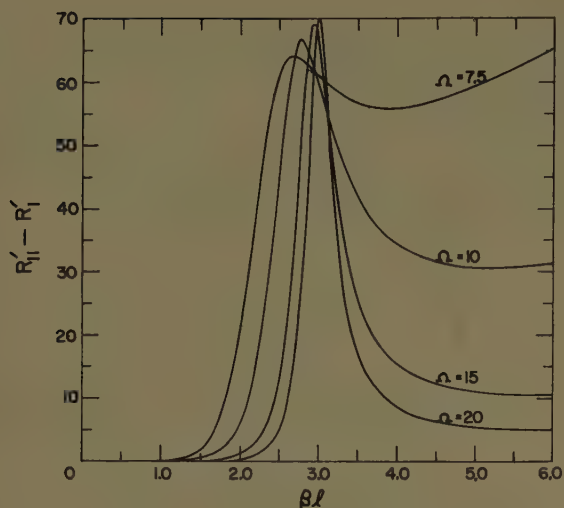


Fig. 3—The parameter,  $R'_{11} - R'_1$ , of cylindrical antennas.

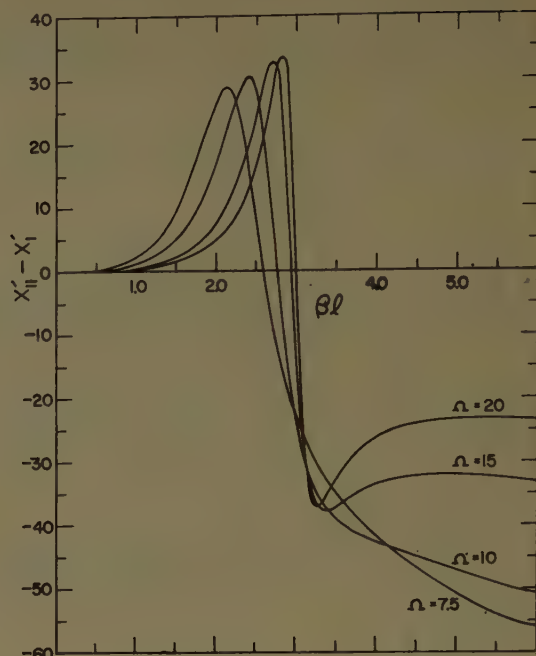


Fig. 4—The parameter,  $X'_{11} - X'_1$ , of cylindrical antennas.

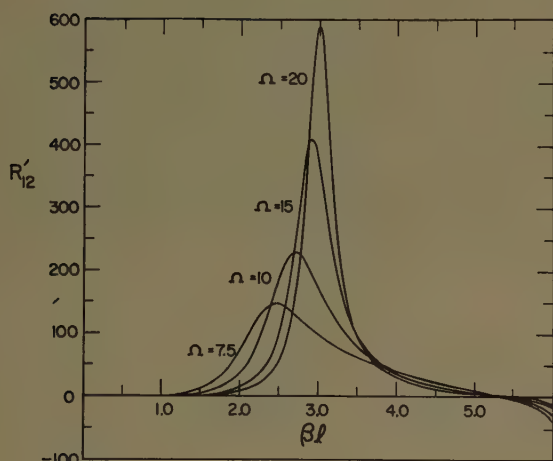


Fig. 5—The parameter,  $R'_{12}$ , of cylindrical antennas.

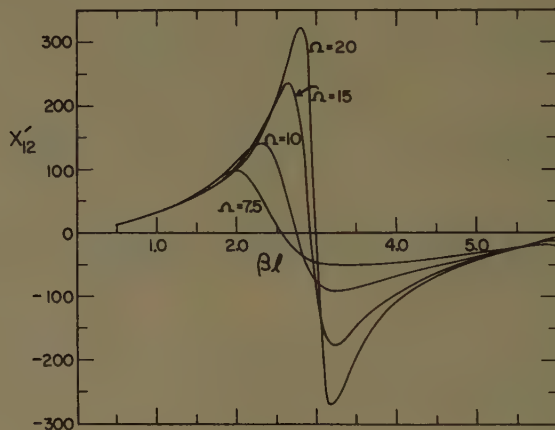


Fig. 6—The parameter,  $X'_{12}$ , of cylindrical antennas.

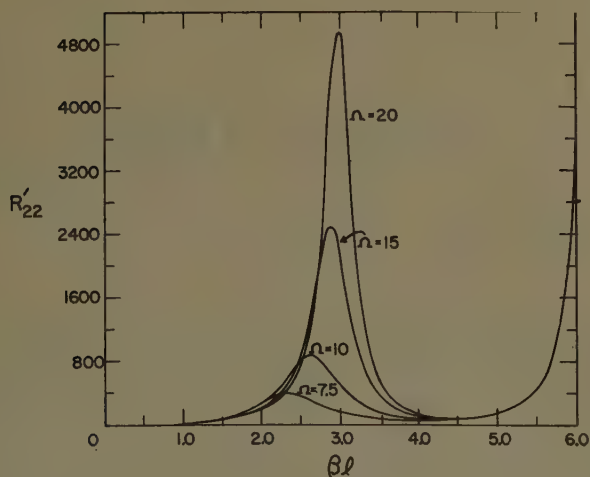


Fig. 7—The parameter,  $R'_{22}$ , of cylindrical antennas.

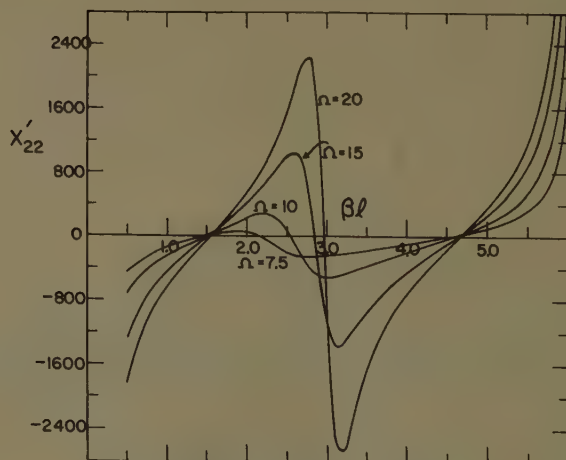


Fig. 8—The parameter,  $X'_{22}$ , of cylindrical antennas.

$$\begin{aligned}
Z_{22} &= j30 \left[ (A + jB) - \frac{(C + jD)^2}{E + jF} \right] = Z_{22}' \\
Z_{11} - Z_1 &= -j30 \left[ \frac{\Delta l}{r_0} e^{-j\beta r_0} \right]^2 \frac{H^2}{E + jF} \\
&= \left[ \frac{\Delta l}{r_0} e^{-j\beta r_0} \right]^2 (Z_{11}' - Z_1') \\
Z_{12} &= j30 \left[ \frac{\Delta l}{r_0} e^{-j\beta r_0} \right] \left[ G - H \frac{C + jD}{E + jF} \right] \\
&= \left[ \frac{\Delta l}{r_0} e^{-j\beta r_0} \right] Z_{12}'
\end{aligned} \quad (28)$$

where  $Z_{11}' - Z_1'$ ,  $Z_{12}'$ , and  $Z_{22}'$  are the parts independent of  $\Delta l$  and  $r_0$  in the expressions of  $Z_{11} - Z_1$ ,  $Z_{12}$ , and  $Z_{22}$ , respectively. The primed impedances depend only on  $A$ ,  $B$ ,  $C$ ,  $D$ ,  $E$ ,  $F$ ,  $G$ , and  $H$  and therefore on  $\beta l$  and  $\Omega$ .

Using (28), the back-scattered field intensity from (8) is:

$$E_r^s = \frac{I_1(0)}{\Delta l} \left[ \frac{\Delta l}{r_0} e^{-j\beta r_0} \right]^2 \left[ (Z_{11}' - Z_1') - \frac{Z_{12}'^2}{Z_{22}' + Z_L} \right] \quad (29)$$

The ratio of the squares of  $|E_r^s|$  and  $|E_0^i|$  from (29) and (2) is

$$\frac{|E_r^s|^2}{|E_0^i|^2} = \frac{1}{900\beta^2 r_0^2} \left| (Z_{11}' - Z_1') - \frac{Z_{12}'^2}{Z_{22}' + Z_L} \right|^2 \quad (30)$$

Therefore, according to (1), the back-scattering cross section is given by

$$\sigma/\lambda^2 = \frac{1}{900\pi} \left| (Z_{11}' - Z_1') - \frac{Z_{12}'^2}{Z_{22}' + Z_L} \right|^2 \quad (31)$$

Since the parameters  $Z_{11}' - Z_1'$ ,  $Z_{12}'$ , and  $Z_{22}'$  in (31) depend only on the geometry of the cylindrical antenna and are independent of the load, one needs only to determine these parameters once in order to determine  $\sigma/\lambda^2$  for a cylindrical antenna with any load impedance.

### NUMERICAL RESULTS

Actual computations have been carried out for cylindrical antennas with the following values of  $\Omega = 2 \ln(2l/a)$ : 7.5, 10, 15, and 20. For each  $\Omega$ ,  $(Z_{11}' - Z_1')$ ,  $Z_{12}'$ , and  $Z_{22}'$  were computed for  $\beta l$  from 0.5 to 6.0 in 0.1 intervals.  $\sigma/\lambda^2$  was computed for different load impedance  $Z_L = \infty$ , 0,  $(75 + j0)$  ohms,  $(300 + j0)$  ohms, and  $Z_{22}^*$ , where  $Z_{22}^*$  is the complex conjugate of  $Z_{22}'$ . When  $Z_L = Z_{22}^*$ , the case will be called matched.

Since the parameters  $(Z_{11}' - Z_1')$ ,  $Z_{12}'$ , and  $Z_{22}'$  are all one needs to determine  $\sigma/\lambda^2$  for an antenna with any load impedance, the results of the real and imaginary parts of  $Z_{11}' - Z_1'$ ,  $Z_{12}'$ , and  $Z_{22}'$ , denoted by  $R_{11}' - R_1'$ ,  $R_{12}'$ ,  $R_{22}'$  and  $X_{11}' - X_1'$ ,  $X_{12}'$ ,  $X_{22}'$ , respectively, are given in Figs. 3-8, p. 144. The back-scattering cross section,  $\sigma/\lambda^2$ , for same load impedance but for different values of  $\Omega$  are given in Figs. 9-13, p. 146. In Fig. 9 for  $Z_L = 0$  case, it is seen that the resonance peaks for

each  $\Omega$  occur at about  $\beta l = \pi/2$ ,  $3\pi/2$  or  $l = \lambda/4$ ,  $3\lambda/4$ . As  $\Omega$  increases, the first resonance peak shifts toward  $\beta l = \pi/2$  in the direction of increasing  $\beta l$ , but the second resonance peak shifts slightly toward  $\beta l = 3\pi/2$  in the direction of decreasing  $\beta l$ . The resonance peaks are sharper for larger values of  $\Omega$ . These phenomena appear also in Fig. 11 for the  $Z_L = (75 + j0)$  ohms case. However, the resonance peaks are relatively flatter. In the case of  $Z_L = (300 + j0)$  ohms (Fig. 12), the resonance peaks almost disappear but one still can recognize them for  $\Omega = 15$  and  $\Omega = 20$ . In Fig. 13 for the  $Z_L = \infty$  case, there is only one peak occurring at a value somewhat below  $\beta l = \pi$  or  $l = \lambda/2$ . The position of the peak shifts toward  $\beta l = \pi$  as  $\Omega$  increases. In all the cases, it is generally true that for the same value of  $\beta l$ , the back-scattering cross section increases as  $\Omega$  decreases except possibly in the neighborhood of resonance.

It is to be emphasized that the present theoretical results check very closely with Sevick's measurements, as shown by Fig. 14, p. 147, which are generally considered to be more accurate than those by Dike and King. Since Dike and King's measured results<sup>1</sup> were presented in relative values, comparisons can only be made on qualitative basis. The qualitative agreement between the present theoretical results and their measured results is better than that between their own theoretical<sup>1</sup> and measured results.<sup>1</sup> Some phenomena are observed both from the present theoretical results and their measured results but not from their theoretical results. These phenomena are: 1) the values of  $\sigma/\lambda^2$  for  $Z_L = 0$  case level off after the second peak for a certain interval of  $\beta l$  for 0.08-inch diameter cylindrical antenna as shown in Fig. 15. 2) The peak flattens as the diameter increases for the matched load case as shown by Fig. 16.

The theoretical results by Dike and King are obtained by using the integral equation method. It is rather difficult to obtain higher order approximations by the integral equation method, because the iteration process involves repeated integrals. As for the variational method, one can obtain higher order approximations systematically by adding more terms in the trial function for  $I_2(z)$ . This will be discussed in the next section.

### HIGHER ORDER APPROXIMATIONS

The trial function for  $I_2(z)$  used in the first order approximation fails to represent  $I_2(z)$  when  $\beta l = 2\pi$  or  $l = \lambda$ . This is a direct consequence of the assumed trial function for  $I_2(z)$ . Since both  $\sin \beta z$  and  $\cos \beta z$  are periodic functions, their values repeat as  $\beta z$  changes by  $2\pi$ . For an antenna with  $l = \lambda$ ,  $I_2(z)$  in (20) cannot satisfy both the conditions  $I_2(\pm l) = 0$  and  $I_2(0) = \text{nonzero feeding current}$ . It is also suspected that the trial function will be inadequate when  $\beta l$  is near to  $2\pi$ . In order to avoid this, the trial function for  $I_2(z)$  is modified with one additional term as follows:

$$I_2(z) = a + b \cos \beta z + c \sin \beta |z| + d \cos \frac{\beta z}{2} \quad (32)$$



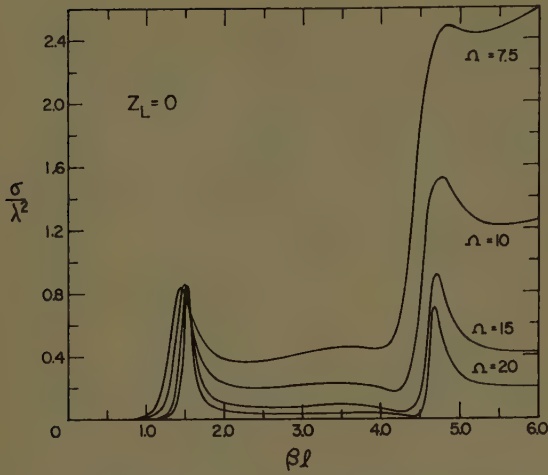


Fig. 9—Broadside back-scattering cross section of center-loaded cylindrical antennas with  $Z_L = 0$ .

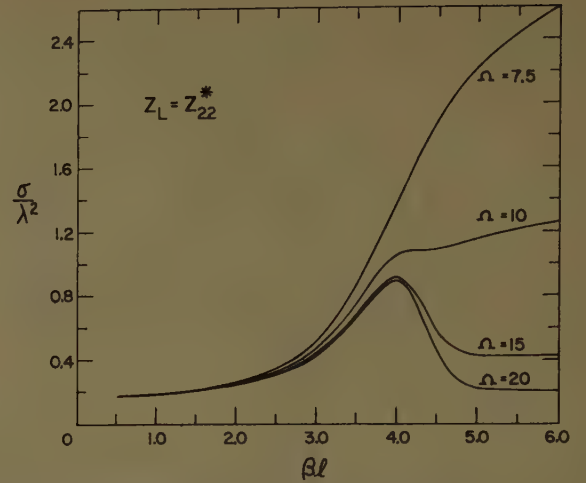


Fig. 10—Broadside back-scattering cross section of center-loaded cylindrical antennas with  $Z_L = Z_{22}^*$ .

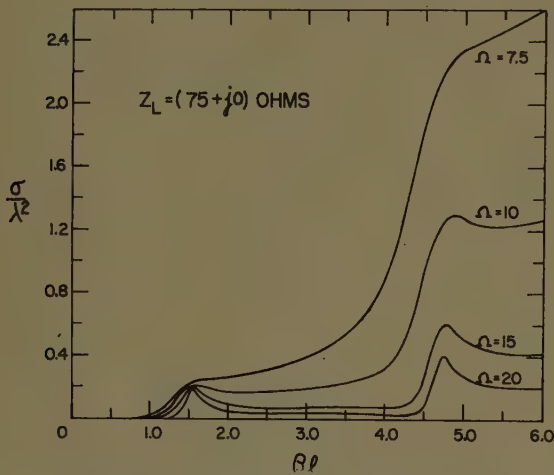


Fig. 11—Broadside back-scattering cross section of center-loaded cylindrical antennas with  $Z_L = (75 + j0)$  ohms.

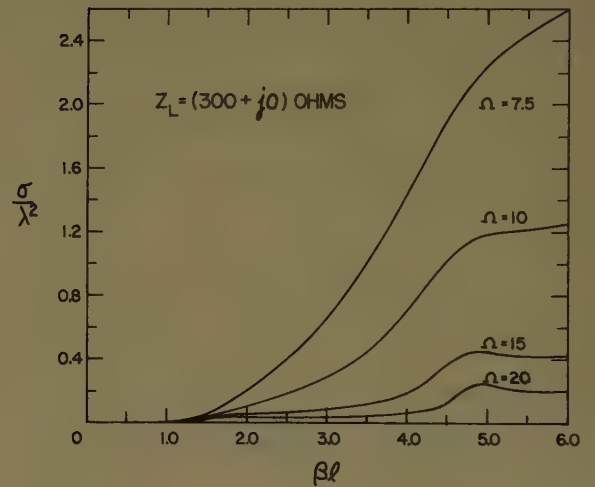


Fig. 12—Broadside back-scattering cross section of center-loaded cylindrical antennas with  $Z_L = (300 + j0)$  ohms.

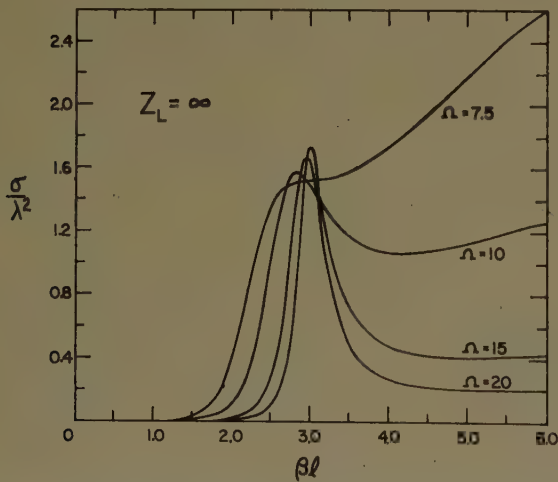


Fig. 13—Broadside back-scattering cross section of center-loaded cylindrical antennas with  $Z_L = \infty$ .

Using the same conditions,  $I_2(0)$  = feeding current and  $I_2(\pm l) = 0$ , constants  $a$  and  $d$  can be eliminated, and (32) becomes

$$I_2(z) = I_{20}(z) + k_1 I_{21}(z) + k_2 I_{22}(z) \quad (33)$$

where

$$k_1 = \frac{c}{1 - \cos \beta l}$$

$$k_2 = \frac{d}{1 - \cos \beta l}$$

$$I_{20}(z) = \frac{\cos \beta z - \cos \beta l}{1 - \cos \beta l}$$

$$I_{21}(z) = \sin \beta(l - |z|) + \sin \beta|z| - \sin \beta l$$

$$I_{22}(z) = (1 - \cos \beta z) \left( 1 - \cos \frac{\beta l}{2} \right)$$

$$- (1 - \cos \beta l) \left( 1 - \cos \frac{\beta z}{2} \right).$$

Then  $k_1$  and  $k_2$  can be determined by the stationary property of the impedances by setting

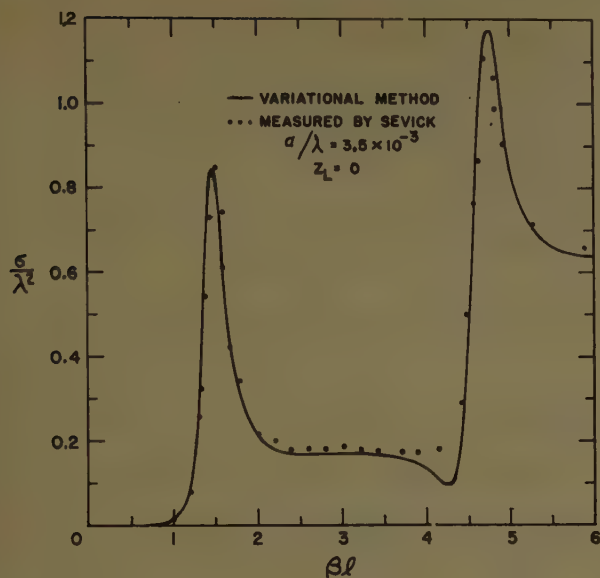


Fig. 14—Broadside back-scattering cross section of cylindrical antennas with  $Z_L=0$  and  $a/\lambda=3.5 \times 10^{-3}$ .

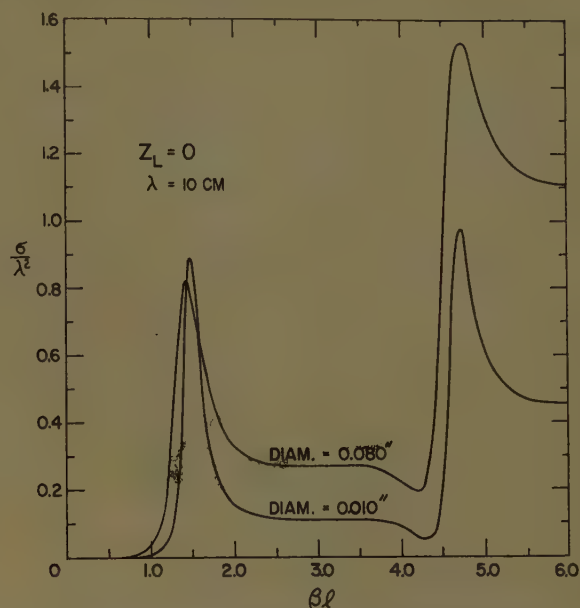


Fig. 15—Broadside back-scattering cross section of cylindrical antennas of fixed diameters with  $Z_L=0$  by the variational method.

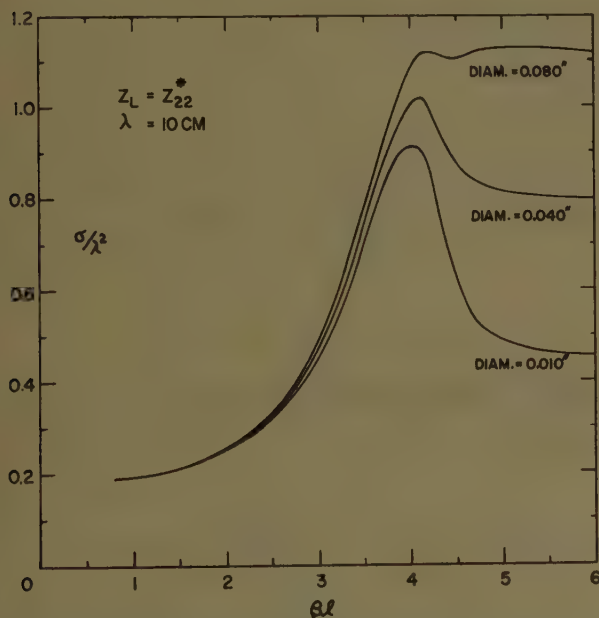


Fig. 16—Broadside back-scattering cross section of cylindrical antennas of fixed diameters with matched load by the variational method.

$$\frac{\partial Z}{\partial k_1} = 0 \quad \frac{\partial Z}{\partial k_2} = 0.$$

Using (33) as a trial function for  $I_2(z)$ , one not only extends  $\beta l$  to cover  $2\pi$  but also improves the approximation. The results obtained by using (33) will be called second order approximations. There is no further analytical difficulty in obtaining second order approximation, because all the additional integrals are of similar types encountered in the first order approximation. Notice that the term  $\cos(\beta z/2)$  is not effective in improving the approximations for small values of  $\beta l$ , say  $\beta l < 2$ , due to the mild variation of  $\cos(\beta/2)$  in that

range. If more accurate results at small values of  $\beta l$  are required, an additional term of the form  $\cos 2\beta z$  may be used. It is believed that the first order approximation by the variational method is satisfactory at smaller values of  $\beta l$ , but much better results for  $\beta l$  near  $2\pi$  can be obtained from a second order approximation by using (33) or by similar modifications, such as adding  $\sin(\beta z/2)$  term or adding both  $\sin(\beta z/2)$  and  $\cos(\beta z/2)$  terms. However, the trial function given in (33) fails again to represent  $I_2(z)$  at  $\beta l = 4\pi$  because of the same reason. In order to extend  $\beta l$  to cover  $4\pi$ , further modifications such as adding  $\cos(\beta z/3)$  or  $\sin(\beta z/3)$  or both may be necessary. Theoretically a trial function for  $I_2(z)$  can be made to cover all ranges of  $\beta l$  and the approximations can be improved indefinitely by adding more terms, but in practice, the order of approximations used is limited by the additional labor involved.

## APPENDIX

### APPROXIMATE RESULTS FOR DIFFERENT INTEGRALS

$$\iint I_{20} \Gamma_{22} I_{20} = j30(A + jB)I_2^2(0)$$

$$\iint I_{20} \Gamma_{22} I_{21} = j30(C + jD)I_2(0)$$

$$\iint I_{21} \Gamma_{22} I_{21} = j30(E + jF)$$

$$I_1(0)\Delta l \int \Gamma_{12} I_{20} = \left[ \frac{\Delta l}{r_0} e^{-j\beta r_0} \right] j30GI_1(0)I_2(0)$$

$$I_1'(0)\Delta l \int \Gamma_{12} I_{21} = \left[ \frac{\Delta l}{r_0} e^{-j\beta r_0} \right] j30HI_1'(0)$$



where

$$\begin{aligned}
 A &= \frac{1}{(1 - \cos L)^2} \left\{ S(4L) + 4 \cos L (L \cos L - \sin L) \right. \\
 &\quad \left. \cdot \left[ \ln \frac{4L}{\alpha} - C(2L) \right] - \frac{8}{\pi} \alpha \sin^2 L - 2 \cos^2 L \sin 2L \right\} \\
 B &= \frac{1}{(1 - \cos L)^2} \left\{ -C(4L) - (4L \cos^2 L - 2 \sin 2L) S(2L) \right. \\
 &\quad \left. + \sin^2 2L \right\} \\
 C &= \frac{1}{1 - \cos L} \left\{ (\sin L) S(4L) + (1 - \cos L) C(4L) \right. \\
 &\quad + 4 \cos L (1 - \cos L - L \sin L) C(2L) \\
 &\quad + 4 \cos L (1 - \cos L) C(L) \\
 &\quad + 4 \sin L (L \cos L - \sin L) \ln \frac{4L}{\alpha} \\
 &\quad + 4(1 - \cos L)^2 \ln \frac{2L}{\alpha} \\
 &\quad \left. - \frac{8}{\pi} \alpha \sin L (1 - \cos L) - (\sin 2L)^2 \right\} \\
 D &= \frac{1}{1 - \cos L} \left\{ (1 - \cos L) S(4L) - (\sin L) C(4L) \right. \\
 &\quad + 4 \cos L (1 - \cos L - L \sin L) S(2L) \\
 &\quad \left. + 4 \cos L (1 - \cos L) S(L) + 2 \sin^2 L \sin 2L \right\}
 \end{aligned}$$

$$\begin{aligned}
 E &= 2 \cos L (1 - \cos L) S(4L) + 2 \sin L (1 - \cos L) C(4L) \\
 &\quad + 4(1 - \cos L)^2 S(2L) - 4L (\sin^2 L) C(2L) \\
 &\quad + 8 \sin L (1 - \cos L) C(L) \\
 &\quad + [4L \sin^2 L - 8 \sin L (1 - \cos L)] \ln \frac{4L}{\alpha} \\
 &\quad - \frac{24}{\pi} \alpha (1 - \cos L)^2 - 2 \sin^2 L \sin 2L
 \end{aligned}$$

$$\begin{aligned}
 F &= 2 \sin L (1 - \cos L) S(4L) - 2 \cos L (1 - \cos L) C(4L) \\
 &\quad - 4L (\sin^2 L) S(2L) - 4(1 - \cos L)^2 C(2L) \\
 &\quad + 8 \sin L (1 - \cos L) S(L) + 4 \sin^4 L
 \end{aligned}$$

$$G = \frac{2}{1 - \cos L} (\sin L - L \cos L)$$

$$H = 2[2(1 - \cos L) - L \sin L]$$

with

$$L = \beta l, \quad \alpha = \beta a$$

$$C(x) = \int_0^x \frac{1 - \cos u}{u} du, \quad S(x) = \int_0^x \frac{\sin u}{u} du.$$

## Electromagnetic Diffraction by Dielectric Strips\*

DAVID C. STICKLER†

**Summary**—In this paper the scattering of a plane wave by a rectangular dielectric strip is calculated by approximating polarization currents in the strip. One advantage of the technique applied here is that no variational calculations are needed. Results of experimental investigation show good agreement with the predicted pattern.

### INTRODUCTION

THE general problem of scattering by dielectric bodies has been studied by various authors<sup>1-3</sup> and since only a few of these problems admit to rigorous solutions, approximate methods are needed to predict the effect of such bodies on an electromagnetic field.

\* Manuscript received by the PGAP, January 12, 1957; revised manuscript received, June 24, 1957. The research reported in this paper was supported in part by the Air Res. and Dev. Command, Wright Air Dev. Center, Wright-Patterson AFB, Ohio, through a contract with the Ohio State University Res. Foundation.

† Antenna Lab., The Ohio State University, Columbus, Ohio.

<sup>1</sup> V. H. Rumsey, "Reaction concept in electromagnetic theory," *Phys. Rev.*, vol. 94, pp. 1483-1491; June 15, 1954.

<sup>2</sup> M. H. Cohen, "Application of the reaction concept to scattering problems," *IRE TRANS.*, vol. AP-3, pp. 193-199; October, 1955.

<sup>3</sup> D. R. Rhodes, "An Investigation of Pulsed Radar Systems for Model Measurements," Antenna Lab., The Ohio State University Res. Foundation, Rep. 475-476; December, 1953. Prepared under Contract No. AF 18(600)-19.

The reaction concept was introduced by Rumsey<sup>1</sup> and extended for the case of dielectric scatterers by Cohen.<sup>2</sup>

Rumsey<sup>1</sup> discussed the problem of scattering by a dielectric body by considering the equivalent electric and magnetic currents of Schelkunoff on the surface of the scatterer. He shows that in bi-static scattering problems several stationary expressions may be derived for the echo. As an example, he considers the echo due to a plane wave normally incident on an infinite dielectric sheet given by two stationary expressions and compares these with the exact solution.

Cohen<sup>2</sup> discussed the problem in a somewhat different manner although he uses the reaction concept. The difference in the approaches made by Rumsey and Cohen is in their choice of currents. Cohen uses the polarization currents, which are volume currents in free space in the volume occupied by the scatterer, and are proportional to the total electric field in the dielectric. They generate the scattered field. Cohen considered the echo from a right circular dielectric cylinder and studied the results from several approximations for the polarization currents. The results of these calculations

were compared with the exact solution. It was found that the best approximation of those considered to the echo area was obtained when the total field in the cylinder was assumed to be the sum of two plane waves. The incident field was considered to be  $\bar{E} = \hat{k} e^{ik_0 x}$  with the  $\bar{E}$  parallel to the axis of the cylinder. The approximation which yielded the best results was given by

$$\bar{E}^i = \hat{k}(\alpha_1 e^{ik_1 x} + \alpha_2 e^{-ik_1 x})$$

where the constants  $\alpha_1$  and  $\alpha_2$  are determined through the stationary expression derived by the reaction concept.

Rhodes<sup>3</sup> set up an integral equation of the second kind involving the incident and total fields. He then obtained an infinite series representation for the total field by successive substitutions. Rhodes also considered the echo from a right circular dielectric cylinder and carried out the calculation retaining one, two, and three terms of the series. However, Rhodes' best calculation compares unfavorably with Cohen's best. The results of Rhodes' work are given in Cohen's paper.

In this paper the total fields in a dielectric strip with a plane wave or a good approximation to a plane wave incident are assumed to be those that would be present in the strip if it were an infinite dielectric sheet with the same thickness and constitutive parameters. The scattered field of the strip may then be calculated by an integration over the volume of the scatterer. This approximation is essentially the same as Cohen's<sup>2</sup> except that in addition the magnitudes of the coefficients  $\alpha_1$  and  $\alpha_2$  are also assumed.

### THE POLARIZATION CURRENTS

The expressions for the polarization currents will now be derived in a slightly more concise form than that given by Cohen.<sup>2</sup> The incident fields, that is, the fields in the absence of the scatterer, must satisfy

$$\nabla \times \nabla \times \bar{E}^i - k_0^2 \bar{E}^i = 0 \quad (1)$$

$$\nabla \times \nabla \times \bar{H}^i - k_0^2 \bar{H}^i = 0 \quad (2)$$

where  $k_0^2 = \omega^2 \mu_0 \epsilon_0$ . The total fields must satisfy

$$\nabla \times \nabla \times \bar{E}^t - k^2 \bar{E}^t = 0 \quad (3)$$

$$\nabla \times \nabla \times \bar{H}^t - k^2 \bar{H}^t = 0 \quad (4)$$

where  $k^2 = \omega^2 \mu_1 \epsilon_1$  in the scatterer and  $k^2 = \omega^2 \mu_0 \epsilon_0$  outside the scatterer. The scattered field is defined by

$$\bar{E}^s = \bar{E}^t - \bar{E}^i \quad (5)$$

Subtracting (1) from (3) and (2) from (4) and substituting for  $\bar{E}^i$  and  $\bar{H}^i$  the following are obtained

$$\nabla \times \nabla \times \bar{E}^s - k_0^2 \bar{E}^s = (k^2 - k_0^2) \bar{E}^t + i\omega \nabla \mu \times \bar{H}^t \quad (6)$$

$$\nabla \times \nabla \times \bar{H}^s - k_0^2 \bar{H}^s = (k^2 - k_0^2) \bar{H}^t - i\omega \nabla \epsilon \times \bar{E}^t \quad (7)$$

The effect of the dielectric scatterer may be replaced by the currents in (8) in free space

$$\bar{J} = -i\omega \epsilon_0 [\mu_r \epsilon_r - 1] \bar{E}^t \frac{\nabla \mu}{\mu_0} \times \bar{H}^t \quad (8)$$

within the scatterer and zero elsewhere.

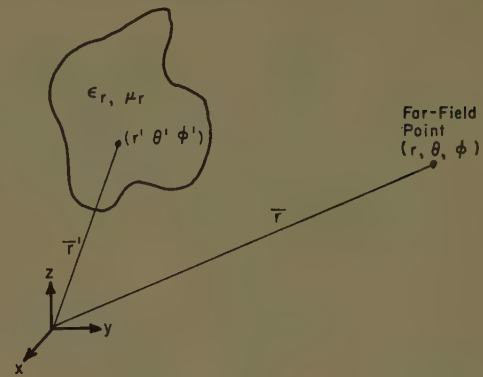


Fig. 1—Geometry for arbitrary scatterer.

In the far-field the scattered electric field is given by

$$\bar{E}^s(\bar{r}) = \frac{k_0^2(\mu_r \epsilon_r - 1)}{4\pi} \frac{e^{ik_0 r}}{r} [\hat{\theta} \hat{\theta} + \hat{\phi} \hat{\phi}] \cdot \int \bar{E}^t(\bar{r}') e^{-ik_0 \bar{r}' \cdot \cos \gamma} dV + \frac{i\omega}{4\pi} \frac{e^{ik_0 \Gamma}}{\Gamma} \quad (9)$$

$$\int \nabla \mu \times \bar{H}^t(\bar{r}') e^{-ik_0 \bar{r}' \cdot \cos \gamma} dV$$

where the integration is taken over the volume of the scatterer and  $\cos \gamma = \sin \theta \sin \theta' \cos(\phi - \phi') + \cos \theta \cos \theta'$ . The coordinate system is shown in Fig. 1.

It will be convenient to express the total electric field in the scatterer in rectangular coordinates

$$\bar{E}^t(\bar{r}') = E_x \hat{i} + E_y \hat{j} + E_z \hat{k} \quad (10)$$

from which it can be shown that

$$E_{\theta}^s(\theta, \phi) = \frac{k_0^2(\mu_r \epsilon_r - 1)}{4\pi} \frac{e^{ik_0 r}}{r} \int (\cos \theta \cos \phi E_x + \cos \theta \sin \phi E_y - \sin \theta E_z) e^{-ik_0 \bar{r}' \cdot \cos \gamma} dV \quad (11)$$

$$E_{\phi}^s(\theta, \phi) = \frac{k_0^2(\mu_r \epsilon_r - 1)}{4\pi} \frac{e^{ik_0 r}}{r} \int (-\sin \phi E_x + \cos \phi E_y) e^{-ik_0 \bar{r}' \cdot \cos \gamma} dV \quad (12)$$

### SCATTERING BY A DIELECTRIC STRIP

Scattering by a dielectric strip as illustrated in Fig. 2 will be considered for the following polarizations.

$$\bar{E}^i = E_z \hat{k} \quad (13)$$

in the  $x$ - $y$  plane (vertical polarization),

$$\bar{E}^i = E_j \hat{j} \quad (14)$$

in the  $x$ - $y$  plane (horizontal polarization). The relative permeability will be considered to be unity.

It is now assumed that the electric field in the dielectric strip with a plane wave incident is the same as that field which would exist in the strip if the strip were an infinite dielectric sheet of the same thickness and permittivity with a plane wave incident at the same angle



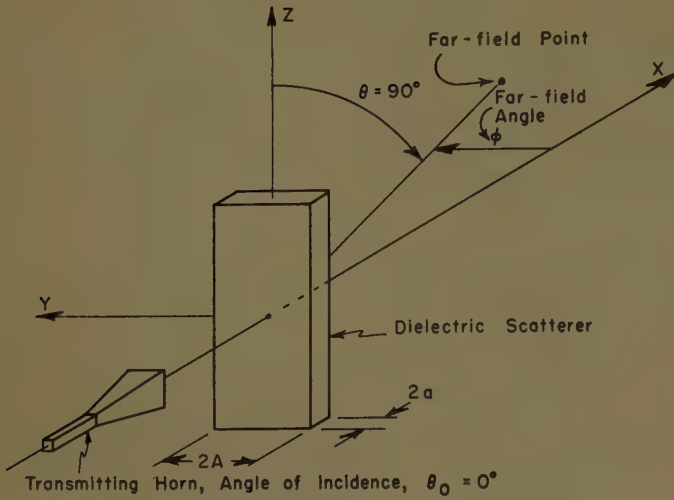


Fig. 2—Geometry for dielectric strip scatterer. The strip is infinite in the  $Z$  direction.

of incidence. In addition to this assumption it is assumed that the  $z$  dependence of the field is separable, that is

$$\bar{E}^i = \bar{E}(x, y)Z(z), \quad (15)$$

when the incident field is that of a typical pyramidal horn. This is an approximation and several methods of circumventing it have been suggested, but the complexity of the calculations increases when this is considered.

For vertical polarization as defined by (13) we shall be interested in the  $E$ -field patterns described by (11) in the  $\theta = \pi/2$  plane. The fields in the dielectric are given by

$$\begin{aligned} \bar{E}^i(x'y'z') \\ = \hat{k}Z(z')TE_0^i e^{ik_0 y'} \sin \theta_0 [e^{ik_{1x'} \cos \theta_1} + K e^{-ik_{1x'} \cos \theta_1}] \end{aligned} \quad (16)$$

where

$$T = \frac{2k_0 \cos \theta_0}{k_0 \cos \theta_0 + k_1 \cos \theta_1} \left[ \frac{e^{i2a(k_1 \cos \theta_1 - k_0 \cos \theta_0)}}{1 - K^2} \right]$$

$$K = \frac{k_1 \cos \theta_1 - k_0 \cos \theta_0}{k_1 \cos \theta_1 + k_0 \cos \theta_0} e^{2ik_{1a} \cos \theta_1}$$

$$k_0 \sin \theta_0 = k_1 \sin \theta_1.$$

Substituting in (11) and integrating we obtain

$$\begin{aligned} E_{\theta^*}(\theta, \phi) = -\sin \theta \left\{ \frac{k_0^2(\epsilon_r - 1)}{\pi} \right\} \frac{e^{ik_0 r}}{r} TE_0^i [Z(\theta)] \\ \left[ \frac{\sin(k_0 A \{\sin \theta_0 - \sin \theta \sin \phi\})}{k_0 \{\sin \theta_0 - \sin \theta \sin \phi\}} \right] \\ \left[ \frac{\sin a \{k_1 \cos \theta_1 - k_0 \sin \theta \cos \phi\}}{\{k_1 \cos \theta_1 - k_0 \sin \theta \cos \phi\}} \right] \\ + \frac{K \sin a \{k_1 \cos \theta_1 + k_0 \sin \theta \cos \phi\}}{\{k_1 \cos \theta_1 + k_0 \sin \theta \cos \phi\}} \end{aligned} \quad (17)$$

where

$$[Z(\theta)] = \int_{z'=-\infty}^{+\infty} Z(z') e^{-ik_0 z' \cos \theta} dz'.$$

Three cases of vertical polarization were considered:

$$\begin{aligned} a = 0.25 \text{ inch} \quad \epsilon_r = 2.4 \quad \theta_0 = 0 \quad A = \begin{cases} 1.4 \text{ inch} \\ 0.3 \text{ inch} \end{cases} \\ a = 0.25 \text{ inch} \quad \epsilon_r = 2.4 \quad \theta_0 = 30^\circ \quad A = 1.4 \text{ inch.} \end{aligned}$$

The plots of the total fields at  $\theta = \pi/2$  are shown in Figs. 3–5. The measured and calculated patterns for the three cases of vertical polarization were correlated as follows. The same incident field was applied in all three cases. It was noted that there was a null in the far-field pattern for the  $\theta_0 = 0, A = 1.4$  inch case at  $\phi = 10^\circ$ . This implied that at  $\phi = 10^\circ$ ,  $E^s(\pi/2, 10^\circ) = -E^i(\pi/2, 10^\circ)$  and hence we were able to determine a constant  $C_v$  which related the scattered and total fields for all  $A$  and  $\theta_0$ . There are obviously more general techniques for relating the fields.

For horizontal polarization as defined by (14) we shall be interested in the  $E_\phi$  pattern as described by (12). We find

$$E_{\phi^*}\left(\frac{\pi}{2}, \phi\right) = -\cos \phi E_{\theta^*}\left(\frac{\pi}{2}, \phi\right) \quad (18)$$

where  $E_{\theta^*}(\pi/2, \phi)$  is given by (17). The plots of the total fields are shown in Figs. 6 and 7. A normalizing constant  $C_h$  was determined in the same manner as  $C_v$ .

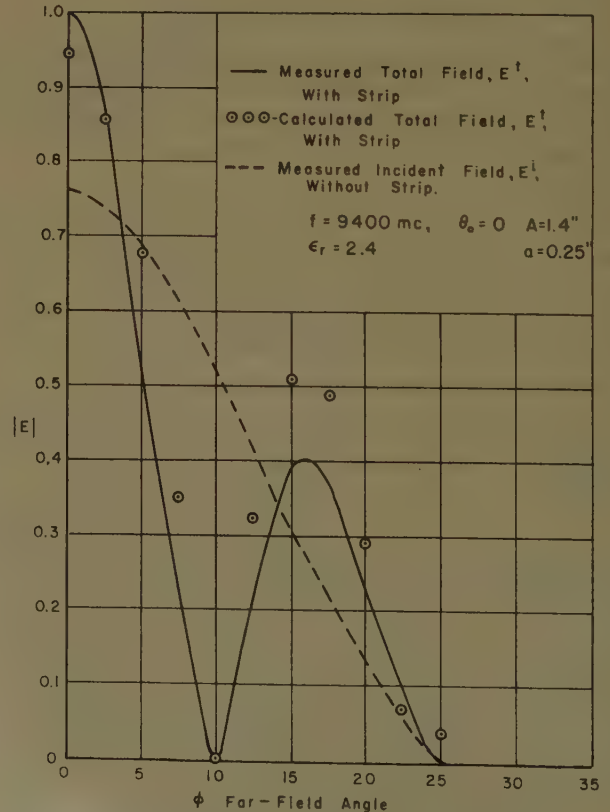


Fig. 3—Far-field pattern of horn and dielectric strip with vertical polarization.

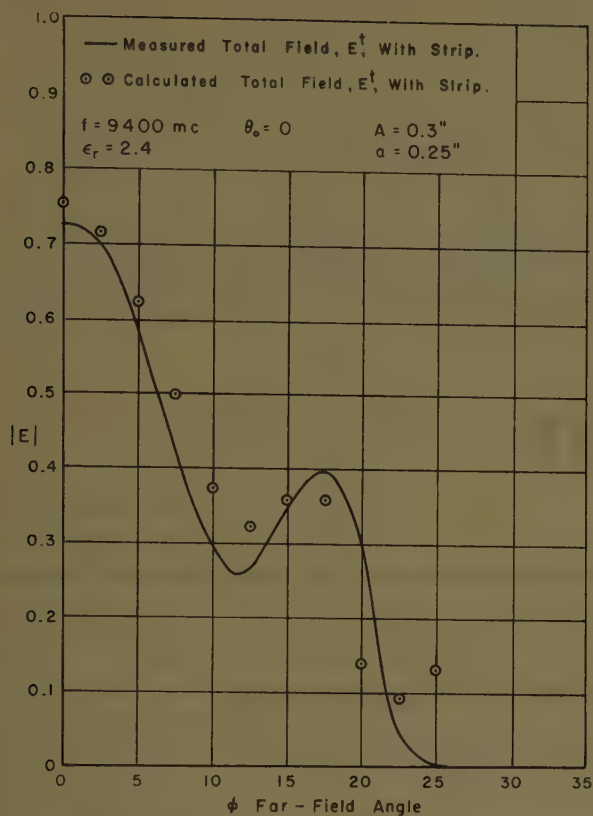


Fig. 4—Far-field pattern of horn and dielectric strip with vertical polarization.

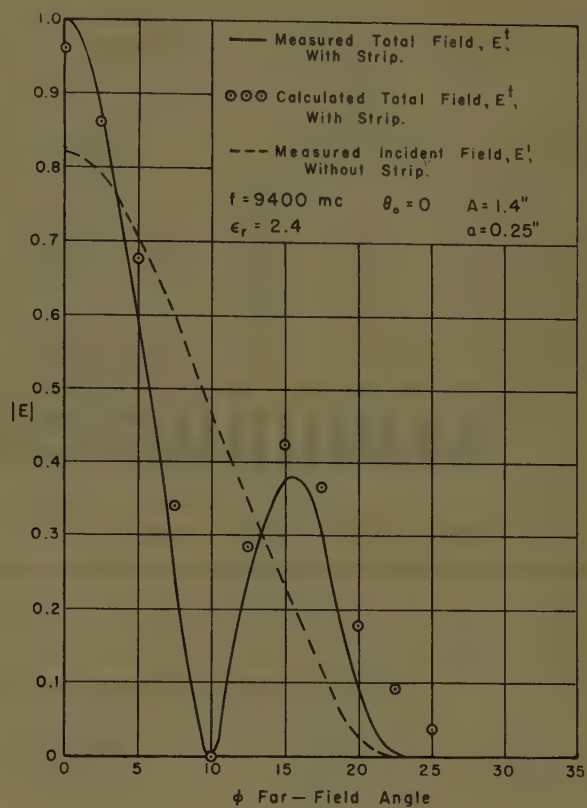


Fig. 6—Far-field pattern of horn and dielectric strip with horizontal polarization.

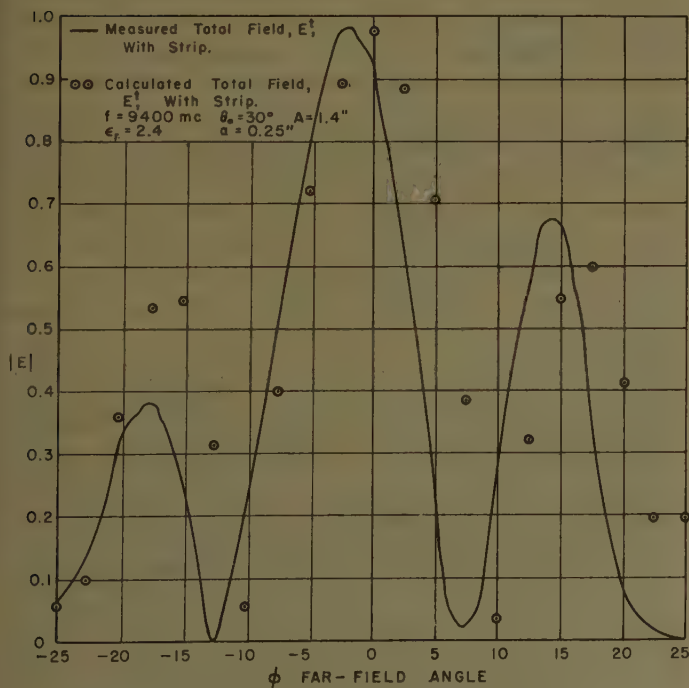


Fig. 5—Far-field pattern of horn and dielectric strip with vertical polarization.

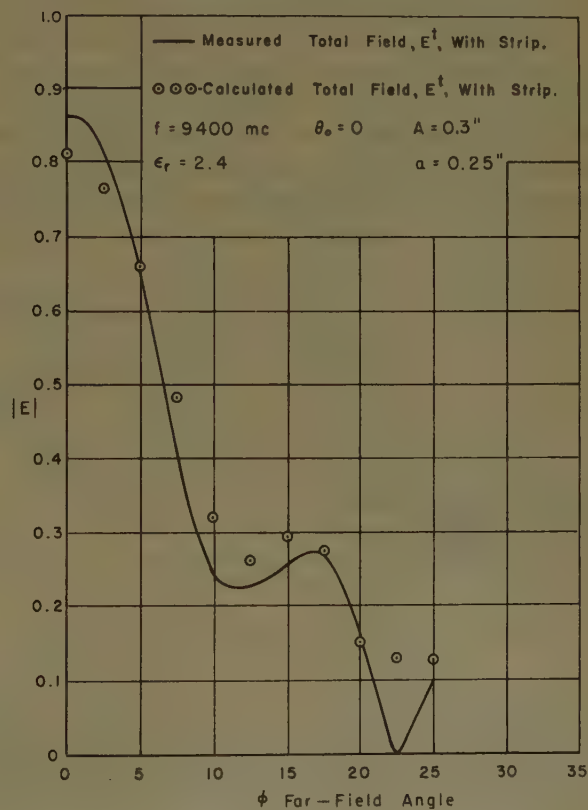


Fig. 7—Far-field pattern of horn and dielectric strip with horizontal polarization.

### CONCLUSION

Using plane-wave plane-sheet theory it is possible to calculate the scattering by a dielectric strip placed in the vicinity of an antenna. The simplicity of the calculations should be noted.

### ACKNOWLEDGMENT

The author is grateful to Dr. J. H. Richmond for his suggestion of the problem and for his continued guidance.



# communication

## A Line Source with Variable Polarization\*

J. N. HINES† AND J. UPSON‡

THE polarization of this line-source antenna can be continuously adjusted from linear polarization to circular polarization (with either sense of rotation) by simply changing the spacing between the line source and the aperture.<sup>1</sup> It consists of a traveling-wave primary radiator mounted in a parallel-plate transmission line that is terminated in a flared (*i.e.*, horn) aperture (see Fig. 1). The primary radiator consists of an array of closely spaced slots cut into the narrow

wall of standard waveguide at an angle of about 45°. Modes with orthogonal electric fields (*i.e.*, the TE and TEM modes) are set up in the parallel-plate line by this arrangement, and *if the primary radiator is aligned parallel to the aperture*, both modes radiate with the same direction of maximum radiation. Since the two modes have different phase velocities, the relative phase of the orthogonal fields in the aperture can be adjusted by changing the distance between the primary radiator and the aperture. This controls the polarization of the radiated field. Circular polarization requires that the two orthogonal components of the radiated field be equal in magnitude as well as 90° out of phase. The angle at which the slots are cut into the waveguide feed can be adjusted to obtain fields of equal strength. In practice an angle of 45° comes quite close to the correct value as indicated by measurements.

Because of the orientation of the slots in the waveguide feed, the linearly polarized field is polarized at an angle of 45°, *i.e.*, either parallel or perpendicular to the slots. Horizontal and vertical polarization can be obtained, if desired, by combining right-circular polarization and left-circular polarization from each half of the line source. For example, if the two circularly polarized fields are in phase, vertical polarization will result; and if they are out of phase, horizontal polarization will result.

The direction of maximum radiation,  $\theta_{\max}$ , is determined solely by the propagation constant in the waveguide. This is given approximately by

$$\cos \theta_{\max} = (\lambda_0/\lambda_g) = \sqrt{1 - (\lambda_0/\lambda_{c0})^2}, \quad (1)$$

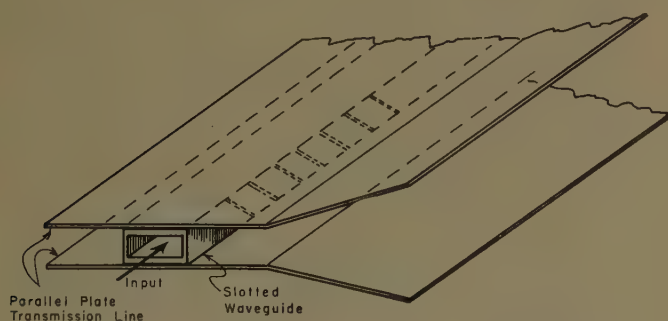


Fig. 1—A sketch of the variably polarized line source.

\* Manuscript received by the PGAP, April 29, 1957; revised manuscript received, October 7, 1957. This work was performed under contract between the Air. Res. and Dev. Command, Wright Air Dev. Center, Wright-Patterson AFB, Ohio, and The Ohio State University Res. Foundation, Columbus, Ohio.

† Antenna Lab., The Ohio State University, Columbus, Ohio.

‡ North American Aviation, Inc., Columbus, Ohio; formerly with Antenna Lab., The Ohio State University.

<sup>1</sup> J. N. Hines and J. Upson, "A Line Source with Variable Polarization," Antenna Lab., The Ohio State University Res. Foundation; November 15, 1956. Prepared under Contract AF 33(616)-3353, Air Res. and Dev. Command, Wright Air Dev. Center, Wright-Patterson AFB, Ohio.

where

- $\lambda_0$ =free-space wavelength
- $\lambda_g$ =guide wavelength
- $\lambda_{cg}$ =free-space cutoff wavelength of the guide  
 $\approx 2 \times$  wide dimension, if slot loading is not too large.

The TEM mode is the dominant mode in the parallel-plate line and it has no cutoff frequency. The cutoff wavelength for the TE mode in the parallel-plate line is given by

$$\frac{1}{\lambda_c^2} = \frac{1}{\lambda_g^2} + \left(\frac{N}{2S}\right)^2, \tag{2}$$

where

- $\lambda_c$ =free-space cutoff wavelength
- $S$ =plate spacing
- $N$ =mode number.

Generally the frequency and direction of maximum radiation (or range of directions) are specified when designing a line-source radiator. When these are known, the cutoff wavelength and hence waveguide cross section can be determined from (1), and the spacing of the parallel-plate line can be obtained from (2).

The relative phase,  $\phi$ , of the TE and TEM fields at any point in the aperture can be changed by varying the distance,  $g$ , between the primary radiator and the aperture. This phase difference is

$$\phi = 2\pi \cos \theta_{\max} \frac{g}{\lambda_0} (\tan \theta_{\max} - \tan \theta_{TE}). \tag{3}$$

$\theta_{TE}$  is the direction of the wave normal of the TE mode in the parallel-plate line and can be determined from

$$\cos \theta_{TE} = \frac{\cos \theta_{\max}}{\sqrt{1 - \left(\frac{N\lambda_0}{2S}\right)^2}}. \tag{4}$$

The relative phase given by (3) is relatively insensitive to small frequency changes since the first term is independent of frequency and the second term is a slowly varying function of frequency. Hence if the magnitudes of the orthogonal components remain constant, the polarization of the field radiated by the line source will not change rapidly with frequency. This was borne out by measurements.

The measured polarization characteristics of this antenna are compared with the theoretical performance in Fig. 2. Measurements were taken in the direction of maximum radiation in the TEM mode's principal  $H$  plane. The sharp cusp is the result of expressing the axial ratio,  $AR$ , in db units. Measurements were also taken for variations in  $g/\lambda_0$  which resulted in circular polarization of the opposite sense to that shown. These data are not plotted, however, since they show the same results.

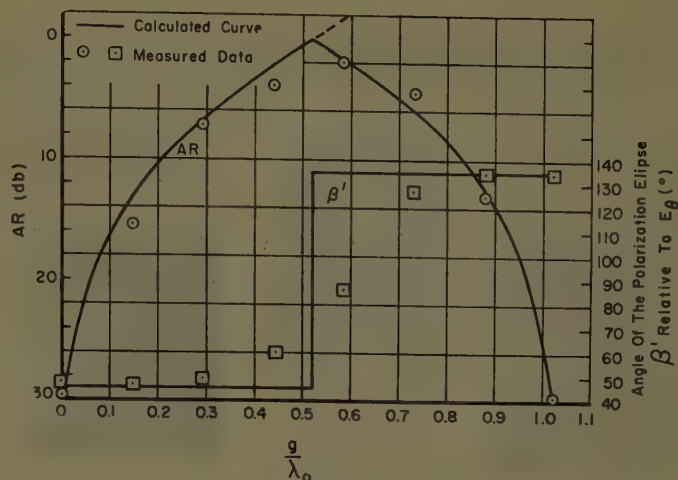


Fig. 2—Plot of the polarization characteristics of the line source antenna as a function of the waveguide to aperture spacing.

TABLE I  
RESULTS OF FREQUENCY CHANGE

Frequency	Axial Ratio	$\theta_{\max}$
16.16 kmc	3.6 db	65.0°
16.22 kmc	4.0 db	63.9°
16.53 kmc	3.5 db	61.7°
17.03 kmc	2.3 db	57.7°
17.24 kmc	2.4 db	56.6°
17.68 kmc	1.5 db	53.7°

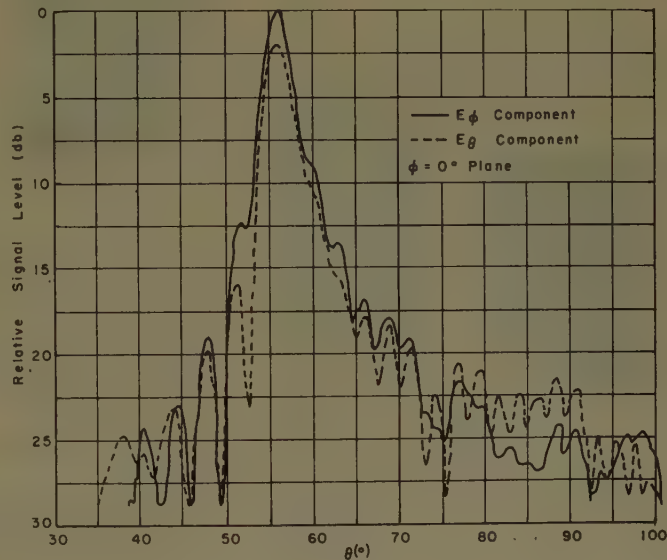


Fig. 3—Radiation patterns of the line source antenna for the near circular polarization case.

The polarization characteristics as a function of frequency for approximately a 10 per cent frequency change are given in Table I. Note the relatively small change in the axial ratio even though the beam scanned through about 10°.

A typical principal-plane radiation pattern showing both field components is shown in Fig. 3 for a case of near-circular polarization.



# Contributors

Richard B. Barrar (M'57) is a native of Dayton, Ohio and received the degree of B.S.E. in engineering physics from the University of Michigan in 1947. He received the M.S. degree in physics in 1948, and the Ph.D. degree in mathematics in 1952, both from the University of Michigan. From 1951 to 1952, he was employed as a research associate at Harvard University in the mathematics department. Dr. Barrar worked from 1952 to 1954, at McMillan Laboratory, Ipswich, Mass. where he did research on radomes and electromagnetic theory. From 1954 to 1957, he was employed as a research physicist at Hughes Aircraft Company where his duties included work on radomes, antennas, and diffraction theory. Dr. Barrar is now head of the Antenna and Propagation Unit at Hoffman Laboratories Inc., Los Angeles.



R. B. BARRAR

Dr. Barrar is a member of Sigma Xi, Phi Kappa Phi, the American Mathematical Society, and the Society for Industrial and Applied Mathematics.

Judd Blass (A'47-M'50) was born in New York, N. Y., on August 25, 1925. He received the B.E.E. degree from Polytechnic Institute of Brooklyn in 1944, and the M.E.E. and D.E.E. degrees from the Polytechnic Institute of Brooklyn in 1947 and 1952. He was a research assistant at the Microwave Research Institute from 1947 to 1950, and was engaged in the study of discontinuity problems in waveguides.



J. BLASS

In 1950, Dr. Blass joined the Raytheon Manufacturing Company as an engineer and worked on radar antenna and microwave oven equipment designs. From 1952 to 1954, he was chief project engineer at Dorne and Margolin, Inc. where he was concerned with the design of aircraft antennas and direction finding systems. Since 1954, he has been with The W. L. Maxson Corporation and is at present manager of the microwave department.

Dr. Blass is a member of Sigma Xi, Tau Beta Pi, and Eta Kappa Nu.

cal engineering from the University of New Hampshire, Durham, N. H., in 1949 and the M.S. degree from Northeastern University, Boston, Mass., in 1956.



L. C. EDWARDS

Since joining Raytheon Manufacturing Company in 1949 he has been engaged in studies of various aspects of ionospheric radio propagation.

Mr. Edwards is a member of Tau Beta Pi.

Robert S. Elliott, for photograph and biography, please see page 333 of the July 1957 issue of these TRANSACTIONS.

Donald A. Hedlund (S'47-A'48-M'53) was born in Youngstown, Ohio on October 10, 1924. He received the B.E. and M.E. degrees from Yale University in 1945 and 1947, respectively.



D. A. HEDLUND

He served as a communication officer in the Naval Reserve during 1945 and 1946. Since 1947 he has been employed by Raytheon Manufacturing Company in experimental and applied research in the field of radio wave propagation. At present he is a section manager in the Communications Department of Raytheon's Wayland Laboratory. The section is engaged in the study of various aspects of propagation as applied to radar and communication problems.

He is a member of Tau Beta Pi.

Yueh-Ying Hu (S'48-A'51-SM'56) was born on May 11, 1918, in Nanking, China. She received the B.S. degree from National Central University in 1940 and the Ph.D. degree from Oregon State College in 1951.



Y. Y. HU

From 1944 to 1947 she was an instructor in National Central University. In 1951, she became an assistant professor of electrical engineering at Syracuse University where she is now an associate Professor.

She is a member of Sigma Xi, and Pi Mu Epsilon.

Joseph B. Keller was born on July 31, 1923, in Paterson, N. J. He received the B.A. and M.S. degrees in physics in 1943 and 1946, respectively, and the Ph.D. degree in mathematics in 1948, all from New York University, New York, N. Y. He was a physics instructor at Princeton University, Princeton, N. J., a research associate at the Columbia University Division of War Research, New York, N. Y., and was Head of the Mathematics Branch of the Office of Naval Research. Since 1946, except for a year at ONR, he has been at New York University where he is now research professor of mathematics.



J. B. KELLER

Dr. Keller has done research in acoustics, fluid dynamics, and electromagnetic theory. In recent years he has been concentrating on diffraction problems.

He is a member of the American Physical Society.

Ray L. Leadabrand (S'49-A'52-M'54) was born in Pasadena, Calif., on October 12, 1927. He received the B.S. degree in communication engineering from San Jose State College, San Jose, Calif., in 1950.



R. L. LEADABRAND

From 1950 to 1952, he was a field engineer for the Philco Corp., in Japan and Korea. While with Philco he was engaged in the installation and testing of antennas and communications equipment. From 1952 to 1955, Mr. Leadabrand was on the staff of the Radio Propagation Laboratory at Stanford University, where he was engaged in research on auroras, sporadic-E, meteors, and related problems. He received the M.S. degree in electrical engineering from Stanford University in 1953. In October, 1955, he joined the staff of Stanford Research Institute as a research engineer in the Special Techniques Group of the Radio Systems Laboratory. Since that time he has been engaged in research on auroral and meteoric propagation.

Mr. Leadabrand is a member of Sigma Xi and the U. S. Committee of URSI.

Bertram R. Levy was born on July 2, 1932, in New York, N. Y. He received the B.A. and Ph.D. degrees in mathematics from New York University, and is at the

present time a research assistant at the Institute of Mathematical Sciences of New York University. In addition to his research activities Dr. Levy has taught in the Communication Development Training Program of Bell Telephone Laboratories and in the Department of Mathematics of New York University.



B. R. LEVY

and Sigma Pi Sigma.



G. C. McCormick (A'54) was born at Paradise, Nova Scotia, Canada on September 20, 1915. He received the B.S. degree from King's-Dalhousie University, Halifax, Nova Scotia, in 1935, and the M.S. degree from Acadia University in 1945. A Ph.D. degree in physics was obtained from McGill University, Montreal, in 1953.



G. C. McCORMICK

Dr. McCormick was lecturer in physics at Acadia University from 1949 to 1951. During 1953-54, he was assistant professor of physics at the University of New Brunswick and in 1954 he joined the staff of the National Research Council of Canada, Radio and Electrical Engineering Division.

He is a member of the Canadian Association of Physicists.



Gilbert H. Owyang was born in Tientsin, China, on July 7, 1925. He received the B.S. degree in electrical engineering from La Universitato Utopia, China, in 1944, and the M.S. degree from Harvard University in 1950.



G. H. OWYANG

From 1944 to 1949, he worked with the Shanghai Power Company, China, as an engineer. He was also been on the engineering staff of Devanco Inc. and Frank L. Capps and Company, both in New York. He is now a research assistant at Gordon McKay Laboratory, Harvard University.

Mr. Owyang is an associate member of the Society of the Sigma Xi.



David I. Paul (M'57) was born in New York, N. Y., on April 4, 1928. He received the M.A. degree in mathematics in 1951, and

the Ph.D. degree in physics in 1956, from the University of California, Los Angeles. While at UCLA, he was a teaching assistant and an associate. Dr. Paul has served as a Communications Officer in the United States Air Force and as a member of the technical staff with the Bell Telephone Research Laboratories and the North American Aviation Co. While at the Bell Telephone Research Laboratories he



D. I. PAUL

worked on scatter and tropospheric propagation studies. He was with the Hughes Aircraft Company, is now a professor at the University of California.

Dr. Paul is a member of Phi Beta Kappa, Pi Mu Epsilon, and Sigma Xi.



Robert L. Pease (SM'56) was born in Fitchburg, Mass., on July 13, 1925. He received the A.B. degree in physics from Miami University, Oxford, Ohio, in 1943, and the Ph.D. degree in physics from M.I.T. in 1950. During the war, he was a naval radar officer.



R. L. PEASE

At present, he is a research physicist in the Antenna Department, Microwave Laboratory, Hughes Research Laboratories, where he is engaged in the study of the propagation and radiation of surface waves.

Dr. Pease is a member of Phi Beta Kappa, Sigma Xi, and the American Physical Society.



Leon Peters, Jr. (S'50-A'51) was born in Columbus, Ohio in 1923. He attended The Ohio State University, receiving the Bachelor of Electrical Engineering degree in 1950, and the Master of Science degree in 1954. Since 1950 he has been employed as a research associate by the Antenna Laboratory at The Ohio State University, where he has been concerned with the properties of radar targets.



L. PETERS, JR.

Mr. Peters is a member of Sigma Xi.



Allen M. Peterson (M'56) was born in Santa Clara, Calif., on May 22, 1922. He attended San Jose State College, San Jose, Calif., from 1939 to 1942. He was associated with the Electronics Group of Sacramento

Air Service Command from 1942 to 1944 and was on active duty with the U. S. Army Air Forces from 1944 to 1946. He received the



A. M. PETERSON

B.S. degree in 1948, the M.S. in 1949, and the Ph.D. in 1952 from Stanford University, all in electrical engineering. From 1947 to the present time, he has been a staff member of the Radio Propagation Laboratory at Stanford University. He is at present Head of the Special Techniques Group of the Radio Systems Laboratory at Stanford Research Institute and assistant professor of the electrical engineering department at Stanford University. Dr. Peterson is the author of more than a dozen papers in the fields of radio propagation and upper atmosphere physics. At Stanford Research Institute he is engaged in research on radio propagation, communications, and radio systems design.

Dr. Peterson is a member of Commission 3 of the United States Committee of URSI and a member of a National Science Foundation Panel charged with planning and reviewing aurora and ionospheric research programs to be conducted during the forthcoming International Geophysical Year.



Lloyd L. Philipson (M'56) was born in Utica, N. Y., on June 19, 1928. In 1950, he received the B.A. degree in mathematics from the University of California at Los Angeles. He also received there the M.A. and Ph.D. degrees in 1951 and 1954, respectively. In 1953-1954, he had a Fellowship from the Institute for Numerical Analysis, National Bureau of Standards.



L. L. PHILIPSON

In 1951, he was employed by the Aerojet-General Corp. where he did applied research on rocket stability. From 1951 to 1954, he worked with numerical analysis at the RAND Corp. and from 1954 to 1955, was employed by Lockheed Aircraft Corp. to do applied research on aircraft sound and vibration problems.

In 1955, he joined Hughes Research Laboratories where he is currently head of the Analysis Group of the Electrical Research Section in the Radome Department, doing work on antenna-radome systems.

Dr. Philipson is a member of Sigma Xi, RESA, Pi Mu Epsilon, the American Mathematical Society, and the Society for Industrial and Applied Mathematics.



Robert E. Plummer was born in Fort Wayne, Ind., on September 26, 1928. He was a member of the United States Navy from



1946 to 1949, serving as an instructor in the Airborne Electronics Maintenance school. He received the B.E.E. degree from the University of Florida, Gainesville, Fla., in 1953, and the M.S. degree in electrical engineering from the University of Southern California, Los Angeles, Calif., in June, 1957. He joined the technical staff of the Research Laboratories, Hughes Aircraft Co. in June, 1953, and has since



R. E. PLUMMER

been engaged in antenna research and development. He is presently head of the Nose Cone Antenna Group of the Antenna Department.

He is a member of Phi Eta Sigma, Phi Kappa Phi, and Sigma Tau.



Laura Ronchi was born in Florence, Italy, on May 7, 1929.

She was graduated with a major in physics from the University of Florence in 1950.



L. RONCHI

delle Ricerche in Florence.



Walter Rotman (A'49-M'55) was born in St. Louis, Mo., on August 24, 1922. He received the B.S. and M.S. degrees from Massachusetts Institute of Technology in 1947 and 1948.



W. ROTMAN

From 1942 to 1945, he served in the Air Force, working on radar equipment. During his student career he worked as a research assistant in the Research Laboratory of Electronics at M.I.T.

In 1948, Mr. Rotman joined the Airborne Antenna Group of the Air Force Cambridge Research Center, where he is now engaged in antenna research. His fields of interest include progressive wave antennas, microwave optical systems, and missile antennas.

Mr. Rotman is a member of RESA and Sigma Xi.



Howard E. Shanks was born January 28, 1933, in Temple City, Calif. He attended Pasadena City College from 1950 to 1952.

At this time he transferred to the California Institute of Technology where he received the B.S.E.E. degree in 1954. He joined the Hughes Aircraft Company under the Master of Science Fellowship Program and received the M.S. degree in physics at the University of California at Los Angeles in 1956. He has been with the antenna department of the Hughes Aircraft Company for the last three years where he



H. E. SHANKS

has worked with the analysis and design of uhf-vhf antennas, the theoretical and experimental research on circular aperture antennas and scattering cross sections, and the study of flush-mounted high speed radar antennas.

Mr. Shanks is completing work for the Ph.D. in physics at UCLA under the Hughes Doctoral Fellowship Program.

He is a member of Tau Beta Pi.



L. M. Spetner (SM'57) was born in St. Louis, Mo. on January 17, 1927. He received a B.S.M.E. degree from Washington University in 1945. After service in the U. S. Navy he returned to Washington University in 1946 and received an appointment as lecturer in the Department of Applied Mechanics until 1947. During this time he also worked as a research engineer on missile guidance and control



L. M. SPETNER

problems with the Washington University Research Foundation.

From 1947 to 1950, he took graduate work in physics at Massachusetts Institute of Technology, doing research in cosmic rays and high energy particles. He received the Ph.D. degree from M.I.T. in 1950. During the summer of 1948 he worked in the servomechanism group at Emerson Electric Co. in St. Louis. From 1949 to 1950, he was a research assistant at M.I.T. and for one semester after receiving his degree he was a research associate.

From 1951 to the present Dr. Spetner has been a physicist with the Applied Physics Laboratory of the Johns Hopkins University where he has been engaged in research in electromagnetic propagation and noise theory.

He is a member of the American Physical Society, an associate member of Sigma Xi, and a member of Tau Beta Pi.



David C. Stickler was born in Piqua, Ohio on April 12, 1933. He attended Case Institute of Technology, Cleveland, Ohio,

and received the Bachelor of Science degree in mathematics from the Ohio State University, Columbus, Ohio, in 1956.



D. C. STICKLER

Since that time he has been a research assistant at the Antenna Laboratory of The Ohio State University where he is working on an advanced degree in electrical engineering. He has been engaged in research in electromagnetic theory and radomes.



Robert L. Tanner, for photograph and biography, see page 243 of the April 1957 issue of these TRANSACTIONS.



Giuliano Toraldo di Francia was born in Florence, Italy, on September 17, 1916. He was graduated with a major in physics from the University of Florence in 1939, and after World War II, he received the Ph.D. degrees in mathematical physics and optics from that University. For some years, he was professor of electromagnetic waves at the University of Florence. In 1952-1953, he was a visiting professor at the Institute of Optics of the University of Rochester.



G. TORALDO DI FRANCIA

At present, he is a professor at the Istituto Nazionale di Ottica and research director at the Centro Microonde del Consiglio Nazionale delle Ricerche in Florence.

Dr. Toraldo di Francia is vice-president of the International Commission of Optics of the International Union of Pure and Applied Physics and a member of the Italian Committee of URSI.



Charles P. Wells was born January 23, 1909, in Tabor, Iowa. He received the B.A. degree with a major in mathematics from Simpson College, Indianola, Iowa, in 1930 and the Ph.D. degree in applied mathematics from Iowa State College in 1935. He served as instructor in mathematics at North Dakota State College from 1934 until 1938, when he went to Michigan State University where he is now professor of mathematics. During World War II, he was an operations analyst with the United States Air Force. His main interests



C. P. WELLS

are in applied mathematics, especially in radiation problems and in particular antenna radiation problems.

He is a member of the American Mathematical Society and the Mathematical Association of America.



Harold A. Wheeler (A'27-M'28-F'35) was born in St. Paul, Minn., on May 10, 1903. He received the B.S. degree in physics from George Washington University, Washington, D. C., in 1925 and did post-graduate studies in physics at Johns Hopkins University, Baltimore, Md., until 1928.

He was employed by the Hazeltine Corp. from 1924 to 1945, advancing to vice-president and chief consulting engineer. Since 1946, he has engaged in independent work as a consulting radio physicist, and since 1947, his principal occupation has been as President of Wheeler Laboratories, Inc. In this capacity, he is directing the Great Neck and Smithtown laboratories, specializing in microwaves and antennas.

His specialization in antennas dates back to "all-wave" antennas for broadcast receivers around 1935, then radar beacon and IFF antennas during World War II, for which he received the Navy Certificate of Commendation. He has published basic studies of "small" antennas and "large" arrays and has directed recent developments in radar antennas for guiding missiles.



H. A. WHEELER

Mr. Wheeler has served IRE in such positions as Director (1934, 1940-1945), chairman of Standards Committee, and chairman of the Long Island Section. He received the Morris N. Liebman Memorial Prize in 1940 for work on some problems of television. He is a Fellow of AIEE and Radio Club of America, associate member of IEE (British), and member of Sigma Xi and Tau Beta Pi.



Charles H. Wilcox (M'56) was born in Rochester, N. Y., on May 21, 1929. He received the B.S. degree in physics from Duke University in 1950, and the M.S. degree in physics from the University of Illinois in 1952.



C. H. WILCOX

From 1952 through 1953, he was a research physicist at the Engineering Experiment Station, Georgia Institute of Technology, Atlanta, Ga. Since 1954 he has been at the Hughes Aircraft Co., Culver City, Calif., in the Microwave Laboratory. He has also been a lecturer in electrical engineering at the University of Southern California. His work has been mainly in the subjects of radio-wave scattering and propagation, and radar systems analysis.

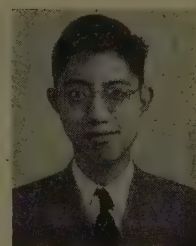


Tai Tsun Wu was born in Shanghai, China, on December 1, 1933. He received the B.S. degree from the University of Min-

nesota, Minneapolis, Minn., in 1953, the M.S. and Ph.D. degrees both from Harvard University, Cambridge, Mass., in 1954 and 1956, respectively.

Since his graduation in 1956 he has been a Junior Fellow of the Society of Fellows at Harvard.

He is a member of Tau Beta Pi, Eta Kappa Nu, Sigma Xi, the American Mathematical Society and the American Physical Society.



T. T. WU



Irving W. Yabroff was born in Oakland, Calif., on January 26, 1928. He served with the U. S. Air Force from 1945 to 1947.



I. W. YABROFF

He received the B.A. degree in psychology and the M.S. degree in electrical engineering from Stanford University, Stanford, Calif., in 1950 and 1953, respectively. He will complete the requirements for the Ph.D. degree at that university in June, 1958.

For the past two years, Mr. Yabroff has held a research assistantship in the Radio Propagation Laboratory at Stanford. Presently, he is at the Stanford Research Institute, Menlo Park, Calif., working on propagation studies and weapons systems analysis.





# SCIENTIFICALLY ORIENTED PEOPLE...

like the results of their work to be elegant in the mathematical sense of "ingenious simplicity," and we are no exception. In fact, we expend a great deal of effort in search of this kind of simplicity. Applied to airborne antennas, "elegant" obviously implies minimum size and weight. These characteristics are equally important to us.

With many of our antennas we believe that a considerable amount of elegance has been achieved. This is true of the family of airborne uhf monopole type radiators which we manufacture. It includes a wide variety of stubs and annular slots, all of which are substantially simpler and smaller than can be obtained through application of the published art. Nevertheless, theoretical considerations indicate that further substantial reductions in size are not impossible.

Efforts to discover elegant means of accomplishing this size reduction will be a small but important part of our activity in the future. We consider this to be a most interesting problem and one to which no extension of conventional techniques may be expected to yield a solution.

We are anxious to add a few senior engineers to our staff. Our laboratory is modern and air-conditioned and our program is very varied. We have about 100 people, and so far as we can determine, we have designed antennas for more different aircraft than any other group in the country of any size. If you are anxious to do original work in this field, please contact Arthur Dorne, President.

**DORNE & MARGOLIN, INC.**  
29 NEW YORK AVENUE  
WESTBURY, N.Y.

## *microwave engineers*

• The Hughes Research and Development Laboratories are engaged in basic and applied research and development programs in a wide variety of fields, including antennas, radomes, microwave and storage tubes, masers, ferrite devices, microwave circuitry, instrumentation, and other fields.

One of the several interesting problems is the design of feedback loops for locking the local oscillator klystron to an available reference signal. The requirements—good stability and low noise in a very trying environment.

*Your inquiry is invited.  
Please write Mr. John Bailey.*

*the West's leader in advanced electronics*

**HUGHES**

RESEARCH & DEVELOPMENT  
LABORATORIES

*Hughes Aircraft Co., Culver City, Calif.*



*For  
Information  
Concerning*

## **ADVERTISING RATES**

### *Contact*

MR. DELMER C. PORTS  
Jansky and Bailey, Inc.  
1339 Wisconsin Ave., N.W.  
Washington 7, D. C.

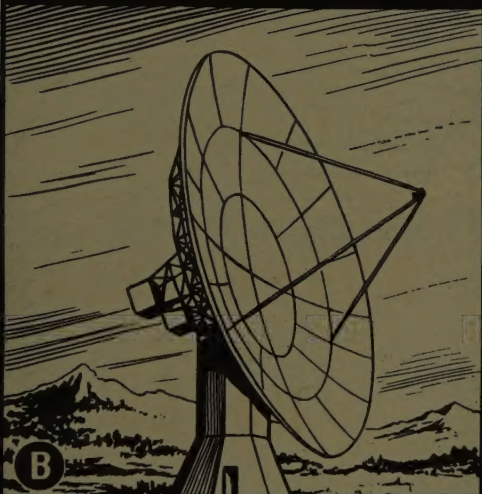
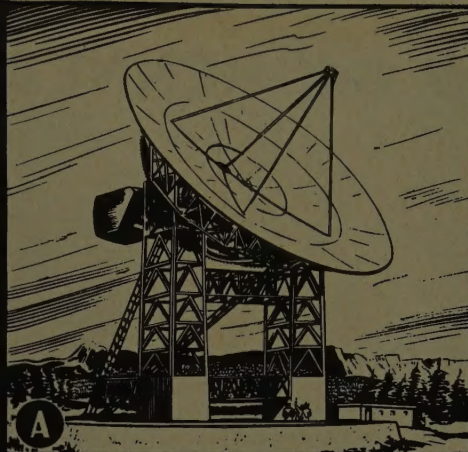
Telephone:  
Federal 3-4800





# GENERAL BRONZE THE LEADER IN LARGE ANTENNA SYSTEM DESIGN

- ANTENNAS
- PEDESTALS
- SERVOS

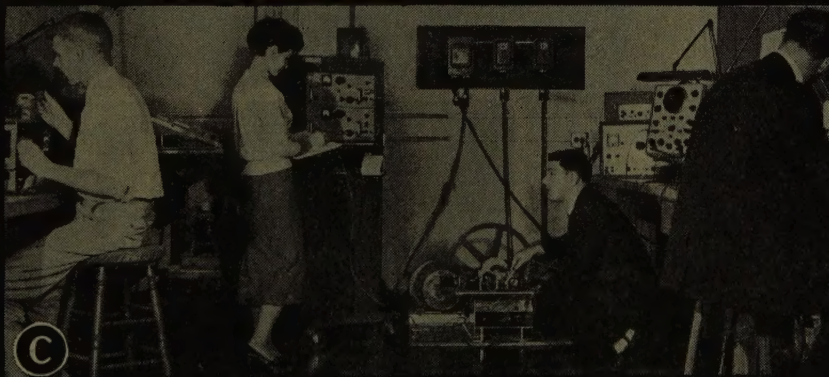


**A** LARGE RADIO TELESCOPE DESIGN  
(as appeared on the cover of PULSE)

**B** 60' TRACKING ANTENNAS, PEDESTALS AND TOWERS FOR THE NATIONAL BUREAU OF STANDARDS

**C** THE GENERAL BRONZE E C SERVO SYSTEM FOR PRECISION CONTROL OF LARGE ANTENNA SYSTEMS

**D** 28' SCATTER ANTENNA WITH THE DEW LINE PROVEN FEED WHICH WESTERN ELECTRIC CALLED "A MILESTONE IN ELECTRONIC HISTORY"



THE GENERAL BRONZE CORPORATION HAS ONE OF THE LARGEST COMPOSITE STAFFS OF MECHANICAL AND STRUCTURAL ENGINEERS INCLUDING SOME OF THE LEADING DESIGNERS OF ANTENNA AND SERVO SYSTEMS.

STANDARD DESIGNS ARE AVAILABLE FOR RADAR AND SCATTER ANTENNA SYSTEMS, HIGH POWER ROTARY JOINTS AND U.H.F. WAVEGUIDE AND WAVEGUIDE TEST EQUIPMENT.

Write for Technical Brochures on General Bronze Antenna System Designs.  
Please specify field of interest.



**GENERAL BRONZE CORPORATION**

711 STEWART AVENUE

GARDEN CITY, N. Y.

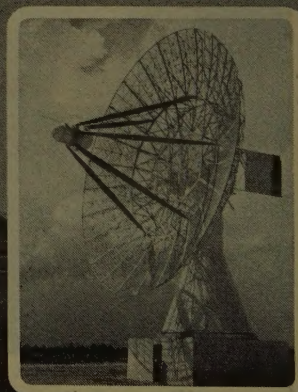


*Big dish with a big job...*

## NEW 84' KENNEDY TRACKING ANTENNA



28' RADAR  
TRACKING ANTENNA



60' TELEMETRY  
TRACKING ANTENNA

**T**OWERING 90 feet above the New England countryside at Westford, Mass., this giant 84' tracking antenna is part of a new, long-range radar installation now studying problems in ballistics missile defense.

Equipped with an elevation-azimuth type mount designed and fabricated in cooperation with M. I. T.'s Lincoln Laboratory, the big dish can make a full 360° horizontal sweep and has a vertical rotating capability of 90°. Like all Kennedy steerable antennas, it features a light weight, aluminum dish supported by a steel pedestal mounted on a concrete base.

This kind of achievement in antenna design and construction is solid proof that Kennedy is the name to remember when you are faced with antenna problems.



ANTENNA EQUIPMENT

**D. S. KENNEDY & CO.**

COHASSET, MASS. — TEL: CO4-1200

*Down-To-Earth SOLUTIONS to  
Out-Of-This-World PROBLEMS*

Tracking Antennas  
Radio Telescopes  
Radar Antennas  
"Trans-Horizon" Antennas  
Ionospheric Scatter







## INSTITUTIONAL LISTINGS

The IRE Professional Group on Antennas and Propagation is grateful for the assistance given by the firms listed below, and invites application for Institutional Listing from other firms interested in the field of Antennas and Propagation.

**ANDREW CORPORATION**, 363 E. 75th St., Chicago 19, Ill.  
Antennas, Antenna Systems, Transmission Lines, Development and Production.

**ANTLAB**, 4950 North High St., Columbus 14, Ohio  
Antenna Pattern Range Systems—Recorders & Mounts.

**BLAINE ELECTRONETICS, INC.**, 14757 Keswick St., Van Nuys, Calif.  
Antennas, Paraboloids, Scale Models, Antenna Radiation Pattern Measurement Towers

**COLLINS RADIO COMPANY**, Cedar Rapids, Iowa  
Antenna Design and Propagation Research Related for Airborne and Ground Communication Systems.

**DEVELOPMENTAL ENGINEERING CORP.**, 1001 Conn. Ave. N.W., Washington, D. C. and Leesburg, Va.  
Research, Development, Installation of Antennas and Antenna Equipment for Super Power Stations.

**THE GABRIEL LABORATORIES**, Div. of the Gabriel Co., 135 Crescent Road, Needham Heights 94, Mass.  
Research and Development of Antenna Equipment for Government and Industry.

**HUGHES AIRCRAFT COMPANY**, Culver City, Calif.  
Research, Development, Mfr.: Radar, Missiles, Antennas, Radomes, Tubes, Solid State Physics, Computers.

**I-T-E CIRCUIT BREAKER CO.**, Special Products Div., 601 E. Erie Ave., Philadelphia 34, Pa.  
Design, Development and Manufacture of Antennas, and Related Equipment.

**JANSKY & BAILEY, INC.**, 1339 Wisconsin Ave. N.W., Washington 7, D. C.  
Radio & Electronic Engineering; Antenna Research & Propagation Measurements; Systems Design & Evaluation.

**MARK PRODUCTS CO.**, 6412 W. Lincoln Ave., Morton Grove, Ill.  
Multi Element Grid Parabolas, Antennas for Two-Way Communications, R & D

**MARYLAND ELECTRONIC MANUFACTURING CORPORATION**, College Park, Md.  
Antenna and System Development and Production for Civil and Military Requirements.

**THE RAMO-WOOLDRIDGE CORPORATION**, Los Angeles 45, Calif.

**TRANSCO PRODUCTS, INC.**, 12210 Nebraska Ave., Los Angeles 25, Calif.  
Res., Design, Dev., & Mfr. of Antenna Systems & Components for Missile, Aircraft & Ground Installations.

**WHEELER LABORATORIES, INC.**, 122 Cutter Mill Road, Great Neck, N. Y.  
Consulting Services, Research and Development, Microwave Antennas and Waveguide Components.

The charge for an Institutional Listing is \$25.00 per issue or \$75.00 for four consecutive issues. Application may be made to the Technical Secretary, The Institute of Radio Engineers, 1 East 79th Street, New York 21, N.Y.